

R
E
S
M

**Research on
Engineering
Structures
Materials**

P-ISSN: 2148-9807 E-ISSN: 2149-4088

www.jresm.org

**Volume
9**

**Issue
4**

**December
2023**

The International Journal of **Research on Engineering Structures and Materials (RESM)** is a peer-reviewed open access journal (p-ISSN: 2148-9807; o-ISSN: 2149-4088) published by MIM Research Group. It is published in February, June, September, and December.

The main objective of RESM is to provide an International academic platform for researchers to share scientific results related to all aspects of mechanical, civil, and material engineering areas.

RESM aims the publication of original research articles, reviews, short communications technical reports, and letters to the editor on the latest developments in the related fields.

All expenditures for the publication of the manuscripts are most kindly reimbursed by *MIM Research Group*. Thus, authors do not need to pay for publishing their studies in the journal.

The scope of the journal covers (but not limited to) behavior of structures, machines and mechanical systems, vibration, impact loadings and structural dynamics, mechanics of materials (elasticity, plasticity, fracture mechanics), material science (structure and properties of concrete, metals, ceramics, composites, plastics, wood, etc.), nano-materials performances of new and existing buildings and other structural systems, design of buildings and other structural systems, seismic behavior of buildings and other structural systems, repair and strengthening of structural systems, case studies and failure of structural systems, safety and reliability in structural and material engineering, use of new and innovative materials and techniques in energy systems and mechanical aspects of biological systems (biomechanics and biomimetics).

The topics covered in JRESM include:

- Structural Engineering
- Mechanical Engineering
- Material Engineering
- Earthquake Engineering
- Nano-technology
- Energy Systems (Focus on Renewable)
- Biomechanics and Biomimetics
- Environment (Material and Engineering System Related Issues)
- Computer Engineering and Data Science (Material and Engineering System-Related Issues)

Abstracting and Indexing

Please visit <http://www.jresm.org> for more information.

Graphics and Design

Yunus Demirtaş

ydemirtas@jresm.net



**RESEARCH on
ENGINEERING STRUCTURES &
MATERIALS**



RESEARCH on ENGINEERING STRUCTURES & MATERIALS

Editorial Board

Editor in Chief

Hayri Baytan Özmen

Usak University

Türkiye

Editors

Canan Kandilli

Usak University

Türkiye

Antonio F. Miguel

University of Evora

Portugal

Michele Barbato

University of California Davis

USA

Alp Karakoç

Aalto University

Finland

Faris Tarlochan

Qatar University

Qatar

Mehmet Palancı

Arel University

Türkiye

Francesco D'Annibale

University of L'Aquila

Italy

Samson Olalekan
Odeyemi

Kwara State University Malete

Nigeria

Saifulnizan Jamian

Universiti Tun Hussein Onn
Malaysia

Malaysia

Chitaranjan Pany

Vikram Sarabhai Space Centre

India

Daniel Cruze

Hindustan Institute of Technology
and Science

India

Badrinarayan Rath

Wollega University

Ethiopia

Taymaz Tabari

Jagiellonian University

Poland

Tamer
Saracyakupoglu

İstanbul Gelisim University

Türkiye

Editorial Office

Publishing Assistant

Yunus Demirtaş

Eskişehir Technical University

Türkiye

Yusuf Öztürk

MIM Resarch Group

Türkiye

Language Editors

Gaye Kuru

Usak University

Türkiye

Mete Çal

Niğde Ömer Halisdemir University

Türkiye

Editorial Board Members

Farid Abed-Meraim	Arts et Metiers ParisTech	France
P. Anbazhagan	Indian Institute of Science	India
Raffaele Barretta	University of Naples Federico II	Italy
R.S. Beniwal	Council of Scientific and Industrial Research	India
Antonio Caggiano	University of Buenos Aires	Argentina
Noel Challamel	University of South Brittany	France
Abdulkadir Çevik	Gaziantep University	Türkiye
J. Paulo Davim	University of Aveiro	Portugal
Hom Nath Dhakal	University of Portsmouth	UK
Ali Faghidian	Islamic Azad University	Iran
S. Amir M. Ghannadpour	Shahid Beheshti University	Iran
Ali Goodarzi	Harvard University	USA
Jian Jiang	National Institute of Standards and Technology	USA
Ramazan Karakuzu	Dokuz Eylül University	Türkiye
Arkadiusz Kwiecien	Cracow University of Technology	Poland
Stefano Lenci	Universita Politecnica delle Marche	Italy
Silva Lozančić	University of Osijek	Croatia
Fabio Mazza	University of Calabria	Italia
Yuan Meini	North University of China	China
Stergios A. Mitoulis	University of Surrey	UK
Vinayagam Mohanavel	Anna University	India
Ehsan Noroozinejad Farsangi	Kerman Graduate University of Technology	Iran
Alaa M. Rashad	Shaqra University	Saudi Arabia
Mohammad Mehdi Rashidi	University of Tongji	China
Pier Paolo Rossi	University of Catania	Italy
Neritan Shkodrani	Polythecnic University of Tirana	Albania
Y.B. Yang	National Taiwan University	Taiwan

Advisory Board

Name and Surname	Affiliation	Country
Waleed A Abbas	University of Technology	Iraq
Muna Khethier Abbass	University of Technology-Iraq	Iraq
Abdul Razak Abdul Karim	University Malaysia Sarawak	Malaysia
Yunika Kirana Abdul Khalik	UNIMAS	India
Mohammad Abdul Mannan	University Malaysia Sarawa	Malaysia
Ahmed Abdullahi	Higher Colleges of Technology	Dubai
Mehmet Ada	Usak University	Türkiye
Mohammad Afrazi	Tarbiat Modares University	Iran
B. Akbari	University of Tehran	Iran
Mustafa Akpolat	Munzur University	Türkiye
Ali Özhan Akyüz	Burdur Mehmet Akif Ersoy University	Türkiye
Waleed Khalid Al- azzawi	Al-Farahidi University	Iraq
Tawalo Ali	Università degli di Napoli Federico II	Italy
Thaer Alrudaini	University of Basrah	Iraq
Raheem Al-Sabur	University of Basrah	Iraq
Denis Anders	Cologne University of Applied Sciences	Germany
Gabriel Arce	Louisiana State University	USA
Nur Farhayu Ariffin	University Malaysia Pahang	Malaysia
E. Arunraj	Karunya Institute of Technology and Sciences	India
Hidayati Asrah	University Malaysia Sabah	Malaysia
Siva Avudaiappan	University of Santiago	Chile
Samuel Awe	Automotive Components Floby AB	Sweden
Chioma Awodiji	University Of Port-Harcourt	Nigeria
Kemal Aydın	Gümüşhane University	Türkiye
Ameer Baiee	University of Babylon	Iraq
Carlos Eduardo Tino Balestra	Western Paraná State University	Brazil

Mohammad Saleh Baradaran	Islamic Azad University of Mashhad	Iran
Peyman Beiranvand	Razi University	Iran
Hadj Bekki	University Ibn Khaldoun of Tiaret	Algeria
Abdelhalim Bensaada	University of Yahia Fares of Medea	Algeria
Mohammed Bentahar	Tahar Moulay University of Saida	Algeria
H. Alperen Bulut	Erzincan University	Türkiye
Esitake Cebolina		Iraq
Halit Cetiner	Isparta University	Türkiye
Kamel Chaoui	Badji Mokhtar University	Algeria
Venkatesh Chava	CVR College of Engineering	India
Maheswaran Chellapandian	Mepco Schlenk Engineering College	India
Xinrong Chengil	Tongji University	China
Sonali Sri Durga Chereddy	CVR College of Engineering	India
Anna Chiaradonna	DICEAA, University of L'Aquila	Italy
Ajay Chourasia	Central Building Research Institute	India
Daniel Cruze	Mohamed Sathak A J College of Engineering	India
Zhaoyan Cui	Nanjing Forestry University	China
Ashish Kumar Dash	Indian Institute of Technology	Indian
Cengiz Görkem Dengiz	Ondokuz Mayıs University	Türkiye
Arindam Dey	Indian Institute of Technology Guwahati	India
Marwan Effendy	Universitas Muhammadiyah Surakarta	Indonesia
Ashraf El-Shamy	National Research Centre	Egypt
Ali Ercetin	Bandırma Onyedi Eylül University	Türkiye
Kemal Ermis	Sakarya University of Applied Science	Türkiye
Uchechi Eziefula	University of Agriculture and Environmental Sciences, Umuagwo	Nigeria
Mingjing Fang	Wuhan University of Technology	China
Christopher Fapohunda	Federal University Oye-Ekiti	Nigeria
Abdelkader Fidjah	University of Djelfa	Algeria
Saeid Foughi	Konya Technical University	Türkiye

Sharanabasava V. Ganachari	KLE Technological University	India
Zhong Ge	Yunnan University	China
Gökhan Gece	Bursa Teknik University	Türkiye
Mahesh Gopal	College of Engineering and Technology	Ethiopia
Chandrasekhar G L Gotur	Atria Institute of Technology	India
Mert Göksüzoğlu	SAMPA	Türkiye
Layachi Guelmine	B.B.A University	Algeria
Kadir Günaydın	GE Aviation, Marmara Technology Center	Türkiye
Endalkachew Mosisa Gutema	College of Engg and Tech	Ethiopia
Ahmet Güral	Gazi University	Türkiye
Hussein Hamada	University Malaysia Pahang	Malaysia
Taihao Han	Missouri University of Science and Technology	USA
Md. Zia Ul Haq	Panjab University	India
Md. Naimul Haque	East West University	India
Noor Sheena Herayani Harith	University Malaysia Sabah	Malaysia
Shrikant Harle	Ram Meghe College of Engineering and Management	India
Catur Harsito	Universitas Sebelas Maret	Indonesia
Muttaqin Hasan	Syiah Kuala University	Indonesia
Maboud Hekmatifar	Islamic Azad University	Iran
Mohammad Heydari Vini	Islamic Azad University	Iran
Qing Hong	Midwestern University	USA
Oleksii Hrechanyi	Zaporizhzhia National University	Ukraine
Md. Saiful Islam	University Putra Malaysia	Malaysia
Mehmet Zerrakki Işık	Batman University	Türkiye
Ghassan Subhi Jameel	University of Anbar	Iraq
Saifulnizan Jamian	University Tun Hussein Onn Malaysia	Malaysia
Girish M. Joshi	VIT University	India
Bhuria Jyothi		Nepal

Arunkumar K		India
Hossein Kabir	University of Illinois	USA
Pulitha Kavetri		Sri Lanka
Mehmet Kaya	Bozok University	Türkiye
Emre Kemer	Usak University	Türkiye
Pallavi Pradeep	Rungta College of Engineering and	
Khobragade	Technology	India
Cemal Kochan	Dokuz Eylul University	Türkiye
Ali Koçak	Yıldız Technical University	Türkiye
Nitin Kumar	University of California Davis	USA
A. Suresh Kumar	Kalasalngam Academy of Research and	
	Education	India
Sanjeev Kumar	Sanjeev Agrawal Global Educational	
	University	India
Josephine Chang Hui		
Lai	University Malaysia Sarawak	Malaysia
Ravichandran M	K. Ramakrishnan College of Engineering	India
Uma Mageshwari		India
Lomesh Mahajan	Dr. Babasaheb Ambedkar Technological	
	University	India
Natt Makul	Phranakhon Rajabhat University	Thailand
Anirban Mandal	National Institute of Technology	India
Tahara Ramadan Md		
Kassim	International Islamic University Malaysia	Malaysia
Priyansha Mehra	Manipal University	India
Adamah Messan	Laboratoire Eco Matériaux de Construction	
	(LEMC)	France
Suruchi Mishra		Malaysia
Khairul Anwar		
Mohamad Said	UNIMAS	Malaysia
Fadzli Mohamed Nazri	University Sains Malaysia	Malaysia
Mohsin Talib		
Mohammed	Kufa University	Iran
Noor Azline Mohd		
Nasir	University Putra Malaysia	Malaysia

Mohd Syahrul Hisyam	University Teknologi MARA (UiTM)	Malaysia
Mohd Sani	Cawangan Pahang	
Mahmoud Mokhtar	Housing & Building National Research Center	Egypt
Alaa M. Morsy	Arab Academy for Science	Egypt
Rini Mulyani	Senior Lecturer at University Bung Hatta, Padang, Indonesia	Indonesia
Yasmin Murad	University of Jordan Amman	Jordan
Nahida Nazim Musayeva	Azerbaijan National Academy of Sciences	Azerbaijan
Arslan Mushtaq	NUST Institute of Civil Engineering	Pakistan
Maheswaran Muthiah	Kalasalangam Academy of Research and Education	India
Madeva Nagaral	Aircraft Research and Design Centre, Hindustan Aeronautics Limited	India
Salem Nawel	University of Gabes	Tunisia
Amarachi Nkwoada	Federal University of Technology Owerri	Nigeria
Mehrab Nodehi	University of California	USA
Samson Olalekan Odeyemi	Kwara State University	Nigeria
Hayri B. Ozmen	Usak University	Türkiye
İbrahim Öz	Ahi Evran University	Türkiye
Gurusamy P Partheeban	Chennai Institute of Technology	India
Pachaivannan	Chennai Institute of Technology	India
Chitaranjan Pany	Vikram Sarabhi Space Center	India
Rajesh Kumar Paswan	National Institute of Technology Jamshedpur	India
Vikas Patel	National Council for Cement and Building Materials	India
Hiteshkumar Patil	Dr. Babasaheb Ambedkar Technological University	India
Zühtü Onur Pehlivanlı	Kırıkkale University	Türkiye
Amin Moslemi Petrudi	Tehran University	Iran
Hemadri Prasad Raju	Sree Vidyanikethan Engineering College	India

Kalappa Prashantha	Adichunchanagiri University	India
Harris Priya	Kurukshetra University	India
Kavendra Pulkit		India
Helogi Putin		India
Ajibola Ibrahim Quadri	Federal University of Technology	Nigeria
Md. Mijanur Rahman	Military Institute of Science and Technology	Bangladesh
Azida Rashidi	UNIMAS	Malaysia
Badrinarayan Rath	Wollega University	Ethiopia
T.V. Reshma		India
Pier Paolo Rossi	University of Catania	Italy
Md Jalal Uddin Rumi	Military Institute of Science and Technology	Bangladesh
Abbasali Sadeghi	Islamic Azad University	Iran
Mohammed A. Sakr	Tanta University	Egypt
M.Helen Santhi	Vellore Institute of Technology	India
Tamer Saraçyakupoğlu	Istanbul Gelişim University	Türkiye
Divya Sharma	NITTTR Chandigarh	India
Fatheali Shilar	Jain College of Engineering Belgaum	India
Lenganji Simwanda	Stellenbosch University	South Africa
Brijesh Singh	National Council for Cement and Building Materials	India
Navdeep Singh	Dr B R Ambedkar National Inst. of Tech.	India
Rami Sldozian	University of Technology	Iraq
M. Somasundaram	PSG College of Technology	India
Rajkumar Srinivasan	SRM TRP Engineering College Irungalur	India
Rianti Dewi Sulamet- Ariobimo	Universitas Trisakti	Indonesia
Marthin Dody Josias Sumajouw	Sam Ratulangi University	Indonesia
Gülsah Susurluk	Beykent University	Türkiye
Jumrik Taipodia	NIT Arunachal Pradesh	India
Aykut Tamer	Imperial College London	England
Chan Sin Tan	University Malaysia Perlis	Malaysia
Hamide Tekeli	Süleyman Demirel University	Türkiye

Delsye Ching Lee Teo	Melbourne Polytechnic	Australia
Mehmet Topuz	Van Yüzüncü Yıl University	Türkiye
Tuan Norhayati Tuan Chik	University Tun Hussein Onn	Malaysia
Hasan Ulus	Selcuk University	Türkiye
Dilay Uncu	Celal Bayar University	Türkiye
Prem Kumar V	VIT Chennai	India
Harinadh	Sri Venkateswara College of Engineering and Technology	India
Vemanaboina		
Tadesse Gameda Wakjira	University of British Columbia	Canada
Gustavo Bosel Wally	Federal University of Rio Grande do Sul	Brazil
Narong Wichapa	Kalasin University	Thailand
I Wiryadi	Mahasaraswati Denpasar University	Indonesia
Omid Aminoroayai Yamani	K. N. Toosi University of Technology	Iran
Guney Guven Yapici	Ozyegin University	Türkiye
Salih Hakan Yetgin	Kütahya Dumlupınar University	Türkiye
Sevim Yolcular Karaoğlu	Ege University	Türkiye
Ana Sakura Zainal Abidin	UNIMAS	Malaysia

In This Issue

Research Article

1101 **Fadhluhartini Muftah, Norizah Omar, Ahmad Rasidi Osman, Mohd Syahrul Hisyam Mohd Sani**

Compression strength behaviour of fibre-reinforced concrete made with hoop-shaped waste polyethylene terephthalate fibre

Research Article

1117 **Darshini Shekhar, Jagdish Godihal**

Sustainable approaches in the built environment with industrial waste and recycled products derived from construction and demolition waste

Research Article

1135 **P.N. Ojha, Abhishek Singh, Amit Trivedi, Brijesh Singh, Nitin Chowdhury**

Evaluation of coal based bottom ash as an alternative to fine aggregate in concrete: recommendations for specifications of bottom ash and its concrete mix design

Research Article

1153 **Anugrah Budi Wicaksono, Hadi Sutantob, Wegie Ruslan**

Effects of immersion in the NaCl and H₂SO₄ solutions on the corrosion rate, microstructure, and hardness of stainless steel 316L

Technical Note

1169 **Chioma Awodiji, Samuel Sule**

Flexural strength and cost performance of tuffcrete concrete

Research Article

1181 **Khaoula Berkas, Kamel Chaoui, Wafia Ghabeche, Latifa Alimi, Abir Guenouche, Fatima Zohra Melais**

Environmental stress cracking of chemically aged HDPE-100 gas pipe under impact fracture mode

Research Article

1201 **Nawel Salem**

Effect of calcined clay on the properties of cementitious mortar reinforced by Posidonia Fiber

Technical Note

1227 **Oguntayo Daniel, Ogundipe Olumide, Daikwo Jemimah, Adeyemi Festus, Aladegboye Oluwasegun**

Moisture susceptibility of waste ceramic tiles modified asphalt mixtures

Research Article

1239 **Jagan Sivamani**

Performance studies on energy efficient paver block with treated recycled aggregate

Research Article

1255 **Jeyashree T M, M S Somesh**

Characteristic study on concrete elements using agrowaste as a replacement of fine aggregate

Research Article

1267 **M. Maheswaran, C. Freeda Christy, M. Muthukannan, K. Arunkumar, A. Vigneshkumar**

Parametric study on the performance of industrial byproducts based geopolymer concrete blended with rice husk ash & nano silica

Research Article

1287 **Yogitha Bayapureddy, Karthikeyan Muniraj, Munireddy Mutukuru Gangireddy**

Characteristic evaluation of concrete containing sugarcane bagasse ash as pozzolanic admixture

Research Article

1309 **Samir Kennouch, Allaoua Belferrag, Djamel Boutoutaou, Samia Bouzouaid, Hachem Chaib**

The effect of using recycled materials (sand and fine powder) from demolished concrete waste in alluvial sand mortar

Research Article

1325 **Pankaj Dhongade, Vikas Sargade**

Study of morphology and effect of compression moulding parameters on mechanical properties of nanoclay/polymer nanocomposites sheet moulding compound

Research Article

1347 **Rashmi Arya, Hari Singh**

Parametric optimization of ball milling process parameters for uniform distribution of particles

Research Article

1361 **Md Ashrafal Alam, Mohammad Al-Amin**

Anchors for shear strengthening of damaged RC beam using bonded steel plate

Research Article

1379 **Abhay Gujar, Sachin Pore**

Bi-diaphragm elastoplastic haunch retrofit solution for ill-detailed RC beam-column joints

Research Article

1403 **Arda Uzunömeroğlu**

Investigation of the effect of boron inhibitor on reinforced concrete by using the accelerated corrosion technique

Research Article

1417 **Thaer Alrudaini**

Estimating vibration period of reinforced concrete moment resisting frame buildings

Review Article

1433 **Banu D. Handono, Ronny E. Pandaleke, Reynaldo J. Sela, Dody M.J. Sumajouw, Steenie E. Wallah, Servie O. Dapas, Reky S. Windah**

The evaluation of behavior of geopolymer reinforced concrete and conventional reinforced concrete beams: A critical review

Research Article

1459 **Ashish Singh, Sasankasekhar Mandal**

Effect of wind and structural parameters on across wind load of super high-rise buildings

Research Article

1477 **Chereddy Sonali Sri Durga, Chava Venkatesh, T. Muralidhararao, Ramamohana Reddy Bellum**

Crack healing and flexural behaviour of self-healing concrete influenced by different bacillus species

Research Article

1489 **Chereddy Sonali Sri Durga, Chava Venkatesh, T. Muralidhararao, Ramamohana Reddy Bellum, B. Naga Malleswara Rao**

Estimation of durability properties of self-healing concrete influenced by different bacillus species

Research Article

1507 **Ajibola Ibrahim Quadri, Lekan Makanju Olanitori, Abdulhakeem Sadiq**

Effect of non-biodegradable waste materials on the strength performance of concrete

Research Article

1521 **Poonam, VP Singh**

Optimizing cost and strength by utilization of blast furnace slag aggregate and recycled concrete sand in concrete using response surface models

Research Article

1543 **Mehmet Cemal Geneş, Pari Yaseen**

Analytical study on seismic strengthening of existing reinforced concrete buildings by implementation of energy absorbers

Review Article

1573 **Aashima Sharma, Heaven Singh**

Evaluation of physical testing for seismic behaviour of tunnels: A comprehensive review

Free access to tables of content, abstracts and full text of papers for web visitors.

Copyright © 2023

Research on Engineering Structures & Materials

MIM Research Group Publications

P-ISSN: 2148-9807

E-ISSN: 2149-4088

<http://www.jresm.org>



ABSTRACTING / INDEXING

The international journal of Research on Engineering Structures and Materials (RESM) is currently Abstracted/Indexed by Asos Indeks, CiteFactor, Cosmos, CrossRef, Directory of Research Journal Indexing, Engineering Journals (ProQuest), EZB Electronic Journal Library, Global Impact Factor, Google Scholar, International Institute of Organized Research (I2OR), International Scientific Indexing (ISI), Materials Science & Engineering Database (ProQuest), Open Academic Journals Index, Publication Forum, Research BibleScientific Indexing Service, Root Indexing, Scopus, Ulakbim TR Index (Tubitak), Universal Impact Factor and under evaluation by many other respected indexes.

Check web site for current indexing info, www.jresm.org

Scopus®





Research Article

Compression strength behaviour of fibre-reinforced concrete made with hoop-shaped waste polyethylene terephthalate fibre

Fadhluhartini Muftah^a, Norizah Omar^b, Ahmad Rasidi Osman^c, Mohd Syahrul Hisyam Mohd Sani^{*d}

Civil Engineering Studies, College of Engineering, Universiti Teknologi MARA (UiTM) Cawangan Pahang, Bandar Jengka, Pahang, Malaysia

Article Info

Abstract

Article history:

Received 28 Jan 2023

Accepted 29 Jul 2023

Keywords:

*Compression strength behaviour;
Fibre-reinforced concrete;
Waste polyethylene terephthalate;
Hoop-shaped fibre;
Environmental problem*

Fibre-reinforced concrete (FRC) is a special concrete incorporated with fibre that can replace reinforced concrete for utilising in structural applications. FRC with plastic waste fibre is introduced in construction to resolve the corrosion problem of the reinforced steel bar in the concrete, resolve the cracking on the concrete and minimise the environmental problem which occurred due to plastic bottle waste disposal and non-biodegradable material. The main objective of this study is to determine the compression strength behaviour of waste Polyethylene Terephthalate (PET) fibre with hoop-shaped in FRC in percentages of 0.1%, 0.2%, 0.3%, 0.4%, 0.5%, 0.6%, 0.7% and 0.8% weight to weight of cement. For that reason, the waste mineral bottle water is collected, cleaned and cut into 100 mm of length and 5 mm of width to propose hoop-shaped waste PET fibre. FRC with waste PET fibre is tested for its workability in fresh conditions and its water absorption and compression strength in hardened conditions. Furthermore, the tensile test is conducted for determining the stress and strain behaviour of waste PET fibre in two conditions; in single and hoop-shaped. From the experimental activity, the waste PET fibre of 0.5% produced the appropriate compression strength value and recorded a percentage difference approximately of 6.33% for 28 days duration as compared with a control mix. In addition, the percentage difference of the water absorption of all mixes is reported to have in the range of 0.25% to 25.96% when compared with the control mix which is tremendously affected the compressive strength.

© 2023 MIM Research Group. All rights reserved.

1. Introduction

For the waste bottle which collected from the mineral water bottle is made of polyethylene terephthalate material. Waste bottle disposal is a known environmental problem faced by all countries in the world now and in the future. This is because the waste bottle is difficult to decompose and not easy to find a landfill site to dump all waste. The waste bottle in the area of dumpsite produced soil pollution, air pollution, water and groundwater pollution and harmful chemical components. Yong et al. [1] reported that the waste product in Malaysia must be managed and organised to ensure the environmental and economic issues can be resolved properly and noted that the waste product with more than 80% was disposed of at dumpsites. Awoyera et al. [2] discussed the effect that occurred due to a high percentage of plastic waste disposal such as drainage blockage which causes the breeding of mosquitoes that are aware of carrying a variety of dangerous diseases and also causes property damage as a result of the massive floods. Yong et al. [1] mentioned about the percentage of solid waste disposal by separating them into 45% of food and organic waste, 13% of plastics, 12% of diapers, 9% of paper and 6% of garden waste. Liang et al. [3] stated that the quantities of plastic waste in industrial solid waste were determined of 42 million

*Corresponding author: msyahrul210@uitm.edu.my

^a orcid.org/0000-0002-3237-132X; ^b orcid.org/0000-0001-9255-3208; ^c orcid.org/0009-0003-9691-544X;

^d orcid.org/0000-0002-7389-483X

DOI: <http://dx.doi.org/10.17515/resm2023.674ma0128>

Res. Eng. Struct. Mat. Vol. 9 Iss. 4 (2023) 1101-1116

tonnes (Mt) and municipal solid waste of 79 Mt in the Asia region and reported total waste plastic in Malaysia for the years 2016, 2017 and 2018 were 2.45 Mt, 2.60 Mt and 2.65 Mt, respectively. Besides, Khoo et al. [4] recorded that the improper waste management of plastic waste, especially during the coronavirus disease (COVID-19) pandemic resulted in an unexpected surge of plastic waste which influenced human health and environmental impact. Plastic waste is disposed of in landfills (40%), disposed of in incinerators approximately (25%), recycled (16%) and left into the environment without any process (19%) [4].

Therefore, the waste bottle can be resolved technically similar to other waste products by going through the 3R process (Reduce, Reuse and Recycle) but reduce and reuse activity are classified as an impossible way for solving the limited dumping area availability. Undoubtedly, the recycling process is a determinant of a better future to reduce pollution and environmental impact that generally could change the world landscape and affect the lives of future generations. The recycling activity is necessary to reduce air pollution due to open burning, waste dumped into landfills, river and sea pollution due to widespread waste disposal and odour pollution due to unsystematic waste management. Recycling activity also is simple, time and energy-consuming practice that can reduce the utilisation of new resources to make new materials for producing consumer products which are harmless to human health. Khatab et al. [5] stated that plastic waste is split into two categories which are recognised as thermoplastic and thermosetting plastic. Thermoplastic is formed by melting with the heat process and hardening with the cooling process; however, thermosetting plastic cannot melt through the heating process [5]. Examples of thermoplastics include polyethylene terephthalate (PET), polypropylene, high-density polyethylene and polystyrene. Examples of thermosetting plastic are melamine, epoxy resin, polyurethane, silicone, phenolic and unsaturated polyester [5]. Ullah Khan and Ayub [6] stated that PET is used broadly in the world because of its properties such as high strength, thermal endurance, chemical endurance, high strength and damage resistance.

Fibre-reinforced concrete (FRC) is categorised as a special concrete added with fibre and the amount of fibre is referred to as the percentage of overall volume or weight of the concrete. Special concrete with outstanding availability and versatility could reduce the cost, especially in production, material and maintenance and also energy consumption. Additionally, reinforced steel bar in concrete is known in construction activity as having high costs in material production and maintenance. Sometimes, the FRC is also recognised as a composite material with the presence of fibre to increase the structural integrity such as durability, fatigue and deformation aspect. There are a lot of advantages of fibre in concrete such as cracking control, shrinkage control, water permeability reduction, strength improvement, segregation and bleeding reduction and shear capacity increment. Borg et al. [7] mentioned about fibre is not only able to reduce cracking due to shrinkage but affected the service period and also the aesthetics of the structure. The addition of fibre especially polymer or plastic to concrete has been investigated to alleviate structural failure or difficulties such as fractures produced by drying and hydraulic retraction (plastic) [8]. The fibre in concrete has existed in different shapes, sizes, lengths and origin materials for instance steel, carbon, glass, natural and synthetic fibre. Nowadays, FRC is becoming popular for adding in concrete in order to reduce the time of construction and cost of production, maintenance and labour and in applications such as pavement, tunnel lining, slope stabilisation, wall and heavy structure. FRC is suitable to classify into three large groups namely; natural fibre, industrial fibre and synthetic fibre. The selection of the fibre in concrete is depended on the application, design and suitability, for example, steel fibre is not appropriately used at offshore or adjacent to extreme chemical activity.

Fibres are observed in flat and circular conditions and verified their capability by using the aspect ratio (length to diameter ratio) of fibre. FRC can replace the traditional method for concreting the structural element which is known as reinforced concrete by using a steel bar in the concrete. In general, the concrete without reinforced is exposed to large cracks or fractures so the fibre in concrete is proposed as a role to form together to reduce cracks and increased the toughness. Furthermore, the utilisation of fibre in concrete which reacts as reinforcement is a technique to recycle and reuse the waste product for producing better strength. Fibre chosen from the waste product is more practical either from the construction site, residential, agricultural or industrial which produced a lot of environmental problems and incurred high costs to disposal or dumping. Industrial waste which is normally obtained from processing, manufacturing, packaging and engineering activity. The proper approach of handling all wastes is required to minimise the negative impacts on society, the economy and the environment. From the observation, the residential and construction activity which in parallel with the increasing of human population, urbanisation and economic development had generated major waste products in Malaysia. The waste bottle is one of the waste products from the residential. Plastic is the world's third largest waste product source and is collected from plastic bags, bottles, and plastic straws [9]. Chen et al. [9] reported that plastic waste contains bisphenols A (BPA), heavy metals, phthalates and flame retardants which caused the environmental problem and human health abnormalities issue. Ncube et al. [10] reported that plastic is a polymer group material with versatile, low cost and unique properties and is used in food packaging which protected the food from the physical, chemical and biological factors. The fibre in concrete is one of the most significant ways for modifying the brittleness of normal concrete and strengthening the concrete [11].

2. Waste PET Fibre in Concrete

The waste bottle is used in concrete either by replacement or added in such as fibre and fine aggregate. The waste bottle is utilised in normal concrete or special concrete. There are many studies on the waste bottle fibre in special concrete for example high strength concrete [12], self-compacting concrete [13], recycled aggregate concrete [14] and ultra-high-performance green concrete [15]. There are many studies on waste bottles as fine aggregate by Fakoor and Nematzadeh [16], Nematzadeh et al. [17], Noroozi et al. [18] and Colak et al. [19]. Besides, many researchers have discussed the combination of waste plastic fibre with other waste materials as replacing traditional material or as an additive. Bui et al. [14] combined the waste PET fibre with woven plastic sack waste and silica fume. Awoyera et al. [2] studied the waste PET fibre with recycled ceramic tile waste as the sand replacement and other combinations for instance palm oil fuel ash as cement replacement [15]. Many researchers have studied waste plastic fibre in concrete with a variety of plastic origins, dimensions, shapes and aspect ratios. Ganesh Prabhu et al. [20] reported studying the utilisation of waste PET fibre with the proportion of 0.5%, 1.0% and 1.5% of the weight of fine aggregate and with a different aspect ratio of 17, 33 and 50, respectively. Faisal et al. [21] recorded the result of the flexural toughness index of concrete with waste PET fibre in ring-shaped with a width of 5 mm is 23.1% and 10 mm is 39.9% of percentage increment. Usmani and Abdul Awal [22] mentioned about the experimental activity of concrete incorporated with waste PET fibre through a variety of fibre lengths of 10 mm, 20 mm and 30 mm and fibre volume of 0.5%, 1.0% and 1.5%, respectively, for hardened concrete testing of splitting tensile, compressive and flexural strength, and fresh concrete testing of density and workability. Aditya Krishna Reddy and Arun Kumar [23] studied the strength, stiffness, Young's modulus and deformation of the waste PET fibre in concrete with the percentage of cement weight of 0.25%, 0.5% and 0.75% and added superplasticiser in the concrete mix of 0.8% by cement weight. De Luna and Ahmed Shaikh [24] noted the experimental activity to determine the anisotropy and bond behaviour of

waste PET fibre in concrete by using pullout, uni-axial tension and three-point flexural. Thomas and Moosvi [25] reported that the result of mechanical and fracture properties of concrete incorporating waste PET fibre of 0.2%, 0.4%, 0.6% and 0.8%, respectively and blended with ordinary Portland cement and metakaolin. Khalid et al. [26] studied the result of the pullout and splitting tensile strength behaviour of FRC made with the addition of waste PET fibre in ring-shaped with widths of 5 mm and 10 mm and compared concrete with synthetic fibre and concrete with waste wires fibre. The ring-shaped or sometimes known as circular and hoop-shaped fibre. Adnan and Dawood [27] stated that concrete with waste PET fibre has shown a decrease in flexural strength but increases the compression strength with 1.5% and 3% of concrete volume. Borg et al. [7] reported that the compression strength of FRC with waste PET fibre either in the straight or deformed condition is reduced by around 0.5% to 8.5% rather than the normal mix and showed that the fibre length of 30 mm provides a better result as compared with the fibre length of 50 mm. The fibre length is not significantly affected the compression strength of the concrete [7].

From the analysis of the literature review, the study on FRC with waste PET fibre is categorised as a study that is still popular nowadays and still ongoing. The size of the waste PET fibre that is normally used is less than 50 mm of length, less than 5 mm of width and added in the FRC with below 1% with various of proportions. There is no information on the previous study which used PET fibre length of more than 50 mm or 100 mm and PET fibre width of 5 mm. The proportion of waste PET fibre in FRC with various proportions with additional of 0.2%, 0.25% and 0.5% but there is an inadequate study with an additional of 0.1%. Additionally, there is no information on added PET fibre in FRC with a complete percentage from the lowest percentage of 0.1% to the highest percentage of 1.0%. The percentage of PET fibre in FRC is calculated based on weight to the weight of cement which is classified as very limited. Additionally, the study on the material and mechanical properties of hoop-shaped PET fibre is still limited and classified as important to ensure the combination of the fibre in FRC is significant. In general, all studies are started with compressive strength before continuing with other testing and thus, the compressive strength data can be considered very important. The main objective of the paper is to determine the compression strength behaviour of FRC with hoop-shaped waste PET fibre in different fibre proportions. The second objective is to determine the surface morphology and mechanical properties of hoop-shaped waste PET fibre before being used in FRC.

3. Specimen Preparation and Experimental Setup

The waste mineral bottle is collected and cleaned from the bottle's surface by using tap water. The specimen of the waste PET fibre is cut into 2 shapes; hoop-shaped (double) and straight (single) shape for the tensile test experiment. The hoop-shaped and straight (single) with 100 mm of length and 5 mm of width is used. The aspect ratio of the waste PET fibre is 20. The fibre is collected from the waste mineral bottle with the same shape and dimension which is chosen only in clear colour and cut accordingly to specific width as shown in Figure 1. The length of the cutting section is based on the circumference of the bottle. The mass of one of the hoop-shaped is 0.5 g. Firstly, the waste PET fibre is tested for determining its surface morphology by using scanning electron microscopy (SEM) and elemental analysis by energy-dispersive x-ray spectroscopy (EDS) technique. A full metallurgical procedure is offered by combining SEM and EDS analysis to provide a thorough chemical composition and elemental investigation.

The traditional materials such as composite Portland cement, natural sand, natural gravel and water are measured accordingly to the weight after calculating based on the density. All concrete ingredients are mixed together and the fibre is added into the mixer slowly at three intervals times to avoid segregation and clotted circumstances. The admixtures

especially superplasticiser is not used in the study because to obtain only the solid result of the traditional concrete ingredient with fibres. Concrete with grade 30 and a water-cement ratio of 0.55 is designed and the waste PET fibre is mixed at 0.1%, 0.2%, 0.3%, 0.4%, 0.5%, 0.6%, 0.7% and 0.8%, respectively, weight to weight of cement. These proportions are selected based on the study by Thomas and Moosvi [25] which was used with an increment of 0.2% and the highest percentage of the fibre is 0.8%. The percentage of the fibre is referred to as the weight of the cement. The mixture with 0% of fibre is known as the control mix. Three samples are prepared for each mix to make up the total number of specimens of 27. The description of the mixes is tabulated in Table 1. The standard procedure that is used and referred to is BS1881-108:1983 for the workability and water absorption test and BS EN12390-3:2002 for the compression strength test.



Fig. 1 Waste PET fibre

Table 1. The mix of the specimen with different percentages of the fibre

No.	Specimen	Percentage of the fibres in the FRC	Weight of the fibres in the FRC
1	M0	0%	0
2	M1	0.1%	10 g
3	M2	0.2%	20 g
4	M3	0.3%	30 g
5	M4	0.4%	40 g
6	M5	0.5%	50 g
7	M6	0.6%	60 g
8	M7	0.7%	70 g
9	M8	0.8%	80 g

The tensile test of the fibre is conducted using a universal testing machine (UTM) loaded with 100 kN load capacity with 0.5 mm/min. The ultimate load and deformation at the ultimate load of the fibre are investigated. The resulting stress versus strain graph of the fibre is analysed. The testing is important for checking the strength due to the bonding criteria before mixing with other concrete ingredients. The testing of the concrete is divided into fresh concrete conditions and hardened concrete conditions. For the fresh concrete condition, the workability test by using the slump test is conducted to obtain the height of the slump. Whilst, the testing of the hardened concrete condition is separated into two categories; water absorption test and compression strength of the FRC. The size of the cube mould of 150 mm × 150 mm × 150 mm is prepared for the compression strength. The compression strength test is utilised in the compression machine with a capacity of 2000 kN for determining the ultimate load and compression strength value. The compression strength test is conducted on samples curing ageing for 7 days (early strength) and for 28 days (mature strength).

4. Result and Discussion

The result and discussion of the study are divided into four parts including surface morphology and elemental analysis of waste PET fibre, mechanical properties of hoop-shaped waste PET fibre, workability of the FRC in fresh conditions, and water absorption and compression strength of the FRC in the hardened condition.

4.1 Surface Morphology and Elemental Analysis of Waste PET Fibre

The surface morphology of the waste PET fibre is observed on the flat surface and the surface of the cut section by using the SEM micrograph. From the SEM micrograph, the analysis of the various materials for surface and surface fractures due to cut activity is completely reported by providing a high-resolution image. Whilst, EDS analysis is reported to provide additional thoughtful of the surface material through the SEM analysis process. The SEM micrograph on the flat surface of waste PET fibre is recorded to have a smooth surface, unfluctuating in terms of elevation and without any hilly conditions as shown in Figure 2(a). Furthermore, the SEM micrograph on the cut section of waste PET fibre is the smooth conditions on the nearest part of the cut section but the cut section region is stated to have an irregular condition as shown in Figure 2 (b) and Figure 2 (c). Figure 2 (c) is illustrated a grainy surface more clearly like a living fungus when compared to Figure 2 (b). This is because there are elements attached before cutting that have been damaged and caused high friction in that area. This condition is shown that it is very suitable when combined with other concrete materials and improved the bond with each other, especially sand and cement. Figure 3 (a) and Figure 3 (b) illustrate the EDS elemental analysis graph for a flat surface and cut section, respectively. The major element which detected in EDS is carbon and oxygen for a flat surface and cut section region as tabulated in Table 2. The percentage difference between the element carbon and oxygen for the flat surface is 54.61% and the cut section is 48.00%. The objective of the surface morphology and elemental analysis of the waste PET fibre is to ensure the waste PET fibre is appropriate when combined with other concrete ingredients.

4.2 Mechanical Properties of Hoop-shaped Waste Polyethylene Terephthalate (PET) Fibre

The ultimate load of the single and double (hoop-shaped) waste PET fibre is 91.773 kN and 236.195 kN, respectively. The result of the mechanical properties of the tensile test is shown in Figure 4. From the stress and strain graph, the single waste PET fibre obtained a low value of ultimate stress with 107.97 MPa when compared with double of hoop-shaped waste PET fibre of 138.94 MPa. The percentage of the difference between single and double (hoop-shaped) waste PET fibre is 22.29%. The strain of the ultimate load of a single waste PET fibre is 0.0234 mm/mm and the double of waste PET waste or hoop-shaped is 0.0397 mm/mm. The percentage difference between single and double (hoop-shaped) is e 41.06%. The elastic modulus (E) of the single and double (hoop-shaped) waste PET fibre is 6.50 GPa and 4.66 GPa, respectively. The elastic modulus of the waste PET fibre with 50 mm of length, 1 mm of diameter and an aspect ratio of 50 is 3.10 GPa (Awoyera et al., 2021). Lastly, the waste PET fibre in double (hoop-shaped) which produced good results is suitable for adding in the FRC and increasing the bond strength between the fibre and concrete material. This is because the hoop-shaped is reported to have two parts and every part has played its role and produced its own initial stress to sustain the tensile load from outside.

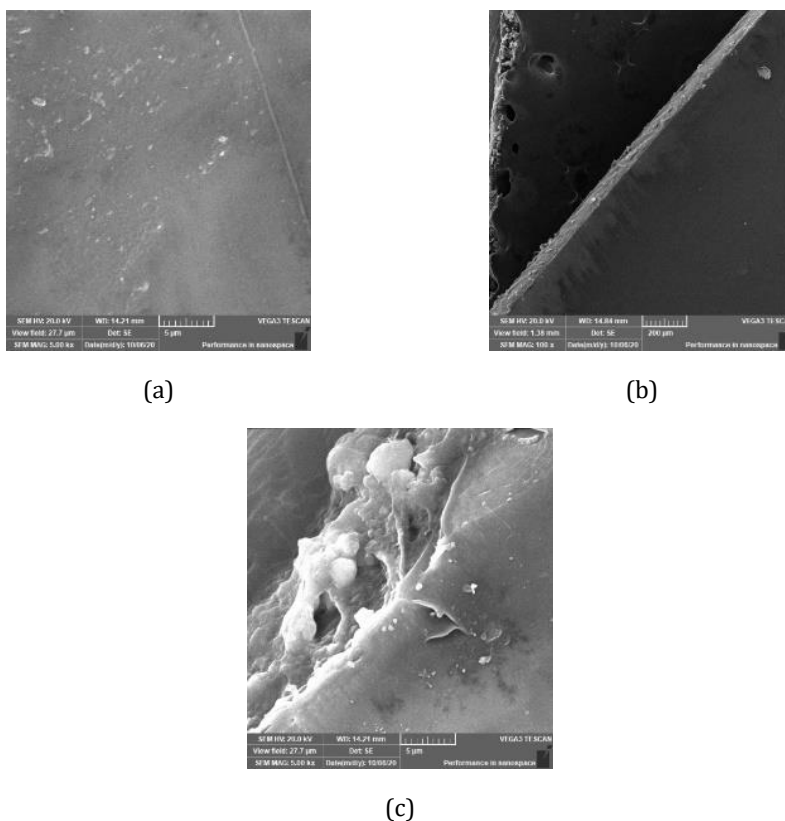


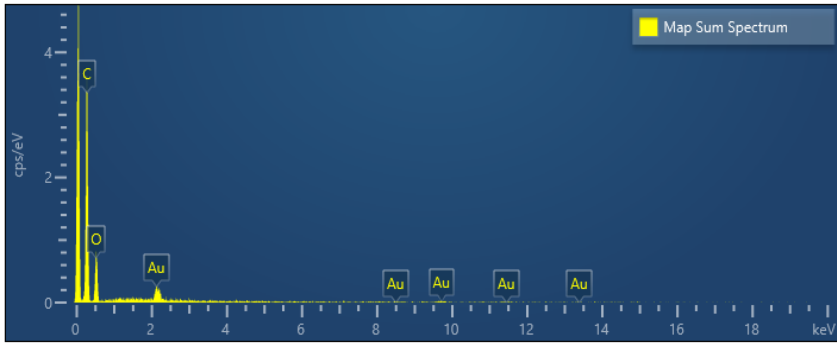
Fig. 2 Surface morphology of the waste PET fibre on (a) flat surface with 5 µm scale, (b) cut section with 200 µm scale and (c) cut section with 5 µm scale

Table 2. EDS Elemental analysis of waste PET fibre

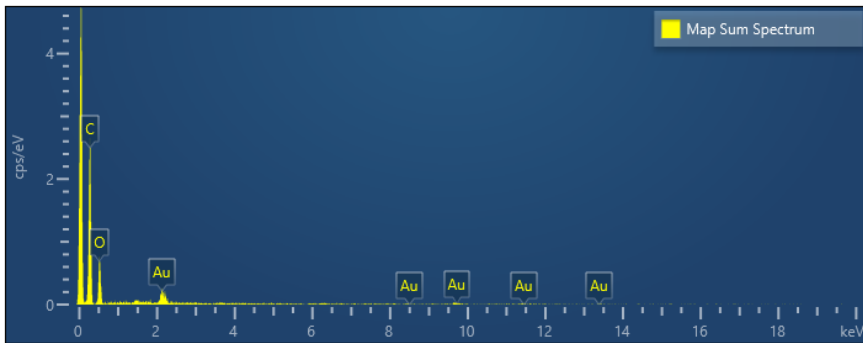
Name of element	Weight (%)	
	Flat Surface	Cut Section
Carbon (C)	68.78	65.79
Oxygen (O)	31.22	34.21

4.3 Workability Test by using Slump Test for Fresh Fibre-reinforced Concrete

The workability of the FRC is important to describe the ability of concrete for mixing, placing and finishing and influenced to strength, appearance and quality of concrete. The process to determine the workability of the FRC is by calculating the height of the slump. Figure 5 illustrates the example of the slump test for different specimens. The workability of the FRC is reduced when the amount of the waste PET fibre increased. The statement is supported by the study by Cui et al. [28] who mentioned about the slump value decreased with an increase in fibre content and length. The study by Nibudey et al. [29] stated the slump decreased with increasing of fibre content and grade of concrete. This situation is due to the waste PET fibre controlling the distribution of the water to overall mixtures. Besides, this fibre is observed to clump during the mixing process, but not too much, although the fibre is added in stages. The height of the slump of the FRC is shown in Figure 6. Smaoui et al. [30] stated that the evidence supports the hypothesis that as the percentage of plastic increases, the density of concrete decreases.



(a)



(b)

Fig. 3 EDS elemental analysis graph of (a) flat surface and (b) cut section.

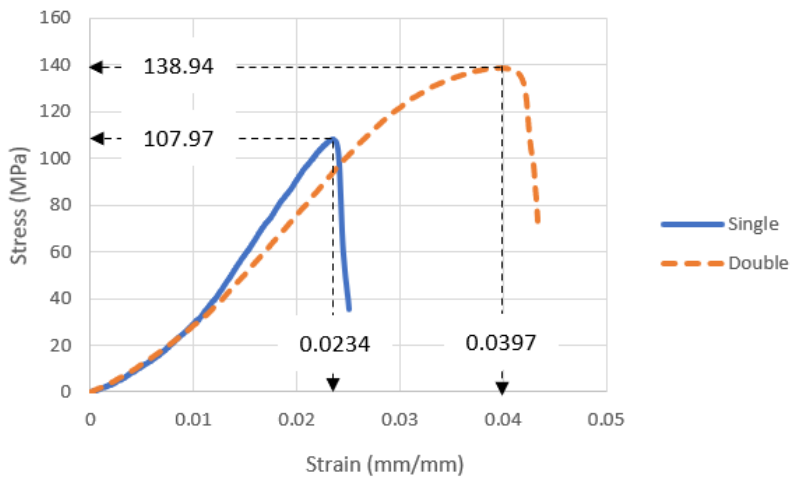


Fig. 4 The result of the stress and strain of the waste PET fibre

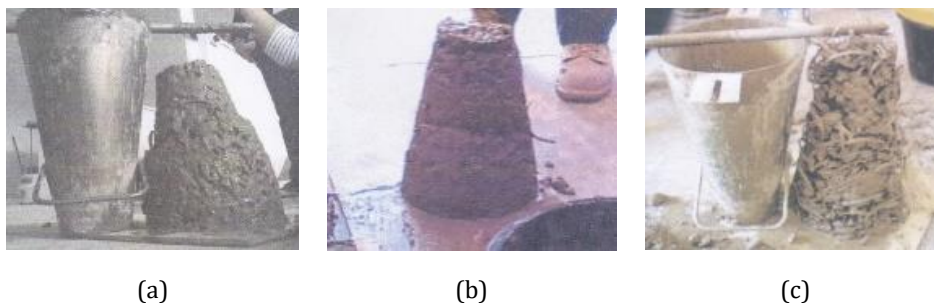


Fig. 5 The slump test of (a) M1 specimen, (b) M6 specimen and (c) M8 specimen

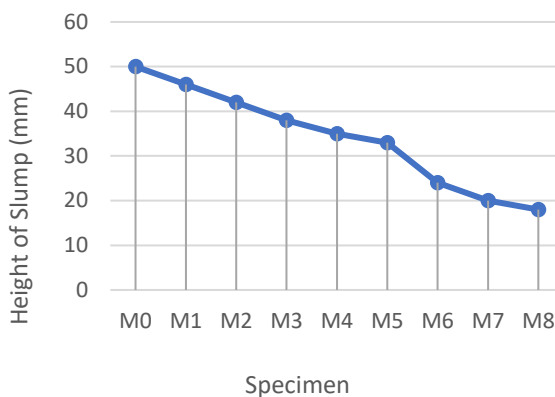


Fig. 6 The result of the slump with the proportion of fibre

The percentage difference between the control mix (M0) and other mixes is reported to have 8% for M1, 16% for M2, 24% for M3, 30% for M4, 34% for M5, 52% for M6, 60% for M7 and 64% for M8, respectively. The workability percentage difference between the highest value of the slump and the lowest value of the slump is 60.87%. The percentage difference between mix and the mix by adding 0.1% of fibre is approximately 8.00% for M0 and M1, 8.70% for M1 and M2, 9.52% for M2 and M3, 7.89% for M3 and M4, 5.71% for M4 and M5, 27.27% for M5 and M6, 16.67% for M6 and M7 and 10.00% for M7 and M8, respectively. From the calculations, the proportion between 0.1% with every mix is reported as below 10% from M1 until M5 but later, the percentage is stated as more than 10%. The degree of workability of the control mix is classified as medium workability and other mixes are categorised as low workability. The low degree of workability is appropriate for applications such as slabs, foundations and pavement.

4.4 Water Absorption Test for Hardened Fibre-reinforced Concrete

The water absorption value of the FRC is shown to increase when the proportion of waste PET fibre increased as illustrated in Figure 7 with a linear relationship. The statement of that water absorption is reduced with increasing of waste PET fibre is proven by the study of Awoyera et al. [2]. Furthermore, 25.77% is reported when comparing the highest value with the lowest value of water absorption. In general, the water absorption for hardened concrete is dependent on the workability of the fresh concrete. When the workability is low, the water absorption is classified as a high condition. Figure 8 shows the percentage difference of the water absorption between each mix with the control mix and between each mix with the mix added by 0.1% of fibre. The percentage difference of all mixes with

control mix is recorded to obtain 0.25%, 1.99%, 8.13%, 12.24%, 19.21%, 20.99%, 21.39%, 25.96% for M1, M2, M3, M4, M5, M6, M7 and M8, respectively. The line of the graph for the percentage difference between each mix with the mix added 0.1% of the fibre is shown having a fluctuation and the graph line of the percentage difference between mix with control mix is illustrated having to approach the linear relationship. Thus, the proportion with an additional of 0.1% of the fibre is shown not significant for water absorption in FRC between each mix.

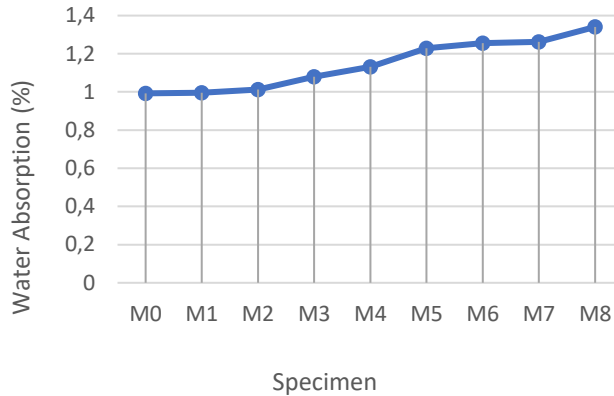


Fig. 7 The water absorption result of the control mix and other mixes

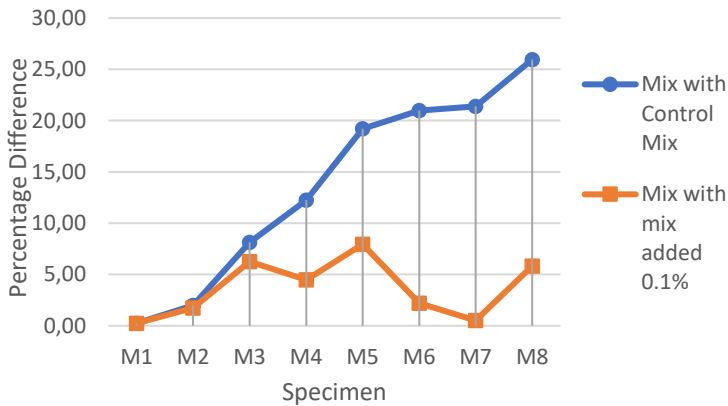


Fig. 8 The percentage difference of the water absorption between each mix with the control mix and between each mix with the mix added 0.1% of fibre

4.5 Compression Strength Test for Hardened Fibre-reinforced Concrete

The ultimate load and compression strength of the FRC at an early and mature age is decreased when the fibre content is increased. This is because the waste PET fibre with high content has affected the bonding between the fibre and other concrete ingredients. Furthermore, the high water absorption has also influenced the compression strength of the FRC. Figure 9 shows the compression strength of the control mix and others mix for 7 days and 28 days. M5 and M8 represented the highest and lowest value, respectively of the compression strength at an early age. The compression strength of the FRC for all mixes at an early stage is stated to obtain less than the control mix and a mix of 0.5% of fibre (M5) is illustrated as the highest value amongst the mix with the percentage difference of 1.86%.

Whilst, the highest value of the percentage difference between the control mix which is more than 10% is reported as 10.30% for M1, 11.66% for M6, 25.23% for M7 and lastly 26.68% for M8. All mixes had not achieved 75% of the design grade. This is because the superplasticiser is excluded in the mixing and the waste PET fibre is kept too long which influenced the problem of clotted fibres.

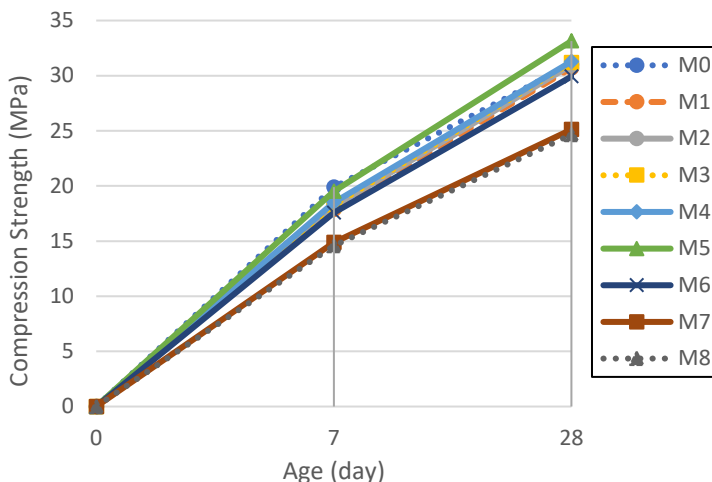


Fig. 9 The compression strength versus curing age relationship

For 28 days duration, the highest value is noted for M5 and the lowest value is reported for M8. All mixes moved slowly to achieve the compression strength at 28 days with more than the design grade except for M6, M7 and M8. Mix with the added fibre of 0.1% and 0.2% at 28 days is reported to have a reduction of compression strength but the compression strength has grown for mix M3 of 0.3% until mix M5 of 0.5%. After the fibre is added more than 0.5%, the compression strength value is decreased as shown in Figure 6. The percentage difference between control mix with M1, M2, M3, M4, M5, M6, M7 and M8 is reported to obtain 1.10%, 0.26%, 0.46%, 0.76%, 6.33%, 3.62%, 19.09% and 20.57%, respectively. Thomas and Moosvi [25] mentioned the fibre added which could improve the compression strength with the maximum fibre of 0.4%. The statement is classified as conservative because 0.5% also produced an increment of the compression strength. Figure 10 illustrates the compression strength with the proportion of waste PET fibre for 7 days and 28 days. The graph pattern of the 7 days and 28 days showed the same pattern and the result of compression strength is in good condition.

5. Comparison Study

The compression study is discussed to verify the result with other previous study results. The comparison study of the compression strength of the FRC with the previous study such as Shinde et al. [31]. The prediction of the compression strength formula by referring to Ojeda [32]. All the compression results of the previous studies are compared by using percentage differences with the result of the experimental. Bui et al. [14] mentioned about the concrete with using waste PET fibre in the proportion of 0.25%, 0.5% and 0.75% and combined with the recycled coarse aggregate and silica fume still produced a reduction in compressive strength. Table 3 tabulates the result of the previous study. The new prediction formula for compression strength at 28 days (f_c), as stated in Eq. (1) by the study of Ojeda [32], is used in the study.

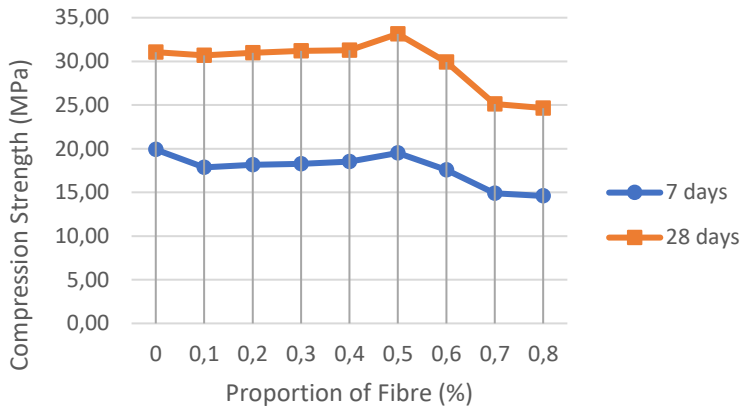


Fig. 10 The compression strength of FRC with waste PET fibre at 7 and 28 days

$$f_c = -31.433w/c - 0.645P + 0.031C + 38.140 \tag{1}$$

where, w/c = water cement ratio, P = plastic content by volume in %, C = cement content (kg/m^3).

Table 3. Description of the previous study on the result of the compression strength

Authors	Description	Proportion of fibre (%)	Compression Strength (MPa)	Percentage Difference (%)	Remarks
Shinde et al. [31]	The FRC with grade 30 and the plasticiser of 0.20% of cement weight is used. The proportion of the fibre with 0.5%, 1.0%, 1.5% and 2.0% of the cement weight is investigated. The length and breadth of the fibre are 50 mm and 2 mm, respectively.	0.5%	25.12 MPa for 7 days and 39.86 MPa for 28 days	22.25% for 7 days and 16.86% for 28 days	The study used a plasticiser in the mixing and the compression strength of the FRC is increased when the fibre is in the percentage of 0.5% and 1.0%. However, the compression strength of the FRC goes down after 1.0%. The percentage difference between 7 days and 28 days is 36.98%. The result showed that more than 0.5% or 1.0% is reported to have a better result compared with other specimens is considered conservative.
Ojeda [32]	The Eq. (1) is used.	0.1%, 0.2%, 0.3%, 0.4% and 0.5%	33.50 MPa, 33.43 MPa, 33.37 MPa, 33.30 MPa and 33.24 MPa	8.35%, 7.40%, 6.52%, 6.07% and 0.30%	The study is compared with the new prediction formula for compression strength at 28 days for 0.1% to 0.5% only. The prediction result of compression strength is calculated and determined the percentage difference. The percentage difference is around 0.3% to 8.35%.

6. Compression and Flexural Strength Relationship

The strength of compression and flexural are often linked. Depending on the particular concrete mix, flexural strength ranges from 10% to 15% of compression strength.

According to standards and previous studies which discussed on the relationship between compression and flexural strength such as the Australian Standard (AS 3600), American Concrete Institute (ACI 363-92) and Smaoui et al. [30], respectively used to determine the prediction of the flexural strength of the concrete. The prediction of the flexural strength of the concrete by referring to Eq. 2 based on AS 3600, Eq. 3 based on ACI 363-92 and Eq. 4 based on a study by Smaoui et al. [30] is used. These equations are important to predict the flexural strength of the concrete without any testing activity or usage of the experiment tool.

$$f_i = 0.6 \sqrt{f_c} \tag{2}$$

$$f_i = 0.94 \sqrt{f_c} \tag{3}$$

$$f_i = 5 \times 10^{-6} (f_c)^{4.0323} \tag{4}$$

where, f_i = flexural strength (MPa).

Figure 11 is shown the result of the prediction of flexural strength by using Eq. 2, Eq. 3 and Eq. 4 from the experimental result of the compression strength of concrete. Eq. 4 is more reliable when compared with other standards.

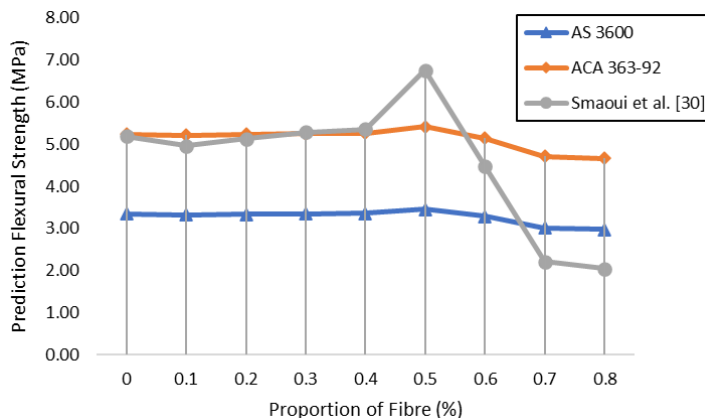


Fig. 11 The prediction flexural strength of all mixes

7. Conclusion

From the observation and analysis of the experimental activity, the following conclusions are drawn and analysed. The ultimate load of the mechanical properties of the fibre in a single shape and hoop-shaped is reported to obtain 91.773 kN and 236.195 kN, respectively. The percentage difference of the ultimate stress between the single shape and hoop-shaped is 22.29%. Furthermore, the strain of the ultimate load and elastic modulus of the hoop-shaped is 0.0397 mm/mm and 4.66 GPa, respectively. The waste PET fibre in hoop-shaped is chosen for adding in the FRC and tightening the bonding between the fibre and other concrete ingredients.

In fresh concrete conditions, the workability of the FRC is reduced when the proportion of the waste PET fibre is increased. All mixes with additional of fibre content are considered as a degree of workability in low conditions and M1 has shown the highest value of the height of slump. The percentage difference between the control mix and M1 is 8.0% and the range from 8% to 65% represents the difference in percentage between the control

mix and other mixes. The water absorption of the FRC is decreased by increasing the waste PET fibre content. M1 and M8 have shown the lowest and highest value of water absorption in FRC, respectively.

The compression strength of FRC is determined as less than 75% of the design grade for all mixes and more than 30 MPa for all mixes except for M6, M7 and M8 at 28 days. The compression strength of FRC is reduced when the amount of the waste PET fibre is more than 0.5%. The percentage difference between the control mix with the highest value of the compression strength for 7 days is 1.86% and for 28 days is 6.33%. The excessive water absorption has also had an impact on the compression strength of the FRC. The compression strength data and information are important for further study and to form the structural elements such as beams, columns or slabs.

For further study, the workability, water absorption and compression strength of the FRC will be able to be resolved if using the superplasticiser or nanomaterial as a replacement or additional material. Thus, adding PET fibre to FRC without any modification, alterations or adjustments is not acceptable. The experimental activity especially the mechanical properties could be extended for tensile and flexural strength, and could be investigated the length and width of waste PET fibre in increasing the strength of the FRC.

Acknowledgement

The authors warmly thank the Universiti Teknologi MARA (UiTM) Cawangan Pahang for the facility support. Sincerest gratitude is extended to the staff and faculty members for providing technical advice and to the College of Engineering of Universiti Teknologi MARA (UiTM) Cawangan Pahang, Kampus Jengka for allowing the use of laboratory machines and equipment.

References

- [1] Yong ZJ, Bashir MJK, Hassan MS. Biogas and Biofertilizer Production from Organic Fraction Municipal Solid Waste for Sustainable Circular Economy and Environmental Protection in Malaysia. *Science of the Total Environment*, 2021; 776: 145961. <https://doi.org/10.1016/j.scitotenv.2021.145961>
- [2] Awoyera PO, Olalusi OB, Iweriebo N. Physical, Strength and Microscale Properties of Plastic Fiber-reinforced Concrete Containing Fine Ceramics Particles. *Materialia*, 2021; 15: 100970. <https://doi.org/10.1016/j.mtla.2020.100970>
- [3] Liang Y, Tan Q, Song Q, Li J. An Analysis of the Plastic Waste Trade and Management in Asia. *Waste Management*, 2021; 119: 242-253. <https://doi.org/10.1016/j.wasman.2020.09.049>
- [4] Khoo KS, Ho LY, Lim HR, Leong HY, Chew KW. Plastic Waste Associated with the COVID-19 Pandemic: Crisis or Opportunity? *Journal of Hazardous Materials*, 2021; 417: 126108. <https://doi.org/10.1016/j.jhazmat.2021.126108>
- [5] Khatab HR, Mohammed SJ, Hameed LA. Mechanical Properties of Concrete Contain Waste Fibers of Plastic Straps. *IOP Conference Series: Materials Science and Engineering*, 2019; 557: 012059. <https://doi.org/10.1088/1757-899X/557/1/012059>
- [6] Ullah Khan S, Ayub T. Flexure and Shear Behaviour of Self-compacting Reinforced Concrete Beams with Polyethylene Terephthalate Fibres and Strips. *Structures*, 2020; 25: 200-211. <https://doi.org/10.1016/j.istruc.2020.02.023>
- [7] Borg RP, Baldacchino O, Ferrara L. Early Age Performance and Mechanical Characteristics of Recycled PET Fibre Reinforced Concrete. *Construction and Building Materials*, 2016; 108: 29-47. <https://doi.org/10.1016/j.conbuildmat.2016.01.029>

- [8] Pereira EL, de Oliveira Junior AL, Fineza AG. Optimization of Mechanical Properties in Concrete Reinforced with Fibers from Solid Urban Wastes (PET Bottles) for the Production of Ecological Concrete. *Construction and Building Materials*, 2017; 149: 837-848. <https://doi.org/10.1016/j.conbuildmat.2017.05.148>
- [9] Chen HL, Nath TK, Chong S, Foo V, Gibbins C, Lechner AM. The Plastic Waste Problem in Malaysia: Management, Recycling and Disposal of Local and Global Plastic Waste. *SN Applied Sciences*, 2021; 3(437). <https://doi.org/10.1007/s42452-021-04234-y>
- [10] Ncube LK, Ude AU, Ogunmuyiwa EN, Zulkifli R, Beas IN. An Overview of Plastic Waste Generation and Management in Food Packaging Industries. *Recycling*, 2021; 6(12): 2-25. <https://doi.org/10.3390/recycling6010012>
- [11] Alsadey S. Utilization of Plastic Bottle Waste in Concrete. *Journal of Biological and Environmental Engineering*, 2016; 1(1): 1-5.
- [12] Mohammed AA, Faqe Rahim AA. Experimental Behavior and Analysis of High Strength Concrete Beams Reinforced with PET Waste Fiber. *Construction and Building Materials*, 2020; 244: 118350. <https://doi.org/10.1016/j.conbuildmat.2020.118350>
- [13] Al-hadithi AI, Noaman AT, Mosleh WK. Mechanical Properties and Impact Behavior of PET Fiber Reinforced Self-compacting Concrete (SCC). *Composite Structures*, 2019; 224: 111021. <https://doi.org/10.1016/j.compstruct.2019.111021>
- [14] Bui NK, Satomi T, Takahashi H. Recycling Woven Plastic Sack Waste and PET Bottle Waste as Fiber in Recycled Aggregate Concrete: An Experimental Study. *Waste Management*, 2018; 78: 79-93. <https://doi.org/10.1016/j.wasman.2018.05.035>
- [15] Alani AH, Bunnori NM, Noaman AT, Majid TA. Durability Performance of a Novel Ultra-high-performance PET Green Concrete (UHPPGC). *Construction and Building Materials*, 2019; 209: 395-405. <https://doi.org/10.1016/j.conbuildmat.2019.03.088>
- [16] Fakoor M, Nematzadeh M. Evaluation of Post-fire Pull-out Behavior of Steel Rebars in High-strength Concrete Containing Waste PET and Steel Fibers: Experimental and Theoretical Study. *Construction and Building Materials*, 2021; 299: 123917. <https://doi.org/10.1016/j.conbuildmat.2021.123917>
- [17] Nematzadeh M, Shahmansouri AA, Fakoor M. Post-fire Compressive Strength of Recycled PET Aggregate Concrete Reinforced with Steel Fibers: Optimization and Prediction via RSM and GEP. *Construction and Building Materials*, 2020; 252: 119057. <https://doi.org/10.1016/j.conbuildmat.2020.119057>
- [18] Noroozi R, Shafabakhsh G, Kheyroddin A, Moghaddam AM. Investigating the Effects of Recycled PET Particles, Shredded Recycled Steel Fibers and Metakaolin Powder on the Properties of RCCP. *Construction and Building Materials*, 2019; 224: 173-187. <https://doi.org/10.1016/j.conbuildmat.2019.07.012>
- [19] Colak AB, Akcaozoglu K, Akcaozoglu S, Beller G. Artificial Intelligence Approach in Predicting the Effect of Elevated Temperature on the Mechanical Properties of PET Aggregate Mortars: An Experimental Study. *Arabian Journal for Science and Engineering*, 2021; 46 (5): 4867-4881. <https://doi.org/10.1007/s13369-020-05280-1>
- [20] Ganesh Prabhu P, Arun Kumar C, Pandiyaraj R, Rajesh P, Sasi Kumar L. Study on Utilization of Waste Pet Bottle Fiber in Concrete. *International Journal of Research in Engineering & Technology*, 2014; 2 (5): 233-240.
- [21] Faisal SK, Irwan JM, Othman N, Wan Ibrahim MH. Flexural Toughness of Ring-shaped Waste Bottle Fiber Concrete. *MATEC Web of Conferences*, 2016; 47: 01002. <https://doi.org/10.1051/mateconf/20164701002>
- [22] Usmani MU, Abdul Awal ASM. Physical, Mechanical and Durable Characteristics of Concrete Incorporating Polyethylene Terephthalate Fiber from Bottle Waste. *Journal of Critical Review*, 2020; 7 (5): 908-916. <https://doi.org/10.31838/jcr.07.05.187>
- [23] Aditya Krishna Reddy K, Arun Kumar C. Study of Mechanical Properties of Concrete using Waste Pet Bottle Fibres for the Reinforcement. *International Journal of Engineering and Management Research*, 2014; 4 (2): 232-240.

- [24] De Luna AM, Ahmed Shaikh FU. Anisotropy and Bond Behaviour of Recycled Polyethylene Terephthalate (PET) Fibre as Concrete Reinforcement. *Construction and Building Materials*, 2020; 265: 120331. <https://doi.org/10.1016/j.conbuildmat.2020.120331>
- [25] Thomas LM, Moosvi SA. Hardened Properties of Binary Cement Concrete with Recycled PET Bottle Fiber: An Experimental Study. *Materials Today: Proceedings*, 2020; 32: 632-637. <https://doi.org/10.1016/j.matpr.2020.03.025>
- [26] Khalid FS, Irwan JM, Wan Ibrahim MH, Othman N, Shahidan S. Splitting Tensile and Pullout Behavior of Synthetic Wastes as Fiber-Reinforced Concrete. *Construction and Building Materials*, 2018; 171: 54-64. <https://doi.org/10.1016/j.conbuildmat.2018.03.122>
- [27] Adnan HM, Dawood AO. Strength Behavior of Reinforced Concrete Beam using Recycle of PET Wastes as Synthetic Fibers. *Case Studies in Construction Materials*, 2020; 13: e00367. <https://doi.org/10.1016/j.cscm.2020.e00367>
- [28] Cui X, Liu G, Wang C, Qi Y. Effects of PET Fibers on Pumpability, Shootability and Mechanical Properties of Wet-mix Shotcrete. *Advances in Civil Engineering*, 2019: 1-14. <https://doi.org/10.1155/2019/2756489>
- [29] Nibudey RN, Nagarnaik PB, Parbat DK, Pande AM. Compressive Strength and Sorptivity Properties of PET Fiber Reinforced Concrete. *International Journal of Advances in Engineering and Technology*, 2014; 7 (4): 1206-1216.
- [30] Smaoui H, Trabelsi A, Kammoun Z, Aouicha B. Mechanical, Physical, Blast Waves and Ballistic Impact Resistance Properties of a Concrete Incorporating Thermally Treated PET Inclusions. *Construction and Building Materials*, 2023; 365: 130088. <https://doi.org/10.1016/j.conbuildmat.2022.130088>
- [31] Shinde TR, Kumar VA, Jadhav RM. Comparative Study of Waste Pet Bottle Fibers and Polypropylene Fiber Reinforced Concrete. *International Journal for Research in Engineering Application & Management*, 2018; Special Issue - ICRTET2018: 854-858.
- [32] Ojeda JP. A Meta-analysis on the Use of Plastic Waste as Fibers and Aggregates in Concrete Composites. *Construction and Building Materials*, 2021; 295: 123420. <https://doi.org/10.1016/j.conbuildmat.2021.123420>



Research Article

Sustainable approaches in the built environment with industrial waste and recycled products derived from construction and demolition waste

Darshini Shekhar ^{a*}, Jagdish Godihal^b

Department of Civil Engineering, Presidency University, Bengaluru, India

Article Info

Abstract

Article history:

Received 07 Feb 2023

Accepted 16 May 2023

Keywords:

*Recycled concrete aggregates;
Hollow cavity blocks;
Compressive strength;
Drying shrinkage;
Structural cost efficiency*

The cost of construction becoming costlier day by day, because of the non-availability of sufficient natural materials. The exploration of natural materials leads to the depletion of natural resources. The increasing fuel prices and other miscellaneous costs make the production of conventional concrete costlier year by year. To address this issue, products derived from recycling construction and demolition waste and industrial waste having similar properties to that of natural aggregates and cement need to be identified, wherein, we can replace these in appropriate proportion to get the desired recycled concrete complement with conventional concrete. To explore this possibility, the study has been carried out by preparing the blocks with circular and rectangular cavities, using recycled concrete aggregate and coal ash. As we are using industrial waste materials this study ascertains the sustainability dimensions like, environmental and economic. An experimental procedure for finding compressive strength, water absorption, density, and drying shrinkage has been carried out. The percentage cost difference between conventional concrete and the recycled concrete block was determined using an economic analysis based on a remote matrix and raw material price. The most suitable proportion is found to be recycled concrete aggregates replacing 70% of natural aggregates and coal ash replacing 35% of cement, satisfying the mechanical properties of blocks but falling short of the durability characteristics. Based on the results, the structural-cost efficiency of distinct cavity blocks has been calculated. The concrete mix design and ideal mix are deduced solely for applications in Indian construction.

© 2023 MIM Research Group. All rights reserved.

1. Introduction

Construction and demolition waste (CDW) accounts for 25–30% of all solid trash generated globally and is thought to produce more than 3 billion tonnes annually. Recycling CDW has been proposed to be necessary for the building industry to be sustainable in a circular economy given this grave environmental issue [1]. “According to a report by the Technology Information Forecasting and Assessment Council (TIFAC), new construction waste in India averages 50 kg per square meter, while the demolition of old buildings produces 300-500 kg per square meter of demolished waste”. If it is presumed that 5% of existing structures are demolished each year, this trash will total 288 million tonnes. Construction and demolition debris comprises two types of waste: recycled concrete aggregate and recycled aggregate made from crushed conventional concrete. According to the Ministry of Urban Development (MoUD) report in India, recycled aggregate can bridge the gap between aggregate demand and supply, with the housing sector reporting a 55,000 million cubic meter aggregate shortage. Recycling construction and demolition waste (CDW) as an alternative concrete aggregate for concrete is one

*Corresponding author: darshinis@presidencyuniversity.in

^a orcid.org/0000-0002-5431-9717; ^b orcid.org/0000-0001-9719-9850

DOI: <http://dx.doi.org/10.17515/resm2023.685ma0207>

Res. Eng. Struct. Mat. Vol. 9 Iss. 4 (2023) 1117-1133

solution to all of these issues. There is a necessity for the creation of "Recycled aggregate concrete" (RAC) where aggregate reprocessing in the years ahead will be required due to a lack of natural resources. The output of fly ash and bottom ash from coal-fired electric power plants emits tonnes of combustion refuse each year. The majority of which is lightweight fly ash and heavier bottom ash that accumulates on the boiler floor, and the bulk of this ash is fated for landfills. Recycling and reusing C&D waste have numerous cost-cutting benefits. The cost of waste disposal land can be reduced, as can the labour costs associated with cleaning landfills. The modern building relies heavily on cement concrete hollow blocks. They are more affordable and superior than burned clay bricks because they are more durable, fire resistant, partially sound resistant, have good thermal insulation, and have a low dead load. Construction can be finished more quickly since concrete hollow blocks are often larger than conventional clay building bricks, require less mortar and are used for both framed, bearing walls, partitions, and panel walls. Recycled aggregate concrete blocks are synthesized, substituting recycled coarse aggregate for natural gravel or pebble and river sand for recycled fine aggregates. The strength of recycled concrete was equivalent to that of conventional concrete, as the ecological and financial benefits are quite good [2]. The material strength of RAC-based concrete is weaker than quartzite aggregate, but they are equivalent to granite aggregate-the second most often used aggregate. As a result, CDW may be utilized to make concrete with a characteristic strength of up to 30 N/mm² when natural aggregate is replaced with 100% recycled coarse aggregate [3]. The recycled aggregate concrete may be used in place of natural coarse aggregates in M20 grade concrete without compromising workability or strength [4]. Hammed (2015) [5] claimed a financial savings of 63.13 percent for recycled aggregate concrete generated by reusing concrete trash to build fresh concrete at the same demolition place. However, the cost savings are 12.62 percent when RAC is produced using recycled concrete aggregate bought from a recycling facility [6]. Increasing the amount of attached old cement mortar with the recycled fine aggregate replacement ratio results in a loss in compressive strength. While using recycled fine aggregate, the greatest compressive strength drop was 6.7%, 11.1%, 31.3%, and 50% for concrete with replacement ratios of 10%, 30%, 50%, and 100%, respectively [7]. It is evident that the compressive strength, regardless of the cement quantity or binder composition, is highly prone to the large subsistence of recycled fine aggregate (RFA) 100% [8,9]. In RAC, two significant elements to examine cost and energy usage. RAC can sometimes be more expensive or use more energy than virgin aggregate and is mostly controlled by travel distances [10]. The highest compressive strength achieved by recycled aggregate concrete cubes treated with epoxy resin with 25% replacement is 38.8MPa. Epoxy resin coating to recycled coarse aggregates reduces water absorption and improves the workability of concrete mix [11]. A sensitivity analysis-based case study in Thailand illustrates the viability of using recycled aggregates from Bangkok's economic aspects. It has been determined that the payback period for investments in recycled aggregate facilities is nine years [12]. The impact of using recycled concrete aggregates (RCA) in addition to superplasticizers on the mechanical, rheological, and overall shrinkage properties of concrete made with natural coarse aggregate and RCA has been studied. To demonstrate the change in mechanical properties and total shrinkage as an attribute of the concrete contents, inferences, and numerical relations are proposed. Concrete's compressive and flexural strengths at 28 days increased when RCA aggregate content is 60%. While the negative effects of using too much superplasticizer can reduce compressive strength by about 21% for materials with low w/c ratios. Concrete with RCA aggregates experiences overall shrinkage that is greater than regular concrete and proportional to the rate of substitution [13]. An experimental program was carried out to investigate the properties of RCA in comparison to natural aggregate. According to close observation, high-quality and acceptable structural concrete can be formed using RAC, which in turn is preliminarily dependent on the characteristics of demolished concrete [14]. Regarding the above-

mentioned mechanical property coming to the durability aspect drying shrinkage is another key feature in the overall design of RCA. The drying shrinkage of RAC is measured over a 70-day test period with a 100% ratio and achieved a 95% rise in drying shrinkage [15]. Following that, researchers used RCAs to partially replace natural coarse aggregates (NCAs) in the preparation of normal- and high-strength RAC with w/c ratios of 0.26-0.75 and reviewed shrinkage actions. The results showed that as the RCA ratios increased, the drying shrinkage of RAC of varying strengths (w/c ratios) increased. These increases, however, ranged, ranging from 0.1% to 121.3% [16]. Good reliable construction is possible to make using RCA. Various mechanical test conducted on concrete where NCA: RCA ratio is 40:60 is found to be the logical and cost-effective and efficient way to use technology in the future [17]. Tyre waste has recently been used in a variety of ways for soil fortification. Waste tyre textile fiber is a byproduct of waste tyre processing. These unique wastes are regularly buried or burned in defiance of international law. This work uses an experimental design to demonstrate that these materials might be recycled and combined with soil to enhance the mechanical qualities of the mixture. According to the test results, adding fiber to the soil increases both its tensile and shear strengths. So, these wastes could be used to improve the mechanical qualities of many types of soils in geotechnical applications rather than being buried or burned [18]. Four different poorly graded sands with various particle size distributions underwent direct shear tests to ascertain their shear behaviors. 4 distinct poorly graded sands, each with a different median diameter have been chosen. Sand with larger particle sizes records a higher friction angle than soils with microscopic particles, according to the results. Also, it emerged from the experiments that sand with larger particle sizes had a higher dilation angle [19]. The present trend emphasizes sustainability in terms of substituting conventional materials with industrial byproducts as an environmentally friendly resource that may aid in the implementation of cost-savings and the use of green products. The concepts of structural efficiency (SE) and cost efficiency (CE) were established and assessed to demonstrate the relationship between compressive strength, toughened density, and cost per hollow block [20]. Portland cement is the principal source of carbon emissions from commercially produced concrete mixtures, accounting for 74% to 81% of total emissions [21]. Cement can be partially replaced by supplementary cementitious materials (SCMs) such as ground granulated blast furnace slag and fly ash and natural aggregates (NA) can be replaced with recycled aggregates (RA) [22]. Furthermore, sustainable recycled aggregate concrete (RAC) helps to limit the depletion of natural mineral resources [23]. SCM incorporation in NAC can lower carbon emissions and concrete costs, whereas partially substituting NA with RA results in equivalent emissions but a slightly higher cost for an equal design strength [24]. Based on the SVAGRIHA assessment, a conventional existing building star rating has been assigned in the case study inquiry on a 3BHK house in Bengaluru, Karnataka, India. According to the investigation, the current building construction practices do not meet the star green rating, so adopting renewable resources and materials with reduced embodied energy would be beneficial. Reducing waste, industrial recycling, efficiently utilizing energy, implementing green technologies, and protecting ecological resources are all examples of sustainable practices [25]. In practice, concrete hollow blocks are built of cement, cementitious ingredients such as fly ash, asbestos and conventional aggregates (M sand of 4.75mm and natural coarse aggregate of size 10mm). In India, a massive chunk of coal ash and construction demolition debris is generated, which is headed for landfills rather than being used as a raw material in concrete. To address this issue, recycling CDW waste to obtain recycled concrete aggregates should be undertaken. Previous research has shown the application of recycled concrete aggregates in combination with coal bottom ash on cubes. Utilizing untreated industrial waste (coal ash) and recycled CDW (RCA) to make circular and rectangular cavity block tests and ascertain the two dimensions of sustainability- enviro and economic centric applied to Indian construction add to new knowledge in this area of research, being a novelty. When coal

ash is combined with water, it exhibits pozzolanic properties that allow it to generate cementitious compounds. Building Materials & Technology Promotion Council Ministry of Housing & Urban Affairs in India has policies to encourage the use of recycled concrete aggregates in building works as a sustainable construction approach. The recovered fine and coarse aggregates have been successfully used and verified for their suitability for use in concrete, with validation performed at the National Council for Cement & Building Materials - NCB Bhawan and other locations. Overall, the addition of recycled aggregates to natural aggregates offers several benefits, including resource efficiency, environmental stewardship, energy and cost savings, waste reduction, performance and adaptability, and regulatory issues.

The present study focuses on preparing recycled concrete hollow blocks of two different cavity shapes: rectangular cavity concrete block (RCB) and circular cavity concrete block (CCB). To create hollow block masonry units, this study aims to replace natural coarse aggregate (NCA) with recycled coarse aggregate (RC_CA), manufactured sand (M sand) with recycled fine aggregate (RC_FA), and cement with coal ash in varying ratios. The key parameter of the study is to find out and compare the compressive strength (f_{ck}), water absorption, density, drying shrinkage test, and cost efficiency study of hardened concrete RCB and CCB samples made of conventional concrete and recycled concrete (coal ash and RCA).

2. Methodology and Experimentation

The two distinct forms of cavity concrete blocks (RCB and CCB) are cast in after performing the basic property test on materials and mix design in accordance with IS 10262 (2019) utilizing conventional, waste and recycled materials. The key test on the concrete hollow block is done following IS 2185 (part 1):2005 specification. Considering the concrete cavity block manufacturing unit to be located at a place, the manufacturing cost of six distinct cavity blocks was investigated in terms of mix proportion dosage and material pricing including shipping expenses. Structural cost efficiency is one of the crucial factors to take into account for sustainability. Based on the strength and density delivered to the cost of producing a concrete cavity block, the structural cost-effectiveness of the specimens is assessed. The cost imposed by various concrete constituents has been compared, and different cavity block grades as per Indian construction scenarios have been illustrated. The sequence of study is shown in Fig. 1.

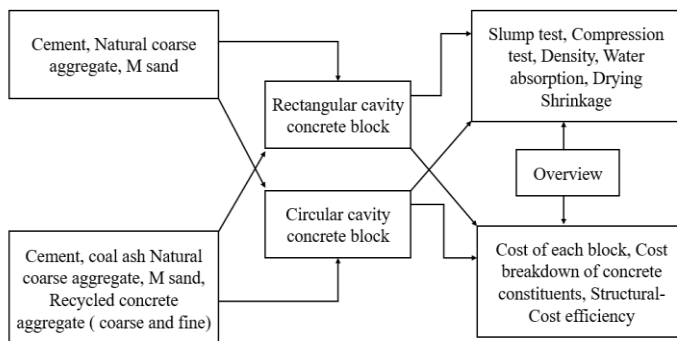


Fig. 1 Methodology for the study

2.1. Materials

M sand, natural coarse aggregate, recycled coarse aggregate (<10mm size), recycled fine aggregate (<4.75mm), OPC cement 53 grade, coal ash, and BASF master glemium

superplasticizer are the components of the concrete block specimen utilized in this study. These materials are used to create cavity concrete blocks in accordance with IS 10262 (2019). RCA is bought from a CD waste recycling plant located near Yelahanka, Bengaluru. Coal ash is collected from the bottom of a furnace in a clay brick manufacturing operation where coal was used as a fuel source and sieved to eliminate undesirable components. Fig. 2 depicts the various materials utilized in the study of mixed-proportion concrete samples that were not subjected to any processing at the casting site. The material's physical appearance is shown below, providing a visual acceptance of the difference between recycled or waste materials and natural materials.



Fig. 2 Concrete materials used in the study

2.2. Mix Design and Mix Proportion

As there is no special mix design for recycled aggregate concrete, the study followed the specifications for conventional concrete (IS 10262-2019). Six concrete mix proportions are considered and 12 concrete hollow blocks type of each 6 rectangular and circular cavity blocks have been cast. The water cement ratio is adjusted based on the RCA water absorption with the addition of recycled concrete aggregate. The mix ratios obtained in this experimental study are. Mix calculation outcomes per unit volume of concrete are displayed in Table 1 along with the mix ratio, which was determined to be 1:1.39:2.91 (cement: fine aggregate: coarse aggregate) for both cavity blocks.

Table 1. Mix proportion of concrete mix design

Mix type	Cement kg/m ³	Coal bottom ash kg/m ³	NCA kg/m ³	RCcA kg/m ³	M sand kg/m ³	RCfA kg/m ³
Mix 1 and 2	483.63	-	1407.36	-	672.24	-
Mix 3 and 4	314.35	169.27	422.46	984.9	201.43	470.56
Mix 5 and 6	265.99	217.63	141.06	1266.3	67.22	605.01

The proportions of RCA in the concrete cavity block mixture are considered as per the IS:383(2016). Table 2 below displays the additional superplasticizer dosage and the water-cement ratio (W/C). Since recycled aggregates often have higher water absorption capabilities, the saturated surface dry conditions of the aggregate were maintained prior to the start of the mixing processes. In order to improve the performance of concrete in terms of workability and compressive strength, the dosage of superplasticizer in RAC is doubled.

Table 2. Different concrete mix percentages for different cavity block specimens

Mixes	Mix Type	HBS	Concrete Mix Ratio	(w/c)	SP %
Mix-1	Conventional concrete	R1,	100% (cement)+100% (NCA)+100%	0.40	0.5%
		C1	(M sand)+SP		
Mix-2	concrete	R2,	100% (cement) + 100% (NCA) +	0.45	-
		C2	100% (M sand)		
Mix-3	concrete	R3,	35% (coal ash)+65% (cement)+70%	0.40	1%
		C3	RCA (Coarse)+30% (NCA)+70% RCA (Fine)+ 30% M sand+SP		
Mix-4	Recycled concrete	R4,	35% (coal ash) + 65% (cement)+70%	0.45	-
		C4	RCA (Coarse)+30% (NCA)+ 70% RCA (Fine)+ 30% M sand		
Mix-5	concrete	R5,	45% (coal ash)+55% (cement)+90%	0.40	1%
		C5	RCA (Coarse)+ 10% (NCA)+90% RCA (Fine)+10% (M sand) +SP		
Mix-6	concrete	R6,	45% (coal ash) + 55% (cement) + 90%	0.45	-
		C6	RCA (Coarse)+ 10% (NCA) + 90% RCA (Fine)+10% (M sand)		

2.3. Preparation of Specimen

Rectangular cavity block (RCB) and circular cavity block (CCB) of size 500*100*100mm maintaining a consistent bed thickness of 25mm are prepared. RCB is provided with a face shell thickness of 25mm and a web thickness of 50mm. In the instance of the CCB block, the face shell thickness is 50mm and the web thickness is 60mm. Compressive strength, water absorption, and block density are calculated as per the IS2185(part 1) 2005 code. Fig. 3 depicts the casting technique used for the study's specimens.



Fig. 3 Casting of RCB and CCB testing specimens for the study

2.4 Basic Property Test of Concrete Materials

The fundamental specifications for concrete constituents used in the mix design for the objective strength M30 are shown in Table 3. The recycled fine aggregate fineness modulus is significantly greater than that of M sand, indicating that RFA is coarser than M sand. As the age of the recycled aggregate increases the specific gravity of the aggregate decreases. The source of the aggregate and the old mortars clinging to it are the key elements impacting the recycled concrete aggregate’s capacity to absorb water. The standard

consistency of coal ash was experimented to be more than cement but was in the limited range as prescribed by IS5513-(1976) and IS4031-1998.

Table 3. Basic material property test result

Concrete Materials	Specific Gravity	Water Absorption (%)	Fineness Modulus
M Sand	2.61	8.1	4.83
RCA (Fine)	2.44	4.74	5.525
Natural Coarse (NCA)	2.54	<1	2.066
RCA (Coarse)	2.24	6.38	1.961
OPC 53 Grade Cement	2.97	NA	NA
Coal Ash	2.41	NA	NA

2.5. Sieve Analysis of Aggregates

The aggregate’s particle size distribution and grading curves are shown in Fig. 4 and Table 4. Despite that both natural and recycled aggregates showed a similar nature, they could not have hindered the workability of fresh concrete. RCA gradation depends on the source of demolished concrete and the recycling method. RCA utilized in the study tends to have a high percentage of finer particles than the conventional aggregate. RCA (fine) falls under Zone 1 and M sand falls in Zone 2 as per the gradation under clause 6.3 in IS 383 (2016). The higher percentage fraction variation is observed in the 300-75-micron sieve in RC_FA and 4.75mm micron sieve in RC_CA.

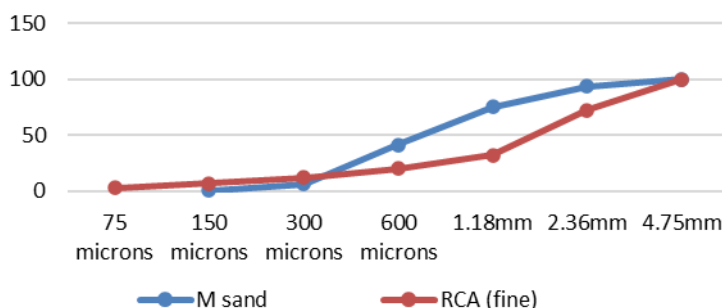


Fig. 4 Grading curve of fine aggregate

Table 4. Particle size distribution of RCA and NCA

IS Sieve	% passing NCA	% passing RCA (coarse)
20mm	100	100
12.5mm	100	99.7
10mm	91.8	83.1
4.75mm	1.6	21.1

2.6 Slump, Compressive Strength, Density, Water Absorption

Concrete workability relates to the uniformity of concrete in the fresh state and is partly related to its yield stress. The workability of the concrete is inferred based on the slump value of the concrete mixture as prescribed in code IS 1199 (2018). Compressive strength test is done in the universal testing machine where plates are kept at the bottom and top of the specimen to prevent failure at the hollow section and to distribute the load equally along the surface area. The procedure specified in IS 2185 (2005) has been followed in terms of block density and water absorption (annexures C and E) calculation.

2.7. Drying Shrinkage Test

The drying shrinkage test is carried out using a length comparator as the tool and is observed in Fig. 5. Six different concrete mix samples are cast in a 7.5x7.5x30 cm mould and left for curing for about 28 days. As the specimens are taken out of the water, each specimen's length must be measured (wet measurement, L1). The samples are then kept in an oven set at 50°C for 44 hours. Samples are described as having a dry length, L2, after being dried in an oven. The formula below is used to calculate the sample's drying shrinkage.

$$\text{Drying shrinkage (\%)} = \frac{(L1 - L2)}{L2 * 100} \quad (1)$$



Fig. 5 Drying shrinkage test using length comparator

2.8. Cost Analysis

Taking into account the concrete hollow block manufacturing facility in Hebbal, Bengaluru. The cost of manufacturing hollow blocks of the various concrete composites considered in the study is calculated by employing recycling and industrial unit vendor selling prices. The cost estimation for the hollow block with superplasticizer added is assumed to be the same as hollow blocks created without superplasticizer. Consequently, the value of the increased master glenium price per block is negligible. Fig. 6 depicts the availability of raw materials concerning the hollow block factory's distance matrix. Recycled aggregates are found to have a net purchasing cost that is half that of natural aggregates. The cost of coal ash is imposed more on transportation than on its retail price.

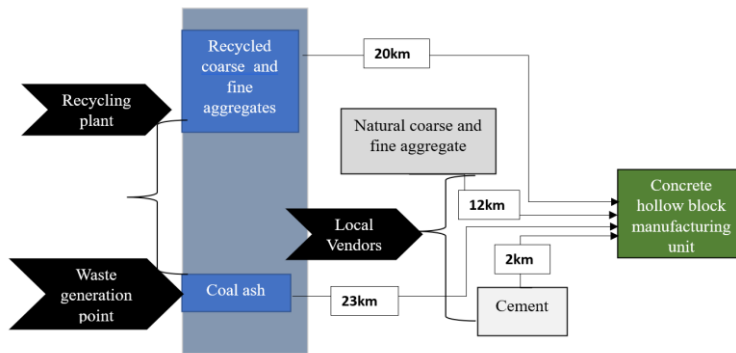


Fig. 6 Distance matrix of cavity block manufacturing unit

2.9. Structural -Cost Efficiency of The Different Cavity and Concrete Composite Block

To compare the conventional and industrial by-product-based hollow blocks, the idea of structural-cost efficiency (SCE) was established and assessed to specimens into a comparable platform. Structural-cost efficiency is calculated by the Equation 2 as mentioned below.

$$SCE = \left(\frac{fck}{D}\right) + \left(\frac{fck}{C}\right) \quad (2)$$

fck = compressive strength of block unit (MPa)

D = Density of the unit block (Kg/m³)

C = Cost per unit block (INR)

3. Results

In this section the results obtained from the study, related to fresh and hardened concrete using various mix proportions have been outlined.

3.1. Fresh Concrete Test

Different slump pattern of various concrete mixtures is observed in Fig. 7. The slump value of the concrete mixture is subsiding as the percentage of RCA increases and the value ranges from 30-65mm which is within the range per code IS 1199 (2018) and is shown in Fig. 8.



Fig. 7 Slump pattern of different concrete mix

In the CDW crushing procedure, the quantity of adhered mortar causes poor workability and large slump loss in recycled aggregate concrete. According to experiment observation, using a superplasticizer is advised to make RAC more workable.

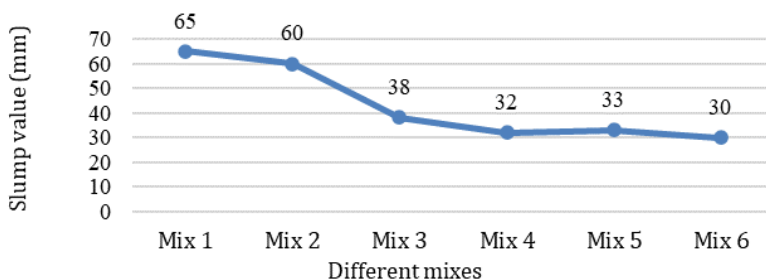


Fig. 8 Slump value of different concrete mix

3.2. Hardened Property Test Results

The compression test of these 12 cavity blocks (RCB and CCB) after 28 days of curing has been performed, and variation in strength test results of a different concrete mixture is shown in Fig. 9. Given the failure status of recycled concrete masonry block, it is clear that the top face and the weak points in joints where penetration cracks had first appeared before the entire specimen was ultimately destroyed. This was primarily caused by grooves on the top surface, making forming a failure surface simple. The lowest and maximum compressive strengths of various RCB and CCB concrete compositions are shown in Table 5. The statistical data are analyzed using R Studio to determine the standard deviation and coefficient of variation for each of the 12 different blocks which are shown in Table 5 below.

Table 5. Summary of test results of compressive strength (fck)

Block type	Minimum fck	Maximum fck	Standard deviation	Coefficient of variation
R1	12.98	13.27	0.1181	0.8981
R2	10.5	11.31	0.3245	2.9723
R3	12.29	12.33	0.2963	2.4508
R4	6.9	7.53	0.2246	3.1195
R5	9.77	10.28	0.1874	1.8785
R6	5.6	6.09	0.2591	4.399
C1	26.78	28.82	0.7404	2.6510
C2	25.1	26.1	0.4123	1.6105
C3	14.99	15.54	0.2198	1.4399
C4	10.65	10.98	0.1238	1.1417
C5	11.25	11.98	0.3035	2.6169
C6	7.12	7.71	0.2250	3.004

The highest strength is achieved by CCB (C1 and C2) and the fck value is ranging from 21.91 MPa without a superplasticizer and 24.92 MPa with a superplasticizer. There is a difference in the characteristic strength between recycled concrete block and conventional concrete block, varying from 41% to 61% less for CCB and 10% to 25% less for RCB. Since coal ash is rehydrating material and contains calcium oxide and recycled aggregates diminishes the aggregate–mortar interfacial transition zone of recycled aggregate concrete, thus declining

its mechanical strength. In the wake of the block's large hollow area and thinner web, RCB's compressive strength is 40%-12% weaker than CCB's for the same concrete mix proportion. The inclusion of a superplasticizer in mixes 3 and 5 increased block strength by up to 40%, owing to the production of a homogeneous mixture with a low water-cement ratio to offset excessive water absorption in recycled aggregate concrete.

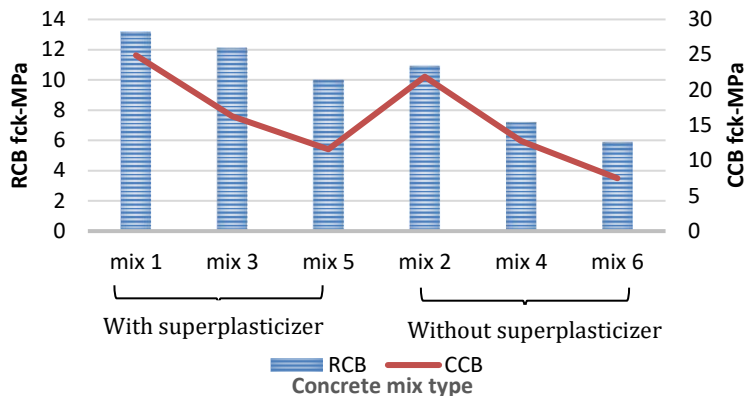


Fig. 9 28 days compressive strength (fck) of different cavity block

3.3. Grading of Conventional Concrete and Recycled Concrete Block

The block density of recycled concrete block is 0.1 times lower than a conventional concrete cavity block. This is due to the porosity and low specific gravity. Water absorption of both RCB and CCB- conventional concrete and recycled aggregate concrete are below 10% which is acceptable in practice. The density of the considered blocks in the study is ranging from 1362- 1940 kg/m³ wherein RCB is less dense compared to CCB due to the increased content of concrete mixtures.

Table 6. Comparison of conventional and recycled concrete block

Specimens	Mix type	Density (kg/m ³)	Water absorption	Block grade
RCB	Mix 5	1362	6.68%	B
	Mix 6		5.59%	
CCB	Mix 5	1752	7.8%	A
	Mix 6		7.49%	
RCB	Mix 3	1565	6.32%	A
	Mix 4		5.99%	
CCB	Mix 3	1835	6.78%	A
	Mix 4		6.56%	
RCB	Mix 1	1633	4.3%	A
	Mix 2		4.4%	
CCB	Mix 1	1940	5.67%	A
	Mix 2		5.9%	

There is a slight decrease in water absorption of the concrete block when a superplasticizer is used due to its adsorption capacity. Water absorbability of concrete increases with the addition of recycled concrete aggregates and the replacement of coal ash. This may be

because of the high-water absorption capacity of the adhered mortar in the recycled concrete. Table 6 presents the grade of each block type made of different concrete mixes based on the obtained water absorption, density, and compressive strength results.

3.4. Drying Shrinkage Test

The shrinkage of the concrete samples regarded for the study after 28 days is depicted in Table 7. Each mix was tested using an average of four samples and the drying shrinkage percentage ranged from 0.009 to 0.084. According to the experimental findings, the increased moisture content and reduced strength of RCA have resulted in increased drying shrinkage of recycled concrete mix.

Table 7. Drying shrinkage of different concrete mixtures

Concrete Mix Type	Drying shrinkage (%)
Mix 1	0.031
Mix 2	0.002
Mix 3	0.075
Mix 4	0.069
Mix 5	0.091
Mix 6	0.084

As per the Indian standard code, the maximum allowable percentage is 0.006%. Recycled concrete mixtures is exhibiting shrinkage of up to 0.09% and the rate of shrinkage in samples with superplasticizer is more. This is primarily because the paste volume increased. Superplasticizers lower the surface tension of the water in the concrete mix, enabling the addition of more water. Due to the increased surface area of the paste particles, moisture in the concrete evaporates, increasing the amount of shrinkage.

3.5. Cost Ratio of RCB and CCB Block Composites

Taking into account the mass of composite materials for RCB and CCB, Fig. 10 and Fig. 11 shows the cost of each material contributing to each cavity block in Indian Rupees (INR-₹). From the surveillance of the below figures, it can be noted that cement is the major expensive component used to make concrete, followed by coarse aggregate and then fine aggregate. RCA incurs more transportation costs than it does net market value.

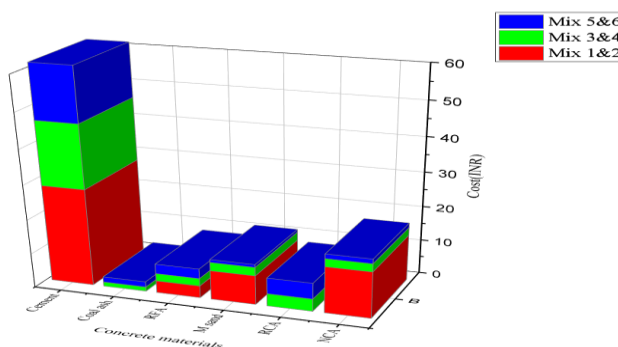


Fig. 10 CCB composites cost ratio (INR)

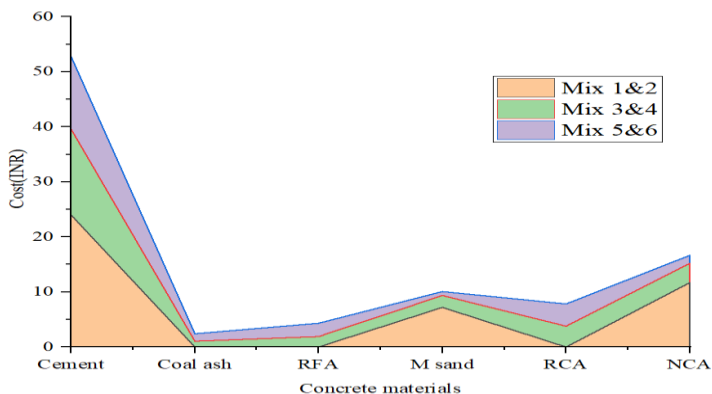


Fig. 11 RCB composites cost ratio (INR)

3.6. Structural-Cost Efficiency of The Different Cavity and Concrete Composite Blocks

The Pricing of two distinct concrete blocks with varying cavities is shown in Fig. 12, along with structural-cost efficiency (SCE) values. Mix (1,2) costs 42.9₹ for one RCB block while one CCB block is 47.82₹. Mix (3,4) RCB costs 32.7₹ and CCB costs 37.4₹. Mix (5,6) costs 29.6₹/CCB and 27.92₹/ RCB. Mix (3,4) and Mix (5,6) cavity blocks have been observed as 23% and 31% less expensive compared to conventional concrete mix (1,2) including transportation costs.

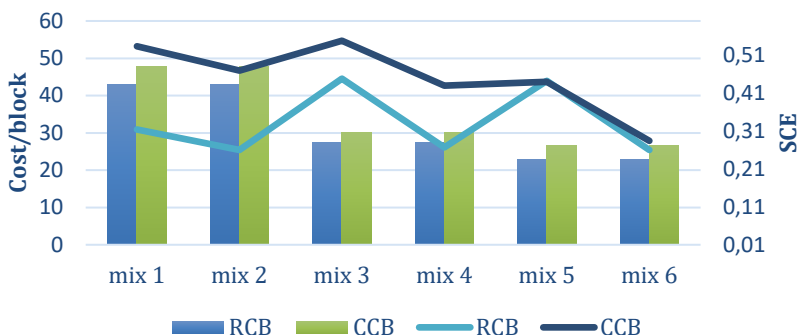


Fig. 12 Structural-Cost efficiency of block

Since RCB blocks have more cavity space and a lower material consumption rate than CCB blocks, they are relatively less expensive. When RCA (fine and coarse) and coal ash are used, mix 3 blocks (RCB, CCB; R3, C3) is found to have the highest structural- cost-effectiveness. SCE increased by about 30% and 3% in the R3 and C3 blocks, respectively, for the conventional block. Meanwhile, SCE in the R5 and C5 blocks was found to be equal.

The government, businesses and the general public must all work together in a concerted effort to promote the use of recycled materials in building construction. The government of India should emphasize increasing the quality of recycled materials and finding novel ways to use them in building construction. Education and awareness initiatives might be developed to spread the word about the advantages of employing recycled materials in building construction. It is advisable to encourage contractors and building firms to use

recycled aggregate by offering incentives. This can aid in the development of a sustainable supply chain for these commodities.

Among the 17 sustainable development goals (SDG) the current research meets the 9th goal: Industry, Innovation, and Infrastructure; the 12th goal: Responsible Production and Consumption; 13th Goal: Climate Action. Using RCA and coal ash to accomplish the 9th Industry, Innovation, and Infrastructure target is one of the 17 Sustainable Development Goals. 12th: Responsible Production and Consumption. 13th Goal: Climate Action. Building sustainable infrastructure with enhanced resource efficiency supports economic development by focusing on cheap and fair public access. Recycling and reusing building and demolition debris could help to achieve sustainable management and efficient use of natural resources. It aids in the creation of jobs by requiring labour from the beginning to the end of the manufacture of recycled concrete aggregates from the source site. Using the approach of substituting possible industrial waste in raw form or recycled pattern would assist to cut carbon dioxide emissions from conventional material production.

Recycled concrete aggregates in concrete production can be used only in metropolitan cities, Since the rate of construction and destruction (C&D) activity is more in these places. Usage of these waste and recycled materials will not be applicable for districts and taluk places because of lower C&D activities and transportation of these waste from large generation areas to smaller towns will negatively impact on enviro and economic dimensions of sustainability.

4. Conclusion

While developing load-bearing wall units that adhere to IS 2183 criteria, supplementary cementitious materials (SCM) such as coal ash up to 45%, can partially substitute cement and natural aggregates can be replaced with recycled concrete aggregates up to 90%. The passive benefits of using recycled concrete aggregates prevent the depletion of natural mineral resources and maintaining sustainable CDW management practices. According to the economic analysis, considerable cost reduction is observed in substituting NCA with RCA. However, the substitution of coal ash for cement has shown a significant impact on cost reduction.

The following conclusions are drawn from the study

- The workability of recycled concrete is lower than conventional concrete mix, but the slump value is within the acceptable limit for concrete masonry as per code IS 1199 (2018). The reduction in slump value is due to contamination of RCA the adhered mortar.
- Recycled coarse and fine aggregates can be used in making hollow block masonry units with a minimum of 5MPa characteristic strength. This can be employed as a load-bearing walling element by replacing natural aggregates of up to 90% by RCA with the addition of coal ash replacement of up to 45% as a supplementary cement material.
- The inclusion of a superplasticizer improved both the slump test and the compressive strength property. It reduced the water content of the mix, enhanced the cement particle spread, and increased compaction effectiveness, resulting in denser concrete. The workability of recycled concrete improved by 14%-16% when 1% SP was added to the cement weight. Superplasticizers can be applied to concrete hollow blocks to increase RAC compressive strength by 40%.
- Since the mass of RCA in unit CCB is greater than that of RCB, the water absorption and density of the CCB block are greater than that of RCB. The density of conventional hollow blocks is larger than recycled concrete hollow block due to

the pore structure of RCA and the low specific gravity of non-conventional materials.

- The RCA severely impacted the recycled concrete 28-day drying shrinkage by up to 0.8% - 0.9% for an RCA replacement ratio of 90%. The drying shrinkage characteristics of recycled concrete hollow blocks are not satisfied. Even though the addition of superplasticizers was supposed to increase workability and compressive strength, the durability property diminished. This is because recycled concrete undergoes bleeding where the water rises to the top of the concrete and volatiles having left voids, which leads to concrete shrinkage.
- Cement is indeed the largest share with the highest consumption cost in the creation of concrete components. Substituting recycled concrete aggregate and coal ash for traditional concrete materials makes it possible to manufacture hollow block walling units with a minimum characteristic strength of 5 MPa at a minimum cost savings of 30%.
- The best mix (mix 3) for both cavity blocks is 35% (coal ash) + 65% (cement)+70% RCA (Coarse)+30% (NCA)+ 70% RCA (Fine)+ 30% M sand+ Superplasticizer. This concrete mix hollow block is considered to be a grade A block with good compressive strength, and high structural-cost efficiency upon improving the drying shrinkage property.

Future scope of the study

- Improve on the durability property of concrete mix (drying shrinkage) where the concentration of recycled aggregate is 70% and coal ash is 35% and above.
- To experiment on different size hollow blocks considering the current project mix proportion.

Acknowledgment

I would like to acknowledge and give my warmest thanks to my research supervisor for his advice and support in carrying me through all the stages to write this research article. My sincere thanks to project students, teaching, and nonteaching staff for their help in carrying experimental project.

References

- [1] Robayo-Salazar R, Valencia-Saavedra W, Mejía de Gutiérrez R. Reuse of powders and recycled aggregates from mixed construction and demolition waste in alkali-activated materials and precast concrete units. *Sustainability*. 2022 Aug 6;14(15):9685. <https://doi.org/10.3390/su14159685>
- [2] Aslani, F, Hou L, Nejadi S, Sun J, & Abbasi S. Experimental analysis of fiber-reinforced recycled aggregate self-compacting concrete using waste recycled concrete aggregates, polypropylene, and steel fibers. *Structural Concrete*. 2019; 20(5): 1670-1683. <https://doi.org/10.1002/suco.201800336>
- [3] Akhtar MF, Naqvi MW, Alam MM, Shariq M. Use of Different Types of Aggregate vis-a-vis Demolition Waste as an Alternate Material for Concrete. In *Urbanization Challenges in Emerging Economies: Resilience and Sustainability of Infrastructure 2018 Dec 13* (pp. 679-690). Reston, VA: American Society of Civil Engineers. <https://doi.org/10.1061/9780784482032.068>
- [4] Prathima, G., Ganesh, B., & Nagaraja, K. P. (2018). Optimum utilization of alternate material for aggregates-An approach for waste management in urban areas for sustainability. In *Urbanization Challenges in Emerging Economies: Energy and Water Infrastructure; Transportation Infrastructure; and Planning and Financing* (pp. 221-

- 231). Reston, VA: American Society of Civil Engineers. <https://doi.org/10.1061/9780784482025.023>
- [5] Hameed, M. Impact of Transportation on Cost, Energy, and Particulate Emissions for Recycled [sic] Concrete Aggregate, Ph.D. Dissertation, University of Florida, Florida. 2009.
- [6] Ohemeng EA, Ekolu SO. Comparative analysis on costs and benefits of producing natural and recycled concrete aggregates: A South African case study. *Case Studies in Construction Materials*. 2020 Dec 1;13:e00450. <https://doi.org/10.1016/j.cscm.2020.e00450>
- [7] Zhang H, Ji T, Zeng X, Yang Z, Lin X, Liang Y. Mechanical behavior of ultra-high performance concrete (UHPC) using recycled fine aggregate cured under different conditions and the mechanism based on integrated microstructural parameters. *Construction and Building Materials*. 2018 Dec 20;192:489-507. <https://doi.org/10.1016/j.conbuildmat.2018.10.117>
- [8] Kim SW, Yun HD. Evaluation of the bond behavior of steel reinforcing bars in recycled fine aggregate concrete. *Cement and Concrete Composites*. 2014 Feb 1;46:8-18. <https://doi.org/10.1016/j.cemconcomp.2013.10.013>
- [9] Kumar R, Gurram SC, Minocha AK. Influence of recycled fine aggregate on microstructure and hardened properties of concrete. *Magazine of Concrete Research*. 2017 Dec;69(24):1288-95. <https://doi.org/10.1680/jmacr.17.00030>
- [10] Rakesh S, Keshava M. A study on embodied energy of recycled aggregates obtained from processed demolition waste. In *Nat. Conf. Recent Trends in Architecture & Civil Engineering Towards Energy Efficient and Sustainable Develop.*, NIT Tiruchirapalli 2019 Jan.
- [11] Zuki SS, Shahidan S, Subramaniam S. Effects of Recycled Aggregate Resin (RAR) in Concrete Material. *International Journal of Sustainable Construction Engineering and Technology*. 2020 Oct 25;11(2):55-64. <https://doi.org/10.30880/ijscet.2020.11.02.006>
- [12] Nitichote, K., & Yodsudjai, W. Recycled Aggregates Production Through Economic Perspectives. *International Journal of Sustainable Construction Engineering and Technology*. 2022; 13(1), 257-263. <https://doi.org/10.30880/ijscet.2022.13.01.022>
- [13] Ait Mohamed Amer A, Ezziiane K, Adjoudj MH. Evaluation of coarse recycled concrete aggregates effect on the properties of fresh and hardened concrete. *Asian Journal of Civil Engineering*. 2021 Sep;22(6):1173-84. <https://doi.org/10.1007/s42107-021-00373-0>
- [14] Kashyap R, Saxena M, Gautam A, Chauhan S, Mourya A, Verma P. A study on recycled lightweight aggregate concrete. *Journal of Building Pathology and Rehabilitation*. 2022 Dec;7(1):28. <https://doi.org/10.1007/s41024-022-00168-z>
- [15] Sri Ravindrarajah R, Tam CT. Properties of concrete made with crushed concrete as coarse aggregate. In *ICE Themes Recycled Aggregates: Use in Concrete 2019* (pp. 87-104). ICE Publishing.
- [16] Shannag MJ. Characteristics of lightweight concrete containing mineral admixtures. *Construction and Building Materials*. 2011 Feb 1;25(2):658-62. <https://doi.org/10.1016/j.conbuildmat.2010.07.025>
- [17] Vaidya OV, Malviya K, Bhirud YL. Strength Characteristics of Concrete Using Recycled Concrete Aggregate. *Vidyabharati Int. Interdiscip. Res. J.* 2021;13:533-8. <https://doi.org/10.17515/resm2022.423st0319tn>
- [18] Fareghian M, Afrazi M, Fakhimi A. Soil Reinforcement by Waste Tire Textile Fibers: Small-Scale Experimental Tests. *Journal of Materials in Civil Engineering*. 2023 Feb 1;35(2):04022402. [https://doi.org/10.1061/\(ASCE\)MT.1943-5533.0004574](https://doi.org/10.1061/(ASCE)MT.1943-5533.0004574)
- [19] Afrazi M, Yazdani M. Determination of the effect of soil particle size distribution on the shear behavior of sand. *Journal of Advanced Engineering and Computation*. 2021 Jun 30;5(2):125-34. <https://doi.org/10.25073/jaec.202152.331>

- [20] Nayaka RR, Alengaram UJ, Jumaat MZ, Yusoff S, Ganasan R. Performance evaluation of engineering properties, radiation shielding, and sustainability of hollow masonry blocks produced using a high volume of industrial by-products. *Journal of Materials in Civil Engineering*. 2021 Mar 1;33(3):04021003. [https://doi.org/10.1061/\(ASCE\)MT.1943-5533.0003558](https://doi.org/10.1061/(ASCE)MT.1943-5533.0003558)
- [21] Flower DJ, Sanjayan JG. Green house gas emissions due to concrete manufacture. *The international Journal of life cycle assessment*. 2007 Jul;12:282-8. <https://doi.org/10.1065/lca2007.05.327>
- [22] Xu B, Bompa DV, Elghazouli AY. Cyclic stress-strain rate-dependent response of rubberised concrete. *Construction and Building Materials*. 2020 Sep 10;254:119253. <https://doi.org/10.1016/j.conbuildmat.2020.119253>
- [23] Knoeri C, Sanyé-Mengual E, Althaus HJ. Comparative LCA of recycled and conventional concrete for structural applications. *The international journal of life cycle assessment*. 2013 Jun;18:909-18. <https://doi.org/10.1007/s11367-012-0544-2>
- [24] Bostanci SC, Limbachiya M, Kew H. Use of recycled aggregates for low carbon and cost effective concrete construction. *Journal of Cleaner Production*. 2018 Jul 10;189:176-96. <https://doi.org/10.1016/j.jclepro.2018.04.090>
- [25] Shekhar D, Godihal J. Sustainability assessment methodology for residential building in urban area-a case study. In *Multi-Hazard Vulnerability and Resilience Building 2023* Jan 1 (pp. 45-59). Elsevier. <https://doi.org/10.1016/B978-0-323-95682-6.00013-9>
- [26] IS 2185(2005)-part 1 Indian Standard concrete masonry units - specification part 1 hollow and solid concrete blocks (Third Revision), Bureau of Indian standards manak bhavan, 9 bahadur shah zafar marc3 new Delhi 110002
- [27] IS 10262 Concrete Mix Proportioning - Guidelines (Second Revision), Bureau of Indian standards manak bhavan, 9 bahadur shah zafar marc3 New Delhi 110002. 2019.
- [28] IS: 1199 -2018 (Part 2) Indian Standard Fresh Concrete -Methods of sampling and analysis of concrete, Bureau of Indian standards manak bhavan, 9 bahadur shah zafar marc3 New Delhi 110002.
- [29] IS383-2016. Indian standard coarse and fine aggregate concrete specification- Third revision

Blank Page



Research Article

Evaluation of coal based bottom ash as an alternative to fine aggregate in concrete: recommendations for specifications of bottom ash and its concrete mix design

P.N. Ojha^a, Abhishek Singh^b, Amit Trivedi^c, Brijesh Singh^{*,d}, Nitin Chowdhury^e

Centre for Construction Development & Research, National Council for Cement and Building Materials, India

Article Info

Abstract

Article history:

Received 17 Mar 2023

Accepted 15 May 2023

Keywords:

*Bottom ash;
Characterization;
Composite fine
aggregate;
Mix design;
Specifications*

Present study is an attempt to develop recommendations for specifications of bottom ash and concrete mix design guidelines by carrying out studies on bottom ash samples collected from 10 thermal power plants across India. Bottom ash samples were evaluated for physical and chemical properties. Composite fine aggregates were prepared by replacing 10-50% of conventional fine aggregate with bottom ash. 70 concrete mix trials were carried out using composite fine aggregates and mixes were evaluated for fresh, hardened and durability properties. Study indicated that maximum replacement of conventional fine aggregate with bottom ash for preparation of OPC based concrete shall not exceed 50% by weight of total fine aggregate and fineness modulus of resultant composite fine aggregate for use in concrete as fine aggregate shall be at least 1.35. The compressive strength of concrete at 28 days for all trials using composite fine aggregates were comparable with compressive strength of control concrete made with 100% conventional fine aggregates. The carbonation depth of control concrete were 6.6 mm to 9.5 mm and for concrete with composite fine aggregates, carbonation depths were 5.5 to 11.0 mm. The RCPT results of all mixes (including control mixes) shows that all mixes are lying in same class of penetrability. The electrical resistivity values of control concrete mixes were 7.1 to 6.1 k-ohm-cm and for concrete with composite fine it was 6.7 to 8.58 k-ohm-cm. Based on the results; recommendations were derived for specification of coal based bottom ash for its utilization as an alternative to conventional fine aggregate in concrete along with guidelines for concrete mix design.

© 2023 MIM Research Group. All rights reserved.

1. Introduction

One of the major components of concrete matrix are aggregates, as they generally occupy more than seventy percent of entire volume of concrete. Natural fine aggregates used in concrete are generally obtained by mining river sand from its bed. As consumption of concrete is increasing exponentially, particularly in developing country like India, it leads to the rapid rise in mining of river sand which leads to ecological problems alongside creating an impact on aquifer of river bed [1]. Therefore, aggressively growing construction industry requires an urgent sustainable alternative to conventional sand. In coal based thermal power plants, bottom ash has to be dumped in an open area nearby power plant, which pollutes the natural water bodies and also reduces the available productive land. The physical properties, chemical properties and the particle gradation of bottom ash are quite similar to that of fine aggregate. Therefore, in past decade, several studies related to physical and chemical evaluation of bottom ash as an aggregate and its

*Corresponding author: brijeshshewgaitr96@gmail.com

^a orcid.org/0000-0003-1754-4488; ^b orcid.org/0000-0002-2343-5934; ^c orcid.org/0000-0002-2594-4679;

^d orcid.org/0000-0002-6512-1968; ^e orcid.org/0009-0003-9374-7663

DOI: <http://dx.doi.org/10.17515/resm2023.710ma0317>

Res. Eng. Struct. Mat. Vol. 9 Iss. 4 (2023) 1135-1152

effect on mechanical and durability performance of concrete has been carried out to investigate the possibility of using bottom ash as an alternative to conventional sand in concrete which has shown encouraging results [1-7]. Bottom ash majorly consists of fused coarser coal ash particles. Bottom ash particles are well graded, have rough texture and are comparatively more irregular, porous and lighter in comparison to conventional sand [2-4]. The size range of bottom ash particles vary from fine aggregate to gravel. Aforementioned properties of bottom ash make it an attractive alternative to natural sand. Cheriaf et al [7] based on morphological study of bottom ash using scanning electronic microscope found that bottom ash is very different as compared to fly ash particles with respect to its shape and surface characteristics. Seals et al [4] evaluated different characteristics of bottom ash from West and reported that density for bottom ash samples varied from 11.6 to 18.4 kN/m³ (standard Proctor density) and optimum moisture content were observed to vary from 12 to 34 [4]. Coarser size of bottom ash along with its surface characteristics like fused, glassy texture makes it an ideal alternative for natural fine aggregates. However, utilization of bottom ash in concrete as fine aggregate is limited due to several technical challenges such as variation in characteristics of bottom ash, water requirement and its contribution in cements hydration [5].

Using bottom ash instead of sand leads to increase in water demand to attain the similar level of workability of concrete in its fresh state because of higher water absorption, irregular shape as well as porous nature of bottom ash particles [6 -10]. Therefore, in case of concrete incorporating bottom ash as replacement of fine aggregate, amount of extra water added to the mix, which just fills up the void and does not participate in lubrication needs to be taken into account [11-13]. Effective water to binder ratio in concrete needs to be appropriately adjusted to take into consideration, the porous nature of bottom ash particles [14]. Kadam et al [15] concluded from their study that with the increase in proportion of bottom ash as fine aggregate, the concrete mix becomes more cohesive resulting in lower workability. Singh and Siddique concluded that with increase in bottom ash proportion in concrete mix causes increase in amount of irregular and porous particles in the mix, which subsequently leads to increase in inter-particles friction [2]. However, some researchers have also found contradicting results [16-17]. Bai et al [18] observed that with increase in coal bottom ash, ball bearing effect increases, leading to better workability. However, most of the researchers have accepted that increasing the percentage level of coal based bottom ash as fine aggregate in concrete leads to increase in water demand to produce a workable concrete mix [19].

Studies carried out in past reveal that porosity of interfacial transition zone (ITZ) between aggregate particles and hydrated cement matrix gets increased with increase in bottom ash proportion in mix and it further leads to accumulation of free water nearby bottom ash particles [2]. Increased porosity and local w/c ratio of ITZ have detrimental effects on mechanical characteristics of concrete, particularly its compressive strength. Past research studies with focus on pozzolanic reactivity of bottom ash conclude that in spite of its relatively low pozzolanic activities it can be utilized to produce durable concrete [20-21]. Ksaibati [22] evaluated the feasibility of coal bottom ash utilisation as a complete aggregate substitution. Samples were prepared using bottom ash from three different sources and results indicated that the optimum asphalt content was higher in the mixture containing bottom ash with similar performance of the bottom ash mix compared control mixture during service period. The coal based bottom ash contains high amount of SiO₂, Al₂O₃, and Fe₂O₃ that enhances pozzolanic effects, mix interlock, and mechanical properties of concrete [23]. Even though pozzolanic potential of bottom ash is less due to its grain size [24], its lower pozzolanic nature does not prove to be any limiting factor for its potential to be utilized as replacement of conventional fine aggregate. On the contrary, any level of contribution due to the pozzolanic action of bottom ash particles improves the hardened

as well as long term durability performance of concrete because of densification of cement matrix with secondary C-S-H formation [25]. Aggarwal et al [26] carried out research experiments on development of concrete mixes by using coal based bottom ash as 40% replacement of conventional fine aggregate (by weight) and found that up to 40% replacement level, mechanical properties like compressive and flexural strength are comparable or higher than control concrete. Arumugam et al [27] carried out lab experiments on preparation of concrete mixes by replacing as much as 60% of conventional fine aggregate with bottom ash and concluded that compressive strength of concrete mixes was higher in comparison to control concrete (without bottom ash), only up to 20% replacement of fine aggregate with bottom ash. Studies conducted by Raju et al [28] on concrete mixes prepared by replacement of up to 30% fine aggregate (by weight) with coal based bottom ash. Enhancement in mechanical properties of concrete mixes such as compressive, flexural and split tensile strength was observed only up to 20% replacement level. Above mentioned studies reveal that it is possible to incorporate and utilize coal based bottom ash as a partial replacement of conventional fine aggregate in cement concrete. Past studies have established the beneficial environmental impact of bottom ash utilisation in concrete as compared to conventional concrete [29-30]. Studies have proved bottom ash as a green and sustainable material that could decrease harmful environmental impact and promote sustainability in concrete production [31-32].

Research Significance:

Bureau of Indian Standards has permitted the use of manufactured aggregates in concrete through IS: 383-2016 [37]. It specifies that coal based bottom ash can be used as to replace conventional sand up to 25% in lean concrete only. However, the standard does not allow the use of coal based bottom ash in plain concrete and reinforced concrete. All across the globe, research studies on application of bottom ash as fine aggregate in concrete have been carried out at replacement levels varying from 10 to 100%. However, for wide use of bottom ash in construction as fine aggregate there is need for development of specification for conformance criteria in terms of physical and chemical parameters, so that end user can evaluate the bottom ash as per recommended specifications for use in concrete. Along with specifications, mix design guidelines and recommendations needs to be formulated for design of concrete mixes using coal based bottom ash as partial replacement of conventional sand in concrete. Present study focuses on development of specification for use of bottom ash as fine aggregate in concrete as well as formulation of guidelines for mix design of concrete mixes using bottom ash as part replacement of conventional fine aggregate.

2. Experimental Plan

Based on previous study conducted by Ojha et al [34-36], on feasibility study on possible utilisation of coal based bottom ash as replacement of conventional sand in concrete, it was concluded that up to 50% replacement of conventional sand with coal based bottom ash is viable in designed concrete mixes without affecting durability performance of concrete. The above recommendation was based on the bottom ash collected from only two sources. To formulate the specifications, in present study bottom ash samples were collected from 10 thermal power plants spread across various regions of India and those samples were characterized for their respective physical and chemical properties. Based on characterization results, specifications of bottom ash will be derived, for its use as a part replacement of conventional fine aggregate. Present study also covers studies on concrete mixes prepared using 21 selected composite fine aggregate (covering bottom ashes from all the sources). All the concrete mixes were evaluated for initial slump, air content, wet density and compressive strength. Durability studies were also carried out on selected concrete mixes. Based on aforementioned studies, mix design guidelines and

recommendations were formulated for use of bottom ash as part replacement of conventional fine aggregate in concrete.

3. Characterization of Bottom Ash Samples

3.1. Physical Characterization

Bottom ash samples collected from 10 thermal power plants were evaluated for their different physical characteristics such as sieve analysis, water absorption, specific gravity, material finer than 75 microns and soundness as per relevant parts of IS 2386. Sieve analysis of bottom ash samples were carried out and fineness modulus was determined and compared with fineness modulus of zone of fine aggregate as specified in IS 383:2016 and the results are given in Table 1.

Table 1. Sieve analysis results (gradation) of bottom ash samples

IS Sieve Size	Percentage Passing (%)									
	Plant No.									
	1	2	3	4	5	6	7	8	9	10
10 mm	100	100	100	100	100	100	100	99	100	98
4.75 mm	98	100	100	94	100	100	97	97	100	94
2.36 mm	96	100	99	87	100	99	95	95	100	88
1.18 mm	94	99	98	80	100	95	91	93	100	80
600 μm	87	93	96	68	99	86	83	89	100	69
300 μm	74	68	81	41	93	62	62	76	98	44
150 μm	37	25	27	15	38	20	28	36	86	15
Fineness Modulus	1.14	1.15	1	2.15	0.67	1.38	1.44	1.15	0.16	2.12
Zone as per IS:383-2016	Finer than ZoneI V	Finer than ZoneI V	Finer than ZoneI V	ZoneI II	Finer than ZoneI V	Finer than ZoneI V	Finer than ZoneI V	Finer than ZoneI V	Finer than ZoneIV	Zone III

Individual grading of all bottom ash indicates that all the bottom ash samples are finer than Zone 4 except bottom ash from plant-4 and plant-10. Fineness modulus of bottom ashes are in the range of 0.16 to 2.15. It is observed that fineness modulus of plant-9 was lowest i.e. 0.16 and that of plant-4 was highest i.e. 2.15. The results of other physical properties of bottom ash samples are given in Table 2 below.

Values of specific gravity of all samples are varying from 1.7 to 2.05 and are observed to be less than the conventional fine aggregate, whose specific gravity values are in the range of 2.6 to 2.9. In case of water absorption (tested as per IS 2386), it was observed that apart from plant-6 and plant-7, water absorption values of other bottom ash samples are in the range of 0.49 to 1.82 and are comparable with conventional fine aggregate. In case of accelerated mortar bar results (conducted as per ASTM 1260), expansion of mortar bars made using bottom ash samples as fine aggregate less than maximum limit (i.e. 0.1 %) as per ASTM C 1260. Therefore, samples of bottom ash from all sources are innocuous in nature. In order to decide specifications for physical characteristics of bottom ash as a replacement to conventional fine aggregate in concrete, requirement in terms of fineness modulus, water absorption, material finer than 75 microns and soundness has been considered to evaluate the bottom ash samples collected from 10 thermal power plants across India by studying its fresh, hardened and durability properties in concrete. Low value of fineness modulus of bottom ash will create issues with fresh concrete properties such as water demand, workability and ratio of coarse to fine aggregate. Limit on water

absorption of bottom ash as a fine aggregate is critical as higher water absorption can lead to higher slump loss and issues with workability of concrete.

Table 2. Results of Physical properties of Bottom Ash Sample

Test Carried out	Source of Bottom Ash Plant No.									
	1	2	3	4	5	6	7	8	9	10
Specific gravity	1.86	1.73	1.75	1.72	2.05	1.7	1.73	1.83	1.98	1.79
Water absorption %	0.64	1.69	1.36	1.23	0.49	6.89	5.19	1.82	1.43	1.52
Material finer than 75 μm % (wet sieving)	5.47	1.67	7.3	3.17	4.53	8.63	8.07	8.43	64.33	2.83
Soundness Na ₂ SO ₄ %	2.53	3.42	1.2	6.15	2.76	3.01	1.37	0.85	0.40	2.09
Organic impurities %	Nil	Nil	Nil	Nil	Nil	Nil	Nil	Nil	Nil	Nil
Clay Lumps %	Nil	Nil	Nil	Nil	Nil	Nil	Nil	Nil	Nil	Nil
Accelerated Mortar Bar ASTM C1260 %	0.04	0.03	0.04	0.02	0.05	0.04	0.05	0.03	0.07	0.06

Limit on material finer than 75 microns is critical as higher value will lead to more water demand and higher dosage of admixture to achieve similar fresh, mechanical and durability performance of concrete as in case of conventional fine aggregate. Higher value of materials finer than 75 microns can affect the compressive strength of concrete negatively. In order to avoid the expansion issues in concrete, the soundness limit are very important and higher soundness value can affect durability properties of concrete due to excessive change in volume of concrete. Based on the Physical characterization of bottom ash samples, it can be inferred that since very low value of fineness modulus of bottom ash will create issues with fresh concrete properties such as water demand, workability, ratio of coarse to fine aggregate, Minimum Fineness modulus of bottom ash has been kept at 1. Maximum value of water absorption of bottom ash to be used in concrete has been kept 2% as same is mentioned in Indian Standard IS: 383-2016 for conventional aggregate to be used in concrete. Maximum value of material finer than 75 μ has been 8.63%, therefore requirements for material finer than 75 μ has been kept at maximum 12%. Maximum value of Soundness of bottom ash by Na₂SO₄ has been observed 6.15%, therefore maximum limit of 10% has been considered. Similarly, maximum limit of soundness with MgSO₄ has been kept at 15%. Currently Indian standard, IS: 383-2016 permits conventional fine aggregate with limit of soundness with 10% and 15% for Na₂SO₄ and MgSO₄ respectively. All the results were well below this limit and same limit as conventional fine aggregate has been kept for bottom ash replacement as fine aggregate.

3.2 Chemical Characterization of Bottom Ash

Bottom ash samples from 10 thermal power plants were evaluated for their different chemical properties such as loss on Ignition, major constituents and minor constituents, total alkali content as Na₂O equivalent, chloride content and total Sulphur as S to establish the specifications of bottom ash. The results of chemical characterization of bottom ash samples have been tabulated in Table-3 below.

Table 3. Characterization of Bottom Ash Samples

Parameters	Source of Bottom Ash									
	Plant No.									
	1	2	3	4	5	6	7	8	9	10
Loss on Ignition %	0.28	0.28	0.78	0.82	0.12	0.19	0.67	2.72	0.41	1.21
SiO ₂ %	61.29	62.37	65.80	66.20	61.95	63.98	65.30	61.05	62.08	66.38
Fe ₂ O ₃ %	8.64	8.06	3.88	4.10	12.63	6.21	4.06	5.86	5.52	4.03
Al ₂ O ₃ %	23.45	22.91	23.89	21.03	19.01	24.48	25.80	24.93	26.65	20.47
CaO %	2.02	2.15	1.02	3.54	1.88	1.05	1.25	1.20	2.21	4.16
MgO %	0.61	0.62	0.92	1.00	0.92	1.44	1.15	1.91	1.27	1.78
Total Sulphur (as S) %	0.33	0.27	0.24	1.50	0.39	0.10	0.10	0.12	0.08	0.17
Na ₂ O _{equi.} %	0.84	1.03	0.88	0.89	0.95	0.69	0.66	1.01	0.73	0.93
Cl %	0.014	0.008	0.010	0.006	0.011	0.011	0.011	0.030	0.010	0.011
SO ₃ %	0.06	0.05	0.09	0.11	0.06	0.93	0.13	0.18	0.14	0.22
TiO ₂ %	1.94	1.67	1.80	1.46	1.70	0.34	0.36	0.35	0.36	0.28
Cr ⁺³ %	0.013	0.012	0.013	0.013	0.013	0.047	0.041	0.041	0.053	0.044

Keeping in view that bottom ash is a man-made material produced from thermal power plants and composition of coal and manufacturing process can have impact on the chemical characteristics of bottom ash which can subsequently affect the fresh, hardened and durability properties of concrete, when bottom ash is used as fine aggregate. The fine aggregates may contain different chemical constituents that react with coarse aggregate or cement paste matrix and form cracks on concrete surface which affects mechanical and durability performance. Therefore, the aggregates must be tested to ensure that such kinds of particles are not present in aggregates. In order, to have uniformity in quality of bottom ash as a fine aggregate and its consistent performance in concrete, limits on loss on ignition, SiO₂ content, MgO content, SO₃ content, acid soluble chloride content, total chloride content and total alkali content as Na₂O equivalent has been considered, Maximum value of loss on ignition was observed 2.72%, therefore requirement for loss on ignition has been kept at maximum 3%. Minimum value of SiO₂ was observed 61.05%, therefore requirement for SiO₂ has been kept Minimum 50%. Maximum value of MgO was observed 1.91%, therefore requirement for MgO has been kept at maximum 3%. Maximum value of SO₃ was observed 0.93%, therefore requirement for SO₃ has been kept at maximum 2%. Maximum value of acid soluble chloride was observed 0.03%, therefore requirement for acid soluble chloride has been kept at maximum 0.04%. Maximum value of Total Chloride was observed 0.048%, therefore requirement for total chloride has been kept at maximum 0.05%. Maximum value of total alkalies as Na₂O equivalent was observed 1.03, therefore requirement for total alkalies as Na₂O equivalent has been kept Maximum 1.5% and this does not have any impact on alkali silica reaction as expansion values in accelerated mortar bar test are within permissible limit.

3.3. Study of Size and Grading of Composite Fine Aggregate for Preparation of Guidelines for Mix Design

In order to effectively utilize bottom ash as fine aggregate in concrete, it is imperative to study the grading and size distribution of bottom ash, as this will affect the fresh concrete properties such as water demand, ratio of coarse aggregate to fine aggregate, workability, air content wet density etc. There was total 10 sources of bottom ash in which Bottom ash from Plant-9 and Plant-1 were not considered in study for formulation of guidelines for

concrete mix design as the bottom ash from Plant-9 was very fine and fineness modulus is comparable with that of coarse fly ash. Whereas, Plant-1 has been shut down permanently. In this study, bottom ash samples from 8 sources (i.e. except Plant-1 and Plant-9) were mixed with fine aggregate from natural source of Zone- II & III and crushed sand of Zone-I, II & III as part replacement of 10%, 20%, 30%, 40% and 50%. Total 200 composite fine aggregate (8 sources of Bottom Ash × 5 Source of fine aggregate × 5 different percentage replacement) were worked out theoretically.

Table 4. Composition of 21 composite fine aggregates selected for further study

Sl. No.	Fineness Modulus	Fineness Modulus Range	Bottom Ash Source	Percentage Replacement	Fine Aggregate Source
CFA-1	1.33	1.33-1.69	Plant-5	50%	Natural Sand Zone-III
CFA-2	1.47		Plant-3	50%	Natural Sand Zone-III
CFA-3	1.55		Plant-8	50%	Natural Sand Zone-III
CFA-4	1.67		Plant-6	50%	Natural Sand Zone-III
CFA-5	1.68		Plant-2	50%	Crushed Sand Zone-III
CFA-6	1.68		Plant-5	40%	Crushed Sand Zone-II
CFA-7	1.71		Plant-2	30%	Natural Sand Zone-III
CFA-8	1.7		Plant-7	50%	Natural Sand Zone-III
CFA-9	1.78	1.7-1.89	Plant-8	40%	Crushed Sand Zone-III
CFA-10	1.8		Plant-5	40%	Natural Sand Zone-II
CFA-11	1.84		Plant-3	30%	Crushed Sand Zone-III
CFA-12	1.97		Plant-7	40%	Crushed Sand Zone-II
CFA-13	1.99	1.9-2.09	Plant-10	20%	Natural Sand Zone-III
CFA-14	2.05		Plant-4	50%	Natural Sand Zone-III
CFA-15	2.06		Plant-3	20%	Crushed Sand Zone-II
CFA-16	2.16	2.1-2.49	Plant-10	50%	Crushed Sand Zone-III
CFA-17	2.25		Plant-8	20%	Natural Sand Zone-II
CFA-18	2.38		Plant-5	30%	Crushed Sand Zone-I
CFA-19	2.41		Plant-4	30%	Natural Sand Zone-II
CFA-20	2.76		Plant-6	20%	Crushed Sand Zone-I
CFA-21	2.61		Plant-10	50%	Crushed Sand Zone-I

Grading of all 200 composite fine aggregates have been calculated mathematically based on weightage average. Fineness modulus values of all the composite fine aggregates are in the range of 1.33 to 3.01 and has been further categorized in 5 different ranges of fineness modulus (i.e. 1.33-1.69, 1.70- 1.89, 1.90-2.09, 2.1-2.49, 2.50- 3.01) on the basis fineness modulus of all zone of sands as mentioned in above table. A matrix was prepared for 200 composite fine aggregate in 5 different ranges. Out of total 200, Composite Fine Aggregate (CFA), 21 composite fine aggregates were selected on the basis of their fineness modulus, criticality and were also selected in such a manner that Bottom ash from all the 8 sources and all types of fine aggregates of different zones are covered for the further studies on concrete mix design. Composite Fine Aggregates (CFA) selected for further study were selected in such a way that they cover different ranges of fineness modulus, different proportions of replacement (i.e. 20, 30, 40 and 50%) and bottom ash samples from all possible sources. Composition of Composite Fine Aggregates (CFA) selected for further study has been tabulated below in table 4.

The actual sieve analysis was carried out for the selected 21 composite fine aggregates from all ranges as mentioned above. The sample of bottom ash was mixed with the fine aggregate as per the percentage of part replacement as mentioned for their respective composite fine aggregates and the fineness modulus was determined experimentally. The fineness modulus of experimentally determined values and mathematically calculated values of all the 21 composite mixes were found to be comparable and were within the deviation of +10%. Sieve analysis along with fineness modulus of aforementioned composite fine aggregates has been tabulated below in Table 5.

Table 5. Sieve analysis results of selected composite fine aggregate

Sieve Size	CFA-1	CFA-2	CFA-3	CFA-4	CFA-5	CFA-6	CFA-7
	% Passing						
10 mm	100	100	100	100	100	100	100
4.75 mm	100	100	100	100	100	100	100
2.36 mm	100	100	95	100	96	95	100
1.18 mm	97	96	96	94	85	80	95
600 µm	88	88	84	84	74	72	86
300 µm	61	55	54	48	56	58	35
150 µm	22	18	23	16	24	29	14
Fineness Modulus	1.32	1.49	1.48	1.58	1.65	1.66	1.70
Sieve Size	CFA-8	CFA-9	CFA-10	CFA-11	CFA-12	CFA-13	CFA-14
	% Passing						
10 mm	100	100	100	100	100	100	100
4.75 mm	100	98	99	99	98	98	98
2.36 mm	99	92	91	92	93	98	95
1.18 mm	92	78	90	84	76	96	88
600 µm	83	74	74	72	60	76	75
300 µm	47	56	46	53	52	33	36
150 µm	18	25	20	23	30	8	12
Fineness Modulus	1.61	1.77	1.8	1.77	1.91	1.91	1.96
Sieve Size	CFA-15	CFA-16	CFA-17	CFA-18	CFA-19	CFA-20	CFA-21
	% Passing						
10 mm	100	100	100	100	100	100	99
4.75 mm	100	98	95	100	94	100	98
2.36 mm	92	86	94	88	92	81	85
1.18 mm	74	79	88	62	84	62	69
600 µm	61	65	66	55	58	44	46
300 µm	44	45	30	44	27	32	31
150 µm	31	19	14	23	12	12	16
Fineness Modulus	1.98	2.08	2.13	2.28	2.33	2.59	2.56

4. Concrete Mix Trials and Determination of Properties of Concrete Mixes in Fresh State and Their Compressive Strength for Formulation of Concrete Mix Design Guidelines

As per guidelines given in IS 10262:2019 [37] for the concrete mix design, concrete mix trials were conducted to determine the parameters required for formulation of guidelines i.e. air content in fresh concrete; water required for workability of fresh concrete for slump 25 mm- 50 mm; additional percentage of water required for every 25 mm increase in slump; estimation of proportion of coarse aggregate (i.e. volume of coarse aggregate per

unit volume of total aggregate). Concrete mix trials were conducted at different water content and different ratios of coarse to fine aggregate to determine the aforementioned parameters. Concrete mix trials were conducted using OPC-43 and 21 number of selected composite fine aggregates at water to binder ratio of 0.5 and for maximum aggregate size of 20 mm. All the mixes were cast without any chemical admixture. Coarse and fine aggregate conforming to IS 383:2016 [33] and OPC-43 grade cement conforming to IS 269:2015 [38] were used for conducting trials and preparation of concrete mixes. The target compressive strength for the mixes designed with composite fine aggregate and control mixes were 31.62 MPa which corresponds to M25 grade concrete mix design. Total 70 concrete mix trials with OPC-43 grade cement using 21 composite fine aggregate were conducted and properties of concrete in fresh state such as air content, wet density and workability in terms of slump were determined. Mixes were also evaluated for compressive strength at 28 days. Several trials were conducted to determine the volume of coarse aggregate per unit volume of total aggregates. Details of all concrete mix trials along with their fresh properties and compressive strength at 7 and 28 days have been tabulated in table 6.

Table 6. Details of trials conducted using composite fine aggregates, fresh properties and compressive strength of trial mixes

Sl. no	Composite fine aggregate	% of bottom ash in composite fine aggregate	Ratio of coarse and fine aggregate	Water kg/m ³	Slump mm	Air Content %	Wet Density kg/m ³	Comp. Strength	
								7 Days MPa	28 Days MPa
1	CFA-1	50%	(70:30)	186	25	1.8	2430	27.35	33
2	CFA-1	50%	(72:28)	186	25	1.6	2400	27.57	36.08
3	CFA-1	50%	(72:28)	194	45	1.4	2428	23.94	31.92
4	CFA-1	50%	(74:26)	194	70	1.2	2391	23.86	32.06
5	CFA-2	50%	(68:32)	194	20	1.8	2381	27.36	34.78
6	CFA-2	50%	(70:30)	194	25	1.4	2405	26.74	33.65
7	CFA-2	50%	(70:30)	202	60	1.2	2389	24.89	32.5
8	CFA-3	50%	(68:32)	194	25	1.3	2417	25.09	32.9
9	CFA-3	50%	(70:30)	194	35	1.3	2443	24.31	32.6
10	CFA-3	50%	(72:28)	194	40	1.3	2396	25.27	34.59
11	CFA-4	50%	(68:32)	194	30	1.7	2438	22.35	33.76
12	CFA-4	50%	(70:30)	194	30	1.5	2470	24.59	34.7
13	CFA-4	50%	(72:38)	194	50	1.3	2430	24.88	35.1
14	CFA-4	50%	(72:38)	202	75	1.5	2466	22.96	33.9
15	CFA-5	50%	(68:32)	194	10	1.9	2415	27.84	35.43
16	CFA-5	50%	(70:30)	194	10	2.0	2400	26.99	34.78
17	CFA-5	50%	(70:30)	204	30	1.9	2396	24.8	35.34
18	CFA-6	40%	(68:32)	194	20	1.5	2437	25.61	35.7
19	CFA-6	40%	(68:32)	202	40	1.5	2419	24.03	34.76
20	CFA-6	40%	(70:30)	202	45	1.2	2410	28.95	35.78
21	CFA-6	40%	(72:28)	202	45	1.0	2425	25.04	34.5
22	CFA-7	30%	(68:32)	194	40	1.2	2453	28.82	35.65
23	CFA-7	30%	(70:30)	194	50	1.5	2471	29.37	36.89
24	CFA-7	30%	(72:28)	194	50	1.7	2462	26.23	34.76
25	CFA-8	50%	(68:32)	194	20	1.5	2442	27.52	34.65
26	CFA-8	50%	(70:30)	194	20	1.5	2469	29.2	35.98
27	CFA-8	50%	(70:30)	202	45	1.4	2427	24.33	34.65
28	CFA-9	40%	(68:32)	194	35	1.8	2404	22.05	33.76
29	CFA-9	40%	(70:30)	194	45	1.6	2396	23.68	33.89
30	CFA-9	40%	(72:28)	194	45	1.9	2384	24.44	35.87
31	CFA-10	40%	(68:32)	194	40	1.5	2393	26.39	35.78

32	CFA-10	40%	(70:30)	194	50	1.5	2426	27.5	35.2
33	CFA-10	40%	(72:28)	194	45	1.5	2412	26.77	34.97
34	CFA-11	30%	(68:32)	194	35	1.7	2453	28.71	34.54
35	CFA-11	30%	(70:30)	194	45	1.2	2468	28.93	35.65
36	CFA-11	30%	(70:30)	202	75	1.1	2441	24.16	34.90
37	CFA-12	40%	(66:34)	194	10	Mix was not cohesive and was not evaluated further			
38	CFA-12	40%	(66:34)	202	25	1.7	2439	26.95	34.7
39	CFA-12	40%	(68:32)	194	25	1.3	2376	24.74	31.87
40	CFA-13	20%	(68:32)	194	25	1.5	2390	26.39	33.43
41	CFA-13	20%	(68:32)	202	35	1.3	2376	24.74	31.87
42	CFA-13	20%	(70:30)	194	20	1.3	2419	27.28	34.8
43	CFA-14	50%	(66:34)	194	40	2.1	2480	27.11	35.89
44	CFA-14	50%	(68:32)	194	40	1.6	2473	27.39	35.5
45	CFA-14	50%	(68:32)	202	60	1.3	2448	26.82	34.6
46	CFA-14	50%	(70:30)	194	50	1.5	2436	29.06	36.1
47	CFA-15	20%	(64:36)	194	30	1.6	2482	24.53	34.87
48	CFA-15	20%	(66:34)	194	30	1.2	2492	26.02	35.76
49	CFA-15	20%	(68:32)	194	35	1.2	2504	24.69	34.7
50	CFA-15	20%	(68:32)	202	50	1.7	2468	22.03	33.85
51	CFA-16	50%	(62:38)	194	10	1.2	2430	28.31	35.6
52	CFA-16	50%	(62:38)	204	70	1.0	2449	24.04	32.8
53	CFA-16	50%	(68:32)	194	45	1.6	2428	22.64	31.6
54	CFA-16	50%	(70:30)	194	90	1.2	2433	22.5	31.9
55	CFA-16	50%	(72:28)	194	95	1.2	2420	25.68	33.76
56	CFA-17	20%	(66:34)	194	40	1.4	2452	26.5	33.52
57	CFA-17	20%	(68:32)	194	60	1.6	2443	26.62	32.90
58	CFA-17	20%	(70:30)	194	80	1.4	2429	26.23	32.97
59	CFA-18	30%	(64:36)	194	40	1.5	2459	26.62	35.7
60	CFA-18	30%	(66:34)	194	50	1.5	2411	28.71	36.76
61	CFA-18	30%	(66:34)	202	80	1.0	2426	28.06	35.98
62	CFA-18	30%	(68:32)	194	40	1.6	2390	27.33	34.76
63	CFA-19	30%	(64:36)	194	50	1.6	2387	24.87	33.32
64	CFA-19	30%	(66:34)	194	50	1.9	2425	26.37	34.7
65	CFA-20	20%	(62:38)	194	45	1.4	2371	29.06	35.8
66	CFA-20	20%	(64:36)	194	55	1.4	2369	30.01	36.12
67	CFA-20	20%	(64:36)	202	90	1.3	2405	28.43	35.56
68	CFA-21	50%	(64:36)	194	50	1.5	2493	27.56	35.89
69	CFA-21	50%	(62:38)	186	10	Mix was not cohesive and was not evaluated further			
70	CFA-21	50%	(62:38)	194	40	1.8	2461	30.89	40.04
71	Control-1	100%	(70:30)	194	75	1.9	2385	32.89	38.25
72	Control-2	100%	(68:32)	209	65	1.6	2421	31.79	37.65

For concrete mixes using composite fine aggregates lying in the fineness modulus range of 1.33-1.69, it was observed that for concrete mix having volume of coarse aggregate per unit volume of total aggregate of 0.72 and water content at 194 kg, the mix was cohesive and desired slump was achieved (i.e. 25 mm- 50 mm) without chemical admixture. Due to very low fineness modulus, the composite fine aggregate percentage was kept low and after further reducing the composite fine aggregate the mix was not found cohesive. For concrete mixes using composite fine aggregates lying in the fineness modulus range of 1.70-1.89, it was observed that for concrete mix having volume of coarse aggregate per unit volume of total aggregate of 0.70 and water content at 194 kg, the mix was cohesive and the desired slump (i.e. 25 mm- 50 mm) was achieved without chemical admixture. For concrete mixes using composite fine aggregates lying in the fineness modulus range of 1.9-2.09, it was observed that for concrete mixes at volume of coarse aggregate per unit volume of total aggregate of 0.68 and water content at 194 kg, the mix was cohesive and required slump (i.e. 25 mm- 50 mm) was achieved. Similarly, for concrete mixes using composite

fine aggregates lying in the fineness modulus range of 2.1-2.49, volume of coarse aggregate per unit volume of total aggregate of 0.66 and water content of 194 kg per cum has been finalized to achieve the slump value of 25 mm- 50 mm. Similarly, for concrete mixes using composite fine aggregates lying in the fineness modulus range of 2.5- 3.01, volume of coarse aggregate per unit volume of total aggregate of 0.64 has been finalized as the fineness modulus of composite fine aggregate is comparable to coarser range of Zone-II and finer range of Zone-I. Along with above, in general for all concrete mix trials using different composite fine aggregates, it was observed that air content of all the mixes were varying from 1.0% to 2.0%. Majority of the values were lying near 1.5%. Therefore, air content of 1.5% shall be considered for the design mix of concrete mix incorporating bottom ash as part replacement of conventional fine aggregates. It was observed that at 194 kg of water per cubic meter of concrete, desired slump (i.e. 25 to 50 mm) was achieved without any chemical admixture. To achieve additional 25 mm slump above 50 mm, additional 4% of water shall be added as per Indian Standard IS: 10262-2019 procedure. The compressive strength of concrete mixes at 28 days of all the trials using composite fine aggregates (containing bottom ash) were comparable with the compressive strength of control concrete mixes made with 100% conventional fine aggregates i.e. natural and crushed sand. Based on above trials the volume of coarse aggregate per unit volume of total aggregate for different ranges of fineness modulus of composite fine aggregate at water to cement ratio of 0.50 and nominal maximum size of aggregate as 20 mm for which the mixes were observed to be cohesive have been tabulated in table 7 for design mix of concrete.

Table 7. Volume of coarse aggregate per unit volume of total aggregate for water-cement ratio of 0.50 and nominal maximum size of aggregate of 20 mm

Fineness Modulus of composite fine aggregate	1.33-1.69	1.7-1.89	1.9-2.09	2.1-2.49	2.5-3.01
Volume of Coarse Aggregate per Unit Volume of total Aggregate	0.72	0.70	0.68	0.66	0.64

5. Studies on Durability Properties of Selected Concrete Mixes

Out of total 70 mixes using OPC-43 cement, 8 concrete mixes were selected for further studies on long term durability related properties of concrete as mentioned below:

- Pore structure using MIP
- Accelerated Carbonation Test at 28 days as per ISO 1920- Part-12
- Rapid Chloride Permeability Test (RCPT) as per ASTM C 1202
- Electrical resistivity of concrete by four-point Wenner Probe method

The mixes were selected keeping in view the fineness modulus of composite fine aggregate to cover the fineness modulus range from 1.33 to 2.25 and the replacement percentage of composite fine aggregate of bottom ash between 20 to 50 percent. This was done to cover that upper, lower and middle range of fineness modulus and replacement percentage of composite fine aggregate and also to cover the maximum number of sources into consideration. Two concrete mixes containing 100% conventional fine aggregates (one concrete mix with 100% natural sand and one concrete mix with 100% crushed sand) were selected to act as control concrete mixes. Further, 6 experimental concrete mixes prepared using composite fine aggregates having different proportions of bottom ash from different sources) were selected. Out of six experimental mix, two mixes had composite fine aggregate containing 20% bottom ash, one mix had composite fine aggregate containing 30% bottom ash and three mixes had composite fine aggregate containing 50% bottom ash as part replacement of conventional fine aggregate.

5.1 Pore Structure Using Mercury Intrusion Porosity (MIP)

Mortar sample extracted from hardened concrete was evaluated for porosity percentage, total pore volume, average pore diameter and median pore diameter using Mercury Intrusion Porosimeter (MIP) equipment. Mercury was intruded into the sample at pressure of 350 MPa for measurement of aforementioned parameters related to pore structure and test results have been tabulated below in table 8 and test setup used for evaluation of parameters associated to pore structure has been shown in figure 1.

Table 8. Pore structure parameters of mixes using Mercury Intrusion Porosity

Mix	Fineness modulus of fine aggregate	Source of Bottom ash	% of bottom ash in fine aggregate	Type of conventional Fine aggregate	Porosity of Mortar using MIP	Total Pore Volume (mm ³ /g)	Average pore diameter (nm)	Median pore diameter (nm)
Mix-1	1.96	-	0%	Natural Sand Zone-3	9.38	45.03	24.39	48.90
Mix-2	2.21	-	0%	Crushed Sand Zone 3	15.93	78.09	26.36	66.05
Mix-3	1.33	Plant-5	50%	Natural Sand Zone 3	14.16	67.69	48.48	221.30
Mix-4	1.68	Plant-2	50%	Crushed Sand Zone 3	12.86	60.68	67.59	165.16
Mix-5	1.7	Plant-7	50%	Natural Sand Zone 3	11.50	51.99	61.34	254.06
Mix-6	1.84	Plant-3	30%	Crushed Sand Zone 3	10.49	50.46	35.33	61.09
Mix-7	1.99	Plant-10	20%	Natural Sand Zone 3	10.58	49.53	52.91	112.02
Mix-8	2.25	Plant-8	20%	Natural Sand Zone 2	7.16	18.72	37.40	147.20



Fig. 1 Test setup for evaluation of pore structure



Fig. 2 Accelerated Carbonation Test

Porosity of control sample (without Bottom ash) was 9.38% to 15.93 %. Whereas, for concrete samples containing composite fine aggregate, porosity values are varying from 7.16 to 14.16%. Total pore volume of control samples (without bottom ash) are 45.03

mm³/g to 78.09 mm³/g. Whereas for concrete samples containing composite fine aggregate values of total pore volume varies from 18.72 to 67.69 mm³/g which is comparable to control concrete.

The average pore diameter of control samples (without bottom ash) are 24.39 nm to 26.36 nm. Whereas, for concrete samples containing composite fine aggregate values of average pore diameter varies from 35.33 to 67.59 nm. Again, the median pore diameter of control samples (without bottom ash) are 48.90 to 66.05 nm. Whereas, for concrete samples containing composite fine aggregate values of average pore diameter varies from 66.09 to 254.06 nm. The results of porosity and total pore volume are in the similar range but wide variation between the average pore diameter and median pore diameter results of concrete with conventional aggregate and composite fine aggregate is seen. With the replacement of bottom ash as a fine aggregate the nucleation sites sometimes gets formed in the cement hydration products and intrusion of mercury in composite fine aggregate though is same, pore diameters are different.

5.2. Carbonation Chamber Used for Accelerated Carbonation Test

Accelerated carbonation test on selected concrete mixes was conducted as per adopted as per ISO 1920 part 12. Concrete specimens (dimension 100 × 100 × 500 mm) were cast and cured in water at temperature of 27 ± 2 °C for 28 days and then conditioned under controlled laboratory environment for 14 days at temperature of 27 ± 2 °C and relative humidity of 65 ± 5 % [39-41]. Carbonation depth of concrete specimen after 70 days of carbonation has been tabulated in table 9 Carbonation chamber used for accelerated carbonation of concrete specimen has been shown in figure 2. The carbonation depth of control concrete samples (without bottom ash) are observed to be 6.6 mm and 9.5 mm. Whereas, for the concrete mixes made with composite fine aggregates, carbonation depths are in the range of 5.5 to 11.0 mm. This suggest that, the carbonation depth values of concrete mixes made with composite aggregate (bottom ash as part replacement of conventional fine aggregate) and control concrete mixes (without bottom ash) are similar and comparable as the range is around 5 to 11 mm for both types of fine aggregate.

5.3. Rapid Chloride Penetrability Test

This test is used to evaluate any material against the chloride ion penetration. RCPT test was carried out as per procedure laid down in ASTM C 1202. This test was carried out on saturated 50 mm thick concrete disc of 100 mm diameter extracted from cylindrical concrete specimen having 100 mm diameter and 200 mm length. The total charge passed (in coulombs) through samples of all the concrete mixes at the age of 28 days is given in table 9 and is related to the chloride ion penetrability class according to the criteria given in ASTM C1202. The RCPT results of all the mixes (including control mixes) shows that all mixes are lying in the same class of penetrability (i.e. 2000- 4000 coulombs, Moderate degree of penetrability). Therefore, performance of concrete mixes prepared with composite fine aggregate against chloride ion penetration is similar and comparable with the control concrete mixes (without bottom ash).

5.4. Electrical Resistivity of Concrete

Electrical resistivity testing of concrete slabs (300 × 300 × 100 mm) was conducted using four-point Wenner probe resistivity meter which is used for in-situ measurement of electrical resistivity in concrete [42-44]. Resistivity meter permits a rapid and non-destructive measurement of the quality of concrete with respect to its resistivity. Test results of concrete resistivity for concrete mixes are given in table 9. The electrical resistivity values of control concrete mixes are 7.1 and 6.1 k-ohm-cm. Whereas concrete mixes with composite fine aggregate are in the range of 6.7 to 8.58 k-ohm-cm. This suggest that, the electrical resistivity values of concrete mixes made with composite aggregate

(bottom ash as part replacement of conventional fine aggregate) and control concrete mixes (without bottom ash) are almost similar and comparable.

Table 9. Accelerated carbonation depth, RCPT and electrical resistivity of selected concrete mixes

Mix	Fineness Modulus of fine aggregate	Bottom ash Source	% Replacement of fine aggregate using bottom ash	Conventional Fine aggregate (Type)	RCPT (Coulombs) After 28 days	Electrical Resistivity (k-Ω-cm) After 28 days	Accelerated Carbonation depth (mm) After 70 days of carbonation
Mix-1	1.96	-	0%	Natural Sand Zone-3	3575	7.1	6.5
Mix-2	2.21	-	0%	Crushed Sand Zone 3	3670	6.1	9.5
Mix-3	1.33	Plant-5	50%	Natural Sand-Zone 3	3446	7.5	10.0
Mix-4	1.68	Plant-2	50%	Crushed Sand-Zone 3	2873	8.58	6.2
Mix-5	1.7	Plant-7	50%	Natural Sand-Zone 3	2874	7.3	6.5
Mix-6	1.84	Plant-3	30%	Crushed Sand-Zone 3	2284	7.5	5.5
Mix-7	1.99	Plant-10	20%	Natural Sand-Zone 3	3194	6.7	11.0
Mix-8	2.25	Plant-8	20%	Natural Sand-Zone 2	3686	7.2	11.0

6. Conclusion and Recommendations

Based on the detailed study done and literature reviewed to develop recommendations for specifications of bottom ash and concrete mix design guidelines by carrying out studies on bottom ash samples collected from 10 thermal power plants across India, the following conclusions and recommendations are drawn:

Based upon the Physical characterization of bottom ash samples, minimum fineness modulus of bottom ash has been kept at 1 as low value of fineness modulus of bottom ash creates issues with fresh concrete properties such as water demand, workability and ratio of coarse to fine aggregate. Maximum value of water absorption of bottom ash to be used in concrete has been kept 2%. Maximum value of material finer than 75 μ has been 8.63%, therefore requirements for material finer than 75 μ has been kept at maximum 12%. Maximum value of Soundness of bottom ash by Na₂SO₄ has been observed 6.15%, therefore maximum limit of 10% has been considered. Similarly, maximum limit of soundness with MgSO₄ has been kept at 15%. Based upon the chemical characterization of bottom ash samples, maximum value of loss on ignition was observed to be 2.72%, therefore requirement for loss on ignition has been kept at maximum 3%. Minimum value of SiO₂ was observed 61.05%, therefore requirement for SiO₂ has been kept Minimum 50%. Maximum value of MgO was observed 1.91%, therefore requirement for MgO has been kept at maximum 3%. Maximum value of SO₃ was observed 0.93%, therefore requirement for SO₃ has been kept at maximum 2%. Maximum value of acid soluble chloride was observed 0.03%, therefore requirement for acid soluble chloride has been kept at maximum 0.04%. Maximum value of Total Chloride was observed 0.048%, therefore requirement for total chloride has been kept at maximum 0.05%. Maximum value of total alkalis as Na₂O equivalent was observed 1.03, therefore requirement for total alkalis as Na₂O equivalent has been kept Maximum 1.5%. Based upon findings and conclusions on

physical and chemical characteristics of bottom ash to be used in concrete as part replacement of fine aggregate, recommendations for specification of physical and chemical characteristics of bottom ash are given below in Table 10 & Table 11.

Table 10. Recommendations for Specification for physical characteristics of bottom ash

Physical Parameter	Requirement
Material finer than 75 μ , % Max	12
Fineness Modulus of Bottom Ash, Min and Max	1 and 4
Water absorption Max	2
Soundness (Na ₂ SO ₄), % Max	10
Soundness (MgSO ₄), % Max	15

Table 11. Recommendations for Specifications for chemical characteristics of bottom ash

Chemical Parameter	Requirement
Loss on Ignition, % Max	3
SiO ₂ , % Min	50
MgO, % Max	3
SO ₃ , % Max	2
SiO ₂ +Al ₂ O ₃ +Fe ₂ O ₃ , % Min	60
Acid Soluble Chloride, % Max	0.04
Total Chloride, %, Max	0.05
Total Alkalies as Na ₂ O equivalent, % Max	1.5

Composite fine aggregate recommended for use in concrete is a mixture of fine aggregate (i.e. natural/ crushed sand) and bottom ash. Conventional fine aggregate is partly replaced with bottom ash in different percentage by weight to make composite fine aggregate of required fineness modulus. Based on the aforementioned trials, recommendations for composite fine aggregate are that composite fine aggregate shall be a mixture of conventional fine aggregate (i.e. natural/crushed sand) and coal based bottom ash. Maximum replacement of conventional fine aggregate with coal based bottom ash for preparation of OPC based cement concrete shall not exceed 50% by weight of total fine aggregate. Sieve analysis of conventional fine aggregate and coal based bottom ash shall be done and fineness modulus of both shall be determined. Conventional fine aggregate shall be replaced by bottom ash in such proportion (not exceeding the permissible limit of 50 %) that fineness modulus of the resultant composite fine aggregate for use in concrete as fine aggregate shall be at least 1.35. The specific gravity of composite fine aggregate (as prepared by the procedure given above) shall be determined mathematically as well as experimentally as per IS 2386.

Based on the aforementioned trials on 70 different concrete mixes, recommendations for concrete mix design using coal based bottom ash as part replacement of conventional sand are that value of entrapped air supposed to be in case of non-air entrained concrete having 20 mm maximum size of aggregate (MSA), shall be taken as 1.50%. In case of availability of experimental site data (at least five air content values for similar mix), actual air content values can be used during concrete mix proportioning. The quantity of water for one cubic meter concrete having MSA 20 mm shall be kept as 194 kg/m³. Aforementioned amount of water has been suggested for concrete mixes made using angular coarse aggregate, having initial slump value of 25 to 50 mm. The amount of water may be tentatively reduced by 10 kg, in case the aggregates are sub-angular in nature, by 15 kg in case of aggregates made

up of gravel along with some quantity of crushed particles and approximately by 20 kg in case the aggregates are rounded gravel to generate similar degree of workability as mentioned in Indian Standard IS: 10262-2019. For each increase or decrease in slump value of around 25 mm, recommended value of water may either be appropriately increased or decreased by approximately 4 percent or it may be established by carrying out appropriate trials. Volume of coarse aggregate per unit volume of total aggregate for concrete mix at w/c of 0.50 and 20 mm MSA shall be 0.72, 0.70, 0.68, 0.66 and 0.64 for composite aggregate having fineness modulus of 1.33-1.69, 1.7-1.89, 1.9-2.09, 2.1-2.49 and 2.5-3.01 respectively as tabulated above in table 7. These suggested proportions may be duly adjusted for concrete mixes prepared at water-cement ratios other than 0.50. The aforementioned proportion of coarse aggregates shall be increased at rate of 0.01, for every decrease in w/c by 0.05 and decreased at rate of 0.01 for every increase in w/c by 0.05. Other mix design parameters, such as maximum water-cement ratio, target mean strength, selection of water cement ratio along with other calculations shall be as per IS 10262: 2019.

References

- [1] Ojha PN, Singh B, Kaura P, Singh A. Lightweight geopolymer fly ash sand: an alternative to fine aggregate for concrete production. *Research on Engineering Structures and Materials*, 2021; 7(3): 375-392. <https://doi.org/10.17515/resm2021.257ma0205>
- [2] Muthusamy K, Rasid MH, Jokhio GA, Mokhtar Albshir Budiea A, Hussin MW, J Mirza. Coal bottom ash as sand replacement in concrete: A review. *Construction and Building Materials*, 2020; 236:117507. <https://doi.org/10.1016/j.conbuildmat.2019.117507>
- [3] Singh M, R Siddique. Effect of coal bottom ash as partial replacement of sand on properties of concrete. *Resour. Conserv. Recycl.*, 2013; 72:20-32. <https://doi.org/10.1016/j.resconrec.2012.12.006>
- [4] Singh N, Shehnazdeep B. Reviewing the role of coal bottom ash as an alternative of cement. *Construction and Building Materials*, 2020; 233:117276. <https://doi.org/10.1016/j.conbuildmat.2019.117276>
- [5] Seals RK, Moulton LK, Ruth BE, Bottom ash: An Engineering Material. *JSMFD, American Society of Civil Engineers*, 1972; 98 (SM4): 311-325. <https://doi.org/10.1061/JSEFAQ.0001741>
- [6] Andrade LB, Rocha JC, Cheriaf M. Aspects of moisture kinetics of coal bottom ash in concrete. *Cement and Concrete Research*, 2007; 37:231-241. <https://doi.org/10.1016/j.cemconres.2006.11.001>
- [7] Ghafoori N, Bucholc L. Investigation of Lignite-Based Bottom Ash for Structural Concrete, *ASCE J. Mater. Civ. Eng.*, 1996; 8:128-137. [https://doi.org/10.1061/\(ASCE\)0899-1561\(1996\)8:3\(128\)](https://doi.org/10.1061/(ASCE)0899-1561(1996)8:3(128))
- [8] Andrade LB, Rocha JC, Cheriaf M. Evaluation of concrete incorporating bottom ash as a natural aggregates replacement, *Waste Manage.*, 2007;27(9):1190- 1199. <https://doi.org/10.1016/j.wasman.2006.07.020>
- [9] Weber S, Reinhardt HW. A new generation of high-performance concrete: concrete with autogenous curing", *Adv. Cem Mater.*, 1997; 6(2): 59-68. [https://doi.org/10.1016/S1065-7355\(97\)00009-6](https://doi.org/10.1016/S1065-7355(97)00009-6)
- [10] Barbare N, Shukla A, Bose A. Uptake and loss of water in cenosphere-concrete composite material, *Cement and Concrete Research*, 2003; 33(10):1681-1686. [https://doi.org/10.1016/S0008-8846\(03\)00148-0](https://doi.org/10.1016/S0008-8846(03)00148-0)
- [11] Kasemchaisiri R, S Tangtermsirikul. A method to determine water retainability of porous fine aggregate for design and quality control of fresh concrete, *Construction and Building Materials*, 2007;21(6):1322-1334. <https://doi.org/10.1016/j.conbuildmat.2006.01.009>

- [12] Ghafoori N, Bucholc J. Investigation of lignite-based bottom ash for structural concrete", *Journal of materials in Civil Engineering*, 1996; 8(3):128-137. [https://doi.org/10.1061/\(ASCE\)0899-1561\(1996\)8:3\(128\)](https://doi.org/10.1061/(ASCE)0899-1561(1996)8:3(128))
- [13] Ghafoori N, Bucholc J. Properties of high-calcium dry bottom ash concrete, *ACI Materials Journal*, 1997; 94(2):90-101. <https://doi.org/10.14359/289>
- [14] Chengzhi Z, Ai Qin W, Mingshu T, Xiaoyu L. The filling role of pozzolanic material, *Cement and Concrete Research*, 1996; 26(6):943-947. [https://doi.org/10.1016/0008-8846\(96\)00064-6](https://doi.org/10.1016/0008-8846(96)00064-6)
- [15] Andrade LB, Rocha JC, Cheriaf M. Influence of coal bottom ash as fine aggregate on fresh properties of concrete, *Construction and Building Materials*, 2009; 23:609-614. <https://doi.org/10.1016/j.conbuildmat.2008.05.003>
- [16] Kadam MP, Patil YD. Effect of sieved coal bottom ash as a sand replacement on properties of cement concrete, *Magazine of Concrete Research*, 2015; 67(5): 227- 234. <https://doi.org/10.1680/macr.14.00179>
- [17] Kou SC, Poon CS, Properties of concrete prepared with crushed fine stone, furnace bottom ash and fine recycled aggregate as fine aggregates, *Construction and Building Materials*, 2009;23:2877-2886. <https://doi.org/10.1016/j.conbuildmat.2009.02.009>
- [18] Gooi S, Mousa AA, Kong D. A critical review and gap analysis on the use of coal bottom ash as a substitute constituent in concrete. *J. Clean. Prod.* 2020: 268:121752. <https://doi.org/10.1016/j.jclepro.2020.121752>
- [19] Bai Y, Darcy F, Basheer PAM. Strength and drying shrinkage properties of concrete containing furnace bottom ash as fine aggregate, *Construction and Building Materials*, 2005;19:691-697. <https://doi.org/10.1016/j.conbuildmat.2005.02.021>
- [20] Nikbin IM, Saman RR, Allahyari H, Damadi M. A comprehensive analytical study on mechanical properties of concrete containing waste bottom ash as natural aggregate replacement", *Construction and Building Materials*, 2016; 121:746-759. <https://doi.org/10.1016/j.conbuildmat.2016.06.078>
- [21] Singh M, Siddique R. Compressive strength, drying shrinkage and chemical resistance of concrete incorporating coal bottom ash as partial or total replacement of sand, *Construction and Building Materials*, 2014; 68:39-48. <https://doi.org/10.1016/j.conbuildmat.2014.06.034>
- [22] Lee HK, Kim HK, Hwang EA. Utilization of power plant bottom ash as aggregates in fiber-reinforced cellular concrete, *Waste Management*, 2010;30:274-284. <https://doi.org/10.1016/j.wasman.2009.09.043>
- [23] Ksaibati K, Stephen J. Utilization of Bottom Ash in Asphalt Mixes; No. MCP Report No. 99-104A. Department of Civil & Architectural Engineering, University of Wyoming; Laramie, USA; 1999.
- [24] Singh N, Mithulraj M, Arya S. Utilization of coal bottom ash in recycled concrete aggregates based self-compacting concrete blended with metakaolin. *Resour. Conserv. Recycl.* 2019; 144:240-251. <https://doi.org/10.1016/j.resconrec.2019.01.044>
- [25] Andrade, LB. Methodology of assessment to use of bottom ash of thermoelectric power plants as aggregate in concrete, M.Sc. Thesis, Department of Civil Engineering, Federal University of Santa Catarina, Santa Catarina, Brazil; 2004.
- [26] Singh, B, Ojha PN, Trivedi A, Patel, V, Arora VV. Development Of Empirical Equations For Prediction Of Flexural And Split Tensile Strength For Normal And High Strength Concrete With Granite And Calc-Granulite Aggregate, *Indian Concrete Journal*, 2021: 95 (11): 36-46.
- [27] Aggarwal P, Aggarwal Y, Gupta SM. Effect of Bottom Ash as replacement of fine aggregate in concrete, *Asian Journal of Civil Engineering (Building and Housing)*, 2007; 8 (1):49-62.
- [28] Arumugam K, Ilangovan R, Manohar JD, A study on characterization and use of pond ash as fine aggregate in concrete, *International Journal of Civil and Structural Engineering*, 2011;2 (2):466.

- [29] Raju R, Paul MM, Aboobacker KA, Strength performance of concrete using bottom ash as fine aggregate", *Int. J. Research Eng. Technol.*, 2014; 2:111-119.
- [30] Jamora JB, Gudia Sel, Go AW, Giduquio MB, Loretero ME. Potential CO₂ reduction and cost evaluation in use and transport of coal ash as cement replacement: A case in the Philippines. *Waste Manag.* 2020; 103:137-145. <https://doi.org/10.1016/j.wasman.2019.12.026>
- [31] Ankur N, Singh N. Performance of cement mortars and concretes containing coal bottom ash: A comprehensive review, *Renew. Sustain. Energy Rev.* 2021; 149: 111361. <https://doi.org/10.1016/j.rser.2021.111361>
- [32] Inayat A, Inayat M, Shahbaz M, Sulaiman SA, Raza M, Yusup S. Parametric analysis and optimization for the catalytic air gasification of palm kernel shell using coal bottom ash as catalyst, *Renew. Energy* 2020; 145:671-681. <https://doi.org/10.1016/j.renene.2019.06.104>
- [33] IS 383. Coarse and Fine Aggregate for Concrete-Specification", Bureau of Indian Standards-New Delhi, India; 2016.
- [34] Ojha PN, Trivedi A, Singh B, Singh A. Evaluation of mechanical and durability properties of concrete made with Indian bottom ash as replacement of fine aggregate, *Journal of Asian Concrete Federation*, 2020;6 (2):50-65. <https://doi.org/10.18702/acf.2020.12.6.2.50>
- [35] Ojha PN, Singh B, Kaura P, Satyakam R. Ash Utilization Strategy in India-A Way Forward, In *Advances in Sustainable Materials and Resilient Infrastructure*, Springer, Singapore, 2022;145-157. https://doi.org/10.1007/978-981-16-9744-9_10
- [36] Ojha PN, Kaura P, Kumar S, Jain H, Singh B, Mittal P. Design of low carbon high performance concrete incorporating ultrafine materials, *Sustainable Structures & Materials, An International Journal*, 2022; 5(1):1-12.
- [37] IS 10262. Concrete Mix Proportioning - Guidelines", Bureau of Indian Standards- New Delhi, India; 2019.
- [38] IS 269. Ordinary Portland Cement- Specifications", Bureau of Indian Standards-New Delhi, India; 2015.
- [39] Arora VV, Singh B, Patel V. Durability and corrosion studies in prestressed concrete made with blended cement, *Asian Concrete Federation Journal*, 2019;5 (1):15-24. <https://doi.org/10.18702/acf.2019.06.30.15>
- [40] Ojha PN, Trivedi A, Singh B, KNS Adarsh, Patel V, Gupta RK. High performance fiber reinforced concrete-for repair in spillways of concrete dams. *Research on Engineering Structures and Materials*, 2021; 7(4):505-522. <https://doi.org/10.17515/resm2021.252ma0128>
- [41] Ojha PN, Singh B, Singh P, Singh A, Mandre MK. Study on effect of fly ash and limestone powder on compressive strength of roller compacted concrete for dam construction, *Journal of Asian Concrete Federation*, 2022;8 (1):37-50. <https://doi.org/10.18702/acf.2022.6.8.1.37>
- [42] Ojha PN, Singh B, Singh A, Patel V, Arora VV, Experimental study on creep and shrinkage behaviour of high strength concrete for application in high rise buildings, *Indian Concrete Journal*, 2021; 95:2:30-42.
- [43] Arora VV, Singh B, Patel V. Durability and corrosion studies in prestressed concrete made with blended cement. *Journal of Asian Concrete Federation*, 2019;5(1):15-24. <https://doi.org/10.18702/acf.2019.06.30.15>
- [44] Arora VV, Singh B, Yadav L. Flexural and fatigue behavior of prestressed concrete beams made with Portland pozzolana cement. *Journal of Asian Concrete Federation*, 2016;2(1):15-23. <https://doi.org/10.18702/acf.2016.06.2.1.15>



Research Article

Effects of immersion in the NaCl and H₂SO₄ solutions on the corrosion rate, microstructure, and hardness of stainless steel 316L

Anugrah Budi Wicaksono^{*a}, Hadi Sutanto^b, Wegie Ruslan^c

Department of Mechanical Engineering, Atma Jaya Catholic University of Indonesia, Jakarta 12930, Indonesia

Article Info

Abstract

Article history:

Received 20 Feb 2023

Accepted 16 May 2023

Keywords:

Corrosion rate;

Stainless steel 316L;

Corrosive medium;

Microstructure;

Material resistance

Stainless steel is one of the materials with excellent corrosion resistance, so it is widely applied in various fields such as the chemical industry, aerospace, power generation, and biomedicine. The environmental condition (neutral, acidic, salty, or basic) is the most important thing to be considered prior to choosing palpable stainless steel materials. In this study, the corrosion behaviors of stainless-steel type SS 316L under exposure immersions in salty and acidic environments using sodium chloride (NaCl) and sulfuric acid (H₂SO₄) solutions were investigated, by referring to a standard method of ASTM G31-72. Scanning electron microscopy (SEM) results revealed that the specimen in NaCl solution exhibited a darker color, and relatively similar shape of cracks are observed. In contrast, the specimen immersed in H₂SO₄ was observed to have a large diagonal crack. The corrosion rate of SS 316L immersed in NaCl was lower with a value of 0.4260 mpy, compared to that of H₂SO₄ which was 2.5141 mpy. The Vickers hardness test showed that the hardness value of NaCl immersion was higher than that of H₂SO₄, which was 6.34% and 1.94%, respectively. It can be concluded that the SS 316L is better used in a salty environment compared to acidic conditions, because the main function of SS 316L is to be able to withstand rust, one of which is caused by chloride compared to other types of stainless-steel.

© 2023 MIM Research Group. All rights reserved.

1. Introduction

Austenitic stainless steel is a common material that has good corrosion resistance, excellent mechanical strength, low thermal expansion, lower process costs, and good reliability [1]. Most manufacturing industries use this material as the primary material for making their products. Stainless Steel AISI 316L (SS 316L) is one of the austenitic stainless steel materials with excellent corrosion resistance, so it is widely applied in various fields such as the chemical industry, aerospace, power generation, and biomedicine [2]. This material is also recommended as a biomaterial due to its low carbon content, which increases its corrosion resistance to chlorinated environments [3,4]. The passive protective layer on the surface of SS material provides high prevention against uniform corrosion in ordinary oxidizing environments but can induce localized forms of corrosion under special conditions [5–7]. The existence of corrosive substances can lead to local passivation degradation and dangerous pitting [8–10]. The exposure of austenitic stainless steel 316L to the high temperature followed by slow cooling in air, such as, during welding, is corresponding to their vulnerability to another type of localized intergranular corrosion. In addition, low-chromium regions are the preferred pathways for crack propagation under other localized corrosion attacks and tensile stresses [11,12].

*Corresponding author: nugrahwicaksono07@gmail.com

^a orcid.org/0000-0002-5571-9448; ^b orcid.org/0000-0002-9632-5883; ^c orcid.org/0000-0001-5141-4615
DOI: <http://dx.doi.org/10.17515/resm2023.695ma0220>

This type of stainless steel is used in medical devices such as implants [13]. Moreover, the high corrosion resistance of SS 316L provides by a thin chromium oxide film that has high stability against corrosion [14,15]. However, this SS 316L material still has some shortcomings; for example, when SS 316L is used as one of the materials for shipbuilding. Marine vessels will come into contact with the marine environment, which contains sodium chloride (NaCl) salt. Therefore this material often experiences pitting-type corrosion due to exposure to seawater and through the deposition of salt in the air, which has high humidity and high chloride concentration [16]. SS 316L is also sensitive to chloride (Cl) compounds in the environment, affecting this material's corrosion resistance. The presence of chloride compounds in the environment can corrode SS 316L and affect its service life.

Recently, the relationship between extreme environments and the pitting corrosion tendency of stainless steel materials has been the field of numerous investigations. Based on the available literature, pH, temperature, and types of the environment play a critical role in the corrosion susceptibility of stainless steel materials [17–19]. A combination of pickling and passivation in aqueous solutions of hydrochloric and nitric acids has been found to be the best choice for rust removal [20]. Several studies have reported the role of MnS inclusions in initiating pitting corrosion in sensitized austenitic SS. Another study compared the effect of different mechanical surface treatments on the pitting resistance of sensitized SS 304 in a 3.5 wt% of NaCl solution [18]. Immersion method has been popular to investigate the corrosion and durability property of stainless-steels. Lieth et al investigated effects of heat treatment on different water condition i.e., sea water, fresh water, and crude oil by immersion method. They found that the severe corrosion occurred in the sea water at high temperature [21]. Another study by Ji et al found that the higher the concentration of the mixed solution and the higher the test temperature, the greater the corrosion rate of 316L stainless steel wire and the lower the breaking strength of 316L stainless steel wire [22]. Adnan et al observed that heat treatment affects the corrosion rate. The annealed sample showed the lowest corrosion rate, while the quenched sample seemed to corrode more compared to the other samples [23]. Moreover, Reda and coworkers have reported some important studies regarding the effect of several environmental aspects on the microstructure of stainless-steel materials have been investigated. They found that hydrogen caused the corrosion and alter the microstructure of electroplated steel alloy 4130 by diffusion mechanism [24]. Next, they also found that heating and solution treatment caused a hardening effect that improved the mechanical and microstructure properties of aluminum-zinc alloy 7075 [25]. Similarly, the heating and solution treatment has been employed on aluminum-copper 2024 alloy, which found that the heating and solution treatment increases the mechanical properties of the steel by short-distance diffusion coupled with precipitation mechanisms [26].

Several studies have been carried out to investigate the resistance of stainless steel materials in solution treatments, including the corrosion rate and hardness of SS 304L in a 0.01M NaCl medium [27]. Improvement of corrosion properties of nanostructured SS 304L in 0.6 M NaCl medium and the effect of incorporation of molybdenum Disulfide (MoS₂) in organic coatings on the corrosion resistance of stainless steel in 3.5% NaCl medium [28]. Furthermore, several other studies also discuss the resistance of 316L when immersed in an H₂SO₄ medium, including the corrosion rate of SS 316L in an H₂SO₄ medium containing the amino acid methionine [29] and the corrosion rate of SS 316L in an H₂SO₄ medium with various temperature treatments [30].

According to the literature, it is reported that the environmental condition (neutral, acidic, salty, or basic) is the most important thing to be considered prior to choose the right stainless steel materials [8,20,31,32]. Nevertheless, the comparison study regarding the corrosion properties of stainless steel, specifically SS 316L, under different conditions is

extremely limited; thus, a comprehensive study that provides a comparison of different environmental conditions on the corrosion behavior of stainless steel materials is urgently needed. Therefore, in this study, the corrosion behaviors of SS 316L under exposure immersions in salty and acidic environments using NaCl and H₂SO₄ solutions were investigated. The ultimate goal of this study is to investigate the effects of acidic and salty conditions on the corrosion behavior of SS 316L. The specimen of SS 316L was immersed in NaCl and H₂SO₄ under the same condition, by referring to a standard method of ASTM G31-72. The corrosion behavior was determined using the corrosion rate and mass loss method. Microstructures of SS 316L of before/after exposure immersion experiment were analyzed using scanning electron microscopy (SEM). Meanwhile, the chemical composition of the specimen was analyzed using energy dispersive spectroscopy (EDS). The mechanical properties of SS 316L before/after treatment were assessed using the Vickers hardness test. Finally, the results of this study was expected to provide recommendations for industry in selecting the right condition for a durable and corrosion-resistant use of SS 316L.

2. Materials and Method

2.1. Materials

A standard stainless steel 316L (SS 316L) plate was supplied from Bozhong Metal Groups, China, which fulfilled the standard specification of SS 316L by ASTM A240 and JIS G4304. The standard composition and mechanical properties of SS 316L that was used in this study are summarized in Table 1 and standard mechanical properties of SS 316L are listed in Table 2. Sodium chloride (NaCl, 99%), sodium hydroxide (NaOH, 99%), and sulfuric acid (H₂SO₄, 98%) that were used for the immersion experiment were provided by Merck, Germany. Deionized (DI) water was always used in chemical solution preparation and all experimentation.

Table 1. Standard additive composition in SS 316L [33,34].

Elementals	Composition (wt%)
C (Carbon)	≤ 0.03
Si (Silicon)	≤ 1.00
Mn (Manganese)	≤ 2.00
P (Phosphorous)	≤ 0.045
S (Sulfur)	≤ 0.045
Cr (Chromium)	16.0 – 18.0
Mo (Molybdenum)	2.0
Ni (Nickel)	10.0

Table 2. Standard mechanical properties of SS 316L [35,36].

Mechanical Properties	Unit	Value
Yield strength	MPa	≥ 200
Tensile strength	MPa	≥ 480
Elongation at break	%	≥ 50
Hardness	HV	≤ 180

2.2. Corrosive Medium Immersion Test

The corrosive medium immersion test was conducted by adapting a standardized method of ASTM G31-72 [37]. This method is commonly used in the determination of laboratory corrosion testing for metals. In this experiment, NaCl and H₂SO₄ were used as the immersion medium that simply represented the salty and acid environments, respectively.

Firstly, 100 mL of NaCl and H₂SO₄ solutions with the same molar concentration (0.017 M) were prepared in a different compartment. After that, a rectangular shape of SS 316L was prepared with a dimension of 20 mm x 10 mm x 2 mm and hanged with a inert rope [38,39]. Fig. 1 depicts the schematic representation of corrosive medium immersion test. The initial weight of the plate was weighed using a precision analytical balance (Precisa Series 390, USA) with an accuracy of 4 significant figure. Then, the SS 316L plates were immersed in both solutions and were left for three days. After three days, the SS 316L samples were taken from the solution and washed with DI water to clean the spent solution [37,39]. The cleansed samples were dried in an oven for four hours until they were completely dried. The samples were put into a desiccator before being weighed, which is noted as the final weight after the corrosion test. Finally, the corrosion rate can be simply determined using Eq. 1 [40,41].

$$C_R = \frac{(W_i - W_f) \times K}{\rho \times A \times t} \quad (1)$$

Where C_R represents the corrosion rate (mils per year/mpy), W_i and W_f are the initial and the final weight (mg) of the sample, respectively. K is a constant in the corrosion rate equation (534), and ρ shows the density of the immersion solution (g/cm³). A is the total surface area of the sample (cm²), and t is the time of exposure (h).

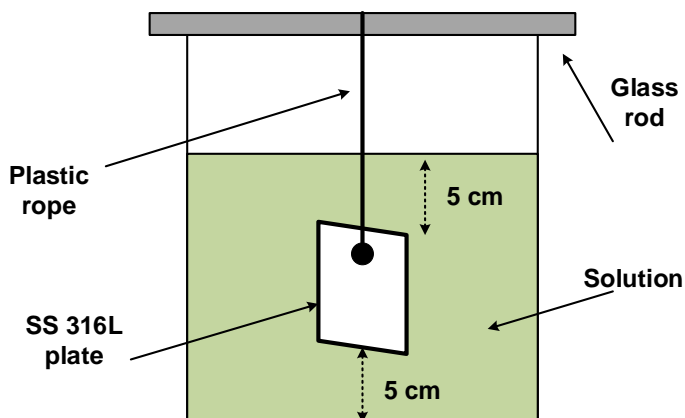


Fig. 1 Schematic illustration of corrosion immersion experiment

2.3. Characterization

Scanning electron microscopy (SEM, Thermo-Fischer Scientific, USA) was performed to capture the surface morphology of the pristine SS 316L and samples after going through the corrosion immersion test. This instrument can provide a surface picture of the samples with some magnifications. To further understand the effects of corrosive medium immersion on the chemical composition of the SS 316L, an energy dispersive spectroscopy (EDS, Thermo-Fischer Scientific, USA) was used. This analysis can show the chemical entities of the samples, which corresponds to the SEM images [42–44]. Therefore, some new insights regarding the effects of corrosive medium immersion using NaCl and H₂SO₄ on the microstructure of SS 316L can be achieved.

2.4. Mechanical Strength Evaluation Using Vickers Hardness Test

Vickers hardness test method was used to evaluate the mechanical strength of the SS 316L before and after corrosion immersion tests. The basic concept of this test is to test the

hardness of the material with a stacker. The shape of this poulder is like a pyramid and is made of square diamonds. The angle produced by Vickers's eye is 136° [45]. To describe the hardness of the sample, Vickers hardness number (VHN) is used, as can be expressed in Eq. 2 [46,47].

$$VHN = \frac{1.854 \times P}{d^2} \tag{2}$$

Where *VHN* stands for Vickers hardness number (kg/μm²). *P* is the applied load (kg), and *d* is the average diagonal length (μm).

3. Results and Discussion

3.1. Effects of Immersion in NaCl and H₂SO₄ on The Mass Reduction and Corrosion Rate of SS 316L

Effects of different types of corrosive medium, which are salty and acidic conditions, on the SS 316L sample were investigated. Table 3 summarizes the data regarding the mass reduction and corrosion rate of SS 316L after being immersed in NaCl and H₂SO₄ solution. According to Table 3, it can be seen that initially, the SS 316L samples had a mass of 2.9796 g and 2.9938 g before being immersed in NaCl and H₂SO₄ solutions. The samples were left for 72 h to assess the corrosion process of SS 316L in salty and acidic conditions. After 72 h, it can be observed that the final weights of both samples are 2.9795 g for immersion in NaCl and 2.9933 g for H₂SO₄. Hence, the weight difference can be simply computed by subtracting the initial and final weights of the samples. It was found that the SS 316L exhibited 0.0001 g of weight loss due to immersion in the NaCl solution. Moreover, the SS 316L possessed a more dramatic weight loss of 0.0005 g when the sample was immersed in the H₂SO₄ solution. The occurrence of weight loss can be due to the reaction between the dominant metal in the SS 316L, which is iron (Fe), and the corrosive solutions. The greater mass reduction represents the greater loss of Fe that can be extracted from the body of SS 316L [48]. The sample that was immersed in H₂SO₄ exhibited greater mass loss. It is explainable that the corrosion reaction in this condition occurs in two ways, namely, the redox corrosion reaction between iron and oxygen and the direct acid leaching due to a large number of H⁺ ions [49]. The reactions can be written as follows [48,50].

Redox reaction mechanisms;

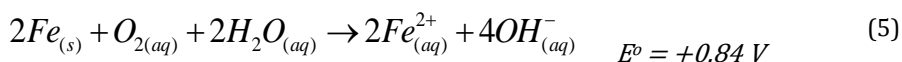
Oxidation reaction:



Reduction reaction:



Overall reaction:



Acid leaching reaction:



On the other hand, the sample that was immersed in NaCl solution seems to have a lower mass loss compared to that of H₂SO₄. It is clearly due to the corrosion reaction that occurred in the NaCl system being just the redox mechanisms (see Eq. 3-5); thus, the mass loss due to corrosion is found lower. Corroboratively, the measured corrosion rate of the SS 316L in H₂SO₄ is way much faster than that of NaCl, with the exact values of 2.5141 mpy and 0.4260 mpy, respectively. The corrosion rate in H₂SO₄ is 5.9 times higher than that in NaCl. Fortunately, the corrosion rate for SS 316L is still acceptable when it falls in the range of 1 – 5 mpy, and when the corrosion rate is < 1 mpy, it is called exceptional [51,52]. Therefore, these results indicate that SS 316L is better used for equipment in a salty environment compared to the acidic one.

Table 3. The mass reduction and corrosion rate of SS 316L after being immersed in NaCl and H₂SO₄ solutions.

Type of solution	Starting date	Finishing date	Duration (h)	Initial weight W _i (g)	Final weight W _f (g)	Weight difference ΔW (g)	Corrosion rate (mpy)
NaCl	2 September 2022	5 September 2022	72	2.9796	2.9795	0.0001	0.4266
H ₂ SO ₄	2 September 2022	5 September 2022	72	2.9938	2.9933	0.0005	2.5176

3.2. Effects of Immersion in Corrosive Medium on The Surface Micromorphology and Chemical Composition of SS 316L

Fig. 2 shows the SEM images and EDS spectra of pristine SS 316L without immersion treatment. It can be seen that the surface micromorphology of the sample is quite uniform without any sign of corrosion. Meanwhile, The SEM test on the sample of SS 316L that was immersed in NaCl solution obtained a hollow structure in stainless steel as a result of immersion for three days, as can be seen in Fig. 3. After experiencing treatment, the material has defects in the microstructure of the material, which can further affect the service life of the material's properties. This also causes a reduction in the mass of the material because cracks and degradation occurred on the surface. This was also reported in a study, they explained that there were long depressions in the diagonal direction after being immersed in the corrosive solution [53]. Moreover, another finding can be observed in Fig. 2 that when stainless steel material is immersed in NaCl solution, some crystal constituents were formed on the surface of the material. The circle image shown is the form of crystallization that occurs when immersing SS 316L in NaCl solution. The type of corrosion occurred in immersion into NaCl solution is uniform corrosion [54].

Moreover, SEM results also show that the corrosion that occurs on SS 316L when immersed in H₂SO₄ solution possesses worse corrosion, with uniform defects observed on the surface of SS 316L as can be seen in Fig. 4. Corrosion occurs almost all over the surface of the specimen, and there are the same depressions and cracks, indicating that the type of corrosion that occurs is a type of uniform corrosion [55–57]. Almost the entire top surface of stainless steel formed new crystals and black spots. However, what distinguishes between the immersion of the two solutions is the erosion of the material when immersed in H₂SO₄ so that in general the hardness value of the specimen immersed in H₂SO₄ is much lower than the specimen immersed in NaCl solution. Then, based on the results of EDS on the test specimens showed that the percentage value of the Fe element was higher in SS 316L specimens immersed in H₂SO₄ solution than in SS 316L specimens immersed in NaCl. specimen immersed in H₂SO₄ is much lower than the specimen immersed in NaCl solution [37]

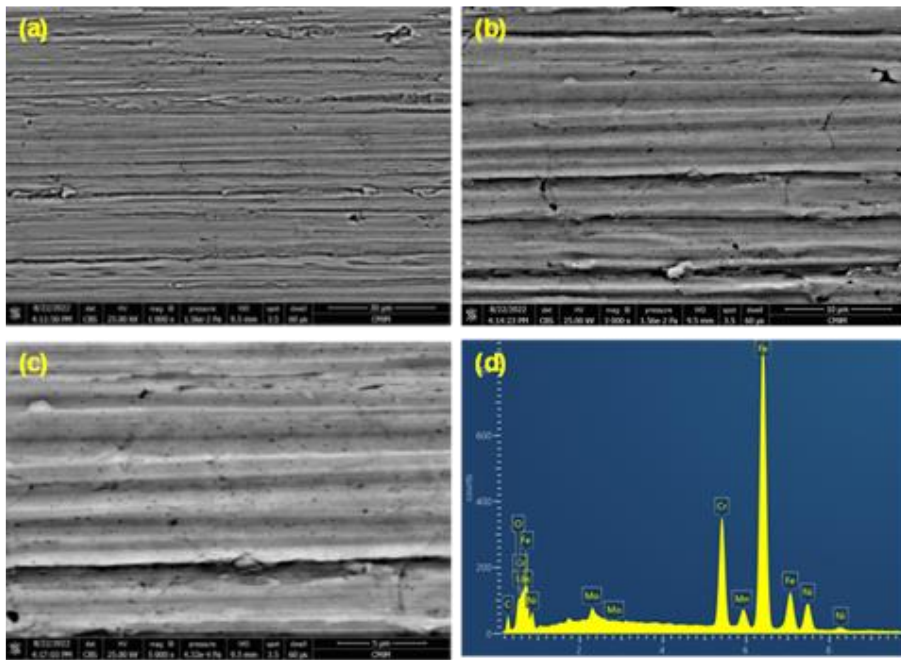


Fig. 2 SEM images of the pristine SS 316L under magnifications of (a) 1000x, (b) 3000x, and (c) 5000x. (d) EDS spectra of pristine SS 316L

The chemical composition of pristine SS 316L and the immersed SS 316L samples in NaCl and H₂SO₄ was analyzed using EDS. Table 4 summarizes the elemental composition of the samples. It is found that the pristine SS 316L consists of 68.1, 16.5, 10.3, 2.9, 1.2, and 1.0% of Fe, Cr, Ni, O, S, and Mn, respectively, which is in similar manner with previous studies [33,34]. While for the sample that immersed in NaCl exhibited compositions of 66.9, 16.4, 10.3, 4.1, 1.2, and 1.1 wt% for Fe, Cr, Ni, O, S, and Mn, respectively. While the sample immersed in H₂SO₄ solution exhibited compositions of 65.7, 15.6, 9.2, 6.5, 1.7, and 1.3 wt%, for Fe, Cr, Ni, O, S, and Mn, respectively. Based on the results, it is found that the immersion process reduced the Fe content and increased the oxygen content. This process followed the corrosion reaction mechanisms as discussed perviously. It is also clearly observed that H₂SO₄ caused worse corrosion on the main metals that constructed the SS 316L, such as Fe, Cr, and Ni, compared to that of in NaCl solution. It can be due to a strong electrochemical reaction between H₂SO₄ and the metals [58,59], as previously discussed in section 3.1. It is also evident by the SEM images that a sample of SS 316L in H₂SO₄ exhibited more defects in its microstructure compared to that of NaCl. The reduction content of constituent metals can alter the mechanical strength of the SS 316L sample [60]. Therefore, it can be concluded that H₂SO₄ caused more serious corrosion activity on SS 316L compared to NaCl.

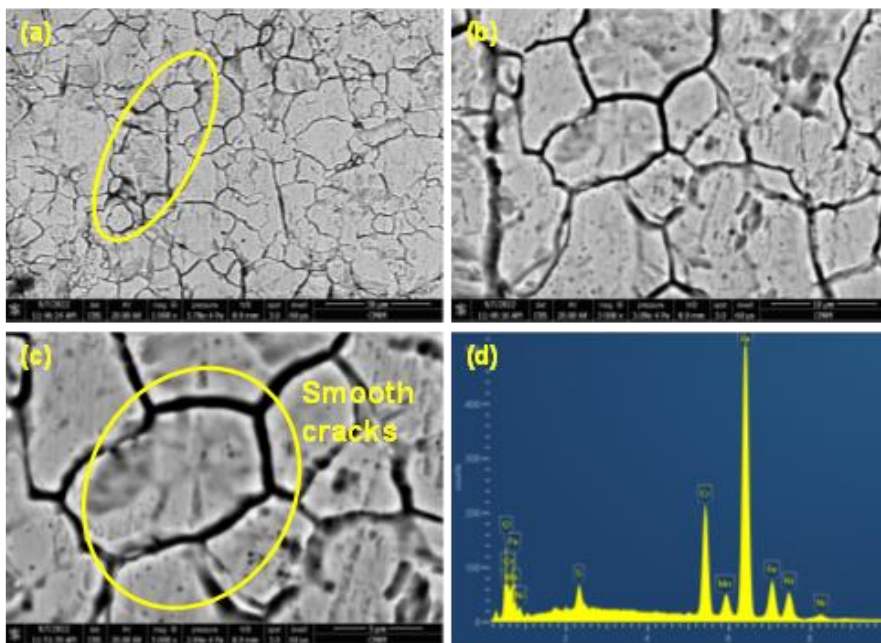


Fig. 3 SEM images of SS 316L sample after immersed in NaCl solution under magnifications of (a) 1000x, (b) 3000x, and (c) 5000x. EDS spectra of SS 316L sample after immersed in NaCl solution

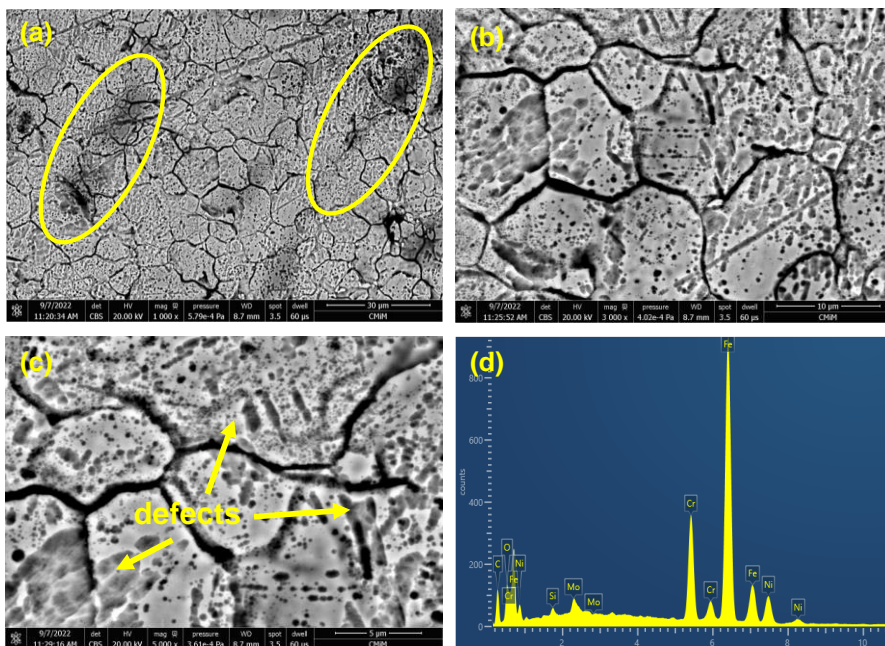


Fig. 4 SEM images of SS 316L sample after immersed in H₂SO₄ solution under magnifications of (a) 1000x, (b) 3000x, and (c) 5000x. EDS spectra of SS 316L sample after immersed in H₂SO₄ solution.

Table 4. Chemical compositions of the SS 316L samples after being immersed in NaCl and H₂SO₄ solutions.

Elementals	Composition (wt%)		
	Pristine SS 316L	SS 316L (NaCl)	SS 316L (H ₂ SO ₄)
Iron (Fe)	68.1	66.9	65.7
Chromium (Cr)	16.5	16.4	15.6
Nickel (Ni)	10.3	10.3	9.2
Oxygen (O)	2.9	4.1	6.5
Sulfur (S)	1.2	1.2	1.7
Manganese (Mn)	1.0	1.1	1.3

3.3. Effects of Immersion in Corrosive Medium on The Hardness Level of SS 316L

Effects of immersion in NaCl and H₂SO₄ solutions on the mechanical strength of SS 316L were assessed through the Vickers hardness test. Fig. 5 shows the results of Vickers hardness numbers (VHN) for three samples, namely pristine SS 316L, SS 316L (H₂SO₄), and SS 316L (NaCl). It can be seen that the pristine SS 316L exhibited a VHN of 159.3 ± 1.32 kg/ μm^2 . The immersed products showed VHN numbers of 169.4 ± 0.52 kg/ μm^2 for SS 316L (NaCl) and 162.4 ± 0.47 kg/ μm^2 for SS 316L (H₂SO₄). It is found that the immersed samples have higher VHN values compared to the pristine SS 316L. It is explainable by the formation of a brittle surface of SS 316L due to the corrosion reactions on the surface. This corroded surface attributes more brittle property due to the oxidation, thus, the immersed samples attributed higher VHN values [61,62]. The HV value increased by 6.34% for materials soaked in NaCl solution, and the value obtained from materials soaked in H₂SO₄ solution increased by 1.94%. Moreover, the SS 316L sample from the NaCl solution has a slightly higher VHN than that of H₂SO₄.

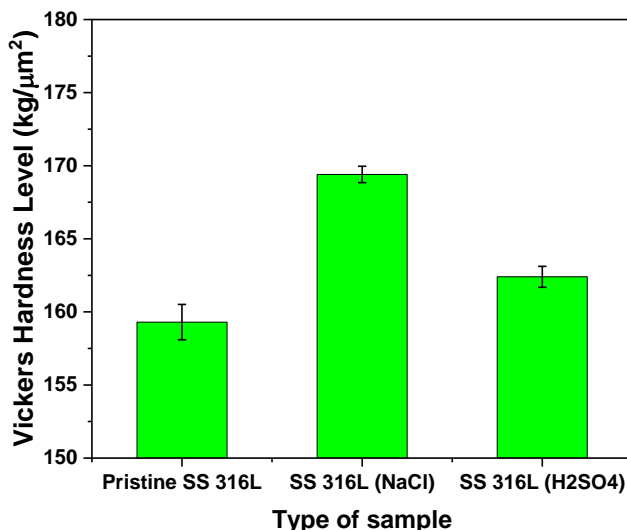


Fig. 5 Results of the hardness of the tested SS 316L samples.

The defect-free corrosion surface can be attributed to enhancing the mechanical strength of the SS 316L sample in NaCl. The generated crystals on the surface of SS 316L can also provide higher mechanical strength [59,63]. The hardness value of SS 316L increased by 6.34% for those immersed in NaCl solution. Therefore, SS 316L itself is widely used for the manufacture of equipment that is in direct contact with salt solutions because the main function of SS 316L is to be able to withstand rust, one of which is caused by chloride [64].

3.4. Effect of pH Variations

Effect of pH variations on the corrosion rate and hardness of the immersed SS 316L was investigated and the results are depicted on Fig. 6. Based on Fig. 6 it can be seen that the corrosion rate of SS 316L decreased significantly with a rise of pH. pH of solution was controlled using NaOH and H₂SO₄. Sample of SS 316L at lowest pH of 1 experienced the highest corrosion rate of 2.5563 mpy, while at pH of 7 and above the corrosion rate remained constant at 0.5317 mpy. pH is a measure of the acidity or basicity of a solution and plays a crucial role in the corrosion of stainless steel. The corrosion of stainless steel is an electrochemical process that involves the transfer of electrons between the metal and its environment. At low pH levels, the concentration of hydrogen ions (H⁺) in the solution increases, leading to an increase in the corrosion rate of stainless steel [65]. Conversely, at higher pH levels, the concentration of H⁺ ions decrease, resulting in a decrease in the corrosion rate [66]. Therefore, pH variations can have a significant impact on the corrosion rate of stainless steel [1]. Similar results have been found that corrosion rate of stainless steels is affected by pH variations. For instance, a study by Samosir in 2017 demonstrated that the corrosion rate of stainless steel increased with a decrease in pH below 4 [67]. On the other hand, maintaining a neutral or higher pH can help reduce the corrosion rate of stainless steel [68]. Therefore, it is crucial to maintain optimal pH levels to minimize the corrosion rate of stainless steel and prolong its lifespan.

Fig. 6 also depicts the effect of pH variations on the hardness of SS 316L samples. It can be seen that the hardness of SS 316L decreased in a pH lower than 7 and higher than 7. The highest hardness value was found at neutral condition (pH=7) and the lowest hardness value was at acidic condition (pH=1). Hardness is an important characteristic of stainless steel, as it determines the material's resistance to wear and deformation. In a study conducted by Saefuloh et al. in 2020, the hardness of stainless steel 304 was measured in corrosive media, including sea water and 3.5% NaCl [65]. The results showed that the hardness of stainless steel decreased as the corrosion rate increased, indicating a negative correlation between hardness and corrosion rate. Additionally, maintaining a high level of hardness in stainless steel is crucial to ensure its durability and longevity in various applications. The pH level of the environment in which stainless steel is used can have a significant impact on its hardness. Research by Garcia-Cabezon et al. in 2022 found that precipitation hardening stainless steel (PH SS) manufactured by selective laser melting had varying levels of hardness depending on the pH level of the environment [69]. Similarly, Saefuloh's research in 2020 showed that the corrosion rate of stainless-steel duplex was affected by the pH level of the environment, but had no significant effect on the level of hardness [65]. However, research by Zai et al. in 2020 found that the high strength and hardness induced by precipitation hardening in PH stainless steels limits their workability [70]. Hence, it is important to balance pH control and hardness in stainless steel applications to ensure optimal performance. The hardness of stainless steel is a critical factor in its performance, and can be influenced by variations in pH levels. While maintaining a high level of hardness is important, it is also crucial to consider the effects of pH control on the material's corrosion resistance and workability. Further research is needed to fully understand the relationship between pH variations and the hardness of stainless steel, and to develop effective strategies for balancing these factors in various applications.

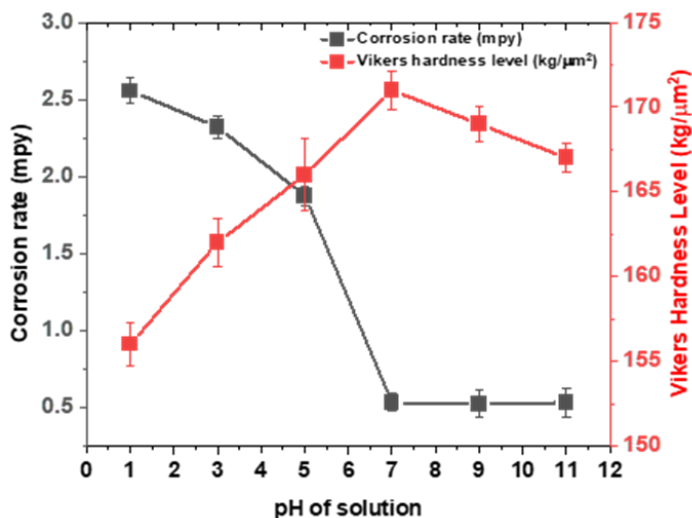


Fig. 6 Effect of pH of solutions on the corrosion rate and hardness of SS 316L

4. Conclusion

In this study, the corrosion behaviors of stainless-steel type SS 316L under exposure immersions in salty and acidic environments using sodium chloride (NaCl) and sulfuric acid (H₂SO₄) solutions were investigated, by referring to a standard method of ASTM G31-72. Scanning electron microscopy (SEM) results revealed that the specimen in NaCl solution exhibited a darker color, and relatively similar shape of cracks are observed. In contrast, the specimen immersed in H₂SO₄ was observed to have a large diagonal crack. It was found that the corrosion resistance of SS 316L immersed in NaCl solution is better because the corrosion rate value is < 1 mpy, which was 0.4260 mpy. This value is in the "excellent" category compared to the corrosion rate value of SS 316L immersed in H₂SO₄ solution, which was 2.5141 mpy in the "excellent" category. This indicates that SS 316L is better placed in a salty environment than in acidic conditions. In the Vickers test, it was found that the value of each material increased not too significantly. The HV value increased by 6.34% for materials soaked in NaCl solution, and the value obtained from materials soaked in H₂SO₄ solution increased by 1.94%. Moreover, the SS 316L sample from the NaCl solution has a slightly higher VHN than that of H₂SO₄. The defect-free corrosion surface can be attributed to enhancing the mechanical strength of the SS 316L sample in NaCl. The generated crystals on the surface of SS 316L can also provide higher mechanical strength. These results indicate that NaCl adds strength to the surface structure of the material compared to the H₂SO₄ solution. Therefore, SS 316L itself is widely used for the manufacture of equipment that is in direct contact with salt solutions because the main function of SS 316L is to be able to withstand rust, one of which is caused by chloride. Finally, it can be concluded that SS 316L used in the marine industry will perform better in terms of resistance and hardness compared to the other industries that often intersect with acidic solutions. It is crucial to maintain optimal pH levels to minimize the corrosion rate of stainless steel and prolong its lifespan. Further research is needed to fully understand the relationship between pH variations and the hardness of stainless steel, and to develop effective strategies for balancing these factors in various applications.

Acknowledgment

The authors thank PT. Cipta Micro Material provided the scanning electron microscopy – energy dispersive spectroscopy (SEM-EDS) analysis for this research. The authors would also acknowledge the Atma Jaya Catholic University of Indonesia and PT. Bina Niaga Multi Usaha for their support for this project.

References

- [1] Yasir M, Danish M, Mia M, Gupta MK, Sarikaya M. Investigation into the surface quality and stress corrosion cracking resistance of AISI 316L stainless steel via precision end-milling operation. The International Journal of Advanced Manufacturing Technology. 2021 Jan 9;112(3-4):1065-76. <https://doi.org/10.1007/s00170-020-06413-4>
- [2] Bordji G, Jouzeau JY, Mainard D, Payan E, Delagoutte+ JP, Netter P. Evaluation of the effect of three surface treatments on the biocompatibility of 316L stainless steel using human differentiated cells. Vol. 17, Biomaterials. 1996. [https://doi.org/10.1016/0142-9612\(96\)82723-2](https://doi.org/10.1016/0142-9612(96)82723-2)
- [3] Yeganeh M, Rezvani MH, Laribaghali SM. Electrochemical behavior of additively manufactured 316L stainless steel in H₂SO₄ solution containing methionine as an amino acid. Colloids Surf A Physicochem Eng Asp. 2021 Oct 20;627. <https://doi.org/10.1016/j.colsurfa.2021.127120>
- [4] Kusworo TD, Kumoro AC, Aryanti N, Kurniawan TA, Dalanta F, Alias NH. Photocatalytic polysulfone membrane incorporated by ZnO-MnO₂@SiO₂ composite under UV light irradiation for the reliable treatment of natural rubber-laden wastewater. Chemical Engineering Journal. 2023 Jan;451:138593. <https://doi.org/10.1016/j.cej.2022.138593>
- [5] Lacerda JC de, Freitas LL de, Brito RF, Moura Filho F, Teixeira RLP. Comparative Study Between Sensitization Degree of the 0.4% Mo Austenitic Stainless Steel and UNS S31803 Duplex Stainless Steel. Materials Research. 2021;24(1). <https://doi.org/10.1590/1980-5373-mr-2020-0408>
- [6] Baser E, Incesu A, Sismanoglu S, Gungor A. Wear performance investigation of AlSi8Cu3Fe aluminum alloy related to aging parameters. Research on Engineering Structures and Materials. 2018; <https://doi.org/10.17515/resm2018.64is0829>
- [7] Balcioglu HE. An investigation on the mechanical strength, impact resistance and hardness of SiC filled natural jute fiber reinforced composites. Research on Engineering Structures and Materials. 2019; <https://doi.org/10.17515/resm2019.131me0529>
- [8] Liu G, Liu Y, Cheng Y, Li J, Jiang Y. The Intergranular Corrosion Susceptibility of Metastable Austenitic Cr-Mn-Ni-N-Cu High-Strength Stainless Steel under Various Heat Treatments. Materials. 2019 Apr 29;12(9):1385. <https://doi.org/10.3390/ma12091385>
- [9] Koç E, Makhlof FMS. Corrosion behavior of heat treated Mg-xZn (x=0.5 - 3) alloys. Research on Engineering Structures and Materials. 2018; <https://doi.org/10.17515/resm2018.69is1007>
- [10] Dalanta F, Kusworo TD, Aryanti N, Othman NH. Optimization of AC/TiO₂/CeO₂ composite formulation for petroleum refinery wastewater treatment via simultaneous adsorption-photocatalytic process using D-optimal mixture experimental design. J Environ Chem Eng [Internet]. 2021 Dec 1 [cited 2021 Oct 24];9(6):106517. <https://doi.org/10.1016/j.jece.2021.106517>
- [11] Zhou W, Ma W, Li Y, Sun Y. Effect of Sensitizing Treatment on the Microstructure and Susceptibility to Intergranular Corrosion of High-Nitrogen Austenitic Stainless Steel. Metallography, Microstructure, and Analysis. 2021 Feb 6;10(1):25-35. <https://doi.org/10.1007/s13632-020-00708-4>

- [12] Bansod A v., Patil AP, Moon AP, Khobragade NN. Intergranular Corrosion Behavior of Low-Nickel and 304 Austenitic Stainless Steels. *J Mater Eng Perform.* 2016 Sep 25;25(9):3615-26. <https://doi.org/10.1007/s11665-016-2221-2>
- [13] Stewart S, Bryant SJ, Ahn J, Hankenson KD. Bone Regeneration. In: *Translational Regenerative Medicine.* Elsevier; 2015. p. 313-33. <https://doi.org/10.1016/B978-0-12-410396-2.00024-4>
- [14] Ayu Arwati IG, Majlan EH, Wan Daud WR, Shyuan LK, Binti Arifin K, Husaini T, et al. Temperature Effects on Stainless Steel 316L Corrosion in the Environment of Sulphuric Acid (H₂SO₄). In: *IOP Conference Series: Materials Science and Engineering.* Institute of Physics Publishing; 2018. <https://doi.org/10.1088/1757-899X/343/1/012016>
- [15] Rusnak CR, Menzemer CC. Fatigue behavior of flush reinforced welded hand-holes in aluminum light poles. *Research on Engineering Structures and Materials.* 2021; <https://doi.org/10.17515/resm2021.248st0122tn>
- [16] Wang H, Wu Y, Sun X, Ling J, Zou D. Corrosion Resistance to Chloride of a Novel Stainless Steel: The Threshold Chloride Value and Effect of Surface State. *Materials.* 2019 Jul 11;12(14):2235. <https://doi.org/10.3390/ma12142235>
- [17] Cheng CQ, Klinkenberg LI, Ise Y, Zhao J, Tada E, Nishikata A. Pitting corrosion of sensitised type 304 stainless steel under wet-dry cycling condition. *Corros Sci.* 2017 Apr;118:217-26. <https://doi.org/10.1016/j.corsci.2017.02.010>
- [18] Ezuber H, Alshater A, Nisar SO, Gonsalvez A, Aslam S. Effect of Surface Finish on the Pitting Corrosion Behavior of Sensitized AISI 304 Austenitic Stainless Steel Alloys in 3.5% NaCl Solutions. *Surface Engineering and Applied Electrochemistry.* 2018 Jan 3;54(1):73-80. <https://doi.org/10.3103/S1068375518010039>
- [19] Tokuda S, Muto I, Sugawara Y, Hara N. Effect of Sensitization on Pitting Corrosion at MnS and CrS in Type 304 Stainless Steel. *J Electrochem Soc.* 2021 Sep 1;168(9):091504. <https://doi.org/10.1149/1945-7111/ac28c6>
- [20] Liptáková T, Bolzoni F, Trško L. Specification of surface parameters effects on corrosion behavior of the AISI 316Ti in dependence on experimental methods. *J Adhes Sci Technol.* 2016 Nov 1;30(21):2329-44. <https://doi.org/10.1080/01694243.2016.1182824>
- [21] Lieth HM, Al-Sabur R, Jassim RJ, Alsahlani A. Enhancement of corrosion resistance and mechanical properties of API 5L X60 steel by heat treatments in different environments. *Journal of Engineering Research.* 2021 Nov 4; <https://doi.org/10.36909/jer.14591>
- [22] Ji JB, Tong J. Corrosion Rate and Mechanical Properties of 316L Stainless Steel Wires in Different Corrosive Conditions. *Applied Mechanics and Materials.* 2013 Dec;441:48-52. <https://doi.org/10.4028/www.scientific.net/AMM.441.48>
- [23] Adham Adnan M, Kee KE, Raja PB, Ismail MC, Kakooei S. Influence of Heat Treatment on the Corrosion of Carbon Steel in Environment Containing Carbon Dioxide and Acetic Acid. *IOP Conf Ser Mater Sci Eng.* 2018 May;370:012039. <https://doi.org/10.1088/1757-899X/370/1/012039>
- [24] Reda Y, El-Shamy AM, Eessaa AK. Effect of hydrogen embrittlement on the microstructures of electroplated steel alloy 4130. *Ain Shams Engineering Journal.* 2018 Dec;9(4):2973-82. <https://doi.org/10.1016/j.asej.2018.08.004>
- [25] Reda Y, Yehia HM, El-Shamy AM. Microstructural and mechanical properties of Al-Zn alloy 7075 during RRA and triple aging. *Egyptian Journal of Petroleum.* 2022 Mar;31(1):9-13. <https://doi.org/10.1016/j.ejpe.2021.12.001>
- [26] Reda Y, Yehia HM, El-Shamy AM. Triple aging of the RRA Al -Cu 2024 alloy and its impact on the mechanical and microstructure properties. *Egyptian Journal of Petroleum.* 2022 Sep;31(3):89-94. <https://doi.org/10.1016/j.ejpe.2022.08.003>
- [27] Mastouri W, Pichon L, Martemianov S, Paillat T, Thomas A. Effect of immersion time at the stainless steel 304L/NaCl (0.01 M) interface. *Journal of Electrochemical Science and Engineering.* 2019 Feb 28;9(2):99-111. <https://doi.org/10.5599/jese.639>

- [28] Olugbade T, Lu J. Enhanced corrosion properties of nanostructured 316 stainless steel in 0.6 M NaCl solution. *J Bio Tribocorros.* 2019 Jun 1;5(2). <https://doi.org/10.1007/s40735-019-0235-7>
- [29] Sung Hong M, Park Y, Gu Kim J, Kim K. Effect of Incorporating MoS₂ in Organic Coatings on the Corrosion Resistance of 316L Stainless Steel in a 3.5% NaCl Solution. <https://doi.org/10.3390/coatings9010045>
- [30] Fossati A, Borgioli F, Galvanetto E, Bacci T. Corrosion resistance properties of glow-discharge nitrided AISI 316L austenitic stainless steel in NaCl solutions. *Corrosion Science - CORROS SCI.* 2006 Jun 1;48:1513-27. <https://doi.org/10.1016/j.corsci.2005.06.006>
- [31] Lv J, Luo H. The Effect of Low Temperature Sensitization on Corrosion Resistance of Ultrafine-Grained Type 321 Stainless Steels. *J Mater Eng Perform.* 2014 Jan 14;23(1):262-7. <https://doi.org/10.1007/s11665-013-0818-2>
- [32] Zhang C, Wei Y, Yang J, Emori W, Li J. Effects of nitric acid passivation on the corrosion behavior of ZG06Cr13Ni4Mo stainless steel in simulated marine atmosphere. *Materials and Corrosion.* 2020 Sep 29;71(9):1576-90. <https://doi.org/10.1002/maco.202011597>
- [33] Attarzadeh N, Molaei M, Babaei K, Fattah-alhosseini A. New Promising Ceramic Coatings for Corrosion and Wear Protection of Steels: A Review. *Surfaces and Interfaces.* 2021 Apr;23:100997. <https://doi.org/10.1016/j.surfin.2021.100997>
- [34] Kong D, Dong C, Wei S, Ni X, Zhang L, Li R, et al. About metastable cellular structure in additively manufactured austenitic stainless steels. *Addit Manuf.* 2021 Feb;38:101804. <https://doi.org/10.1016/j.addma.2020.101804>
- [35] Zaffora A, di Franco F, Santamaria M. Corrosion of stainless steel in food and pharmaceutical industry. *Curr Opin Electrochem.* 2021 Oct;29:100760. <https://doi.org/10.1016/j.coelec.2021.100760>
- [36] Eshkabilov S, Ara I, Sevostianov I, Azarmi F, Tangpong X. Mechanical and thermal properties of stainless steel parts, manufactured by various technologies, in relation to their microstructure. *Int J Eng Sci.* 2021 Feb;159:103398. <https://doi.org/10.1016/j.ijengsci.2020.103398>
- [37] Beeharry P, Surnam BYR. Atmospheric Corrosion of Welded Mild Steel. *Mater Today Proc.* 2018;5(2):7476-85. <https://doi.org/10.1016/j.matpr.2017.11.419>
- [38] Lieth HM, Al-Sabur R, Jassim RJ, Alsahlani A. Enhancement of corrosion resistance and mechanical properties of API 5L X60 steel by heat treatments in different environments. *Journal of Engineering Research.* 2021 Nov 4; <https://doi.org/10.36909/jer.14591>
- [39] Alaskari, Liptakova T, Fajnor P, Halamova M. Mechanical surface treatments effects on corrosion of AISI 316 Ti stainless steel in chloride environments. *Journal of Engineering Research.* 2014 Sep 7;2(3):20. <https://doi.org/10.7603/s40632-014-0020-1>
- [40] Orlikowski J, Szociński M, Żakowski K, Igliński P, Domańska K, Darowicki K. Actual field corrosion rate of offshore structures in the Baltic Sea along depth profile from water surface to sea bed. *Ocean Engineering.* 2022 Dec;265:112545. <https://doi.org/10.1016/j.oceaneng.2022.112545>
- [41] Wang Z, Zhao Y, Liu M, Shen H, Fang Q, Yao J. Investigation of the effects of small flow rate and particle impact on high temperature CO₂ corrosion of N80 steel. *Corros Sci.* 2022 Dec;209:110735. <https://doi.org/10.1016/j.corsci.2022.110735>
- [42] Putignano A, Tosco V, Monterubbianesi R, Vitiello F, Gatto ML, Furlani M, et al. Comparison of three different bulk-filling techniques for restoring class II cavities: μ CT, SEM-EDS combined analyses for margins and internal fit assessments. *J Mech Behav Biomed Mater.* 2021 Dec;124:104812. <https://doi.org/10.1016/j.jmbbm.2021.104812>
- [43] Sargam Y, Wang K. Quantifying dispersion of nanosilica in hardened cement matrix using a novel SEM-EDS and image analysis-based methodology. *Cem Concr Res.* 2021 Sep;147:106524. <https://doi.org/10.1016/j.cemconres.2021.106524>

- [44] Greer MC, MacDonald BL, Stalla D. Cobalt, lead, and borax: Preliminary LA-ICP-MS and SEM-EDS analysis of Late-18th- to Mid-19th-century British refined earthenware glazes. *J Archaeol Sci Rep.* 2021 Jun;37:103013. <https://doi.org/10.1016/j.jasrep.2021.103013>
- [45] Donmez MB, Olcay EO, Demirel M. Influence of coloring liquid immersion on flexural strength, Vickers hardness, and color of zirconia. *J Prosthet Dent.* 2021 Oct;126(4):589.e1-589.e6. <https://doi.org/10.1016/j.prosdent.2020.11.020>
- [46] Hu X, Li J, Wang Z, Wang J. A microstructure-informatic strategy for Vickers hardness forecast of austenitic steels from experimental data. *Mater Des.* 2021 Mar;201:109497. <https://doi.org/10.1016/j.matdes.2021.109497>
- [47] Chu H, Wang T, Han L, Cao L, Guo MZ, Liang Y, et al. Vickers hardness distribution and prediction model of cement pastes corroded by sulfate under the coexistence of electric field and chloride. *Constr Build Mater.* 2021 Nov;309:125119. <https://doi.org/10.1016/j.conbuildmat.2021.125119>
- [48] Tang C, Wang X, Zhang Y, Liu N, Hu X. Corrosion behaviors and kinetics of nanoscale zero-valent iron in water: A review. *Journal of Environmental Sciences.* 2022 Dec;
- [49] Fan X, Guan X, Ma J, Ai H. Kinetics and corrosion products of aqueous nitrate reduction by iron powder without reaction conditions control. *Journal of Environmental Sciences.* 2009 Jan;21(8):1028-35. [https://doi.org/10.1016/S1001-0742\(08\)62378-5](https://doi.org/10.1016/S1001-0742(08)62378-5)
- [50] CHEN J, ZHANG Q. Effect of electrochemical state on corrosion-wear behaviors of TC4 alloy in artificial seawater. *Transactions of Nonferrous Metals Society of China.* 2016 Apr;26(4):1011-8. [https://doi.org/10.1016/S1003-6326\(16\)64164-X](https://doi.org/10.1016/S1003-6326(16)64164-X)
- [51] Chmelko, Šulko M, Garan M, Zvirko O, de Jesus AMP. Influence of additional factors on the integrity of pipelines with small corrosion defects. *Procedia Structural Integrity.* 2022;42:315-20. <https://doi.org/10.1016/j.prostr.2022.12.223>
- [52] Costa EM, Dedavid BA, Santos CA, Lopes NF, Fraccaro C, Pagartanidis T, et al. Crevice corrosion on stainless steels in oil and gas industry: A review of techniques for evaluation, critical environmental factors and dissolved oxygen. *Eng Fail Anal.* 2023 Feb;144:106955. <https://doi.org/10.1016/j.engfailanal.2022.106955>
- [53] Wu X, Liu Y, Sun Y, Dai N, Li J, Jiang Y. A discussion on evaluation criteria for crevice corrosion of various stainless steels. *J Mater Sci Technol.* 2021 Feb;64:29-37. <https://doi.org/10.1016/j.jmst.2020.04.017>
- [54] Li X, Gong J. Effects of steel liner corrosion on the leak-tightness of prestressed concrete containment structure under severe accident loads. *Ann Nucl Energy.* 2023 Jan;180:109487. <https://doi.org/10.1016/j.anucene.2022.109487>
- [55] Xiao Z, Liu J, Jiang Z, Luo L, Huang Q. Corrosion behavior and mechanism of CLAM and 316L steels in flowing Pb-17Li alloy under magnetic field. *Nuclear Engineering and Technology.* 2022 Jun;54(6):1962-71. <https://doi.org/10.1016/j.net.2021.12.020>
- [56] Wongpanya P, Wongpinij T, Photongkam P, Siritapetawee J. Improvement in corrosion resistance of 316L stainless steel in simulated body fluid mixed with antiplatelet drugs by coating with Ti-doped DLC films for application in biomaterials. *Corros Sci.* 2022 Nov;208:110611. <https://doi.org/10.1016/j.corsci.2022.110611>
- [57] Li H, Liu W, Chen L, Fan P, Dong B, Ma Z, et al. Corrosion crack failure analysis of 316L hydraulic control pipeline in high temperature aerobic steam environment of heavy oil thermal recovery well. *Eng Fail Anal.* 2022 Aug;138:106297. <https://doi.org/10.1016/j.engfailanal.2022.106297>
- [58] Dong Y, Li J, Xu D, Song G, Liu D, Wang H, et al. Investigation of microbial corrosion inhibition of Cu-bearing 316L stainless steel in the presence of acid producing bacterium *Acidithiobacillus caldus* SM-1. *J Mater Sci Technol.* 2021 Feb;64:176-86. <https://doi.org/10.1016/j.jmst.2020.05.070>
- [59] Zhao R, Xu W, Yu Q, Niu L. Synergistic effect of SAMs of S-containing amino acids and surfactant on corrosion inhibition of 316L stainless steel in 0.5 M NaCl solution. *J Mol Liq.* 2020 Nov;318:114322. <https://doi.org/10.1016/j.molliq.2020.114322>

- [60] Lodhi MJK, Deen KM, Haider W. Corrosion behavior of additively manufactured 316L stainless steel in acidic media. *Materialia* (Oxf). 2018 Oct;2:111-21. <https://doi.org/10.1016/j.mtla.2018.06.015>
- [61] Li Z, Chai L, Tang Y, Zhang C, Qi L, Zhang K, et al. 316L stainless steel repaired layers by weld surfacing and laser cladding on a 27SiMn steel: A comparative study of microstructures, corrosion, hardness and wear performances. *Journal of Materials Research and Technology*. 2023 Jan; <https://doi.org/10.1016/j.jmrt.2023.01.162>
- [62] Guo H, Wei H, Li G, Sun F. Experimental research on fatigue performance of butt welds of corroded Q690 high strength steel. *J Constr Steel Res*. 2021 Sep;184:106801. <https://doi.org/10.1016/j.jcsr.2021.106801>
- [63] Ruiz-Menéndez G, Andrade C, Carro-Sevillano G, Peña C, Adeva P, Medina J, et al. Identification of the failure mode of corroding steel rebars in a viaduct in service through hardness measurements. *Results in Engineering*. 2022 Mar;13:100331. <https://doi.org/10.1016/j.rineng.2022.100331>
- [64] Pathote D, Jaiswal D, Singh V, Behera CK. Electrochemical corrosion behavior of tantalum coated 316L stainless steel by D.C. Magnetron sputtering for orthopedic applications. *Applied Surface Science Advances*. 2023 Feb;13:100365. <https://doi.org/10.1016/j.apsadv.2022.100365>



Technical Note

Flexural strength and cost performance of tuffcrete concrete

Chioma Awodiji^{*a}, Samuel Sule^b

Department of Civil and Environmental Engineering, University of Port-Harcourt, Rivers State, Nigeria

Article Info

Abstract

Article history:

Received 04 Apr 2023

Accepted 18 Jul 2023

*Axion liquid polymer;
Axion white tuffcrete
powder;
Comparative cost
analysis;*

This study investigated the flexural strength of tuffcrete concrete in relation to nominal concrete. Tuffcrete concrete (TC) was made from Portland cement (PC), tuffcrete white powder (TWP), river sand, granite chippings, tuffcrete liquid polymer (TLP), and water. A prescribed mix of 1:2:2 (binder: sand: granite) with a diluted polymer-binder ratio of 0.6 was adopted. TWP replaced PC in percentages of 0%, 5%, 10%, 15%, 20%, and 30%. 10 liters of TLP were diluted in 200 liters of water to make the water for mixing the concrete. 12 concrete standard beams of size 100mm x 100mm x 400mm were generated and hardened in water at ambient temperature for 28 days before being laid open for flexural testing. A comparative cost analysis was also carried out on the TC with respect to regular concrete. The workability of the fresh TC was highly enhanced due to the addition of the TWP. A 69.57% increase in slump was obtained by replacing PC with just 5% TWP. Slump values kept on getting bigger as the percentage of TWP incorporation grew. However, the flexural strength of TC reduced as more and more TWP was added to the mix. Flexural strength results ranged from 9.38 N/mm² at 0% inclusion of TWP to 4.38 N/mm² at 30% introduction of TWP. The best substitution of PC with TWP was at 5% with a flexural strength value of 7.22 N/mm². Cost analysis revealed that the amount for making TC is greater than that of normal concrete, mainly due to the addition of the TLP, and this does not impact positively on the flexural strengths achieved. Nevertheless, PC replacement with TWP reduced the cost of binding material. In conclusion, the use of tuffcrete concrete based on flexural strength alone may be discouraged due to cost. But improved strength properties could still be achieved with better mix designs.

© 2023 MIM Research Group. All rights reserved.

1. Introduction

Concrete, which is a universally accepted material used for construction purposes, is produced primarily by mixing Portland cement, sand, gravel, or granite chippings with water in prearranged quantities in order to reach preferred properties. The mixture is usually allowed to gain strength before it can adequately carry a load. The combination of the cement and water forms a paste that aids in bonding the aggregates in the mixture. The use of concrete for construction works in Nigeria is on the rise as more developmental facilities are put up to meet the pressing basic needs of an increasing population.

However, the continuous collapse of these concrete structures is becoming very worrisome. Between October 1974 and November 2022, Nigeria documented about 541 building collapse incidences, and 61 of these happened in 2022 [1]. According to [2], an extraordinary degree of collapse occurred in 2014, while the greatest number of deaths recorded was in 2016 under the review period. The outcomes of these building collapses are seen in the loss of money invested and lives, the wastage of materials, the contractor's influence being badly affected, higher maintenance costs, the deterrent beauty of the building, and the bad reputation of the owners [3].

*Corresponding author: chioma.awodiji@uniport.edu.ng

^a orcid.org/0000-0003-3575-1405; ^b orcid.org/0009-0009-5412-2648

DOI: <http://dx.doi.org/10.17515/resm2023.731ma0404tn>

Res. Eng. Struct. Mat. Vol. 9 Iss. 4 (2023) 1169-1179

In summary, the major cause of building and structural collapses in Nigeria is corrupt practices in the construction industry. This is seen in the use of non-professionals in construction work, the use of sub-standard materials, shoddy work, and the non-compliance and enforcement of building code specifications by clients, contractors, and regulatory bodies for selfish reasons. [4]. Therefore, in order to alleviate the frequent occurrence of collapse of concrete structures, new materials with enhanced load-bearing and weathering properties are being investigated. This study seeks to investigate the flexural strength performance of Tuffcrete concrete since this type of concrete is gaining more and more popularity as an alternative to nominal concrete in Nigeria and is mostly applied in concrete pavement construction [5].

Tuffcrete concrete is a mixture of PC, Axion TWP, Axion TLP, water, rivers sand and crushed granite. The Axion tuffcrete white powder and liquid polymer are products of Axion Global Engineering Limited which is a subsidiary of Axion Canada. Their use in concreting is believed to have a lot of advantages over the use of conventional concrete. In 2022, approval was given by the Nigerian Federal Capital Development Authority (FDCA) for the employment of the Canadian-made Axion tuffcrete lightweight concrete system in the development of feasible building projects in Abuja [6]. The body also gave instructions to ministries responsible for road construction in the country to partner with research and tertiary institutions towards the application of research data in line with the use of tuffcrete in concrete making.

According to [7], the use of tuffcrete concrete in pavement construction is expected to improve the waterproofing effect of the pavement, reduce its rate of contraction and expansion, and enable the pavement to attain more load-bearing capacity than nominal concrete, depending on the mix design. This will make the road pavement last longer and live out its intended useful life without failing. In addition, tuffcrete concrete is expected to eliminate the use of damp-proof courses in foundation construction, is good for repairing damaged and old concrete, and results in a lighter-weight concrete than normal concrete. [6] stated that the product saves time and money and can reduce material and labor costs by 4%.

The rise in the use of these products for concrete production, especially in the construction of pavements, has necessitated the need to study the concrete material. However, it was observed from the literature review that very few scientific investigations on this product have been published online, making it very difficult to access information on previous related studies. So, the present study is intended to fill this knowledge gap.

The flexural strength of concrete is its capacity to withstand collapse via bending. This mechanical strength is the basis for the design of concrete roads. According to [8], the design of concrete pavement is done with a 4.5 MPa flexural strength at 28 days, based on third-point loading. Thus, the use of Tuffcrete concrete in the construction of Nigerian roads has made it very important to study the flexural strength property of the material. This will enable concrete designers to know how well the concrete is performing under flexure.

As earlier noted, not many researchers have published online materials on the use of Tuffcrete concrete in construction work. Nevertheless, only a very few published articles on TC were accessed via the internet. Some unpublished materials were also accessed from the Port-Harcourt warehouse of the Axion company in Rivers State, Nigeria. [9], in their study on the strength of steel-fibro tuffcrete element, observed a flexural strength range of 9MPa to 14MPa for tuffcrete concrete. These values expanded by 37% when the concrete was tested with the fibers, reinforcing rods and form work in place. [10], considered the inclusion of volcanic tuff as a substitute for Portland cement and tuff sand in mortar production, and recorded the best 28-day flexural strength result of 12.5 MPa at 50% replacement of Portland cement. At 28 days, strength readings of 5.7 MPa, 3.7 MPa, and 2.3 MPa were obtained with 25%, 75%, and 100% inclusions, respectively.

[11] worked with the addition of lava tuffs to implement concrete behavior. In concrete production, they replaced Portland pozzolan cement with 0%, 5%, 10%, 15% and 20% volcanic tuff and reported that the flexural strength of the concrete decreased as the percentage of the tuff increased. The maximum flexural strength of about 3.1MPa was established at 0% and, with 20% inclusion, a minimum flexural strength of 1.3MPa was obtained. As more volcanic tuff is added to the concrete mixture, it has been demonstrated that the amount of cement will decrease and thus hamper the hydration process leading to reduction in the generation of the strength gaining compounds such as C_2S and C_3S . [11] also observed that as the percentage of substitutable value was increasing, the slump of the concrete began to decrease. This was due to the high porous nature of volcanic tuff that make it able to suck up mixing water from the concrete.

[12] reported that a common problem for polymer-cement mixtures is that their compressive strength is generally modest because of a lack of joint bonding between two dissimilar phases in the concrete structure. However, the concrete showed improvements in all areas of performance. Studies by [13] showed that the durability and adhesion strength of cementitious materials are enhanced by including a very low amount of water-soluble polymer, thereby enabling them to be used as repair materials. An increase in workability as a result of polymer plasticizing and the effect of air entrainment was observed. It was noted that, compared to conventional concrete, a greater retention of water had been observed which led to more flowing mortar. This was effective in reducing the mortar's bleeding and, therefore, increasing concrete homogeneity by regulating segregation of new mixes. However, due to the increased entrained air, the mechanical properties of the concrete have been reduced.

2. Materials and Methods

The materials and methods adopted in this study are discussed as follows:

2.1. Materials

The following materials were used for producing the tuffcrete concrete: Portland cement (PC), tuffcrete white powder (TWP), river sand, granite chippings, tuffcrete liquid polymer (TLP), and water. The 42.5N grade of Dangote 3X brand portland cement was used. It meets the requirements of the specification for cement [14]. Axion tuffcrete white powder and liquid polymer were purchased from the Axion Chemical warehouse located along Aba Express-way, Iribe, Port-Harcourt, Rivers State Nigeria. According to [15], the TWP is a product marketed under and protected by a registered trade name. It acts as a molecular binding agent which meets the specifications of chemical resistance and durability. The TLP plays the role of a molecular activator that provides high resistance to aggressive liquids and chemicals in concrete. It is a water-soluble polymer. The chemical and physical property test results for the TWP and TLP are presented in Table 3 and Table 4.

At the Choba campus of the University of Port Harcourt, water (free of dirt and organic matter) was obtained. From a construction site on the university's campus, river sand was purchased. Granite-crushed rocks with nominal sizes of 19mm were used as coarse aggregate. The sieve analysis tests on the aggregate, according to [16], displayed that aggregates were uniformly graded accordingly.

2.1.1 Mix proportioning

Standard concrete beams of 100mm x 100mm x 400mm were prepared according to [17] and cured in water for 28 days, as illustrated in Figure 1 and Figure 2 accordingly. A prescribed mix of 1:2:2 (binder: sand: granite) at a 0.6 diluted polymer/cement ratio was investigated. Water for mixing concrete was prepared by diluting 10 liters of polymer in 200 liters of water. Portland cement was replaced by tuffcrete white powder in percentages of 0%, 5%, 10%,

15%, 20%, and 30%, respectively. Two specimens were made for each mix ratio, leading to a total of 12 concrete beams. The mix proportions of the tuffcrete concrete are shown in Table 1.

Table 1. Concrete mix proportion of tuffcrete concrete

Mix No.	Mix proportions of concrete				Dil. poly-cement ratio	Mix proportioning by weight of one concrete beam of size 100mmx100mmx400mm (kg/m ³)					
	PC	TWP	Sand	Granite		PC	TWP	Sand	Granite	Water	Liquid polymer
F1	1	0	2	2		480	0	960	960	288	14.4
F2	0.95	0.05	2	2		456	24	960	960	288	14.4
F3	0.90	0.10	2	2	0.60	432	48	960	960	288	14.4
F4	0.85	0.15	2	2		408	72	960	960	288	14.4
F5	0.80	0.20	2	2		384	96	960	960	288	14.4
F6	0.70	0.30	2	2		336	144	960	960	288	14.4



Fig. 1 Concrete beams



Fig. 2 Curing of beams by total immersion in water

2.2 Methods

Methods applied in the study of tuffcrete concrete include chemical and physical property tests on the TWP and TLP, slump tests of fresh concrete, flexural strength tests on hardened concrete, and a cost analysis of the use of tuffcrete in concrete production.

2.2.1 Physical and chemical Property Tests on the TWP and TLP

The chemical composition of the TWP and TLP was obtained in accordance with [18] using the X-Ray Fluorescence (XRF) method. Results obtained are shown in Tables 3 and 4. The physical properties of the materials were also measured, and the values determined are presented in the same tables.

2.2.2 Slump Test

The workability of the fresh concrete paste was accessed using the slump test in accordance with [19], as depicted in Figure 3. The values obtained are presented in Figure 5.



Fig. 3 Slump test on fresh concrete

2.2.3 Flexural Strength Test

The flexural strength of the hardened concrete was ascertained by testing the specimen under flexure using a universal testing machine in accordance with [20]. The equation (1) was used to calculate the flexural strength of the concrete. While, Figure 4 shows the experimental procedure carried out in the laboratory.

$$\text{Flexural strength (N/mm}^2\text{)} = 3PL/2bd^2 \quad (1)$$

Where, P is the fracture load (N); b is the average specimen width at fracture (mm); D is the average specimen depth at fracture (mm).



Fig. 4 Flexural strength test of concrete beam

2.2.3 Cost Analysis of Producing TC

Costing to determine and compare the total amount of money for producing a cubic meter of tuffcrete concrete beam as well as conventional concrete was done. Table 2 shows the current values of the constituents of tuffcrete concrete that were used in carrying out the analysis. The results of this analysis are given in Table 5.

3. Results and Discussions

3.1 Chemical and Physical Properties of TWP and TLP

The results of the chemical and physical property test conducted on TWP and TLP are depicted in Table 3 and Table 4 as follows:

Table 2. Current market prices of Tuffcrete concrete components

S/No.	Constituents	Market procurement pattern	Unit cost (₦ per Kg)
1.	Cement	₦4,500 per 50kg bag	90.00
2.	Granite	₦420,000 per 30ton (30,000kg)	14.00
3.	Sand	₦43,000 per 30ton (30,000kg)	1.43
4.	Water	₦3,500 per 1000kg	3.50
5.	Tuffcrete white powder	₦2,500 per 50kg	50.00
6.	Tuffcrete liquid polymer	₦25,000 per 10kg	2500

Table 3. Chemical property test for TWP and TLP

S/N	OXIDES	TWP (%)	TLP (%)
1.	CaO	4.83	1.58
2.	SiO ₂	68.24	0.73
3.	AL ₂ O ₃	5.37	2.69
4.	Fe ₂ O ₃	3.74	0.31
5.	MgO	2.60	0.84
6.	Na ₂ O	0.23	0.03
7.	K ₂ O	3.69	0.29
8.	SO ₃	0.72	0.17
9.	TiO ₂	0.42	0.02
10.	ZnO	0.08	1.34

Table 4. Physical property test for TWP and TLP

S/N	Properties	TWP	TLP
1.	Bulk density	10.28KN/m ³	1.088g/ml
2.	pH	7.98	5.78
3.	Color	White	Black
4.	Electrical conductivity	-	136.6µS/cm
5.	Porosity	68%	-
6.	Particle size	43.2µm	-
7.	WHC	55.76%	-

The combination of the oxides of aluminum, iron, and silicon gave a total percentage of 77.35%. This exceeded the specification given by [21] that states that the summation of these three oxides in a binding material for concrete production must not be less than 70%. AL₂O₃ was at 5.37%, SiO₂ at 68.24%, and Fe₂O₃ at 3.74%.

3.2 Slump

Fig. 5 reveals that the replacement of PC with TWP improved the workability of the fresh concrete. A drastic rise in this property of the concrete was observed from 0% to 5% replacement. Slump values rose from 5.09mm to 40.5mm at these points accordingly. Values kept increasing steadily from 5% up till 30% substitution. Slump value at 30% inclusion was 80.5mm. Therefore, a percentage increase in slump of 1481.53% was observed between 0% to 30% TWP addition. Due to the high porosity of the TWP (68%), it is expected that the workability of the concrete should reduce as the content of TWP increased. This is because, there are much voids that could assimilate mixing water from the fresh concrete. But this was not the case. According to [9], the use of water-soluble polymer in concrete making creates an air entrainment and plasticizing effect in the concrete leading to more water being retained in the mix. This makes concrete to be more flowable.

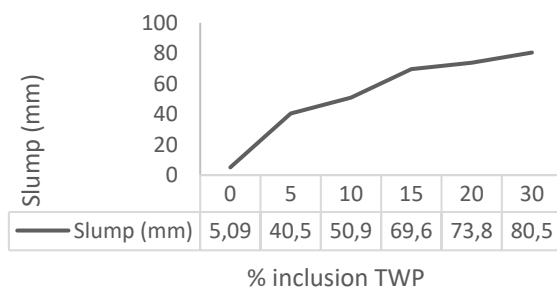


Fig. 5 Slump (mm) vs. % inclusion of TW

3.3. Flexural Strength

Fig. 6 shows the behavior of the flexural strength of the TC as the content of TWP increased. A boost in the amount of TWP lowered the flexural strength of the concrete. Nominal concrete had the largest value at 9.38 N/mm². This dropped to 7.22 N/mm² at 5% replacement, which was quite a significant drop. A very slight reduction in strength was observed between 5% and 10% as the flexural strength value dropped further to 7.20 N/mm². At 15% substitution, a remarkable reduction in strength was seen as values reduced further to 5.84 N/mm². Steady lessening of strength continued up to 30% replacement. Strength at this point was 4.38 N/mm². An optimal percentage replacement of 5% was achieved in the study, leading to a percentage strength reduction of 23.03% at that point.

The decrease in strength as more TWP was added into the concrete mix is due to the fact that lesser quantities of the strength giving compounds (i.e., the tricalcium silicate and the dicalcium silicate) were produced. This occurred because the addition of TWP in the cement slowed down the process of cement hydration that forms these compounds. As earlier observed, the inclusion of the TWP improved the workability of the fresh concrete due to polymer plasticization and air entrainment [13]. But, as the workability improved, the flexural strength of the concrete decreased.

3.4 Cost Analysis of Tuffcrete Concrete to Conventional Concrete

Table 5 illustrates the cost of each item for making concrete in Nigerian naira (₦) per cubic meter. Considering Table 5, the cost of producing a cubic meter of tuffcrete concrete increased far more than that of conventional concrete for all percentage replacements studied. A sudden increase in cost of production of 59.4% was witnessed between 0% and 5% incorporation. However, this rise was a result of the addition of TLP to the mixture and not due to the replacement of PC with TWP. In fact, the replacement of PC with TWP led to a gradual and

overall cost reduction of about 9.76% from 0% to 30% replacement when the cost of TLP was excluded from the analysis, as presented in Figure 8. This means that the main source of the high cost of tuffcrete concrete production when compared to nominal concrete is the incorporation of the TLP in the mixture. As the amount of TWP substitution increased above 5%, the cost of producing TC began to drop gradually as shown in Figure 7.

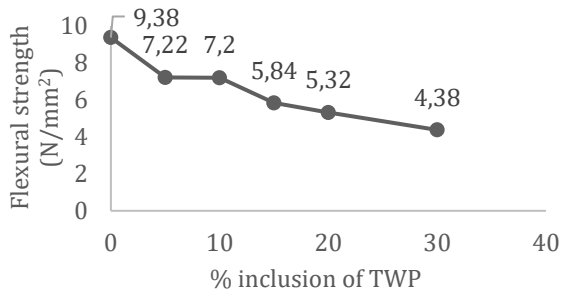


Fig. 6 Relationship between flexural strength (N/mm²) and % inclusion of TWP

Table 5. Cost of concrete constituent materials

S/ No	% repl.	Cement	Granite	Sand	Water	TWP	TLP	Total cost of TC	Total cost of TC- cost of TLP	% Diff. of cost
1	0	43,200	13,440	1,372.80	1008	0	0	59,021	59,021	0
2	5	41,040	13,440	1,372.80	1008	1200	360 00	94,061	58,061	38
3	10	38,880	13,440	1,372.80	1008	2400	360 00	93,101	57,101	39
4	15	36,720	13,440	1,372.80	1008	3600	360 00	92,141	56,141	39
5	20	34,560	13,440	1,372.80	1008	4800	360 00	91,181	55,181	39
6	30	30,240	13,440	1,372.80	1008	7200	360 00	89,261	53,261	40
Average =									39	

4. Conclusions

In this work, the flexural strength of tuffcrete concrete and its cost implications were investigated compared to conventional concrete. A specified mix ratio of 1:2:2 (binder:sand:granite chipping) at a 0.6 diluted polymer/cement ratio was studied. The binders, which were PC and TWP, were combined in such a way that they replaced PC with 0% to 30% of TWP one after the other. This study revealed that this substitution greatly improved the workability of the fresh concrete, making the concrete a very flowable one that can be finished very smoothly. The concrete produced can be classified as having medium workability and is suitable for normal reinforced concrete works with manual compaction, and heavy reinforced concrete works with vibration as the mode of compaction. Since the TWP content has a great impact on the workability of the concrete, the mix design of tuffcrete concrete should be done considering that the water-cement ratio must be minimal. This is expected to improve the strength of the concrete. Although, the effect of the TLP in the concrete was not specifically studied in this work, the presence of polymers in fresh concrete have been proven to improve workability as a result of the entrainment of air and plasticization of the concrete. This may have been one of the reasons why the fluidity of the concrete was greatly improved.

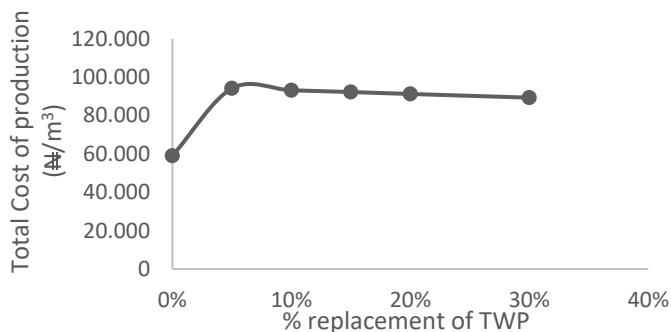


Fig. 7 Relationship between total cost of production vs. % replacement

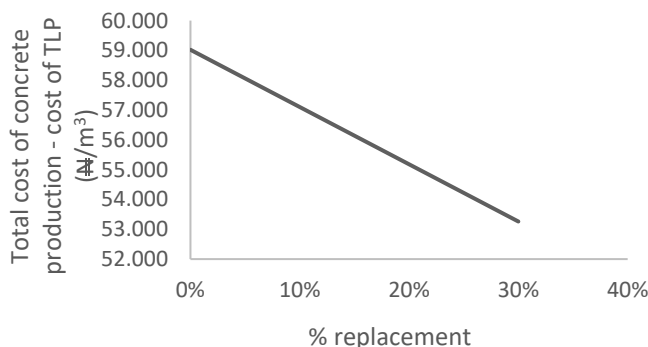


Fig. 8 Relationship between total cost of concrete production less cost of TLP (₦) vs. % replacement

Introduction of the TWP into the concrete mix lessened the flexural strength of the concrete. 0% inclusion of TWP gave the greatest flexural strength result, while 5% addition of TWP was seen as the best percentage insertion for the attainment of the finest strength of 7.22N/mm². 30% replacement generated a strength value of 4.38N/mm². There was no significant drop in strength between 5% and 10% replacements. The drop in strength could be attributed to the decrease in the content of cement in the concrete, effect of air entrainment, and plasticizing of the polymer within the cement matrix. However, strength is expected to increase at older age.

The cost of producing tuffcrete concrete was way higher than that of nominal concrete by reason of the insertion of TLP into the mix. The addition of TWP resulted in cost savings with regards to cement consumption. But this advantage was overtaken by the increased cost of the TLP. A 59.4% increase in cost was observed between 0% and 5%. However, after the 5% substitution, the cost kept decreasing slightly. At intervals of 5% and 10%, the cost dropped by 1.02%. Between 5% and 15%, a cost reduction of 2.04% was obtained. Between 5% and 20%, the cost was reduced by 3.1%, and a drop of 5.10% was observed between 5% and 30%.

A future examination of the effect of TLP in the concrete should be carried out so as to ascertain its advantage in the production of the tuffcrete concrete. There is also a need to study the microstructure of tuffcrete concrete in order to gain a better understanding of its makeup. This will enable the mix designer to understand the parameters to improve upon so as to have a very strong and durable concrete with properties that counter the higher cost of its production over that of conventional concrete.

Acknowledgement

We would like to acknowledge the great assistance given to us by Ovu-Eleonu Fortune and Faithful Peter with regards to the practical works at the laboratory.

References

- [1] Nigeria records 61 incidents of building collapse in 2022-Report [Internet]. [cited 2023 March 16] Available from: <https://tribuneonlineng.com/nigeria-records-61-incidents-of-building-collapse-in-2022-report/>
- [2] Odeyemi SO, Giwa ZT, Abdulwahab R. Building collapse in Nigeria (2009-2019), causes and remedies. Journal of Science and Engineering Production. 2019, 1(1):122-135. Available from: https://www.researchgate.net/profile/Odeyemi-Samson-O/publication/334002053_Building_Collapse_in_Nigeria_2009-2019_Causes_and_Remedies_-_A_Review/links/5d129a3192851cf4404c263e/Building-Collapse-in-Nigeria-2009-2019-Causes-and-Remedies-A-Review.pdf
- [3] Adebowale PA, Gambo MD, Ankeli IA, Dabara DI. Building collapse in Nigeria: Issues and challenges. Conference of the International Journal of Arts and Science, 2016, 9(1):99-108. Available from: https://www.researchgate.net/publication/334431926_BUILDING_COLLAPSE_IN_NIGERIA_ISSUES_AND_CHALLENGES
- [4] Obodoh D, Amade B, Obodoh C, Igwe C. Assessment of the effects of building collapse risks on the stakeholders in the Nigerian built environment. Nigerian Journal of Technology. 2019, 38 (4):822-831. <https://doi.org/10.4314/njt.v38i4.2>
- [5] About Axion tuffcrete [Internet]. 2023 [cited 2023 March 16]. Available from: <https://axioncanada.com/tuffcrete.html>
- [6] Onyedinefu O. FCDA approves use of axion tuffcrete light weight concrete system. [Internet]. 2023 [cited 2023 March 12]. Available from: <https://businessday.ng/real-sector/article/fcda-approves-use-of-axion-tuffcrete-light-weight-concrete-system/>
- [7] Axion Flyer [Internet]. 2023. [cited 2023 March 16]. Available from: <https://axioncanada.com/download/AXION-FLYER.pdf>
- [8] American Standard Testing Method ASTM C78. Standard method for flexural strength of concrete using simple beam with third-point loading, 2009.
- [9] Khasauov YM, Atabieva MM, Chochaer AA. Strength of the monolithic coverings with non-flexible formwork of steel fibro-tuffcrete element. IOP conference series: Material Science and Engineering. 913, 022046; 2020. <https://doi.org/10.1088/1757-899X/913/2/022046>
- [10] Al-zou'by J, Al-zzboon KK. Effect of volcanic tuff on the characteristic of cement mortar. Ceramica. 2014, 60(354):279-284. <https://doi.org/10.1590/S0366-69132014000200018>
- [11] Edris, WF, Abdelkader, S., Salama, A. H. E., Sayed, A. A. A. Concrete behavior with volcanic tuff inclusion. Civil Engineering and Architecture. 2021, 9(5): 1434-1441. <https://doi.org/10.13189/cea.2021.090516>
- [12] Liang R, Liu Q, Hou D, Li Z and Sun G. Flexural strength enhancement of cement paste through monomer incorporation in-situ bond formation. Cement and Concrete Research. 2022, 152, 106675. <https://doi.org/10.1016/j.cemconres.2021.106675>
- [13] Knapten E, Beelden S, and Generat V. Water soluble polymeric modifiers for cement mortar and concrete. [Internet]. 2023. Available from: bwk.kuleuven.be/mat/publications/internationalconference/2007-knapten-watersoluble-conmat.pdf
- [14] Nigerian Industrial Standard NIS 444-1. Composition, specification and conformity criteria for common cements, 2003.

- [15] Axion tuffcrete white powder [Internet]. 2021 [cited 2023 March 16]. Available from: https://m.facebook.com/axionafricadotcom/posts/the-axion-tuffcrete-white-powder-is-a-proprietary-formulation-which-act-as-a-mol/1141218339697087/?_rdr
- [16] American Standard Test Measurement ASTM C136-06. Standard test method for sieve analysis of fine and coarse aggregate, 2006.
- [17] Bureau of Indian Standards IS 516. Methods of tests for strength of concrete, 1959.
- [18] American Standard Test Measurement ASTM C18. Guide to ASTM test methods for the analysis of petroleum products and lubricants, 1994.
- [19] British Standard BS 1881-102:1983. Testing concrete - method for determination of slump, 1983.
- [20] British Standard BS 1881-118. Testing concrete - method for determination of flexural strength, 1983.
- [21] American Standard Test Measurement ASTM C618. Standard specification for coal, fly-ash and raw or calcined natural pozzolan for use in concrete, 2022.

Blank Page



Environmental stress cracking of chemically aged HDPE-100 gas pipe under impact fracture mode

Khaoula Berkas^{1,a}, Kamel Chaoui^{*1,b}, Wafia Ghabeché^{2,c}, Latifa Alimi^{3,d}, Abir Guenouche^{1,e}, Fatima Zohra Melais^{4,f}

¹Mechanics of Materials and Industrial Maintenance Research Laboratory (LR3MI), Mechanical Eng. Dept., Faculty of Technology, Badji Mokhtar University, PO Box 12, 23005 Annaba, Algeria

²Electrical Eng. Dept., Faculty of Technology, Abderahmane Mira University, Targa Ouzemour, 06000 Béjaia, Algeria

³Research Center in Industrial Technologies (CRTI), PO Box 64, Chéraga, 16014 Algiers, Algeria

⁴Civil Eng. Dept., Faculty of Technology, Badji Mokhtar University, PO Box 12, 23005 Annaba, Algeria

Article Info

Abstract

Article history:

Received 11 Apr 2023

Accepted 01 Jul 2023

Keywords:

Polyethylene pipe;
Ageing effects;
Sorption;
Charpy fracture energy;
Fracture surface

High-density polyethylene (HDPE) pipes are widely employed for urban gas, water and sewage transportation networks because of economic considerations and very satisfactory lifetimes. As they are straight forwardly designated for numerous hostile conditions, the stress cracking resistance needs to be investigated in combination with ageing in controlled environments. This study is set to investigate long-term sorption experiments followed by Charpy fracture tests using the same arc-shaped specimens machined from HDPE pipe. Chemically ageing media are deionized water (DW) and both hydrochloric (HA) and acetic acids (AA). For the first 4 weeks, it is found that % weight change increased drastically for HA medium. Then, for the next 30 weeks period, the inverse situation took place as the % weight change for HA diminished tending nearly to zero while it augmented for DW and AA environments. Within the first week, the impact fracture energy of HDPE decreased for all media and then increased substantially for both acids well above the as-received (AR) reference line. Charpy energy experienced a monotonic decrease for DW as swelling enhancement is promoted in the absence of plasticized material. After 7 months ageing, both acids show much higher Charpy energies than AR and DW specimens and a substantial increase in ductility. The resilience changes with respect to AR tests are respectively +110%, +75% and -25.8% for HA, AA and DW. It is accepted that strong acids (i.e., HA) easily deplete antioxidants and carbon black mixed with the resin. The combined effects of both mechanical and chemical processes can serve a more representative durability studies of HDPE pipes including ESC phenomenon.

© 2023 MIM Research Group. All rights reserved.

1. Introduction

Numerous methods have been developed to characterize the mechanical resistance of high-density polyethylene (HDPE) pipes based on diverse approaches [1-4]. Some of these methods have been suitably worked out and then adapted to evolve towards standard tests used by manufacturers in order to guarantee safety, quality and the best possible durability for the products. However, mechanical resistance is not the only assurance for HDPE pipes conveying water or extremely dangerous fluids such as natural gas in urban areas. The effect of the

*Corresponding author: chaoui.kamel@univ-annaba.dz

^aorcid.org/0009-0004-4393-2817; ^borcid.org/0000-0001-6532-9462; ^corcid.org/0000-0003-1423-3203;

^dorcid.org/0000-0003-4359-3566; ^eorcid.org/0009-0006-3148-1849; ^forcid.org/0000-0003-4709-8247

DOI: <http://dx.doi.org/10.17515/resm2023.737ma0411>

Res. Eng. Struct. Mat. Vol. 9 Iss. 4 (2023) 1181-1199

environmental service conditions must be included in order to obtain the best assessment taking into account the limitations to which plastic pipes are truly subjected to. For this reason, customary mechanical tests and their standards devoted to plastic pipes are extended to account for new design constraints, material conditioning and environmental factors during global durability characterization [5,6]. For polymers, various mechanical tests have been extended to such influence commonly known as Environmental Stress Cracking Resistance (ESCR) [7].

A number of mechanical tests are frequently used to determine the performance of polymers under impact conditions including Charpy, Izod and Falling Weight Impact. Today, Charpy fracture energy is recognized as a product property and a ranking basis for plastic pipe materials. Indeed, the superior performance of HDPE over MDPE (Medium Density Polyethylene) pipes is deduced from Charpy fracture tests, performed at 20°C and 1.6 m/s, which showed 15 and 24 kJ/m² respectively [5,8]. Also, it is established that impact loading based on ISO 17281 standard is the best example to obtain semi-brittle fracture in HDPE which is the key mechanism that resists crack propagation. Alternatively, the Charpy test described in ISO 179 is intended to measure toughness reflecting a combination of brittle and crazing mechanisms at the maximum force together with the absorbed energy by shear yielding [9,10]. The comparison between fracture mechanics-based analysis of instrumented Charpy impact test data for a set HDPE pipe grades and data of the conventional Charpy impact test concluded that the latter is established as a robust reproducible measure of the resistance to rapid crack propagation (RCP) [9]. Likewise, a formal brittle fracture mechanism is also revealed when analyzing semi-crystalline polymers pipes subjected standard impact tests and low temperatures [9,11].

ASTM-D1693 is a standard test method for Environmental Stress-Cracking (ESC) of ethylene plastics as it aims determining their vulnerability to Slow Crack Growth (SCG) in contact with chemical agents [12]. Usually, it uses notched bent strip (or U-shaped) specimens immersed in a controlled environment. However, a careful review of the specialized literature relevant to ESC of HDPE pipe does not show any experimental work using arc-shaped specimens chemically aged and tested under impact mode. PE pipe arc-shaped specimens have been mentioned in published studies dealing with standardization and mechanical aspects faraway from chemical ageing effects [13-17]. For instance, it is proposed for SCG a quantitative relationship between the fibrillar texture and corresponding applied load [13]. Likewise, few approaches are developed for radial impact plane strain fracture toughness parameters based on GIC which is characterized by the elastic critical strain energy release rate or J_{1C} which is characterized by the elasto-plastic J-integral. These toughness measurements are obtained from non-standard polyethylene arc-shaped specimens under either bending or tension modes [14-16]. Distinctly, the evolution of GIC in the radial direction is also discussed using Charpy fracture energies measured from machined arc-shaped specimens with variable HDPE pipe thicknesses [17].

The utmost risky situation causing irreversible property degradation and durability loss for HDPE pipes is ESC phenomenon as it is induced by various environmental reactions in the presence of effective external mechanical and/or thermal loads [18,19]. Depending on the nature and the possibility of amalgamation, aggressive agents may be acting alone or mutually. The most encountered ageing environments leading to HDPE degradation are frequently triggered by thermal effects, humidity or mineralized waters, hydrocarbons and fuels, alkali and acidic solutions, solvents, oxygen, chlorine, UV rays and living micro-organisms [6,7,18,19].

In the case of acids, several studies have shown the generally adverse effects on both structure and on physical properties of HDPE and polypropylene (PP) as shown in Table 1a for the case of transportation pipes [20-24] and in Table 1b for others specific applications [25-28].

Table 1a. Literature survey of HDPE pipe interactions with sulfuric and hydrochloric acids

HDE Product	Testing Conditions	Aging time (d)	Observations	Ref.
Pipe	33% H ₂ SO ₄ , ATR FTIR, 75°C	30 min.	Structural changes identified by ATR FTIR, Formation of a sulfonic group and olefinic initiation, H ₂ SO ₄ attacks and destroys carbonyl impurities Probably incorporated during polymerization.	[20] ; 1985
Gas Pipe	20% H ₂ SO ₄ , Tensile, 25°C	90	H ₂ SO ₄ solution affects the HDPE filament structure, Decrease of E and ε _y by 58.5% and 32% respectively, Across pipe wall, lowest E values are at outer layers.	[21] ; 2009
Pipe, Grade 80	20% H ₂ SO ₄ , Tensile, 25°C	7	External, intermediate and internal layers are considered, Values of E decreased by 60%, 58% and 56% respectively, Increase of ultimate strain ε _f across the pipe wall thickness.	[22] ; 2013
Pipe	Mixture: H ₂ SO ₄ /SO ₄ ²⁻ Tensile, 25°C, pH=1	168	Sorption experiments: HDPE shows a Fickian diffusion, Sorption rate: 0.008%; hydrolysis is invoked, Increased σ _y (+26%) and significant decrease in ε _y (~74%), Both crystallinity and density are augmented.	[23] ; 2014
Pipe	HCl, (5,10, 20%) Roughness, DSC, 25°C	129	increase of roughness with acid concentration, Crystallinity drop (~ 33%) with acid concentration, Important loss of fracture strength.	[24] ; 2015

Indeed, damage degrees, following exposure to H₂SO₄ or HCl acids over variable ageing periods, are complex and multifaceted [27,29]. Significant alterations of HDPE structure together with preminent increases and/or decreases in mechanical and thermal properties are observed. When mechanical loads, thermal effects and exposition to chemically aggressive conditions are combined, resulting polymer degradations and service lifetime reduction may become even more significant [20,25-28].

HDPE pipe networks for transmission and distribution of fluids fall in the category of fluid-polymer interactions. This infers that physico-chemical phenomena such as diffusion, surfaces, and solubility are unquestionably implicated somehow and instigate certain negative effects on product performance. The solubility parameter (δ) approach as defined by Hansen is required to explain sorption observations. Such parameter typically includes the effects of 3 cohesive forces, i.e., dispersive, polar and hydrogen bonding forces [29,30]. It is understood that whenever the solubility parameters (based on dispersive forces) of both the polymer and an ageing liquid are closer, environmental stress cracking (ESC) becomes possible. Hansen’s work [30] summarizes diffusion coefficients measurements in polymers for different concentrations, anomalous type absorption rates, reporting concentration

profiles for anomalous diffusion involving surface resistance and explaining water blisters formation in polymers due to saturation. On the other hand, Hansen’s approach is also utilized to characterize physical affinities (i.e., solubility, chemical resistance, permeability...) for polymers, surface wettability and ultimately to correlate ESC occurrence in polymers using the relative energy difference number [30].

Table 1b. Literature survey of some specific cases involving HDPE or PP in interactions with sulfuric or hydrochloric acids

HDE Product	Testing Conditions	Aging time (days)	Observations	Ref.
PE coating	10% HCl, thermal expansion, 50°C	1	Effects of H ₂ O and 10% HCl are not significant on melting, Small increase in linear thermal expansion coefficient.	[25] ; 2019
	30% H ₂ SO ₄ , Room T°	7 years	Liquid accumulation at polymer liner surface, Plasticization effects take place, Observed damage due to surface pulverization.	
Liner coating	H ₂ SO ₄ 50,70,80 and 90%, Heated up to 70°C.		Increase in melting temperature (aging in 50%), Crystallization degree increase (hot acid), Melting point gradually decreased as high concentrations affect the molecular structure.	[26] ; 2021
	H ₂ SO ₄ 70 - 90%, FTIR, heated 70°C	20	Detection of unsaturated double & triple bonds, Presence of carbonyl groups, Molecular structure is affected by high acid concentrations, Damage : Chain scission, dehydrogenation, oxydation.	
HDPE Micro-Plastic	H ₂ SO ₄ 70°C FTIR	7	Chemical changes: color alterations of white and black, Morphological deformation and surface sulfonation, No changes or new signals in the FTIR spectrum.	[27] ; 2022
			3.5% crystallinity decrease after HCl treatment,	
PP sheet	6% HCl, Drying: 70°C for 3h	60	Overall PP polymer orientation: it becomes less orderly, Tensile tests: expression of more brittleness after exposure, 5.6% reduction in tensile strength.	[28] ; 2018

The objective of this study is to investigate simultaneously acidic liquid sorption and Charpy fracture energy of HDPE pipes. Specifically, the proposed testing specimens are non-standard arcs directly machined from an HDPE gas pipe [14-17]. The effects of ageing in deionized water and acidic environments on sorption and fracture energies are discussed for different periods of immersion.

2. Experimental Procedures

This section presents as-received (AR) material characteristics, sample preparation and both sorption and Charpy testing conditions. The raw material is a high-density polyethylene extruded by CHIALI Co. (Sidi Bel-Abbes, Algeria) as HDPE-100 gas pipe. It should be noted that it is a very resistant pipe and is manufactured to last in service well above the 100 years limit. Its dimensions are 200 mm in OD with an SDR of 17.6 and it is pigmented with carbon black. Table 2 summarizes its typical characteristics.

Table 2. Some physical and chemical properties of HDPE-100 gas pipe material

Property	Limit values	ISO Standard
Density, (g/cm ³)	0.95–0.98	1183
MFI at 190°C; 21.6 kg, (g/10min)	0.75	1133
Carbon Black content, (%)	2.0 – 2.5	6964
OIT at 200°C, (min.)	≥ 20	11357-6
Elastic Modulus, (MPa)	550 – 1460	
Yield Stress, (MPa)	20 – 30	527-1
Elongation at break, (%)	≥ 350	
Toughness, (K _{IC} , MPa.√m)	2 – 5	13586 (ASTM E-399)
Shore D hardness, (at 20°C)	59	868
Resistance to cracking in surface-active environment, (mm/day)	≤15	(ASTM D-1693)
SCG Resistance, (Notched tube, 80°C, 165 h, 8.6 bars; thickness > 5mm)	No break	13479

Arc-shaped specimens are prepared directly from the pipe in order to preserve most of the specific morphological variances and residual stresses imparted by the extrusion manufacturing process. Cutting is accomplished using a TOKADA 16D20 lathe at a cutting speed of 380 mm/min. while the 2 mm deep V-notch is milled on a M-HURON 55 milling machine at 486 mm/min. The arc width is 24 mm and the notch is sharpened with a one-pass razor blade (Fig. 1a, 1b) [31] Abir. Other details on machining and testing are available elsewhere [17,21,22,24].

The conditioning environments are presented in Table 3. These are (1) deionized water (DW), (2) 5% acetic acid (AA: CH₃COOH) and (3) 20% hydrochloric acid (HA: HCl) [32]. The ageing durations are 7, 14, 28 and 210 days at laboratory condition (atmospheric pressure and ~ 22°C). All specimens are weighted using an OHAUS electronic scale (max. 220 g; ±10⁻³) and then conditioned in sealed glass containers within a controlled laboratory chamber (Fig. 1c).

The tests are carried out on a ZWICK 5113 Charpy impact tester controlled with a testXpert© Software. The device complies with the standards DIN EN ISO 179, DIN 50115, DIN 53453 and ASTM D 6110-97 for Charpy tests, while for impact tensile tests, it fulfills the requirements of the standards DIN EN ISO 8256 and ISO 8256 for (Fig. 1d).

In this specific case, two methods may be considered to study HDPE ductility: (i) % cross-sectional area reduction from arc-shaped specimens and (ii) % strain at failure from standard tensile testing [33,34]. Strain failure may also be considered from HDPE filaments tensile data, available in literature [21]. Fracture surface areas measurements are achieved using the free and open-source software “ImageJ” [35]. It is mostly employed for image treatment to assess differences as they appear in the aftermath of an altering event in terms of surface area and

pixel value statistics. For the present situation, ImageJ is used as a tool for fracture surface analysis from low magnification digitized pictures.

Table 3. Number of tested specimens and characteristics of conditioning liquids

Medium	Chemical formula	Nb spec.	Manufacturer	[Conc.]	pH solution	Aggressiveness (Lab. T°, [32])
Deionized Water (DW)	H ₂ O	25	SARL. AA, Ain-Smara (Algeria)	-	5.7	HDPE resistant for T ≤ 60°C
Acetic Acid (AA)	CH ₃ COOH	20	ETS. NAIDJA, (Algeria)	5%	4	
Hydrochloric Acid (HA)	HCl	20	CARLO ERBA REAGENTS (France)	20%	0.5	

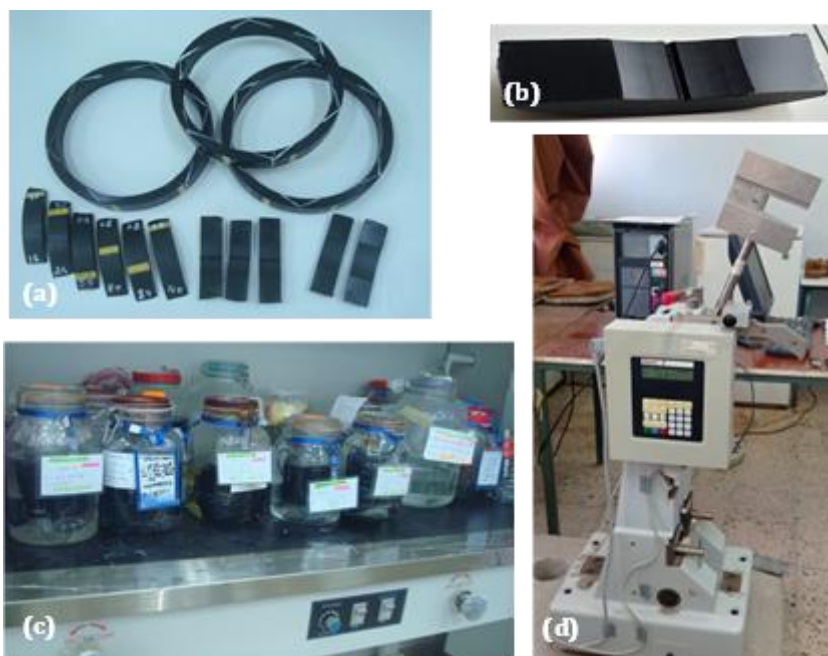


Fig. 1 (a) Cut and milled arc-specimens from pipe rings, (b) inner side notch, (c) Glass containers for aging in aggressive environments, (d) Zwick Charpy testing instrument

3. Results and Discussion

3.1. Liquid Sorption

The adopted approach in this experimental procedure is designed to have an idea about the % mass variation under the effect of liquid sorption by the HDPE arc-shaped samples before impact testing. This method allows subsequent mechanical characterization tests to be carried out on the very aged specimens. The % mass variation, presented in Figure 2 as a function of the square root of elapsed time, is calculated according to equation (1):

$$\frac{\Delta m}{m_0} = \frac{m_t - m_0}{m_0} \quad (1)$$

where m_0 and m_t are the masses measured initially and at time t , respectively.

For the environments considered in this study, different phenomena are observed during the 7 months immersion. DW medium is characterized by a relatively slow initial sorption phase (0-7 days) followed by an acceleration between 14 and 28 days and ultimately an evolution towards a form of saturation (equilibrium). This behavior is more or less similar to that of CH_3COOH , which shows an equilibrium starting the 14 days period up to 7 months. The limit sorption levels by HDPE for these 2 fluids remain below 0.04% with a concretization of a saturation-like plateau beyond the one-month period. Alternatively, the HCl case is divided into 2 parts showing a significant sorption after 14 days approaching 0.06% and followed by an accentuated desorption up to 7 months passing even below those of DW and CH_3COOH . Similar sorption data are presented in literature for DW and HCl [23].

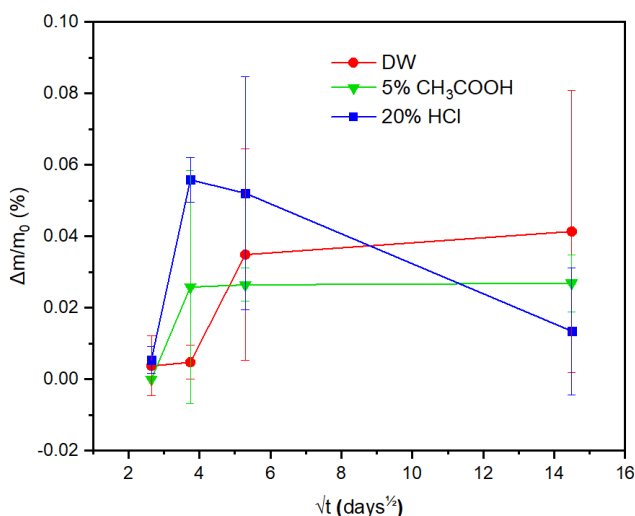


Fig. 2 Weight % change as a function of time (\sqrt{t} (Days^{1/2})) for HDPE exposed to different media: DW, 5% CH_3COOH and 20% HCl solutions

Based on Weitsman's categorization which lists different encountered sorption curves shapes, it is concluded that the 3 media considered in this study are of types (B), (LF: Linear Fickian) and (D) respectively for DW, AA and HA [36]. Generally, water sorption is identified as Type B for both polymer and composite materials. Such curve characterizes the condition of two-stage diffusion where weight gain data are related with mild fluid effects and are essentially reversible upon drying [19,36]. On the other hand, Type D curves agree with weight loss attributed to chemical and/or physical break-down of HDPE. Mainly, it is caused by leaching along interphase regions, as well as by hydrolysis, i.e., the disjoining of side groups from the backbones of the HDPE chains followed by chain scissions which is an irreversible response leading ultimately to structural failure as reported [36].

On the basis of the previously discussed solubility parameter approach, the short-term sorption order (HA, DW and AA) is explained. In the long-term, hydrochloric acid (HA) causes an increase in the crystallinity by crystallization chemistry and the resulting chain scissions together with the reorganization in crystalline clusters may play a barrier role as regards of fluid passage. In addition, the phenomenon of plasticization prevents any diffusion of HA and

a reactive polymer degradation is initiated. For other semi-crystalline polymers, energy-dispersive X-ray analysis revealed a chlorine pic after exposure to HA, indicating a chemical attack by chlorination reaction [28]. In the case of a contact between plasticized PVC and acetic acid, a simultaneous diffusion takes place as the liquid moves into, and plasticizer out of the polymer. Usually, such mass transfer is an unsteady state diffusion-controlled process [28]. Some experimental observations for HDPE interactions with acids are summarized in Tables 1a and 1b.

3.2. Impact Fracture Energy

This study examines four specific aspects associated with ESC of HDPE pipes: (i) manufacturing of non-standard arc-shaped specimens, (ii) chemically ageing in DW, acetic and hydrochloric acids for several months, (iii) measuring sorption/desorption based on actual specimens and (iv) testing under impact loading (Charpy). Such investigation is considered as a reasonable continuation for a lot of experimental work willing to introduce ESC phenomenon following the extension of the standard ISO/DIS 17281 as proposed by Niglia et al. [14] and others [15-17]. In the case of AR specimens, Fig. 3a shows the buckled final forms after impact testing. Post-failure observation shows significant deformation and an irreversible crack opening forming inconstant acute angles. The fast crack propagation covers more than 95% of specimen thickness. Total separation into two parts did not occur for AR tested specimens implying some ductility especially towards the final propagation stages (outermost pipe layers) and a substantial residual toughness left over. When using an instrumented impact tester, literature shows that for a width to crack length ratio (a/w) of 0.2, the maximum load at break attained 375 N within 1.10 ms. Moreover, increasing the (a/w) ratio, resulted in lower breaking load as the ligament is shortened [14]. However, for chemically aged ones, a few specimens are torn apart upon impact suggesting a material resistance loss and a factual evolution towards some kind of brittleness. This explanation is drawn from long-term testing of polyethylene pipes as damage mechanisms such as oxidation, polymer plasticization, chain scission and chemical degradation are found to take place lowering drastically the material strength. Measured Charpy impact fracture energies for one lot of HDPE specimens are presented in Fig. 3b.

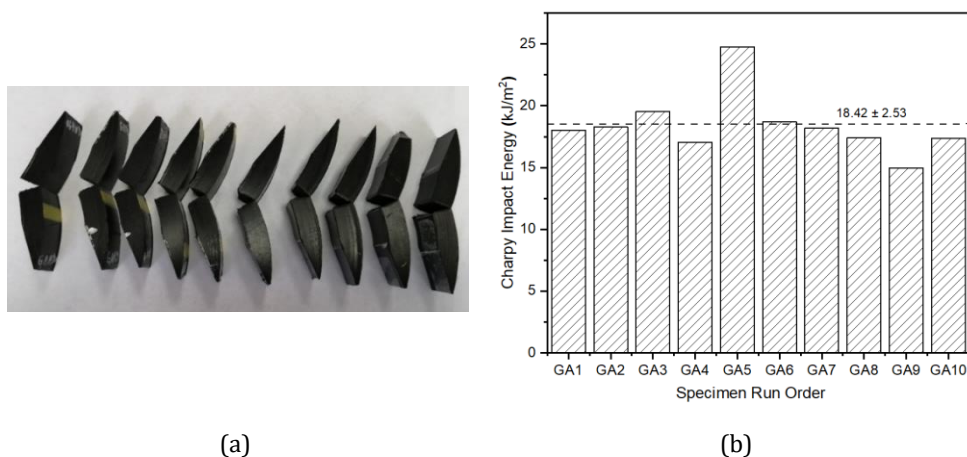


Fig. 3 (a) Ultimate shape of fractured arc-shaped specimens (GA: Gas As-received pipe), (b) Recorded impact fracture energy (Dashed line: mean value)

Good reproducibility is observed with 18.42 kJ/m² as an average value. Generally, such specific measurements based on arcs and different loading schemes are experimentally or

numerically utilized to obtain further fracture parameters such as GIC and JIC without the effects of chemical environments. Therefore, it was not possible to make appropriate comparisons with available literature [14-17]. However, when using standard specimens, Leever et al. presented closer Charpy fracture energies of 17 kJ/m² and 23 kJ/m² respectively for MDPE and HDPE at 20°C [8]. Table 4 summarizes previous impact experimental studies carried out in LR3MI laboratory on HDPE arcs provided by different manufacturers [31-33].

Table 4. Charpy fracture energy (arc-shaped HDPE specimens from local pipe manufacturers)

Pipe Lots	HDPE Grade (Manuf. year)	OD (mm); <SDR>	Width (mm)	Nb. of specimens	Charpy Fract. Energy (kJ/m ²)	Ref.
1	HDPE-80, SARL TUNEX, (Oran), Gas (2010)	125	8	16	14.53 ± 4.89	[37]; 2012
2	HDPE-100 TUBOGAZ Co., (Annaba), Water (2021)	200 <17.5>	24	12	15.95 ± 2.43 *	[38]; 2021
3	HDPE-100K-PLAST Co., (Sétif), Gas (2020)	200 <17.5>	24	10	22.67 ± 1.96 *	[31]; 2022
4	HDPE-100 CHIALI Co., (Sidi Bel-Abbès), Gas (2019)	200 <17.5>	24	10	18.42 ± 2.53 *	This Study

(*) With razor cut.

Although, pipe dimensions and polymer resins are not similar, it is concluded that measured Charpy fracture energies present consistent results and allow ranking of resins.

For chemically aged specimens, Charpy fracture energy results versus elapsed time are depicted in Fig. 4. A great contrast is unveiled between the AR specimens and those aged in DW on one side and the two remaining acids (AA and CA). It is noted that the divergence in impact resistance becomes broader as the exposure time goes longer. Indeed, during the first 28 days, the fracture energy remained underneath the AR reference line for all studied media. Beyond this period, the curves diverged above and beneath the AR boundary. At 7 months of ageing, the effect of DW reduced the impact fracture energy by -25.8%, while AA and HA showed surprisingly raised values respectively by +75.3% and +110%. It should be remembered that after 28 days, a significant increase in desorption took place exclusively for HDPE specimens exposed to hydrochloric acid (Fig. 2).

For a tentative to correlate between sorption results and Charpy fracture energies as a function of ageing times, the following cases are discussed:

Case 1 (7 days ageing): On one hand, all sorption data for DW, AA and HA are below 0.005% (Fig. 2) while the Charpy energies remain rather close to each other and well below the AR ones (Fig. 4). These circumstances may imply that one week is a rather short period not fit to observe clear changes for such bulky samples.

Case 2 (14 – 28 days ageing): In this timespan, both acids (AA and HA) continue to follow the same pattern for Charpy energies while HA started undergoing a relative desorption which becomes more pronounced in the next period (Type D). After 4 weeks ageing, ranking from higher to lower, % sorption data and Charpy energies (CE) may be presented as follows:

$$\left(\frac{\Delta m}{m_0}\right)_{HCl} > \left(\frac{\Delta m}{m_0}\right)_{DW} > \left(\frac{\Delta m}{m_0}\right)_{CH_3COOH} \tag{2}$$

$$CE_{As-Received} > CE_{HCl} > CE_{CH_3COOH} > CE_{DW} \tag{3}$$

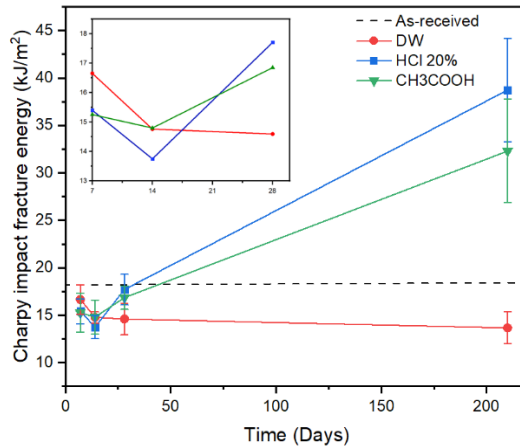


Fig. 4 Fracture Impact Energy as a function of time aged in DW, 5% CH₃COOH and 20% HCl solutions, (Dashed horizontal line refers to as-received case)

It is noticed that HDPE shows a higher sorption of HA with respect to DW and AA (Eq. (2); Fig. 2). At the same time, the Charpy energy associated with HA exceeds that of AA indicating that polymer brittleness is rapidly increasing with strong acids (Eq (3); Fig. 4). It can also be alleged that DW absorption may cause a further reduction of impact energy because of the capability of continued swelling.

Case 3 (210 days ageing): For long-term immersion, the fast desorption experienced by HA is the most striking event compared to AA and DW curves (Fig. 2). Meanwhile, DW continued to diffuse into HDPE following the stipulated Type B sorption [24,36] and causing depletion of antioxidants and other stabilizers [39]. It can be inferred that impact DW fracture energy will remain for a while below that of AR. Between 4 and 7 weeks, the AA percent weight uptake by HDPE describes a clear linear Fickian curve and remains lower than 0.027%. In addition, Charpy energies of HA and AA augmented rapidly and departed away from the AR reference line. Both observations are summarized below:

$$\left(\frac{\Delta m}{m_0}\right)_{DW} > \left(\frac{\Delta m}{m_0}\right)_{CH_3COOH} > \left(\frac{\Delta m}{m_0}\right)_{HCl} \tag{4}$$

$$CE_{HCl} > CE_{CH_3COOH} > CE_{As-Received} > CE_{DW} \tag{5}$$

Both HCl and DW environments' positions in Eqs. (4)-(5) are completely reversed, i.e., the most absorbing samples give the lowest Charpy energy and vice versa. As mentioned earlier material deterioration is occurring gradually within the HDPE structure all along with hydrolysis and readiness for ultimate failure in strong acids. The evolution towards a limit of water swelling (saturation) and its reversibility are major guarantees for the integrity preservation of the HDPE structure.

3.3 Fracture Surface Analysis

Fracture surface analysis is a necessary step in order to understand the mechanisms that led to crack initiation and its propagation during laboratory tests or under service conditions. Qualitative and even quantitative information can be extracted and may provide valuable information to formulate reasonable interpretations. Although some published work is devoted to the subject of Charpy tests on PE, there remains very little, if any, that relates to the effects of ESC caused by acidic media on HDPE-100 intended for Natural Gas transmission [8,10,13,14]. Figs. 5-7 present photomicrographs at low magnification in order to reveal different surface elementary occurrences associated with rapid crack propagation.

At this step, it is useful to remind that each picture shows the two faces of the newly created surfaces side-by-side. Scrutinizing each fracture surface and its symmetrical part should facilitate identifying macroscopic features and some of their details. Horizontal arrows indicate the crack propagation direction in both surfaces. Therefore, these figures illustrate representative fracture surfaces for AR and aged specimens in DW, AA and HA. Globally, each picture shows a notch strip, a fine razor cut trace, an initiation crack jump followed by one or more striations and a final arrest line [10,13]. The inclined dashed arrows (1) and (2) point to the limits of two main crack jumps in all pictures (Figs. 5-7). The first jump usually corresponds to a “craze zone” which is a signature representing the initiation phase of the crack extension. It is characterized by a progressively vanishing fibrillation (whitened surface elements) surrounded by a “halo” (arrow 1) [10,40].

Fig. 5 is a typical fracture surface of an as-received specimen, i.e., no prior chemical ageing is performed. The segment “ b_1 ” designates the first jump span corresponding to the initiation craze zone size at the impact moment. It is understood that tested arcs undergo a rotation at about half crack length marking another particular brittle-like crack jump (Arrow 2).

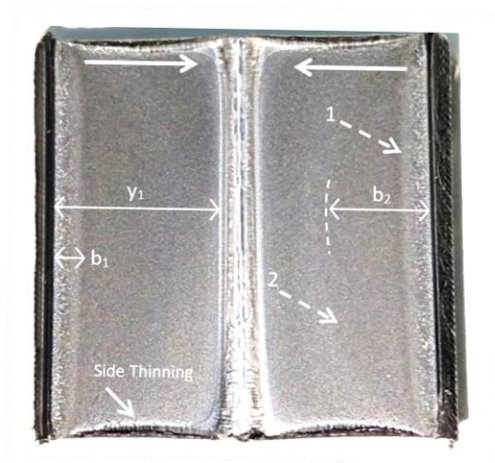


Fig. 5 A photomicrograph of global fracture surface from an unaged specimen (AR);

X~3.5; Horizontal arrows indicate CP direction

The segment “ b_2 ” designates the jump span in the brittle-like propagation zone (Fig. 5). Finally yielded HDPE material causes transverse specimen thinning, known as “shear lips”, to appear on either side of the propagating crack. The distance between initiation and final crack arrest line (large scale yielding) is denoted “ y_1 ” which will be used later for comparisons. Similarly, figure 6 illustrates the fracture surfaces of specimens aged in DW and AA. The surface marks corresponding to the effect of ageing and to crack propagation are also imprinted. The two

crack jumps are still identifiable; arrows (1) and (2) with shear lips in DW and AA. The observed fracture surface appears rough with a tendency to surface fragility probably under the effect of long-term sorption, although the quality of the external and internal surfaces of the pipe are not much affected by DW. Moreover, it should be noted that there is a weak participation of DW in the oxidation processes; that is, the structural properties of HDPE such as crystallinity and OIT are little affected [24].

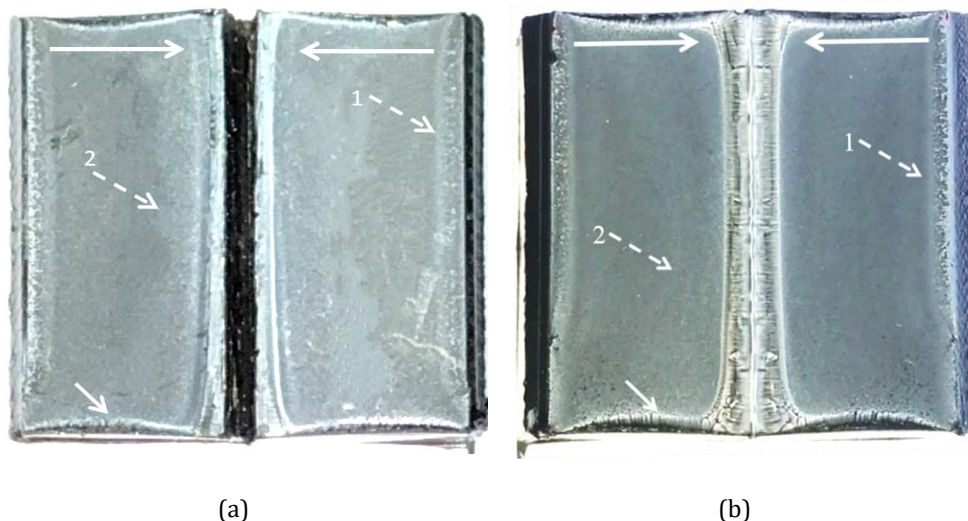


Fig. 6 Photomicrographs of global fracture surface from 7-month aged specimens in (a) DW and (b) 5% CH₃COOH (AA); X~3.5; Horizontal arrows indicate CP direction

Fig. 7 illustrates the fracture surfaces after 7 months ageing in hydrochloric acid for 2 identical specimens failed in the same conditions (HA-1 and HA-2). It is concluded that HA seems to be more damaging than AA (Fig. 6b) which showed a surface relatively similar to that of DW (Fig. 6a). The fibers within the craze zone are quite strained, the b_2 limit is rather diffuse and the side thinning is significant. The HA craze zone extent represented by distance b_1 (see Fig. 5) is larger than that of AA (Fig. 6b). On the other hand, the limits of b_2 are easily distinguishable and definitely imprinted on the surfaces (Figs. 7a-7b). The fracture surface is unquestionably of brittle nature as it exhibits localized areas with pulled out material; arrows (3); (Fig. 7a). By improving the picture contrast, the trail of the craze zone is made visible with stretched fibers and its complementary "Halo".

Also, embrittlement is much more pronounced at the crack arrest line as indicated by arrows (4). Table 5 recapitulates the quantified parameters (b_1 , b_2 and y_1) as explained in Fig. 5 and the relevant comments after 7 months of exposure. It appears that both (%) thinning and b_1 are amplified for the HA while DW and AA have similar tendencies (lower thinning and lower b_1). The b_2 parameter remains a rough approximate for both DW and AA. Nevertheless, the parameter y_1 is practically the same for all environments suggesting that the final crack arrest line occurred in comparable conditions.

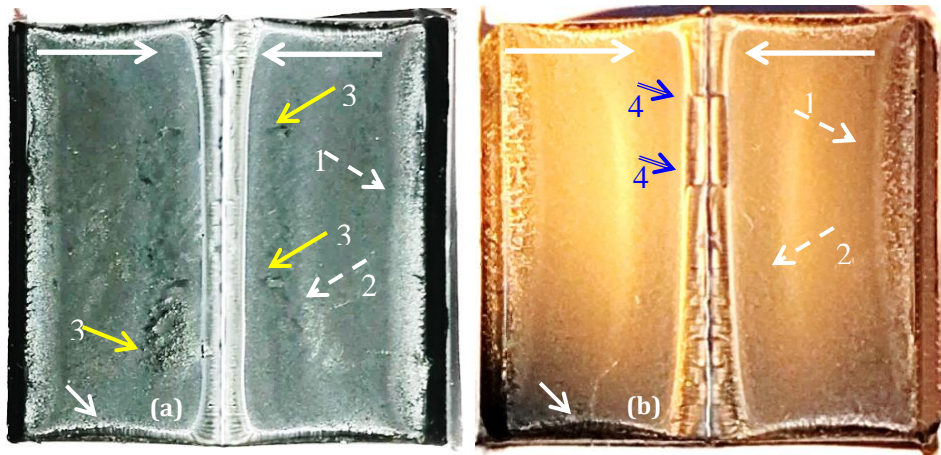


Fig. 7 Photomicrographs of two global fracture surfaces after 7 months aging in 20% HCl at different contrasts, (a) regular back and white image and (b) enhanced image (polarized light observation); X~3.5; Horizontal arrows indicate CP direction

Table 5. Thinning, bands and yielding positions from fracture surface after 7 months aging

Aging Medium	$\Delta t/t_0$ (%)	Initiation jump, (b ₁ , mm)	Propagation band, (b ₂ , mm)	Onset yielding (y ₁ , mm)	Optical observations
As-Received (AR)	6.14	4.0	16.2	26.5	Drawn-out fibrils within b ₁ , Smooth propagation surface, Diffuse limits of b ₂ band
DW	5.83	3.8	14.4	26.3	Whitened initiation line, Less dense fibrils within b ₁ , Dispersed fibrils around b ₂ , Sample breaking into 2 parts.
CH ₃ COOH (AA)	5.67	3.7	20.1	25.9	Highly drawn matter at initiation front, Elongated fibers within b ₁ , b ₂ : very diffuse (blurred), Substantial shear lips (yielding)
HCl* (HA-1)	7.40	5.5	16.5	26.3	Larger b ₁ , Highly yielded fibrils in b ₁ , Distinguishable b ₂ limits, Large surface embrittlement, b ₂ : Zone of material uprooting.
HCl* (HA-2)	7.56	5.3	16.3	26.5	Larger b ₁ , highly yielded fibers, Unambiguous b ₂ limits, Coarse fracture surface in the propagation zone (nearby b ₂).

* Identical samples tested in the same conditions. HA-1 (Fig. 7a) and HA-2 (Fig. 7b).

3.4 Ductility Analysis

Since this study presents Charpy fracture data using chemically aged non-standard arch-shaped specimens, it is noteworthy to investigate the ductility associated with plastic pipe testing. It is fundamentally accepted that ductility is by far one of the most significant intensive mechanical properties for structural and pressure vessel materials. It is defined as tensile plasticity because it is governed by strain hardening rate in the last tensile test stages. As a consequence, one way to improve material ductility needs to increase strain hardening rate through microstructure modification [33,34, 41,42]. During laboratory testing and accreditation steps, ductility of HDPE pipes is a major factor for detecting early deformations due to overpressure or high mechanical loads. Therefore, this property contributes to establish safe installation and functioning conditions and also to prevent unexpected catastrophic failures.

At least, two methods are employed to approach ductility from destructive mechanical testing of HDPE pipes. Conventionally, the limiting estimate of ductility is taken as the recorded strain at failure (ϵ_f) from a standard tensile test. Alternatively, overall ductility is usually expressed whensoever achievable by percent cross-sectional area reduction (A_r) at break (eq. 6):

$$\% A_r = \frac{A_0 - A_f}{A_0} \tag{6}$$

where A_0 and A_f are respectively initial and final cross-sectional areas of failed component. Using ImageJ® Software the fracture surfaces of Figures 5-7 are analyzed to obtain changes in cross-sectional areas as a function of ageing times and environments. The calculation operations must be carried meticulously. Figure 8 summarizes the findings when equation (A) is applied for a 7 months ageing period.

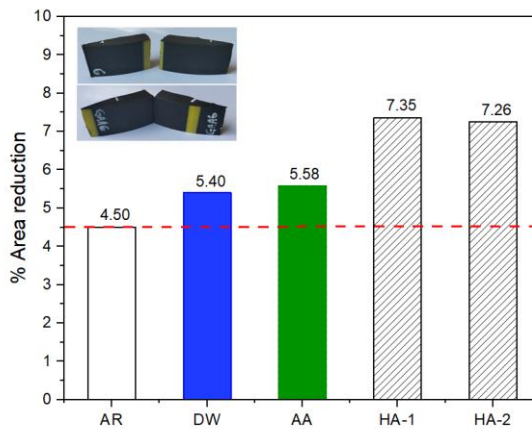


Fig. 8 Percent ductility for unaged (AR) and aged HDPE-100 in DW, AA and HA (7 months ageing period)

The first indication is that ductility of aged HDPE in HA rose by 39% compared to as-received (AR) specimens. This is an important information about the role of hydrochloric acid in increasing solubility and plasticization of semi-crystalline polymers such as polyethylene [28,33,34]. Secondly, for acetic acid (AA) ageing, ductility rise is limited only to 19% since AA is ranked as a weak acid and its behavior in this case is close to that of deionized water (DW) with 17%.

Literature does not provide impact ductility data for aged arc-shaped HDPE pipes. However, when considering filaments machined from HDPE pipes and aged in aggressive environments for 3 months [21], it is possible to discuss ductility in terms of strain at failure (ϵ_f). The latter property is dependent on the strain-hardening capacity of the material. It is found that ductility is increased to 900% (H₂SO₄), 1400% (crude oil) and 850% (Toluene-Methanol mixture) as compared to 700% for As-Received (AR) specimens. The rank according decreasing strain at failure is as follows [21]:

$$\epsilon_f (\text{crude oil}) > \epsilon_f (\text{Toluene-Methanol}) > \epsilon_f (\text{H}_2\text{SO}_4) > \epsilon_f (\text{AR}) \quad (7)$$

It is concluded that both methods (%Ar and ϵ_f) agree that aggressive environments augment ductility because of triggering degradation processes such as solubilization and plasticization of HDPE [28,33,34,36]. It is accepted that %Ar and ϵ_f measure different types of material behavior. Strain at failure is mostly affected by uniform elongation as it depends on strain hardening while %Ar is ultimately a measure of the deformation required to produce fracture and initiate the material necking propagation [43].

4. Conclusion

This work is proposed to investigate a new adaptation for non-standard specimens to study at the same time sorption and mechanical resilience properties of HDPE gas pipes after long-term chemical ageing. The following conclusions are made:

- For reasons related to the preservation of the thermomechanical history imparted by the extrusion process of HDPE-100 pipes and by handling/storage methods, the choice of non-standard specimens might be favored in order to implement, much more representative environmental stress cracking experimental studies and to extend actual testing standards.
- The designated procedure allowed obtaining necessary information to characterize sorption of weak and strong acids. Within 2 weeks, HDPE-100 resin experienced maximum swelling of HCl (20%). Then, a nearly total desorption took place progressively during the next 28 weeks.
- According to Weitsman's sorption labeling, deionized water, acetic and hydrochloric acids in contact with HDPE-100 resin are respectively Type (B), Type LF and Type (D). It is recognized that water sorption curve symbolizes the condition of a two-stage diffusion. For the strong acid, the behavior of sorption/desorption is in agreement with chemical and physical degradation of the resin and antioxidant depletion.
- Deionized water experienced a slow and monotonic decrease of Charpy energy which can be attributed according to literature to the absence of plasticized material resulting in and enhanced swelling. For the 7 months ageing period, both acids show much higher Charpy energies than as-received and deionized water cases. For HCl (20%), the increase is 110% and for CH₃COOH (5%), it is 75% compared to as-received Charpy energy, while deionize water experienced a 25.8% decrease. It implies that HCl and CH₃COOH made the HDPE resin more resilient but brittle as inferred from fractography and literature.
- Fractographic analyzes show that crack initiation is driven by a craze zone, the size of which corresponds to b_1 distance worked out from post-failure surface observation. As expected, crack propagation is completed by a crack arrest line defining the y_1 parameter. Side thinning (or "shear lips") and craze zone size (b_1 parameter) are amplified for acids while the distance to final yielding (y_1 parameter) remained almost constant for all environments.
- The results suggest that the various deformations incurred by aged material represent a global and realistic effect of chemical and mechanical processes induced over time. It

is believed that such combination can serve for a more representative studies of durability/reliability for HDPE pipes in interaction with service environments. The prospects will still open with the provision of other characterizing measurements related to ESC phenomenon.

- Ductility is approached using % cross-sectional area reduction at break. For HA and AA ageing, it increased respectively by 39% and 19% compared to as-received specimens. This is another good indication about hydrochloric acid contribution into solubility and plasticization of HDPE. This finding is corroborated from literature using strain at failure (ϵ_f) as a measure of ductility for chemically aged HDPE filaments.

Abbreviations

AA	Acetic acid;
A_0	Initial cross-sectional area (%);
A_f	Final cross-sectional area (mm^2);
Ar	Area reduction (mm^2);
AR	As-received;
CE	Charpy energy;
DW	Deionized water;
ESC	Environmental stress cracking;
ESCR	Environmental stress cracking resistance;
GA	Gaz pipe, As-received;
HA	Hydrochloric acid;
HDPE	High-density polyethylene;
LF	Linear Fickian;
MDPE	Medium density polyethylene;
MP	Micro plastics;
OD	Outer diameter;
PE	Polyethylene;
PP	Polypropylene;
RCP	Rapid crack propagation;
SCG	Slow crack growth;
SDR	Standard dimension ratio;

Nomenclature:

b_1	Extent initiation jump (mm);
b_2	Extent propagation jump (mm);
δ	Solubility parameter ($\text{MPa})^{1/2}$
ϵ_f	strain at failure (%);
G_{IC}	Elastic fracture toughness (kJ/m^2);
J_{IC}	Elasto-plastic fracture toughness (kJ/m^2);
m	Mass (g);
m_0	Initial mass (g);
OIT	Oxidation induction time (min.);
t	Time (hours or days);
t_0	Initial thickness (mm);
y_1	Distance to final crack arrest line (mm);
Δt	Thickness change (mm);

Acknowledgements

This research has been conducted within a PRFU project (2019-2022). The authors would like to express their gratitude to Algerian companies: STMP CHIALI (Sidi Bel-Abbès) and Sarl TUBOGAZ (Annaba) for pipe supply, and AMM-Sider SPA (El-Hadjar) for machining operations. They are also thankful to LCG (Civil Eng. Lab.) and LCOA (Appl. Organic Chemistry Lab.). Interesting discussions with LR3MI members are well appreciated.

Funding

Work partially funded by DGRSDT-MESRS (Ministry of Higher Education and Scientific Research, Algeria) and LR3MI (UBM Annaba). [PRFU Project Code: A11N01UN230120190008], Mechanical behavior and remaining service life of polyethylene pipes subjected to operational and environmental conditions.

References

- [1] ISO 1167-1 (2006) Thermoplastics pipes, fittings and assemblies for the conveyance of fluids –Determination of the resistance to internal pressure–, Part 1: General method. 8. http://www.driso.ir/standards/iso/ISO_1167_1_2006,Thermoplastics.pdf
- [2] ASTM D5045 (2014) Standard Test Methods for Plane-Strain Fracture Toughness and Strain Energy Release Rate of Plastic Materials. 10.
- [3] American Water Works Association, PE Pipe - Design and Installation (2006) Manual of water supply practices – AWWA M55 (# 30055PA), 1st Ed., Denver, CO., 151. <https://www.awwa.org>
- [4] The Plastics Pipe Institute (2008) Handbook of Polyethylene Pipe: Inspections, Tests and Safety Considerations, Chap. 2, 2nd Ed., Irving, TX, 15-41 https://www.plasticpipe.org/MunicipalIndustrial/Shared_Content/Shop/PE-Handbook.aspx
- [5] Makris KF, Langeveld J, Clemens FHLR. A review on the durability of PVC sewer pipes: research vs. practice, *Structure & Infrastructure Eng.*, 2020; 16(6): 880 - 897. <https://doi.org/10.1080/15732479.2019.1673442>
- [6] Zanzinger H, Engelsing K, Hausmann S. Durability of polyethylene geopipes for landfill applications after several years in service. 10th Inter. Conf. on Geosynthetics, ICG'2014, 2014.
- [7] Plastic failure analysis and prevention, J. Moalli Ed., Society of Plastics Engineers, SPE, Norwich, NY, 2001.
- [8] Leever P S, Yayla P, Wheel M A. Charpy and dynamic fracture testing for rapid crack propagation in polyethylene pipe. *Plastics, Rubber and Composites Processing and Applications.* 1992; 17(4): 247 - 253. <https://www.researchgate.net/publication/287994808>
- [9] Deblieck RAC, Van Beek DJM, McCarthy M, Mindermann P, Remerie K, Langer B, Lach R, Grellmann W. A Simple Intrinsic Measure for Rapid Crack Propagation in Bimodal Polyethylene Pipe Grades Validated by Elastic-Plastic Fracture Mechanics Analysis of Data from Instrumented Charpy Impact Test. *Poly. Eng. & Sci.* 2016; 1-9. <https://doi.org/10.1002/pen.24380>
- [10] Andreassen E, Nord-Varhaug K, Hinrichsen EL, Persson AM. Impact fracture toughness of polyethylene materials for injection moulding. Conf. PPS07EA, Polymer Processing Society, Gothenburg, Sweden, 2007. <https://www.researchgate.net/publication/237272308>
- [11] Domaneschi M. Experimental and numerical study of standard impact tests on polypropylene pipes with brittle behaviour. *Proceedings of the Institution of Mechanical Engineers, Part B: Journal of Engineering Manufacture.* 2012; 226(12):2035 - 2046. <https://doi.org/10.1177/0954405412461983>

- [12] ASTM-D1693. Standard Test Method for Environmental Stress-Cracking of Ethylene Plastics. Book of Standards. 11. 2021.
- [13] Lee CS, Epstein MM. Fracture Surface Features of Polyethylene Pipe Samples. *Polymer Eng. & Sci.*, 1982; 22(9): 549 - 255. <https://doi.org/10.1002/pen.760220906>
- [14] Niglia J, Cissilino A, Seltzer R, Frontini P. Determination of impact fracture toughness of polyethylene using arc-shaped specimens. *Engineering Fracture Mechanics*, 2002; 69(12):1391-1399. [https://doi.org/10.1016/S0013-7944\(02\)00008-5](https://doi.org/10.1016/S0013-7944(02)00008-5)
- [15] Özbek P, Argyrakis C, Leever P. Fracture mechanics analysis of arc shaped specimens for pipe grade polymers. *Polymer Testing*. 2009; 28(3):357 - 361. <https://doi.org/10.1016/j.polymertesting.2009.02.001>
- [16] Liang H, Yang CD, Ceng-dian L. The determination of JIC for polyethylene pipe using non-standard arc-shaped specimen. *Int. J. of Pres. Ves. and Pip.*, 1999; 76(9):647 - 651. [https://doi.org/10.1016/S0308-0161\(99\)00032-0](https://doi.org/10.1016/S0308-0161(99)00032-0)
- [17] Kaddeche M, Chaoui K, Belhadi S, Yaltese M-A. Study of impact fracture toughness variations through polyethylene pipe wall. *Congrès Français de Mécanique*. 2019. Brest, France, 13. <https://cfm2019.sciencesconf.org/246487/document>
- [18] Broughton WR, Maxwell AS. *Environmental Ageing of Polymeric Materials, A National Measurement Good Practice Guide*, 2007; No. 103, NPL, Teddington, UK, 103. <https://eprintspublications.npl.co.uk/3866/1/mgpg103.pdf>
- [19] Ghabeche W, Chaoui K. Revue des interactions physico-chimiques du polyéthylène extrudé sous forme de tubes avec des environnements agressifs (Environmental Stress Cracking of High Density Polyethylene Pipes: A Review, *Revue des Sciences et de Technologie, SYNTHESE*, 2021 ; 27(2):1 - 22. <https://www.asjp.cerist.dz/en/downArticle/34/27/2/173061>
- [20] Cameron GG, Main BR. The action of concentrated sulphuric acid on polyethylene and polypropylene: Part 2-Effects on the polymer surface. *Polym. Degrad. & Stab.*, 1985; 11(1):9 - 25. [https://doi.org/10.1016/0141-3910\(85\)90113-2](https://doi.org/10.1016/0141-3910(85)90113-2)
- [21] Rehab-Bekkouche S, Ghabeche W, Kaddeche M, Kiass N, Chaoui K. Mechanical behaviour of machined polyethylene filaments subjected to aggressive chemical environments. *MECHANIKA*, 2009; 3(77):40 - 46. <http://mechanika.ktu.lt/index.php/Mech/article/view/15233>
- [22] Alimi L, Chaoui K, Ghabeche W, Chaoui W. Short-term HDPE pipe degradation upon exposure to aggressive environments. *Mater Tech.*, 2013; 101 :701 - 709. <https://doi.org/10.1051/mattech/2013083>
- [23] Lasfar S, Mouallif I, Latrach HA, Chergui M, Choukir A, Diab A. Gravimetric, mechanical and chemical characterization of different materials used in sewers systems: Polyvinyl chloride (PVC), polypropylene (PP) and high-density polyethylene (HDPE), aged in sulfuric acid at 60°C. *Int. J. Eng. & Sci.*, 2015; 5(4)1-10. www.researchinventy.com
- [24] Ghabeche W, Alimi L, Chaoui K. Degradation of plastic pipe surfaces in contact with an aggressive acidic environment. *30th Int Conf TMREES'15. Energy Procedia*, 2015; 74:351-364. <https://doi.org/10.1016/j.egypro.2015.07.625>
- [25] Aiduganov D, Balkaev D, Varfolomeev M, Emelianov D. Effect of formation water and hydrochloric acid on the physical and chemical properties of polymer materials of high-pressure pipelines used for transportation of crude oil. *Int. Conf. Corrosion in the Oil and Gas Industry, E3S Web of Conferences* 121. 04001:4-8. 2019. <https://doi.org/10.1051/e3sconf/201912104001>
- [26] Liu C, Tang C, Wang S. Ageing of polyethylene thermoplastic liner exposed to sulfuric acid corrosive environments. *ICAMMT'21, J. of Physics: Conference Series* 1885(3):1-8. 2021. <https://doi.org/10.1088/1742-6596/1885/3/032061>
- [27] Lee HB, Lee KS, Kim SJ, Choi BI, Go BR, Rhu CJ, Han TH. Effect of Chemical Agents on the Morphology and Chemical Structures of Microplastics. *Polymers*, 2022; 14, 4353:3 - 15. <https://doi.org/10.3390/polym14204353>

- [28] Agrawal S, Ingle N, Maity U, Jasra RV, Munshi P. Effect of Aqueous HCl with Dissolved Chlorine on Certain Corrosion-Resistant Polymers, 2018; ACS Omega, 3, 6692 – 6702. <https://doi.org/10.1021/acsomega.8b00515>
- [29] Hansen CM. Hansen solubility parameters, a user's handbook, CRC, Boca Raton, FL., 2000. <https://pdfs.semanticscholar.org/2b33/89e52b0f4e42d0aaf4a1bd2b91f308d874e6.pdf>
- [30] Hansen CM. Aspects of solubility, surfaces and diffusion in polymers, Progress in Organic Coatings, 51, 2004; p. 55 - 66. <https://doi.org/10.1016/j.porgcoat.2004.05.002>
- [31] Guenouche A (2022). Etude de l'effet de l'acide sulfurique et d'un solvant à base de toluène-méthanol sur la résistance aux chocs d'un tube HDPE (gaz). Master of Science, Mech. Eng. Dept., Badji Mokhtar University, Annaba, Algeria.
- [32] The Plastics Pipe Institute. Chemical resistance of plastic piping materials, Updated Technical Report, TR-19. 2020. <https://www.plasticpipe.org/>
- [33] Zhu Y T, Wu XL. Ductility and plasticity of nanostructured metals: differences and issues. Materials Today Nano, vol. 2, pp. 15 - 20, 2018. <https://doi.org/10.1016/j.mtnano.2018.09.004>
- [34] Hocker SJA, Kim WT, Schniepp HC, Kranbuehl DE. Polymer crystallinity and the ductile to brittle transition. Polymer. vol. 158, no. October, pp. 72-76, 2018. <https://doi.org/10.1016/j.polymer.2018.10.031>
- [35] T. Ferreira and W. Rasband, ImageJ User Guide ImageJ, vol. 1.46r, 2012. <https://imagej.nih.gov/ij/docs/guide/user-guide.pdf>
- [36] Weitsman YJ. Fluid effects in polymers and polymeric composites. Chapter 4, pages 31-32, Mechanical Engineering Series, Frederick F. Ling Editor-in-Chief, Springer, 2012; New York. <https://doi.org/10.1007/978-1-4614-1059-1>
- [37] Chabbi A (2012). Etude de la résistance des matériaux polymériques et composites en interaction avec des fluides. Mémoire de Magistère, Mech. Eng. Dept., Larbi Ben M'Hidi University, Oum El-Bouaghi, Algeria.
- [38] Lalaymia I (2021). Rupture des tubes en HDPE sous le mode impact : effets de quelques milieux agressifs. Master of Science, Mech. Eng. Dept., Badji Mokhtar University, Annaba, Algeria.
- [39] Yu W, Sedghi E, Nawaz S, Hjertberg T, Oderkerk J, Costa FR, Gedde UW. Assessing the long-term performance of polyethylene stabilized with phenolic antioxidants exposed to water containing chlorine dioxide. Polymer Testing, 2013; 32, 359 - 365. <https://doi.org/10.1016/j.polymertesting.2012.12.003>
- [40] Thuy M, Pedragosa-Rincón M, Niebergall U, Oehler H, Alig I, Böhning M. Environmental Stress Cracking of High-Density Polyethylene Applying Linear Elastic Fracture Mechanics. Polymers, 2022; 14, 2415:1- 21. <https://doi.org/10.3390/polym14122415>
- [41] Savini G, Oréfice RL. Super ductility in HDPE/EVA blends triggered by synthetic amorphous nanocalc. J. Polym. Res., 2021; vol. 28, N° 1. <https://doi.org/10.1007/s10965-020-02389-7>
- [42] Reano AF, Guinault A, Richaud E, Fayolle B. Polyethylene loss of ductility during oxidation: Effect of initial molar mass distribution. Polym. Degrad. Stab., 2018; vol. 149, pp. 78 - 84. <https://doi.org/10.1016/j.polymdegradstab.2018.01.021>
- [43] Gedney R, Measuring the Ductility of Metals, Qual. Mag., 2007; N° 781, pp. 1-5. <http://www.qualitymag.com/articles/89228-measuring-the-ductility-of-metals>

Blank Page



Research Article

Effect of calcined clay on the properties of cementitious mortar reinforced by Posidonia Fiber

Nawel Salem^{1,2}

¹Civil Eng. Dept., National School of Engineers of Gabes, University of Gabes, Gabes-Tunisia.

²Laboratory of Civil Eng., National School of Engineers of Tunis, University of Tunis El Manar, Tunisia

Article Info

Abstract

Article history:

Received 5 May 2023

Accepted 14 Aug 2023

Keywords:

Posidonia-oceanica fibers;

Calcined clay;

Physical properties;

Hygroscopic

properties;

Rheological properties;

Mechanical properties

Posidonia fiber has a negative visual impact on tourism and produces bad odors due to the decomposition of microorganisms. Thus, its recovery for waste recycling and other sustainable uses is encouraged. In this context, the objective of this work was to study the influence of calcined clay as a mineral coating for fibers and the surface treatments (hydro-thermal by water boiling and chemical treatment by NaOH) on the durability of Posidonia fiber and to evaluate their effect on the physical and hygroscopic properties, rheological, mechanical and micro-structural performances, and chemical attack of cementitious mortars with supplementary materials. An experimental study was carried out by varying volume ratios (5%, 12.5%, and 20%). The effects of these treatments on the physical, thermal and morphology properties of the fibers were determined. The water absorption of mortar reinforced by fibers coated with calcined clay decreased compared to composite reinforced by fibers treated without coating. The calcined clay makes the fibers relatively less hydrophilic. According to the various mechanical tests, adding treated Posidonia fibers in a pozzolanic matrix improves the composite properties.

© 2023 MIM Research Group. All rights reserved.

1. Introduction

Because of the various ecological and environmental problems, extensive research has been conducted over the recent decades on the use of vegetable fibers, e.g., flax, hemp, date palm, and jute, as reinforcing materials. These fibers are biodegradable and renewable [1, 2, 3]; however, they are hydrophilic because they are removed from cellulose. Generally, plant fibers are physically characterized by their density, length, and diameter [4]. The low density of plant fibers gives these materials specific mechanical properties [5]. Plant fibers are distinguished by their chemical composition, i.e., cellulose, hemicelluloses, lignin, pectin, waxes, and water [6], which determines the physical properties of fibers [7]. Plant fibers trap water between micro-fibrils due to the presence of hemicelluloses. This hydrophilic character is an essential feature to consider in the case of vegetable fibers. Indeed, water will influence the behavior of cementitious composites in the hardened state (mechanical properties, porosity, etc.) and the fresh state (workability and flow time) ([5, 8]. Furthermore, fluid movement is a central feature of the durability of cement materials [9, 10, 11].

Cement composites reinforced with natural fibers have recently been considered a viable alternative to traditional composites (steel and synthetic fibers). However, the main hurdle in their application remains their lack of long-term durability in the highly

Corresponding author: naoual.salem@enig.u-gabes.tn

<https://orcid.org/0000-0002-2294-5561>

DOI: <http://dx.doi.org/10.17515/resm2023.759ma0505>

Res. Eng. Struct. Mat. Vol. 9 Iss. 4 (2023) 1201-1226

alkaline environment of the Portland cement matrix. Several studies have revealed that plant fibers exhibit limited resistance to alkalis [7, 12, 13, 14]. Alkaline environments, especially in lime released by cement during hydration, limit the use of fibers in cement, as lime causes fiber degradation or tensile strength decrease. Fiber degradation in the cement matrix occurs because of the dissolution of lignin and hemicelluloses due to the adsorption of calcium and hydroxyl ions [12, 13, 15]. In addition, a change in the method of fibers' fracture was noticed after long-term aging. Fiber mineralization is caused by the migration of hydration products (calcium hydroxide) on the fiber's surface and into the fibrous cell (lumen) simultaneously after prolonged contact with the cement matrix, causing deterioration and hardening of its structure. As a result, the fibers become brittle, and the transfer of strength between them and the matrix will be limited [7, 12, 13, 14, 15, 16]. Therefore, two solutions have been proposed to protect natural fibers from degradation in cementitious composites. The first solution is the modification of the matrix by decreasing its alkalinity, and the second entails treating the fibers' surface before adding them to the matrix [12, 13, 14].

The use of low-alkali cementitious the most widely used method of reducing matrix alkalinity. Some researchers suggest replacing part of the cement with slag, fly ash, or pozzolanic materials. For example, materials based on natural volcanic ash, metakaolin, and calcined clay can improve the durability of composites [7, 17, 18]. Calcined clays are recognized as pozzolanic substances because of their composition, silica or silica-alumina compounds [19, 20]. Using natural calcined clay as a supplementary cementitious material that substitute's part of cement in concrete is gaining significant attention [21]. Its application not only helps decrease the cement content in concrete production but also enhances the strength and durability of structural concrete [21, 22, 23]. Incorporating calcined clay is crucial in influencing the mechanical properties of mortars and concrete [17, 21, 24]. Calcium Aluminates hydrates (CAH) and calcium silicate hydrate (CSH) intensify as the addition percentage rises. These compounds play a significant role in enhancing the strength of the material, likely influenced by the mineral content. Besides, their chemical reaction with the calcium hydrate (CH) released during cement hydration further enhances this strength [21, 25]. Additions reduce pores sizes and change their distribution [18, 21, 24]. The introduction of pozzolans results in closed porosity, leading to enhanced mechanical strength and durability. This improvement is attributed to the increased formation of CSH and the lack of interconnected pores. Consequently, integrating pozzolans into the cement promotes better hydration, reduces the number of pores, and decreases the volume of mixing water.

Thus, the coating of lignocellulose fibers can be achieved with a pozzolanic material, such as metakaolin [26] and silica fume [14], to reduce water absorption of fibers and thus increase the mechanical properties and fiber/matrix adhesion. Fiber absorption has been reduced, and the probability of a cavity between the fiber and the matrix is lower [8]. The replacement of cement with metakaolin and bentonite improves the sisal fibers' durability in cement-based materials as they increase their flexural strength [15]. Wei et al. [27] reported that adding supplementary cement materials (metakaolin, fly ash, etc.) could significantly slow down the degradation of natural fibers.

Fiber surface treatment is needed to improve the fiber/matrix interface, moisture resistance, and fluid absorption [10, 11]. Alkaline treatment partially removes hydrophilic hydroxyl groups of natural fibers. It makes the fiber surface rougher. Naiiri et al. [28] studied the surface modification of palm fibers, and they showed that treatment with soda at a concentration of 1% for one hour improves tensile strength, which may be attributed to an increase in the arrangement of the cellulose and a decrease in the lignin content in the fiber. After alkaline treatment, the removal of amorphous parts increases

the crystallization rate of the fibers [29]. They can also be easily treated with other chemicals, such as silane or acetic acid [28,30, 31,32].

Research on composite materials incorporating vegetable fibers has shown that the mechanical properties of composites improve. Ajouguim et al. [33, 34, 35] highlight the shift from a fragile composite to a ductile composite that exhibits controlled post-peak behavior. However, this change in behavior does not always lead to an improvement in bending resistance [36]. Generally, the compressive strength of composites is not significantly affected by the incorporation of vegetable fibers [7]. Asma et al. [4] show that compressive strength decreases with fiber volume. Chafei [8] asserts that incorporating flax fibers reduces compressive strength significantly. This decrease is due to poor fiber/matrix adhesion and the increased size and number of occluded pores in cement [31]. However, other researchers attributed this reduction to an increase in the number of defects and a non-homogeneous distribution of fibers. Composite porosity increases with the volume fractions of fibers, leading to a decreased density of composites and decreased mechanical properties [7].

The Posidonia fiber represents natural resources found on the beaches of the Mediterranean in the form of balls carried by the waves. Despite its crucial ecological role in protecting against erosion, it has a negative visual impact on tourism and produces bad odors due to the decomposition of microorganisms [37]. Thus, the recovery of Posidonia for waste recycling and other sustainable uses is encouraged. Several researchers have studied the effect of adding Posidonia fiber to a cement matrix on the physical, mechanical, thermal, and morphological properties. The results show that the bio-composite gives better bending resistance, higher ductility, lower density, and a better matrix/fiber interface than conventional cement materials [32, 38, 39, 40].

The present work aimed to study the effect of calcined clay as a mineral coating for fibers and surface treatments (hydro-thermal by water boiling and chemical treatment by NaOH) of Posidonia fiber on the physical and hygroscopic properties, rheological, mechanical, and micro-structural performances, and chemical attack of cementitious mortars with supplementary materials.

2. Experimental Program

2.1. Materials and Characterization

2.1.1 Sand Cement and Calcined Clay

A Portland cement type CEM I 42.5 MPa and standard sand of EN 196-1 were used. Moreover, calcined clay at 600°C for one hour of calcination [17] was used as a mineral coating. The physical and mechanical properties, such as pycnometer density, Blaine surface area, average particle diameter, and pozzolanic activity index, were measured (Table1). The chemical composition and X-ray diffraction curve (mineralogical composition) of calcined clay were determined (Table 2 and Fig 1).

Table1. Properties of calcined clay

Properties	Calcinedclay (600°C/1h)
Density	2.48
The Blaine area(m ² /Kg)	457
Average Particle diameter (μm)	0.96
Pozzolanic activity index	1.19

The chemical composition was determined by X-ray fluorescence. The results of the chemical analysis of calcined clay at 600°C show that their main constituents were silica (45.54%), alumina (16.71%), and iron oxide (11.11%). The calcined clay is a good pozzolanic addition in that the total percentage of SiO₂, Al₂O₃, and FeO are greater than 70% (73.26%)

Table2. Chemical composition of calcined clay

% by mass	SiO ₂	Al ₂ O ₃	Fe ₂ O ₃	CaO	MgO	SO ₃	k ₂ O	Na ₂ O	TiO ₂	CaCO ₃	LOT
600°C/1h	45.54	16.71	11.11	8.96	1.81	1.84	1.05	1.24	0.03	13.7	13.8

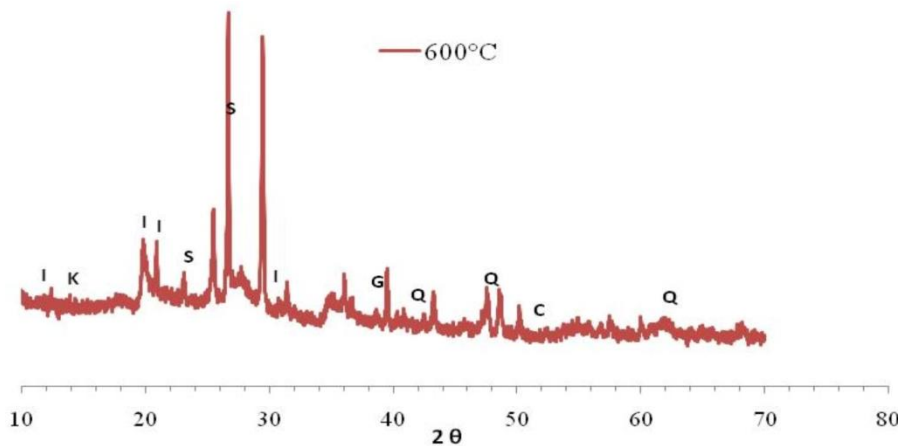


Fig. 1 Mineralogical composition of calcined clay (S: Smectite, I: Illite, K: Kaolinite, C: Calcite, Q: Quartz, G: Geothite)

2.1.2 Posidonia Oceanica Fibers

a. Extraction of Raw Fibers

The physical and mechanical properties of Posidonia fibers are comparable to other natural fibers commonly used in composites. Posidonia fiber is a natural fiber composed of celluloses (48.4%), lignin (23.12%), and hemicelluloses (18.9%) with a tensile strength equal to 5MPa [40].

The fiber of Posidonia oceanica, in the form of balls, was collected directly on the beach in Gabes-Tunisia. They are made of naturally agglomerated fibers. First, a manual extraction was necessary to separate the fibers and then rinsing in water several times to facilitate the removal of impurities, followed by drying in the air for days and in an oven at 65°C. After drying, crushing was carried out using a crusher (Retsch SM 100) to refine the size of the fibers and ensure the distribution and homogenization between the fibers and the matrix (Fig 2).

b. Surface Treatment of Raw Fibers

In this study, raw and crushed fibers are referred to as (T0). Two treatments were planned: a first combined treatment (T1): hydro thermal and chemical by NaOH for different fractions (0%, 5%, 12.5%, and 20%), and a second treatment (T2) combined

and coated by calcined clay (12.5% E). Given the hydrophilic nature, the properties of the fibers had to be modified by surface treatments to make them hydrophobic.



Fig. 2 Fibers from *Posidonia Oceanica* after crushing and sieving

The crushed fibers were boiled in water in a container for 30 minutes. Then, they were rinsed with water to remove impurities and organic matter, especially sugars [1]. Hydro-thermal treatment alone does not profoundly affect the structure of the fibers. It is used only for the extraction of water-soluble materials [41]. Hence, additional treatment was proposed. In most cases, the chemical treatment of fibers with NaOH can improve their physical, mechanical, and insulating properties and promote their implementation, whether molded in the form of wool or mixed with materials (gypsum, cement matrix, etc.) [3].



Fig. 3 Fibers treated and coated with calcined clay

Mercerization of fibers promotes fibrillation, eliminates hemicelluloses, and makes the surface rougher [41]. In the present study, boiled fibers were immersed in NaOH solution with a molar concentration of 0.4 M for 2 hours. Subsequently, after chemical treatment, the fibers were rinsed with water to remove traces of NaOH and impurities until neutralization by checking the pH. Given that the interstitial alkaline solution of the cement matrix decreases the fibers' durability and causes their degradation and microstructure modification [33, 34, 35], the mineral coating with a pozzolanic material

was considered. This treatment consists of mixing treated fibers thermally and chemically with calcined clay to reduce the strong water absorption and make it waterproof and hydrophobic (Fig 3) [7].

2.1.3. Mixture Proportion

The composite consisted of a binder (90% cement + 10% calcined clay), water, and sand to form the matrix and the treated Posidonia fibers as reinforcement. The fibers were previously dried in an oven until a constant mass. The cement was initially mixed with 10% of calcined clay and water for a Water-Binder (W/B) ratio equal to 0.5 (by mass). Afterward, the fibers and standard sand were added, in the wet state, for a Sand-Binder (S/B) ratio equal to 3 (by mass) to have better mixture homogeneity. The volume fractions of the fibers of the entire mix (sand: cement: water) were 0%, 5%, 12.5%, and 20%. Vegetable fibers have a significant impact on the handling and homogeneity of composites. For this reason, the mixing protocol is crucial as it affects the properties in the hardened and fresh state composite. Moreover, some protocols apply only to standardized mortars; thus, the presence of fibers is not taken into account [7], which is why a mixing plan that is more suited to the presence of fibers was developed. Some measures may be taken during the mixing process to reduce the effects of agglomeration. The fibers are usually added gradually at the end of the mixing process once the other ingredients are mixed [7]. Another critical aspect of the handling is the agglomeration of the fibers and the formation of pellets during mixing. The degree of agglomeration depends on the fraction volume, the length (crushing of fibers) and type of fibers used, and the maximum aggregate size in the composite. Fiber agglomeration should be avoided as it would affect resistance negatively. The mortar was put in cubic molds ($4 \times 4 \times 4 \text{ cm}^3$) to determine physical properties, in prismatic molds ($4 \times 4 \times 16 \text{ cm}^3$) for flexural and compressive strengths, and in cylindrical ones ($11 \times 22 \text{ cm}^2$) for Brazilian tensile test (Fig 4). The molds were removed after 24h, and the samples were kept in water for 90 days.



Fig. 4 Cast samples to physical and mechanical properties

2.2. Test Methods

2.2.1. Rheological Properties

The workability of the pozzolanic mortar was determined to study its rheological behavior. The test was performed in accordance with NF P18-452.

2.2.2. Physical Properties

To determine the water-accessible porosity and bulk density of mortars, the gravimetric method was used in accordance with NF P18-459.

2.2.3. Hygroscopic Properties

a. Absorption-Sorption

To follow the water imbibitions kinetics of the mortars and in accordance with ASTM C1585-20, the samples were placed in an oven, with a gradual temperature rise of up to 80°C and obtaining a constant dry mass obtention. Then, a protective coating with an epoxy resin was applied to the circumference to avoid the accessibility of water from the sides. The samples were weighed, and then one side was put in contact with water up to 2 mm in height. The samples were taken after 15 min, 1h, 2h, 3h, 4h, 1d, 2d, 3d, 4d, and 7d. The mass gain due to water absorption was measured, and the capillary absorption coefficient (C) was calculated.

b. Moisture Diffusion Under Controlled Relative Humidity

The performance of mortar subjected to aggressive environments is a function of the penetrability of the pore system. The material is partially charged with moisture when exposed to a humid or aggressive atmosphere. The specimen is conditioned in an environment with controlled relative humidity to induce a consistent moisture condition in the capillary pore system. The moisture absorption or moisture diffusion kinetics of fiber-reinforced pozzolanic cementitious composites was measured (NF EN ISO 12571). These composites were previously dried in the oven at 80°C until a stabilized mass. The experimental device was composed of a sealed container to place the composites above a saline solution of a mass concentration of 35.9g NaCl/100g of water (HR= 79%). The samples were taken after 15min, 1h, 2h, 3h, 4h, 1d, 3d, 4d, and 7 days. Also, the moisture content of mortar in a controlled relative humidity environment (W) and the diffusion coefficient (D) were calculated.

2.2.4. Mechanical Properties

The mechanical tests for mortars were carried out in accordance with NF EN 196 and NF P18-400 standards.

2.2.5. Chemical Attack

To assess the samples' durability and chemical resistance to chemical attack (ASTM C267-20), we examined the change in specimens' weight and measured their compressive strength at 90 days of samples immersed in sodium chloride (NaCl). All specimens were compared before and after exposure.

2.2.6. Morphological Study

Scanning electron microscope (SEM-EDX) observations were used to compare the effect of fiber treatment on morphology, the interface matrix/fiber, and the pores size of the mortars.

3. Results and Discussions

3.1. Effect of Surface Treatment of Fibers

3.1.1. Physical Characterization

Fig 5 presents the particle size distribution of raw Posidonia fiber determined after sieving by laser diffraction apparatus. The raw and treated fiber exhibited a modal distribution. Table 3 shows that treated fibers' specific surface area (SSA) is higher compared to untreated fibers. It is a modification of the structure and the fibers. The mean diameter of treated fibers is higher, which could be attributed to an agglomeration effect [31].

Table3. Particle size distribution of treated and untreated Posidonia fibers

	SSA (m ² /Kg)	D ₅₀ (um)
Raw fiber T0	143.3	75
Treated fiber T1	153.1	85

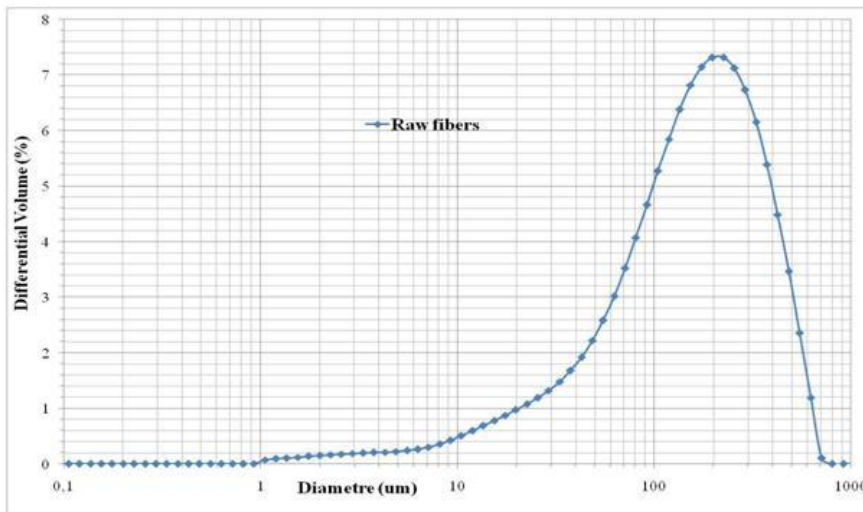


Fig. 5 The particle size distribution of raw Posidonia Fibers after sieving

To measure the fibers' water absorption (Fig 6), the natural water content, and the densities (Table4), the tests carried out were based on an experimental protocol developed by the RILEM TC 236-BBM group [7]. Fig 7 presents the percentage of mineral (C %) and organic (O %) composition of raw and treated Posidonia fibers determined by calcinations at 550°C.

Fibers treated with sodium hydroxide are lighter than raw fibers due to the removal of extractable and non-cellulosic materials on the fiber wall (lignin, sugar, etc.) [3]. The natural water content of treated fibers (T1) is lower than that of raw fibers, which explains the presence of organic matter in the raw fibers. The organic matter contents of the raw and treated Posidonia fibers are respectively 93.54% and 86.5%. Posidonia fibers have high organic matter content than the treated fibers. This finding shows that

alkaline treatment appears to be effective for the removal of impurities and non-organic matter (sugars).

Table4. Physical properties of raw and treated fiber

Properties	Raw fiber	Treated fiber by NaOH
Bulk density (g/cm ³)	0.18	0.15
Density (g/cm ³)	1.49	1.34
Natural water content (%)	12.66	11.85

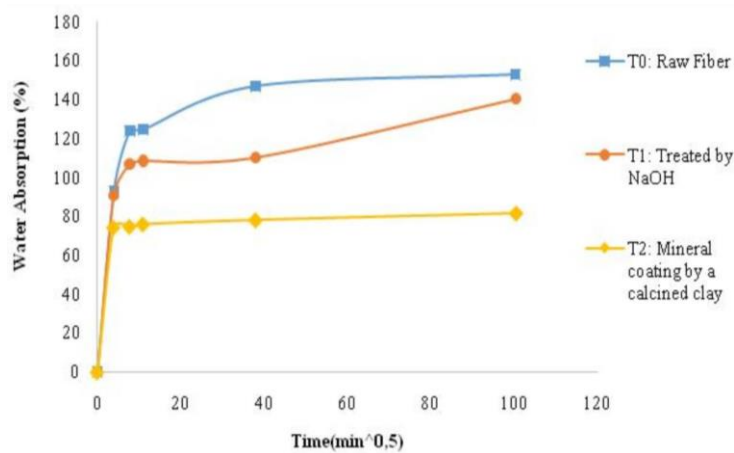


Fig. 6 Water absorption of raw and treated Posidonia fibers

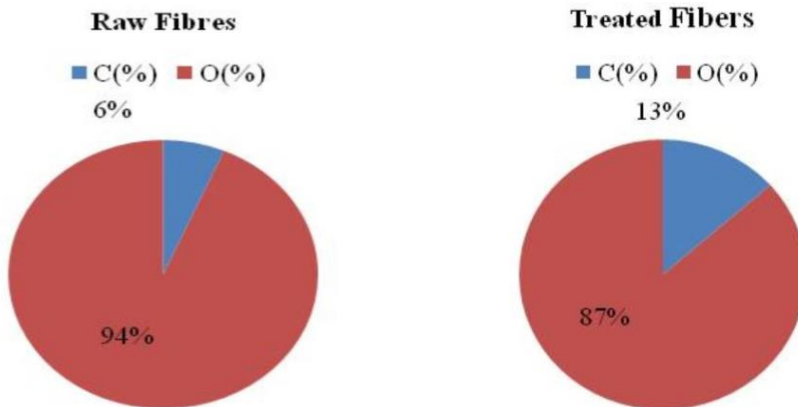


Fig. 7 The percentage of mineral (C %) and organic (O %) composition of raw and treated fibers

The general shape of the water absorption curves of raw and treated Posidonia plant fibers is similar to that of other plant fibers found in the literature [5, 7]. For Posidonia fibers, two stages of absorption can be distinguished: First, the mass of the samples increased rapidly during the first 15 minutes of immersion. In less than 60 minutes, the raw Posidonia fiber had absorbed almost 123%. Second, a continuous slow absorption occurred after two hours of immersion. Many properties of plant fibers, including physical and mechanical, are affected by water absorption [42]. Raw Posidonia fibers can

absorb up to 146% of their mass after 24 hours of immersion. This high absorption capacity is mainly due to the capillary action produced by the high porosity of these fibrous structures and the presence of hydroxyl (-OH) and amorphous groups in the cellulosic structure of plant fibers. In the long term, this will result in significant dimensional changes in the fiber within the matrix [42]. Regardless of the type of fiber used, the literature on using plant fiber in the cement matrix indicates that a plant fiber absorbs much water and, in some cases, more than its weight. Fibers' water absorption kinetics allows knowing their intrinsic properties [43]. Indeed, the soda treatment has improved the Posidonia fiber absorption performance. On the contrary, another previous study also noted that the hydrophilic content of NaOH-treated fibers increased significantly [5].

3.1.2. Structural characterization

The treatment of Posidonia fibers with NaOH has an apparent effect on the infrared spectra (Fig 8). The Fourier transform infrared (FTIR) obtained using a spectrometry infrared UV allows checking the removal of lignin, pectin, and hemicelluloses. The alkaline treatment modifies the structure of the Posidonia fibers and reduces the intermolecular and intra-molecular hydrogen bond between the hydroxyl groups of cellulose and hemicelluloses of the vegetable fiber. After 2 hours of immersion in NaOH, the alkaline treatment causes damage to some components of Posidonia fiber, including lignin and hemicelluloses, which will be almost dissolved and extracted from the fiber. Indeed, the comparison of the two spectra shows the disappearance in the spectra of treated fibers of peaks at 1591 cm^{-1} and 1417 cm^{-1} attributed to lignin, pectin, and hemicelluloses [44, 45]. The decrease in band intensity at 2911 cm^{-1} presents the valence vibration of the C-H group of the CH_2 bond. In addition, the intensity of the absorption peak between 3100 and 3800 cm^{-1} is attributed to the hydroxyl groups of cellulose increases after treatment, confirming the increase in the cellulose content in the treated fibers [1, 46].

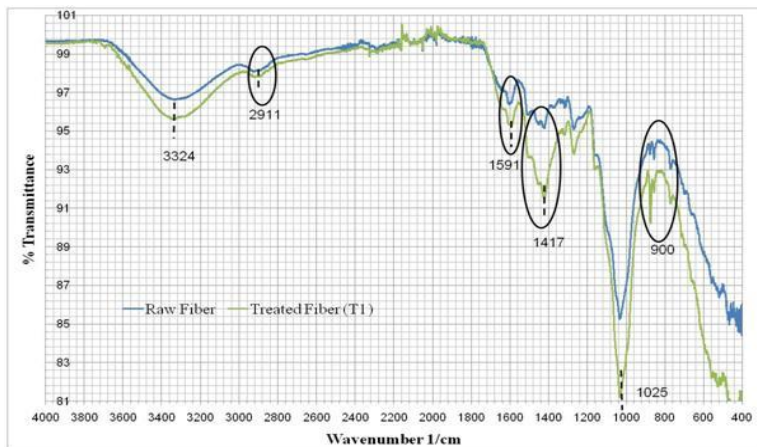


Fig. 8 FTIR spectra of raw and treated fibers

3.1.3. Thermal characterization

Differential thermal analysis (DTA) and thermo gravimetric analysis (TGA) were determined simultaneously in a Setaram differential calorimeter device (SETSYS evolution) with argon shielding gas and Helium, an inert gas. A finely ground sample was introduced into an oven where the temperature was raised from room temperature to 600°C at a speed of $10^{\circ}\text{C}/\text{min}$. The DTG curves shown in Fig 9 depict two endothermic

peaks. Between 50°C and 100°C, the Posidonia fibers samples lost a small amount of mass due to evaporation and moisture removal from the fibers. It was thermally stable up to 220°C [47]. For raw fibers, the first peak at low temperatures (290°C) is the temperature of hemicelluloses decomposition. This peak does not exist for treated fibers, proving that hemicelluloses have been removed. The second peak is associated with the decomposition of cellulose and lignin (315°C for treated fibers and 330°C for raw ones) [1, 11, 46]. The treatment with NaOH is effective since the thermal stability is related to the level of cellulose decomposed during processing. The de-polymerization of hemicelluloses and cellulose is due to improved thermal stability. Hemicelluloses and lignin are amorphous and begin to degrade before cellulose, which is very crystalline [10, 46].

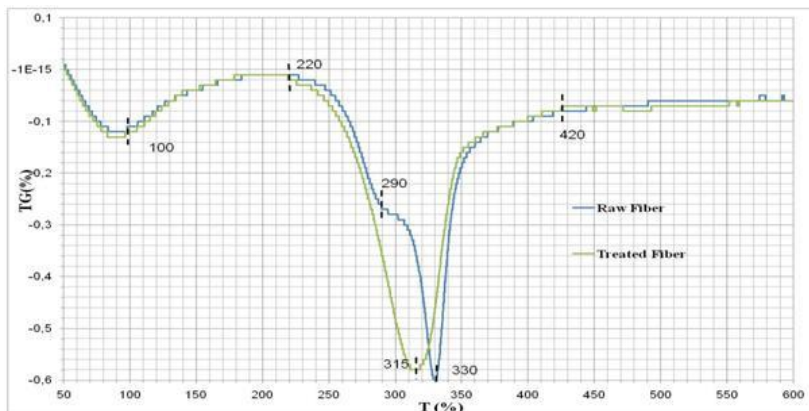


Fig. 9 The DTG of raw and treated fibers

3.2. Workability

Fig 10 shows the flow time of mortar for different volumetric fractions measured using the workability meter. The reference mortar (non-fibrous) has a soft consistency (fluid) with a flow time equal to 10 seconds. The flow time measured on the mortar (T1 (5%)) is in the order of 20 seconds.

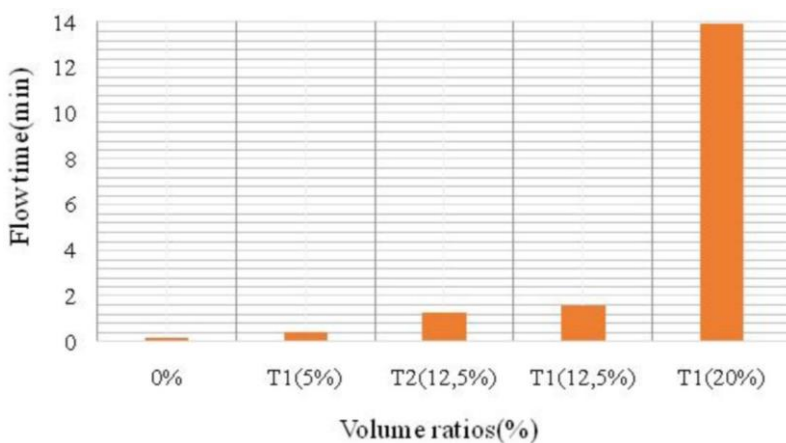


Fig. 10 Mortars flow time of raw and treated fibers

There is an increase in flow time with the fraction of fibers (Chafei et al., cited by [7]). However, mortar (T1 (20%)) has poor workability (stiff consistency) with a flow time of

about 14 minutes. Finally, mortar (T2 (12.5%)) flow time is equal to 1.23 minutes, which is lower than mortar (T1 (12.5%)) (1.57 minutes). For the same Water/Binder (W/B) ratio and considering the high absorption capacity of fiber during the first 15 minutes (Fig 6), the flow time increased (Fig 11). The addition of fiber to a pozzolanic mineral matrix leads to decreasing its workability, which can be corrected by an adjustment of the W/B ratio. There is a loss of workability due to the high water-absorption power of the fibers [4, 14].

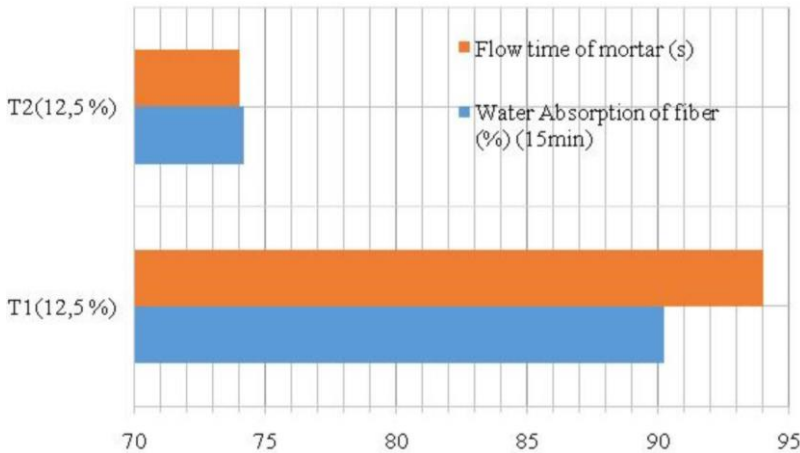


Fig.11 Effect of treatment on flow time of mortars and water absorption of fibers

3.3. Bulk Density and Water-Accessible Porosity

Fig 12 shows a significant decrease in density when Posidonia fibers are incorporated. The embedded mortar of 20% fiber has the lowest density, 6% less than the reference mortar, and has a greater porosity (14.27%). The porosity of the composite increases with the volume fractions, which can be explained by the fact that using fibers can create more voids and promote the accessibility of water. This increase can be caused by the swelling of fibers in the fresh mortar. These release the water absorbed, which creates voids and increases the porosity in the matrix [33, 34, 35, 48].

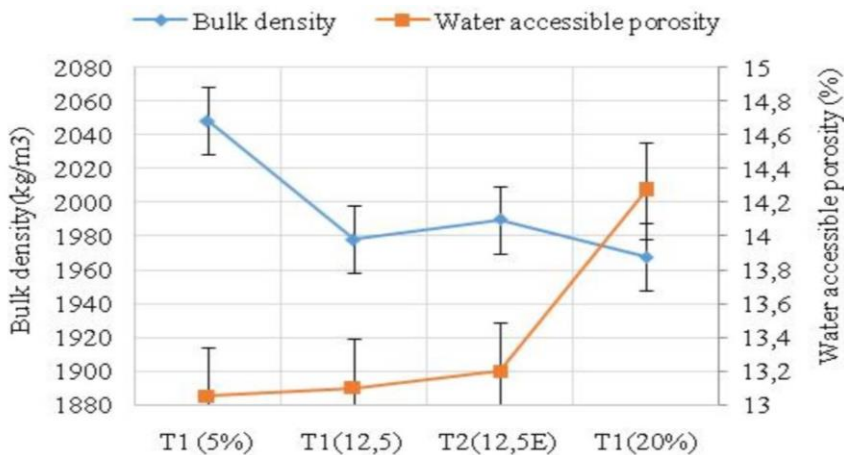


Fig. 12 Effect of treatment on bulk density and water accessible porosity of the mortars

3.4. Imbibition Kinetics

Fluid movement is a crucial feature of cement materials' durability[49]. The capillary absorption coefficients(C (Kg/m^2)) of the composites (12.5%) for different treatments are shown in Fig 13. The embedded mortar of 20% fiber has the highest capillary absorption. The incorporation of vegetable fibers in composites is known to increase their porosity [35, 50]. The absorption of composite water reinforced by fibers coated by calcined clay is lower than that of composite reinforced by NaOH-treated fibers without coating. This decrease is due to the reduced number of pores through the mineral coating treatment. Water diffusion is related to several factors, such as porosity, moisture, volume fraction of fibers, temperature, and matrix viscosity [51, 52]. Water absorbed by fibered composites represents the mobility and movement of liquid in the capillary pores due to capillary absorption [53]. The Posidonia fibers absorb water, causing hygroscopic swelling and changing their mechanical and physico-chemical properties [31]. The water absorption ensures the durability of the composite. The water diffusion kinetics in the composite is based on Fick models. The water absorption behavior is initially linear (Fickian diffusion); slows down until the moisture level approaches saturation level. Quasi-linear variation provides information on the diffusivity of water molecules and indicates the speed of water penetration into the material [54]. The water intake increases with the fiber fractions. This increase is related to the hydrophilic character of fibers and the formation of hydrogen bonds between water molecules and the hydroxyl and carboxyl groups of fibers present in pectin, hemicelluloses, and cellulose [54,55, 56, 57]. Increasing the fractions of the fibers improves their separation and dispersion in the composite, thus promoting water absorption in these composites because of a specific surface that is more important for the best separated fibers. The calcined clay decreases the fibers' hydrophilic nature due to a better adhesion to the fiber/matrix interface. The volume and porosity at the interface decrease, hence a reduction in the free space for water circulation and storage [55]. The coating agent decreases the number of short chains at the interface and makes OH clusters of fibers less accessible to water molecules [58, 59].

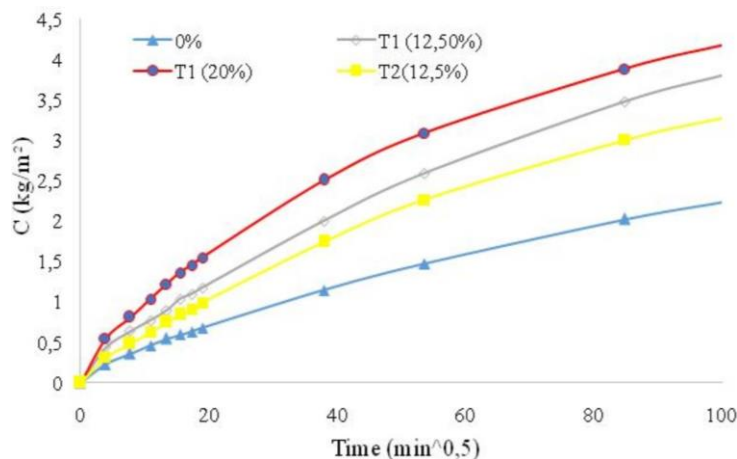


Fig. 13 Effect of treatment and volume ratios on water absorption coefficient of the mortars

3.5. Moisture Diffusion Under Controlled Humidity

The moisture content under controlled humidity (W) (79%) of the composites as a function of time is illustrated in Figs 13 and 14. The water content increases over time;

This finding is expected because mortars are packed in an environment with high relative humidity. As expected, the water intake was very fast from the first hours and then slowed down to stabilize. The water content (Fig14) and the diffusion coefficient (Table 5) increase with fiber content. There is a 27% increase for the 20% volume fraction. Composites reinforced by coated fibers were found to absorb less moisture, proving that the treatment of mineral coating by pozzolanic materials makes it relatively less hydrophilic (Fig 15). Water absorption capacity and humidity are directly related to the presence of voids and the fiber/matrix interface [53]. High moisture absorption results in a low fiber/matrix interface and poor stress transfer. Alkaline treatment reduces moisture absorption, decreases the hydrogen bonding capacity of cellulose, and eliminates open hydroxyl groups that tend to bind to water molecules. It dissolves hemicelluloses and disrupts the hydrogen bond in the network structure, thus increasing surface roughness [31, 58, 59].

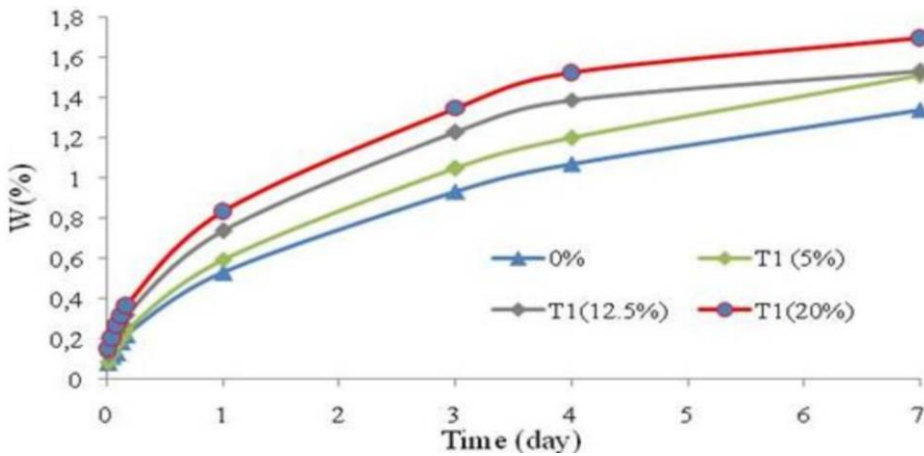


Fig. 14 Effect of volume ratios on water content under controlled humidity (79%) of the mortars

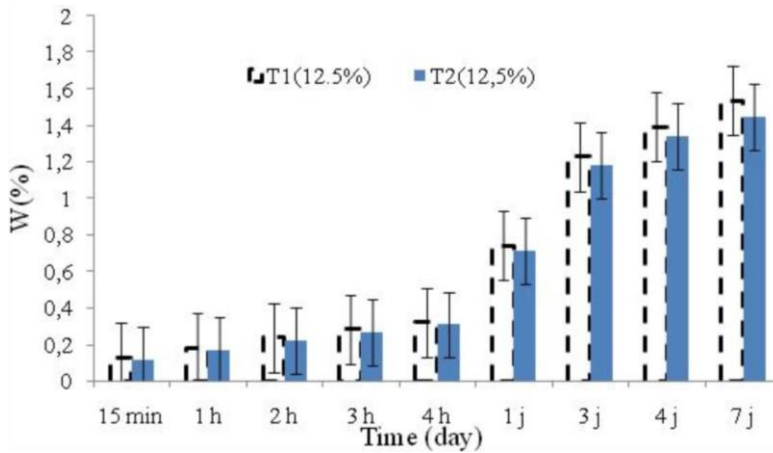


Fig. 15 Effect of treatment on water content under controlled humidity (79%) of the mortars

Table5. Effect of fiber fraction on the diffusion coefficient

		D (m ² /s)	n<0.5 (Fick models)
T1	0%	5.7E-10	0.463
	5%	5.7E-10	0.463
	12.50%	8.46E-10	0.417
	20%	8.83E-10	0.421
12,5%	T1 (12.5%)	8.46E-10	0.417
	T2 (12.5%)	8.7E-10	0.404

3.6. Mechanical Properties

The results of the splitting tensile test in long-term (90 days) for different volume fractions and surface treatments are shown in Fig 16. There is a loss of ductility and an increase in resistance to the appearance of the first crack. The same results were found by Sedan et al. using hemp fibers and Canovas et al. using sisal fibers, cited by [7]. In mechanical studies on fiber-cement composites, the authors report that, in most cases, the ductility decreases over time, and the mechanical properties change considerably due to the reduced ductility of the material [4]. The factors contributing to the loss of ductility are the degradation of fibers in the alkaline matrix by partial dissolution of cellulose, hemicelluloses, and lignin and the decomposition according to two phenomena. The first was peeling off by the formation of iso-saccharine acids (CH₂OH) that would break away from the chain. The hemicelluloses are more sensitive to peeling off. The second was the alkaline hydrolysis that consists of dividing the molecular chain and reducing the degree of fibers' polymerization [7,14].

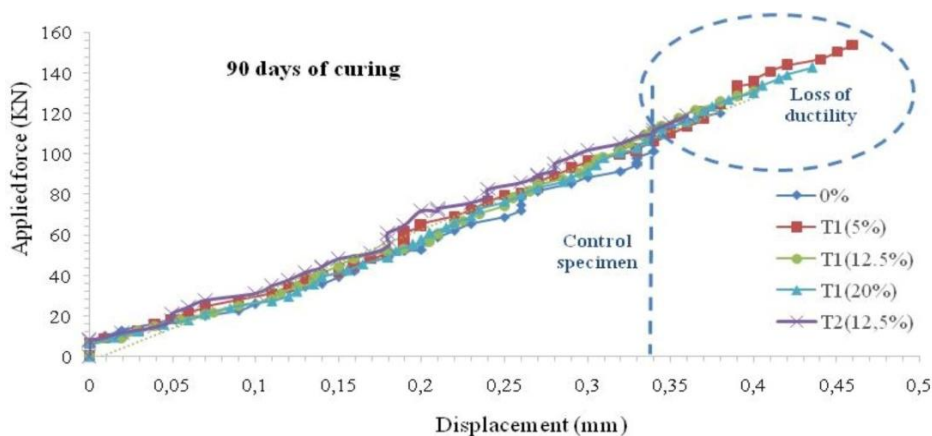


Fig. 16 Effect of treatment on splitting tensile strength of the mortars

The experimental results of the flexural strength (σ_f) at 28-day and 90-day for different volume fractions and surface treatment are shown in Fig 17. As can be seen in the figure, the tensile strength of the composite reinforced by fiber (T1 (5%)) improves compared to the reference composite, with a 1.5% increase. This finding can be attributed to the improvement of the fiber/matrix interface [38] and the pozzolanic reaction of calcined clay [18]. It eliminates the phenomenon of fiber mineralization and improves mechanical resistance. The reduction in the long-term bending strength of 12.5% and 20% volume fractions may be due to surface defects increase and higher porosity [33]. There is also a low variation (Fig17) in the bending resistance of composite reinforced by treated and coated fibers (T2), with an increase of 2.8% compared to (T1). The mineral coating seems to improve the fiber/matrix adhesion.

Fig18 shows that the compressive strength (σ_c) decreases with the addition of fibers. Several authors explain this decrease by the increase in pores in the mixture via oculus air and, thus, the reduction in the cohesion of the fibrous matrix [7, 31]. The increase in the percentage of fiber leads to a decrease in the amount of heat released following the hydration reaction, which explains the decrease in strength of 12.5% and 20%. This finding is probably due to the residual sugars present in the structure of fibers; accordingly, the hydration reaction can be inhibited [34].

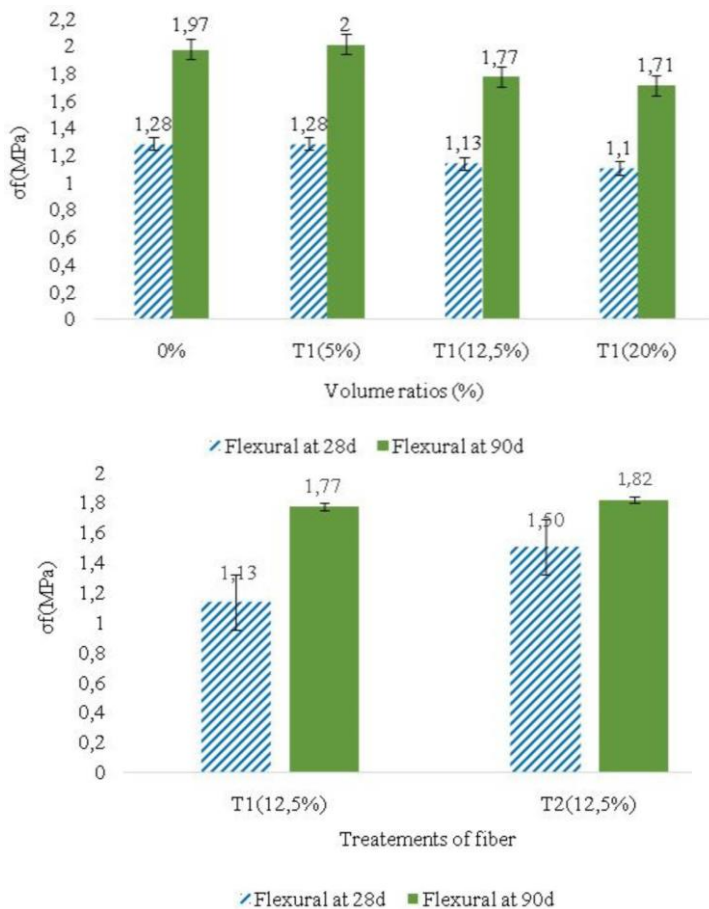


Fig. 17 Effect of volume ratios and treatment on flexural strength of the mortars

Adding fiber helps trap air inside the matrix and reduce its compactness. Abida [53] claims that this finding may be due to the orientation of the fibers during the preparation phase, which allows the agglomeration in the matrix and the non-homogeneous distribution of fibers. However, the best compressive strength is obtained for 5% fibers, with an 11% increase over the reference composite. This finding is consistent with that of Allegue et al. [38]. The alkaline treatment decreases the absorption rate of the fibers, explaining the resistance gain [53]. Also, fig 18 depicts a low variation in the compressive strength of the composites reinforced by the fibers treated and coated by the calcined clay (T2) compared to (T1). Mineral coating for fibers seems to improve the mechanical properties of composites. The larger the volume, the more likely it is to find notable defects that can lead to the breakdown of the fibers. In addition, it has been shown that fiber ruptures are due to a larger size but not to the number of defects [60]. Composite

characteristics are determined by fiber, matrix composition, and fiber-matrix interface [61].

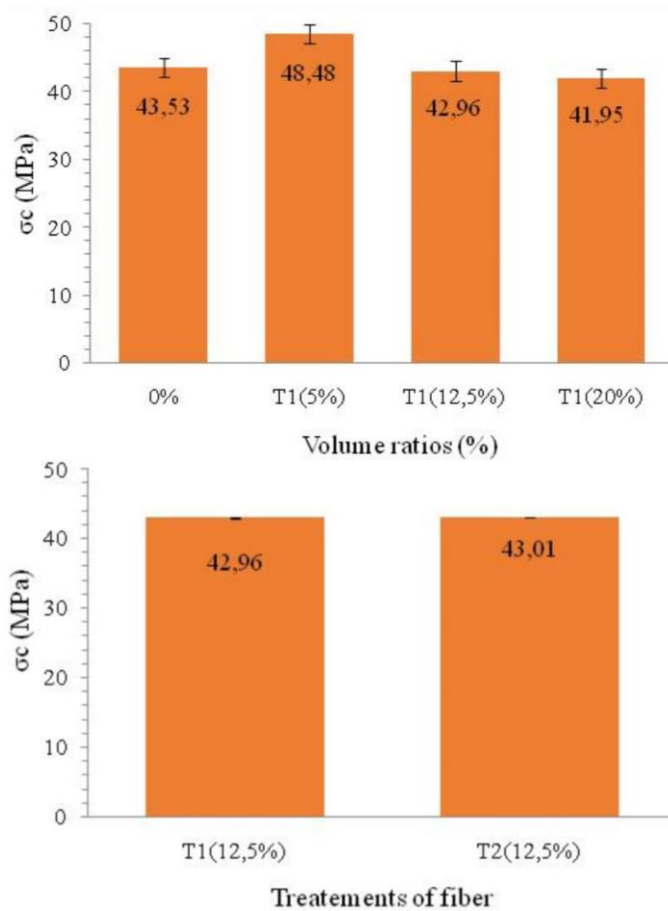


Fig. 18 Effect of volume ratios and treatment on compressive strength of the mortar (90days of curing)

3.7. Alkaline Degradation by Sodium Chloride (NaCl)

Fig 19 shows that the density of the mortars increases after 90 days of immersion in an alkaline solution. This increase is due to a swelling of the composites and the formation of calcium chloride. In the same vein, Asma [4] showed swelling of composites reinforced by Diss fibers after immersion in seawater. Fibers cause volume variation in all composite directions [33]. It is also noted (Fig 20) that the coating treatment by the calcined clay reduces the loss of strength, which can be explained by the rapid reduction of the calcium hydroxide in the cement paste caused by the pozzolanic reaction of the calcined clay [18].

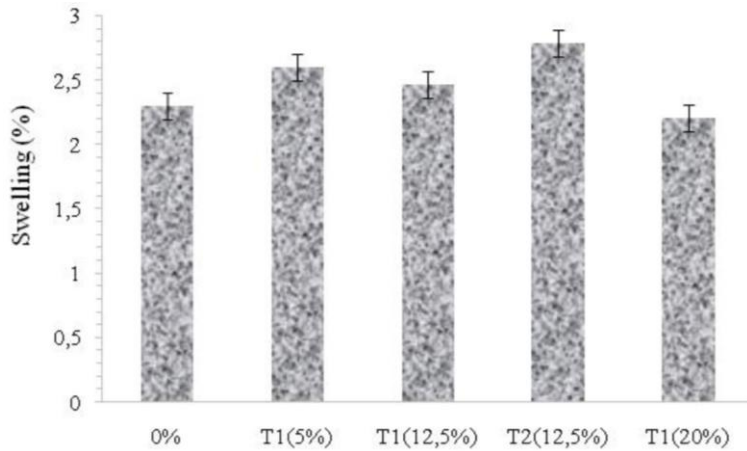


Fig. 19 Swelling of mortars after 90 days of immersion in chloride sodium chloride(NaCl)

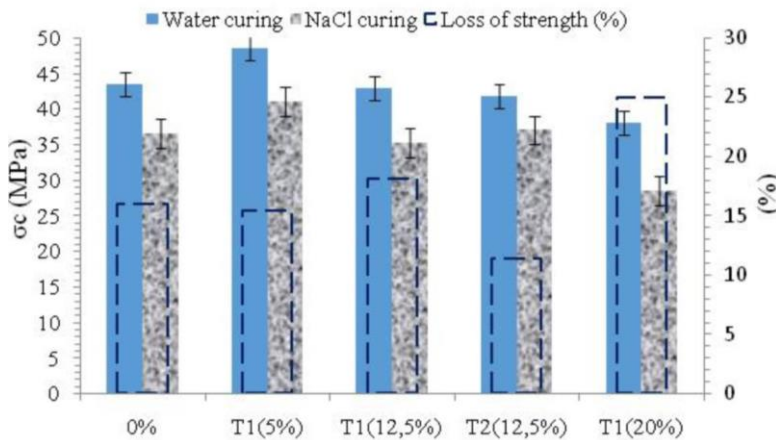


Fig. 20 Reduction in compressive strength of mortars after 90 days of immersion in chloride sodium chloride(NaCl)

3.8. SEM Microstructure Study

The shape of the fibers influences the interface and the anchoring with the matrix. The tubular form has a high adhesion as the fibrillar fibers form massively. This form absorbs more water, which can cause a durability problem. The nature of the fibers directly affects water absorption and the formation of barriers. There is an increase in the roughness of fiber surfaces after alkaline treatment. This regularity improves the adhesion between the fibers and the matrix. It can be suggested that there is also a reduction in impurities, lignin, and hemicelluloses [13, 16, 33]. Fig 21, 22 and 23 shows the SEM-EDX micrographs of Posidonia fibers before and after treatment. To determine the efficacy of the treatment with NaOH (Na^+), the amount of Na^+ in the treated fibers is evaluated. An additional peak shows the presence of the Na^+ molecule resulting from the performed chemical treatment. The results confirm the presence of a chemical reaction between Posidonia fibers and NaOH. Table 6 presents the major compositional elements (oxygen (O) and carbon (C)) of raw and treated fiber and traces for silica (Si), alumina (Al), and iron (Fe), indicating the typical residual elements for plant biomass fibers and calcined clay (siliceous aluminous nature).

Untreated fibers have a thin layer of grass, wax, and impurities deposited on the surface. The hydrothermal and alkali treatment removes the weak external layer of the fibers, such as wax, lignin, and hemicelluloses. It creates a rough surface morphology resulting in better adhesion with the mortar matrix. A small canal with little pores confirms the porosity structure of the fiber. Mineral coating over the Posidonia surface provides a waterproof film that reduces water absorption from the matrix. A combined treatment would create both surface roughening and waterproofing effects [62]. The molecules of the matrix can be fixed to the surface of the fiber by a chemical reaction or adsorption, which determines the adhesion strength of the interface. In some cases, the interface may consist of additional components, such as an adhesive or an intermediate layer between the two components of the composite material. Due to the presence of cellulose and lignin hydroxyl groups, natural fibers can be modified. Surface properties, such as wettability, adhesion, surface tension, fiber surface roughness, and porosity, can be improved by treatment. These surface irregularities play a crucial role in the mechanical connection of the interface with the matrix [61]. The addition of Posidonia fibers allows the creation of voids inside the matrix leading to poor adhesion between fibers and the matrix. The mineral coating treatment by calcined clay minimizes voids (Fig 24 and 25).

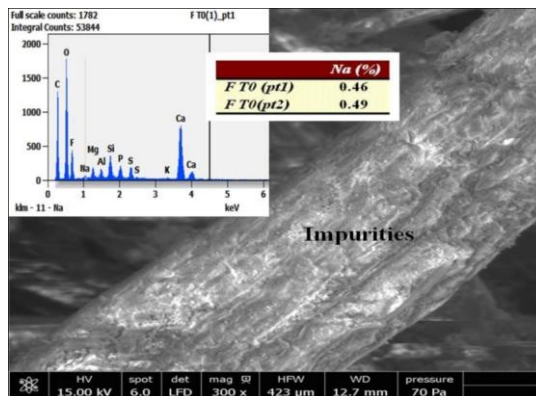


Fig. 21 SEM-EDX micrographs of Posidonia fibers before treatment

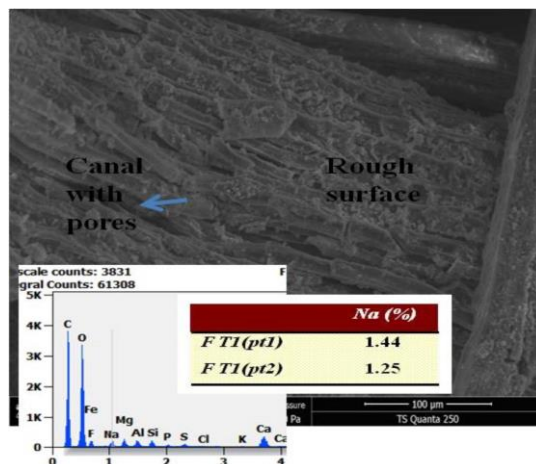


Fig. 22 SEM-EDX micrographs of Posidonia fibers after treatment (alkali and hydrothermal treatment)

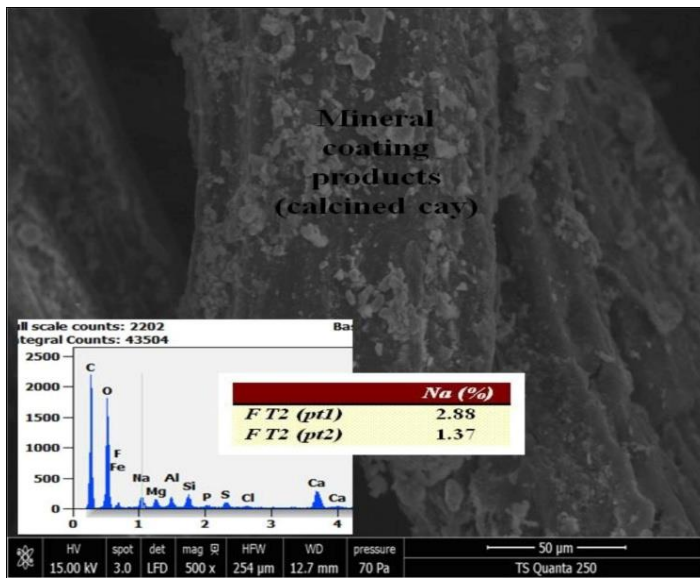


Fig. 23 SEM–EDX micrographs of Posidonia fibers with mineral coating (x100)

Table6. Compositional elements of raw and treated fibers

	Atom %	C	O	Si	Al	Fe
F T0	Point(1)	15.95	38.47	2.02	0.71	0.57
	Point(2)	14.30	34.33	0.98	0.60	-
F T1	Point(1)	40.29	51.01	0.65	0.80	0.25
	Point(2)	37.71	50.77	0.73	0.76	0.21
F T2	Point(1)	39.65	47.18	1.67	1.19	0.40
	Point(2)	23.46	59.05	3.42	2.03	0.62

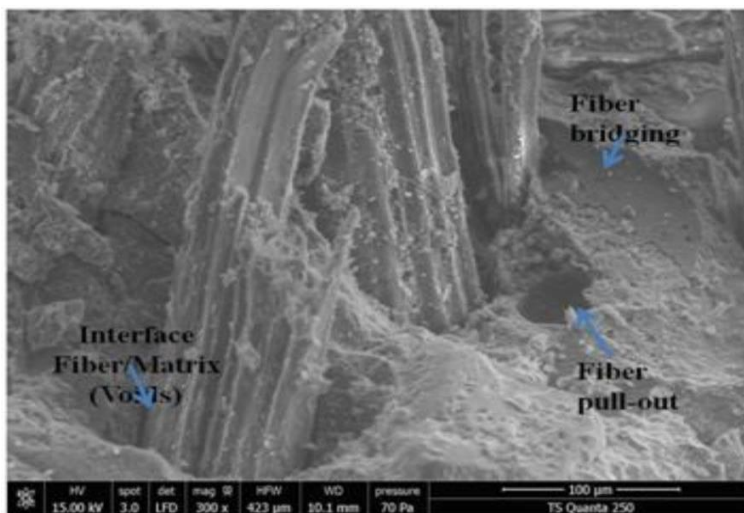


Fig. 24 SEM micrographs of mortars (12.5%) alkali and hydrothermal treatment

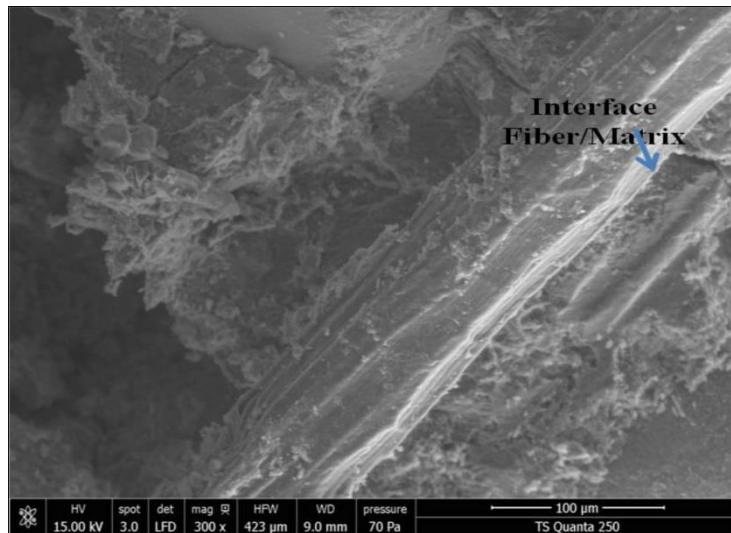


Fig. 25 SEM micrographs of mortars with mineral coating (x100)

5. Conclusions

Based on the analysis of the physical and hygroscopic properties, rheological, mechanical, and micro-structural performances, and chemical attack of cementitious mortars with supplementary materials (calcined clay) incorporating *Posidonia* fibers, the following conclusions can be drawn:

- Fiber characterization showed that alkaline treatment was effective in removing non-cellulosic materials and reducing water absorption from fibers.
- The incorporation of *Posidonia* fibers (volume fraction 5%, 12.5%, and 20%) in composite seems to reduce the usability in the fresh state significantly.
- A decrease in the water absorption of composite reinforced by fibers coated with calcined clay compared to composite reinforced by fibers treated with NaOH without coating. This decrease is due to the reduced number of pores through the mineral coating treatment.
- The maximum moisture content increases with the fiber content.
- The mineral coating treatment by the pozzolanic material makes the fibers relatively less hydrophilic.
- The tensile test shows a long-term loss of ductility and an increase in resistance to the appearance of the first crack.
- The flexural test shows an improvement in strength with the addition of treated *Posidonia* fibers up to an optimum of 5% by volume of fibers. This finding may be explained by the improvement of the fiber/ matrix interface and the pozzolanic reaction of calcined clay, which eliminates the phenomenon of fiber mineralization. However, beyond that percentage, resistance decreases, which may be due to the increase in surface defects.
- The highest compressive resistance was obtained at 5% volume fraction. The alkaline treatment decreases the absorption rate of the fibers, explaining the gain in resistance, and then decreases with the increase in the volume fraction of the fibers.

- The density of the mortars increases after 90 days of immersion in an alkaline solution. This increase is due to a swelling of the composites and the formation of calcium chloride. Fibers cause volume variation in all composite directions.
- The coating treatment by the calcined clay reduces the loss of strength after 90 days of immersion in an alkaline solution, which can be explained by the rapid reduction of the calcium hydroxide in the cement paste caused by the pozzolanic reaction of the calcined clay.

Future Scope and Limitations of The Study

Following the results of this research, other methods, such as lime or plasma treatment, can be proposed for the surface treatment of fibers. It is necessary to study the durability of composite reinforced by Posidonia fibers, such as the determination of migration coefficient and chloride diffusion, freeze-thaw test, and hygro-thermal behavior. It is advisable to study the behavior in adverse environments such as acid environments and elevated temperatures.

References

- [1] Yahiaoui L. Caractérisation d'un composite à la rupture à base des fibres végétales (Diss), PhD Thesis, Abbas Stif University, Algeria, 2018.
- [2] Zahra NF, Fayrouz Z, Lamis A, Mondher Z. Mechanical Performance of Doum Palm Fiber-Reinforced Plaster Mortars. Proceedings of the 7th Conference on Design and Modeling of Mechanical Systems, Hammamet, Tunisia, March, 473-482, 2018. https://doi.org/10.1007/978-3-319-66697-6_46
- [3] Hamdaoui O. Caractérisation thermique et mécanique de fibres naturelles d'origine marine en vue de leur utilisation dans les matériaux de l'habitat, PhD Thesis, Paris Est University, France, 2018.
- [4] Asma S. Elaboration des composites cimentaires à base de fibres végétales locales (le diss): caractérisation, durabilité et application au cas de la maçonnerie, PhD Thesis, Badji Mokhtar University, Algeria, 2015.
- [5] Bouhadjila Y, Rahem Z. Traitement des fibres de palmier dattier. Science, 2019 ; 39 : 331-334.
- [6] Cisse O. Caractérisation du comportement hygro-mécanique des fibres libériennes élémentaires issues du chanvre, PhD Thesis, Cheikh Anta Diop University, Senegal, 2014.
- [7] Page J. Formulation et caractérisation d'un composite cimentaire biofibré pour des procédés de construction préfabriquée, PhD Thesis, Normandie University, France, 2017.
- [8] Chafei S. Influence de différents traitements sur les comportements rhéologique et mécanique d'un composite cimentaire mortier-fibres de lin, PhD Thesis, Caen University, France, 2014.
- [9] Kareche A. Étude des matériaux à base de bois de palmier dattier: durabilité, dégradation et propriétés structurales et de transfert, PhD Thesis, Batna 2 University, Algeria, 2014.
- [10] Kareche A, Agoudjil B, Haba B, Boudenne A. Study on the durability of new construction materials based on mortar reinforced with date palm fibers wastes. Waste and biomass valorization, 2020; 11: 3801-3809. <https://doi.org/10.1007/s12649-019-00669-y>
- [11] Kareche A. Durabilité et dégradation des composites bio-sourcés à base de bois de palmier dattier, PhD Thesis, Batna 2 University, 2020.

- [12] Wei J, Meyer C. Degradation mechanisms of natural fiber in the matrix of cement composites. *Cement and concrete Research*, 2015; 73: 1-16. <https://doi.org/10.1016/j.cemconres.2015.02.019>
- [13] Merta I, Poletanovic B, Kopecskó K. Durability of natural fibres within cement-based materials. *Review. Concr. Struct. Hung. Group, Fib*, 2017; 18: 10-15.
- [14] Page J, Libessart L, Djelal C, Gonon M, Laiymani I. Feasibility of Using Biomass Fly Ash in Cementitious Materials. *Multidisciplinary Digital Publishing Institute Proceedings*, 2019; 34: 12. <https://doi.org/10.3390/proceedings2019034012>
- [15] Wei J, Meyer C. Degradation of natural fiber in ternary blended cement composites containing metakaolin and montmorillonite. *Corrosion Science*, 2017; 120: 42-60. <https://doi.org/10.1016/j.corsci.2016.12.004>
- [16] Merta I, Kopecskó K, Tschegg EK. Durability of hemp fibers in the alkaline environment of cement matrix. 8th RILEM international symposium on fibre reinforced concrete, University of Minho, Guimarães, Portugal, 2012.
- [17] Nawel S, Mounir L, Hedi H. Effect of temperature on pozzolanic reaction of Tunisian clays calcined in laboratory. *SN Applied Sciences*, 2020; 2: 1-14. <https://doi.org/10.1007/s42452-020-1935-9>
- [18] Salem N, Ltifi M, Hassis H. Mechanical and durability study of Tunisian calcined clay in lightweight concrete of expanded clay. *European Journal of Environmental and Civil Engineering*, 2021; 25: 2257-2276. <https://doi.org/10.1080/19648189.2019.1624625>
- [19] Chakchouk A, Trifi L, Samet B., Bouaziz S. Formulation of blended cement: Effect of process variables on clay pozzolanic activity. *Construction and Building Materials*, 2009; 23:1365-1373. <https://doi.org/10.1016/j.conbuildmat.2008.07.015>
- [20] Fernandez R, Martirena F, Scrivener KL. The origin of the pozzolanic activity of calcined clay minerals: A comparison between kaolinite, illite and montmorillonite. *Cement and concrete research*, 2011; 41: 113-122. <https://doi.org/10.1016/j.cemconres.2010.09.013>
- [21] Jaskulski R, Józwiak-Niedźwiedzka D, Yakymchko Y. Calcined clay as supplementary cementitious material. *Materials*, 2020; 13: 4734. <https://doi.org/10.3390/ma13214734>
- [22] Kasaniya M, Thomas MD, Moffatt EG. Efficiency of natural pozzolans, ground glasses and coal bottom ashes in mitigating sulfate attack and alkali-silica reaction. *Cement and Concrete Research*, 2021; 149: 06551. <https://doi.org/10.1016/j.cemconres.2021.106551>
- [23] Cordoba, G., & Irassar, E. F. (2021). Sulfate performance of calcined illitic shales. *Construction and Building Materials*, 291, 123215. <https://doi.org/10.1016/j.conbuildmat.2021.123215>
- [24] Cordoba GP, Zito SV, Sposito R, Rahhal VF, Tironi A, Thienel C, Irassar EF. Concretes with calcined clay and calcined shale: workability, mechanical, and transport properties. *Journal of Materials in Civil Engineering*, 2020; 32: 04020224. [https://doi.org/10.1061/\(ASCE\)MT.1943-5533.0003296](https://doi.org/10.1061/(ASCE)MT.1943-5533.0003296)
- [25] Msinjili NS, Gluth GJ, Sturm P, Vogler N, Kühne HC. Comparison of calcined illitic clays (brick clays) and low-grade kaolinitic clays as supplementary cementitious materials. *Materials and Structures*, 2019; 52: 1-14. <https://doi.org/10.1617/s11527-019-1393-2>
- [26] Magniont C. Contribution à la formulation et à la caractérisation d'un écomatériau de construction à base d'agroressources, PhD Thesis, Toulouse 3 University, France, 2010.
- [27] Wei J, Ma S, D'Shawn GT. Correlation between hydration of cement and durability of natural fiber-reinforced cement composites. *Corrosion Science*, 2016; 106: 1-15. <https://doi.org/10.1016/j.corsci.2016.01.020>

- [28] Naiiri F, Lamis A, Mehdi S, Redouane Z, Mondher Z. Performance of lightweight mortar reinforced with doum palm fiber. *Journal of Composite Materials*, 2021; 55: 1591-1607. <https://doi.org/10.1177/0021998320975196>
- [29] Borchani KE. Développement d'un composite à base d'un polymère biodégradable et de fibres extraites de la plante d'Alfa, PhD Thesis, Lyon University, France, 2016.
- [30] Amroune S. Caractérisations mécaniques et étude de l'endommagement des matériaux composites renforcés par des fibres de palmier, PhD Thesis, Guelma University, Algeria, 2016.
- [31] Lahouioui M, Arfi RB, Fois M, Ibos L, Ghorbal A. Investigation of fiber surface treatment effect on thermal, mechanical and acoustical properties of date palm fiber-reinforced cementitious composites. *Waste and Biomass Valorization*, 2019; 1-15. <https://doi.org/10.1007/s12649-019-00745-3>
- [32] Hamdaoui O, Limam O, Ibos L, Mazioud A. Thermal and mechanical properties of hardened cement paste reinforced with Posidonia-Oceanica natural fibers. *Construction and Building Materials*, 2021; 269: 121339. <https://doi.org/10.1016/j.conbuildmat.2020.121339>
- [33] Ajouguim S, Abdelouahdi K, Waqif M, Stefanidou M, Saâdi L. Modifications of Alfa fibers by alkali and hydrothermal treatment. *Cellulose*, 2019; 26: 1503-1516. <https://doi.org/10.1007/s10570-018-2181-9>
- [34] Ajouguim S, Page J, Djelal C, Waqif M, Saâdi L. Impact of Alfa fibers morphology on hydration kinetics and mechanical properties of cement mortars. *Construction and Building Materials*, 2021; 293: 123514. <https://doi.org/10.1016/j.conbuildmat.2021.123514>
- [35] Ajouguim S, Stefanidou M, Abdelouahdi K, Waqif M, Saâdi L. Influence of treated bio-fibers on the mechanical and physical properties of cement mortars. *European Journal of Environmental and Civil Engineering*, 2022; 26: 3120-3135. <https://doi.org/10.1080/19648189.2020.1782773>
- [36] Kriker A, Debicki G, Bali A, Khenfer MM, Chabannet M. Mechanical properties of date palm fibres and concrete reinforced with date palm fibres in hot-dry climate. *Cement and Concrete Composites*, 2005; 27: 554-564. <https://doi.org/10.1016/j.cemconcomp.2004.09.015>
- [37] Borum J. European seagrasses: an introduction to monitoring and management, C. M. Duarte, T. M. Greve, & D. Krause-Jensen (Eds.), M & MS project, 2004: 67-71.
- [38] Allegue L, Zidi M, Sghaier S. Mechanical properties of Posidonia oceanica fibers reinforced cement. *Journal of Composite Materials*, 2015; 49: 509-517. <https://doi.org/10.1177/0021998314521254>
- [39] Jedidi M, Abroug A. Valorization of Posidonia oceanica Balls for the Manufacture of an Insulating and Ecological Material. *Jordan Journal of Civil Engineering*, 2020; 14.
- [40] Benjeddou O, Jedidi M, Khadimallah MA, Ravindran G, Sridhar J. Effect of Posidonia oceanica Fibers Addition on the Thermal and Acoustic Properties of Cement Paste. *Buildings*, 2022; 12:909. <https://doi.org/10.3390/buildings12070909>
- [41] Hassan MZ, Roslan SA, Sapuan SM, Rasid ZA, Mohd Nor AF, Md Daud MY, Mohamed Yusoff MZ. Mercerization optimization of bamboo (*bambusa vulgaris*) fiber-reinforced epoxy composite structures using a box-behnken design. *Polymers*, 2020; 12: 1367. <https://doi.org/10.3390/polym12061367>
- [42] Thuault A, Eve S, Blond D, Bréard J, Gomina M. Effects of the hydrothermal environment on the mechanical properties of flax fibres. *Journal of composite materials*, 2014; 48: 1699-1707. <https://doi.org/10.1177/0021998313490217>
- [43] Baley C, Gomina M, Breard J, Bourmaud A, Davies P. Variability of mechanical properties of flax fibres for composite reinforcement. A review. *Industrial Crops and Products*, 2020; 145: 111984. <https://doi.org/10.1016/j.indcrop.2019.111984>

- [44] Bodirlau R, Teaca CA, Spiridon I. Chemical modification of beech wood: Effect on thermal stability. *BioResources*, 2008; 3: 789-800. <https://doi.org/10.15376/biores.3.3.789-800>
- [45] May C, Moussa A. Chemical and structural analysis of lignocellulosic biomass of *Ampelodesmos mauritanicus* (DISs) and *Stipatenacissima*. *Wood Res*, 2018; 63: 699-712.
- [46] Bouhamed N. Elaboration et caractérisation d'un matériau composite à base de farine de bois d'olivier, PhD Thesis, Normandie University, Sfax University, Tunisia, 2020.
- [47] Zhang J, Koubaa A, Xing D, Liu W, Wang Q, Wang X, Wang H. Improving lignocellulose thermal stability by chemical modification with boric acid for incorporating into polyamide. *Materials & Design*, 2020; 191: 108589. <https://doi.org/10.1016/j.matdes.2020.108589>
- [48] Marvila MT, Rocha HA, de Azevedo ARG, Colorado HA, Zapata JF, Vieira CMF. Use of natural vegetable fibers in cementitious composites: Concepts and applications. *Innovative Infrastructure Solutions*, 2021; 6: 1-24. <https://doi.org/10.1007/s41062-021-00551-8>
- [49] Amriou A. Evaluation de la durabilité du béton par essais de perméabilité à l'eau sous conditions climatiques et chimiques préjudiciables, PhD Thesis, M'sila University, Algeria 2017.
- [50] Bamaga SO. A Review on the Utilization of Date Palm Fibers as Inclusion in Concrete and Mortar, *Fibers*, 2022; 10: 35. <https://doi.org/10.3390/fib10040035>
- [51] Jain D, Kamboj I, Bera TK, Kang AS, Singla RK. Experimental and numerical investigations on the effect of alkaline hornification on the hydrothermal ageing of Agave natural fiber composites. *International Journal of Heat and Mass Transfer*, 2019; 130: 431-439. <https://doi.org/10.1016/j.ijheatmasstransfer.2018.10.106>
- [52] Radzi AM, Sapuan SM, Jawaid M, Mansor MR. Effect of alkaline treatment on mechanical, physical and thermal properties of roselle/sugar palm fiber reinforced thermoplastic polyurethane hybrid composites. *Fibers and Polymers*, 2019; 20: 847-855. <https://doi.org/10.1007/s12221-019-1061-8>
- [53] Abida M. Comportement hygroscopique et couplage hygromécanique dans les composites lin/époxy: approche expérimentale multi-échelle et modélisation, PhD Thesis, Normandie University, France, 2018.
- [54] Placet V. Influence de traitements hygrothermiques sur les propriétés mécaniques de composites à fibres végétales (Effect of hygro-thermal treatment on the mechanical properties of natural fibres composites, *JNC*, 2009; 16: 10.
- [55] Placet V, Cisse O, Boubakar ML. Influence of environmental relative humidity on the tensile and rotational behaviour of hemp fibres. *Journal of Materials Science*, 2012; 47: 3435-3446. <https://doi.org/10.1007/s10853-011-6191-3>
- [56] Francois C, Plasseraud L, Pourchet S, Boni G, Placet V, Fontaine S, Champion D. Étude d'un procédé de traitement innovant des fibres de chanvre sous condition de fluide supercritique et propriétés induites, *JNC*, 2017; 20.
- [57] Berges M, Piezel B, Person V, Corn S, Léger R, Fontaine S, Placet V. Microstructure et vieillissement hygrothermique de composites renforcés de fibres de lin unidirectionnelles, *JNC*, 2017; 20.
- [58] Rabii H. Étude du vieillissement de composites renforcés par des fibres naturelles: application bâtiment, PhD Thesis, Paris Est University, 2016.
- [59] Ibro MA. Vers la prédiction des cinétiques de rééquilibrage entre 2 milieux initialement en conditions de saturation différentes, PhD Thesis, Paul Sabatier-Toulouse III University, 2020.

- [60] Baley C. Influence of kink bands on the tensile strength of flax fibers. *Journal of materials science*, 2004; 39: 331-334. <https://doi.org/10.1023/B:JMSC.0000007768.63055.ae>
- [61] El Omari H. *Matériaux Lignocellulosiques Fonctionnels à partir de plantes vivaces marocaines et de pâtes commerciales*, PhD Thesis, Quebec University, 2016.
- [62] Ajouguim S, Page J, Djelal C, Waqif M, Saadi L. Performance of Alfa fibres in cementitious materials exposed to diverse surface treatments. *Construction Technologies and Architecture*, 2022; 1: 660-667. <https://doi.org/10.4028/www.scientific.net/CTA.1.660>



Technical Note

Moisture susceptibility of waste ceramic tiles modified asphalt mixtures

Oguntayo Daniel^{*1,a}, Ogundipe Olumide^{2,b}, Daikwo Jemimah^{3,c}, Adeyemi Festus^{4,d}, Aladegboye Oluwasegun^{3,e}

¹Department of Civil Engineering, Confluence University of Science and Technology, Osara, Nigeria

²Department of Civil Engineering, Ekiti State University, Ado-Ekiti, Nigeria

³Department of Civil Engineering, Landmark University, Omu-Aran, Nigeria

⁴Department of Civil Engineering, Ajayi Crowther University, Oyo, Nigeria

Article Info

Article history:

Received 04 July 2023

Accepted 11 Sep 2023

Keywords:

Waste ceramic tiles;
Durability;
Asphalt mixtures;
Tensile strength ration;
Retained strength index;
Construction and demolition waste

Abstract

Waste ceramic tiles have been recognized as viable in producing asphalt mixtures. However, the primary concern is the assurance of its durability, especially in terms of moisture damage. Therefore, this research aims to investigate the moisture susceptibility of asphalt mixtures incorporating waste ceramic tiles (WCT). The coarse aggregates of 25 mm size were partially replaced with WCT at 0%-50% proportions. The Marshall Method of mix design was used to calculate the optimum bitumen content (OBC) at various levels of WCT replacement. Utilizing the retained strength index (RSI) and tensile strength ratio (TSR) tests, the moisture susceptibility of the mixes compacted at OBC was assessed. The results indicate that the continuous increase of WCT leads to decreased TSR and RSI values. The RSI ranges from 91.10%-81.90%, 74.91%-61.07% and 47.89%-41.05% at 1, 3, and 7-day curing, respectively. The TSR ranges from 89.27-74.73%, 71.48-63.81% and 58.02-46.79% at 1, 3, and 7-day curing, respectively. Nevertheless, it was determined that the WCT-modified asphalt mixtures met the TSR and RSI standards for asphalt mixtures with satisfactory moisture resistivity performance at 1 and 3 days of curing. For satisfying performance of WCT-modified asphalt mixtures, the study recommends an optimum proportion of 30% WCT.

© 2023 MIM Research Group. All rights reserved.

1. Introduction

Most of the construction and demolition (C&D) wastes produced by Nigeria's building industry throughout time is solid waste; ceramic tiles contribute the highest percentage of waste within the C&D wastes [1-2]. According to Ramirez et al. [3] about 54% of the C&D waste in the stony fraction comes from ceramic tiles. Most of these waste ceramic tiles are not recycled and instead end up in landfills, taking up valuable space and costing money in landfilling [4-5]. However, disposal of waste ceramic tiles in landfill can be minimized if it can be re-utilized. For instance, waste ceramic tiles can be recycled into aggregate, which has a better crushing value, impact value, and abrasion value than natural crushed stone [6]. It is also relatively hard and has a significant specific gravity value [7]. Hence, utilizing used ceramic tiles instead of expensive or scarce natural resources will save expenses, consecutively decrease the amount of space needed for disposal, and minimize other costs [8-9].

Past research has addressed asphalt mixture production using waste ceramic tiles in several forms. In Muniandy et al. [10], the performance of recycled ceramic waste as aggregates in asphalt mixtures was conducted. Marshall characteristics and resilient

*Corresponding author: dnloguntayo@gmail.com

^a orcid.org/0000-0003-0400-6103; ^b orcid.org/0000-0002-2783-1336; ^c orcid.org/0009-0006-5864-8135;

^d orcid.org/0009-0004-5266-8261; ^e orcid.org/0000-0002-0850-2414

DOI: <http://dx.doi.org/10.17515/resm2023.798ma0704tn>

modulus were used as the performance indicators. It was demonstrated that ceramic waste aggregates could be employed in the pavement construction industry and provide cost and environmental efficiency advantages. The waste ceramic powder was investigated for viability as an alternative filler for asphalt mastics by Rochlani et al. [11]. They discovered ceramic powder could be employed as an efficient filler substitute in asphalt, having comparable fatigue performance to that of limestone mastic while having higher stiffness, better ageing properties, increased bitumen-filler interaction, and rutting resistance. While waste ceramic tiles have been recognized as viable in the production of asphalt mixtures, the primary concern is the assurance of their durability concerning their moisture damage. To provide excellent service, the asphalt mixtures must remain durable over their intended life span. However, the durability of the asphalt mixtures is seriously affected due to moisture-induced damage [12]. According to Soenen et al. [13], one of the main reasons flexible pavements fails is their vulnerability to moisture, which lowers their durability. Moisture damage in asphalt mixtures is defined as the "degradation of mechanical properties of the material due to the presence of moisture in a liquid or vapour state" [14]. Moisture weakens the cohesiveness in the asphalt mixtures and the adhesion between the aggregate and the asphalt in asphalt mixtures [15]. Hence, the aggregates' type and properties are crucial in preserving the solid bond with asphalt in the presence of water [15]. Therefore, to better understand how moisture affects the performance of WCT-modified asphalt mixtures, this study aims to investigate the effect of moisture on the hot mix asphalt mixtures incorporating waste ceramic tiles as aggregate for sustainable pavement works. For this purpose, WCT was used to replace granite at a proportion of 0-50% for the asphalt mixtures. Marshall immersion and indirect tensile strength assessed the asphalt mixtures' moisture susceptibility.

2. Materials and Methods

2.1. Materials

2.1.1. Waste Ceramic Tiles

The waste ceramic tiles (WCT) were obtained from the Landmark University, Omu-Aran, Nigeria, construction site. The waste ceramic tiles were crushed and graded (as shown in Fig. 1). The properties of the waste ceramic tiles are shown in Table 1.

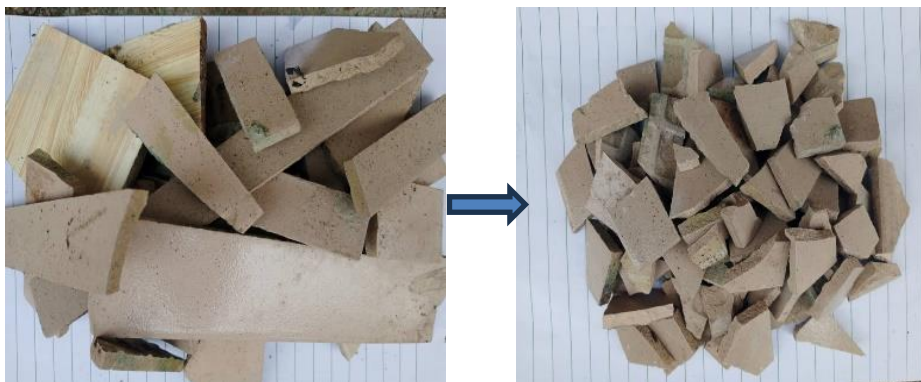


Fig. 1 Waste ceramic tiles

2.1.2. Aggregate

The coarse aggregates utilized were granite with particle sizes of 25 mm for a typical binder course. The fine aggregate used was the stone dust. The coarse and fine aggregate was sourced from a quarry site in Omu-Aran, Nigeria. The properties of the aggregates are

shown in Table 1, and the aggregate gradation for the bituminous mixtures is shown in Fig. 2.

Table 1. Aggregate properties

Test	Specification	Results	
		Granite	WCT
Abrasion test	≤35	20.7	18.0
Flakiness	≤35	11.6	17.9
Aggregate crushing value	≤30	17.2	14.33
Water Absorption	≤0.5	0.10	0.18
Aggregate impact value	≤30	16.8	24.2
Fine Aggregate			
Specific Gravity	≤3	2.7	2.7
Bulk Density		217.3 kg/m ³	

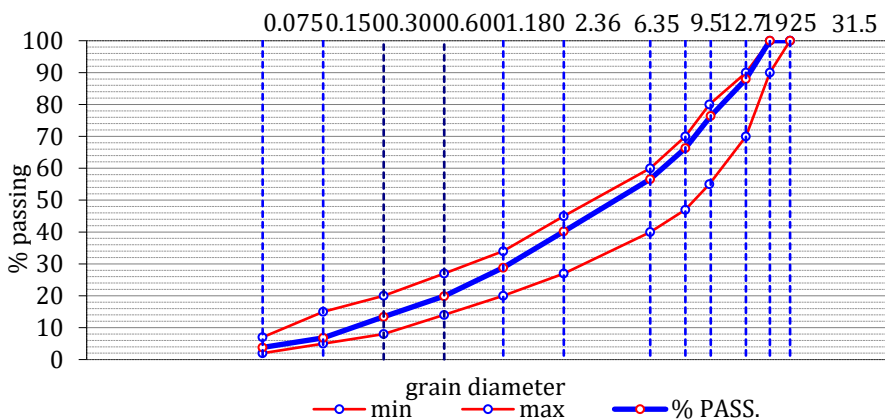


Fig. 2 Aggregate gradation for the asphalt mixtures

2.1.3. Bitumen

The bitumen used was grade 60/70, sourced from a local market in Omu-Aran, Nigeria. The bitumen properties are shown in Table 2.

Table 2. Bitumen properties

Test	Specification	Result
Specific Gravity	1.01-1.06	1.03
Penetration (mm)	60-70	63
Softening Point (°C)	45-56	52.4
Ductility (cm)	Min. 75	110
Solubility in CS ₂ (Petrol was used)	Min. 99.5	99.9
Flash and fire point (°C)	Min. 250	Flash=311 Fire=320
Minimum Loss on Heat for 5 hours at 163°C	Max. 0.2	0.08
Drop in Penetration after heating	Max. 20	13.1

2.2. Materials

Table 3 displays the material quantities utilized to create the asphalt mixtures. Stone dust and HWA were used as fillers in 1200 g aggregates pre-heated between 160 and 1780C. At 1500C, the chosen bitumen content was melted. The steel bowl was used to combine the bitumen and aggregates. A mixing temperature of roughly 1850C was used to combine the mixture completely. The mixture was compressed in a fore-heat Marshall mould by giving each face of the sample 75 blows. In Kara and Karacasu [16], an optimum of 30% WCT was achieved for the HMA. This study considered a variation in the WCT between 0% and 50% at an interval of 10% to replace 25 mm granite in the preparation of the asphalt mixtures.

Table 3. Mix proportion

SN	% WCT	CA: 25mm (%)	CA: 20mm (%)	FA (%)	MF (%)
1	0	40	20	25	15
2	10	40	20	25	15
3	20	40	20	25	15
4	30	40	20	25	15
5	40	40	20	25	15
6	50	40	20	25	15

Note: WCT= waste ceramic tiles, CA= Coarse Aggregate, FA= Fine Aggregate and MF= Mineral Filler

2.3. Laboratory Investigations

2.3.1 Marshall Test to Determine the Optimum Bitumen Content (OBC)

To produce hot mix asphalt (HMA) with the appropriate qualities, the optimum bitumen content was determined using a Marshall method for designing hot asphalt mixtures. Using six different bitumen concentrations (ranging from 5% to 8%), three of 1200 g in weight were prepared per the ASTM D1559 [17] standard. For different bitumen amounts, the Marshall properties of the asphalt mix, including stability, flow, density, the percentage of air voids in the entire mix, and the proportion of voids filled with bitumen, were obtained.

2.3.2 Tensile Strength Ratio (TSR) Test

The tensile strength ratio test is a technique for calculating the strength loss resulting from damage caused by stripping (of the asphalt from the aggregate) while subject to accelerated water conditioning that is controlled in a laboratory. AASHTO T 283 [18] evaluates stripping in Hot Mix Asphalt (HMA) using the indirect tensile strength test (Fig. 3a). After sample conditioning, strength retention is assessed using the Tensile Strength Ratio (TSR). The TSR is performed on two different types of HMA samples. One kind is used as a control (unconditioned) and kept at 25°C temperature. The other type is conditioned by submerging in water and soaking for 1, 3, and 7 days. The TSR value was calculated using Eq. 1.

$$TSR = \frac{T_{wet}}{T_{dry}} \times 100 \quad (1)$$

Where: TSR = Tensile strength ratio, T_{dry} = Average tensile strength of unconditioned samples, T_{wet} = Average tensile strength of conditioned samples.



Fig. 3 Specimen under (a) ITS test (b) Marshall Stability test.

2.3.3 Marshall Immersion Test

The Marshall Immersion test establishes how much cohesiveness is lost when water contacts compacted asphalt mixtures made with asphalt cement. This technique measures the strength loss brought on by water's impact on compacted bituminous mixtures. The specimens are divided as part of the conditioning procedure before the test. One pair is kept in a water bath at 60 °C for 1, 3, and 7 days. The other pair, however, is kept at ambient temperature.

Both specimens are put under a simple compression load after the curing days, with a constant deformation speed of 5.08 mm/min, until they break (as illustrated in Figure 2b). The maintained strength value for each set can be found in this method. The retained strength index (RSI) is the test's outcome, which assesses the specimens' susceptibility to water action. This index is calculated using Eq. 2.

$$RSI = \frac{S_1}{S_2} \times 100\% \quad (2)$$

Where; RSI = Retained Strength Index; S_1 = Marshall Stability with soaking time of 30 min at a temperature of $\pm 60^\circ\text{C}$; S_2 = Stability after immersion at a temperature of $\pm 60^\circ\text{C}$.

2.3.4 Statistical Analysis

Analysis of variance (ANOVA) single factor test was conducted to check the statistical significance of the different proportions of WCT on the moisture susceptibility of the asphalt mixtures. The probability or p-value was considered 0.05 as the level of significance for the hypothesis test.

4. Results and Discussion

4.1. Effects of WCT on the Marshall Properties

The result obtained from study the effect of waste ceramic tiles replacement on the optimum bitumen content (OBC) is shown in Fig. 4. There was an increase in OBC up to 20% addition of WCT and a decrease with further addition of WCT. Nevertheless, the obtained bitumen contents are all within the acceptable variation of 4-7% for a binder course application as stipulated by the General Specification for Roads and Bridges of

Nigeria [19]. Furthermore, this variation in OBC as the proportion of WCT increases was also noted by Huang et al. [20].

The Marshall properties of WCT-modified asphalt mixtures at OBC are depicted in Fig. 5. It was observed that, whilst the stability and flow values of WCT-modified asphalt mixtures are within the acceptable variation (minimum 3.5 kN and 3-5 mm for stability and flow, respectively) as per General Specification for Roads and Bridges of Nigeria [19], a decrease in stability and an increase in flow and volume of mineral aggregates (VMA) as the proportion of WCT increases is observed. It can be said that the large sizes of WCT reduced the stability in the asphalt mix and increased the voids and flow in the mixture resulting from the bitumen content. This result is in contrast to the study conducted by Muniandy et al. [10]. Their study observed an increase in stability for the WCT-modified mixtures compared to the control.

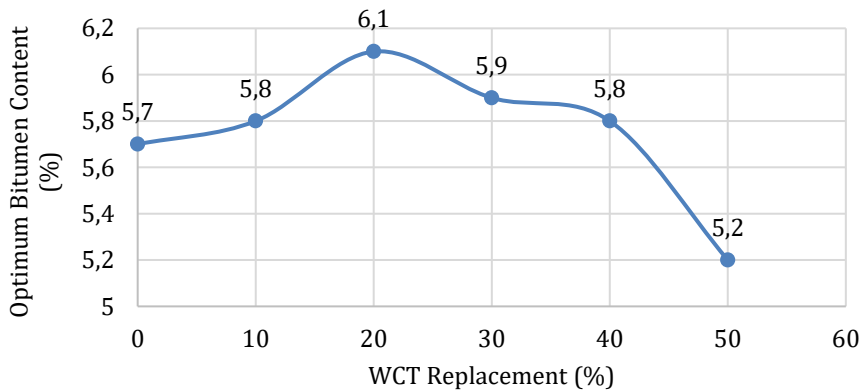


Fig. 4 OBC of WCT-modified asphalt mixtures

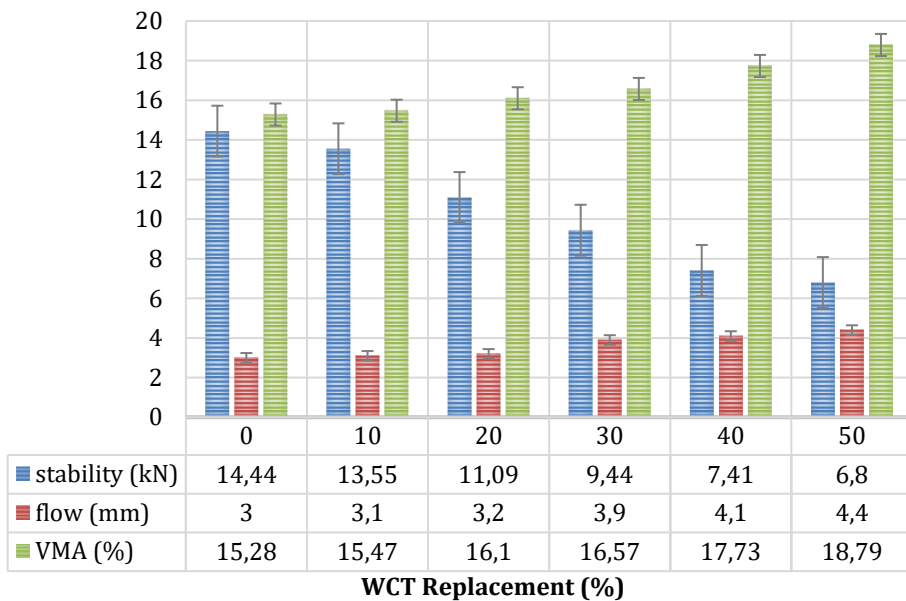


Fig. 5 Marshall Properties of WCT-modified asphalt mixtures

4.2. Tensile Strength Ratio of WCT-modified Asphalt Mixtures

Fig. 6 shows the WCT-modified mixes' indirect tensile strength (ITS) values for both wet and dry conditions. Results showed that increasing WCT steadily until it reaches 30% causes an increase in the tensile strength of the unconditioned samples and then decreases afterwards. Also, for the conditioned samples, an increase in the WCT decreased the tensile strength of the modified mixtures. The strength reduction may result from bitumen and aggregate losing their adherence [21-22].

Fig. 7 depicts the TSR values obtained for WCT-modified asphalt mixtures. It can be seen that the addition of WCT decreases the TSR of the modified asphalt mixtures, which could be due to the loss of adhesion between the binder and aggregate [21-22]. Generally speaking, a higher TSR value means that the mixture will work well and have good resistance to moisture damage [23]; hence, WCT as an aggregate in asphalt mixtures will not guarantee a suitable performance and will likely be susceptible to moisture damage. In the study conducted by Silvestre et al. [24], they also reported a poor behaviour of WCT-modified asphalt mixtures to moisture. Furthermore, the TSR value decreases as the soaking duration increases. However, adding WCT up to 30% at 24-hour soaking duration meets the criteria of a minimum TSR value of 80%.

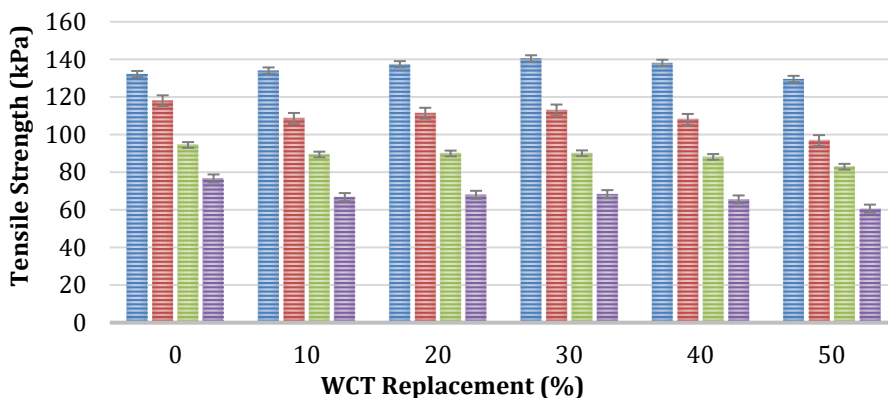


Fig. 6 ITS of WCT-modified asphalt mixtures

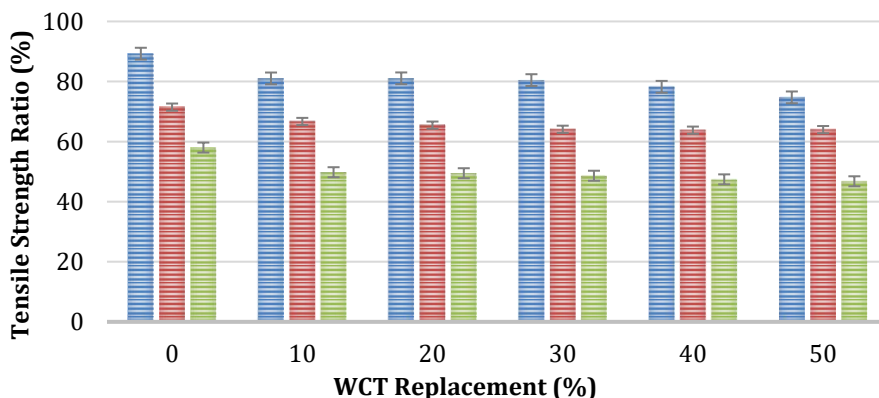


Fig. 7 Tensile strength ratio of WCT-modified asphalt mixtures

4.4. Retained Strength Index of WCT-Modified Asphalt Mixtures

Fig. 8 shows the RSI values obtained for WCT-modified asphalt mixtures. It can be seen that the RSI values decreased on the increment of the WCT at day 1, 3, and 7 days of curing. The decrease in the RSI indicates the WCT-modified mixture's vulnerability to water attack [25]. The RSI ranges from 91.10-81.90%, 74.91-61.07% and 47.89-41.05% at 1, 3, and 7-day curing, respectively. The Marshall Immersion test uses an RSI value of a minimum of 70% to assess whether a mixture is sensitive to moisture. Therefore, except for 50% WCT at 3-day curing, the RSI of all the mixtures at 1, 3-day curing are above 70% and, consequently, durable and suitable for use.

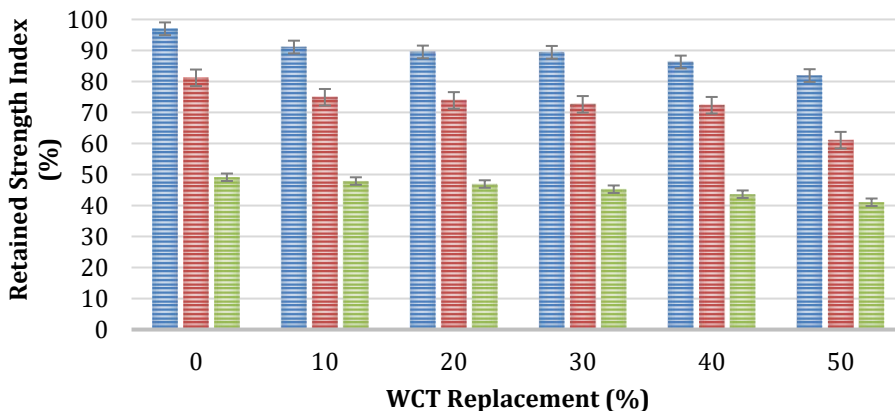


Fig. 8 RSI properties of WCT-modified asphalt mixtures

4.5. ANOVA Results of WCT-Modified Asphalt Mixtures

The ANOVA test results for the proportion of WCT on the moisture susceptibility properties of asphalt mixtures is shown in Table 4. The proportions of WCT are, as indicated in the Table, significantly different at a 5% probability level. This implies that the WCT proportions greatly influence the asphalt mixtures moisture damage properties such as tensile strength, TSR and RSI.

Table 4 ANOVA test for the influence of WCT on Asphalt mixture moisture susceptibility

Properties	Source of variation	Degree of freedom	Sum of squares	Mean square	F test	P Value	Significance																				
ITS	Between groups	5	383.87	76.77	0.0913	0.9926	Yes																				
	Within groups	18	15138.69	841.04				TSR	Between groups	5	225.92	45.18	0.189	0.961	Yes	Within groups	12	2858.44	238.20	RSI	Between groups	5	339.38	67.88	0.1394	0.979	Yes
TSR	Between groups	5	225.92	45.18	0.189	0.961	Yes																				
	Within groups	12	2858.44	238.20				RSI	Between groups	5	339.38	67.88	0.1394	0.979	Yes	Within groups	12	5843.91	486.99								
RSI	Between groups	5	339.38	67.88	0.1394	0.979	Yes																				
	Within groups	12	5843.91	486.99																							

5. Conclusions

To provide excellent service, the asphalt mixtures must remain durable over their intended life span. However, the durability of the asphalt mixtures is seriously affected due to moisture-induced damage. Due to the susceptibility of asphalt mixtures to moisture deterioration, many kinds of distress are accelerated, reducing the pavement's lifespan. In this study, the moisture performance of waste ceramic tiles modified asphalt mixtures was conducted. For this purpose, the Marshall test determined the asphalt mixture's properties and the asphalt mixes' susceptibility to moisture by the Marshall immersion and indirect tensile strength (ITS) tests. The significant findings of this study are as follows:

- There was an increase in OBC up to 20% addition of WCT and a decrease with further addition of WCT. The obtained OBC are all within the acceptable variation of 4-7% for a binder course application as stipulated by the General Specification for Roads and Bridges of Nigeria.
- There was a decrease in stability from 14.44-6.8 kN as the proportion of WCT increases. Nonetheless, the stability values of WCT-modified asphalt mixtures are within the acceptable limits as per General Specification for Roads and Bridges of Nigeria.
- The unconditioned samples' tensile strength increases as WCT increases to 30% and then decreases; indicating that 30% WCT is the optimum value for WCT in WCT-modified asphalt mixtures.
- The TSR of the modified asphalt mixtures decreases from with the addition of WCT, which could be due to the loss of adhesion between the binder and WCT aggregate. The TSR ranges from 89.27-74.73%, 71.48-63.81% and 58.02-46.79% at 1, 3, and 7-day curing, respectively.
- The RSI values decreased on the increment of the WCT, which indicates the WCT-modified mixture's vulnerability to a water attack. The RSI ranges from 91.10-81.90%, 74.91-61.07% and 47.89-41.05% at 1, 3, and 7-day curing, respectively.
- The mixes were found to satisfy the TSR and RSI standards for asphalt mixtures with adequate moisture resistivity performance at 1 and 3 days of curing duration, even though the inclusion of WCT reduces the TSR and RSI.
- The ANOVA test proved that statistically, the proportion of WCT have significance on the moisture susceptibility of asphalt mixtures.
- Future research is recommended to improve the moisture damage of WCT-modified asphalt mixtures.

References

- [1] Zimbili O, Salim W, Ndambuki M. A review on the usage of ceramic wastes in concrete production. *International Journal of Civil, Environmental, Structural, Construction and Architectural Engineering*. 2014 Jan 4;8(1):91-5.
- [2] Juan A, Medina C, Guerra MI, Morán JM, Aguado PJ, Sánchez de Rojas MI, Frías M, Rodríguez O. Re-use of ceramic wastes in construction. *Ceramic materials*. 2010 Sep 28:197-214.
- [3] Ramirez J, Remolisan C, Coscos MJ, Canseco-Tuñacao HA. Integrating Fine Ceramic Tile Aggregates in Concrete Hollow Blocks. In *IOP Conference Series: Earth and Environmental Science* 2023 May 1 (Vol. 1184, No. 1, p. 012023). IOP Publishing. <https://doi.org/10.1088/1755-1315/1184/1/012023>
- [4] Cabalar AF, Hassan DI, Abdulnafaa MD. Use of waste ceramic tiles for road pavement subgrade. *Road Materials and Pavement Design*. 2017 Jul 4;18(4):882-96. <https://doi.org/10.1080/14680629.2016.1194884>

- [5] Awoyera PO, Ndambuki JM, Akinmusuru JO, Omole DO. Characterization of ceramic waste aggregate concrete. HBRC journal. 2018 Dec 1;14(3):282-7. <https://doi.org/10.1016/j.hbrj.2016.11.003>
- [6] Senthamarai RM, Manoharan PD. Concrete with ceramic waste aggregate. Cement and concrete composites. 2005 Oct 1;27(9-10):910-3. <https://doi.org/10.1016/j.cemconcomp.2005.04.003>
- [7] Paul SC, Faruky SA, Babafemi AJ, Miah MJ. Eco-friendly concrete with waste ceramic tile as coarse aggregate: mechanical strength, durability, and microstructural properties. Asian Journal of Civil Engineering. 2023 May 23:1-1. <https://doi.org/10.1007/s42107-023-00718-x>
- [8] Ali AM. Laboratory Evaluation of the Mechanical Performance of Hot Mix Asphalt Modified with Ceramic Waste Powder as Filler. Journal of Engineering Science and Technology. 2022 Aug;17(4): 2861-76.
- [9] Silvestre R, Medel E, García A, Navas J. Using ceramic wastes from tile industry as a partial substitute of natural aggregates in hot mix asphalt binder courses. Construction and Building Materials. 2013 Aug 1; 45: 115-22. <https://doi.org/10.1016/j.conbuildmat.2013.03.058>
- [10] Muniandy R, Ismail DH, Hassim S. Performance of Recycled Ceramic Waste as Aggregates in Asphalt Mixtures. J. Traffic Transp. Eng. 2019;7: 237-45. <https://doi.org/10.17265/2328-2142/2019.06.001>
- [11] Rochlani M, Canon Falla G, Wellner F, Wang D, Fan Z, Leischner S. Feasibility study of waste ceramic powder as a filler alternative for asphalt mastics using the DSR. Road Materials and Pavement Design. 2021 Nov 2;22(11):2591-603. <https://doi.org/10.1080/14680629.2020.1778508>
- [12] Oguntayo D, Ogundipe O, Aladegboye O, Ogunkunbi G, Babatunde Y, Aransiola O. Performance Evaluation of Hospital Waste Ash-Modified Asphalt Mixtures. Advances in Civil Engineering. 2023 Jul 11; 2023. <https://doi.org/10.1155/2023/6880766>
- [13] Soenen H, Vansteenkiste S, Kara De Maeijer P. Fundamental approaches to predict moisture damage in asphalt mixtures: State-of-the-art review. Infrastructures. 2020 Feb 21;5(2):20. <https://doi.org/10.3390/infrastructures5020020>
- [14] Caro S, Masad E, Bhasin A, Little DN. Moisture susceptibility of asphalt mixtures, Part 1: mechanisms. International Journal of Pavement Engineering. 2008 Apr 1;9(2):81-98. <https://doi.org/10.1080/10298430701792128>
- [15] Xiao Z, Chen M, Wu S, Xie J, Kong D, Qiao Z, Niu C. Moisture susceptibility evaluation of asphalt mixtures containing steel slag powder as filler. Materials. 2019 Sep 30;12(19):3211. <https://doi.org/10.3390/ma12193211>
- [16] Kara C, Karacasu M. Use of ceramic wastes in road pavement design. In Proceedings of the world congress on new technologies. Barcelona, Spain 2015 Jul (pp. 226-6).
- [17] American Society for Testing and Materials, ASTM (1993). Standards section 4 vol. 4.03, ASTM-D1559-1993 Philadelphia.
- [18] AASHTO T 283
- [19] Federal Ministry of Works and Housing. General specification for roads and bridges. Fed Highw Dep. 1997;2: 145-284.
- [20] Huang Q, Qian Z, Hu J, Zheng D. Evaluation of stone mastic asphalt containing ceramic waste aggregate for cooling asphalt pavement. Materials. 2020 Jul 2;13(13):2964. <https://doi.org/10.3390/ma13132964>
- [21] Karmakar S, Majhi D, Roy TK, Chanda D. Moisture damage analysis of bituminous mix by durability index utilizing waste plastic cup. Journal of Materials in Civil Engineering. 2018 Sep 1;30(9):04018216. [https://doi.org/10.1061/\(ASCE\)MT.1943-5533.0002366](https://doi.org/10.1061/(ASCE)MT.1943-5533.0002366)
- [22] Ameri M, Ziari H, Yousefi A, Behnood A. Moisture susceptibility of asphalt mixtures: Thermodynamic evaluation of the effects of antistripping additives. Journal of Materials

- in Civil Engineering. 2021 Feb 1;33(2):04020457. [https://doi.org/10.1061/\(ASCE\)MT.1943-5533.0003561](https://doi.org/10.1061/(ASCE)MT.1943-5533.0003561)
- [23] Nataadmadja AD, Prahara E, Setyandito O, Ananditha RW. Evaluation of moisture susceptibility of hot mix asphalt. In AIP Conference Proceedings 2019 Dec 27 (Vol. 2202, No. 1). AIP Publishing. <https://doi.org/10.1063/1.5141719>
- [24] Silvestre R, Medel E, García A, Navas J. Utilizing recycled ceramic aggregates obtained from tile industry in the design of open graded wearing course on both laboratory and in situ basis. *Materials & Design*. 2013 Sep 1; 50: 471-8. <https://doi.org/10.1016/j.matdes.2013.03.041>
- [25] Joni HH, Abed AH. Evaluation the moisture sensitivity of asphalt mixtures modified with waste tire rubber. In IOP Conference Series: Earth and Environmental Science 2022 (Vol. 961, No. 1, p. 012029). IOP Publishing. <https://doi.org/10.1088/1755-1315/961/1/012029>

Blank Page



Research Article

Performance studies on energy efficient paver block with treated recycled aggregate

Jagan Sivamani

Department of Civil Engineering, Sona College of Technology, India

Article Info

Abstract

Article history:

Received 25 May 2023

Accepted 10 Aug 2023

Keywords:

Recycled aggregates;

Bio-treatment;

Carbonation;

Paver block;

Strength;

Water absorption;

Impact energy

Extensive research was performed to investigate the concrete properties (hardened and durability) with finer and coarser recycled aggregates. Fewer studies have discussed on the effect of bio-treatment to recycled aggregates in concrete to overcome its higher water absorption characteristics. However, the studies on the use of bio-treated recycled aggregates as alternative to natural aggregates in real time traffic applications needs to be increased. This paper investigates the feasibility of utilization of recycled coarse aggregate (RCA), recycled fine aggregate (RFA), bio-deposited recycled coarse aggregate (BRCA) and carbonated recycled fine aggregate (CRFA) in the production of sustainable paver blocks for various traffic volumes. The RCA was bio-treated with *Bacillus sphaericus* at 105 cells/ml and RFA was carbonated at 0.2 bar to produce hexagonal paver blocks of 80 mm thickness. The research involves the determination of density, strength and water absorption of paver blocks at suitable ages. The strength of bio-deposited and carbonated paver blocks was reduced by only 6.13% and 8.9% and the water absorption bio-deposited and carbonated paver blocks was increased by only 2.86% and 1.24% compared to conventional paver block. The impact energy of bio-deposited and carbonated paver blocks was 18.6% and 17% lesser compared to conventional paver block. Microstructural investigations through scanning electron microscope (SEM) and X-ray diffraction (XRD) illustrates the CaCO_3 formation that seals the crevice on the recycled aggregate and improves the properties of paver block.

© 2023 MIM Research Group. All rights reserved.

1. Introduction

The circular economy of a country aims at sustainable utilization of waste raw materials in the production of energy efficient products and ensuring cleaner energy. The waste management policies of 3R approach (Reduce, Recycle and Reuse) has diversified to 4R approach (Reduce, Recycle, Reuse and Recovery). Under such circumstances, the most prominent municipal solid waste generated out of construction activities namely Construction and Demolition (C&D) wastes takes its prime importance in 4R approach. C&D wastes, an outcome of demolition and rehabilitation activities in construction include concrete, bricks, steel, wood, plastics etc. in suitable proportions depending upon the structure. These wastes either dumped in landfill or used in temporary/unimportant works affecting the integrity of environment in the former and inefficient utilization strategy in the latter. On a whole, nearly 30% of wood, 45% of gravel, sand is being utilized by construction industries every year globally [1]. Nearly 10-15% of the materials end up as waste resulting in generation of municipal solid waste leading to disposal problems [2]. In India, every year around 150 MT of C&D wastes are generated which is nearly 40% of the those produced globally [3]. The Centre for Science and Environment (CSE) updates that only 1% of C&D wastes were being recycled out of 150 MT generated posing serious threat to the environment. Similarly, in other countries like USA, China etc. the generation

Corresponding author: jagan.civil@sonatech.ac.in

orcid.org/ 0000-0002-4196-7803

DOI: <http://dx.doi.org/10.17515/resm2023.778ma0525>

Res. Eng. Struct. Mat. Vol. 9 Iss. 4 (2023) 1239-1253

of C&D wastes are increasing on a large scale alarming the effective recycling and reutilization. Meanwhile, it is well known that the construction activities depend prominently on natural resources as their source of raw materials resulting in the scarcity. This eventually necessitates the concept of recycling and reuse of construction wastes effectively again in the construction activities.

Extensive researches were carried out with the utilization of recycled construction wastes as fine aggregate (RFA) and coarse aggregate (RCA) in the concrete. Higher utilization of RFA and RCA in the concrete affects the concrete properties due to its inferior quality ensuing from higher porosity [4-7]. So, the researches focus on suitable treatments to RCA and RFA to enhance its quality by reducing its water absorption. Such treatments include acids, carbonation, bio-deposition, slurries, polymers etc. [8-13]. These treatments either involve in removal or coating of adhered mortar as it possesses micro-cracks that increases the porosity. However, the feasibility of utilization of RCA and RFA in the real time traffic/structural applications still needs to be investigated on a larger scale. Researcher [14] used recycled aggregates and crushed clay bricks in the paver block production and infer that higher utilization of recycled aggregates and crushed bricks increased the water absorption of paver block and that eventually reduces the performance of paver blocks and optimized utilization (50%) of both meet the least requirements as defined in AS/NZS 4455 (Grade B) of paver blocks. However, the author [15] reviewed the effective utilization of RCA and RFA in various construction applications and infer that progression of detailed specification on utilization of recycled aggregates reduced the risk factor of its utilization in real time applications that might reduce its environmental impact and scarcity problems. Meanwhile, [16] used dry, washed and pre-saturated RCA and RFA and found that paver-blocks with washed recycled aggregates exhibit required minimum standards with water absorption less than 5% of the control. The use of recycled asphalt pavement as aggregates in the manufacture of pervious paver blocks and found that higher grading resulted in 23.6% reduction in strength and finer grading resulted in 43% reduction in the strength compared to conventional blocks [17]. Researcher [18] produced 80 mm I shaped paver block with RCA and found the optimal replacement of 60% without a significant reduction in strength, density and impact energy. The replacement beyond 60% reduced the strength of the paver block by 13.7% and increased the water absorption by 72%.

Similarly, use of both RCA and crusher dust infer that RCA can be replaced up to 45% for river gravel and crusher dust can be replaced up to 100% for river sand to produce strength equivalent to designated M40 grade for medium volume traffic volume applications [19]. Also, the study observed nearly 44% cost reduction in the production of 1 cu.m of paver blocks. Researcher [20] manufactured paver block and kerb stones with both RCA and RFA and observed optimal replacement of 25% of both RCA and RFA obtained the minimum requirements as per EN 1338. It is also suggested for its applicability in the pedestrian areas or light traffic volume conditions. The properties of bio-blocks with recycled aggregates infer that the unconfined strength of bio-blocks shows a minimum difference of 10% in strength and reduction in the water absorption by 58% [21]. The study also infers that the thermal resistance of bio blocks with natural coarse aggregate (NCA) and RCA was better at both high and low temperatures, but the strength of bio blocks with RCA was lesser compared to those with NCA but it eventually increases with increase in the CaCO₃. It could be observed that relative application of RCA under various traffic volume conditions exhibit the minimum requirement for pedestrian walk (low volume) as specified in the standards. However, the effect of treated RCA and RFA on the behaviour of paver block under various traffic volume conditions has to be investigated. This study examines the effect of both treated RCA and RFA in the manufacture of energy efficient paver blocks wherein the RCA was treated with *Bacillus sphaericus* at 105cells/ml and RFA was carbonated at 0.2 bar.

2. Materials and Methods

2.1. Concrete Materials

This study involves six different aggregates such as natural fine aggregate (NFA) with relative size of 2.36 mm~4.75 mm, natural coarse aggregate (NCA) with relative size of 10 mm~20 mm, RFA and RCA with size equivalent to NFA and NCA, bio-deposited recycled coarse aggregate (BRCA) with size equivalent to NCA and carbonated recycled fine aggregate (CRFA) with size equivalent to NFA. Fig. 1(a) shows the visual of RCA and Fig. 1(b) shows the visual of RFA used. Both the finer and coarser fractions were obtained by recycling the concrete wastes dumped as a result of casting works of students in the institution premises. The concrete wastes collected (the compressive strength and materials used in its manufacture) as boulders were sorted wherein the large boulders were broken with hammers and further recycled into required fractions, sieved and used as RCA and RFA. Fig. 2(a) depicts the gradation curves of RCA and Fig. 2(b) depicts the gradation curves of RFA. In this study, both RCA and RFA were thoroughly washed to remove the silt particles and pre-saturated to ensure SSD prior to its use in the experimentation. The pre-washing and pre-saturation of RCA and RFA will ensure the workability loss and resolve the delinquent of its higher porosity ensuing from the adhered mortar. Whilst, ordinary portland cement (OPC) with a characteristic strength of 43 N/mm² was used in the concrete mix. Potable tap water with basic pH value was used in manufacture and curing operations.

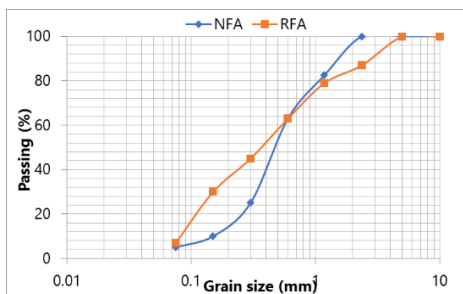


(a)

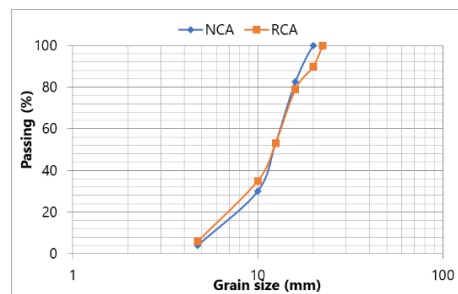


(b)

Fig. 1 (a) Visual of RCA, (b) Visual of RFA



(a)



(b)

Fig. 2 (a) Gradation curves of RCA, (b) Gradation curves of RFA

2.2. Treatments to Recycled Aggregates

Extensive research on recycled aggregate concrete (RAC) infers that higher porosity in RCA and RFA affects the concrete properties [22-24]. To reduce the porosity, the RCA was treated with *Bacillus Subtilis* and the RFA was treated with CO₂. The strains of *Bacillus subtilis* were obtained and cultured in an Agar Medium consisting of 0.5% peptone, 0.3% beef extract and 0.5% NaCl. To prepare the agar medium, 30 g of agar concentrate was dissolved in 1000 ml of distilled water. The mixture is heated during stirring to allow the complete dissolution of the agar precipitate. It is then autoclaved at 120°C for 15 minutes and cooled. The cooled mixture is then transferred to Petri plates and kept undisturbed to congeal. The strains of *Bacillus subtilis* were added along agar medium, incubated at 37°C and shaken at 175 rpm for 48 hours. The grown culture is diluted and spread out on agar plates to calculate the cell count and obtained 7×10^5 cells/ml. Fig. 3 shows the culture solution of *Bacillus Subtilis*, which is used for bio-deposition treatment. The bio-deposition to RCA was performed under laboratory conditions, wherein the collected RCA was surface saturated and air-dried to reach SSD condition. It is then saturated in the cultured solution for 24 hours. The RCA was removed from the cultured solution and immersed in the bio-deposition medium for 72 hours. After 72 hours, the RCA was removed, surface washed and dried at room temperature to produce bio-deposited recycled coarse aggregate (BRCA).

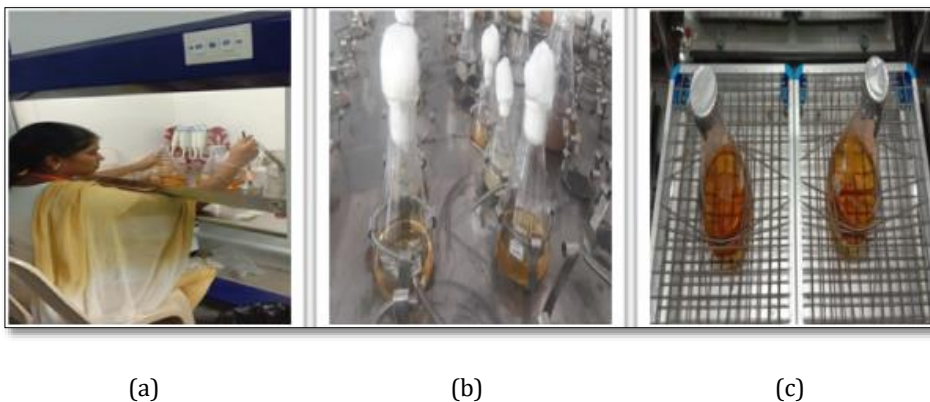


Fig. 3 (a) Preparation of culture medium, (b) Centrifuging, (c) Cultured solution

In carbonation treatment, the RFA was treated with locally available CO₂ (99.5% purity) in the fabricated carbonation set up at 20°C with an R.H. of 60%, as shown in Fig. 4. The carbonation chamber with RFA was subjected to 0.4 bar pressure for 24 hours. It is then allowed to cool at room temperature and used as carbonated recycled fine aggregate (CRFA).

2.3. Concrete Mix and Concrete Testing

The concrete mixtures were prepared with RCA, RFA, BRCA and CRFA as per IS 10262 (2019) [25] for M40 grade to manufacture paver -block for low and medium traffic applications. In this study, eleven concrete mixtures with different percentages of the RCA, RFA, BRCA and CRFA were manufactured to evaluate the suitability of manufactured hexagonal shaped paver blocks for the above said traffic conditions. The NCA and NFA was substituted with 25%, 50% and 100% of RCA and RFA by its weight. The raw material quantities for paver block preparation were given in the table 1 as per IS 10262 (2019). The concrete mixes with NCA were manufactured with normal mixing approach (NMA) and the concrete mixes with RCA and RFA were manufactured with two-stage mixing

approach (TSMA) [26]. The RCA in the mixes tend to absorb water resulting in workability loss, so as to compensate the NMA was altered to TSMA, wherein 50% of water is added to compensate the absorption by RCA and rest 50% is added to overcome workability loss [27-29]. The concrete mixes prepared with NMA and TSMA were fabricated into hexagonal shaped paver block with 125 sq.mm side area and 80 mm thickness. The ingredients required for the paver-block manufacture were confirmed for its physical properties as per IS 383 (2016) [30]. The paver blocks manufactured with NMA and TSMA were tested for its density, compressive strength, tensile strength, flexural strength, impact strength and water absorption. To determine the density, the paver block is oven dried for 7 days and the density was calculated with the dry weight as per IS 15658 (2006) [31]. The compressive strength of the paver block was determined at 28 days as per IS 15658 (2006) [31]. The paver blocks are cured for 28 days at $20 \pm 5^\circ\text{C}$, taken out, wet surfaces are wiped off and the specimens after drying were kept in such a way that the surfaces are properly aligned with the bearing plates in the compression testing machine (CTM). The specimens are loaded at a rate of $15 \pm 3 \text{ N/mm}^2$ per minute and the maximum load at failure is determined. The compressive strength of the paver block was determined at 28 days as per IS 15658 (2006) [31]. The paver block is placed in such a way that shortest length passes through the center of planar area. The specimens were loaded gradually corresponding to stress of 0.05 MPa and the tensile strength of the paver block is calculated using the equation (1).



Fig. 4 Carbonation treatment to RFA

$$\text{Tensile strength} = \frac{0.637 * P}{s} \quad (1)$$

Where, P is ultimate failure load; S size of the specimen

The flexural strength of the paver block was determined at 28 days as per IS 15658 (2006) [31]. The 28-days cured specimens were loaded in the universal testing machine at a rate of 6kN/min and with the maximum load at failure, the flexural strength is calculated using the equation (2)

$$\text{Flexural strength} = \frac{3Pl}{2bd^2} \quad (2)$$

Where, P is ultimate failure load; l – length of the specimen; b – breadth of the specimen; d – depth of the specimen

The water absorption of the paver block was determined at 28 days as per IS 15658 (2006) [31]. The paver block after 28 days of curing were wiped with dry cloth and oven dried at

107 ± 7°C and the difference in wet weight and dry weight were measured to determine the water absorption. To determine the impact energy, a 4.5 kg steel ball is allowed to fall freely from 3m height at the center of the specimen. The number of the blows at which the specimen fails were determined and the impact energy is calculated using the equation (3)

$$\text{Impact energy} = \frac{N \cdot w \cdot v^2}{2} \quad (3)$$

Where N is number of times of free fall of steel ball; w is the weight of the ball; v is the velocity of the steel ball

3. Results and Discussions

3.1. Material Properties

3.1.1 Chemical Constituents

The predominant compounds in the natural aggregates are its SiO₂ (quartz) constituting nearly 90% of weight, 1.5% of CaO, 4-5% of Al₂O₃ and 1-2% of Fe₂O₃ and MgO. In case of recycled aggregates, the constituents include SiO₂ (73-78%), Al₂O₃ (5-6%), CaO (5-6%), Fe₂O₃ (1-2%) and MgO (1-2%). The equivalence in the constituents with varying percentages defines the suitability of replacement of NCA and RCA. The ordinary portland cement (OPC) comprises of nearly 60% of CaO, 21% of SiO₂, 6% of Al₂O₃, 3% of Fe₂O₃, 2.5% of MgO and 7.5% of other minor constituents. Table 1 shows the chemical constituents of the materials used in the study.

Table 1. Chemical constituents

S.No	Constituents	Percentage (%)		References	
		Natural Aggregate	Cement	Natural Aggregate	Cement
1	SiO ₂	90	21		
2	CaO	1.5	60		
3	Al ₂ O ₃	4-5	6	[16, 20]	[14, 17]
4	Fe ₂ O ₃	1-2	3		
5	MgO	1-2	2.5		

3.1.2 Physical and Micro-Structural Properties

Table 2 depicts the variation in the physical properties of NFA, RFA, NCA, RCA, BRCA and CRFA. The density and specific gravity of RCA and RFA were found to be lower than those of NCA and NFA. The specific gravity of RCA and RFA was 13.5% and 6.2% lower compared to NCA and NFA and similarly, the bulk density of RCA and RFA was 9.5% and 10.54% lesser compared to NCA and NFA. Concerning to water absorption, the water absorption of RFA and RCA was 88.57% and 85.80% more compared to NFA and NCA. Similarly, the crushing index, impact value and abrasion value of RCA was 19.10%, 34.73% and 38.2% more compared to NCA. Except for water absorption, all of the physical properties of recycled aggregates were inferior to natural aggregates but within the limitations of IS 383 (1970). The inferior quality of RCA and RFA was attributed to the incidence of smeared mortar on its surface [5, 6]. The crushing of concrete fractions of recycled aggregates results in the formation of micro-cracks on the adhered mortar surface and that eventually increases the porosity and affects its quality. However, the water absorption of RFA was higher than RCA as the more crushing stages is involved in the reducing the particle size

resulting in the increases micro-cracks and silt content [6, 15]. This could be eventually observed with 45.7% increase in the silt content in RFA compared to NFA resulting in higher water absorption. Such inferior properties of RCA and RFA could reduce its utilization in real time applications and thus both RCA and RFA was treated to improve its properties. The specific gravity of CRFA and BRCA was 2.41% and 5.57% more compared to RFA and RCA and the bulk density of CRFA and BRCA was 9.7% and 4.15% more compared to RFA and RCA. The water absorption of CRFA and BRCA was 85.3% and 79.44% lower compared to RFA and RCA, but 21.8% and 30.95% more compared to NFA and NCA. Similarly other properties of CRFA and BRCA was better compared to RFA and RCA owing to the treatments. In carbonation treatment, the CO_2 reacts with the $\text{Ca}(\text{OH})_2$ on the smeared mortar to form CaCO_3 that deposits on the RFA and seals the micro-cracks and improves its properties [12]. The bio-deposition of RCA precipitates CaCO_3 due to the urea hydrolysis that increases the nucleation sites for CaCO_3 [5, 11]. The precipitated CaCO_3 bonds on the RCA, either seals on the surface or impregnates into the micro-pores of the RCA and improves its properties.

Table 2. Physical properties of aggregates

S. No	Description	NFA	RFA	CRFA	NCA	RCA	BRCA
1	Specific gravity	2.58	2.42	2.48	2.74	2.37	2.51
2	Bulk Density (kg/m^3)	1602	1433	1587	1631	1476	1540
3	Water absorption (%)	0.93	8.14	1.19	0.87	6.13	1.26
4	Crushing index (%)	-	-	-	20.41	25.23	21.67
5	Impact value (%)	-	-	-	17.23	26.4	24.51
6	Abrasion value (%)	-	-	-	21.38	34.6	31.76
7	Fineness modulus	3.07	3.52	-	6.87	7.32	-
8	Silt content	2.5	4.61	-	-	-	-

The XRD patterns of NCA, RCA, BRCA, CRFA is shown in the Fig. 5. Fig. 5(a) shows the XRD pattern of NCA, Fig. 5(b) shows the XRD pattern of RCA, Fig. 5(c) shows the XRD pattern of BRCA and Fig. 5(d) shows the XRD pattern of CRFA. The maximum 2θ (Diffraction angle from incident ray) was observed at 30 with NCA, between 60 to 70 with RCA, 20 to 30 with BRCA and 20 to 30 with CRFA. The peak in NCA pattern specify the incidence of SiO_2 , $\text{NaAlSi}_3\text{O}_8$, and CaCO_3 , with the highest being SiO_2 . This might be advantageous in the development of a C-S-H that endorses the concrete strength. In RCA, the peak signifies the calcite compound ensuing from the cement mortar and traces of SiO_2 . In BRCA, higher peaks are observed with calcite similar to RCA but the intensity is more compared to RCA. This could be the CaCO_3 precipitated as a result of microbial activity in addition to the traces of $\text{Ca}(\text{OH})_2$ from the smeared mortar. In CRFA, similar to BRCA, the evidence of $\text{Ca}(\text{OH})_2$ and CaCO_3 was observed, wherein the former was due to the cement mortar and latter due to the interaction of $\text{Ca}(\text{OH})_2$ with CO_2 to form CaCO_3 .

The SEM images of NCA, RCA, BRCA, CRFA is shown in the Fig. 6. Fig. 6(a) shows the SEM image of NCA, Fig. 6(b) shows the SEM image of RCA, Fig. 6(c) shows the SEM image of BRCA and Fig. 6(d) shows the SEM image of CRFA. In NCA, high angular dense particles were observed due to its grading whereas in RCA, few traces of adhered mortar were observed on the angular particles owing to the crushing of RCA to required particle size. In BRCA and CRFA, CaCO_3 deposition were observed on the surface of RCA and RFA resulting in the improvement in their properties. The former is due to the urea lytic activity of bacteria whereas the latter is due to the carbonation.

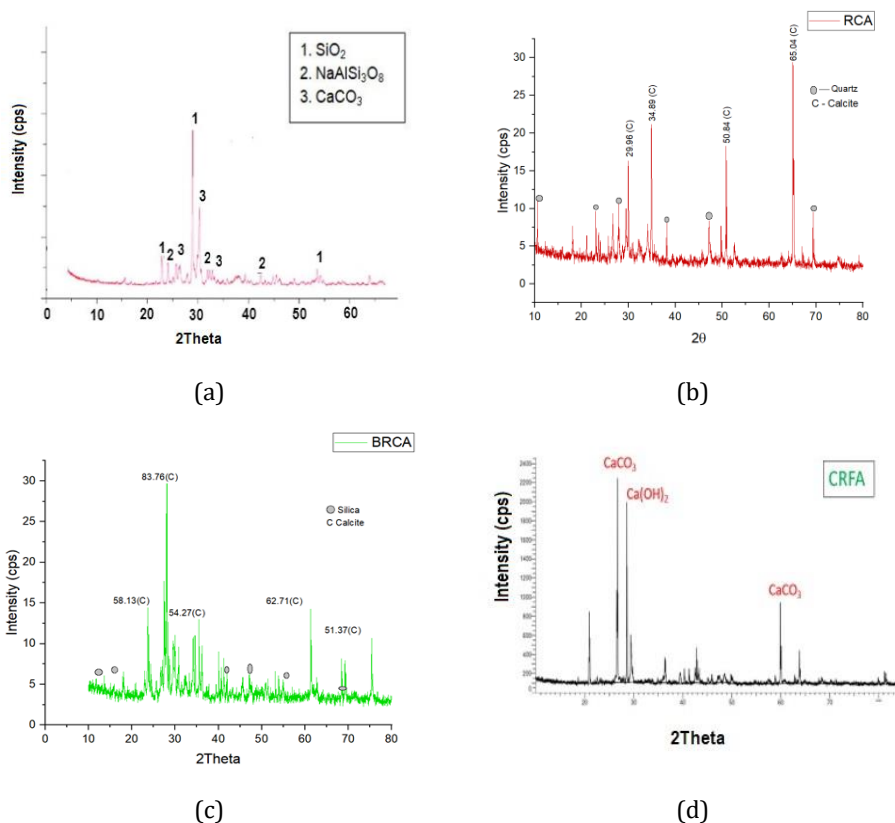


Fig. 5 (a) XRD of NCA, (b) XRD of RCA, (c) XRD of BRCA, (d) XRD of CRFA

3.1.3 Concrete Properties

The compressive strength of the paver block with different mix combinations at 28 days is given in the Fig. 7. The compressive strength of RC-25-RF-0 was 1.47% more compared to the conventional block. Nevertheless, the compressive strength of RC-50-RF-0 and RC-100-RF-0 was 12.01% and 17.64% lesser compared to the conventional paver block. The compressive strength of RC-0-RF-25, RC-0-RF-50 and RC-0-RF-100 was 9.35%, 14.61% and 22.70% lesser compared to conventional paver block. The reduction in the strength is ascribed to the higher porousness of recycled aggregates owing to the micro-cracks on the smeared mortar from the recycling process [10, 22]. It could be observed that with the use of RFA, the decline in the strength is more compared to RCA owing to the increase in the recycling stages to reduce its particle size. The increase in the recycling stages intensifies the micro-cracks resulting in higher porousness compared to RCA and thus higher reduction in the strength of RAC. However, with 100% of RCA and RFA, the strength of paver block was reduced by nearly 30% compared to conventional paver block. In RAC, apart from the higher porosity, the weak interfacial transition zone (ITZ) in RAC was another predominant factor. NAC comprises NCA, matrix, and an ITZ between matrix and NCA, whereas RAC comprises RCA (RFA), matrix, and two ITZ. The first ITZ is between old and original mortar, and the second is between original mortar and RCA (RFA). The former ITZ in the RAC is the weakest zone ensuing from the micro-cracks on RCA (RFA) that weaken its adherence with the new cement mortar.

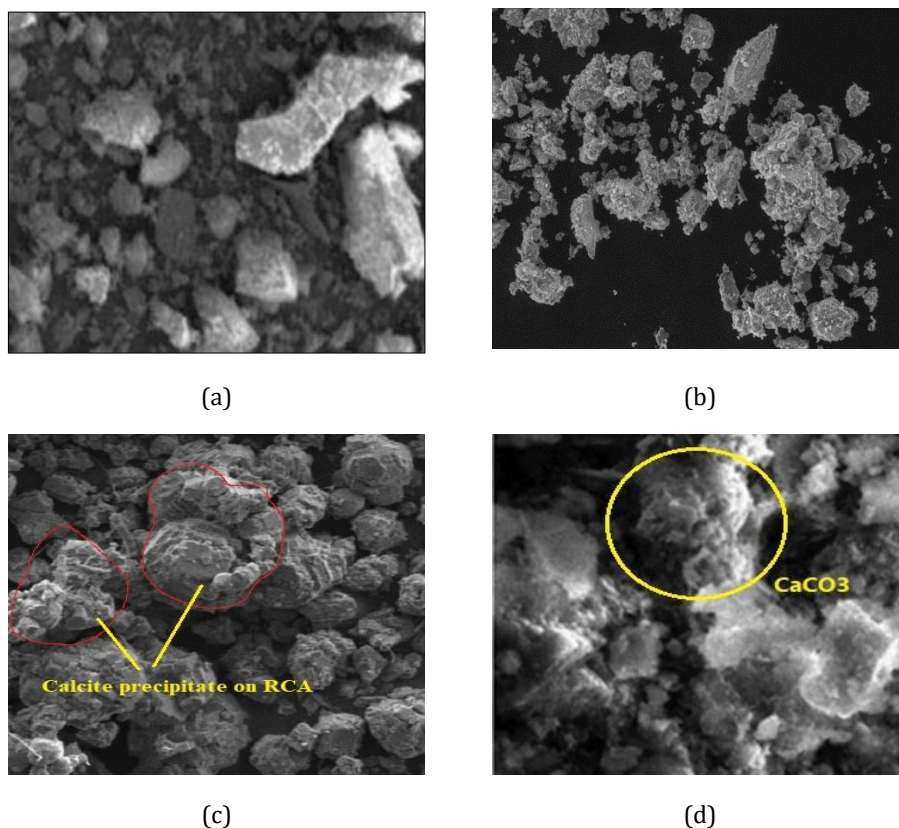


Fig. 6 (a) SEM image of NCA, (b) SEM image of RCA, (c) SEM image of BRCA, (d) SEM image of CRFA

The carbonation to RFA and bio-deposition to RCA tend to improve the strength of the RAC. The strength of BRC-100-RF-0 was only 6.13% lesser compared to RC-0-RF-0, but 12.26% more compared to RC-100-RF-0 and 25.36% more compared to RC-100-RF-100. The deposition of CaCO_3 on the micro-cracks of the RCA reduces the water absorption and improves its strength. The strength of RC-0-CRF-100 was only 8.9% lesser compared to RC-0-RF-0, but 15.07% more compared to RC-0-RF-100 and 23.02% more compared to RC-100-RF-100. The interaction of CO_2 with $\text{Ca}(\text{OH})_2$ forms CaCO_3 that lessens the water absorption of paver block and improves its strength. It could also be observed that higher efficiency was observed with carbonation treatment rather than bio-deposition treatment. This is because owing to finer particle size with increased crack width on adhered mortar surface of RFA, the rate of impregnation of CaCO_3 into the micro-cracks was higher whereas with bio-deposition the crack width is less resulting in CaCO_3 deposition on the surface rather than impregnation into the cracks [13, 21].

The tensile strength of the paver block with different mix combinations at 28 days is shown in the Fig. 8. The tensile strength of RC-25-RF-0, RC-50-RF-0 and RC-100-RF-0 was 1.47%, 7.83% and 20.54% lesser compared to the conventional paver block. The compressive strength of the paver block with RC-0-RF-25, RC-0-RF-50 and RC-0-RF-100 was 0.81%, 10.27% and 25.67% lesser compared to conventional paver block. Similar to compressive strength, higher reduction in tensile strength was observed with RFA than RCA. However, the tensile strength of RC-100-RF-100 was reduced by nearly 28% compared to conventional paver block. Similar to compressive strength, the carbonation treatment to

RFA and bio-deposition treatment to RCA tend to improve the tensile strength of the RAC. The tensile strength of BRC-100-RF-0 was only 11.08% lesser compared to RC-0-RF-0, but 10.63% more compared to RC-100-RF-0 and 18.84% more compared to RC-100-RF-100. The strength of RC-0-CRF-100 was only 14.6% lesser compared to RC-0-RF-0, but 13% more compared to RC-0-RF-100 and 15.50% more compared to RC-100-RF-100. The justification of variation in tensile strength is equivalent to that of mechanism behind the improvement in the compressive strength of the paver block.

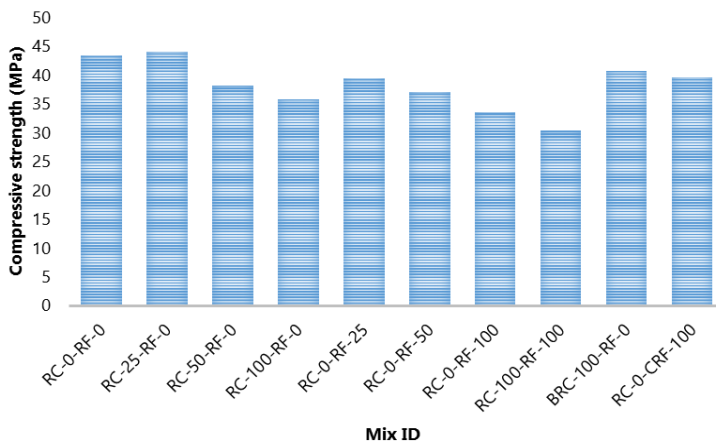


Fig. 7 Compressive strength of the paver block

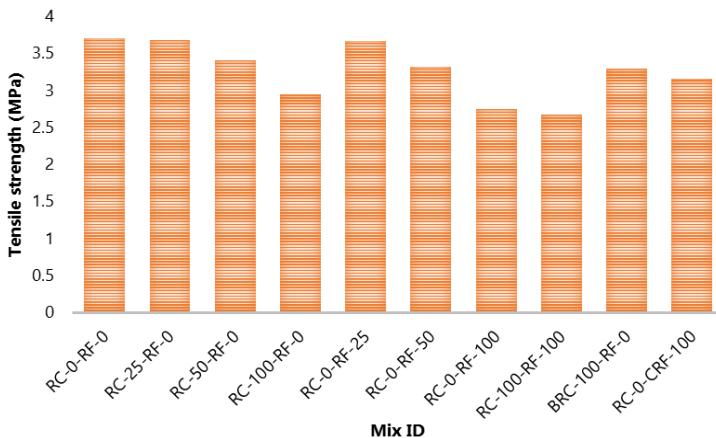


Fig. 8 Tensile strength of the paver block

The flexural strength of the paver block with different mix combinations at 28 days is shown in the Fig. 9. The flexural strength of RC-25-RF-0 was 0.65% more compared to conventional paver block, however the flexural strength of RC-50-RF-0 and RC-100-RF-0 was 6.27% and 9.3% lesser compared to the conventional paver block. The flexural strength of RC-0-RF-25, RC-0-RF-50 and RC-0-RF-100 was 4.76%, 7.57% and 12.12% lesser compared to conventional paver block. Similar to compressive strength and tensile strength, higher reduction in flexural strength was observed with RFA than RCA. However, with 100% of RCA and RFA, the flexural strength of paver block was reduced by nearly 16.23% compared to conventional paver block. Similar to compressive strength, the carbonation treatment to RFA and bio-deposition treatment to RCA tend to improve the

flexural strength of the RAC. The flexural strength of BRC-100-RF-0 was only 3.24% lesser compared to RC-0-RF-0, but 6.26% more compared to RC-100-RF-0 and 13.42% more compared to RC-100-RF-100. The strength of RC-0-CRF-100 was only 4.54% lesser compared to RC-0-RF-0, but 7.93% more compared to RC-0-RF-100 and 12.24% more compared to RC-100-RF-100. The justification of variation in flexural strength is equivalent to that of compressive strength and tensile strength of the paver block.

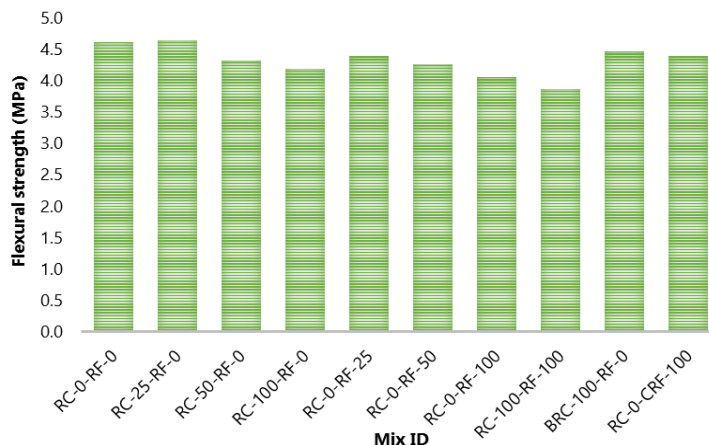


Fig. 9 Flexural strength of the paver block

The water absorption of the paver block with different mix combinations at 28 days is shown in the Fig. 10. The water absorption of RAC paver block with 25%, 50% and 100% of RCA was 4.01%, 9% and 15.17% more compared to conventional paver block. The increase in the water absorption is due to the higher porousness of the RCA and that eventually increases the water absorption of the paver block. The water absorption of RAC paver block with 25%, 50% and 100% of RFA was 5.75%, 18.24% and 22.51% more compared to conventional paver block. The porosity of RFA was higher compared to RCA resulting in higher water absorption. The recycling of concrete fractions of C&D wastes to finer particles increases the crack width ensuing in higher water absorption than RCA [14, 23]. The water absorption of RC-100-RF-100 was 25.19% more compared to conventional paver block. However, after treatments to RFA and RCA, the water absorption of paver block tends to reduce. The water absorption of BRC-100-RF-0 was only 2.86% more compared to RC-0-RF-0 and the water absorption of RC-0-CRF-100 was only 1.24% more compared to RC-0-RF-0. The bio-deposition of RCA precipitates CaCO_3 that bonds on the surface of RCA [13, 21] whereas carbonation treatment to RFA produces CaCO_3 that impregnates into the micro-cracks of the RFA resulting in the reduced water absorption compared to the paver block with untreated RCA and RFA [2, 4, 12].

The impact energy of the paver block with different mix combinations at 28 days is shown in the Fig. 11. The impact energy of RC-0-RF-0 is 11000 kN.mm and the impact energy of the paver block with 25%, 50% and 100% of RCA was 1.36%, 29.15% and 67% lesser compared to conventional paver block. The reduction in the impact energy of paver block is directly related to the increase in the impact value of the RCA. The impact value of RCA was 34.73% more compared to NCA eventually causing lesser resistance of paver blocks to impact load. The impact energy of paver block with 25%, 50% and 100% of RFA was 2.91%, 30.45% and 69% lesser compared to conventional paver block. The impact energy of RC-100-RF-100 was 70% lesser compared to RC-0-RF-0. The impact energy of paver block with RFA is further reduced compared to those with RCA owing to the reduced impact resistance of RFA compared to RCA [18, 19]. The impact energy of BRC-100-RF-0

and RC-0-CRF-100 was only 18.6% and 17% lesser compared to RC-0-RF-0 and 59.44% and 62.65% more compared RC-100-RF-0 and RC-0-RF-100. The improvement in the impact value of RCA and RFA due to treatments eventually improves the impact energy of the paver blocks for its suitable application.

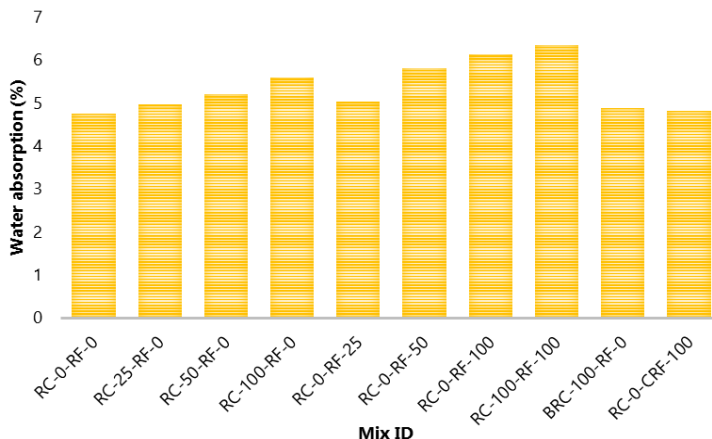


Fig. 10 Water absorption of the paver block

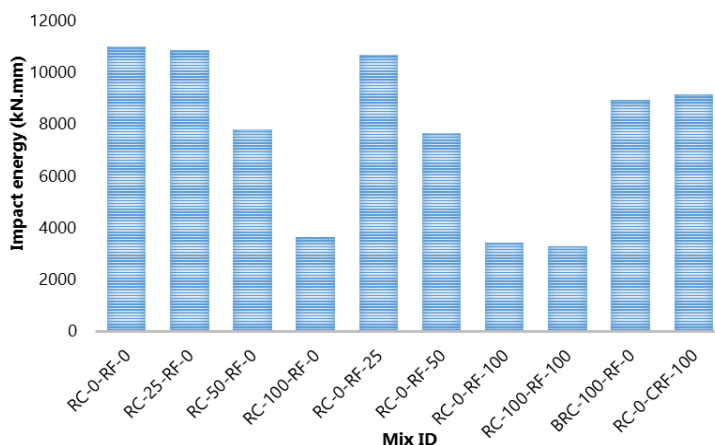


Fig. 11 Impact energy of the paver block

4. Conclusions

In this research, use of NCA, NFA, RCA, RFA, BRCA and CRFA in the production of energy efficient paver blocks were studied and the following inferences were made as follows:

- The specific gravity of RFA and RCA was 6.2% and 13.5% lesser compared to NFA and NCA, however the specific gravity of CRFA and BRCA was 2.41% and 5.57% more compared to RFA and RCA. The bulk density of RCA and RFA was 9.5% and 10.54% lesser compared to NCA and NFA but the bulk density of CRFA and BRCA was 9.7% and 4.15% more compared to RFA and RCA. The water absorption of RFA and RCA was 88.57% and 85.80% more compared to NFA and NCA while the water absorption of CRFA and BRCA was 85.3% and 79.44% lower compared to RFA and RCA, but 21.8% and 30.95% more compared to NFA and NCA. The carbonation

treatment to RFA and bio-deposition of RCA seals the micro-cracks on the adhered mortar and improves its properties.

- The compressive strength of paver block with 100% of RCA and RFA was 17.64% and 22.70% lesser compared to the conventional paver block. However, the compressive strength of paver block with 100% of BRCA and CRFA was 12.26% and 15.07% more compared to those with 100% of RCA and RFA. Similar variations in trend were observed with tensile strength and flexural strength.
- The water absorption of paver block with 100% of RCA and RFA was 15.17% and 22.51% more compared to conventional paver block, The water absorption of paver block with 100% of BRCA and CRFA was only 2.86% and 1.24% more compared to conventional paver block.
- The impact energy of paver block with 100% of RCA and RFA was 67% and 69% more compared to conventional paver block, however the impact energy of paver block with 100% of BRCA and CRFA was 59.44% and 62.65% more compared to those with 100% of RCA and RFA.

From the study, it could be inferred that paver block manufacture with 25% of RCA tend to withstand the required 40 MPa strength for medium traffic conditions. However, upon treatments, the paver block prepared with 100% of BRCA and 100% of CRFA exhibit 40.85 MPa and 39.61 MPa which is ample for M40 grade ensuing its suitability in medium volume traffic applications.

Nomenclature

NCA	: Natural coarse aggregate	RCA	: Recycled coarse aggregate
NFA	: Natural Fine aggregate	RFA	: Recycled fine aggregate
BRCA	: Bio-deposited recycled coarse aggregate	CRFA	: Carbonated recycled fine aggregate
XRD	: X-ray diffraction	SEM	: Scanning electron microscope
RAC	: Recycled aggregate concrete	C&D	: Construction & Demolition
T SMA	: Two-stage mixing approach	NMA	Normal mixing approach

Acknowledgement

The research work does not involve any funding from external source. The author would like to thank the almighty and the management of Sona College of Technology for extending their support in carrying out the research work.

References

- [1] Santamouris M, Vasilakopoulou K. Present and future energy consumption of buildings: Challenges and opportunities towards decarbonization. *Advances in Electrical Engineering, Electronics and Energy*, 2021; 1: 100002. <https://doi.org/10.1016/j.prime.2021.100002>
- [2] Katz, A. Treatments for the Improvement of Recycled Aggregate. *ASCE Journal of Materials in Civil Engineering*, 2004; 16 (6); 597-603. [https://doi.org/10.1061/\(ASCE\)0899-1561\(2004\)16:6\(597\)](https://doi.org/10.1061/(ASCE)0899-1561(2004)16:6(597))

- [3] Jain, MS. A mini review on generation, handling, and initiatives to tackle construction and demolition waste in India. *Environ. Technol. Innov*, 2021; 22: 101490. <https://doi.org/10.1016/j.eti.2021.101490>
- [4] Jagan S, Neelakantan TR, Reddy L, Gokul Kannan R. Characterization study on recycled coarse aggregate for its utilization in concrete - A review. *Journal of Physics: Conference series*, 2020; 1706: 012120. <https://doi.org/10.1088/1742-6596/1706/1/012120>
- [5] Jagan S, Neelakantan TR, Saravana Kumar P, Mugesh Kanna C, Vignesh Harish H, Akash MR. Efficient Utilization of Recycled Concrete Aggregates for Structural Applications - An Experimental Study. *Lecture Notes in Civil Engineering*, 2021; 97: 567-579. https://doi.org/10.1007/978-3-030-55115-5_52
- [6] Sony N, Shukla D. Analytical Study on Mechanical Properties of Concrete Containing Crushed Recycled Coarse Aggregate as an Alternative of Natural Sand. *Construction and Building Materials*, 2021; 266: 120595. <https://doi.org/10.1016/j.conbuildmat.2020.120595>
- [7] Ahmed AM, Roua SZ, Tuqa WA. Evaluation of high-strength concrete made with recycled aggregate under effect of well water. *Case Studies in Construction Materials*, 2020; 12: 00338. <https://doi.org/10.1016/j.cscm.2020.e00338>
- [8] Pawluczuk E, Wichrowska KK, Bołtryk M, Jiménez JR, Fernández JM. The Influence of Heat and Mechanical Treatment of Concrete Rubble on the Properties of Recycled Aggregate Concrete. *Materials*, 2019; 12: 367. <https://doi.org/10.3390/ma12030367>
- [9] Al-Bayati HKA, Das PK, Tighe SL, Baaj H. Evaluation of various treatment methods for enhancing the physical and morphological properties of coarse recycled concrete aggregate. *Construction and Building Materials*, 2016; 112: 284-298. <https://doi.org/10.1016/j.conbuildmat.2016.02.176>
- [10] Verma A, Babu VS, Arunachalam S. Characterization of recycled aggregate by the combined method: Acid soaking and mechanical grinding technique. *Materials Today: Proceedings*, 2021; 49: 230-238. <https://doi.org/10.1016/j.matpr.2021.01.842>
- [11] Jagan S, Neelakantan TR, Saravanakumar P. Performance enhancement of recycled aggregate concrete - An experimental study. *Applied science and Engineering progress*, 2022; 15: 5212. <https://doi.org/10.14416/j.asep.2021.07.003>
- [12] Kou SC, Bao-Jian Z, Chi-Sun P. Use of a CO2 curing step to improve the properties of concrete prepared with recycled aggregates. *Cement & Concrete Composites*, 2014; 45: 22-28. <https://doi.org/10.1016/j.cemconcomp.2013.09.008>
- [13] Jagan S, Neelakantan TR, Padma Lakshmi, M. Enhancement on the properties of recycled coarse aggregate through bio-deposition - An experimental study. *Materials Today Proceedings*, 2022; 49: 1141-1147. <https://doi.org/10.1016/j.matpr.2021.06.009>
- [14] Poon CS, Chan D. Paving blocks made with recycled concrete aggregate and crushed clay brick. *Construction and Building Materials*, 2006; 20: 569-577. <https://doi.org/10.1016/j.conbuildmat.2005.01.044>
- [15] Silva RV, Brito J, Dhir RK. Use of recycled aggregates arising from construction and demolition waste in new construction applications. *Journal of Cleaner Production*, 2019; 236: 117629. <https://doi.org/10.1016/j.jclepro.2019.117629>
- [16] Pederneiras CM, Durante MDP, Amorim EF, Ferreira RL. Incorporation of recycled aggregates from construction and demolition waste in paver blocks. *Rev. IBRACON Estrut. Mater*, 2020; 13: e13405. <https://doi.org/10.1590/s1983-41952020000400005>
- [17] Saboo N, Prasad AN, Sukhija M, Chaudhary M, Chandrappa AK. Effect of the use of recycled asphalt pavement (RAP) aggregates on the performance of pervious paver blocks (PPB). *Construction and Building Materials*, 2020; 262: 120581. <https://doi.org/10.1016/j.conbuildmat.2020.120581>

- [18] Attri GK, Sandeep Shrivastava, Gupta RC. Paver blocks manufactured from construction & demolition waste. *Materials Today Proceedings*, 2020; 27: 311-317. <https://doi.org/10.1016/j.matpr.2019.11.039>
- [19] Attri GK, Gupta RC, Sandeep Shrivastava. Effect of demolished concrete and stone crusher dust on properties of M40 grade paver blocks. *Materials Today Proceedings*, 2021; 44: 4330-4336. <https://doi.org/10.1016/j.matpr.2020.10.553>
- [20] Llanes MC, Romero M, Gazquez MJ, Bolivar JP. Recycled Aggregates from Construction and Demolition Waste in the Manufacture of Urban Pavements. *Materials*, 2021; 14: 6605. <https://doi.org/10.3390/ma14216605>
- [21] Javadi AS, Badiie H, Sabermahani M. Mechanical properties and durability of bio-blocks with recycled concrete aggregates. *Construction and Building Materials*, 2018; 165: 859-865. <https://doi.org/10.1016/j.conbuildmat.2018.01.079>
- [22] Andal J, Snehata M, Zacarias P. Properties of concrete containing recycled concrete aggregate of preserved quality. *Construction and Building Materials*, 2016; 125: 842-855. <https://doi.org/10.1016/j.conbuildmat.2016.08.110>
- [23] Koper A, Koper W, Koper M. Influence of raw concrete material quality on selected properties of recycled concrete aggregates. *Procedia Engineering*, 2017; 172: 536-543. <https://doi.org/10.1016/j.proeng.2017.02.063>
- [24] Ozbakkaloglu T, Gholampour A, Xie T. Hardened and Durability Properties of Recycled Aggregate Concrete: Effect of Recycled Aggregate Properties and Content. *Journal of Materials in Civil Engineering*, 2018; 30: 04017275. [https://doi.org/10.1061/\(ASCE\)MT.1943-5533.0002142](https://doi.org/10.1061/(ASCE)MT.1943-5533.0002142)
- [25] IS 10262 (2019). Guidelines for concrete mix design proportioning. Bureau of Indian Standards. New Delhi, India.
- [26] Tam VWY, Gao XF, Tam CM. Micro structural analysis of recycled aggregate concrete produced from two stage mixing approach. *Cement and Concrete Research*, 2005; 35: 1195-1203. <https://doi.org/10.1016/j.cemconres.2004.10.025>
- [27] Tam VWY, Tam CM. Diversifying two-stage mixing approach (TSMA) for recycled aggregate concrete: TSMA and TSMA_{sc}. *Construction and building Materials*, 2008; 22: 2068-2077. <https://doi.org/10.1016/j.conbuildmat.2007.07.024>
- [28] Jagan S, Neelakantan TR, Saravanakumar P. Mechanical properties of recycled aggregate concrete surface treated by variation in mixing approaches. *Revista de la construccion*, 2021; 20: 236-248. <https://doi.org/10.7764/RDLC.20.2.236>
- [29] Saravanakumar P, Manoj D, Jagan S. Properties of concrete having treated recycled coarse aggregate and slag. *Revista de la construccion*, 2021; 20: 249-258. <https://doi.org/10.7764/RDLC.20.2.249>
- [30] IS 383 (1970). Specification for coarse and fine aggregate for concrete. Bureau of Indian Standards. New Delhi, India.
- [31] IS 15658 (2006). Precast concrete blocks for paving. Bureau of Indian Standards. New Delhi, India.

Blank Page



Research Article

Characteristic study on concrete elements using agro-waste as a replacement of fine aggregate

Jeyashree T M^{*a}, M S Somesh^b

Department of Civil Engineering, Faculty of Engineering and Technology, SRM Institute of Science and Technology, Kattankulathur, Tamil Nadu 603 203, India

Article Info

Article history:

Received 13 Jun 2023

Accepted 14 Aug 2023

Keywords:

Rice husk ash;

Coconut shell powder;

Saw dust;

Agro-waste;

Mechanical properties

Abstract

Concrete is the predominant material that is commonly used for all construction engineering practices and the demand for concrete ingredients has increased nowadays. Utilization of agricultural waste helps in meeting the demand and the present study focused on replacement of fine aggregate with agro-waste. Agro-wastes such as Rice Husk Ash, Saw Dust, and Coconut Shell powder were utilized as a replacement for fine aggregate. An experimental investigation was carried out on concrete specimens with varying proportions of 2%, 4%, 6%, and 8% of agro-waste to the weight of fine aggregate. Agro-waste was equally proportioned for the replaced weight of fine aggregate. Agro-waste concrete was compared with conventional concrete (100% - M sand) for the improvement in mechanical properties by examining the results of compressive strength test and split tensile strength test. Also, the performance of concrete specimens was also determined by non-destructive testing. The optimization of the concrete mix for the addition of agro-waste was obtained based on the strength characteristics. The effectiveness of utilizing agricultural waste in concrete with rebars was studied using the chloride ingress test and Open Circuit Potential test. The experimental findings show that 2 to 4% of agro-waste can be utilized efficiently as fine aggregate replacement.

© 2023 MIM Research Group. All rights reserved.

1. Introduction

Concrete is composed of cement which binds fine aggregate together with coarse aggregate. The scarcity of river sand is increasing nowadays and to meet the current demand, many researchers are focusing on fine aggregate replacement with industrial waste, agricultural waste, and domestic waste. Generally, agricultural wastes such as groundnut shells, sugarcane bagasse ash, oyster shell, tobacco waste, Saw Dust (SD), cork, Rice Husk Ash (RHA), and giant reed ash are used as substitute for fine aggregate. These additives preserve the environment as they are non-toxic, biodegradable, and also reduce cost and energy consumption [1, 2]. The consumption of natural resources also gets reduced with the reuse of agricultural waste in concrete [3]. Utilization of agricultural waste helps in meeting the demand for sand and also helps in solving the disposal problem of agricultural waste. Also, sustainable and eco-friendly construction can be made possible by employing agricultural waste as natural aggregate replacement [4].

As a preliminary study, a comprehensive review was carried out with the help of PRISMA (Preferred Reporting Items for Systematic Reviews and Meta-Analyses) [5] to identify the agricultural waste used in concrete by researchers in the past. The review was conducted using the SCOPUS database and the keywords "concrete" and "agricultural waste" were added to analyze the articles focusing on utilizing agricultural waste or agro-waste in concrete. The search resulted in 605 documents (as on May 24, 2023). Virtual Operating

*Corresponding author: jeyashrm@srmist.edu.in

^a orcid.org/0000-0003-4420-573X; ^b orcid.org/0009-0008-5099-2251

DOI: <http://dx.doi.org/10.17515/resm2023.799ma0613>

Res. Eng. Struct. Mat. Vol. 9 Iss. 4 (2023) 1255-1266

System (VOS) viewer was used to extract the network of keywords and their co-occurrences. Fig. 1 shows the network diagram extracted from VOS viewer. From Fig. 1, it was observed that the most widely used agricultural waste in concrete is rice husk ash, sugar cane bagasse ash, palm oil ash, and coconut shells, (listed in ascending order in terms of keywords occurrences). Also, the keywords including self-compacting concrete, lightweight concrete, and geopolymer concrete were observed and these keywords highlight the effective utilization of agro-waste in enhancing concrete's strength and durability. Many of these studies focused on finding mechanical and durability properties of concrete containing agro-waste.

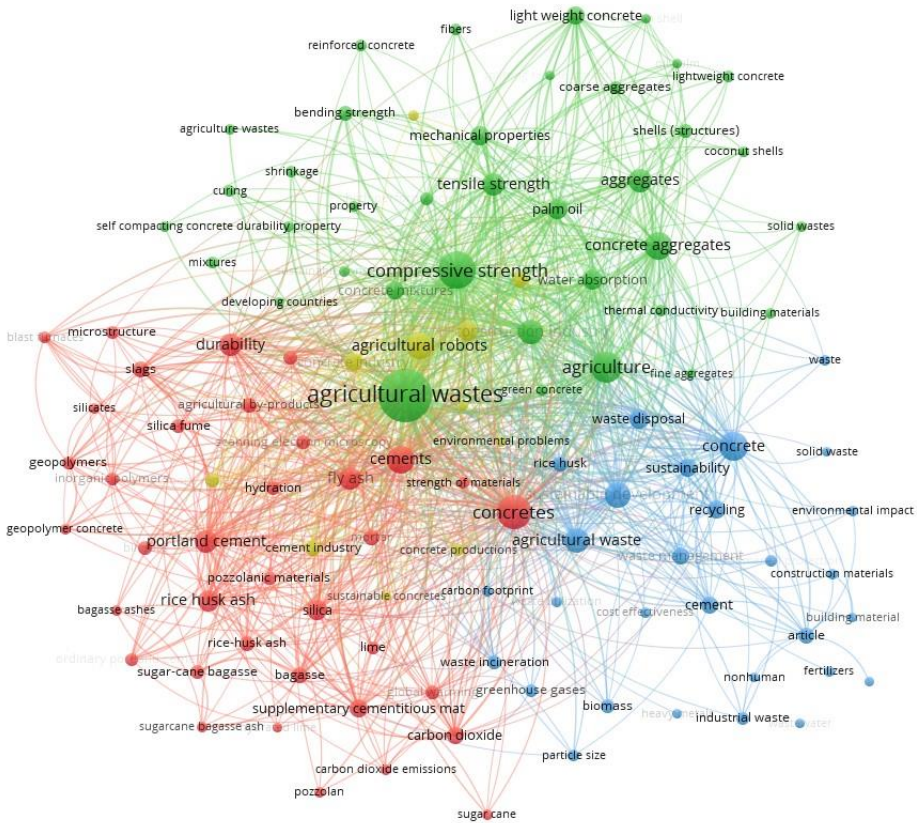


Fig. 1 Network of keywords on utilization of agricultural waste in concrete [Source: VOS viewer]

The current study is mainly concentrated on partial replacement of fine aggregate with eco-friendly additives like Coconut Shell powder (CNS); Saw Dust (SD); Rice Husk Ash (RHA) along with M - Sand to improve the characteristics of concrete. The addition of agro-waste materials (bagasse ash + cork) as fine aggregate replacement in mortar tends to increase the resistance of chloride penetration and improved the cyclic performance of mortar specimens with agro-waste [6]. The utilization of RHA in concrete leads to a reduction in the volume of pores at all ages and decreases the chloride ion penetration [7]. Implementation of ground RHA in concrete with recycled aggregate increased compressive strength, however the modulus of elasticity of concrete declined to that of conventional

concrete as RHA concentration increased [8]. The rice husk ash is found effective as a replacement for sand up to 10% [9]. The presence of CSH gel and $\text{Ca}(\text{OH})_2$ in concrete with addition to the agro-waste attributed to greater strength and other properties in comparison with conventional concrete for lesser content of agro-waste [10]. Utilization of RHA and Bagasse Ash in Self Compacting Concrete (SCC) resulted in the densification of the microstructure of concrete due to the filler effect and secondary CSH gel formation by pozzolanic reaction [11]. RHA as a partial replacement for fine aggregate is observed to enhance the thermal insulation of the concrete [12]. Being an alternate material for natural sand, the greatest choice for fine aggregate replacement in concrete is sawdust ash because of its unique properties [13]. Fine aggregate replacement by sodium-silicate treated sawdust by 5% is determined as an optimum percentage based on strength characteristics [14]. Coconut shell is a potential agricultural waste resource that can be utilized as a sustainably imperative material in concrete [15]. Use of partial coconut shell aggregate results in the production of concrete with good binder quality [16]. The cost of production of concrete with coconut shell powder gets reduced by 5.87% for 30% replacement of fine aggregate in comparison with conventional concrete [17]. Hence, the efficient usage of coconut shell powder, rice husk ash, and saw dust has been experimentally proven for its effectiveness as replacement for fine aggregate. The present study aims to investigate the combined effect of RHA, SD and CNS as replacement for fine aggregate.

2. Research Significance

The utilization of agricultural waste in concrete helps in producing sustainable concrete. The disposal of huge amounts of waste generates land pollution and effective utilization of agricultural waste results in energy conservation and conservation of natural resources. Hence, amending the agro-waste with the partial replacement for fine aggregate can eradicate the environmental issues. This type of concrete also helps in promoting a sustainable environment.

3. Materials

3.1. Coarse Aggregate

The specific gravity and bulk density were found as per IS: 2386 (Part III)-1963 [25] and the values were 2.89 and 1.56 kg/m^3 respectively. The water content present in the aggregate was found to be 0.35% and the maximum size of aggregate used was 20 mm.

3.2. Cement

Cement being a binding material possesses both adhesive and cohesive characteristics. Grade 53 Ordinary Portland Cement (OPC) was used for casting the specimens. The consistency was found to be 31% and the initial setting time was 39 minutes determined as per IS: 4031 – 5:1988 [27]. The specific gravity was obtained as 3.16 (as per IS:4031 – 11:1988) [28] and the fineness of cement was obtained as 5% (as per IS:4031 – 1:1988) [26].

3.3. Fine Aggregate

M – Sand which was crushed and broken into pieces from hard granite rocks was used as fine aggregate. M – Sand available at nearby places was considered for experimental investigation. The specific gravity of M- sand was 2.63 and its fineness modulus was 3.978. According to IS: 383 - 2016 [21], M- sand is classified as Zone II.

3.4. Rice Husk Ash (RHA)

Rice husk is the primitive element of the agro material, where the external covering, the husk is non-edible and can be used as an intrinsic material for improvement of strength in

concrete. Rice husk ash possesses greater pozzolanic reactions which enriches the performance of the concrete [8]. The rice husk had a specific gravity of 2.27. The fineness modulus was determined as 4.31.

3.5. Coconut Shell Powder (CNS)

The coconut shell, which is mostly available in countries like India, Sri Lanka, and Malaysia produces copious quantities of shell which creates problems with disposal; this coconut shell can be dried, powdered, and used as a replacement for fine aggregate in construction industries. The specific gravity of coconut shell powder was determined as 1.2. This possesses a cellulose content of 43.44% which can be one of the reasons for enrichment for strength and possess 45.84% of lignin, and hemicellulose of 0.25% which acts as an impulse for its usability as concrete ingredients [18]. The fineness modulus was determined as 2.46.

3.6. Saw Dust (SD)

Saw dust is a fundamental by-product obtained from the wooden industry and it is easily flammable when it is incautious in disposal. The specific gravity of sawdust was obtained as 2.15. The fineness modulus was obtained as 4.03. The chemical composition of the cement, M-sand, Rice Husk Ash and Saw Dust are given in Table 1.

Table 1. Chemical composition of cement, M-sand, RHA and SD

Composition (%)	Cement	M-sand	Rice Husk Ash	Saw Dust
SiO ₂	22.34	68.67	85.02	68.5
Al ₂ O ₃	4.98	15.92	0.53	4.63
Fe ₂ O ₃	4.54	4.98	0.44	3.47
CaO	60.12	2.97	1.51	9.70
MgO	1.22	-	0.42	5.19
SO ₃	2.56	-	1.62	0.33
Na ₂ O	0.36	0.98	1.10	0.07
K ₂ O	0.51	1.21	2.16	0.23
Loss On Ignition	3.29	3.55	4.93	-

4. Mix Design

The properties of materials were evaluated and based on which the mix proportions were obtained for concrete grade M30 as per Indian Standard IS:10262-2019 [29]. Table 2 shows the adopted mix design for the present study. Batching, mixing, and casting of specimens with agro-waste was done similarly to conventional concrete. Agro-waste was replaced for the weight of fine aggregate by 2%, 4%, 6%, and 8% (with an equal proportion of RHA, CNS, SD for the percentage of replaced fine aggregate). First, the required quantity of cement, M-sand, RHA, CNS, and SD were mixed dry until a uniform mix was obtained and then the content was added to the coarse aggregate in the mixer. Initially, the concrete ingredients were allowed for dry mixing, further required quantity of water was added slowly and mixed to obtain the concrete with the required consistency. Workability of concrete with 100% M-sand was obtained as 100 mm and the slump value decreased by 15% for 8% agro-waste concrete specimens.

5. Methodology and Testing of Concrete Specimens

The mechanical properties of M30 concrete grade were determined according to Indian Standard recommendations. The concrete cube of size 150 × 150 × 150 mm, and concrete cylinder with 150 mm diameter and 300 mm height were casted, cured and tested to determine the strength characteristics of concrete. The preparation of the agro-waste

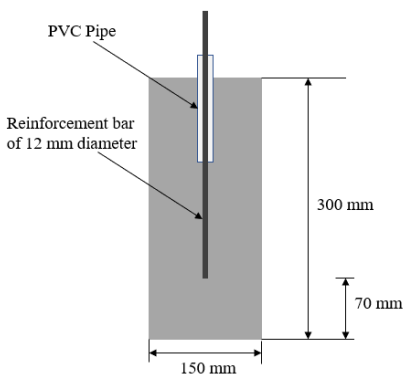
concrete was same as conventional concrete, but it includes the addition of agro-waste materials. Rice husk ash, coconut shell powder, and sawdust were equally proportioned, batched, and mixed. The varying percentages to which agro-wastes was replaced for fine aggregate in concrete are 2%, 4%, 6%, and 8% by weight. The concrete specimens were also tested for non-destructive testing to check the concrete quality. The non-destructive testing was performed as per IS: 13311 (Part 1 and 2): 1992 [22, 23]. Based on the experimental test results, the optimum mix was arrived for adding agro-waste to concrete. The optimum mix was used to cast the concrete cylinders with rebars to study the permeability of concrete.

Table 2. Composition of concrete ingredients

Description	Composition
Water cement ratio	0.42
Coarse aggregate	1234 kg/m ³
Fine aggregate	664 kg/m ³
Cement	381 kg/m ³
Mix ratio	1: 1.74: 3.24
Adopted water content	160 litres

5.1. Open Circuit Potential Test

Six numbers of concrete cylinders with rebars were cast with 0% (2), 2% (2), and 4% (2) of agro-waste as replacement for fine aggregate as shown in Fig. 2. Open Circuit Potential test [24] and chloride ingress test were performed on concrete cylinders with rebars to determine the permeability of the hardened concrete. The studies were also conducted to investigate the efficacy of using agro-waste in concrete. Cylinders with rebars were dried in the open air for 24 hours after 28 days of curing. The dried specimens were immersed in 3.5% NaCl for 60 days. The potential readings were measured periodically for 60 days.



a) Details of concrete cylinders with rebar

b) Cast cylinders with rebar

Fig. 2 Casting of cylinder specimens with rebar

5.2. Chloride ingress test

A chloride ingress test was used to find the chloride content that penetrated the concrete cylinders after exposure to 3.5% NaCl for 60 days. The core concrete sample from the cylinders was made into fine powder. Concrete samples passing through a 425-micron sieve were collected and weighed for 20 grams. The 20 grams of powder was mixed with

distilled water of 100 ml. The prepared sample was placed in a shaker for 1 hour and was filtered with a filter paper. The filtered sample was utilized for the determination of chloride content. The amount of chloride content was measured and the increase or decrease in chloride content was correlated to the permeability of the concrete.

6. Results and Discussion

6.1. Compressive Strength Test

A compressive strength test was performed for the conventional concrete with 100% M-sand and agro-waste concrete after the required days of 3-, 7-, 14- and 28-days water curing. Table 3 shows the compressive strength results for both concrete with 100% M-Sand and agro-waste concrete with 2 - 8% of agro-waste as fine aggregate replacement. From Table 3, it was observed that agro-waste concrete has achieved the required design target strength except for agro-waste concrete specimens with 8% of agro-waste.

Table 3. Compressive strength of concrete

% of agro-waste	Compressive strength - 3 days (N/mm ²)	Compressive strength - 7 days (N/mm ²)	Compressive strength - 14 days (N/mm ²)	Compressive strength - 28 days (N/mm ²)
0%	21.38	27.59	38.46	41.2
2%	19.26	23.3	37.06	37.7
4%	21.83	26.96	38.30	39.8
6%	17.23	25.42	29.83	34.26
8%	9.8	22.12	23.03	27.35

From Fig. 3, it was inferred that the pattern of the compressive strength gain curve remains the same for concrete with 100% M-sand and agro-waste concrete with 2% and 4% of agro-waste. Also, it was observed that the addition of agro-waste does not affect the early-age strength development of concrete.

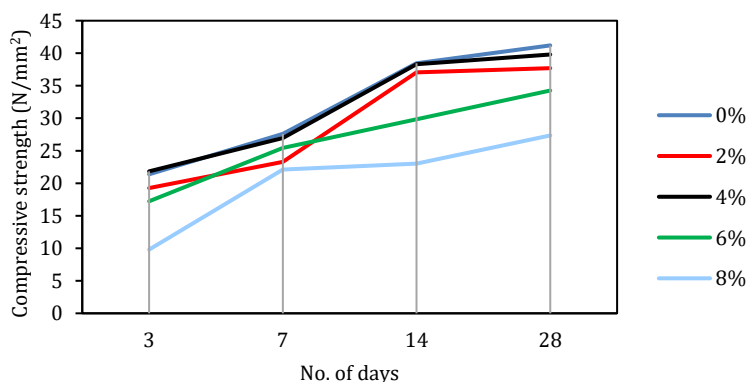


Fig. 3 Compressive strength of concrete specimens for varying percentage of agro-waste

Fig. 4 represents the compressive strength variation for agro-waste concrete to the varying percentages of agro-waste materials. From the 28-day test results, it is inferred that agro-waste concrete with 4% replacement has good performance compared with other agro-waste concrete specimens. Also, it is inferred that the addition of agro-waste for replacement of fine aggregate beyond 6% results in a decrease in compressive strength by

approximately 27%. All the concrete specimens with agro-waste concrete were found to have compressive strength value lesser than conventional concrete but the required target strength has been achieved with the replacement by 4% of agro-waste. The decrease in compressive strength with an increase in agro-waste content can be attributed due to the water absorption by RHA [8, 19], SD, and CNS [17]. The decrease in compressive strength with the increase in agro-waste beyond 10% was also observed by previous researchers [8, 17, 19, 20].

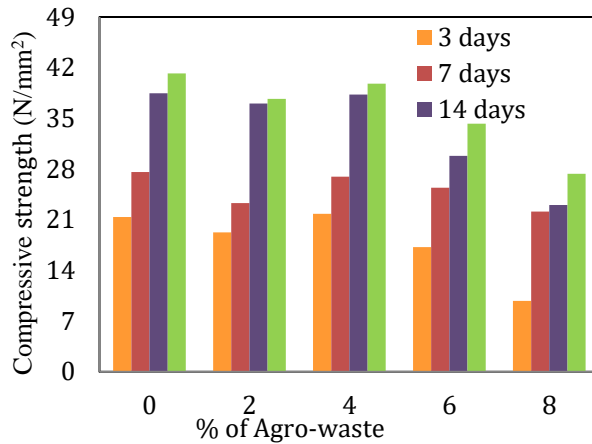


Fig. 4 Compressive strength of concrete with varying % of Agro-waste

6.2. Split Tensile Strength

The split tensile strength was performed for varying percentages of agro-waste in which the 4% confirms again to be an optimized percentage as it possesses the value of 2.94 N/mm². Fig. 5 shows a graphical depiction of the 28-day split tensile strength results. The results from split tensile strength test follows a similar trend to compressive strength test results and from the test results it was observed that 4% of agro-waste can be replaced for fine aggregate using M- Sand.

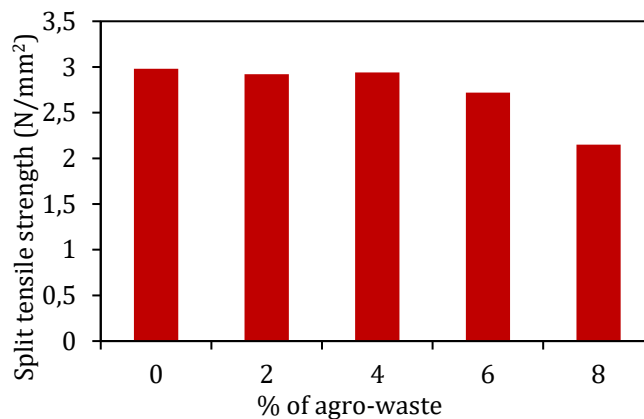


Fig. 5 Split tensile strength of concrete with varying % of agro-waste

6.3. Rebound Hammer Test

The rebound hammer results for agro-waste concrete specimens are up to scratch compared to standard concrete. The rebound value obtained for 4% of agro-waste concrete is 31.0 whereas for conventional concrete it gives 31.4. Table 4 shows the rebound value and the corresponding compressive strength for specimen with varying percentages of agro-waste. Test results show that concrete specimen with 4% of agro-waste shows fairly good surface characteristics with compressive strength of 28 N/mm² when compared with other agro-waste concrete specimens.

Table 4. Rebound hammer values with varying % of agro-waste

Specimen with agro-waste	Rebound number value	Compressive strength (N/mm ²)	Concrete quality as per IS: 13311 [23]
0%	31.4	29	Fair
2%	29.9	27.5	Fair
4%	31.0	28	Fair
6%	28.8	27	Fair
8%	27.6	26	Fair

6.4. Ultrasonic Pulse Velocity Test

Table 5 shows the quality of concrete determined based on pulse velocity. The test findings show that the quality of concrete cubes containing 0%, 2% and 4% agro-waste is excellent. The homogeneity of concrete was maintained with the replacement of fine aggregate by agro-waste. An increase in agro-waste percentage beyond 4% results in the reduction of uniformity of concrete mixes and this can be due to the fact that the addition of agro-waste beyond 4% results in non-uniform packing and unequal dispersion of agro-waste into concrete.

Table 5. Ultrasonic pulse velocity test results with varying % of agro-waste

Specimen with agro-waste	Velocity (km/s)	Concrete quality as per IS: 13311 [22]
0%	4.61	Excellent
2%	4.58	Excellent
4%	4.60	Excellent
6%	4.33	Good
8%	3.98	Good

6.5. Open Circuit Potential Test

The results obtained on 6 concrete cylinders for 60 days are given in Fig. 5. It was observed from the test results that the corrosion rate for agro-waste concrete with 2% and 4% of agro-waste was lesser in comparison with concrete with 100% M-sand (0% of agro-waste). Also, the trend in the increase in potential values for concrete specimens was noticed with the increase in days. The corrosion condition was defined based on potential values in ASTM C876 [24] and the risk of corrosion is highlighted in Fig. 6. The corrosion rate was initially low from 1 to 11 days for all specimens; intermediate corrosion risk was observed from 12 to 55 days, and agro-waste concrete specimens were subjected to intermediate corrosion risk at the end of 60 days. A high risk of corrosion was observed in conventional concrete specimens from 55 to 60 days. The improvement in the performance of agro-waste concrete can be due to the micro-filling effect of RHA within the cement particles [19]. The hydration products get distributed in a homogenous manner and make the concrete matrix denser with the addition of RHA [7]. Thus, the addition of agro-waste resulted in improved performance in terms of micro-filling ability.

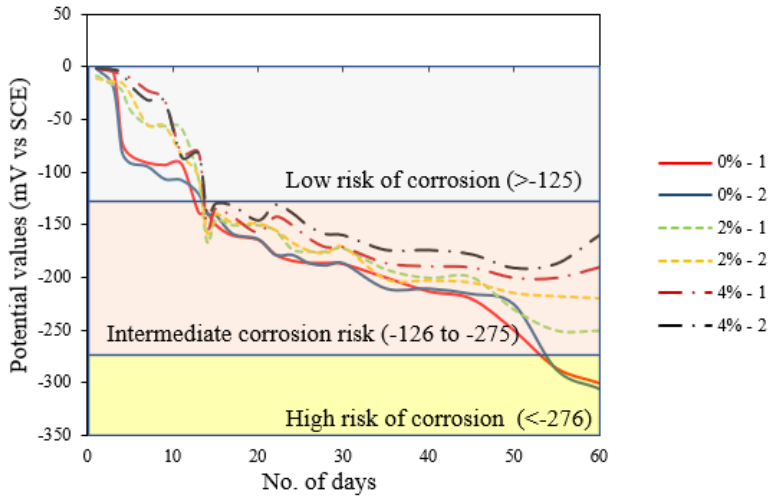


Fig. 6 Potential values for concrete specimens with 0%, 2% and 4% of agro-waste

6.6. Chloride Ingress Test

The quantity of chloride penetrated through the concrete specimens was determined using the chloride ingress test and the chloride content was determined by titration against silver nitrate solution with potassium chromate 5% as the indicator. Table 6 gives the quantity of chloride content penetrated through the concrete specimens and it is clear that agro-waste concrete specimens had a lesser amount of chloride penetrated. Hence, the permeability of concrete had been improved with the utilization of agro-waste as a replacement for fine aggregate.

Table 6. Chloride content for concrete specimens with 0%, 2% and 4% of agro-waste

% of agro-waste	Mean value of silver nitrate solution (ml)	Obtained chloride content (mg/L)	% Decrease in chloride content with respect to conventional specimen
0	10.50	149.1	-
2	9.55	135.6	9.02
4	9.30	132.0	11.47

7. Conclusion

Experimental investigation was performed to ascertain the robust strength of utilizing agro-waste in concrete for 0%, 2%, 4%, 6% and 8% as fine aggregate replacement and the strength characteristics were determined to find the optimized percentage. The following concluding remarks are arrived based on the results from experimental investigation:

- It is recommended to utilize agro-waste with an equal proportion of rice husk ash, sawdust, and coconut shell powder as a replacement for fine aggregate from 2% to 4% by weight.
- It is profound that 4% of agro-waste was obtained to be an optimized percentage for agro-waste concrete as the laboratory results are more convincing for 4% compared with conventional concrete (100% M-sand). The compressive strength and split tensile strength obtained for 4% are also more competent and comparable to conventional concrete.

- Based on the test results from non-destructive testing, it is observed that the surface characteristics and homogeneity of concrete were not affected with the addition of agro-waste up to 4% as a replacement for fine aggregate.
- The addition of agro-waste beyond 4% was found to be ineffective, as evidenced by the lower performance of 6% and 8% agro-waste concrete specimens.
- The experimental results from the OCP test shows that the potential values are lesser for agro-waste concrete specimens in comparison with concrete specimens with 100% M-sand. Also, the chloride content penetrated into the concrete core is lesser for agro-waste concrete specimens. Hence, it is inferred that agro-waste had the micro-filling ability that resulted in the reduction of permeability of concrete specimens. Thus, the replacement of fine aggregate by agro-waste between 2% to 4% is effective in concrete elements with rebars.
- The utilization of agro-waste in concrete will reduce conventional material usage and also it is an environmentally benign. Hence effective utilization of agro-waste will be substantial to the environment.

Acknowledgement

This study acquired no funding from government, commercial, or non-profit organisations. The authors are thankful to the Concrete laboratory, Department of Civil Engineering, SRM Institute of Science and Technology, for their constant support by providing laboratory facilities.

References

- [1] Kumar MV, Lemessa K. Behaviour of Concrete with Agro and Industry Waste as a Replacement for Constituent Materials. *American Journal of Engineering Research*, 2017;6: 79-85.
- [2] He J, Kawasaki S, Achal V. The utilization of agricultural waste as agro-cement in concrete: A review. *Sustainability*, 2020;12(17): 6971. <https://doi.org/10.3390/su12176971>
- [3] Rashad A. Cementitious materials and agricultural wastes as natural fine aggregate replacement in conventional mortar and concrete. *Journal of Building Engineering*, 2016;5: 119-141. <https://doi.org/10.1016/j.jobe.2015.11.011>
- [4] Hakeem IY, Amin M, Agwa IS, Abd-Elrahman MH, Abdelmagied MF. Using a combination of industrial and agricultural wastes to manufacture sustainable ultra-high-performance concrete. *Case Studies in Construction Materials*, 2023: e02323. <https://doi.org/10.1016/j.cscm.2023.e02323>
- [5] Wasim M, Vaz Serra P, Ngo TD. Design for manufacturing and assembly for sustainable, quick and cost-effective prefabricated construction - a review. *International Journal of Construction Management*, 2020: 31: 1-9.
- [6] Prusty JK, Basarkar SS. Concrete using agro-waste as fine aggregate for sustainable development-built environment - A review. *International Journal of Sustainable Built Environment*, 2016;5: 312-333. <https://doi.org/10.1016/j.ijbsbe.2016.06.003>
- [7] Ramasamy V. Compressive Strength and Durability Properties of Rice Husk Ash Concrete. *KSCE Journal of Civil Engineering*, 2011;16: 93-102. <https://doi.org/10.1007/s12205-012-0779-2>
- [8] Tangchirapat W, Buranasing R, Jaturapitakkul C, Chindapasirt P. Influence of rice husk-bark ash on mechanical properties of concrete containing high amount of recycled aggregates. *Construction and Building Materials*, 2008;22: 1812-19. <https://doi.org/10.1016/j.conbuildmat.2007.05.004>

- [9] Poudyal P, Jha AK. Experimental Study on the Properties of Concrete with the Partial Replacement of sand by rice husk. Proceedings of IOE Graduate Conference, 191-195, 2016.
- [10] Godwin IA, Deborah N, Ponraj J, Blesscho RV, Stephen C. Experimental Investigation on the Mechanical and Microstructural properties of Concrete with Agro waste. Indian Journal of Engineering and Technology, 2018;14419: 33-37. <https://doi.org/10.14419/ijet.v7i3.12.15858>
- [11] Hasnain MH, Javed U, Ali A, Zafar MS. Eco-friendly utilization of rice husk ash and bagasse ash blend as partial sand replacement in self-compacting concrete. Construction and Building Materials, 2011; 121753.
- [12] Rashad A. Cementitious materials and agricultural wastes as natural fine aggregate replacement in conventional mortar and concrete. Journal of Building Engineering, 2016;5: 119-141. <https://doi.org/10.1016/j.jobbe.2015.11.011>
- [13] Mageswari M, Vidivelli B. The use of sawdust ash as fine aggregate replacement in concrete. Journal of Environmental Research and Development, 2009;3: 720-726.
- [14] Siddique R, Singh M, Mehta S, Belarbi R. Utilization of treated saw dust in concrete as partial replacement of natural sand. Journal of Cleaner Production, 2020;261: 121226. <https://doi.org/10.1016/j.jclepro.2020.121226>
- [15] Algaifi HA, Shahidan S, Zuki SSM. Mechanical properties of coconut shell-based concrete: experimental and optimisation modelling. Environmental Science Pollution Research, 2022;29: 21140-21155. <https://doi.org/10.1007/s11356-021-17210-1>
- [16] Mo KH, Thomas BS, Yap SP, Abutaha F, Tan CG. Viability of agricultural wastes as substitute of natural aggregate in concrete: A review on the durability-related properties. Journal of Cleaner Production, 2020;275: 123062. <https://doi.org/10.1016/j.jclepro.2020.123062>
- [17] Azunna SU, Aziz FN, Cun PM, Elhibir MM. Characterization of lightweight cement concrete with partial replacement of coconut shell fine aggregate. SN Applied Sciences, 2019; 1: 1-9. <https://doi.org/10.1007/s42452-019-0629-7>
- [18] Satyanarayan KG, Kulkarni AG, Pohati PK. Structure and Properties of coir fibers. Proc. Indian Academic. Science (Engineering Science) 4, 419-436@printed in India 1981. <https://doi.org/10.1007/BF02896344>
- [19] Sua-Iam G, Makul N. Utilization of limestone powder to improve the properties of self-compacting concrete incorporating high volumes of untreated rice husk ash as fine aggregate. Construction and Building Materials, 2013;38: 455-464. <https://doi.org/10.1016/j.conbuildmat.2012.08.016>
- [20] Meko B, Ighalo JO. Utilization of Cordia Africana wood sawdust ash as partial cement replacement in C 25 concrete. Cleaner Materials, 2021;1: 100012. <https://doi.org/10.1016/j.clema.2021.100012>
- [21] IS 383: 2016. Coarse and Fine Aggregate for Concrete - Specification (Third Revision), Bureau of Indian standards, New Delhi, 2016.
- [22] IS 13311 - Part 1. Non-destructive testing of concrete - Methods of test - Ultrasonic Pulse Velocity, Bureau of Indian Standards, New Delhi, 1992.
- [23] IS 13311 - Part 2. Non-destructive testing of concrete - Methods of test - Rebound Hammer, Bureau of Indian Standards, New Delhi, 1992.
- [24] ASTM C876-09. Standard test method for corrosion potentials of uncoated reinforcing steel in concrete, Annual Book of ASTM standards, Philadelphia.
- [25] IS 2386 - Part 3: 1963. Methods of test for aggregates for concrete, PART III: Specific Gravity, Density, Voids, Absorption and Bulking). Bureau of Indian Standards, New Delhi.
- [26] IS 4031 - Part 1:1996. Method of Physical Tests for Hydraulic Cement (Part 1 Determination of Fineness by Dry Sieving). Bureau of Indian Standards, New Delhi.

- [27] IS 4031 - Part 5:1988. Method of Physical Tests for Hydraulic Cement (Part 5 Determination of Initial and Final Setting Times). Bureau of Indian Standards, New Delhi.
- [28] IS 4031 - Part 11:1988. Method of Physical Tests for Hydraulic Cement (Part 11 Determination of Density). Bureau of Indian Standards, New Delhi.
- [29] IS 10262: 2019. Concrete Mix Proportioning - Guidelines. Bureau of Indian Standards, New Delhi.



Research Article

Parametric study on the performance of industrial byproducts based geopolymer concrete blended with rice husk ash & nano silica

M. Maheswaran^{*1,a}, C. Freeda Christy^{1,b}, M. Muthukannan^{2,c}, K. Arunkumar^{3,d},
A. Vigneshkumar^{1,e}

¹ Department of Civil Engineering, Kalasalingam Academy of Research and Education, Tamilnadu, India

² Department of Civil Engineering, KCG College of Technology, Tamilnadu, India

³ Department of Civil Engineering, Mangalam College of Engineering, Kottayam-686631, Kerala, India

Article Info

Abstract

Article history:

Received 03 July 2023

Accepted 11 Sep 2023

Keywords:

Geopolymer concrete;
Industrial-byproducts;
Workability;
Strength properties;
Ambient curing

In this study, Geopolymer concrete (GPC) blended with fly ash (FA), ground granulated blast furnace slag (GGBS), rice husk ash (RHA), and nano-silica (NS) developed and investigated in three aspects: In the first aspect of GPC (FA+GGBS), FA varied from 0-100% of GGBS at 10 % intervals to determine the optimum proportion of FA-GGBS. In the second aspect of GPC (FA+GGBS+RHA), RHA varied from 0-25% of FA at 5% intervals with a constant of 30% GGBS attained from the first aspect of the study. In the third aspect of GPC (FA+GGBS+RHA+NS), NS was replaced with 1, 3, and 5% with the optimum proportions of GGBS (30%) and RHA (15%) obtained from the first and second aspects of the study. The fresh and hardened properties of GPC were obtained at 7 and 28 days under ambient curing. The compressive strength improved while FA was replaced by GGBS (0-100%) from 27.75 to 45 MPa. Meanwhile, workability has decreased to 0.81 from 0.97. Hence, the optimized proportion of FA and GGBS was obtained as 70:30 from the workability aspect. RHA replacement provided compressive strength increment up to 15% (39.5 MPa), but workability gradually decreased (0.92 to 0.84) from 0 to 25%. So, the optimum proportion of RHA was achieved by 15% from the second aspect. In the third aspect, the workability increased from 0.89 to 0.92 while NS replacement (0-3%) with FA. Also, compressive strength has improved from 39.52 to 41.95 MPa. Thus, the optimized NS proportion gained at 3% of NS. Overall, this study provides a view of industrial by-product utilization as part of GPC in optimal proportions.

© 2023 MIM Research Group. All rights reserved.

1. Introduction

The building sector is growing rapidly due to urbanization [1]. Therefore, globally the need for cement production has also risen with infrastructure development [2]. Generally, cement-based concrete is widely used in the building industry [3, 4]. Moreover, the cement industry releases carbon dioxide (CO₂) of 0.85 - 1 ton during the manufacturing processes of one-ton cement which is part of global warming. Furthermore, it estimates that airborne CO₂ emissions are between 5-7% [5-8]. Much recent research has shown interest in finding a substitute material to replace cement [9] with Geopolymer Concrete (GPC), which uses pozzolanic materials and alkali activators [10]. GPC is an environmentally safe alternative to traditional cement-based concrete and contributes to reduce CO₂ emissions. The emissions from geopolymer binders' production are significantly lower compared to cement, possibly around 0.1 to 0.3 tons of CO₂ per ton [11, 12]. Joseph Davidovits invented

*Corresponding author: m.mahe29@gmail.com

^a orcid.org/0000-0001-6913-3141; ^b orcid.org/0000-0002-6929-310X; ^c orcid.org/0000-0003-1912-3513;

^d orcid.org/0000-0002-5745-6864; ^e orcid.org/0009-0003-4755-8669.

DOI: <http://dx.doi.org/10.17515/resm2023.809ma0703>

Res. Eng. Struct. Mat. Vol. 9 Iss. 4 (2023) 1267-1285

Geopolymer (GP) in 1978 as an alternative to cement [13]. GP is an inorganic aluminosilicate polymer group produced by reacting aluminosilicate materials and a higher amount of silicon and aluminum with the alkaline activator solution (AAS) [14].

Generally, Fly ash (FA) and Ground Granulated Blast Furnace Slag (GGBS) are the industrial and steel plant by-products as main precursors used in GPC [15]. AAS is a mixture of Sodium Silicate (Na_2SiO_3) or Potassium Silicate (K_2SiO_3) and Sodium Hydroxide (NaOH) or Potassium Hydroxide (KOH) [16]. However, sodium-based solutions are more economical than potassium-based solutions [17]. FA is pulverized fuel ash from exhaust gases of coal-based thermal power plants by-product that improves the rheology and alkali-aggregate reaction of artificial pozzolan due to the high amorphous silica content [18]. Overall, FA generation of 300-600 MT in 2020, occupied up to 3235 km² of land for disposal, and India produced 271 MT of FA from 200 power plants during 2021-2022 [19]. GGBS is a solid waste discharged in high quantities by the iron and steel industry. The global GGBS production was 377 MT in 2021. The benefits of GGBS on concrete improves the strength, decreases the voids, and reduces the permeability. Also, it can generate heat during the hydration process and reduce water demand from the alkali-silica reaction [20–22].

Rice husk (RH) is a by-product of rice mill from paddy. It is usually obtained from rice husk burning and contains silica ash after being removed from cellulose and lignin. 35 MT of RHA has been produced annually from 140 MT of RH obtained from 700 MT of rice production [23]. Rice husk is burnt to 300-700 degrees Celsius and made into ashes [24]. Rice Husk Ash (RHA) is a fine active silica material with numerous merits, including strength enhancement, durability, and cost-effectiveness. RHA utilization in concrete is the best solution for waste disposal and reduce carbon dioxide emissions. It gives better strength due to high amorphous silica content, high surface area, and porous structure [25–28]. Generally, FA blends with similar high-silica sources materials like GGBS, Silica fume, RHA, and Nano silica to form a suitable chemical composition of geopolymers [29]. GP has the potential to develop environment-friendly materials by using by-products that are harmful to the environment [30].

1.1. Nano Material

In recent years, Nano materials usage in construction has significantly enhanced the performance of the materials. Nowadays, one of the nanomaterials called Nano Silica (NS) is used in concrete technology, as nano-sized particles act as nano additives [31]. It improves the cementitious matrix, hydration, mechanical properties, and concrete microstructure due to its high specific area. It can improve the density binder matrix that decreases porosity and self-healing ability [32]. Also, it is a cost-effective and eco-friendly material that reduces CO₂ emissions. It was found that a small dosage of NS improved the early age and 28-day strength gain of GP concrete through the attributed effect, pozzolanic reaction [33] its pore-filling properties and reactive pozzolans [34]. It accelerates the polymerization rate and facilitates the development of C-S-H and N-A-S-H in natural pozzolan-based GPC [35]. Since NS particles possess a large surface area, the polymerization process is accelerated [36]. Silica or silicon dioxide nanoparticles increases the mechanical properties [37–39]. GPC is resistant to inflammable and chemical problems [40]. It has low creep and less shrinkage and achieves quick setting time and improved the strength [41].

1.2. Review on Literatures

Globally, extensive researchers have been conducted in the field of GPC to find alternate materials to cement and other precursors. For instance, FA (75%) and GGBS (25%) at various concentrations of NaOH from 8 to 16 M with Na_2SiO_3 to NaOH ratio from 0.5 to 3.0 were analyzed for the optimum molarity and obtained as 14 M with $\text{Na}_2\text{SiO}_3/\text{NaOH}$ ratio

as 2.5 in GPC [42]. In addition, GPC made with FA, GGBS, alccofine (0-15%), naphthalene-based superplasticizers (1.5%) were cast to determine the strength. The results proved that GPC attained more strength at 40% FA, 50% GGBS, and 10% alccofine than OPC [43]. Moreover, FA was replaced with RHA to enhance the performance of GPC [44, 45]. However, only 10% of RHA can be replaced with GGBS to gain maximum strength [46]. Overall, it was found that RHA incorporation in GPC can act as additional cementitious material with pozzolanic reaction, binder formation, strength enhancement, and reduces the environmental impact.

On the other hand, the addition of RHA (1.2%) and NS (1%) with FA has improved the strength in GPC which reveals incorporation of NS increases the reactivity and workability of concrete. Hence, NS improve the strength and durability of the GPC [47]. Another study attempted to determine the workability and strength properties of GPC blended with Waste Glass Powder (WGP), FA, GGBS, and MK. The experimental result revealed that GPC with GGBS (55%), WGP (35%), and MK (10%) attained 12% of strength increment [48]. Furthermore, GGBS was replaced with red mud (0-30%) in KOH and K_2SiO_3 as AAS solution to analyze applicability of alternate materials in GPC. The increase in the red mud proportion with GGBS reduced the workability and enhanced the strength up to 12% [49].

Recently, the strength properties of GPC with RHA, FA, GGBS, and nano TiO_2 (NT) were studied and obtained the maximum strength of 16 % increase with RHA (10%) and TiO_2 (4%) incorporated GPC specimens [50]. Although, 20% of RHA addition produced maximum strength with MK (20%), FA (30%), and GGBS (30%), but further addition of the RHA reduced GPC strength [27]. GPC developed from FA, nano-clay (NC), and NT enhanced strength at 1% of NC and 1.25% of NT. Furthermore, it increased the density of GPC and reduced the pores [51]. Also, another study investigated the modified GPC with NS (0-2.5%) and Silica fume (SF) (0-2.5%) with FA (70%) and GGBS (30%) and obtained as 1.5% as the optimum of both NS and SF [50–52]. NS, micro silica, and alkali-activated slag-based GPC were examined and the addition of 3% NS improved the strength and reduced beyond this limit [53].

Overall, GPC with FA, GGBS, MK, SF, RHA, alccofine, red mud, on various combinations of these materials are investigated to gain the optimum strength FA, a primary GPC binder, has growing demand, so it needs to find an alternative. NS is cementitious material and have superior qualities such as improvement of mechanical properties, durability, workability, and shrinkage reduction. It also enhances bond strength and helps mitigate alkali-silica reaction. These significances make nano silica a valuable additive for improving the performance of GPC structures. This study explores the development of GPC using industrial by-products like FA, GGBS, RHA and NS and to arrive the optimum proportions for workability and strength from different combinations of industrial by products.

2. Materials and Methods

2.1. Fly Ash (FA)

FA is a thermal power plant by-product and can act as primary source material. The FA was obtained from Tuticorin thermal power plant for the study. Class F FA is considered as per ASTM C618 [54] with light grey in color, and has a specific gravity of 2.30. Scanning Electron Microscope (ZEISS EVO18 CARL, Germany) equipped with Energy Dispersive X-Ray Spectroscopy (EDX) is non-destructive method and used to analyses the quantitative elemental composition of FA, GGBS, RHA, NS at 1500 magnification, 20 kV acceleration voltage and resolution of 129 (eV). EDX spectrum shows the elemental composition of FA shown in Fig. 1.

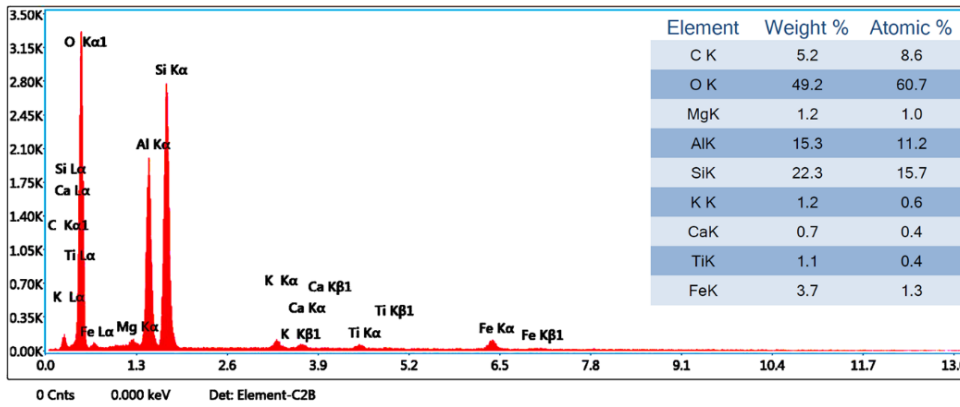


Fig. 1 Elemental compositions of FA from EDX Spectrum

The active silica (SiK-22.3%) and alumina (AlK-15.3%) were found utmost quantity compared to other elements in Class F Fly ash (FA) from EDX spectrum. Where k factor (K electrons, closest to the nucleus, are n=1 electrons) represents the net-count ratios of characteristic or intensity X-rays of sample measurement divided by standard of known or reference sample.

2.2. Ground Granulated Blast Furnace Slag (GGBS)

GGBS is a secondary source material obtained from iron industry byproducts. It was obtained from JSW steels for the study. It is white in color with specific gravity of 2.90 and the chemical compositions of GGBS are shown in Fig. 2.

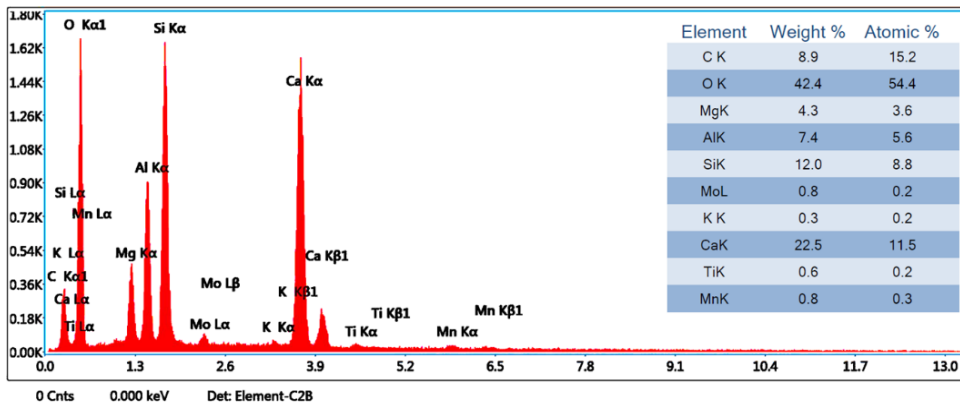


Fig. 2 Elemental compositions of GGBS from EDX Spectrum

The EDAX spectrum of GGBS appears calcium (CaK-22.5%), active silica (SiK-12%), alumina (AlK-7.4%) and magnesium (MgK-4.3%) are presented maximum amount compared to other elements in Class F Fly ash.

2.3. Rice Husk Ash

RHA is an agriculture by-product from rice mills. It is generated by flaming the RH under a specific temperature. It is obtained from a local rice mill plant for the study. It is dark grey color and has a specific gravity of 2.18. The elemental compositions of RHA from EDX spectrum are shown in Fig. 3.

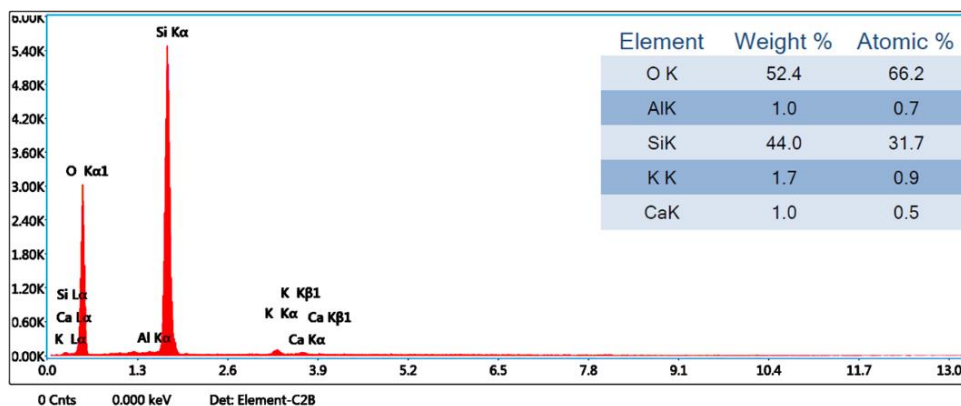


Fig. 3 Elemental compositions of the RHA from EDX Spectrum

From Fig. 3, active silica (SiK-44%) is presented maximum amount compared to other elements in RHA. Oxides are presented due to atmospheric oxygen and potassium and calcium are available in minimum amount which represented in Fig. 3.

2.4. Nano Silica (NS)

NS is in powdered form and purchased from Astra Chemicals, Chennai. It helps in the formation of aluminosilicate gel and contains more silica content in it.

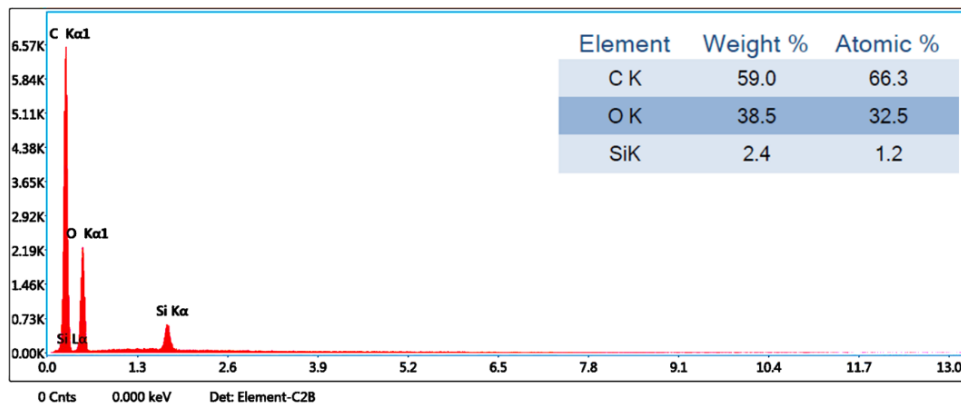


Fig. 4 Elemental compositions of the NS from EDX Spectrum

It is white in color with a specific gravity of 2.4 and elemental composition of NS shown in Fig. 4. The presence of active carbon (CK-59%), oxygen (38.5%) and active silica (SiK-2.4%) was shown in Nano Silica (NS) from spectrum. EDX spectrum proved that pure nano silica was taken for this study. Excess EDX spectrum peak of carbon was presented due to that carbon tape was used to conduct the analysis and oxides due to atmospheric oxygen. Hence, the after deduction of carbon and oxides, the 100% of silica content is available in the sample from Fig. 4.

2.5. Aggregates and Alkaline Liquids

In this study, locally available CA and M sand with the grade of fine aggregate confirmed to Zone-II as per IS383 (2016) [55] and the specific gravity as 2.62 CA of 20 mm size with a specific gravity of 2.91 and density of 1750 kg/m³ was used. Na₂SiO₃ and NaOH mixture can act as AAS. The specific gravity of NaOH and Na₂SiO₃ were 1.47 and 1.60, respectively.

The workability and the compressive strength of GPC can be enhanced with, the 13 Molarity concentration of NaOH solution [56].

2.6. Experimental Procedure

The NaOH and Na₂SiO₃ solution were used as alkaline liquids. Na₂SiO₃ and NaOH ratio was taken as 1:2.5 and the A/B ratio is fixed as 0.55 [57, 58]. 13M was prepared by dissolving 377 grams of NaOH pellets in a liter of distilled water [59]. The NaOH solution has been mixed 24 hours before casting the specimen. The sodium silicate is mixed with NaOH solution before casting.

Table.1 Mix proportions of GPC with various binder combinations

MIX ID	FA %	GGBS %	RHA %	NS %	FA (kg/m ³)	GGBS (kg/m ³)	RHA (kg/m ³)	NS (kg/m ³)
Optimization of binder ratio (FA and GGBS)								
GPG0	100	0	0	0	550	0	0	0
GPG10	90	10	0	0	495	55	0	0
GPG20	80	20	0	0	440	110	0	0
GPG30	70	30	0	0	385	165	0	0
GPG40	60	40	0	0	330	220	0	0
GPG50	50	50	0	0	275	275	0	0
GPG60	40	60	0	0	220	330	0	0
GPG70	30	70	0	0	165	385	0	0
GPG80	20	80	0	0	110	440	0	0
GPG90	10	90	0	0	55	495	0	0
GPG100	0	100	0	0	0	550	0	0
Optimization of RHA								
GPR0	70	30	0	0	385	165	0	0
GPR5	65	30	5	0	357.5	165	27.5	0
GPR10	60	30	10	0	330	165	55	0
GPR15	55	30	15	0	302.5	165	82.5	0
GPR20	50	30	20	0	275	165	110	0
GPR25	45	30	25	0	247.5	165	137.5	0
Optimization of Nano Silica								
GPN0	55	30	15	0	302.5	165	82.5	0
GPN1	54	30	15	1	297	165	82.5	5.5
GPN3	52	30	15	3	286	165	82.5	16.5
GPN5	50	30	15	5	275	165	82.5	27.5

The precursors such as FA, GGBS, RHA, and NS under various combinations were mixed with alkaline liquids along with the aggregates. After mixing, the concrete mixture was transferred into 150×150×150 mm cubes, 150×300 mm cylinder moulds, and 100×100×500 mm prism. Triple specimens were cast for every GPC mix proportions and the cube, cylinder and prism specimens were removed from the moulds and cured at ambient temperature after 24 hours of casting.



Fig. 5 Specimens preparation and test setup of compression (cube), split tensile (cylinder) and flexural (prism)

The cube specimens have undergone compression test as per ASTM C63 [60] and split tensile strength tests have been carried out on the cylinder specimen as per ASTM C496 [61]. A concrete prism is used to analyze flexural strength as per IS 516-1959 at 7 and 28 days [62]. The preparation and testing of specimens shown in Fig. 5

3. Results and Discussions

3.1. Workability and Strength

Workability is obtained for freshly mixed GPC that is to be placed and compacted for the uniform flow of mix in the concrete without segregation. The GPC workability is determined from the standard compaction factor test as per IS 1199-1959 [61]. The workability of FA-GGBS with 0-100% proportions range from 0.97 to 0.81 of compaction factor value shown in Fig. 6. The workability is reduced with the increase in GGBS proportions.

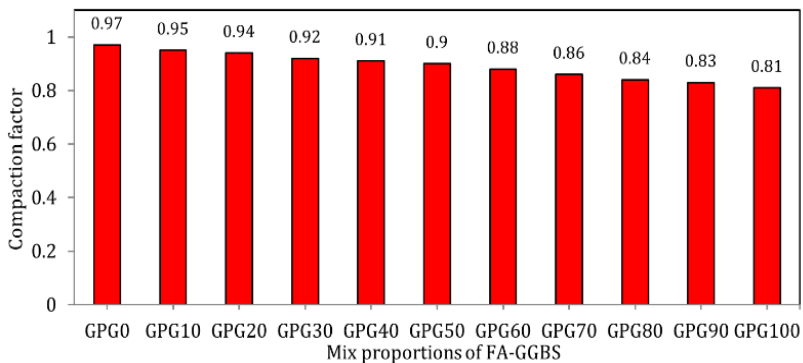


Fig. 6 Compaction factor value for proportions of FA and GGBS

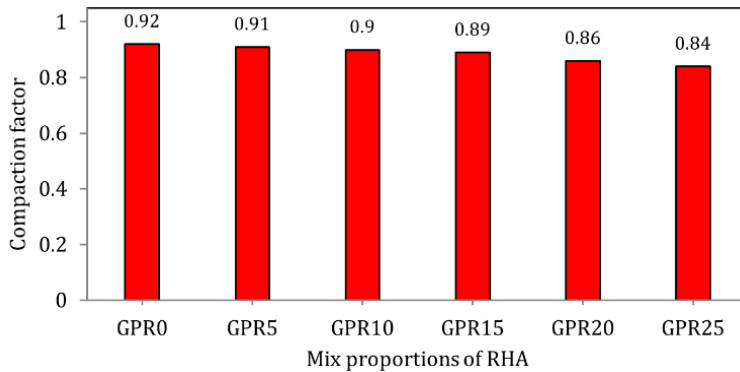


Fig. 7 Compaction factor value for proportions of FA, GGBS, and RHA

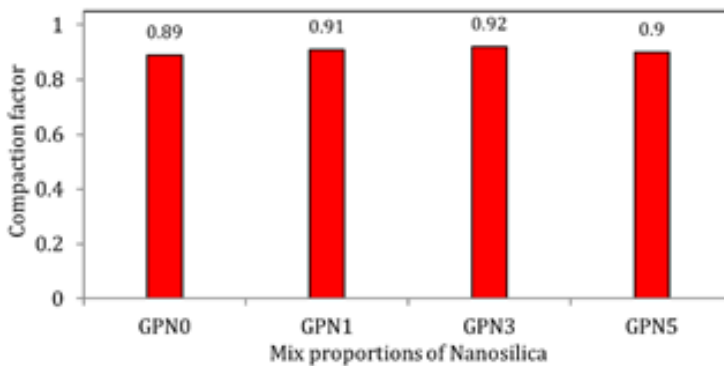


Fig. 8 Compaction factor value for proportions of FA, GGBS, RHA, and NS

According to IS 456-2000, compaction factor 0.85 to 0.92 were considered the medium degree of workability. Hence, the optimum workability is fixed as 0.92, which is medium degree workability obtained at GPC30 from Fig. 6. The workability of GPC based RHA with 0-25% proportions was performed by compaction factor experiment, and the results range from 0.92 to 0.84 shown in Fig. 7. The workability declined in higher RHA proportions. Based on the strength factor, the optimum degree of workability is obtained as 0.89. GPC workability improved from 0.89 to 0.92 at 3% of NS, and it declined to 0.90 at 5% shown in Fig. 8. Hence the optimum workability of NS mixed GPC is obtained at 0.92, which is a medium degree of workability at 3% of NS.

3.1.1 Optimization of FA-GGBS Proportion

The FA-GGBS based GPC was optimized based on the mechanical properties such as compressive strength (CS), split tensile strength (STS) and flexural strength (FS) test. The Mix ID GPG0 to GPG100 was analyzed for the CS, STS and FS test. CS of FA-GGBS proportion at 7-days and 28-days ranges from 13.60 to 29.75 MPa and 27.75 to 45 MPa from Fig. 9. GPC strength increased when GGBS content increased with FA, but workability decreased with the increase of GGBS. STS at 7-days and 28-days ranges from 0.95 to 3.4 MPa and 1.95 to 5.1 MPa from Fig.10. GPC strength increased when GGBS content increased with FA, but workability decreased with the increase of GGBS. So, GPG30 was fixed as the optimum FA-GGBS proportion which is 2.8 MPa at 28 days. FS ranges at 7-days and 28-days from 3.15 to 4.95 MPa and 3.95 to 6.50 MPa indicated in Fig. 11. GPC strength increased when GGBS content increased with FA, but workability decreased with the increase of GGBS. So, GPG30

was fixed as the optimum FA-GGBS proportion at workability factor which is 4.85 MPa at 28 days. Overall, the optimum CS, STS, and FS were obtained from GPG30 at 28 days.

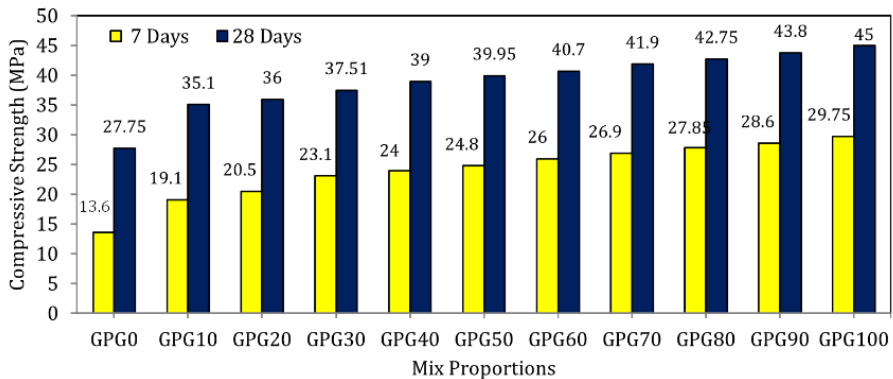


Fig. 9 Compressive strength test for proportions of FA and GGBS

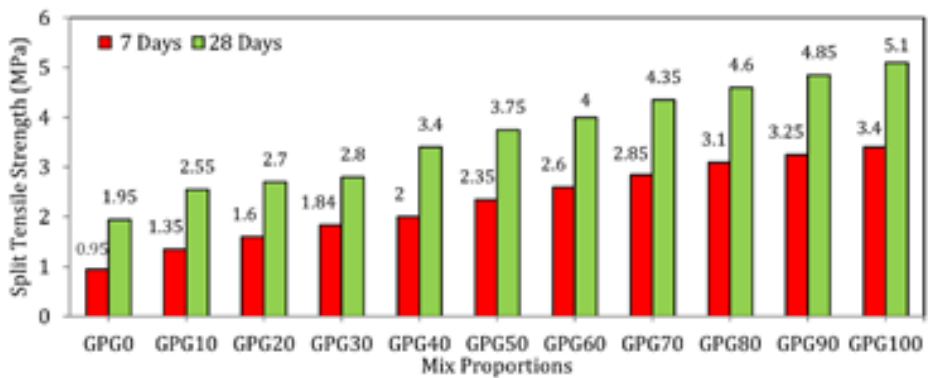


Fig. 10 Split tensile strength test for proportions of FA and GGBS

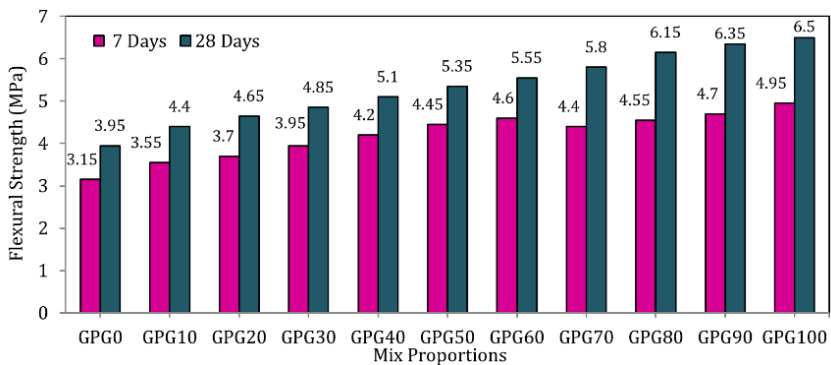


Fig. 11 Flexural strength test for proportions of FA and GGBS

3.1.2 Optimization of RHA proportion

The RHA was optimized with FA and GGBS (30%) based on the value of CS, STS and FS. The optimized proportion of FA-GGBS is taken with constant GGBS proportion and the FA is varied with RHA from 0 to 25% at an interval of 5%. CS of GPC with RHA proportion increases up to 15%, after that the strength decreased. CS of RHA proportions 0 to 15% at

7-days and 28-days ranges from 23.1 to 25.15 MPa and 37.51 to 39.5 MPa and 20% were 22.8 and 37.9 MPa, and for 25% were 21.1 and 36.2 MPa indicated from Fig.12. So, GPR15 was fixed as the optimum RHA-FA-GGBS proportion based on strength concern which is 39.5 MPa at 28 days.

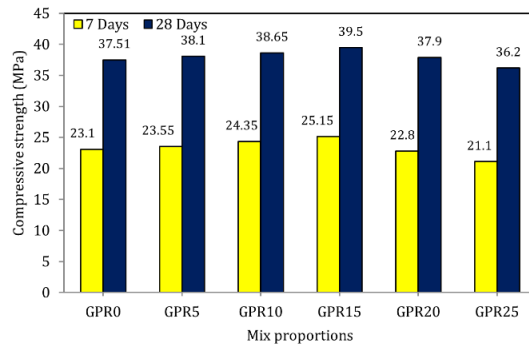


Fig. 12 Compressive strength tests for proportions of FA, GGBS, and RHA

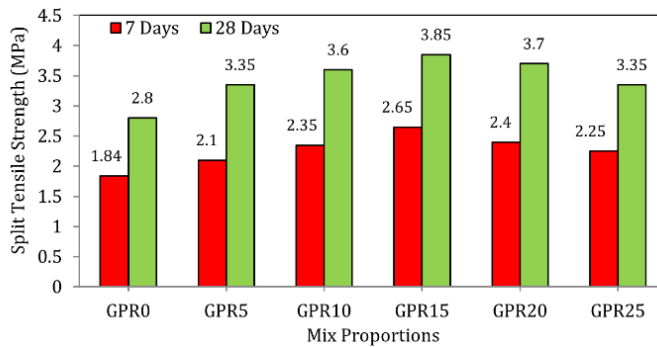


Fig. 13 Split tensile strength tests for proportions of FA, GGBS, and RHA

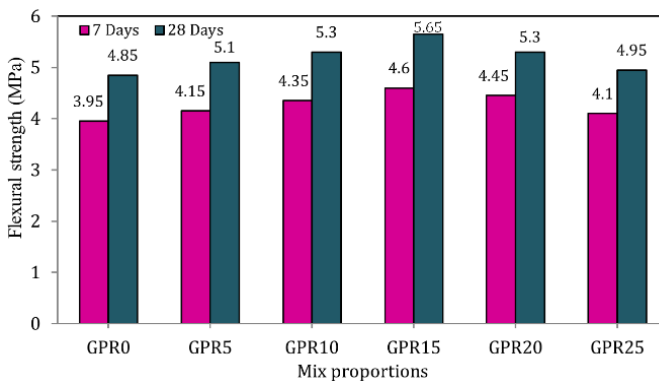


Fig. 14 Flexural strength tests for proportions of FA, GGBS, and RHA

STS of GPC with RHA proportion increases up to 15%, after which the strength decreased. CS of RHA proportions 0 to 15% at 7-days and 28-days ranges from 1.84 to 2.65 MPa and 2.8 to 3.85 MPa and 20% were 2.4 and 3.7 MPa, and for 25% were 2.25 and 3.35 MPa indicated from Fig.13. So, GPR15 was fixed as the optimum RHA-FA-GGBS proportion for strength concern which is 3.85 MPa at 28 days. FS of GPC with RHA proportion increases up to 15% after strength decreases beyond 15%. CS of RHA proportions 0 to 15% at 7-days

and 28-days ranges from 3.95 to 4.6 MPa and 4.85 to 5.65 MPa and 20% were 4.45 and 5.3 MPa, and for 25% were 4.1 and 4.95 MPa indicated from Fig.14. Based on the strength concern, GPR15 was fixed as the optimum RHA-FA-GGBS proportion was obtained as 5.65 MPa at 28 days.

3.1.3 Optimization of NS Proportion

Optimization of NS was determined for FA, GGBS (30%) and RHA (15%). The GGBS and RHA proportions were kept constant, and the FA varied with NS from 0 to 5% at an interval of 0, 1, 3, and 5%. CS, STS, FS test results were plotted for GPN0 to GPN5 in Fig. 15-17.

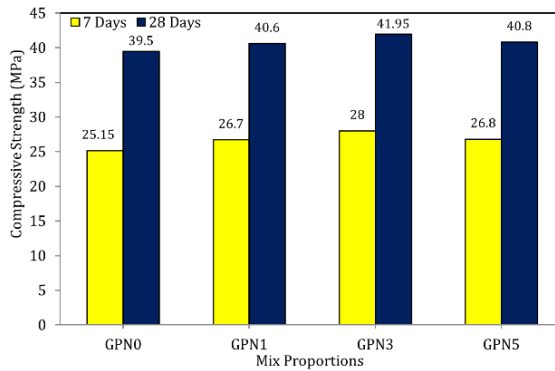


Fig. 15 Compressive strength tests for proportions of FA, GGBS, RHA, and NS

CS increased with NS proportion increased up to 3%, and the strength reduced beyond 3%. CS of NS proportions 0 to 3% at 7-days and 28-days ranges from 25.15 to 28 MPa and 39.5 to 41.95 MPa, whereas for 5% is 26.8 MPa and 40.8 MPa. STS increased with NS proportion increased up to 3%, and the strength reduced beyond 3%. STS of NS proportions 0 to 3% at 7-days and 28-days ranges from 2.65 to 3.4 MPa and 3.85 to 4.25 MPa, whereas for 5% is 3.15 MPa and 4.2 MPa. FS increased with NS proportion increased up to 3%, and the strength reduced beyond 3%. FS of NS proportions 0 to 3% at 7-days and 28-days ranges from 4.6 to 4.95 MPa and 5.65 to 6.1 MPa, whereas for 5% is 4.7 MPa and 5.75 MPa.

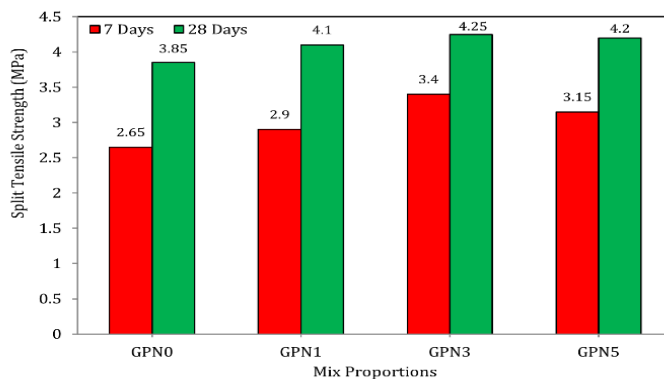


Fig. 16 Split tensile strength tests for proportions of FA, GGBS, RHA, and NS

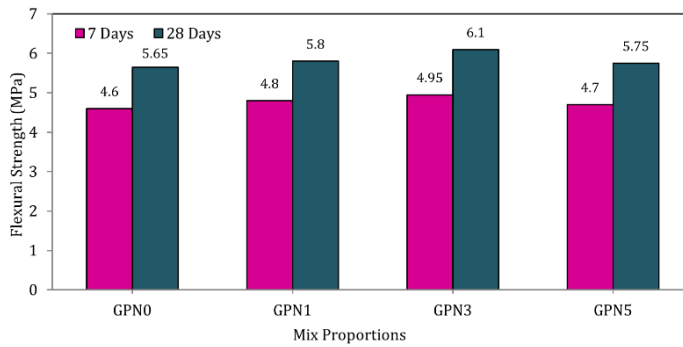
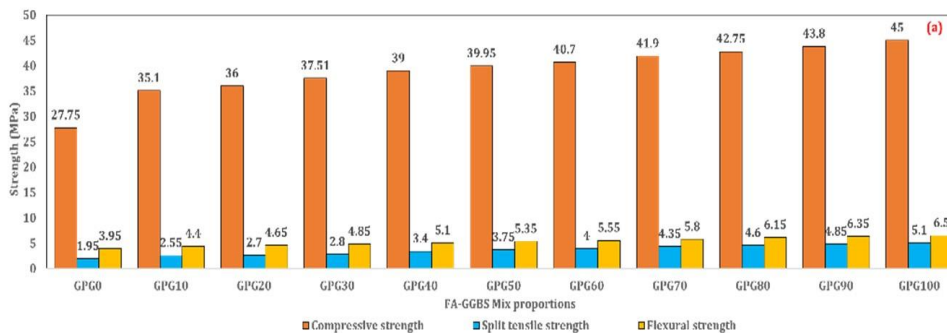


Fig. 17 Flexural strength tests for proportions of FA, GGBS, RHA, and NS

3.1.4 Combined and Optimum Strength of GPC

The combined CS, STS and FS of GPC with FA-GGBS shown in Fig. 18 (a-c). From Fig. 19, the GPC30 provides the test results of CS, STS, FS as 37.51, 2.8, 4.85 MPa, respectively. Also, the workability taken in to the account to obtained the optimum proportion as GPC30. The CS, STS, FS of GPC with different RHA proportion shown in Fig. 19. As the result of strength decrement beyond 15%, the optimum RHA proportion taken as GPR15 can deliver 39.5, 3.85, 5.65 MPa of CS, STS, FS, respectively. Fig. 19 shows the NS optimum proportions fixed as GPN3 (CS-41.95 MPa, STS-4.25 MPa, FS-6.1MPa) due to strength decreased after 3% of NS replacement.

The addition of GGBS influences the strength of GPC due to the higher calcium content than FA and aluminosilicate ratio, which improves the pozzolanic reaction. At the same time, Higher calcium content decreases the workability by reducing setting time in the GPC mix [63, 64]. Also, RHA addition provides supplementary cementitious material and increases the strength of GPC due to its high silica content and pozzolanic properties. However, it reduced more than 15% of RHA addition, causing a reduction of the aluminosilicate ratio in the GPR20 and GPR25. Simultaneously, RHA addition can decrease the workability of the GPC mix due to its finer particle size and higher surface area, which can absorb more water [65, 66]. Moreover, NS addition produces better strength than other GPC mixes due to its highly reactive pozzolanic material. Initially, workability increased up to 3% because the extremely finer particles of NS act as lubricants between particles, thus reducing friction and improving flowability. Simultaneously, it declined after 3% of NS addition due to a high surface area that adsorbs more water [67, 68].



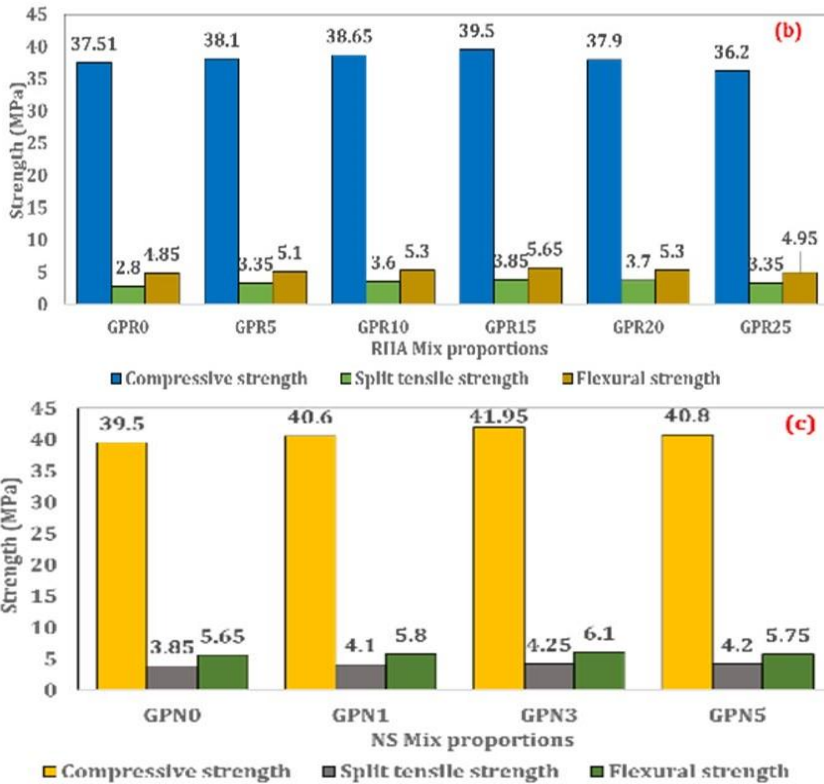


Fig. 18 Combined strength of GPC

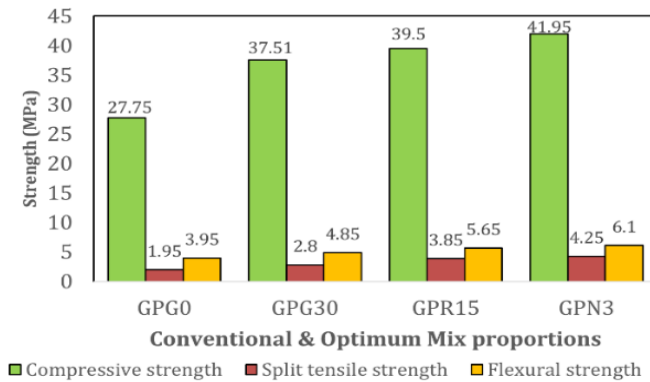


Fig. 19 Optimum strength of GPC

4. Conclusions and Future Research Directions

GPC is an environmentally safe concrete that reduces CO₂ emissions from cement production by replacing cement with industrial waste including FA and GGBS. There has been limited research on the effect of RHA and NS on GPC. Therefore, this study investigated the workability and strength characteristics of GPC incorporated with FA, GGBS, RHA, and NS. The following conclusions were drawn according to results obtained from GPC specimens.

- In the first aspect, with the increase in GGBS content the strength increased, and at the same time, the workability decreased in GPC specimens. Hence, the optimum proportion of 30% GGBS and 70% FA gave the optimum workability and strength at GPG30 mix. Considering all this, strength of GPC is influenced by GGBS in the initial fresh stage.
- In the second aspect, the addition of 15% RHA, 30% GGBS, and 55% FA obtained maximum strength and decreased the strength beyond 15% of RHA. The optimized RHA of 15% RHA gave the optimum workability and strength at GPR15 mix. Hence, GPC strength has increased significantly due to silica in RHA improved the polymer bonds.
- In the third group, 3% of NS, 15% of RHA, 30% of GGBS, and 52% of FA provide optimum strength and better workability at GPN3 due to the pore-filling effect, and the strength decreased beyond 3% as NS fills unreacted areas of GGBS and increased the of GPC strength.

Overall, the study results encourage the use of industrial by-products such as FA, GGBS, RHA, and NS in GPC to reduce the environmental damage from traditional cement production and CO₂ emission. This research recommends to utilizes the FA-GGBS-based GPC to achieve target mean strength. However, to promote sustainability with desired mean strength, this study would suggest replacing up to a certain percentage of RHA with FA. Moreover, to obtain strength with workability, the combination of NS with RHA, GGBS, and FA provides greater development than other combinations. Hence, GPC is a promising sustainable engineering composite material and could be used effectively for building materials.

Also, this paper suggests as future directions for the current study may be the synthesis of RHA-based sodium silicate for GPC and the resistance and volume expansion test on GPC that lay a strong foundation for the research and development in the field of Geopolymer concrete. The high energy required for the manufacturing process of Na₂SiO₃ is high and emits CO₂ from its production. So, Na₂SiO₃ may be substituted by synthesized sodium silicate solution from RHA and NS. Generally, Na₂SiO₃ was produced from the fusion of pure silica sand and sodium carbonate in furnaces at a melting temperature of 1400° Celsius. It emits anthropogenic gases such as CO₂, NO_x, SO_x, and dust that decrease the sustainability of GPC production. However, RHA-based Na₂SiO₃ has been substituted for commercial Na₂SiO₃ due to the equivalent weight ratio of SiO₂/Na₂O, and the process of RHA-based Na₂SiO₃ was comparatively simple and processes such as chemical synthesization by reflux or hydrothermal from RHA and NaOH mixture under minimum temperature from 80° to 140° Celsius. Therefore, the silica-rich RHA-based Na₂SiO₃ is enhancing sustainability by controlling harmful gas emissions during synthesization.

4.1. Assumptions and Limitations of the Study

- The influence of FA, RHA, GGBS, and NS in GPC has not been studied from microstructural analysis such as XRD, FTIR, SEM and EDX. Fresh and mechanical properties test results are assumed to be the effect and impact of materials that are used in GPC.
- The specimens were cured under ambient curing, and the temperature fluctuation might not affect the strength parameters.

Acknowledgement

The Author M. Maheswaran is grateful acknowledges to the International Research Centre (IRC), Kalasalingam Academy of Research and Education (KARE) for providing a University Research Fellowship (URF) and Instrumental research facilities from Geopolymer Laboratory.

References

- [1] Thakur M, Bawa S. Self-compacting geopolymer concrete: A review. *Materials Today: Proceedings*. 2022 Jan 1;59:1683-93. <https://doi.org/10.1016/j.matpr.2022.03.400>
- [2] Elahi MM, Hossain MM, Karim MR, Zain MF, Shearer C. A review on alkali-activated binders: Materials composition and fresh properties of concrete. *Construction and Building Materials*. 2020 Nov 10;260:119788. <https://doi.org/10.1016/j.conbuildmat.2020.119788>
- [3] Shaikh FU. Mechanical and durability properties of fly ash geopolymer concrete containing recycled coarse aggregates. *International Journal of Sustainable Built Environment*. 2016 Dec 1;5(2):277-87. <https://doi.org/10.1016/j.ijsbe.2016.05.009>
- [4] Abdullah WA, Ahmed HU, ALshkane YM, Rahman DB, Ali AO, Abubakr SS. The Possibility of Using Waste Plastic Strip to Enhance the Flexural Capacity of Concrete Beams. *Journal of Engineering Research*. 2021 Aug 22;9(ICRIE).
- [5] Davidovits J. Environmentally driven geopolymer cement applications. In *Proceedings of 2002 Geopolymer Conference*. Melbourne, Australia 2002 Oct 28.
- [6] Turner LK, Collins FG. Carbon dioxide equivalent (CO₂-e) emissions: A comparison between geopolymer and OPC cement concrete. *Construction and building materials*. 2013 Jun 1;43:125-30. <https://doi.org/10.1016/j.conbuildmat.2013.01.023>
- [7] Jindal BB, Sharma R. The effect of nanomaterials on properties of geopolymers derived from industrial by-products: A state-of-the-art review. *Construction and Building Materials*. 2020 Aug 20;252:119028. <https://doi.org/10.1016/j.conbuildmat.2020.119028>
- [8] Ganesh AC, Muthukannan M. Development of high performance sustainable optimized fiber reinforced geopolymer concrete and prediction of compressive strength. *Journal of Cleaner Production*. 2021 Feb 1;282:124543. <https://doi.org/10.1016/j.jclepro.2020.124543>
- [9] Provis JL, Palomo A, Shi C. Advances in understanding alkali-activated materials. *Cement and Concrete Research*. 2015 Dec 1;78:110-25. <https://doi.org/10.1016/j.cemconres.2015.04.013>
- [10] Abdollahnejad Z, Mastali M, Falah M, Luukkonen T, Mazari M, Illikainen M. Construction and demolition waste as recycled aggregates in alkali-activated concretes. *Materials*. 2019 Dec 3;12(23):4016. <https://doi.org/10.3390/ma12234016>
- [11] Alhawat M, Ashour A, Yildirim G, Aldemir A, Sahmaran M. Properties of geopolymers sourced from construction and demolition waste: A review. *Journal of Building Engineering*. 2022 Jun 1;50:104104. <https://doi.org/10.1016/j.jobe.2022.104104>
- [12] Jwaida Z, Dulaimi A, Mashaan N, Othuman Mydin MA. Geopolymers: The Green Alternative to Traditional Materials for Engineering Applications. *Infrastructures*. 2023 May 23;8(6):98. <https://doi.org/10.3390/infrastructures8060098>
- [13] Davidovits J. Geopolymeric reactions in archaeological cements and in modern blended cements. *Concr. Int*. 1987 Dec;9:23-9.
- [14] Qaidi SM, Tayeh BA, Zeyad AM, de Azevedo AR, Ahmed HU, Emad W. Recycling of mine tailings for the geopolymers production: A systematic review. *Case Studies in Construction Materials*. 2022 Jun 1;16:e00933. <https://doi.org/10.1016/j.cscm.2022.e00933>
- [15] Singh RP, Vanapalli KR, Cheela VR, Peddireddy SR, Sharma HB, Mohanty B. Fly ash, GGBS, and silica fume based geopolymer concrete with recycled aggregates: Properties and environmental impacts. *Construction and Building Materials*. 2023 May 16;378:131168.
- [16] Davidovits J. Global warming impact on the cement and aggregates industries. *World resource review*. 1994 Apr 4;6(2):263-78.
- [17] Hemalatha P, Ramujee K. Influence of nano material (TiO₂) on self compacting Geo

- polymer concrete containing Flyash, GGBS and wollastonite. *Materials Today: Proceedings*. 2021 Jan 1;43:2438-42. <https://doi.org/10.1016/j.matpr.2021.02.279>
- [18] Christy C, Tensing D. Effect of class-F fly ash as partial replacement with cement and fine aggregate in mortar. *Indian Journal of Engineering & Materials Sciences* Vol 17, p.140-144 (2010).
- [19] Qadir SU, Raja V, Siddiqui WA, Mahmooduzzafar, Abd_Allah EF, Hashem A, Alam P, Ahmad P. Fly-ash pollution modulates growth, biochemical attributes, antioxidant activity and gene expression in *pithecellobium dulce* (Roxb) benth. *Plants*. 2019 Nov 20;8(12):528. <https://doi.org/10.3390/plants8120528>
- [20] Kumar GV, Nivas KN, Kumar AS, Jyothirmai VV, Rao MD. Performance of M 30 grade concrete by replacing cement with GGBS and fine aggregate with quarry dust (2023).6510-6521
- [21] Farooq F, Jin X, Javed MF, Akbar A, Shah MI, Aslam F, Alyousef R. Geopolymer concrete as sustainable material: A state of the art review. *Construction and Building Materials*. 2021 Nov 1;306:124762. <https://doi.org/10.1016/j.conbuildmat.2021.124762>
- [22] Granulated Ground Blast Furnace Slag (GGBFS) Market Analysis: Industry Market Size, Plant Capacity, Production, Operating Efficiency, Demand & Supply, End-User Industries, Demand by Type, Sales Channel, Company Share, Foreign Trade, Regional Demand, 2015-. In: CHEMANALYST. [https://www.chemanalyst.com/industry-report/granulated-ground-blast-furnace-slag-ggbfs-market-713#:~:text=The global market size of with a CAGR of 3.20%25](https://www.chemanalyst.com/industry-report/granulated-ground-blast-furnace-slag-ggbfs-market-713#:~:text=The%20global%20market%20size%20of%20with%20a%20CAGR%20of%203.20%25).
- [23] Solomon AE, Woubishet ZT, Vo DH, Yehualaw MD. Rice Husk Ash in Concrete. *Sustainability*. 2023;15(1):137. <https://doi.org/10.3390/su15010137>
- [24] Faried AS, Mostafa SA, Tayeh BA, Tawfik TA. The effect of using nano rice husk ash of different burning degrees on ultra-high-performance concrete properties. *Construction and Building Materials*. 2021 Jul 5;290:123279.
- [25] Hwang CL, Huynh TP. Effect of alkali-activator and rice husk ash content on strength development of fly ash and residual rice husk ash-based geopolymers. *Construction and Building Materials*. 2015 Dec 30;101:1-9. <https://doi.org/10.1016/j.conbuildmat.2015.10.025>
- [26] Basri MS, Mazlan N, Mustapha F, Ishak MR. Correlation between compressive strength and fire resistant performance of rice husk ash-based geopolymer binder for panel applications. In MATEC web of conferences 2017 (Vol. 97, p. 01025). EDP Sciences. <https://doi.org/10.1051/mateconf/20179701025>
- [27] Babu GK, Rao KV, Dey S, Veerendra GT. Performance studies on quaternary blended Geopolymer concrete. *Hybrid Advances*. 2023 Apr 1;2:100019. <https://doi.org/10.1016/j.hybadv.2023.100019>
- [28] Yusuf AA, Inambao FL. Characterization of Ugandan biomass wastes as the potential candidates towards bioenergy production. *Renewable and Sustainable Energy Reviews*. 2020 Jan 1;117:109477. <https://doi.org/10.1016/j.rser.2019.109477>
- [29] Wongpa J, Kiattikomol K, Jaturapitakkul C, Chindapasirt P. Compressive strength, modulus of elasticity, and water permeability of inorganic polymer concrete. *Materials & Design*. 2010 Dec 1;31(10):4748-54. <https://doi.org/10.1016/j.matdes.2010.05.012>
- [30] Kaur K, Singh J, Kaur M. Compressive strength of rice husk ash based geopolymer: The effect of alkaline activator. *Construction and Building Materials*. 2018 Apr 30;169:188-92. <https://doi.org/10.1016/j.conbuildmat.2018.02.200>
- [31] Althoey F, Zaid O, Martínez-García R, Alsharari F, Ahmed M, Arbili MM. Impact of Nano-silica on the hydration, strength, durability, and microstructural properties of concrete: A state-of-the-art review. *Case Studies in Construction Materials*. 2023 Mar 15:e01997. <https://doi.org/10.1016/j.cscm.2023.e01997>
- [32] Zhang Z, Li Z, He J, Shi X. High-strength engineered cementitious composites with nanosilica incorporated: Mechanical performance and autogenous self-healing

- behavior. *Cement and Concrete Composites*. 2023 Jan 1; 135:104837.
<https://doi.org/10.1016/j.cemconcomp.2022.104837>
- [33] Aly S, Achraf A, Mohamed Z. Beneficial use of nano-silica in concrete: A review. *Trends in Civil Engineering and its Architecture*. 2018;1(1):1-3.
<https://doi.org/10.32474/tceia.2018.01.000105>
- [34] Rahmawati C, Aprilia S, Saidi T, Aulia TB, Hadi AE. The effects of nanosilica on mechanical properties and fracture toughness of geopolimer cement. *Polymers*. 2021 Jun 30;13(13):2178. <https://doi.org/10.3390/polym13132178>
- [35] Ibrahim M, Johari MA, Maslehuddin M, Rahman MK. Influence of nano-SiO₂ on the strength and microstructure of natural pozzolan based alkali activated concrete. *Construction and Building Materials*. 2018 Jun 10;173:573-85.
<https://doi.org/10.1016/j.conbuildmat.2018.04.051>
- [36] Deb PS, Sarker PK, Barbhuiya S. Sorptivity and acid resistance of ambient-cured geopolimer mortars containing nano-silica. *Cement and Concrete Composites*. 2016 Sep 1;72:235-45. <https://doi.org/10.1016/j.cemconcomp.2016.06.017>
- [37] Singh LP, Ali D, Tyagi I, Sharma U, Singh R, Hou P. Durability studies of nano-engineered fly ash concrete. *Construction and Building Materials*. 2019 Jan 10;194:205-15. <https://doi.org/10.1016/j.conbuildmat.2018.11.022>
- [38] Singh LP, Ali D, Sharma U. Studies on optimization of silica nanoparticles dosage in cementitious system. *Cement and Concrete Composites*. 2016 Jul 1;70:60-8.
<https://doi.org/10.1016/j.cemconcomp.2016.03.006>
- [39] Singh LP, Zhu W, Howind T, Sharma U. Quantification and characterization of CSH in silica nanoparticles incorporated cementitious system. *Cement and Concrete Composites*. 2017 May 1; 79:106-16.
<https://doi.org/10.1016/j.cemconcomp.2017.02.004>
- [40] Guades EJ. Experimental investigation of the compressive and tensile strengths of geopolimer mortar: The effect of sand/fly ash (S/FA) ratio. *Construction and Building Materials*. 2016 Nov 30;127:484-93.
<https://doi.org/10.1016/j.conbuildmat.2016.10.030>
- [41] Soutsos M, Boyle AP, Vinai R, Hadjierakleous A, Barnett SJ. Factors influencing the compressive strength of fly ash based geopolymers. *Construction and Building Materials*. 2016 May 1;110:355-68.
<https://doi.org/10.1016/j.conbuildmat.2015.11.045>
- [42] Verma M, Dev N. Sodium hydroxide effect on the mechanical properties of flyash-slag based geopolimer concrete. *Structural Concrete*. 2021 Jan;22: E368-79.
<https://doi.org/10.1002/suco.202000068>
- [43] Srinivas Reddy K, Bala Murugan S. A Study on Strength Properties and Cost Analysis of Industrial Byproduct-Based Ternary Blended Geopolimer Concrete. In *Emerging Technologies for Agriculture and Environment: Select Proceedings of ITsFEW 2018 2020* (pp. 95-106). Springer Singapore.
- [44] Ramani PV, Chinnaraj PK. Geopolimer concrete with ground granulated blast furnace slag and black rice husk ash. *Gradevinar*. 2015 Sep 11;67(08.):741-8.
<https://doi.org/10.14256/JCE.1208.2015>
- [45] Das SK, Mishra J, Singh SK, Mustakim SM, Patel A, Das SK, Behera U. Characterization and utilization of rice husk ash (RHA) in fly ash-Blast furnace slag based geopolimer concrete for sustainable future. *Materials Today: Proceedings*. 2020 Jan 1;33:5162-7.
<https://doi.org/10.1016/j.matpr.2020.02.870>
- [46] Dara DR, Bhogayata AC. Experimental study of RHA-FA based geopolimer composites. *Int J Sci Res Dev*. 2015;3(4):1615-7.
- [47] Nuaklong P, Jongvivalsakul P, Pothisiri T, Sata V, Chindaprasirt P. Influence of rice husk ash on mechanical properties and fire resistance of recycled aggregate high-calcium fly ash geopolimer concrete. *Journal of Cleaner Production*. 2020 Apr 10;252:119797. <https://doi.org/10.1016/j.jclepro.2019.119797>

- [48] Manikandan P, Natrayan L, Duraimurugan S, Vasugi V. Influence of waste glass powder as an aluminosilicate precursor in synthesizing ternary blended alkali-activated binder. *Silicon*. 2022 Aug;14(13):7799-808. <https://doi.org/10.1007/s12633-021-01533-2>
- [49] Shilar FA, Ganachari SV, Patil VB, Khan TY, Javed S, Baig RU. Optimization of alkaline activator on the strength properties of geopolymer concrete. *Polymers*. 2022 Jun 16;14(12):2434. <https://doi.org/10.3390/polym14122434>
- [50] Chiranjeevi K, Vijayalakshmi MM, Praveenkumar TR. Investigation of fly ash and rice husk ash-based geopolymer concrete using nano particles. *Applied Nanoscience*. 2023 Jan;13(1):839-46. <https://doi.org/10.1007/s13204-021-01916-2>
- [51] Jumaa NH, Ali IM, Nasr MS, Falah MW. Strength and microstructural properties of binary and ternary blends in fly ash-based geopolymer concrete. *Case Studies in Construction Materials*. 2022 Dec 1;17:e01317. <https://doi.org/10.1016/j.cscm.2022.e01317>
- [52] Mustakim SM, Das SK, Mishra J, Aftab A, Alomayri TS, Assaedi HS, Kaze CR. Improvement in fresh, mechanical and microstructural properties of fly ash-blast furnace slag based geopolymer concrete by addition of nano and micro silica. *Silicon*. 2021 Aug;13:2415-28. <https://doi.org/10.1007/s12633-020-00593-0>
- [53] Behfarnia K, Rostami M. Effects of micro and nanoparticles of SiO₂ on the permeability of alkali activated slag concrete. *Construction and building materials*. 2017 Jan 30;131:205-13.
- [54] ASTM Committee. "ASTM C618-19 (2019) Standard specification for coal fly ash and raw or calcined natural pozzolan for use in concrete. ." Barr Harbor Drive, West Conshohocken: Annual Book of ASTM Standards
- [55] Indian Standards IS 383 (2016):Coarse and Fine Aggregate for Concrete-Specification. Bur. Indian Stand. BIS, New Delhi India 110002
- [56] Patankar SV, Ghugal YM, Jamkar SS. Mix design of fly ash based geopolymer concrete. In *Advances in structural engineering: Materials*, volume three 2015 (pp. 1619-1634). Springer India.
- [57] Anuradha R, Sreevidya V, Venkatasubramani R, Rangan BV. Modified guidelines for geopolymer concrete mix design using Indian standard.
- [58] Rao GM, Venu M. Mix design methodology for fly ash and GGBS-based geopolymer concrete. *Adv Struct Eng*. Springer, Singapore. 2020 May 13:173-81.
- [59] Rajamane NP, Jeyalakshmi R. Quantities of sodium hydroxide solids and water to prepare sodium hydroxide solution of given molarity for geopolymer concrete mixes. Indian Concrete Institute Technical Paper, SRM University, India. 2014 Aug.
- [60] American Society for Testing and Materials (2001) *Astm C39/C39M. Stand Test Method Compressive Strength Cylind Concr Specimens 04:1-5*
- [61] ASTM C. Standard test method for splitting tensile strength of cylindrical concrete specimens. C496/C496M-11. 2011.
- [62] Indian Standard Method of Test for Strength of concrete (1959) IS: 516-1959. Bur Indian Stand BIS, New Delhi India 110002
- [63] Jayanthi V, Avudaiappan S, Amran M, Arunachalam KP, Qader DN, Delgado MC, Flores EI, Rashid RS. Innovative use of micronized biomass silica-GGBS as agro-industrial by-products for the production of a sustainable high-strength geopolymer concrete. *Case Studies in Construction Materials*. 2023 Jul 1;18: e01782. <https://doi.org/10.1016/j.cscm.2022.e01782>
- [64] Singh RP, Reddy PS, Vanapalli KR, Mohanty B. Influence of binder materials and alkali activator on the strength and durability properties of geopolymer concrete: A review. *Materials Today: Proceedings*. 2023 May 20. <https://doi.org/10.1016/j.matpr.2023.05.226>
- [65] Varma VC, Nagaraju TV, Raju JN, Alisha SS, Chaitanya MS. Understanding the potential role of precursor content in the geopolymer concrete strength development. *Materials*

- Today: Proceedings. 2023 May 20. <https://doi.org/10.1016/j.matpr.2023.05.227>
- [66] Patel YJ, Shah N. Development of self-compacting geopolymer concrete as a sustainable construction material. *Sustainable Environment Research*. 2018 Nov 1;28(6):412-21. <https://doi.org/10.1016/j.serj.2018.08.004>
- [67] Ahmed HU, Mohammed AS, Faraj RH, Qaidi SM, Mohammed AA. Compressive strength of geopolymer concrete modified with nano-silica: Experimental and modeling investigations. *Case Studies in Construction Materials*. 2022 Jun 1;16:e01036. <https://doi.org/10.1016/j.cscm.2022.e01036>
- [68] Ahmed HU, Mohammed AS, Mohammed AA. Fresh and mechanical performances of recycled plastic aggregate geopolymer concrete modified with Nano-silica: Experimental and computational investigation. *Construction and Building Materials*. 2023 Aug 29;394:132266. <https://doi.org/10.1016/j.conbuildmat.2023.132266>

Blank Page



Research Article

Characteristic evaluation of concrete containing sugarcane bagasse ash as pozzolanic admixture

Yogitha Bayapureddy^{1,a*}, Karthikeyan Muniraj^{1,b}, Munireddy Mutukuru Gangireddy^{2,c}

¹Dept. of Civil Engineering, Vignan's Foundation for Science, Technology, and Research, Vadlamudi, Guntur 522213, A P, India

²Department of Civil Engineering, Andhra University, Visakhapatnam, A P, India

Article Info

Abstract

Article history:

Received 12 July 2023

Accepted 13 Aug 2023

Keywords:

Sugarcane bagasse ash concrete;
Pozzolanic reactivity;
Microstructure;
Strengths;
Sorptivity;
Acid attack;
Mass loss;
Strength loss

This study presents the influence of sugar cane bagasse ash (SCBA) as pozzolanic material on the microstructure, strength and durability properties of concrete. To enhance the pozzolanic properties of raw SCBA, it is incinerated at 6000C for 2 hours in muffle furnace at the rate of 100C/min and ball-milled for 240 minutes to increase its fineness more than cement. SCBA is pre-treated to remove adhered water molecules by heating to 100°C for 24 hours and then it is characterised by SEM/EDS, XRF, FTIR and TGA tests to assess the microstructural properties. In this study cement is replaced by SCBA with 5,10,15,20 and 25% by weight of cement to examine the mechanical and durability properties of concrete. The optimum dosage of SCBA is determined based on various tests conducted on concrete and it is found to be 15%. The tests conducted are compressive strength, split tensile strength, sorptivity, and acid resistance. A maximum strength gain is observed with 15% replacement of cement by SCBA with an increment of 14.8%, 20% and 18.2% for compressive strength at 28, 56 and 90 days, respectively, due to enhanced pozzolanic reactivity and improved microstructure of SCBA concrete and split strength is increased in the range of 16% to 18% over the reference concrete mix. The sorptivity of SCBA concrete is found to reduce by 24.4% compared to reference mix at 15% replacement. The mass loss, strength loss, and dimensional loss are studied on concrete samples based on acid resistance test. The SCBA blended concrete with 15% replacement of cement showed the least acid durability lost factor which is 305.5 with sulphuric acid and 351.72 with hydrochloric acid.

© 2023 MIM Research Group. All rights reserved.

1. Introduction

Agro-based industries generates huge amount of rice husk ash, sugarcane bagasse ash, palm oil fuel ash, wheat straw ash containing inorganic, carbon-rich, fibrous particles causing air, soil and water pollution due to their improper disposal. These ashes have the major composition of carbon and silica oxides which are can be used for enhancing pozzolanic reactivity. Hence, they have wide potential in replacement of cement in concrete composites as mineral admixtures in finely divided form [1-5].

Cement is an important ingredient of concrete which is a widely used material in construction industry. However, concrete has several drawbacks such as low tensile strain, poor microstructure, high permeability and low durability characteristics in aggressive environment. To overcome these drawbacks, supplementary cementitious materials (pozzolans) are widely used in concrete composites. Fly ash, ground granulated blast furnace slag, meta-kaolin, and silica-fume are the commonly used admixtures because of the high silica, alumina and iron oxides content and less loss of ignition. Several studies

*Corresponding author: yogitha0607@gmail.com

^a orcid.org/0000-0003-0876-6919; ^b orcid.org/0000-0001-9961-2098; ^c orcid.org/0000-0002-7889-5655
DOI: <http://dx.doi.org/10.17515/resm2023.819ma0712>

Res. Eng. Struct. Mat. Vol. 9 Iss. 4 (2023) 1287-1307

reported that SCBA is highly siliceous and possesses pozzolanic properties as it contains all the elements present in ordinary Portland cement. A comprehensive review on bagasse ash as pozzolanic material is presented by Thomas et al. [6].

The performance of SCBA in pavement concreting, and soil stabilization is examined by Batool et al. [7]. Characterization of laboratory bagasse ash (LBA), filter bagasse ash (FBA), and bottom bagasse ash (BBA) has been performed by Frías et al. [8]. LBA obtained by heating at 400 °C for 20 minutes and 800 °C for 60 minutes has shown the highest lime fixation, exhibiting excellent pozzolanic performance compared to BBA and FBA. BBA is observed to be inert because of over-crystallisation and adhered sand particles, represented as quartz in XRD studies.

Arif et al. [9] studied the performance of bagasse ash on cement, mortar, and concrete. The effect excess lime in cement pastes even after the pozzolanic reaction due to the absence of semi-amorphous SCBA and phase transition at high temperature on pozzolanic activity are examined. The pozzolanic activity index higher than 75% due to the filler effect with the replacement levels of 5, 10, and 15% is reported. Arif et al. [10] studied the deterioration in conventional and SCBA concretes with SCBA as a replacement of sand. Mortar cubes are cast and exposed to Na₂SO₄ diluted by 1% in water for 28 and 90 days. It is observed that SCBA is unreactive, and mass loss is less for 10 % and 15% replacements.

Mali and Nanthagopalan [11] observed recalcination of SCBA at 600-700°C as optimum temperature to maintain the inherently amorphous nature to exhibit a good pozzolanic reactivity by confirming with the modified Chapelle test and Frattini test. The effect of calcination temperature and fineness on the pozzolanic performance of bagasse ash is also reported by Bahurudeen et al. [12, 13]. Reduction in fineness and loss of ignition (LOI) is highly recommended to improve the reactivity. ASTM C-618 recommended a maximum LOI of 12 % beyond which the ash cannot be called class F pozzolans [14].

The effect of inclusion of pozzolanic sugarcane bagasse ash on rheology, durability and strength properties with various replacement levels is reported in few studies with significant improvement in these properties. The 10% sugarcane bagasse ash replacement level is observed to be optimum for significant improvement concrete properties [15-19]. Subramaniyan and Sivaraja [20] discussed the performance of SCBA concrete with 0% to 40% replacements of cement on workability, mechanical and durability of SCBA concrete. Durability is assessed using sulphate attack, chloride attack, rapid chloride permeability and sorptivity tests. The strength and durability properties of SCBA concrete are shown to be improved due to pozzolanic reactivity and filler effect of SCBA in concrete mix.

Chindaprasirt et al. [21] assessed the mechanical and durability properties, chloride resistance and microstructure of Portland fly ash cement concrete containing high volume bagasse ash. It is shown that the addition of high-volume SCBA into the concrete mix reduced the water demand and chloride penetration depth due to the reduction of critical pore size resulting from the synergistic effect. Rajasekhar et al. [22] examined the durability characteristics of ultra high strength concrete with treated sugarcane bagasse ash. The ultra high strength gain of 70% with SCBA as admixture attaining 160 MPa at an optimum replacement of 15% is reported along with the resistance to chloride ion penetration and decreased sorptivity.

Tripathy and Acharya [23], Prabhath et al. [24] presented the reviews on characterization of bagasse ash and its use in concrete as a supplementary binder and reported the studies on rheology, strength and durability of SCBA modified concrete. An optimum replacement of 20% is shown to be effective as a supplementary binder and filler material.

Zareei et al. [25] studied the microstructure, strength, and durability of eco-friendly concretes containing sugarcane bagasse ash. It is concluded that incorporation of SCBA up

to 5% improved the performance of concrete in terms of strength, durability and impact resistance.

From previous researches it is observed that optimum replacement dosage of SCBA is varying from 5-20% in production of concrete. The improvement of properties of cement mortar or concrete depend on several factors such as pre-treatment conditions, chemical composition, LOI, and particle size distribution or specific surface area or fineness of SCBA. A detailed investigation is necessary to understand the material properties of SCBA to bring out into the existing usage. Besides, limited studies are observed on acid resistivity of SCBA based concrete.

The present study deals with characterization of locally available SCBA after heating at 600°C for 2 hours followed by ball milling of 240 minutes to enhance the material properties and understanding its morphology by SEM, TG/DTA, and FTIR analysis. The suitability of SCBA is examined for strength and durability studies on standard concrete by replacing cement with SCBA by 5, 10, 15, 20 and 25%. A reference mix of M₃₅ grade is used to compare the results of the strength and durability parameters of SCBA concrete. The influence of SCBA is examined on compressive strength, split tensile strength, capillary sorption, and acid resistivity to find the optimum replacement level.

1.1. Research Significance

Cement is the most energy intensive material in concrete production. To minimize the environmental hazards from cement industry, there is a need to use less energy intensive materials. Efforts are being made to find supplementary materials to replace cement. SCBA has such potential. This paper deals with the physiochemical characterization of SCBA and its influence on the properties of concrete and provides information on SCBA modified concrete with respect to strength and durability of standard concrete.

2. Materials and Methods

2.1 Materials

Ordinary Portland Cement (OPC) of compressive strength 53 MPa at 28 days confirming to IS 12269 (2013) [26], granite originated coarse aggregates of 20 mm and 12mm size, and river sand confirmed to IS 383: 2016 [27] are used in the present study for concrete mix design. Results of sieve analysis are presented in Fig. 1.

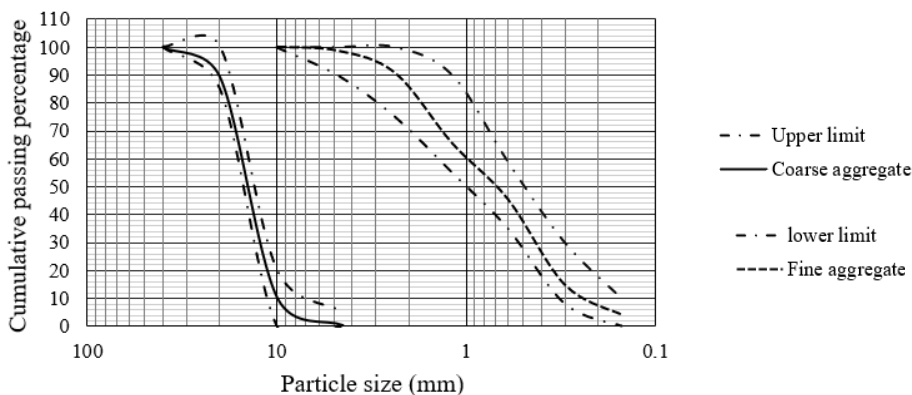


Fig. 1 Sieve analysis of coarse and fine aggregate

SCBA is collected from local sugar mills and pre-treated at 100°C to remove the moisture before mixing with OPC. Further, SCBA is heated at 600°C for 2 hours and pulverized to

micro-size (finely divided) by ball milling for 240 minutes to crush the quartz-silica and improve the specific surface area of SCBA particles. Standard sand is used to carry out the strength activity test of SCBA.

2.2 Physical Properties

Specific surface area, soundness, specific gravity of the cement, raw bagasse ash and processed ash are measured confirmed to IS 1727:1967 [28] and loss of ignition (LOI) determined according to IS 4032(1985) [29] by Blaine's air permeability apparatus Soundness test is performed using Le-Chatelier's apparatus to confirm the presence of magnesium in cement pastes which causes volumetric change. Specific gravity is an indirect measure of carbon content. Lower specific gravity leads to low reactivity due to the high porosity, volumetric change and water retention among particles. So, specific gravity is tested to find the influence on the pozzolanic reactivity of concrete.

2.3 Micro-Structural Studies

SCBA is tested in its as-received form and tailored to suit the properties of cement. VEGA 3 SBH (TESCAN Brno SRO) Scanning electron microscope is used to understand the morphology of SCBA and concrete samples. A beam of electrons is allowed to pass through a vacuum medium, only to hit the amorphous sample, which tends to generate secondary electrons, backscattered electrons and x-rays. The images and refracted electrons data from SEM associated with EDS are used to study the bagasse ash's particle size, texture and elemental composition. Mass loss of sugarcane bagasse ash with temperature change is studied by thermos-gravimetric analysis associated with DTG and DTA by Hitachi STA 7200. The energy absorption of the sample is determined to identify the SiO₂ functional group using Fourier transformation infrared spectroscopy (FTIR). XRF study is done to find the complete composition of the sample which is used to characterize the output of experimental result.

2.4 Strength Activity Index (SAI):

SAI is determined by casting 3 cubes of SCBA based motors and 3 cubes of OPC motors of 50 mm size on each side as specified by IS 1727:1967[28]. The compressive strength test of the cubes is evaluated to find the percentage of SAI by the following formula:

$$\text{Strength Activity Index (SAI)} = \frac{A}{B} \times 100$$

A= Average compressive strength of SCBA motor

B=Average compressive strength of control mix

2.5 Mechanical Properties:

Normal Concrete of M35 grade is prepared according to IS 10262:2019 [30] as a reference mix. The mix proportions of ingredients are shown in Table 1. A poly-carboxylate ether-based superplasticizer is used to attain the desired workability of concrete. Compressive strength and split tensile strength tests are conducted according to IS 516:1959 [31] on standard samples. 90 concrete cubes of 150 mm size for compressive strength and 90 cylinders of 300 x 150 mm for split tensile strength were cast conforming to IS 5816:1999 [32] to understand the behaviour of SCBA concrete in compression and tension. Samples were cured in potable water of pH 7, free from chemicals and particulate solids for 3, 7, 28, 56 and 90 days.

For each variable of compressive strength, mean of 3 samples is taken to present the final test results after finding the difference between the samples is less than 15% of mean compressive strength. The test results of the samples are taken as average of the strength of three specimens after checking the variation which is less than 15% of the average[7].

Table 1. Materials used in the present study (Kg/m³)

% SCBA replaced	Cement (Kg)	SCBA (Kg)	Aggregates (Kg)	Sand (Kg)	Water (Kg)	Plasticizer (Kg)
0	383.16	0	1287.4	674.37	172.42	3.83
5	364.00	19.16	1287.4	674.37	172.42	3.83
10	344.84	38.32	1287.4	674.37	172.42	3.83
15	325.68	57.48	1287.4	674.37	172.42	3.83
20	306.52	76.63	1287.4	674.37	172.42	3.83
25	287.37	95.80	1287.4	674.37	172.42	3.83

2.6. Durability Properties

Sorptivity is the measure of the surface porosity of concrete. ASTM C 1585:2013 [33] is used to perform this test and study the level of the permeability of the samples on the surface of adsorption. The circumference of the sample is sealed to stop the ingress of molecules from the non-experimental surfaces. The results of sorptivity are evaluated from the formula;

$$I = m_t / ad \tag{1}$$

where I = the absorption in mm, m_t = change in mass of the specimen in gm at time t , a = the exposed area of the specimen, in mm², and d = the density of the water in g/mm³.

2.7. Acid Resistivity

An acid tolerance test is conducted on 100 mm cube samples which are cured in water for 28 days with 3% HCl and H₂SO₄ as per ASTM C666 [34] and tested according to ASTM C267-01 [35]. The effect of acid reaction on cement compounds is studied by exposing the samples to acid media in the laboratory with respect to stability of dimensions, mass loss and strength loss of concrete and assessed the effects with following procedures.

- The change in diagonal dimensions is evaluated before and after immersing the samples in an acid bath, and an acid attack is noted from the formula
 Acid attack factor = $(\Delta A/A) * 100$,
 ΔA = Change in dimensions with respect to immersion for 28 days,
 A = Original dimensions before immersion.
- Mass loss is the effect of acid on turning the calcium hydroxide into a white precipitate, which affects the bonding properties of concrete.
 Mass loss factor (%) = $(\Delta M/M) * 100$,
 ΔM = Change in mass with respect to immersion for 28 days,
 M = Mass of OPC/SCBA concrete before acid attack.
- The mechanical properties of acid-immersed samples are evaluated to find the resistance to chemical attack and the integrity of the concrete. The strength of samples is taken at the age of 28 days curing, and it is calculated as
 Strength loss factor (%) = $(\Delta C/C) * 100$
 ΔC = Compressive strength changed due to acid attack,
 C = Compressive strength of reference samples (0% SCBA) at 28 days.

The durability loss due to several factors are studied from the following formula.

$$\text{Acid durability loss factor (ADLF)} = (\text{Mass loss}) * (\text{Strength loss}) * (\text{Dimension loss})$$

3. Results and Discussion

3.1. Physical Properties

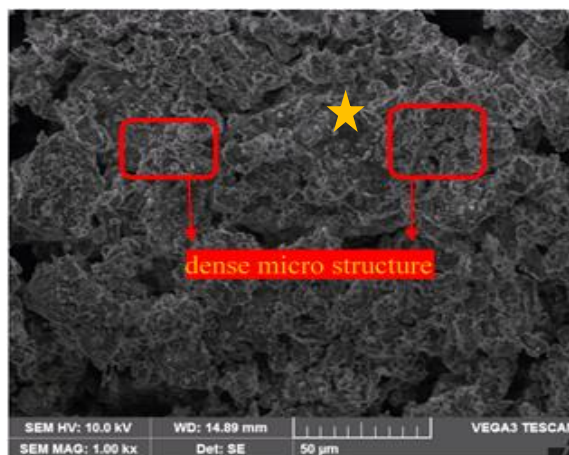
Results in Table 2 shows the soundness of SCBA is observed to be within the limits of 10mm. Due to pre-treatment, there appeared to be mass loss and particle morphology in SCBA. Presence of high carbon, organic substances lead to high LOI. Reduction in LOI and specific gravity resulted from testing the sample at 1000⁰C heated for 30 minutes is observed in the present study. Studies reported a low binding property and poor pozzolanic reactivity due to high LOI [14, 19]. High LOI leads to less reactivity as reported by earlier studies. Increased specific surface area in SCBA from 132 m²/Kg to 441 m²/Kg is resulted from grinding the particles.

Table 2. Physical properties of SCBA and OPC

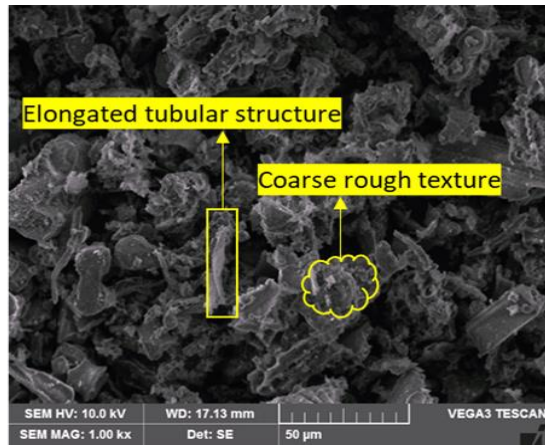
Property	Raw SCBA	Processed SCBA	OPC
Specific surface area (m ² /Kg)	132	441	300
Specific gravity	1.8	2.00	3.15
Soundness (mm)	2.1	1.79	1.80
LOI (%)	22.5	4.20	3.00

3.2. Micro-Structural Properties

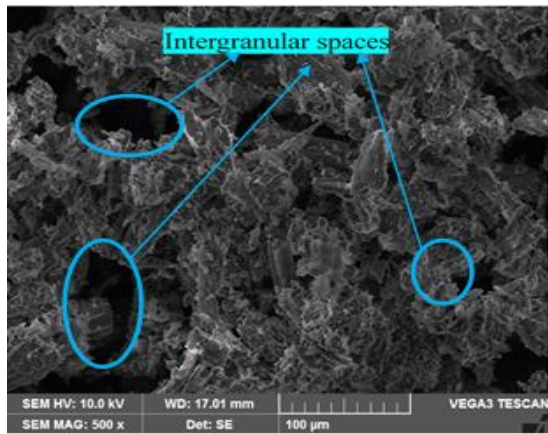
SEM micrographs of OPC and SCBA show a variation in particle size, texture, and package density. Fig 2(a) represents a thick and densely packed molecular structure of OPC. In SCBA samples, SEM micrographs shown in Fig. 2(b) depicts tubular, flaky, cylindrical, coarse, and rough textured structure. Rough texture replicates the original particle texture of SCBA whose particle size was above 150 microns. Researches noted that the rough texture led to water retention and reduced flowability of SCBA while mixing with concrete ingredients [11]. Fig. 2(c) shows higher spaces between the particles which reduced density of SCBA and resulted in low specific gravity. Fig. 2(d) shows voids on the surface of SCBA particles resulted from partial or improper combustion.



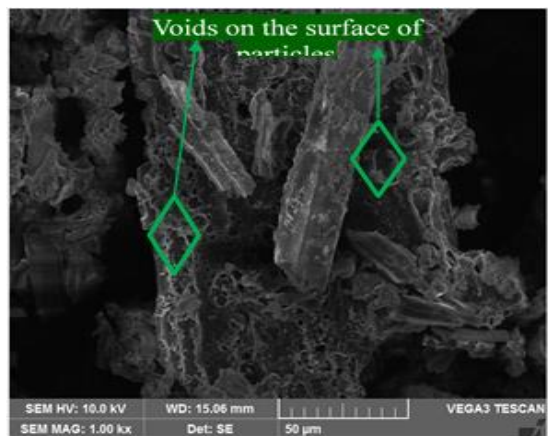
(a)



(b)



(c)



(d)

Fig. 2 SEM images of OPC and SCBA

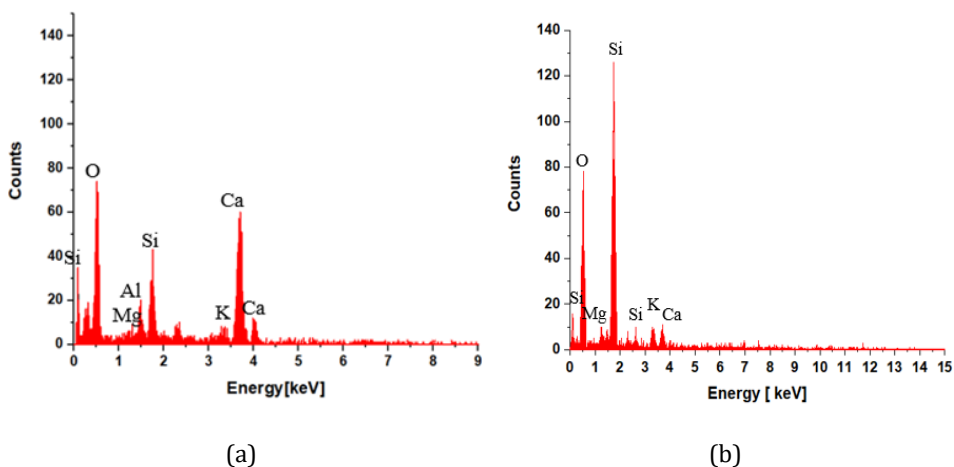


Fig. 3 EDS of OPC and SCBA

Elemental composition of OPC and SCBA, associated with SEM from Fig. 3 indicates that silica oxide dominates other elemental oxides in SCBA, and Ca dominates in OPC. The results of EDS are presented in Table 3. The total oxide composition of silica, alumina and iron are found to be 79.45% which satisfies the minimum criteria of class N pozzolan [36]. Fig.4 shows FTIR spectra with a huge peak with a wavenumber of 1048 due to stretching of SiO₂ ions after absorbing the energy. Mali and Nanthagopalan [11] observed broad peak at 1104 cm⁻¹ which is recognized as vibration of Si-O bond.

Table 3. Mineral composition of OPC and SCBA

Mineral Oxides	Raw SCBA	Processed SCBA	OPC
SiO ₂	43.10	68.38	19.82
CaO	3.45	5.26	63.2
Al ₂ O ₃	4.42	5.25	4.08
Fe ₂ O ₃	6.45	5.82	3.28
MgO	2.13	2.65	4.32
Na ₂ O	1.23	0.06	0.05
K ₂ O	2.55	2.62	0.78

Thermo-gravimetric analysis (TGA) studies are conducted to find the amount of organic and inorganic composition in material. Results are shown in Fig. 5. The volatile, thermal sensitive and non-metallic oxides are expected to exhibit their behaviour when exposed to gradual heating. From previous thermo-gravimetric analysis on mass loss of rice husk ash particles, there appeared 3 major peaks. In 1% of total weight reduction, 5.87% of weight loss is due to elimination of water molecules, 48.05% due to active pyrolysis and 20.14% due to passive pyrolysis [37]. In present study, SCBA shows a weight loss from 100 to 95.8% with a major weight loss in 2 peaks. Out of total mass loss of 4.2%, a loss of 48% occurred between 85 to 100 °C and 28.25% between 200 to 300 °C due to removal of water molecules and CO₂, caused by heating after which temperature gets flattered. DTA graph (Fig. 4) shows an exothermic hump from 100°C to 400°C and a gradual decrease from 400°C onwards showing a release of thermal energy caused by decomposition. The results agree with LOI and TGA studies.

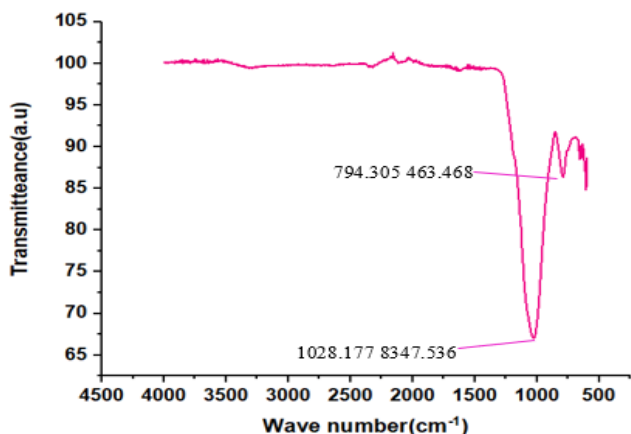
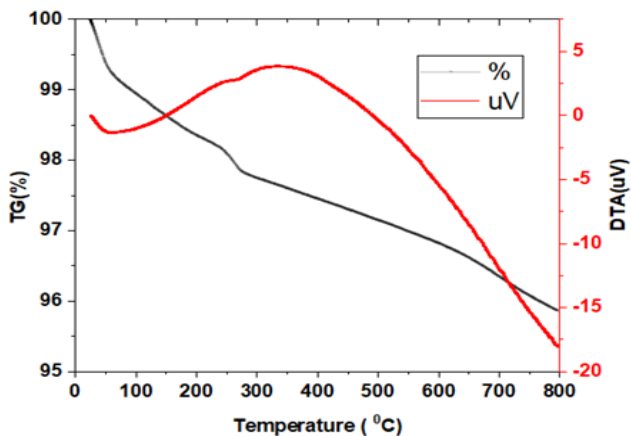
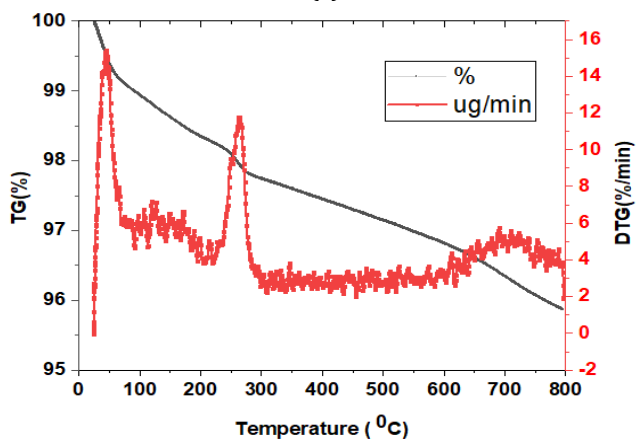


Fig. 4 FTIR of SCBA



(a)



(b)

Fig. 5 TGA of SCBA

The pozzolanic reactivity of SCBA is observed by strength activity index at 28 days. Results show an activity index of 82.98% for SCBA motors showing a reactivity of SCBA particles with OPC.

3.3. Mechanical Properties of Concrete

3.3.1. Compressive Strength

Conventional concrete and SCBA modified concrete are cured for 3, 7, 28, 56 and 90 days to study the effect of curing on the compressive strength of SCBA concrete. The results are shown in table 4. Fig. 6 depicts the results of compressive strength. Increase in strength is observed in all ages and replacement levels of SCBA and increased with the age of curing. SCBA samples exhibit strength gain from day 3 onwards, continued till 7 days. At 28 days, highest strength gain is observed in 15% replaced SCBA concrete. Ganesan et al. [38] observed similar results; an optimum replacement of 10% among 5,10,15,20,25 and 30% replacements of SCBA in concrete samples mix designed for a characteristic compression strength of 25 MPa, crediting the enhanced particle morphology of SCBA resulted from pre-heating at 650°C. Till 20% replacement, the strength attained is similar to conventional concrete. Andrade et al. [39] found an increase of 3.72%, 22.56% and 20% for 5, 10 and 15% replacements due to physical effect, dense packing and pozzolanic reaction. Several researchers reported the strength gain with an optimum replacement of 5 to 15% with an increase in properties of concrete [13]. The results vary by different pre-treatment conditions, chemical composition, and material properties of SCBA.

Table 4 Compressive strength of SCBA concrete

% of SCBA	3 days	7 days	28 days	56 days	90 days
OPC	2.125	30.25	44.12	46.12	47.11
5% SCBA	2.250	31.13	46.45	47.15	47.58
10% SCBA	2.300	32.64	48.32	50.00	50.53
15% SCBA	2.502	34.10	50.50	55.21	55.67
20% SCBA	2.125	31.00	44.10	46.20	47.26
25% SCBA	2.100	30.25	43.08	45.23	47.00

Bahurudeen et al. [40], Jagadeesh [41] observed strength gain in concrete and mortars at an optimum replacement of 25% at the 28 days curing due to pozzolanic reactivity resulted from enhanced material properties of SCBA. In the present study, there appeared an increment in strength due to the pozzolanic effect resulting from the pre-treatment of SCBA. After an optimum replacement of 15%, there appeared a reduction in strength compared to SCBA but an increase in strength (20% replaced SCBA concrete) compared to conventional concrete due to the filler effect (which gave the strength results similar to conventional concrete) and a reduction in strength at 25% due to dilution effect resulted from the exhaustion of free lime and inert SCBA particles. Among all the specimens, maximum strength gains of 55.65, 55.52 and 50.50 MPa are observed at 90, 56, and 28 days of curing, respectively, with 15% SCBA samples. The highest strength at 90 days is due to extended hydration period. A reduction in strength at 25% replacement of SCBA is observed because of the inertness of SCBA. The high volume of bagasse ash has reduced the proportion of cement, reducing the compressive strength of concrete. SCBA can be used as a filler material at a replacement of 20% as the strength of SCBA concrete is similar to OPC. SCBA can be used to replace cement by 5,10 and 15% in concrete due to its high silica

content and attaining higher strength than conventional concrete due to reaction with free lime, forming additional C-S-H bonds as a result of pozzolanic reactivity [42].

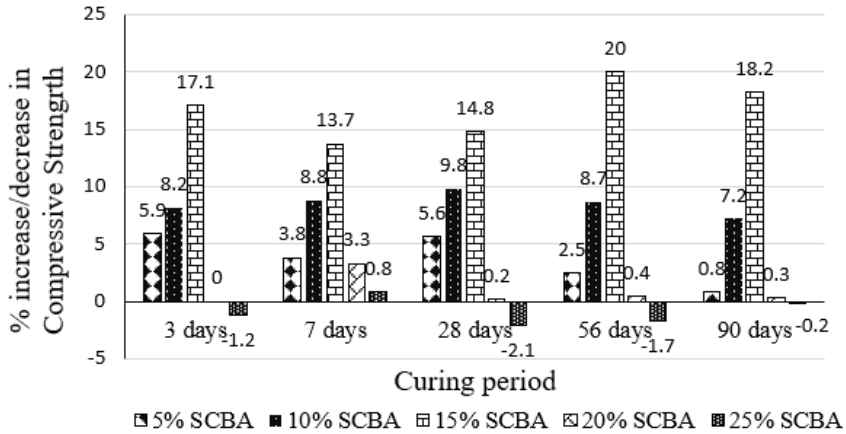


Fig. 6 Results of compressive strength of SCBA concrete

The powdered sample is collected from the core of the concrete cube, after conducting compressive strength test. The micro-structure evaluation is carried out by conducting SEM/EDS tests on the powdered samples.

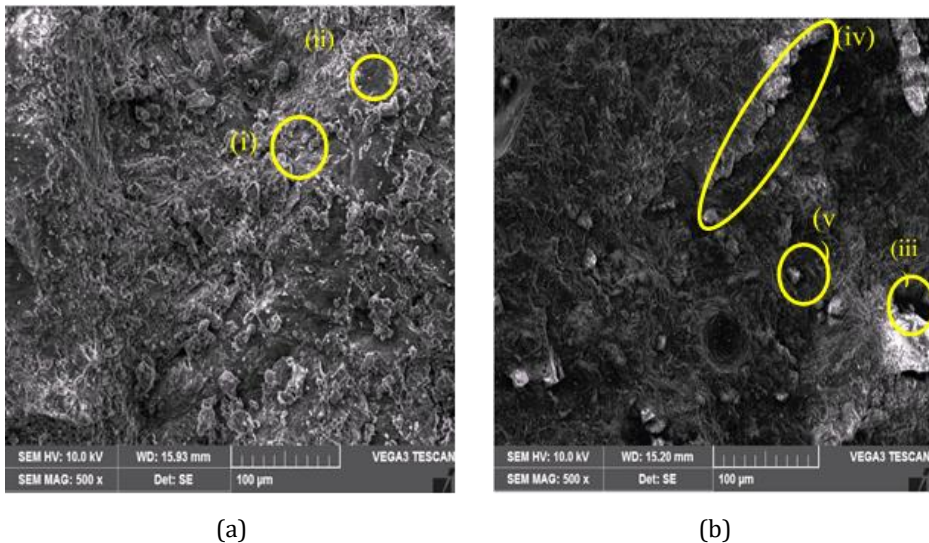


Fig. 7 (a) SEM images of hydrated SCBA concrete at 28 days of curing (b) SEM images of hydrated conventional concrete at 28 days of curing.

Fig. 7 shows SEM analysis of hydrated SCBA and conventional concretes. Visual inspection of micrographs in Figs. 7(a) and 7(b) revealed that SCBA has formed a dense micro-structure with the reaction products varying with the availability of water molecules and calcium silica oxides. Fig. 7(a) shows the formation of hardened concrete. (i) a non-porous hardened compound (ii) thick dense, fibrous formation is identified as C-S-H gel from EDS (Fig. 8) studies and comparative study with previous literature. SEM images in Fig. 7(b) show a complex structure of conventional concrete with (iii) micropores of higher radius,

(iv) appearance of fissure due to a weak bonding between few compounds at 28 days and
 (v) unreacted particles in the composition of OPC samples.

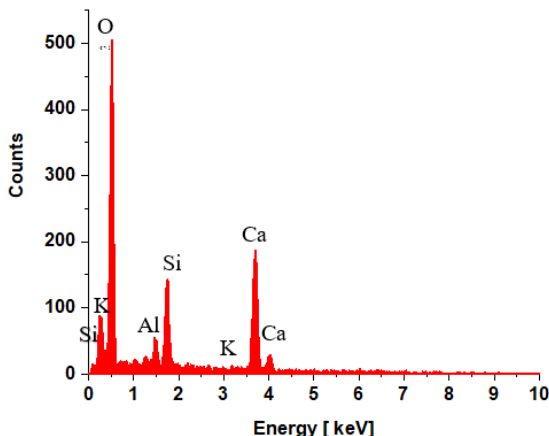


Fig. 8 EDS at (v) showing presence of Calcium-Silica as major composition along with Aluminium and Potassium oxides

3.3.2. Split Tensile Strength

The numerical results of tensile strength of conventional and SCBA concretes are presented in Table 5 and Fig. 9. For structural applications, tensile strength is important to know the resistance of concrete under tensile and flexural stresses. This strength increased continuously with increase in SCBA up to 15% and then showed the decreasing trend. The highest split tensile is observed in 15% replaced SCBA samples at all ages of curing compared to the reference concrete. The highest tensile strength 5.6 MPa in 56 days and 5.7 MPa in 90 days cured samples is observed with 15% SCBA. The increase in this strength is attributed to the additional C-S-H bonds formed by pozzolanic reactivity and the enhanced hydration. The reactive silica of SCBA has bonded with Ca (OH)₂ and water, which has led to the additional formation of C-S-H gel, increasing the strength and stiffness of concrete.

Table 5 Split tensile strength of SCBA concrete (MPa)

% of SCBA	3 days	7 days	28 days	56 days	90 days
OPC only	0.225	3.10	4.50	4.80	4.92
5% SCBA	0.270	3.25	4.80	4.90	5.10
10% SCBA	0.225	3.30	5.13	5.35	5.36
15% SCBA	0.270	3.50	5.30	5.60	5.77
20% SCBA	0.241	3.36	4.75	5.03	4.75
25% SCBA	0.224	3.20	4.44	4.50	4.72

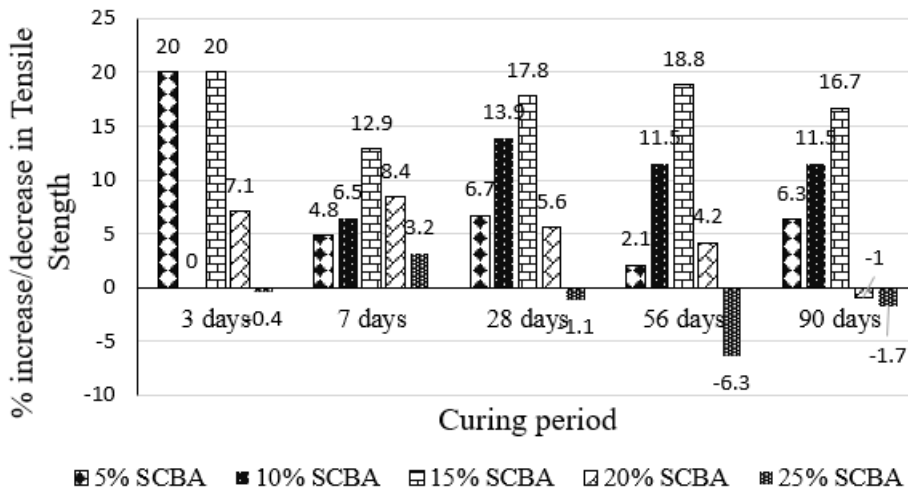


Fig. 9 Results of split tensile strength of concrete

3.3.3. Sorptivity

The change in weight of concrete discs (samples) is noted with reference to time in intervals of 1, 5, 10, 20, 30 and 60 minutes till 9 days according to ASTM C-1585 and represented in Fig. 10. The saturation level is shown with no gain in weight of the sample and steady absorption rate.

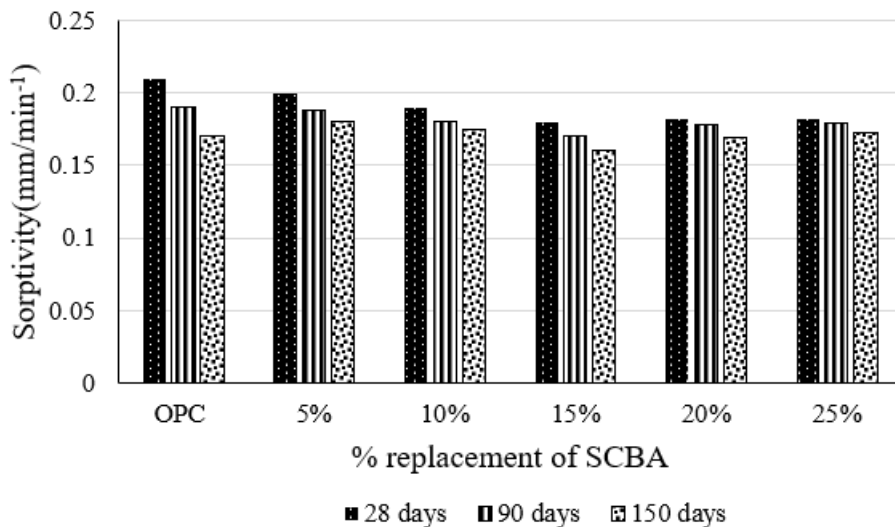


Fig. 10 Sorptivity of SCBA concrete

The sorptivity values of the concrete specimen with OPC retain high moisture content due to high porosity, observed at the end of the saturation period of 28, 90 and 150 days, with values of 0.21, 0.19, 0.17 mm/min^{1/2} as shown in Fig. 10. Bahurudeen and Santhanam [36] found a deviation of the Sorptivity index results from other permeability tests at 56 days showing a least absorption rate at 5% replacement of SCBA. In the present study, the sorptivity experiment for 28, 56 and 90 days of curing are conducted to assess a

comparative performance. Sealing of the surface of the specimen on circumference allows permeability uni-directionally which is equally exposed to cement matrix and coarse aggregate. The present study allows high saturation conditions by extended curing of 56 and 90 days. Results in Fig. 11 show that the moisture content is found to be minimum in samples of 15% replacement which is 88.1, 81 and 76.2 for 28, 90, and 150 days, respectively. The reduction in moisture content is attributed to filler effect and the fragmentation of pores due to the pozzolanic reactivity of SCBA, which has reduced the porosity and capillarity of water molecules. Similar results were observed in sorptivity tests carried out by Muthadhi and Kothandaram [43] in rice-husk ash which kept reducing with an increment in the replacement level of rice husk ash in 5,10, 15, 20 % with an optimum replacement level of 20%.

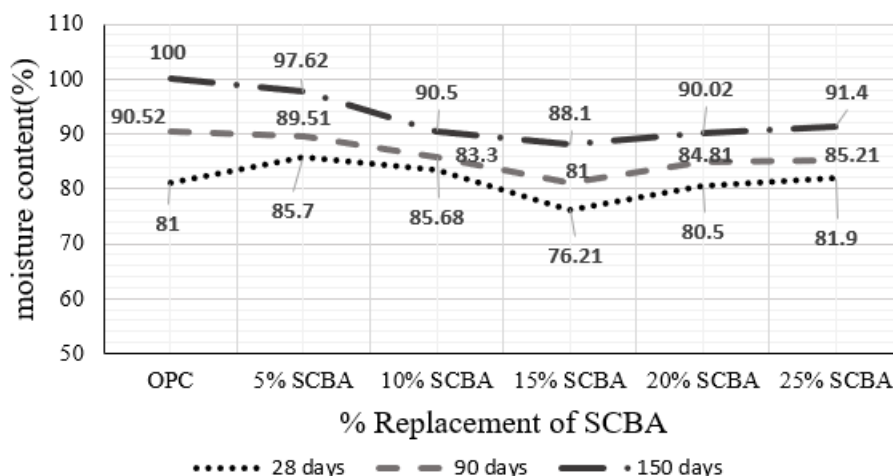


Fig. 11 Change in moisture content with change in replacement level of SCBA

3.3.4. Acid Resistivity

Samples cured for 28 days are collected, surface rubbed with soft cloth are weighed and dimensions are measured. The mass loss, strength loss and dimension loss are calculated and results are tabulated below (Table 6 and Table 7). Cement-based materials deteriorate in acidic atmospheres due to the high alkaline nature of OPC. Calcium silicates, on hydration, is expected to form C-S-H and free lime; forms an insoluble organic compound calcium sulphate ($\text{CaSO}_4 \cdot 2\text{H}_2\text{O}$) in the presence of sulphuric acid. Instead of hardening, weak bonds develop between the molecules leading to reduction in strength [44]. Joshaghani and Moieni [45] observed an increase in the mass of OPC and SCBA samples due to the formation of ettringite and gypsum when the samples were cured in Na_2SO_4 at 28 days and a decrease in mass at 360 days. In present study, it is observed that the dimension, strength and mass losses are reduced in SCBA samples with replacement levels of 5,10,15,20 and 25%.

Degrading the outer layer by precipitating portlandite increases the intensity of acidic corrosion into inner layers either by pores or through the transportation of ions. Gutberlet et al. [46] studied the effect of degradation by HCl and observed a mass loss due to the dissolution of portlandite from de-calcification of C-A-S-H in hydrated samples cured for 90 days. HCl tends to form a layered structure due to the formation of Friedel’s salt and ettringite in the presence of magnesium. Silica gel and silica polymorphs agglomerated at the transition zone initiate the layering, which has high intensity of chlorine attack on

concrete. From the durability loss index results from present study, it is understood that the concrete produced with OPC and SCBA showed less reactivity in H₂SO₄ atmosphere compared to that in HCl. It is observed that the loss in durability caused by mass loss, which showed a co-relation coefficient value 0.987 and 0.989 for curing conditions in H₂SO₄ and HCl. Figure 12 shows the formation of white precipitate around cementitious compounds in acid-cured samples. Improper hydration, dissolution of calcium ions, and deterioration of internal structure has led to mass reduction of concrete.

Table 6 Effect of HCl on SCBA concrete at the age of 28 days curing

% of SCBA	Mass loss factor (%)	Dimension loss factor (%)	Strength loss factor (%)	Durability loss factor (%)
OPC	3.28	2.520	70.25	580.65
SCBA 5%	3.15	2.458	68.74	532.23
SCBA 10%	2.54	2.357	68.10	407.70
SCBA 15%	2.20	2.358	67.80	351.72
SCBA 20%	2.80	2.490	68.00	474.10
SCBA 25%	2.81	2.474	68.67	477.39

Table 7 Effect of H₂SO₄ on SCBA concrete cured for 28 days

% of SCBA	Mass loss factor (%)	Dimension loss factor (%)	Strength loss factor (%)	Durability loss factor (%)
OPC	3.20	2.50	68.50	548.00
SCBA 5%	3.12	2.45	67.20	510.38
SCBA 10%	2.50	2.35	66.32	389.63
SCBA 15%	2.03	2.34	65.00	305.50
SCBA 20%	2.75	2.40	65.53	432.50
SCBA 25%	2.71	2.47	65.62	437.62

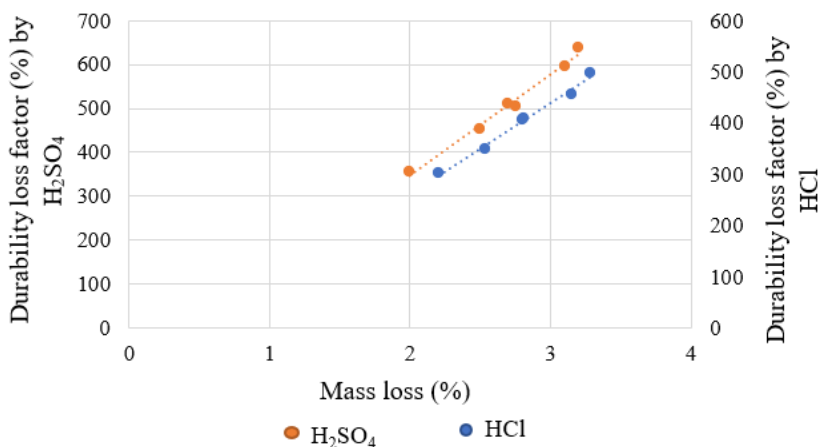


Fig. 12 Co-relation between mass loss and durability of concrete

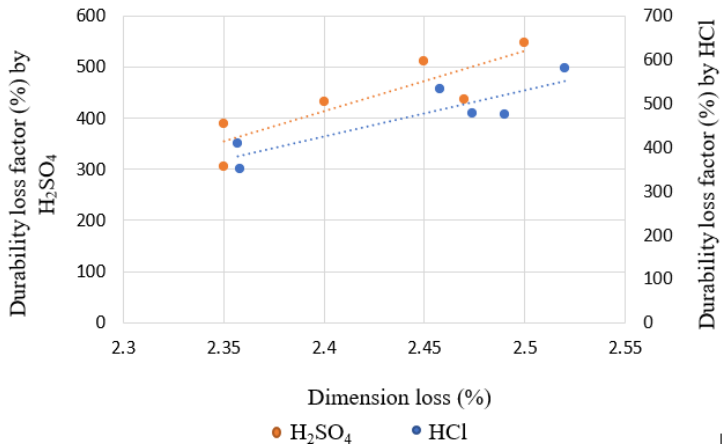


Fig. 13 Co-relation between dimension change and durability of concrete

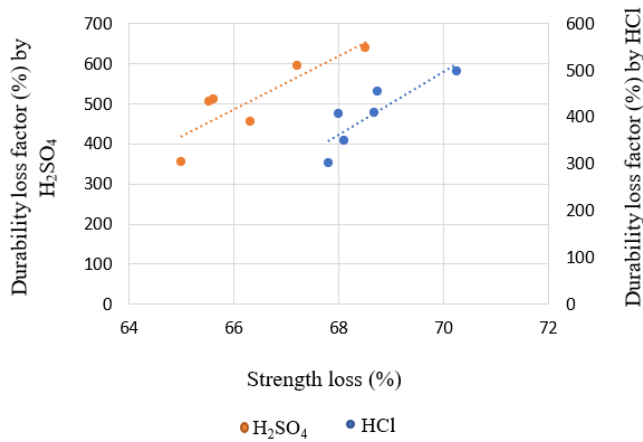


Fig. 14 Co-relation between strength loss and durability of concrete

Table 8 Correlation between the durability properties of concrete cured in acid solution

Acid environment	Factor affected	Regression Equation	R ²
H ₂ SO ₄ acid	Mass loss	y = 197.58x - 97.847	0.9870
	Strength loss	y = 57.709x - 3392.4	0.7483
	Dimension loss	y = 1186.2x - 2433.3	0.7552
HCl acid	Mass loss	y = 207.74x - 110.36	0.9890
	Strength loss	y = 78.854x - 4938.2	0.7297
	Dimension loss	y = 1056.1x - 2109.2	0.7841

There is a reduction in strength, dimension change and mass loss due to HCl and H₂SO₄ in all the samples. Table 6 and 7 show that the highest loss is caused in conventional concrete due to the excess calcium levels present in OPC, which precipitates in presence of HCl and H₂SO₄. While silica being a semi metallic compound, doesn't precipitate and react as

aggressive as OPC. It is difficult to evaluate the durability quotient when several parameters judge deterioration. Co-relation between the individual factors is plotted and represented in figure 12, 13 and 14 where the influence of both the acids on the three properties of concrete is observed. The linear regression graphs shown in Table 8 indicated that mass loss of acid cured samples had highest correlation of 0.97 and 0.98 with maximum durability loss of concrete.

3.3.5. SEM Analysis of Acid Cured Concrete

There appears to be a white precipitate around hydrated samples resulting from dissolution. The following conclusions are drawn from the micro-structural analysis of SCBA concrete exposed to H_2SO_4 .

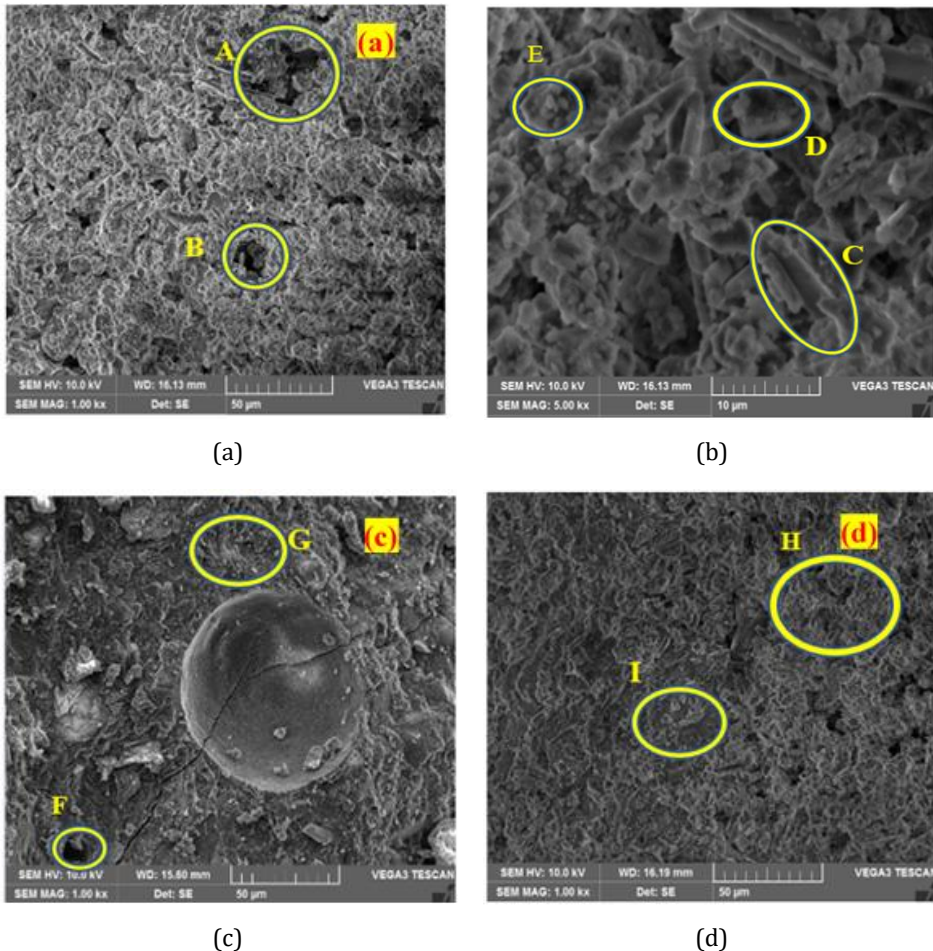


Fig. 15 SEM images of SCBA concrete at 28 days

- A - Hydration of concrete with high porosity,
- B - Presence of voids and white precipitate around hydrated samples,
- C - Unreacted SCBA particle,
- D - Higher magnification of C-S-H, white precipitate around the hydrates,
- E - White precipitate found all over the matrix,
- F - Unreacted portion with low density of cement matrix,

- G - Hydrated portion.
- H,I- C-S-H in acidic medium

Microscopic images of hardened concrete cured in acid solution is shown in Figure 15. Fig. 15(a) shows the complete hydrated concrete in the presence of dilute sulphuric acid. Despite the presence of acid, there appeared a hydration. However, weak bonding between the cementitious particles is represented as white precipitate in Fig. 15 (b). Fig. 15 (c) depicts a porous concrete matrix in H and completely hardened matrix in I where G also shows similar texture which is formed due to C-S-H. Micro voids and cracks are appeared in Fig. 15(d). The elemental composition shows the presence of sulphur along with Ca, Al and silica oxides as observed in EDS studies shown in Figure 16.

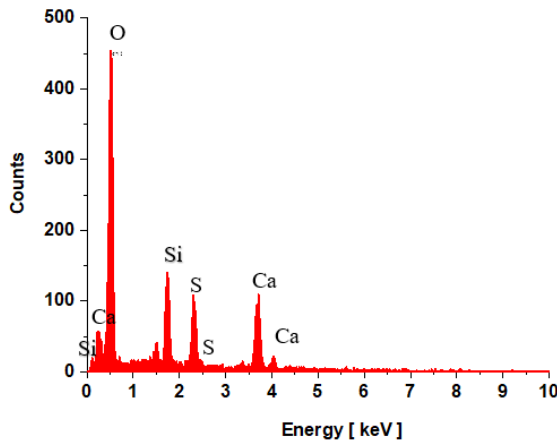


Fig. 16 EDS for SCBA concrete cured in H_2SO_4

4. Conclusions

An in-depth investigation on the material properties of SCBA and its performance in SCBA-modified concrete is assessed from mechanical, durability and micro-structural tests. The following conclusions are drawn from the results and discussion:

- Silica dioxide is found as major composition of SCBA from EDS and FTIR test results; which is an important elemental oxide for pozzolanic reaction. TGA studies show a mass loss around 100 and 250°C conforming the presence of moisture entrapped between the particles along with CO_2 . SEM images show a non-spherical, elongated particle shape and rough-granular texture and is highly porous topography of SCBA. Studies on physical properties show that pre-treatment has increased the fineness, and reduced the carbon content and LOI, enhancing the material properties of SCBA. Strength Activity Index test confirms the pozzolanic reactivity of treated sugarcane bagasse ash.
- The highest compressive strength as 55.65 MPa at the age of 90 days curing and highest split tensile strength as 5.35 MPa at 56 and 90 days of curing are found in 15% replaced SCBA concrete due to pozzolanic reactivity of SCBA with cement. At 20% and 25% replacements, the compressive strength gain has started reducing, however, SCBA concrete attained the mean target strength of 43.25 MPa as per design specifications.

- The water sorptivity of SCBA samples is found to be reduced in all the samples containing SCBA. Least moisture content of 88.1%, 81% and 76.21% is found in 28, 90 and 150 days of curing in 15% SCBA concrete. The discretization of pores resulting from pozzolanic reactivity has enhanced the micro-structure of SCBA concrete. Further, SCBA particles acted as fillers in capillary pores, obstructing water molecules' ingress into the concrete. A reduction in resistivity of water molecules in 20% and 25% is observed because of reduced C-S-H matrix.
- OPC and 5% SCBA samples exposed to HCl suffered maximum durability loss with Acid Durability Loss Factor (ADLF) of 580.65% and 532.23%. Unlike other durability test results, SCBA concrete has shown high resistance to acid attack with 10%, 15%, 20%, 25% replacement levels due to the inert reaction of silica to HCl and H₂SO₄.
- The conclusions suggest that SCBA can be used as mineral admixture after selective pre-treatment at an optimum replacement of 15% to enhance the strength, durability, and acid resistivity of concrete.

Acknowledgement

The authors are thankful to the Vignan's Foundation for Science, Technology, and Research (Deemed to be University) for infrastructure, lab facilities, and constant support for this research work.

References

- [1] Bayapureddy Y, Muniraj K, Mutukuru MRG. Sugarcane bagasse ash as supplementary cementitious material in cement composites: strength, durability, and microstructural analysis. *J Korean Ceram Soc* [Internet]. 2020 Sep 20;57(5):513–9. Available from: <https://link.springer.com/10.1007/s43207-020-00055-8>
- [2] Ajith G, Shanmugasundaram N, Praveenkumar S. Effect of mineral admixtures and manufactured sand on compressive strength of engineered cementitious composite. *J Build Pathol Rehabil* [Internet]. 2021;6(1):1–9. Available from: <https://doi.org/10.1007/s41024-021-00137-y>
- [3] Palaskar SM, Vesmawala GR. Effect of SCBA and GGBFS on the performance of binary and ternary blended concrete. *Res Eng Struct Mater*. 2023; 9(2): 405-419. <http://dx.doi.org/10.17515/resm2022.626st1229>
- [4] Jahanzaib Khalil M, Aslam M, Ahmad S. Utilization of sugarcane bagasse ash as cement replacement for the production of sustainable concrete – A review. Vol. 270, *Construction and Building Materials*. Elsevier Ltd; 2021.
- [5] Jittin V, Minnu SN, Bahurudeen A. Potential of sugarcane bagasse ash as supplementary cementitious material and comparison with currently used rice husk ash. *Constr Build Mater* [Internet]. 2021 Mar; 273:121679. Available from: <https://linkinghub.elsevier.com/retrieve/pii/S0950061820336837>
- [6] B.S. Thomas a b c, J. Yang a b h, A. Bahurudeen d, J.A. Abdalla c, R.A. Hawileh c, H.M. Hamada e, S. Nazar a b, V. Jittin d K A f g. Sugarcane bagasse ash as supplementary cementitious material in concrete – a review. *Mater Today Sustain*. 2021;15.
- [7] Batool F, Masood A, Ali M. Characterization of Sugarcane Bagasse Ash as Pozzolan and Influence on Concrete Properties. *Arab J Sci Eng* [Internet]. 2020;45(5):3891–900. Available from: <https://doi.org/10.1007/s13369-019-04301-y>
- [8] Frías M, Villar E, Savastano H. Brazilian sugar cane bagasse ashes from the cogeneration industry as active pozzolans for cement manufacture. *Cem Concr Compos*. 2011;33(4):490–6.
- [9] Arif E, Clark MW, Lake N. Sugar cane bagasse ash from a high efficiency co-generation boiler: Applications in cement and mortar production. *Constr Build Mater* [Internet].

- 2016; 128:287–97. Available from: <http://dx.doi.org/10.1016/j.conbuildmat.2016.10.091>
- [10] Arif E, Clark MW, Lake N. Sugar cane bagasse ash from a high-efficiency co-generation boiler as filler in concrete. *Constr Build Mater* [Internet]. 2017;151:692–703. Available from: <http://dx.doi.org/10.1016/j.conbuildmat.2017.06.136>
- [11] Mali AK, Nanthagopalan P. Thermo-mechanical treatment of sugarcane bagasse ash with very high LOI: A pozzolanic paradigm. *Constr Build Mater*. 2021 Jun 21;288.
- [12] Bahurudeen A, Wani K, Basit MA, Santhanam M. Assessment of Pozzolanic Performance of Sugarcane Bagasse Ash. *J Mater Civ Eng*. 2016;28(2):1–11.
- [13] Cordeiro GC, Barroso TR, Toledo Filho RD. Enhancement the Properties of Sugar Cane Bagasse Ash with High Carbon Content by a Controlled Re-calcination Process. *KSCE J Civ Eng*. 2018;22(4):1250–7.
- [14] Cordeiro GC, Toledo Filho RD, Fairbairn EMR. Effect of calcination temperature on the pozzolanic activity of sugar cane bagasse ash. *Constr Build Mater*. 2009 Oct;23(10):3301–3.
- [15] Cordeiro GC, Tavares LM, Toledo Filho RD. Improved pozzolanic activity of sugar cane bagasse ash by selective grinding and classification. *Cem Concr Res*. 2016 Nov 1; 89:269–75.
- [16] Katare VD, Madurwar M V. Experimental characterization of sugarcane biomass ash – A review. *Constr Build Mater* [Internet]. 2017; 152:1–15. Available from: <http://dx.doi.org/10.1016/j.conbuildmat.2017.06.142>
- [17] Jittin V, Bahurudeen A. Evaluation of rheological and durability characteristics of sugarcane bagasse ash and rice husk ash based binary and ternary cementitious system. *Constr Build Mater* [Internet]. 2022 Jan; 317:125965. Available from: <https://linkinghub.elsevier.com/retrieve/pii/S0950061821036977>
- [18] Srinivasan R, Sathiya K. Experimental Study on Bagasse Ash in Concrete. *Int J Serv Learn Eng Humanit Eng Soc Entrep*. 2010;5(2):60–6.
- [19] Priya KL, Ragupathy R. Effect of Sugarcane Bagasse Ash on Strength Properties of Concrete. *Int J Res Eng Technol*. 2016;05(04):159–64.
- [20] Subramaniam KS, Sivaraja M. Assessment of sugarcane bagasse ash concrete on mechanical and durability properties. *Adv Nat Appl Sci*. 2016;10(9).
- [21] Chandragiri P, Kroehong W, Damrongwiriyanupap N, Suriyo W, Jaturapitakkul C. Mechanical properties, chloride resistance and microstructure of Portland fly ash cement concrete containing high volume bagasse ash. *J Build Eng* [Internet]. 2020 Sep;31:101415. Available from: <https://linkinghub.elsevier.com/retrieve/pii/S2352710219310162>
- [22] Rajasekar A, Arunachalam K, Kottaisamy M, Saraswathy V. Durability characteristics of Ultra High Strength Concrete with treated sugarcane bagasse ash. *Constr Build Mater* [Internet]. 2018;171:350–6. Available from: <https://doi.org/10.1016/j.conbuildmat.2018.03.140>
- [23] Tripathy A, Acharya PK. Characterization of bagasse ash and its sustainable use in concrete as a supplementary binder – A review. Vol. 322, *Construction and Building Materials*. Elsevier Ltd; 2022.
- [24] Prabhat N, Kumara BS, Vithanage V, Samarathunga AI, Sewwandi N, Maduwantha K, et al. A Review on the Optimization of the Mechanical Properties of Sugarcane-Bagasse-Ash-Integrated Concretes. *J Compos Sci*. 2022; 6(10).
- [25] Zareei SA, Ameri F, Bahrami N. Microstructure, strength, and durability of eco-friendly concretes containing sugarcane bagasse ash. *Constr Build Mater*. 2018 Sep 30;184:258–68.
- [26] IS-12269: Specification for 53 grade ordinary Portland cement. *Bur Indian Stand* [Internet]. 1987;New Delhi,India. Available from: <https://law.resource.org/pub/in/bis/S03/is.12269.b.1987.pdf>

- [27] IS 383(1970): Specification for Coarse and fine aggregates from natural sources for concrete.
- [28] BIS. IS 1727 (1967): Methods of test for pozzolanic materials. 1968;
- [29] IS-4032 1985. Method of chemical analysis of hydraulic cement. Indian Stand. 1985;1-47.
- [30] Indian Standards B. IS 10262 (2009): Guidelines for concrete mix design proportioning.
- [31] IS 516. Method of Tests for Strength of Concrete. Bur Indian Stand. 1959;1-30.
- [32] IS 5816-1999. Indian standard Splitting tensile strength of concrete- method of test. ur Indian Stand. 1999;1-14.
- [33] ASTM C 1585(2013): Standard test method for measurement of rate and absorption by hydraulic cement concrete.
- [34] ASTM C666-97: Standard test method for resistance of concrete to rapid freezing and thawing.
- [35] ASTM C 267: Standard test methods for chemical resistance of mortars, grouts and monolithic surfacing and polymer concretes.
- [36] Bahurudeen A, Santhanam M. Influence of different processing methods on the pozzolanic performance of sugarcane bagasse ash. *Cem Concr Compos.* 2015;56:32-45.
- [37] F. Hincapié Rojas D, Pineda Gómez P, Rosales Rivera A. Production and characterization of silica nanoparticles from rice husk . *Adv Mater Lett.* 2019;10(1):67-73.
- [38] Ganesan K, Rajagopal K, Thangavel K. Evaluation of bagasse ash as supplementary cementitious material. *Cem Concr Compos* [Internet]. 2007 Jul;29(6):515-24. Available from: <https://linkinghub.elsevier.com/retrieve/pii/S0958946507000418>
- [39] Andrade Neto J da S, de França MJS, Amorim Júnior NS de, Ribeiro DV. Effects of adding sugarcane bagasse ash on the properties and durability of concrete. *Constr Build Mater.* 2021;266.
- [40] Bahurudeen A, Kanraj D, Gokul Dev V, Santhanam M. Performance evaluation of sugarcane bagasse ash blended cement in concrete. *Cem Concr Compos* [Internet]. 2015 May;59:77-88. Available from: <https://linkinghub.elsevier.com/retrieve/pii/S0958946515000347>
- [41] Jagadesh P, Ramachandramurthy A, Murugesan R, Sarayu K. Micro-analytical studies on sugar cane bagasse ash. Vol. 40, S^o adhan^a. 2015.
- [42] Raheem AA, Ikotun BD. Incorporation of agricultural residues as partial substitution for cement in concrete and mortar – A review. *J Build Eng* [Internet]. 2020;31(July 2019):101428. Available from: <https://doi.org/10.1016/j.job.2020.101428>
- [43] Muthadhi A, Kothandaraman S. Optimum production conditions for reactive rice husk ash. *Mater Struct Constr.* 2010;43(9):1303-15.
- [44] Allahverdi A, Skvara F. Acidic corrosion of hydrated cement based materials. *Ceram – Silikáty.* 2000;3(44):114-20.
- [45] Joshaghani A, Moeini MA. Evaluating the effects of sugar cane bagasse ash (SCBA) and nanosilica on the mechanical and durability properties of mortar. *Constr Build Mater.* 2017 Oct 15;152:818-31.
- [46] Gutberlet T, Hilbig H, Beddoe RE. Acid attack on hydrated cement - Effect of mineral acids on the degradation process. *Cem Concr Res* [Internet]. 2015;74:35-43. Available from: <http://dx.doi.org/10.1016/j.cemconres.2015.03.011>

Blank Page



Research Article

The effect of using recycled materials (sand and fine powder) from demolished concrete waste in alluvial sand mortar

Samir Kennouche ^{*1,2, a}, Allaoua Belferrag ^{1,2, b}, Djamel Boutoutaou ^{1,2, c}, Samia Bouzouaid ^{1,2, d}, Hachem Chaib ^{1,2, e}

¹Department of Civil Engineering and Hydraulics, University Kasdi Merbah Ouargla, Ouargla 30000, Algeria

²Laboratoire d'Exploitation et Valorisation des Ressources Naturelles en Zones Arides, Ouargla 30000, Algeria

Article Info

Abstract

Article history:

Received 12 Jul 2023

Accepted 21 Aug 2023

Keywords:

Mortar;

Alluvial sand;

Recycled sand;

Concrete waste powder fine;

Compressive strength;

Shrinkage;

Design management;

Geometric modeling;

Engineering analysis;

Finite Element Method

This article evaluates the possibility of a mortar preparation incorporating recycled demolition concrete waste (RDCW). These allow mortars to be produced in two ways: the first in the form of recycled aggregates (RA) to partially replace alluvial sand (AS) (natural sand) and the second in the form of the fine fraction of the waste concrete powder (CWPF) obtained by screening recycled sand (RS) from construction and demolition waste (CDW) to replace Portland cement in the production of composites. The CWPF fraction used is composed of particles having a diameter of less than 0.08 mm. Mortar mixtures were designed with three different RS replacement ratios (0%, 15% and 25%) and varying percentages of CWPF (5%, 10% and 15%). The W/C ratio was designed in 0.53 for all mixes. Mechanical properties such as compressive strength and rheological properties (shrinkage) of the prepared mortars were studied. The results show that the material studied has lower mechanical properties than an ordinary mortar, but these are acceptable and indicative, except that the mixture prepared with 75% A Sand 25% Reregister an increase in mechanical resistance at (long term) 90 days. The reverse is true for shrinkage, where adding RS and CWPF with percentages up to 15% and 10% respectively has a positive effect on the mortars studied. These results contribute to the use of FCPW in composites products.

© 2023 MIM Research Group. All rights reserved.

1. Introduction

Over the last few decades, concrete has been estimated to be the second most used material in the world after water [1]. This consumption will continue to grow in the future due to increased urbanization. But this urban development poses environmental problems in terms of preserving natural resources. Indeed, the construction and demolition (C&D) industry in the civil engineering sector accounts for a significant proportion of waste production.

Each year, it is estimated that around 300 million tonnes of construction waste are produced in the United States and almost 80 million tonnes in Japan; over 500 million tonnes are produced in Europe; 200 million tonnes of concrete waste are produced in China [2], 300 million tonnes in France [1] and 70 million tonnes in Brazil [3]. The situation is the same as in France, where landfill costs vary widely and recycling rates are still very low.

*Corresponding author: pknsamir@gmail.com

^a orcid.org/0009-0000-0350-2223; ^b orcid.org/0009-0003-8864-8708; ^c orcid.org/0009-0005-0283-4863;

^d orcid.org/0009-0006-4022-553X; ^e orcid.org/0009-0003-9008-5633

DOI: <http://dx.doi.org/10.17515/resm2023.820ma0712>

Res. Eng. Struct. Mat. Vol. 9 Iss. 4 (2023) 1309-1324

In the UK, the average cost of landfill is estimated at £15/t (around €18.8/t), representing a total cost to the cement industry of £11.25 million/year (around €15.5 million/year). These figures are currently set to rise due to the observed increase in energy prices. In Australia, inert construction waste accounts for 82% of construction and demolition waste, of which 43% is landfilled. The cost of landfilling in Western Australia has been estimated at between \$6 and \$10/t. Reliable statistics are also a problem in Malaysia, where the identification of construction and demolition waste is not yet effective, and even more so in Kuwait, where up to 33% of landfills are illegal.

In Algeria, and given the development of the building and public works sector in recent years, as well as the growing number of construction sites and deconstruction of illegal sites, the said building and public works sector constitutes the 1st source of massive flows. According to 2016 estimates, the quantity of construction waste generated amounted to 11 million tons.

Any construction or deconstruction site affects the environment through the construction materials themselves, the production of waste and the discharge of pollutants into the air and water, and, indirectly, through the energy requirements of the structures built and the spaces they occupy. Through the *Stratégie Nationale de Gestion Intégrée des Déchets à l'horizon 2035*, the French government aims to reduce the environmental impact of inert waste by installing crushers and sorting destroyed materials.

Studies [4] have shown that recycled gravel can be reused without difficulty in the formulation of concrete. Recycled sand, on the other hand, is more difficult to use. The latter is rich in fines (<0.063 mm), which have a negative impact on workability and increase mix absorption. To avoid this problem, several solutions are applied, such as sieving the fine part of the recycled sand or adding admixtures.

However, for economic reasons, these solutions are not satisfactory. In fact, the use of recycled sand is not authorized for the production of structural concrete, nor is it permitted for the production of prefabricated elements. However, during the demolition waste crushing phase, the quantity of sand by mass can reach half the total quantity of recycled aggregates, so work is needed on incorporating the fines fraction (0.08-5mm) of recycled aggregates into mortars and concretes.

In addition to the problem of generating demolition concrete waste CDW, the environmental impact of cement manufacture, cement production emits a very large quantity of carbon dioxide gas [5 and 6], with CO₂ emissions having a negative impact on the environment. According to several studies, the cement industry is responsible for around 75% of global CO₂ emissions [7]; [6]; [8]; [9]; to reduce this problem, a solution has been proposed by several studies such as , which use materials partially replacing cement in their work [10], this solution a way to reduce CO₂ emissions from clinker and cement production plants and or used recycled waste as a cement additive [6]; [9]; [11,12 and 13];

In the same context [3] note in their work that there is a need for work on the use of this fraction of recycled fine aggregates. Several studies have been aimed at replacing sand or gravel, but few at replacing cement with CDW. For this reason, the present work aims to produce a new binder from the screening of recycled sand to separate the fine fraction < 0.08mm and use it as a substitute for Portland cement. Moreover, in the context of the circular economy, this research is intended as a solution to reduce CO₂ emissions from cement manufacturing plants, and also to the difficulty of disposing of CDW. Mortar, by its very nature, is made up of an essential internal element: fine sand.

In Algeria, large quantities of alluvial rolled silica sand are used to manufacture concrete and mortar. However, excessive extraction of these sands has contributed significantly to

resource depletion, while also having a detrimental impact on the environment. Parts of the world are experiencing this situation, and must now look for alternative materials to meet the growing demand for concrete and mortar aggregates.

There is another type of sand, available in large quantities locally and presenting no major environmental problems: dune sand, which despite its abundance remains relatively unknown in the construction industry. Its quantity amounts to billions of m³, it is available on nearly 60% of the territory and some of its physico-chemical characteristics suggest that it could be adopted as a building material, thus striking a balance between environmental protection constraints and economic and social considerations.

This study will then consider proposing a more atypical alternative: the crushing of recycled sand for incorporation into cementitious materials as a mineral input. According to the literature, this idea has been applied by replacing part of the cement with the fine sand obtained. To test the influence of this incorporation on the mechanical strength of cementitious materials (particularly compressive strength) [14].

The aim of this study is to evaluate the potential of crushed concrete sand and crushed concrete fines recovered from the demolition and maintenance of old reconfigured houses, as well as from construction waste, to be incorporated as sand and substituted in cementitious materials, In order to reduce the cost of using natural materials on the one hand and on the other hand to save the environment.

2. Study Materials

2.1. Sand

The recycled sand used as a corrector in this study comes from the residues of a concrete landfill. This recycled sand (0/4 mm) is obtained by crushing concrete waste and sieving fig. 3. The results of the physical characterization of this sand are presented in Table 1. The particle size analysis curve for this sand is illustrated in figure 1. This recycled sand is a coarse sand with a uniform particle size ($U_c = 7.8$) still spread out ($R_c = 1.98$). Their fineness modulus is 3.36.

The sand equivalent value (80.50%) shows that sand is suitable for mortar making. alluvial sand (AS) was taken from career of Hassi Sayah in the area of Ouargla (Algeria). From the results shown in Table 1, we note that the water absorption of recycled sand is almost three times higher than that of alluvial dune sand. This can be explained by the high porosity induced by the presence of a certain proportion of cement in the recycled sand, in addition to the fines from the crushing of concrete waste having a high proportion (> 5%) with a very high specific surface area. The determination of sieve analysis and calculation of fineness modulus (FM) were carried out in accordance with NF P 18-560, sand equivalency (SE) was measured by NF P 18-598. The specific and apparent density and the absorption test were conducted in accordance with NF P 18-555.



Fig. 1 Preparation of recycled sand by sieving



Fig. 2 photo of sand used

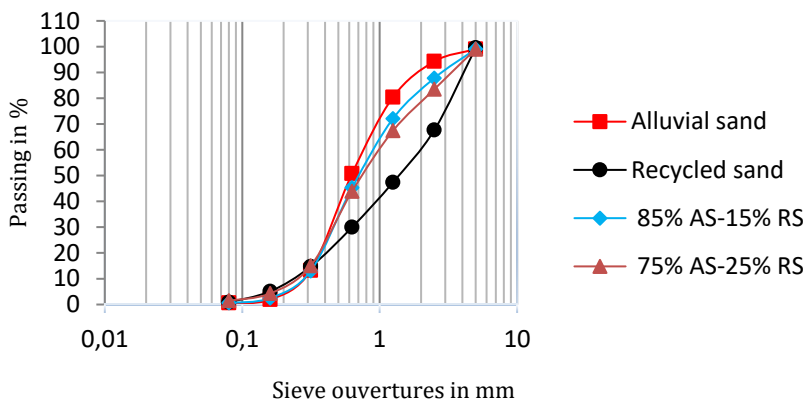


Fig. 3 Grain size distribution of used sand

Table 1. Physical properties of the sands used.

	Alluvial sand (AS)	Recycle d sand (RS)	Corrected sand formulations	
			85% AS + 15% RS	75% DS + 25% RS
Specific density (g/cm ³)	2,51	2,50	2,58	2,66
Apparent density (g/cm ³)	1.47	1,63	1,57	1,58
Water absorption (%)	0.6	8,20	///	///
Fineness modulus	2.60	3,36	2,78	2,80
Sand equivalency (%)	73	80,50	///	///

2.2. Cement

The cement used is a CPJ-CEM II 42.5 N artificial Portland cement, according with standard NF EN 197-1. It has a density of 3.10 g/cm³ and a specific surface area of 3240 g /cm²

Tables 2 and 3 present the chemical analysis and physical and mechanical properties of this cement, respectively. In compliance with standard NF P 15-301194.

Table 2. The chemical analysis of the cement used revealed the existence of the elements which are presented

Chemical analyzes	Lossonignition (NA S042) (%)	Sulphate content (SO3) (%)	MgO magnesium oxide content (%)	Chloride content (NA S042) (%)
Value	10,0 ± 2	2,5 ± 0,5	1,7 ± 0,5	0,02 – 0,05

Table 3. Physical and mechanical characteristics of cement used

	Start setting (min)	End of setting (min)	Cs ₂₈ (MPa)	Cs ₂ (MPa)
CPJ-CEM II	150 ± 30	230 ± 50	≥ 42,5	≥ 10,0

2.3. The Fines Powder

In this study we used the fines powder from recycled concrete (CWPF) obtained by crushing concrete and sieving in the laboratory fig. 4 (a and b) these fines the idea was applied

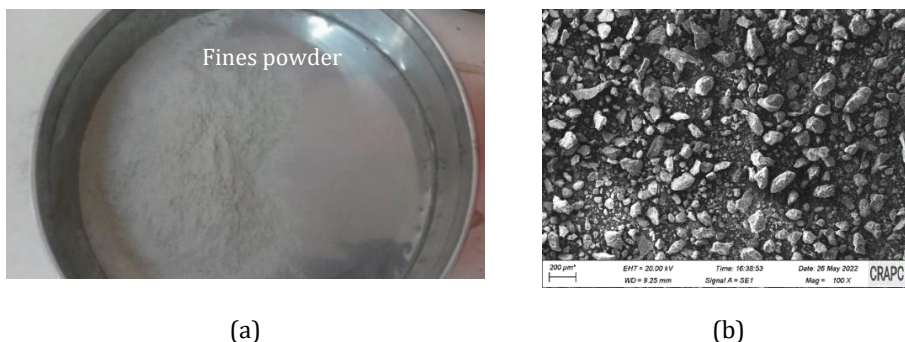


Fig. 4 (a) Photo of the fine powders used, (b) SEM images of the fine powders used

in this work by substituting part of the cement by the fine.

Table 4. Absolute density and specific surface of the CWPF and CPJ-CEM II used

Materials	Portland cement	Fine powder
Absolute density pabs (g/cm ³)	3.10	2.43
Blaine specific surface (cm ² /g)	3240	6520

These results show that the Blaine specific surface area of fine powders is higher than that of CPJ-CEM II 42.5 N cement. This can be explained by the effect of successive crushing and the friability of the raw material, rich in limestone and cementitious materials.

2.3.1 Method of Manufacturing Fines

Recycled aggregate fines powder from crushed concrete waste (RAF): "recycled aggregate fines". A crushing-screening method is used to obtain fines of less than 80μm. In the case of concrete, the 16 x 32 cm cylindrical and 4 x 4 x 16 cm prismatic specimens were previously crushed by compression and traction melting to obtain pieces smaller than 5 cm. This facilitated processing in the crusher. The recycled RA 0/4 aggregates were fed

directly into the crusher. The small granular size of the selected sample saved time and energy. The machine used is a jaw crusher.

The method consists of successively crushing materials with decreasing jaw opening. At the end of each crushing stage, the material is sieved to 80 μm . All particles rejected at this sieve are reintroduced for a new crushing stage, while those passing at 80 μm are retained fig. 5. These operations are repeated until the jaw opening can no longer be reduced. We have chosen to screen at 80 μm because this size is close to the D_{max} conventionally used for mineral additions.



Fig. 5 Preparation of fines by sieving

2.4. Water

The water used for mortar production in this study is potable water. Its quality complies with the requirements of standard NFP 18-404.

3. Experimental Methods

3.1 Characterization of Study Sands

Sand specific gravity, apparent density and absorption were determined in accordance with standard NF P 18-554. Sand particle size analysis by sieving was carried out in accordance with standard NF P 18-560, on aggregate samples ranging in size from 4 to 0.08 mm. Sand equivalence (SE) was carried out in accordance with standard NF P 18-598.

3.2. Fines Characterization Methods

The absolute density is measured by the pycnometer method in accordance with standard EN 1097-6. The specific surface (S_s) is measured by the Blaine method standardized according to NF EN 196-6. Scanning Electron Microscope (SEM) analysis is performed on a field effect microscope.

The SEM is coupled to an energy dispersive spectrometer (EDS). The advantage of using this device is to visualize particle structure on polished sections or pellets, to carry out spot chemical analysis of each mineralogical phase and finally to quantify the proportions by image analysis. The tests are secondary electron mode and backscattered electron mode.

3.4. Mortar Formulation and Sample Preparation

The formulation method adopted is the same as for normal mortar (standard NF EN 196-1). Determination of water content is based on the workability test. The "Water/Cement" ratio ($W/C = 0.53$) was obtained from this test table 5.

Four alluvial sand mortar formulations were prepared and studied, designated as follows:

- M-AS: mortar based on alluvial sand (natural sand) and 0% fines (control)
- M1-ASRSF0: mortar based on 85% alluvial sand and 15% recycled sand
- M2-ASRSF0: mortar based on 75% alluvial sand and 25% recycled sand

The rate of massive fines participation (CWPF) was varied from 5%, 10% and 15% for each mortar formulation. Details of the composition of the different formulations tested are given in Table 5.

Table 5. Composition of the formulations studied

Formulation (1 m ³)	Alluvial Sand (kg)	Recycled Sand (kg)	Cement (kg)	Fines powder (kg)	Water (l)	W/C
M-AS	1425.9	0,00	444.9	0,00	217.8	0,53
M-ASF5	1425.9	0,00	444.6	35.1	217.8	0.53
M-ASF10	1425.9	0,00	421.2	46.8	217.8	0.53
M-ASF15	1425.9	0,00	397.8	70.2	217.8	0.53
M1-ASRSF0	1193.4	210.6	479.7	0,00	217.8	0,53
M1-ASRSF5	1193.4	210.6	444.6	35.1	217.8	0.53
M1-ASRSF10	1193.4	210.6	421.2	46.8	217.8	0.53
M1-ASRSF15	1193.4	210.6	397.8	70.2	217.8	0.53
M2-ASRSF0	831,37	554,25	461,87	0,00	217.8	0,53
M2-ASRSF5	1053	351	444.6	35.1	217.8	0.53
M2-ASRSF10	1053	351	421.2	46.8	217.8	0.53
M2-ASRSF15	1053	351	397.8	70.2	217.8	0.53

The mortar samples prepared were 4 x 4 x 16 cm³ in size. Sand and cement were dry-mixed for 60 s, then water was added. The molds were filled in two layers, each vibrating for 30 s. After 24 h of curing, the mortar specimens were removed from their molds and kept fully immersed in water at a temperature of 25 ± 2°C for 14 days. Then removed from the water and exposed to laboratory conditions (Temperature = 30 ± 5 °C, Humidity = 25 ± 2 %). Figs 6-7 show the photos of the mixed constituents and the test specimens of the mortars prepared respectively.

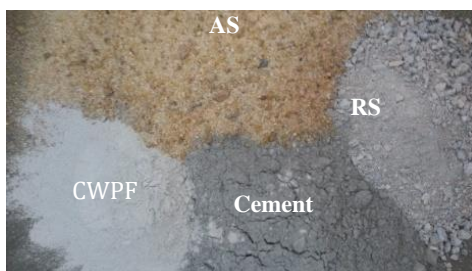


Fig. 6 Dry material mixtures



Fig. 7 Mixture specimens

3.5. Workability

The workability of mortars is measured with a workability meter according to standard NF P 15-437, the test for measuring the flow time of fresh concrete exposed to vibrations.

3.6. Mechanical Testing Techniques

The compressive strength of the mortar samples was measured with the prepared mortar samples (three per age) at ages of 28 and 90days according to the recommendations of NF

EN 196-1 using a hydraulic press with a displacement speed of 0.2 mm/min. The sample is placed between two metal plates in the compressive test machine, shown in Fig.8.



Fig. 8 Compressive test showing the crushing of specimen.

3.7. Shrinkage Test

The unstressed shrinkage test was carried out according to NF P 15-433 (AFNOR, 1994). The results presented are average values of three measurements. These were carried out using a shrinkage meter Fig.9 with an accuracy of ± 5 mm/m. The first shrinkage reading was taken after demolding the specimens at 24 hours followed by further measurements up to 90 days of age. The shrinkage meter can be reliably calibrated with an invar bar before each measurement. The weight loss of the specimens over time was studied along with the shrinkage measurements.



Fig. 9 Shrinkage measurement

4. Results and Discussion

4.1. The Surface Texture of Recycled Sand and Fine Powder

Fig. 10 show the surface texture of RS, which is extremely porous and rough), which may contribute to an increase in the surface area bound to the aggregate-rock interface [15].

An energy dispersion spectroscopy (EDS) analysis of the surface of the RS Fig.10 and table 5 revealed the presence of several elements such as dominant silicon, calcium and aluminum Table 6. This, explained by the presence of old mortar pate coated the RS grains. The same has been observed in several studies [15-16]. From the results obtained by the energy dispersive spectroscopy (EDS) analysis shown in fig. 11 and table 7, it can be seen that CWPF is rich in limestone and cementitious elements such as calcium, aluminum and silicon, with percentages close to those of portland cement, which justifies its use as a replacement for cement in the manufacture of mortars and concretes.

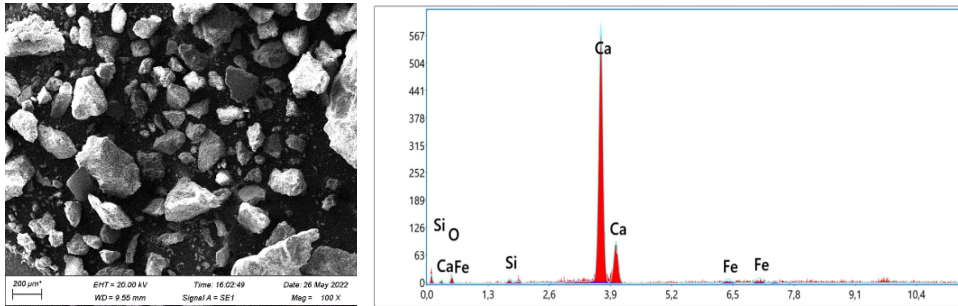


Fig. 10 Analysis of the surface texture of RS

Table 6. Smart quantitative results

Element	OK	SiK	CaK	Fek
% of mass	9.57	0.56	86.69	3.118

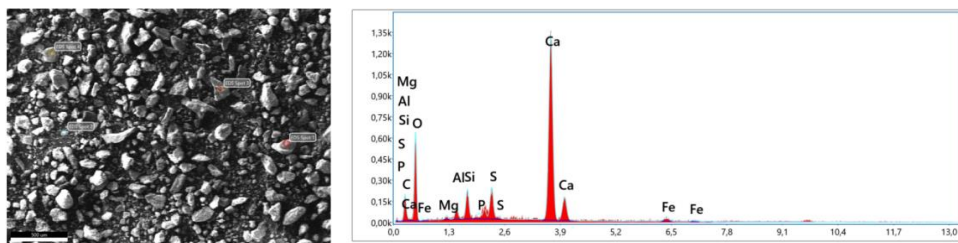


Fig. 11 Analysis of the surface texture of CWPF

Table 7. Smart quantitative results

Element	CK	OK	MgK	AlK	PK	SK	SiK	CaK	Fek
% of mass	7.19	41.76	0.51	1.35	2.88	0.63	3.82	39.68	2.19

4.2. The Effect of Adding Recycled Sand on Mechanical Strength

Fig. 12 shows the compressive strength of M-AS, M1-ASRS and M2-ASRS specimens over time. The compressive strength of the three mixes after 28 days of curing was around 45.1 MPa, 42.2 MPa and 36.3 MPa respectively. The M-AS mixture showed a higher strength than the M1-ASRS and M2-ASRS mixtures, with increases at 28 days of 6.43% and 19.51% respectively. This can be explained by the fact that the presence of RA increases the porosity of the mixture, which translates into a decrease in the strength of mortars containing RS compared to mortars without added RS (control).

Similar observations by [17] who observed in their work that mixes with waste incorporation show reduced compressive strength compared to mixes without incorporation. At 90 days, the compressive strength pattern changed, as the M1-ASRSF0 mortar recorded a decrease in strength of 7.95%, compared to M-ASRSF0, while the M2-ASRSF0 mixture gave more strength than the mixture of a percentage 1.04%, this a slight increase in the resistance of M2-ASRS compared to M-ASRS is due is that the recycled sand, rich in particles of diameters between 0.08 mm and 0.63 mm and containing anhydrous cement, in the presence of water in the long term, the latter reacts to form new hydrates by pozzolanic reactions, which have a positive effect on the resistance [18], while the void-filling effect of these fine RS grains minimizes the percentage of pores. On the other hand, the increase in resistance is probably also due to the nature of the recycled aggregates and the resistance of the demolition concrete which produces these aggregates.

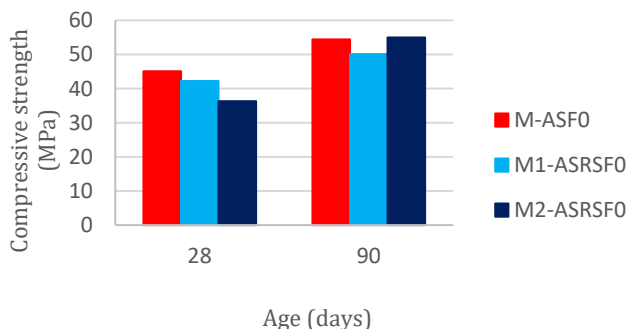


Fig. 12 compressive strength of mixtures without adding CWPF

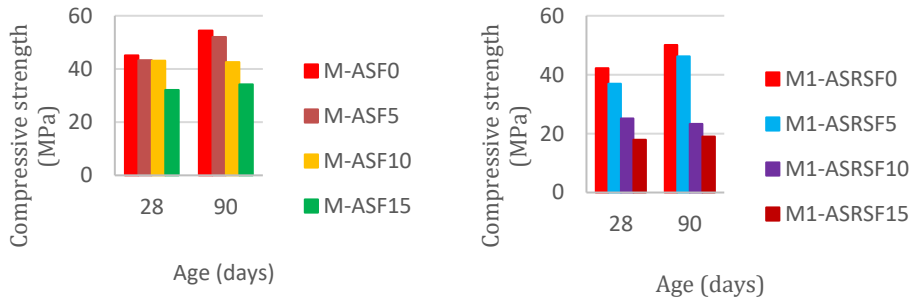
4.2.2. The Effect of Adding Recycled Fine Powder on Mechanical Strength

The results of the compressive strength of mortars prepared with different sands used and with contents of Portland cement replacement by (CWPF) are presented in figure 13. The results obtained show a decrease in compressive strength in all mortar types studied compared to the mortar (control) without replacement (0%).

Figs.13 (a, b, c and d) show that the addition of fine demolition concrete waste in substitution of Portland cement resulted in a decrease in compressive strength compared with mortars without replacement (0%). However, the mortars produced have acceptable strengths for making mortars to NBR 16697 [19]. These results encourage the use of fine CW fractions as cement substitutes for both economic and environmental reasons. We also note that the control concretes M-ASF, M1-ASRS and M2-ASRS show the best strength results compared with mortars made with recycled fine concrete.

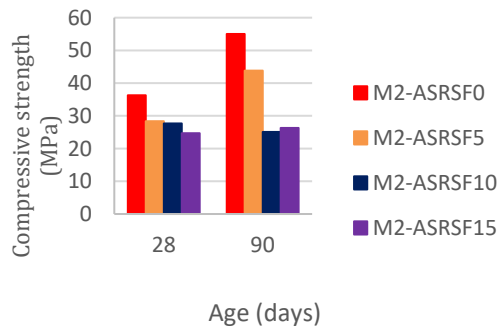
Fig. 13 (a) shows the strength of M-AS concretes with and without the addition of CWPF at 28 and 90 days. It can be seen that the strength of M-ASF5, M-ASF10 and M-ASF15 mixtures decreased by 3.97%, 4.43% and 28.82% respectively, and by 4.46%, 21.73% and 37.17% at 90 days respectively, compared with the M-AS control mortar. Fig. 13.b shows a similar decrease in strength of M1-ASRS mortar (85%AS-15%RS) at 28 days, compared with M1-ASRSF5, M1-ASRSF10 and M1-ASRSF15 mixtures.

This difference is of the order of 18.12%, 44.3% and 60.24% respectively. Figure 13.c also shows a decrease in strength of M2-ASRS (75%AS-25%RS) compared with M2-ASRS, M2-ASRS and M2-ASRS mortar at 28 days of the order of 37.1%, 38.62% and 45.28% respectively.

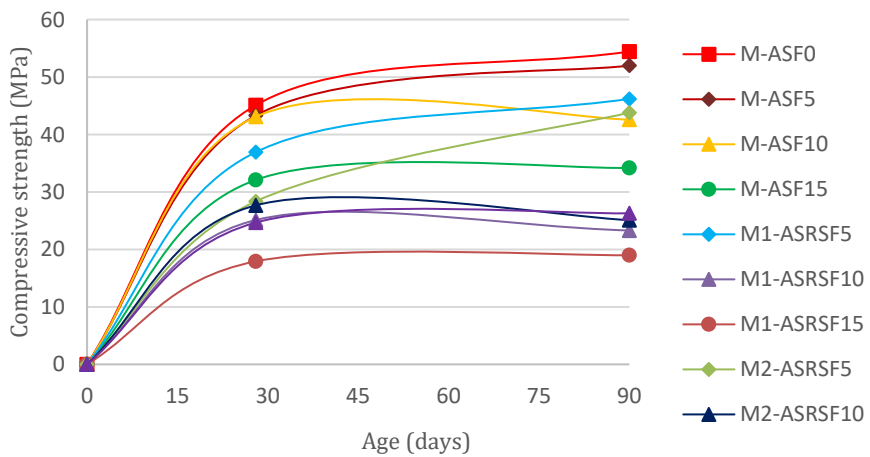


(a) M-AS with and without CWPF

(b) M1-ASRS with adding CWPF



(c) M2-ASRS with adding CWPF



(d) compressive strength of all mixtures studied in comparison

Fig. 13 Compressive strength of mixtures with and without addition of fine powder as a function of time

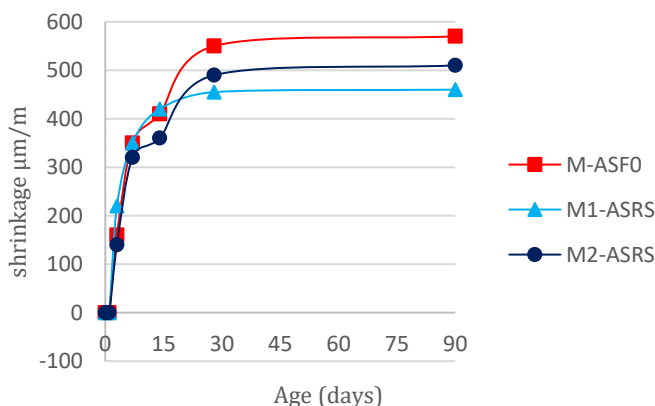
4.3. The Effect of Adding Recycled Sand and Fine Powder on Shrinkage

mixes is similar during the curing time, which resulted in an increase in drying shrinkage as a function of time, this shrinkage is greater in the first 28 days, this due to water evaporation, beyond this period a slight increase observed in all types of mortars studied, similar results were observed in the study of [20]. But the results obtained show a decrease in the shrinkage of alluvial sand mortars mixed with M1-ASRS and M2-ASRS recycled sand compared with mortars made with 100% M-AS alluvial sand.

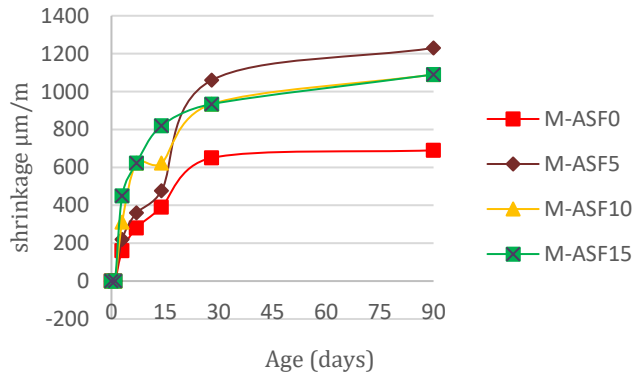
These decreases are respectively of the order of 17.27% and 10.90% at 28 days and of the order of 19.30% and 7.02% at 90 days. The same was observed in the work of [21-18], who found that the addition of AR had a positive effect on shrinkage. As a result, M1-ASRS mortar shows the lowest shrinkage relative to M2-ASRS. This increase in shrinkage is due to the presence of a large quantity of RS, which increases the W/C ratio during mixing, and also to the nature of RS, despite this, the shrinkage of M2-ASRS remains lower than that of M-AS. It can therefore be said that the incorporation of RS in percentages of up to 25% improves the shrinkage of alluvial sand.

The same was observed in the work of [22] where they stated that the addition of RA had a negative influence on the shrinkage phenomenon. Figs. 14 (b, c, d et e). show that incorporating up to 10% CWPF has a positive effect on shrinkage, where mortars M1-ASRSF5 and M1-ASRSF10% show a decrease in shrinkage, this decrease being 4.61% and 6.92% at 28 days and 2.9% and 10. 14% at 90 days on the other hand, above 10% CWPF, there is an increase in shrinkage compared with M-AS mortar.

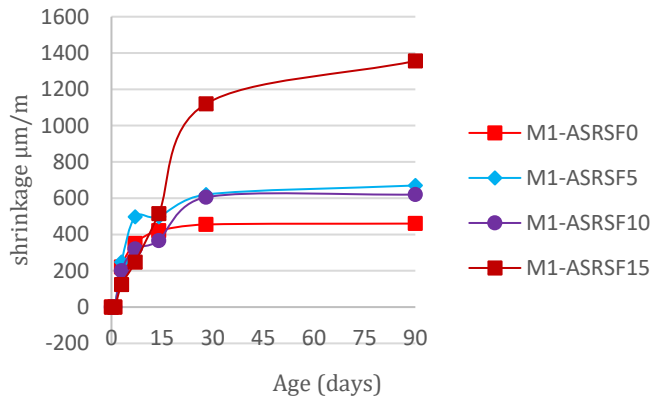
The probable reason for the improvement in the shrinkage phenomenon is the effect of filling the interstitial voids with CWPF, which creates a very dense microstructure which limits microcracking and internal movements of alluvial sand mortars, and also due to the presence of non-hydrated cementitious material, the latter forming hydrates in the presence of water, resulting in long-term internal hardening that limits shrinkage. These results show that the addition of up to 10%CWPF has a positive effect on the shrinkage of alluvial sand.



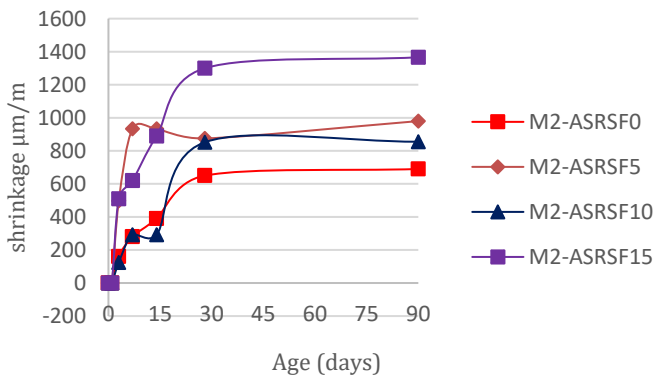
(a) M-AS, M1-ASRS et M2-ASRS without CWPF



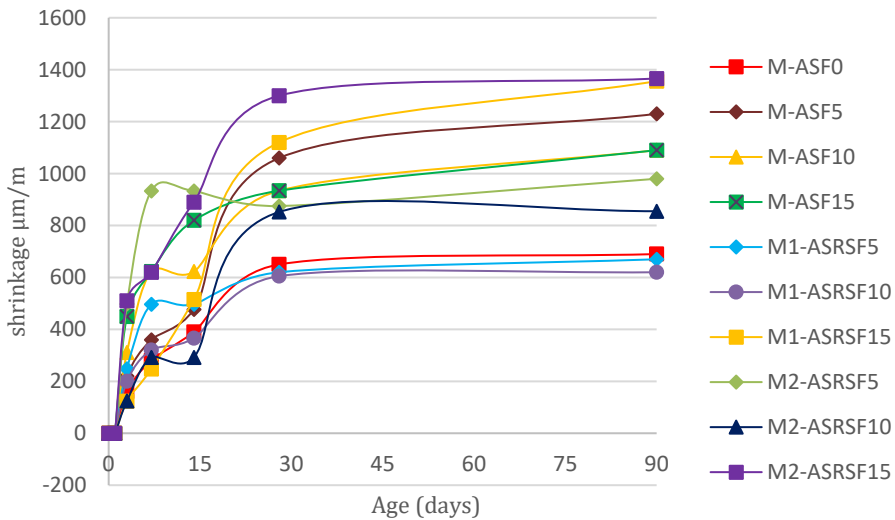
(b) M-AS with and without CWPF



(c) M1-ASRS with adding CWPF



(d) M2-ASRS with adding CWPF



(e) Shrinkage of all mixtures studied in comparison

Fig. 14 Shrinkage of mixtures with and without addition of fine powder as a function of time.

5. Conclusions

The study of all the results concerning the mechanical and rheological characteristics of alluvial sand mortars has enabled us to identify the main findings of this work:

- The addition of demolition sand, which contains a high proportion of fine elements to alluvial sand, helps to fill the voids between the grains of alluvial sand thanks to the fine elements. On the other hand, the alluvial sand grains fill the voids between the coarse demolition sand grains, resulting in a well-balanced grain gradient.
- Correcting the grading of recycled sand with silty sand had a positive effect on improving physical properties (fineness modulus).
- Replacing more than 30% of the natural sand with recycled sand, the mixed sand may lose certain physical properties such as fineness modulus.
- Incorporating recycled sand into the alluvial sand mortar mixture slightly reduces the mechanical strength of the mortar studied.
- Some samples made up of alluvial sand and demolition sand gave better strength results than the mortar sample made up of 100% alluvial sand, and this is of course due to the origin of the recycled aggregates and the strength of the demolished concrete.
- A mixture containing 25% recycled sand showed better compressive strength over the long term (90 days) than a 100% AS mixture.
- Some of the physical properties of CWPF were close to those of Portland cement, encouraging and enabling its use as a substitute for a percentage of synthetic cement to reduce carbon dioxide emissions from cement plants.
- The incorporation of RS and CWPF in the alluvial sand slurry mixture reduced the mechanical strength of the slurry studied.

- As for the effect of incorporating demolition aggregates on the shrinkage of the mortar studied, it varied between an improvement on some samples and an increase on others.
- The incorporation of 15% and 25% alluvial sand in the mortar showed improved shrinkage compared with the 100% AS mixture.
- Mixtures with 15% RS, 5% replacement and 10% CWPF showed improved shrinkage compared with the other mixtures.
- The addition of 15% recycled sand and 10% CWPF to alluvial sand mortar showed positive results, encouraging the use of recycled concrete waste as an alternative to sand and cement, for economic and environmental reasons as part of the valorization of construction waste.

Acknowledgement

We thank the CRAPC laboratory (University of Ouargla) for its help in carrying out the EDS analysis.

References

- [1] Etude de faisabilité. (2011). Projet R&D. PN Recybéton (RECYclage complet des BETONS).
- [2] Xiao J, Li W, Fan Y, Huang X. An overview of study on recycled aggregate concrete in China (1996-2011). *Construction and Building Materials*, 31, 364-383, 2012. <https://doi.org/10.1016/j.conbuildmat.2011.12.074>
- [3] Ulsen C, Kahn H, Hawlitschek G, Masini EA, Angulo SC, John VM. Production of recycled sand from construction and demolition waste. *Construction and Building Materials*, 40, 1168-1173, 2013. <https://doi.org/10.1016/j.conbuildmat.2012.02.004>
- [4] Pacheco-Torgal F, Tam VWY, Labrincha JA, Ding Y, de Brito J. *Handbook of recycled concrete and demolition waste*. Woodhead Publishing, Oxford, 2013.
- [5] Possan E, Thomaz WA, Aleandri GA, Felix EF, dos Santos ACP. CO₂ uptake potential due to concrete carbonation: a case study. *Case Stud. Constr. Mater.*, 2017. <https://doi.org/10.1016/j.cscm.2017.01.007>
- [6] Mehta PK, Monteiro PJM. *Concrete: Microstructure, Properties, and Materials*. McGraw-Hill Education, 2014.
- [7] Boden TA, Andres RJ. *Global CO₂ emissions from fossil-fuel burning*. Cement Manuf. Gas Flaring. 1751-2014, 2017.
- [8] NOAA, 2020. Earth system research laboratory. Global monitoring division. Trends in atmospheric carbon dioxide [WWW document] Earth Syst. Res. Lab.
- [9] Scrivener KL. SPECIAL ISSUE-Future Cements Options for the future of cement. *Indian Concr. J.* 2014.
- [10] Scrivener KL, John VM, Gartner EM. Eco-efficient cements: potential economically viable solutions for a low-CO₂ cement-based materials industry. *Cement Concr. Res.* 114, 2e26, 2018. <https://doi.org/10.1016/j.cemconres.2018.03.015>
- [11] Puerta-Falla G, Kumar A, Gomez-Zamorano L, Bauchy M, Neithalath N, Sant G. The influence of filler type and surface area on the hydration rates of calcium aluminate cement. *Construct. Build. Mater.* 96, 657e665, 2015. <https://doi.org/10.1016/j.conbuildmat.2015.08.094>
- [12] Gastaldi D, Canonico F, Capelli L, Buzzi L, Boccaleri E, Irice S. An investigation on the recycling of hydrated cement from concrete demolition waste. *Cement Concr. Compos.* 2015. <https://doi.org/10.1016/j.cemconcomp.2015.04.010>
- [13] Wang J, Mu M, Liu Y. Recycled cement. *Construct. Build. Mater.* 190, 1124e1132, 2018. <https://doi.org/10.1016/j.conbuildmat.2018.09.181>

- [14] Ma X, Wang Z. Effect of Ground Waste Concrete Powder on Cement Properties. *Advances in Materials Science and Engineering*. Article ID 918294, 2013 . <https://doi.org/10.1155/2013/918294>
- [15] da S. Ferreira RL, Anjos MAS, Ledesma EF, Pereira JES, Nóbrega AKC. Evaluation of the physical-mechanical properties of cement-lime based masonry mortars produced with mixed recycled aggregates, *Mater. Construcción*. 70 (2020) 210. <https://doi.org/10.3989/mc.2020.02819>
- [16] Abreu V, Evangelista L, de Brito J. The effect of multi-recycling on the mechanical performance of coarse recycled aggregates concrete, *Constr. Build. Mater.* 188 (2018) 480-489. <https://doi.org/10.1016/j.conbuildmat.2018.07.178>
- [17] Ozalp F, Yılmaz HD, Kara M, Kaya O, Sahin A. Effects of recycled aggregates from construction and demolition wastes on mechanical and permeability properties of paving stone, kerb and concrete pipes. *Construct. Build. Mater.* 110, 17e23, 2016. <https://doi.org/10.1016/j.conbuildmat.2016.01.030>
- [18] S. Jesus et al. Rendering mortars with incorporation of very fine aggregates from construction and demolition waste / *Construction and Building Materials* 229 (2019) 116844. <https://doi.org/10.1016/j.conbuildmat.2019.116844>
- [19] Abnt, 2017a. NBR 16605: Portland Cement and Other Powdered Material - Determination of the Specific Gravity
- [20] Ledesma EF, Jiménez JR, Ayuso J, Fernández JM, de Brito J, Maximum feasible use of recycled sand from construction and demolition waste for eco-mortar production - Part-I: ceramic masonry waste, *Journal of Cleaner Production* 2014. <https://doi.org/10.1016/j.jclepro.2014.10.084>
- [21] A. Mardani-Aghabaglou et al. Improving the mechanical and durability performance of recycled concrete aggregate-bearing mortar mixtures by using binary and ternary cementitious systems/ *Construction and Building Materials* 196 (2019) 295-306 <https://doi.org/10.1016/j.conbuildmat.2018.11.124>
- [22] Li L, Liu W, You Q, Chen M, Zeng Q. Waste ceramic powder as pozzolanic supplementary filler of cement for developing sustainable building materials. *J. Clean. Prod.* 259, 120853, 2020. <https://doi.org/10.1016/j.jclepro.2020.120853>



Research Article

Study of morphology and effect of compression moulding parameters on mechanical properties of nanoclay/polymer nanocomposites sheet moulding compound

Pankaj Dhongade ^{*a}, Vikas Sargade ^b

Dept. of Mechanical Eng., Dr. Babasaheb Ambedkar Technological University, Maharashtra, India

Article Info

Abstract

Article history:

Received 18 Jan 2023

Accepted 24 May 2023

Keywords:

Nanoclay;

Sheet moulding

compounds;

Compression moulding;

X-ray diffraction

analysis;

Tensile testing;

Flexural testing

Owing to the much larger surface (or interface) area per unit volume, drastic difference in material behaviour can be observed between the conventional and nanostructured materials. A nanostructured material can have totally different properties from a larger-dimension material of the same composition because many of the important chemical and physical interactions are governed by the surfaces. This study considers polymer nanocomposites in the form of sheet moulding compounds. The polymer nanocomposite is formed by adding surface modified Montmorillonite nano-clay as a major nano-material to the SMC composite material so as to enhance the material properties. This study considers fabrication and characterization of polymer nanocomposite by employing the compression moulding technique. Scanning electron microscopy has revealed that though the polymer nanocomposites improve the material properties but its fabrication should be carefully carried out in order to avoid formation of irregularities in the material. The x-ray diffraction results confirmed the retention of crystallinity of the polymer nanocomposites. Upon characterization it has been observed that the material properties like tensile strength, percentage elongation and flexural strength are enhanced. The hardness of the polymer nanocomposite material is slightly improved and the specific gravity is also found to be slightly decreasing making the nano-clay composite lighter.

© 2023 MIM Research Group. All rights reserved.

1. Introduction

1.1 Sheet Moulding Compound (SMC)

The SMC are fiber-reinforced thermosetting semi-finished products, preferably fabricated using compression moulding method [1]. Sheet moulding compounds composites are high-strength, cost-effective composites, with the combination of fillers, fiber reinforcement, thermosetting resin [2], and other additives for special aims that are manufactured by thermo-compression process. The clay (improved surface), calcium carbonate (reduced cost), talc (improved temperature resistance), hollow glass microspheres (weight reduction, thermal insulation), alumina trihydrate (fire retardance), and mica (improved weathering), are the common material used as fillers. The unsaturated polyester (UP), vinyl ester (VE), phenolic or a modified vinyl urethane are mostly preferred for Thermosetting resin [3]. SMC has the major advantage of being able to be manufactured in medium to high volumes [4] but also has many other advantages offered by composites such as light weight, lower tooling costs, and reduced costs by parts integration. The electrical engineering components, construction industry and automotive sector main sections of applications for SMC components. The cabinets, switches and insulating units

*Corresponding author: dhongadepankaj@gmail.com

^a orcid.org/0000-0001-5557-7104; ^b orcid.org/0000-0001-8855-112X

DOI: <http://dx.doi.org/10.17515/resm2023.651me0118>

Res. Eng. Struct. Mat. Vol. 9 Iss. 4 (2023) 1325-1345

needed in the electrical sector, are produced from SMC. The components like coverings of mudguards, trunk lids, loading areas, and fenders needed for the automotive industry, are made of SMC [5]. SMCs are commonly used in automotive industry for its excellent chemical resistance, long-life service, and most importantly, the light-weight of the structural components [6].

1.2. Polymer Nanocomposites

Owing to the much larger surface (or interface) area per unit volume, drastic difference in material behaviour can be observed between the conventional and nanostructured materials. A nanostructured material can have totally different properties from a larger-dimension material of the same composition because many of the important chemical and physical interactions are governed by the surfaces [7, 8]. For the fiber and layered material, a change in particle diameter, layer thickness, or fibrous material diameter from the micrometer to nanometer range, will affect the surface area-to-volume ratio by three orders of magnitude [9]. So, the larger surface area per unit volume can be observed for the nanocomposites that uses very small sizes (in nanometer) of reinforcement material. Nanofibers or nanotubes (1-dimensional) and nanofibers (2-dimensional) [10] facilitates for the high aspect ratios of the particulate constituent which results in good reinforcing efficiency. By adding just enough amount of a low-volume fraction of fillers, the desired performance can be achieved for the polymer nanocomposites and these fillers usually contributes only marginally to the final weight and cost [11].

1.3 Effect of Nanomaterials on Mechanical Properties

The performance of nanocomposites depends on various characteristics of the nanoparticles, such as its size, aspect ratio, specific surface area, and physical/chemical compatibility with the matrix and also on the properties of constituents, composition [12]. Enhanced flexural strength enhances resistance offered to bending and shear loads of a composite material. It has been found by Xu and Hoa [13] that adding a low weight percentage of nano clay to the fiber/epoxy composites improved its flexural strength by 38%. Another study by Shettar et al. has [14] considered the study of tensile and flexural strength of epoxy/nano clay nanocomposites with varying amount of nano clay (1%, 2%, 3%, 4% and 5% wt.) and found that the resistance of the material to tension and bending has been increased after reinforcement of nano clay from 0% to 2% but with reinforcement higher than 3%, the performance got degraded. It has been reported by Pol and Liaghat [15] that using organically modified montmorillonite nano clay (Cloisite 30B) with 3% wt. (out of 0%, 3% and 5%, 7%, and 10% wt. samples) in glass fiber/epoxy significantly increases the tensile strength and impact strength that decreases upon increasing amount of reinforcement of nano clay beyond 3%. Burmistr et al. [16] investigated the variation of tensile strength of nanocomposites formed by using organo-modified clay as a reinforcement material in the base material of polypropylene, polystyrene, and polyamide, and found that the tensile strength and tensile modulus increases up to certain amount of reinforcement after which the tensile strength decreases. A study by Quigley and Baird [17] showed that adding organic modified nano clay up to 7.6 % wt. (out of 0.9, 3.2, 4.9, 7.6, and 9.2 % wt.) in to nylon 6 using supercritical carbon dioxide (scCO₂) as a processing aid, has significantly improved the tensile modulus of the nanocomposite as compared to the base material. Chan et al. [18] considered the study of tensile strength of epoxy/nano clay nanocomposites with varying amount of organomodified montmorillonite nano clay (1%, 3%, 4%, 5%, 7% and 9% wt.) and found that the tensile strength has been increased after reinforcement of nano clay from 0% to 5% but with reinforcement higher than 5%, the performance got degraded.

The abovementioned literature review strongly advocates about using nano-clay as an addition to base material so as to improve several mechanical properties like tensile

strength, tensile modulus, and flexural strength. So, this study will also consider the nano-clay as an important nano-material for improving performance of the material. The readers who are more interested in knowing more about polymer nanocomposites that has higher mechanical properties are encouraged to study articles by Zhade et al. [19] (for tensile strength), Rafiee and Shahzadi [20] (for tensile modulus).

1.4 Necessity of Reducing Weight

One of the major fields of application of polymer composites is automotive industry and it is important to understand the necessity of weight reduction of the components used in the automotive industry. The use of vehicles is increasing day by day resulting in increasing consumption of fossil fuels. This ultimately contributes considerably to the climate change by increasing the amount of greenhouse gases in the environment. Increased use of lightweight materials decreases the energy consumption and hence greenhouse gas emissions [21]. The lightweight components made of glass-fiber reinforced polymers are shown to outperform their steel counterparts over the full life cycle mainly due to the reduced fuel consumption of the vehicle in the use phase [22]. Light weighting has been identified as a cross cutting technology with promising approach to meet the Corporate Average Fuel Economy (CAFÉ) standards, as 10% reduction in the vehicle weight can result in 6–8% increase in fuel efficiency in case of vehicle with conventional internal combustion engine while in case of a battery-electric vehicle fuel efficiency increases by up to 10% [23]. Similar to automotive industry, several other industries will also benefit by reducing the weight of the components.

The current study has major objective of preparing a polymer nanocomposite SMC material that will be beneficial for many applications which will have many desirable properties that are previously mentioned in this section. To achieve the major objective following sub-objectives are decided first one being fabrication of Nano clay composite SMC using compression moulding technique, second one being sample preparation of Nanocomposite SMC in sizes required as per the ASTM or any other standards for particular mechanical tests, and third being studying mechanical properties of polymer Nanocomposite SMC material. After accomplishment of the third sub-objective suggestions regarding usefulness of this newly formed nanocomposite SMC in the different fields of engineering world can be decided.

2. Methodology of Fabricating Polymer Nanocomposite

2.1 Measurement of Constituents of Polymer Nanocomposite

The important part of fabrication of the nanocomposite SMC is the additive nanomaterial that is responsible for enhancing many properties of the material as compared with the properties of the base material. The nanomaterial considered for addition to the base material is nano-clay. The nano-clay used in this study is Montmorillonite clay-based material which has its surface modified by using dimethyl dialkyl (C14-C18) amine with content of 35-45 % (on mass basis). The nano-clay has bulk density ranging from 200 kg/m³ to 500 kg/m³. The nano-clay has average particle size of 13 µm has Beige coloured appearance.

The thermosetting resin, fillers, fibre reinforcement, and other additives required for simplifying the production process of the nanocomposite SMC material. Unsaturated polyester isophthalic resin (Grade-Polypol 1053) is the thermosetting resin material taken into consideration in this investigation. The Polypol 1053 is a condensation polymer prepared by the reaction of polyols (also known as polyhydric alcohols), organic compounds with multiple alcohol or hydroxyl functional groups, with unsaturated dibasic acids. This resin is based on isophthalic acid which is an organic compound with the

formula $C_6H_4(CO_2H)_2$. The filler material is calcium carbonate, and the reinforcing element is chopped roving of E-glass fibres with random orientation and length of 1" (one inch). For ease of fabrication, additional materials including catalysts, mould release agents, and other added elements are also required. In this investigation, organic peroxide is employed as a catalyst and zinc stearates as a mould release agent. In the matrix material, additional additive components like pigment and inhibitors are also incorporated.

It is necessary to know some important characteristics of the materials utilised for fabricating the nanocomposite SMC before actually proceeding for the fabrication and for accomplishing that, some measurements are required. These measurements include of the measurement of viscosity and moisture content of the resin material and of the filler material. For the Brookfield Viscometer is used for the measurement of the viscosity, while the Karl Fischer Titrator is used for the measurement of moisture content.

2.1.1 Viscosity Measurement

The viscosity measurement is carried out by using the Brookfield Viscometer which works on the principle of the rotational viscometry. The amount of torque needed to rotate an item, such as a spindle, in a fluid is gauged and correlated with the viscosity of the fluid. The torque is applied through a calibrated spring to a disc or bob spindle submerged in the fluid, and the amount of torque is correlated with the viscous drag of the test fluid against the spindle [24]. It is possible to compare the Brookfield viscosities of non-Newtonian fluids, obtained under the same test settings (model, spindle, speed, temperature, test time, container, and any other sample preparation techniques that can have an impact on the behaviour of the fluid). Most of the times the trial-and-error methodology is adopted for choosing right spindle and speeds, when creating a new test technique. The effective test procedure produces a percentage torque reading between 5 to 100. The rheological behaviour of the test fluid can be monitored by using the same spindle at various speeds. But the Brookfield viscometer cannot be used for accurate rheometry because assigning a single shear rate is not possible due to the geometry of fluid around a revolving bob or disc spindle in a big container. The Brookfield Viscometer used in this study can be seen in Fig. 1.



Fig. 1 Digital Brookfield Viscometer

The Digital Brookfield Viscometer of DV2T model is used for this study. The number of spindles available are 4 and the number of speeds available are 18, ranging from 0.3 rpm

to 100 rpm. The range of viscosity that can be measured is from 15 to 2000000 mPa.s (mPa.s is Millipascal×seconds).

The use of second number spindle is recommended for the measurement of slurry viscosity. The spindle speed is kept constant at 20 rpm for 30 seconds to take the reading and then the viscosity running test is started. After 30 seconds, the measured value of viscosity is shown by the Brookfield viscometer.

2.1.2 Measurement of Moisture Content

Karl Fischer Titrator is the equipment used for the measurement of moisture content. The equipment, as the name suggests, works on the principle of Karl Fischer titration, which is a traditional titration technique used in chemical research to identify minute amount of water in a sample using coulometric or volumetric titration. In this titration, the amount of water content in a sample is evaluated by measuring the amount of water consumed during a redox reaction of Sulphur dioxide with iodine. In this simple reaction, exactly one molar equivalent of water gets used. The titration is continued by the addition of Iodine to the solution and is stopped when the amount of Iodine in the solution is overly present, which can be determined using potentiometry. The Karl Fischer titration is the go-to method for determining the amount of water because of its specificity, accuracy, and measuring speed.



Fig. 2 Karl Fischer Titrator

The Karl Fischer Titrator shows the Karl Fischer factor for the particular sample quantity. After that it sucks the reagent into the glass flask to find out the moisture content in the sample. The Karl Fischer Titrator used in this study can be seen from Fig. 2. The Karl Fischer Titrator uses volumetric method with vessel capacity of 200 ml. The dispensing resolution is 0.01 ml while the measuring range is 100 ppm to 100% with appropriate sample quantity. The titrator has fixed end point confirmation time of 20 seconds.

2.1.3 Measurement of Number of Ends

The filler and thermosetting resin material demand for the measurement of viscosity and the moisture content while only visual inspection is sufficient for the assessment of the reinforcement material. Chopped roving of E-glass fiber is the reinforcing element of the polymer matrix nanocomposite material considered in this study. By doing the visual inspection of glass fiber roving, the number of ends is measured. The chopped roving of E-glass fiber, used in this study can be seen in Fig. 3.



Fig. 3 E-glass fiber Chopped roving of length 1" (inch)

The characteristics of the various materials considered during the fabrication of the polymer matrix nanocomposite material and determined after completing the measurement are found to be as mentioned in

Table 1. Characteristics of raw materials of polymer matrix nanocomposite material **Hata! Başvuru kaynağı bulunamadı.**

After considering the characterization using abovementioned procedure, the constituents of polymer nanocomposite undergo mechanical mixing processing.

2.2 Dispersion of Nanomaterial into Unsaturated Polyester Resin

The mixture of powder and additives is added into the unsaturated polyester resin in order to have proper dispersion of filler material. Then at the operating speed of 700 to 800 rpm, the mixing is carried out for 10 minutes. The nano clay (surface modified Montmorillonite clay) is the nanomaterial used as the principal addition to base material. A high shear mechanical disperser operating at 1250 rpm, is used for 20 minutes to accomplish the dispersion of the nano clay into the unsaturated polyester resin. The dispersion of nano clay in to the unsaturated polyester resin can be seen in Fig. 4.

The spreading of matrix material on lower and upper sheet during the formation of SMC of polymer composite material needs to be carefully done so as to have the proper bonding between different materials used for polymer nanocomposite. The wetting characteristics of the material affects the bonding i.e. the highly viscous matrix material will not wet properly which may further result in several manufacturing defects in the polymer nanocomposite material. So, the in-process inspection is very important to monitor the values of viscosity. The viscosity of matrix material is measured by employing Brookfield Viscometer as a part of the in-process inspection during the dispersion process.



Fig. 4 Dispersion of Nano-clay in unsaturated polyester resin

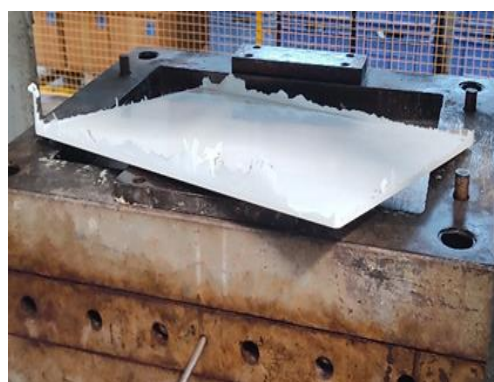
After considering the processing of the constituents, the preparation of polymer nanocomposite SMC is started using compression moulding method.

2.3. Compression Moulding Method

The samples are prepared using compression moulding technique with variation in amount of nano clay, moulding temperature and moulding pressure. There are three stages of compression moulding. The first stage consists of placing the polymer nanocomposite SMC sheet on the lower platen of a hot mould for some time (in seconds) before the mould is closed. Then the sheet is squeezed at a slow closure velocity of (in the range of few millimeters per second) in the second stage [25]. This stage results in considerable deformation of the SMC inside the mould cavity. The mould is kept closed after it gets filled, during a third curing stage for a period of 180 seconds.



(a)



(b)

Fig. 5 Sample sheet from compression moulding (a) Charge preparation (b) Moulded plate

The moulding of SMC sheet is carried out using compression moulding machine with capacity of 100 tons. The size of moulded sheet is $350 \times 250 \times 3.2$ mm.

3. Experimentation

3.1 Design of Experiments

For exploring the relationships efficiently and development of greater understanding of the key parameters [26], the design of experiments is very important. The design of experiments also helps in proper planning and execution of the experiments. In this study, the polymer nanocomposite SMC is prepared using compression moulding method by varying different parameters. The number of factors and the levels of those factors affecting the performance of the nanocomposite material (in terms of different properties of materials) are needed to be decided so as to start the procedure of design of experiments. The three important factors affecting the performance, considered in this study are, amount of nano-clay added to base material, moulding pressure and moulding temperature. For these abovementioned three factors two different values of those factors are considered, as mentioned in Table 2.

Table 2. Parameters affecting performance with its amount

Parameter	Amount
Nano-clay (Phr)	0.2 and 0.4
Moulding Temperature ($^{\circ}\text{C}$)	150 and 160
Moulding Pressure (kg/cm^2)	120 and 130

The full factorial design consisted of 8 runs with all the possible combination of amount of reinforcement, temperature and pressure applied during compression moulding. The experimentation is carried out as per the design of experiment mentioned in the Table 3.

Table 3. Design of Experiments

Run	Nano clay (Phr)	Temp. ($^{\circ}\text{C}$)	Pressure (Kg/cm^2)
1	0.2	150	120
2	0.4	150	120
3	0.2	160	120
4	0.4	160	120
5	0.2	150	130
6	0.4	150	130
7	0.2	160	130
8	0.4	160	130

3.2 Sample Preparation

The samples are prepared as per recommendations for tensile, flexural and hardness test, with variation of different parameters. The samples are prepared from a sheet of the nanocomposite material formed by compression moulding. The geometric layout of the samples needed for different tests can be seen in Fig. 6.

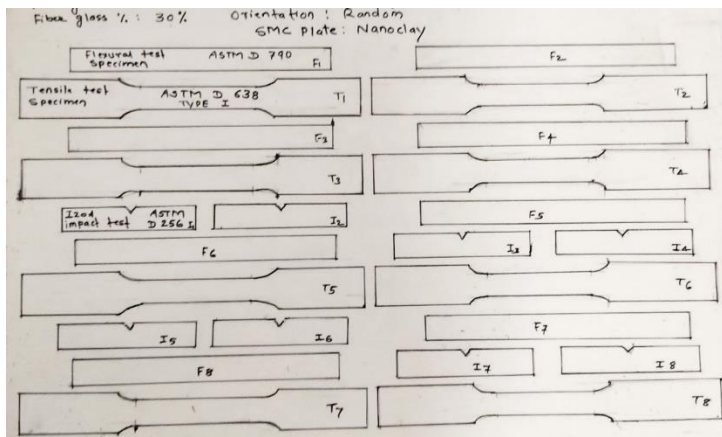


Fig. 6 Layout of the samples from a sheet needed for tensile (T) and flexural (F) tests

4. Characterization of Material Properties

4.1 Morphological Characterization

The Scanning Electron Microscopy (SEM) is one of the major primary diagnostic methods employed for the visualization of the morphology of the surface of the substances like polymers or its composites. In SEM, scanning of the cross-section of the polymer sample is carried out to obtain an image, using a focused electron beam. The atoms and the electrons in the cross-section interact with each other and lead to a variety of detectable signals that reveal details about the surface topography and composition of the sample. The electron beam is typically scanned in a raster scan pattern, and an image is created by fusing the position of the beam with the detected signal [27].

This study is carried out using NOVA NAMOSEM 450 model of Field Emission Scanning Electron Microscope (FE-SEM) that has the Magnification capacity of 20X to 1,000,000X and the images are processed using xT microscope Server. Understanding and locating the irregularities due to agglomeration, void formation and crack formation is the main motive of carrying out the morphological study using SEM.

4.2 X-ray Diffraction Analysis

In order to create polymer nano composites, various nanomaterials in the form of platelets, fibres, and spheroids have been used. Nanomaterials are frequently used in the form of nano clays (mainly layered silicates), nano silica, nanotubes, and nanofibers. The surface chemistry of nanoparticles is frequently further optimized to influence the performance of nanocomposites, resulting in improved nanoparticle dispersion, stronger polymer-particle interactions, and improved polymer adherence to the nanoparticle [28]. X-ray diffraction spectroscopy (XRDS) commands an important position in characterizing and optimizing these interactions.

Utilizing the fundamental tool of X-ray diffraction (XRD), standard studies of the crystallographic materials, including polymers, have been conducted for material characterization. Traditionally, XRD has been used to investigate the crystalline and amorphous structure of polymers, composites, and fillers. The XRD facilitates to the analysis of material using different types of characterizations like phase composition, composition variations, crystallite size and shape, orientation, lattice distortions and faulting, in-situ structure development of nano materials. XRD technique has earned

acolades and has been seen as an attractive tool owing to its simplicity, reliability, non-destructive nature and the quantitative information that can be collected.

4.3 Characterization of Tensile Strength

The tensile strength of the sample is checked using the tensile test carried out using A H25KS model of Universal Testing Machine. For selecting the specimen size and for conducting the tensile test, ASTM D 638 Type I standards for tensile test are followed. The specimen samples size is decided to be $165 \times 13 \times 3.2$ mm. The moulded specimen sample tested at head displacement speed of 2 mm/min.

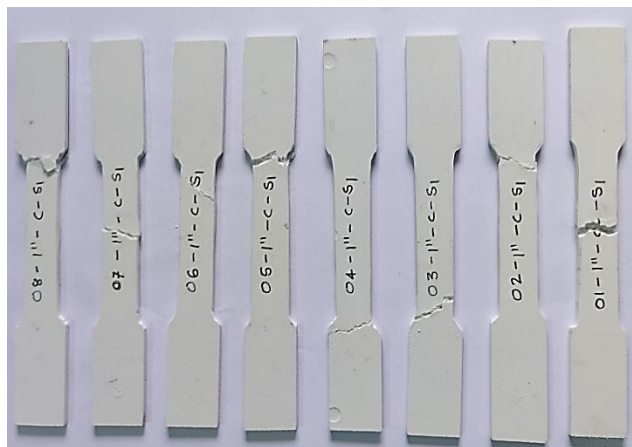


Fig.7 Samples used for the tensile test

4.4 Characterization of Flexural Strength

The flexural strength of the sample is checked using Universal Testing Machine. For selecting the specimen size and for conducting the tensile test, ASTM D 790 standards for flexural test are followed. The specimen samples size is decided to be $127 \times 12.7 \times 3.2$ mm. The moulded specimen sample tested at head displacement speed of 2 mm/min.

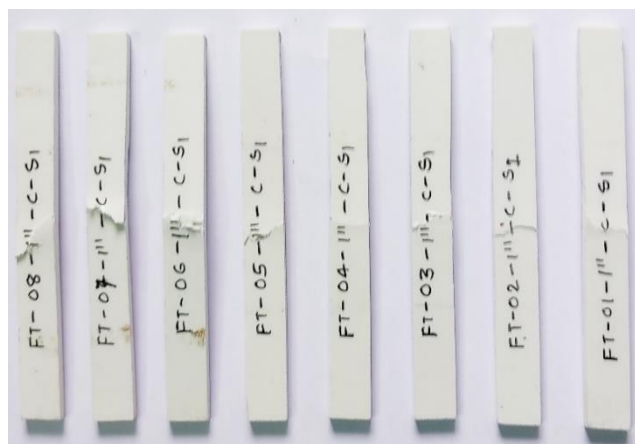


Fig.8 Samples used for the flexural test

The Universal Testing Machine used for the flexural test has specifications similar to that is being used for the tensile test.

4.6 Characterization of Hardness

The moulded specimen samples are tested according ASTM D 2583-07 standard. The specimen samples size is decided to be $25 \times 25 \times 3.2$ mm. The total four samples are prepared for the test. The hardness of the sample is checked using the hardness test carried out using Barcol hardness impressor.



Fig. 9 Barcol hardness impressor

5. Results and Discussion

5.1 Scanning Electron Microscope Imaging

In this study, the specimens failed in the tensile test are used for the SEM image analysis. Fracture surface of tensile test sample coated with 5 nm of platinum to avoid the charging effect.

5.1.1 Agglomeration of Filler

The degree to which the material properties of a polymer nanocomposite are strengthened depends on the filler's distribution over the polymer matrix. Material scientists concentrate on enhancing the polymer-filler interaction, or bonding between fillers and the polymer basis, while making composites. However, because the fillers prefer to bind with one another rather than the polymer matrix, the fillers may gather into clusters or clouds. This kind of bonding is referred to as filler-filler interaction. Increased filler-filler interaction degrades a polymer composite's material quality. When viewing a greyscale SEM image, as can be seen in Fig. 10, the agglomerates are clearly visible in white colour.

5.1.2 Void Formation

The majority of polymer nanocomposite materials exhibit volume dilatation when subjected to forces that cause elongation. At small strains, the material reacts by deforming between its segments in an elastic and inelastic manner. At higher stresses, cavitation-induced volume dilatation is seen [29]. Due to the fact that it reduces a polymer nanocomposite specimen's ability to support loads, the void formation phenomena has received extensive research. Voids (between crystal lamellae) are easily generated in uniaxial tension because tie chain molecules disentanglement and/or rupture are

encouraged, leading to inter-lamellar slip, which prevents significant strain hardening. [30]. When viewing a greyscale SEM image, as can be seen in Fig. 10, the micro voids, are clearly visible in dim grey colour with its dimensions mentioned in green colour.

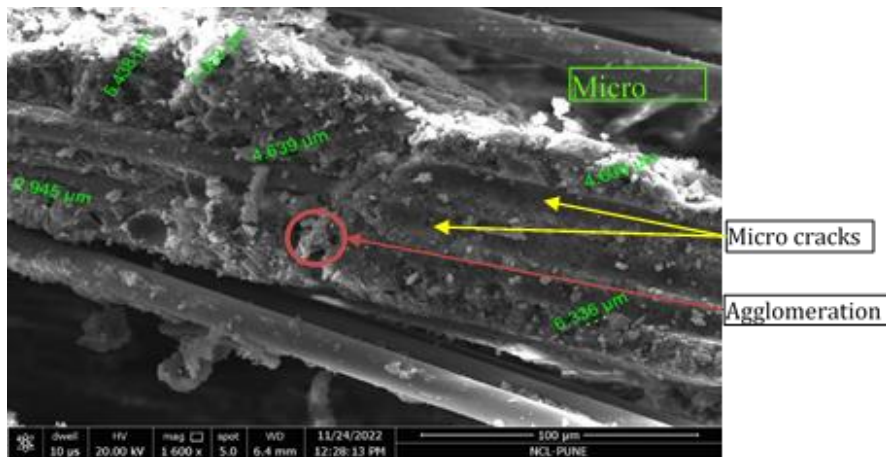


Fig. 10 SEM image showing various irregularities

5.1.3 Crack Formation

Before the start of crack initiation, a number of physical and mechanical phenomena, such as the presence of interfaces and interfacial layers around particles that cause changes in material properties, the triggering of fibrillation and crazing due to the formation of voids, and scaling or confinement effects brought on by the small sizes of the constituent structural elements, occur in nanostructured polymers. In order to prevent void coalescence, the size of the voids should be smaller (with dimensions of few nano meters) in case of unavoidable occurrence of void formation [31]. If there is formation of larger voids upon cavitation and – by coalesce of voids formed in closely connected polymer nanocomposite particles – give rise to crack formation and premature fracture. Two of the micro cracks that are formed in the sample can be observed in Fig. 10.

5.2 X-ray Diffraction Analysis

A single XRD reflection consists of various independent basic parameters and each of them possesses its own physical meaning [2]. The Bragg's diffraction angle (the angle between the incident rays and the diffracting planes) graphically exhibits the peak position. The size of sub-micrometer crystallites in a solid is related to the width of a peak in a diffraction pattern by the Scherrer particle size. So, in getting the dimensions of the particles, the width of an XRD peak plays a pivotal role. The peak shape comprehensively issues the effects of both crystalline size and lattice strain. The sharp peaks are often observed in case of powder XRD which can be seen in Fig. 11. Peak intensity is a reflectance of both absorption and amount of phase in the mixture. The diffraction angle, geometry of instrument, phase diffraction feature, and crystal structure affects the value of peak intensity.

The X-ray diffraction of powder of nano-clay composite SMC weighing 5 gm is carried out at different diffraction angle (2θ) from 10° to 80° . The results, as indicated in Fig. 11, shows highly crystalline peaks for the sample with 0.2 phr observed at diffraction angles of 23.40° , 29.72° , 36.29° , 39.75° , 43.50° , 47.85° , 48.85° with highest peak having intensity of 6558 at 29.72° . For the sample with 0.4 phr observed at diffraction angles of 23.19° ,

29.57°, 36.12°, 39.59°, 43.33°, 47.72°, 48.67° with highest peak having intensity of 6075 at 29.57°. As per the Bragg's equation, peak position (diffraction angle) is a function of the distance (d_{hkl}) between reflection planes (hkl) and in this case the distance between reflection planes varies from 3.7967 Å to 1.8620 Å. The equation known as "Scherrer's equation" is frequently used to calculate the size (diameter) of crystallites from recorded diffraction peak profiles by substituting the FWHM (full width at half its maximum intensity) for the integral width for the corresponding peak. In the current study the diameter of the crystallite is found to be 316 Å.

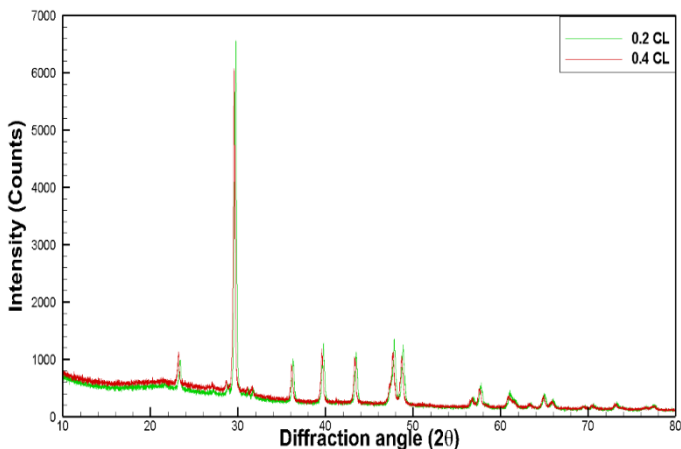


Fig. 11 X-ray diffraction diffractogram of nanocomposite formed using nano-clay

These multiple peaks indicate that the polymer nanocomposite is crystalline [31], however, the intensity at the peak decreases when the amount of nano clay is increased from 0.2 phr to 0.4 phr. The crystallinity is proof that there exists a strong bonding between the several additives used in the formations of polymer nanocomposite.

5.3 Effect of Amount of Reinforcement on Mechanical Properties

The detailed result on properties of nanocomposites formed by varying different parameters like amount of nano clay, temperature and pressure applied during compression moulding, can be seen in Table 4.

Table 4. Tensile and flexural properties of the samples

Run	Nano clay (Phr)	Tem p. (°C)	Pressure (Kg/cm ²)	Tensile strength (MPa)	Flexural strength (MPa)	Elongation (%)
1	0.2	150	120	98.2	191.4	5.17
2	0.4	150	120	102.6	195.4	6.28
3	0.2	160	120	99.6	191.8	5.68
4	0.4	160	120	103.8	198.3	7.11
5	0.2	150	130	101.5	193.5	5.48
6	0.4	150	130	104.3	198.7	7.66
7	0.2	160	130	98.8	192.6	5.24
8	0.4	160	130	104.6	199.4	7.91

By comparing the results of the samples of 2nd, 4th, 6th, and 8th run with the results of the samples of 1st, 3rd, 5th, and 7th run, respectively, it can be concluded that for all the values of temperature and pressure of compression moulding, the tensile strength, the flexural strength, and the percentage elongation of the nanocomposite increases with increase in amount of nano clay material. This means that the polymer nanocomposite with more amount of reinforcement offers more resistance to the tensile and bending load than that with low amount of reinforcement which ultimately means that the ductility of the polymer nanocomposite with more amount of reinforcement is higher than that with low amount of reinforcement. This underlines the importance of formation of polymer nanocomposite from the base material so as to improve the performance against tensile and bending load.

5.4 Effect of Temperature of Compression Moulding

The performance enhancement of the nanocomposites in terms of the tensile strength, as can be seen from Fig. 12, improves negligibly with increase in temperature for all the samples except the samples with 0.2 Phr of nano-clay and 130 kg/cm² of operating pressure. The maximum improvement in the tensile strength is found to be 1.4 %.

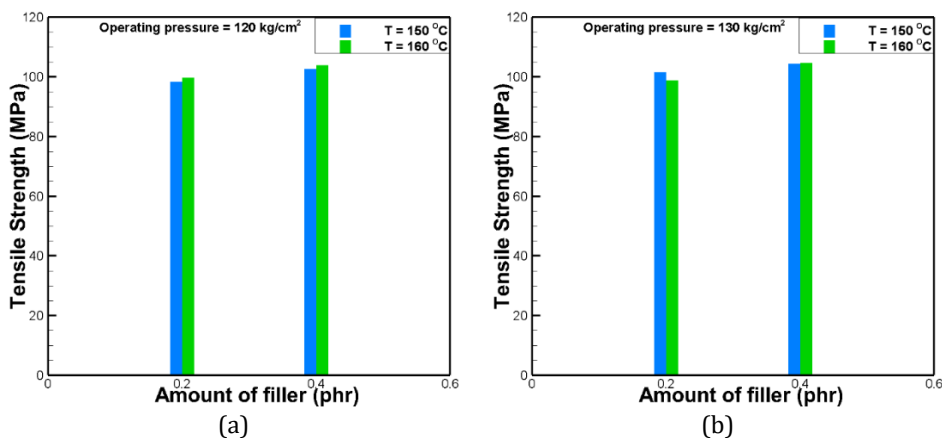


Fig. 12 Effect of compression moulding temperature on tensile strength of nano-clay nanocomposite at operating pressure of (a) 120 kg/cm² (b) 130 kg/cm²

The performance enhancement of the nanocomposites in terms of the flexural strength, as can be seen from Fig.13, improves negligibly with increase in temperature for all the samples except the samples with 0.2 Phr of nano-clay and 130 kg/cm² of operating pressure. The maximum improvement in the flexural strength is found to be 1.5 %.

The performance enhancement of the nanocomposites in terms of the percentage elongation, as can be seen from Fig.14, improves with increase in temperature for all the samples except the samples with 0.2 Phr of nano-clay and 130 kg/cm² of operating pressure. The maximum improvement in the percentage elongation is found to be 13.2 %.

It is noteworthy that the performance of the samples with 0.2 Phr of nano-clay and 130 kg/cm² in terms of tensile strength, flexural strength and the percentage elongation, deteriorates with increase in operating temperature. This means that with lower amount of filler and applied pressure, the increase in temperature may be causing weakening of bonding between the nano-clay and the base material resulting in decrement in the resistance offered by nanocomposite to the tensile and bending load.

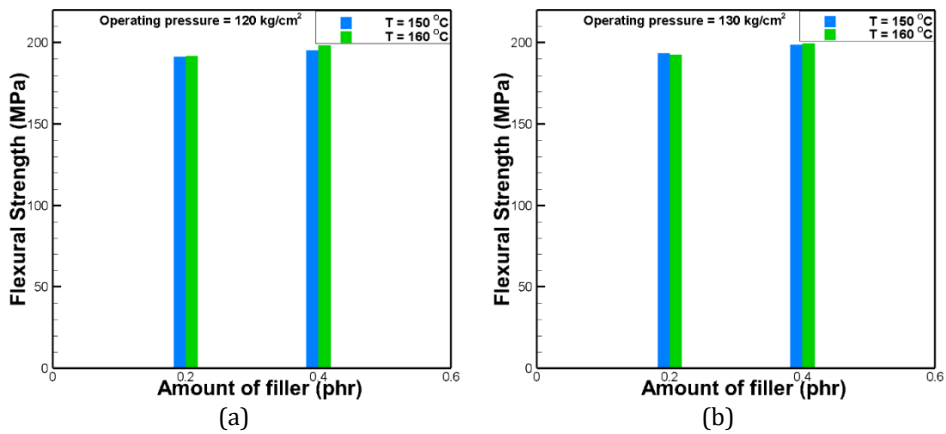


Fig.13 Effect of compression moulding temperature on flexural strength of nano-clay nanocomposite at operating pressure of (a) 120 kg/cm² (b) 130 kg/cm²

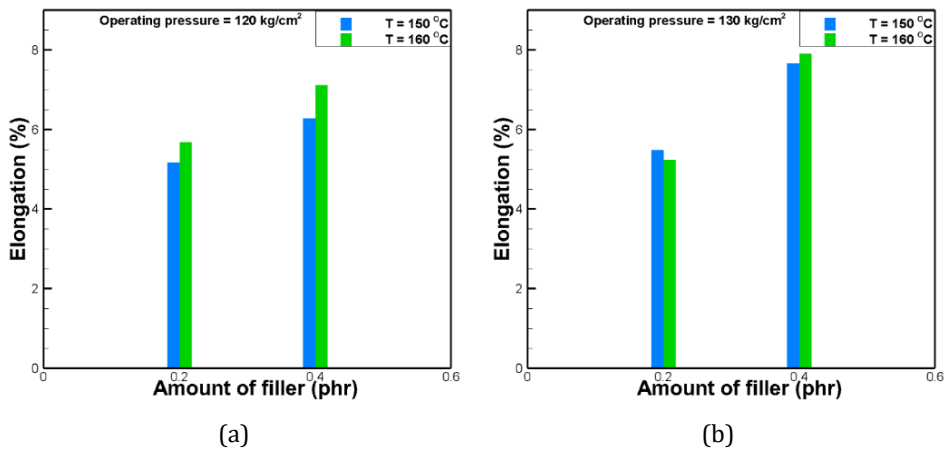


Fig.14 Effect of compression moulding temperature on percentage elongation of nano-clay nanocomposite at operating pressure of (a) 120 kg/cm² (b) 130 kg/cm²

Also, when the composite does not completely melt or flow at low mould temperatures, glass fiber impregnation is decreased. If the heating temperature is below a certain level during the moulding process, the resin cannot completely melt or flow, resulting in excessive flow viscosity and insufficient saturation; if the heating temperature is above a certain level, the resin will degrade, reducing its mechanical performance. A composite material can never revert to its initial state once it has solidified. Cross-links, which are three-dimensional molecule chains, may have formed as a result. In order to prepare the composite to be extremely strong and thermally resilient, the curing temperature needs to be raised. Beyond the critical mould temperature, the matrix starts to degrade and the fibers start to disorder, leading to brittleness and reduced strength. As it has been found that the increment in moulding temperature enhances the mechanical properties of the composite, it can be safely said that the operating temperature used in this study is less than the critical mould temperature.

Table 5. Barcol hardness and specific gravity of the samples

Run	Nano clay (phr)	Temp. (°C)	Pressure (Kg/cm ²)	Barcol hardness	Specific gravity
2	0.4	150	120	47	1.711
4	0.4	160	120	48	1.694
6	0.4	150	130	48	1.699
8	0.4	160	130	49	1.690

The detailed results of Barcol hardness test and measurement of specific gravity for fixed amount of filler of 0.4 phr, and variable temperature and pressure applied during compression moulding, can be seen in Table 5. For applied pressures of 120 kg/cm² and 130 kg/cm², the performance of nano-clay composites, in terms of Barcol hardness and specific gravity, slightly enhances with increase in temperature (decrement in specific gravity is desirable).

5.5 Effect of Applied Pressure of Compression Moulding

The performance enhancement of the nanocomposites in terms of the tensile strength, as can be seen from Fig. 15, improves negligibly with increase in pressure for all the samples except the samples with 0.2 Phr of nano-clay and 160 °C of operating temperature. The maximum improvement in the tensile strength is found to be 3.4 %.

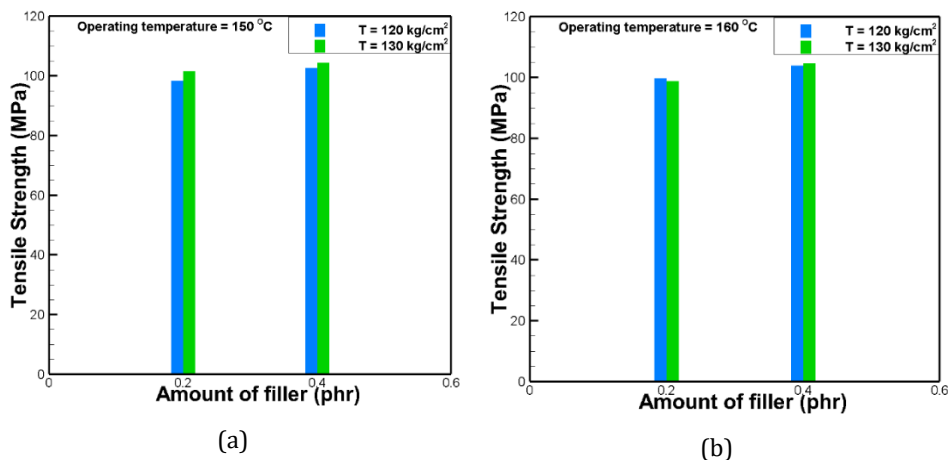


Fig. 15 Effect of compression moulding pressure on tensile strength of nano-clay nanocomposite at operating temperature of (a) 150 °C (b) 160 °C

For samples with 0.2 Phr and 0.4 Phr of nano-silica and 150 °C and 160 °C of operating temperature, the performance of the nanocomposites in terms of the flexural strength, as can be seen from Fig. 16, improves negligibly with increase in pressure. The maximum improvement in the flexural strength is found to be 1.7 %.

The performance enhancement of the nanocomposites in terms of the percentage elongation, as can be seen from Fig. 17, improves with increase in pressure for all the samples except the samples with 0.2 Phr of nano-clay and 160 °C of operating temperature. The maximum improvement in the percentage elongation is found to be 22 %.

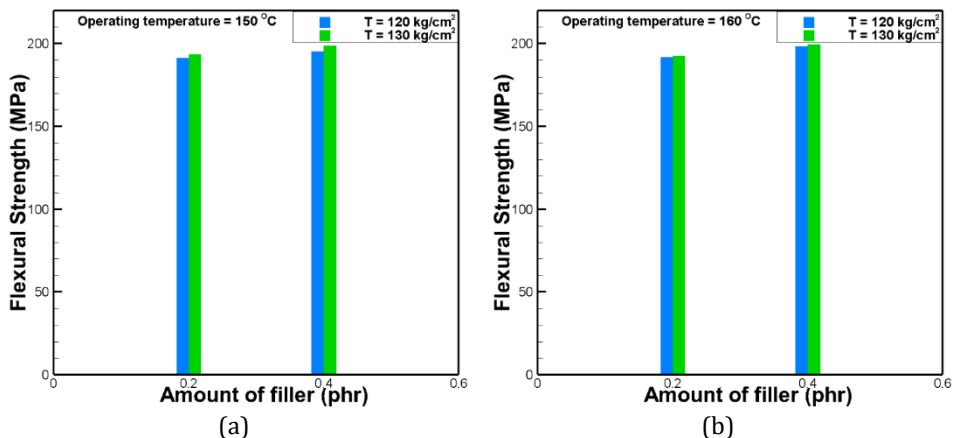


Fig. 16 Effect of compression moulding pressure on flexural strength of nano-clay nanocomposite at operating temperature of (a) 150 °C (b) 160 °C

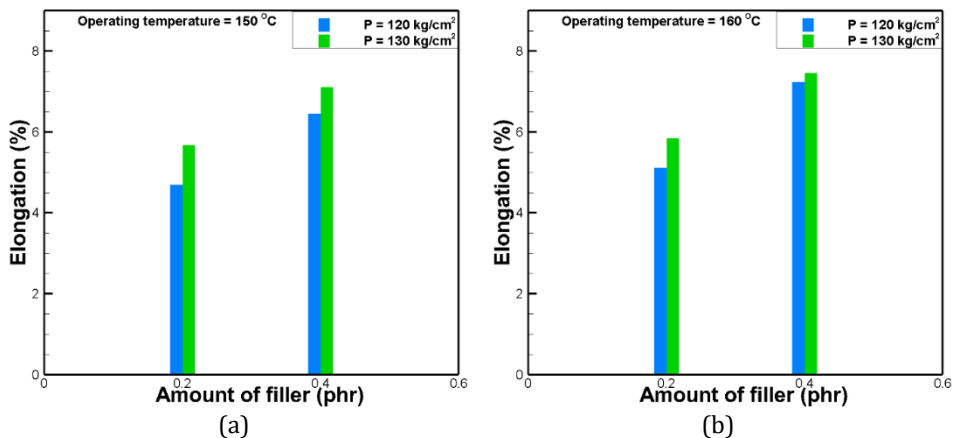


Fig. 17 Effect of compression moulding pressure on percentage elongation of nano-clay nanocomposite at operating temperature of (a) 150 °C (b) 160 °C

The melting point of the polymer is raised by the pressure used during compression moulding. More of the initial crystallinity is preserved in the polymer when the melting point rises. The polymer consolidates better under the higher pressure. Various mechanical properties, like tensile and flexural properties, of the moulded part are directly impacted by the consolidation of the part. When compared to weakly consolidated components, well-consolidated parts offer higher resistance to the various types of mechanical loads.

The results of Barcol hardness test and specific gravity measurement for fixed amount of nano-silica filler of 0.4 phr, and variable temperature and pressure applied during compression moulding, can be seen in Fig.18.

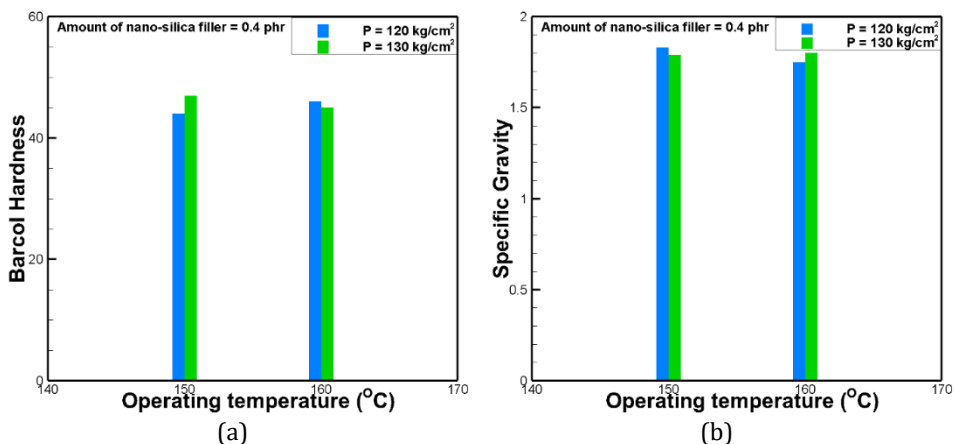


Fig.18 For the samples with the amount of nano-clay filler to be 0.4 phr, effect of compression moulding pressure on (a) Barcol hardness (b) Specific gravity

For temperature of 150 °C the performance of nano-clay composites, in terms of Barcol hardness and specific gravity, slightly enhances with increase in pressure. The opposite trend in the performance in terms of Barcol hardness and specific gravity, is observed at the operating temperature of 160 °C.

5.6 Performance Comparison of Nano Clay Composite And Base Material

The tensile strength, flexural strength and % elongation of the base material is 81.2 MPa, 171.3 MPa, and 5.06% while from Table 4, it can be seen that the maximum value of the tensile strength, flexural strength and % elongation for the Nano clay composite is 104.6 MPa, 199.4 MPa and 7.91%. This means that the tensile strength, flexural strength and % elongation of the base material can be enhanced by 28.82 %, 16.40 % and 56.32 %, respectively by reinforcement of nano clay. The Barcol hardness and specific gravity of the base material is 47 and 1.715 while from Table 5, it can be seen that the maximum value of the Barcol hardness is 49 and the minimum value of the specific gravity is 1.69, for the Nano clay composite. It has to be noted that the reduction in the specific gravity is the desirable result. This means that the performance of the base material in terms of Barcol hardness and specific gravity can be slightly enhanced by 4.26 % and 1.46 %, respectively by reinforcement of nano clay.

6. Conclusions

This study has considered characterization in the form of various mechanical tests and analysis methods. The major conclusions that can be drawn from the study are as mentioned below.

- The irregularities like agglomeration of filler material, formation of micro voids and micro cracks, that can be clearly seen from the SEM images, are needed to avoided during the fabrication of polymer nanocomposites, in order to enhance the performance of the nonocomposites.
- X ray diffraction results has shown multiple peaks which are indirect indication of the crystalline nature of polymer nanocomposite. Also, the intensity of the peaks got decreased after increasing the amount fnano clay from 0.2 phr to 0.4 phr.

- The tensile strength, flexural strength, and the percentage elongation of the nanocomposite material enhances with increase in amount of reinforcement material, at any moulding temperature and pressure.
- At lower moulding pressure, the increase in temperature enhances the of tensile strength, flexural strength, and the percentage elongation for both the values of amount of reinforcement whereas at higher moulding pressure and amount of reinforcement, the increase in temperature decreases the of tensile and flexural strength.
- At lower moulding temperature, the increase in pressure enhances the of tensile strength, flexural strength, and the percentage elongation for both the values of amount of reinforcement whereas at higher moulding temperature and lower amount of reinforcement, the increase in pressure decreases the of tensile strength, flexural strength, and the percentage elongation.
- The increase in the moulding temperature and pressure, increases the Barcol hardness test and decreases the specific gravity (which is desirable), but by very small amount.
- It has been revealed that the polymer nanocomposite becomes more ductile (by virtue of enhancement of tensile strength and the percentage elongation by 29% and 56%) and offers more resistance to bending (by virtue of enhancement of flexural strength by 16%), as compared to its base material.
- Barcol hardness test and measurement of specific gravity has revealed that there is improvement in the performance of the polymer nanocomposite as compared to that of base material, but by very less amount.

References

- [1] Orgéas L, Dumont PJ. Sheet molding compounds. Wiley encyclopedia of composites. 2011 Sep 16:1-36. <https://doi.org/10.1002/9781118097298.weoc222>
- [2] Shirinbayan M, Fitoussi J, Meraghni F, Surowiec B, Laribi M, Tcharkhtchi A. Coupled effect of loading frequency and amplitude on the fatigue behavior of advanced sheet molding compound (A-SMC). Journal of Reinforced Plastics and Composites. 2017 Feb;36(4):271-82. <https://doi.org/10.1177/0731684416682853>
- [3] Amos SE, Yalcin B. Hollow glass microspheres for plastics, elastomers, and adhesives compounds. Elsevier; 2015 Apr 30. <https://doi.org/10.1016/B978-1-4557-7443-2.00003-7>
- [4] R. Brooks. Design and Applications - Composites in Automotive Applications: Design. Comprehensive Composite Materials. Pergamon Press; 2000. <https://doi.org/10.1016/B0-08-042993-9/00120-0>
- [5] Gortner F, Schöffler A, Fischer-Schuch J, Mitschang P. Use of bio-based and renewable materials for sheet molding compounds (SMC)-Mechanical properties and susceptibility to fungal decay. Composites Part C: Open Access. 2022 Mar 1;7:100242. <https://doi.org/10.1016/j.jcomc.2022.100242>
- [6] Shirinbayan M, Rizi HB, Abbasnezhad N, Tcharkhtchi A, Fitoussi J. Tension, compression, and shear behavior of advanced sheet molding compound (A-SMC): Multi-scale damage analysis and strain rate effect. Composites Part B: Engineering. 2021 Nov 15;225:109287. <https://doi.org/10.1016/j.compositesb.2021.109287>
- [7] Schadow K. MEMS/Nanotechnology Integration. Nanotechnology Aerospace Applications. 2005:8-1.
- [8] Hussain F, Hojjati M, Okamoto M, Gorga RE. Polymer-matrix nanocomposites, processing, manufacturing, and application: an overview. Journal of composite materials. 2006 Sep;40(17):1511-75. <https://doi.org/10.1177/0021998306067321>

- [9] Thostenson ET, Li C, Chou TW. Nanocomposites in context. *Composites science and technology*. 2005 Mar 1;65(3-4):491-516. <https://doi.org/10.1016/j.compscitech.2004.11.003>
- [10] Luo JJ, Daniel IM. Characterization and modeling of mechanical behavior of polymer/clay nanocomposites. *Composites science and technology*. 2003 Aug 1;63(11):1607-16. [https://doi.org/10.1016/S0266-3538\(03\)00060-5](https://doi.org/10.1016/S0266-3538(03)00060-5)
- [11] Naskar AK, Keum JK, Boeman RG. Polymer matrix nanocomposites for automotive structural components. *Nature nanotechnology*. 2016 Dec;11(12):1026-30. <https://doi.org/10.1038/nnano.2016.262>
- [12] Stojić J, Raos P, Milinović A, Damjanović D. A Study of the Flexural Properties of PA12/Clay Nanocomposites. *Polymers*. 2022 Jan 21;14(3):434. <https://doi.org/10.3390/polym14030434>
- [13] Xu Y, Van Hoa S. Mechanical properties of carbon fiber reinforced epoxy/clay nanocomposites. *Composites Science and Technology*. 2008 Mar 1;68(3-4):854-61. <https://doi.org/10.1016/j.compscitech.2007.08.013>
- [14] Shettar M, Kowshik CS, Manjunath M, Hiremath P. Experimental investigation on mechanical and wear properties of nanoclay-epoxy composites. *Journal of Materials Research and Technology*. 2020 Jul 1;9(4):9108-16. <https://doi.org/10.1016/j.jmrt.2020.06.058>
- [15] Pol MH, Liaghat G. Investigation of the high velocity impact behavior of nanocomposites. *Polymer Composites*. 2016 Apr;37(4):1173-9. <https://doi.org/10.1002/pc.23281>
- [16] Burmistr MV, Sukhyy KM, Shilov VV, Pissis P, Spanoudaki A, Sukha IV, Tomilo VI, Gomza YP. Synthesis, structure, thermal and mechanical properties of nanocomposites based on linear polymers and layered silicates modified by polymeric quaternary ammonium salts (ionenes). *Polymer*. 2005 Dec 12;46(26):12226-32. <https://doi.org/10.1016/j.polymer.2005.10.094>
- [17] Quigley JP, Baird DG. Improved mechanical properties of organoclay/nylon 6 nanocomposites prepared via a supercritical carbon dioxide-aided, melt blending method. *Polymer Composites*. 2015 Mar;36(3):527-37. <https://doi.org/10.1002/pc.22969>
- [18] Chan ML, Lau KT, Wong TT, Ho MP, Hui D. Mechanism of reinforcement in a nanoclay/polymer composite. *Composites Part B: Engineering*. 2011 Sep 1;42(6):1708-12. <https://doi.org/10.1016/j.compositesb.2011.03.011>
- [19] Zhade SK, Chokka SK, Babu VS, Srinadh KS. A review on mechanical properties of epoxy-glass composites reinforced with nanoclay. *Epoxy-Based Composites*. 2022 May 25.
- [20] Rafiee R, Shahzadi R. Mechanical properties of nanoclay and nanoclay reinforced polymers: a review. *Polymer Composites*. 2019 Feb;40(2):431-45. <https://doi.org/10.1002/pc.24725>
- [21] Kim HC, Wallington TJ. Life-cycle energy and greenhouse gas emission benefits of lightweighting in automobiles: review and harmonization. *Environmental science & technology*. 2013 Jun 18;47(12):6089-97. <https://doi.org/10.1021/es3042115>
- [22] Koffler C. Life cycle assessment of automotive lightweighting through polymers under US boundary conditions. *The International Journal of Life Cycle Assessment*. 2014 Mar;19:538-45. <https://doi.org/10.1007/s11367-013-0652-7>
- [23] The United States Department of Energy, Quadrennial Technology Review pp. 39, 2011. <https://www.energy.gov/sites/prod/files/ReportOnTheFirstQTR.pdf>. accessed on 28th September 2022 at 09:16 pm
- [24] Viscometer Brookfield <https://mapiem.univ-tln.fr/Rheometer-BROOKFIELD-rvt.html>, accessed on 28th September 2022 at 09:16 pm.
- [25] Dumont P, Orgéas L, Favier D, Pizette P, Venet C. Compression moulding of SMC: In situ experiments, modelling and simulation. *Composites Part A: Applied Science and*

- Manufacturing. 2007 Feb 1;38(2):353-68. <https://doi.org/10.1016/j.compositesa.2006.03.010>
- [26] Ahmed W, Jackson JM. Emerging nanotechnologies for manufacturing. William Andrew; 2014 Sep 15.
- [27] Kundu S, Jana P, De D, Roy M. SEM image processing of polymer nanocomposites to estimate filler content. In 2015 IEEE International Conference on Electrical, Computer and Communication Technologies (ICECCT) 2015 Mar 5 (pp. 1-5). IEEE. <https://doi.org/10.1109/ICECCT.2015.7226104>
- [28] Thomas S, Rouxel D, Ponnamma D, editors. Spectroscopy of polymer Nanocomposites. William Andrew; 2016 Feb 16.
- [29] Michler GH, Von Schmeling HH. The physics and micro-mechanics of nano-voids and nano-particles in polymer combinations. Polymer. 2013 Jun 7;54(13):3131-44. <https://doi.org/10.1016/j.polymer.2013.03.035>
- [30] Pawlak A, Galeski A. Cavitation and morphological changes in polypropylene deformed at elevated temperatures. Journal of Polymer Science Part B: Polymer Physics. 2010 Jun 15;48(12):1271-80. <https://doi.org/10.1002/polb.22020>
- [31] Jian Z, Hejing W. The physical meanings of 5 basic parameters for an X-ray diffraction peak and their application. Chinese journal of geochemistry. 2003 Jan;22:38-44. <https://doi.org/10.1007/BF02831544>

Blank Page



Research Article

Parametric optimization of ball milling process parameters for uniform distribution of particles

Rashmi Arya^{*a}, Hari Singh^b

Department of Mechanical Engineering, National Institute of Technology, Kurukshetra

Article Info

Abstract

Article history:

Received 14 June 2023

Accepted 04 Sep 2023

Keywords:

Uniform distribution;

Taguchi approach;

Optimization;

APS;

EFO;

Ball mill

This paper represents the uniform distribution of particles in a mixture of Silicon Nitride and Hexagonal Boron Nitride using Ball milling process. Here, a novel attempt is made to quantify the uniform distribution of particles in terms of the Experimental Fraction of Observations. The effects of process parameters on Average Particle Size and Experimental Fraction of Observations were studied. Taguchi Methodology was used for Design of Experiments in this study. Optimal factor level settings corresponding to the individual responses were found. Analysis of Variance was conducted as well for both the responses. The mean predicted values of responses and the 95% confidence intervals for the same were also calculated. The confirmation test results are found to lie between the predicted confidence Intervals for both the confirmation experiments and population.

© 2023 MIM Research Group. All rights reserved.

1. Introduction

Ceramics play a vital role in today's era due to their properties like low density, high strength, good chemical inertness and high hardness. These materials have applications in industries, space technology and biomedicine to manufacture cutting tool tips, wear parts, rotors for the turbochargers of diesel engines, dental implants and prostheses (1–3).

Silicon Nitride (Si_3N_4) and Hexagonal Boron Nitride (hBN) are recognized to be the most important engineering ceramics among the ceramic materials. Si_3N_4 has low dielectric constant, high fracture toughness, high strength, low dielectric loss, excellent wear resistance, good oxidation resistance and creep resistance; and Si_3N_4 based ceramics are used to manufacture units and parts operating under severe thermal and mechanical loading (4,5). hBN has properties like low dielectric constant, stable at high temperatures, less chemically reactive, high thermal conductivity, non-toxicity and environmental safety (6,7). Such ceramics find applications in metal industry, chemical engineering, lubricating materials, high temperature furnaces, and thermal protection systems (8). The hBN particles provide a self-lubrication property (9).

Both these ceramics, Si_3N_4 and hBN, were milled together to attain uniform distribution of particles. Ball mill remains the most economical method for this purpose and was used to homogenize the distribution of particles and making finer mixture (10). There are several process variables affecting the outcome of the ball milling process. Pengfei Zhang et al. (11) researched the structure of SiBCN powders while performing ball milling. They studied the impact of speed, Ball to Powder Weight Ratio (BPR) and milling time on the morphology of powder. Pardeep Sharma et al. (12) had mechanically alloyed B_4C (more than 99.6% purity) and Si_3N_4 powder for 100 hrs of milling time. Hongju Qiu et al. (13) prepared nano-sized

*Corresponding author: rarya121212@gmail.com

^a orcid.org/0000-0002-1809-6333; ^b orcid.org/0000-0001-6120-9746;

DOI: <http://dx.doi.org/10.17515/resm2023.800me0614>

Res. Eng. Struct. Mat. Vol. 9 Iss. 4 (2023) 1347-1359

6MgO–2Y₂O₃–ZrO₂ powders by combining ball mill and co-precipitation. They studied the impact of milling time on ZrO₂ crystal particles. N. Hlabangana et al. (14) varied the grinding media size and feed material particle size distribution to optimize the milling efficiency. Grinding media filling, powder filling and the mill rotational speed were constant parameters in their study. A. Wagih et al. (15) had used a dynamic model to anticipate the particle size after the ball mill. Ball size, milling time and milling speed were the parameters optimized by them. S. Tahamtan et al. (16) used ball milling to mill Alumina powder with Al and Mg so as to use this mixture for further stir casting process. Fatih Erdemir (17) investigated the impact of ball milling input parameters on the particle size and X-ray peak ratios using RSM.

From literature survey, it is revealed that there has been almost a complete dearth of literature on optimization of process parameters of Ball Milling process using Design of Experiments (DOE) approach. A novel term Experimental Fraction of Observations (EFO) has been proposed by the authors in the literature to quantify the uniform distribution of particles. In this research study, a novel attempt has been made to ascertain the optimal settings of the ball milling process parameters for achieving optimal values Average Particle Size (APS) and EFO using Taguchi's Design of Experiments approach.

2. Experimental Details

The procedure from raw material selection to the confirmation tests is shown in Fig. 1.

2.1. Machine Used

The jar milling machine available at Advance Tribology Lab of the Institute was used to homogenize the powders. The diameter of the balls used was 6mm in the ball milling process.

2.2. Raw Materials

The Si₃N₄ and hBN were used as the raw materials with purity level of 99.5%. The APS range of both powders was 5-50 microns as procured from the supplier. The Scanning Electron Microscopy (SEM) images of raw Si₃N₄ and hBN are shown in Fig. 2 (a) and Fig. 2 (b) respectively.

2.3. Selection of Process Parameters

Milling Time, BPR, and Milling Speed were the three process variables chosen for ball milling process. These were selected based on literature survey and pilot experimentation using One Variable at a Time Approach. The ranges of these parameters are given in Table 1.

2.4. Measurement of Responses

APS and EFO were the responses considered in this research work. The APS was calculated by taking the average of 320 observations of particle size from SEM images. There was a total of four SEM images taken from four different locations from the same sample. The scale for SEM image was fixed to 50 µm. Then 80 readings of particle size were taken from each SEM image.

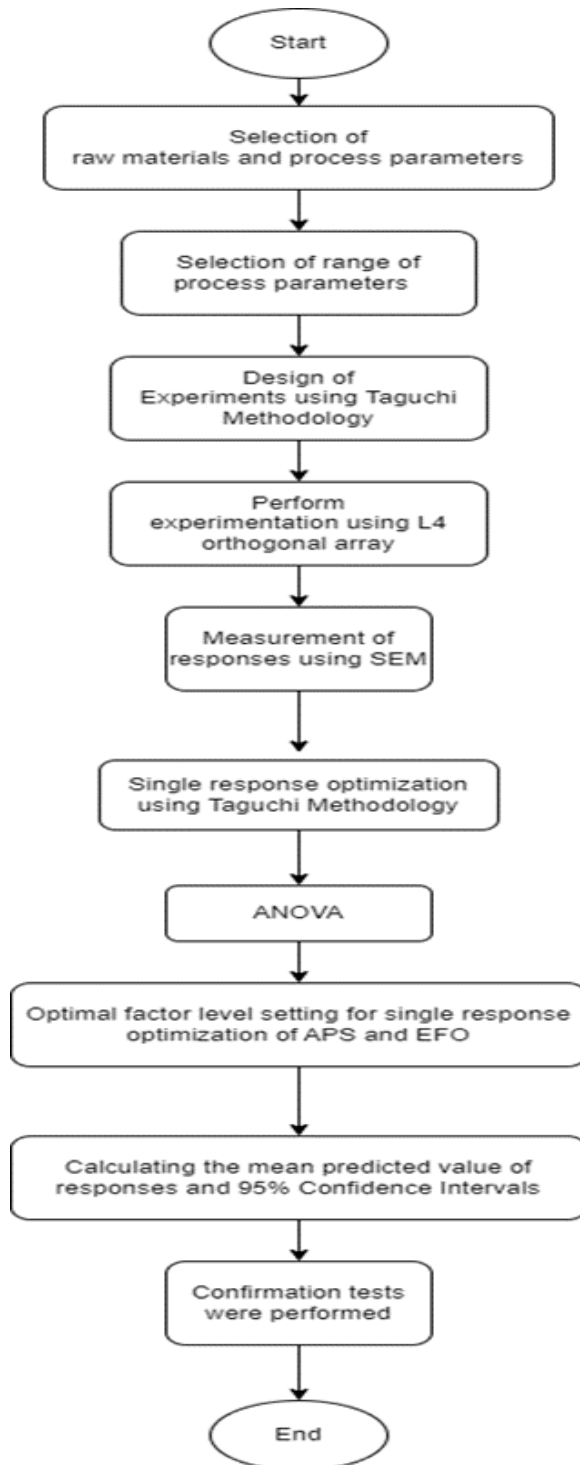


Fig. 1 Experimental methodology

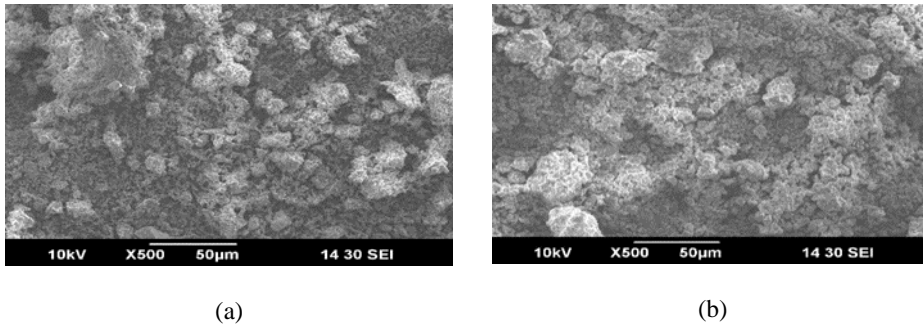


Fig. 2 (a) SEM image of Silicon Nitride; 2(b) SEM image of Hexagonal Boron Nitride

Table 1. Range of process parameters

Process Parameters	Range
Milling Time	1.5-2.5 hrs
BPR	8:1-12:1
Milling Speed	300-500 rpm

ImageJ software was used to calculate APS. A novel parameter EFO was proposed in this study to quantify the uniform distribution of particles which is given by Equation 1. The uniform distribution of particles was quantized in terms of observations falling under 4 sigma (σ) limit. This level of performance yields a product that is free from defects 99.349% of the time.

$$\text{Exp. fraction of observations (EFO)} = \frac{\text{Number of observations within } 4\sigma \text{ limits}}{\text{Total number of observations}} \quad (1)$$

Here, the 4 σ limits = mean \pm 2 σ ; σ = Standard Deviation

So, the number of observations falling between mean \pm 2 σ and divided by the total number of observations is the EFO. The EFO is calculated by ImageJ software and Origin software. The Origin software was used to plot the Histogram according to APS. The calculations for EFO are reported in Table 2 corresponding to 1st set of replicated experiments.

2.5. Experimental Design Methodology

DOE is a statistical method which facilitates to plan, gather data, statistically examine and look into the effect of more than one process parameter simultaneously on the response (18). Taguchi methodology is a technique which helps to study, analyze and optimize the influence of different process parameters simultaneously on the responses using Orthogonal Array and Signal to Noise Ratio (SNRA). The SNRA determines the most robust combination of input process parameters from variation within the results. By maximizing the SNRA, the loss associated can be minimized (19).

Table 2. Calculated values of EFO for 1st set of replicated experiments

	Particle size (µm) lower limit (m- 2sigma)	Particle size(µm) upper limit (m+2 sigma)	Particles falling under m+4sigma limit	EFO
Experiment 1	3.2879	19.2634	309	0.9656
Experiment 2	3.1174	26.4207	307	0.9594
Experiment 3	4.8810	19.7800	310	0.9688
Experiment 4	4.3680	17.5171	311	0.9719

$$MSD_{SB} = \frac{1}{N} \sum_{k=1}^N x_k^2 \tag{2}$$

$$MSD_{LB} = \frac{1}{N} \sum_{k=1}^N \frac{1}{x_k^2} \tag{3}$$

Where N=No. of repetitions, x_k=value of characteristic in kth observation

$$SNRA = -10 \log MSD \tag{4}$$

Table 3. Experimental data for APS

S.No.	Milling Time (hrs)	BPR	Milling Speed (rpm)	APS (µm)			
				R1	R2	R3	SNRA value
1	1.5	8:1	300	11.2757	10.9642	11.1052	-20.9188
2	1.5	12:1	500	14.7909	14.5981	14.6751	-23.3394
3	2.5	8:1	500	12.3305	12.5725	12.8832	-22.0057
4	2.5	12:1	300	10.9425	10.5698	10.7258	-20.6259

Table 4. Experimental data for EFO

S.NO.	Milling Time (hrs)	BPR	Milling Speed (rpm)	EFO			
				R1	R2	R3	SNRA value
1	1.5	8:1	300	0.9656	0.9658	0.9655	-0.3038
2	1.5	12:1	500	0.9594	0.9599	0.9591	-0.3594
3	2.5	8:1	500	0.9688	0.9690	0.9685	-0.2756
4	2.5	12:1	300	0.9719	0.9699	0.9709	-0.2565

In this paper, Taguchi methodology was used for DOE. L4 orthogonal array was selected as an experimental design matrix for investigating three factors having two levels each. The nature of APS was minimizing in nature, so Mean Squared Deviation (MSD) formula for ‘Smaller the Better’ type of response was used to calculate SNRA as given by Equations 2 and 4. The MSD for ‘Larger the better’ type of response was considered to calculate SNRA

for EFO as this response was maximizing in nature given by Equations 3 and 4. Tables 3 and 4 represent the calculated values of APS and EFO corresponding to Taguchi's L4 array with 3 replications. The SNRA values have also been included in the last columns of the Tables.

3. Results and Discussions

The average particle sizes of raw Si_3N_4 and hBN were calculated as $14.5997 \mu\text{m}$ and $20.9046 \mu\text{m}$ respectively as shown in Fig. 3 (a) and Fig. 3 (b). The Fig. 2(a) and Fig. 2(b) depict non-uniform distribution of particles of Si_3N_4 and hBN. The range of particle size for hBN was from $4.5100 \mu\text{m}$ to $90.8430 \mu\text{m}$ and it was from $3.9520 \mu\text{m}$ to $49.8010 \mu\text{m}$ for Si_3N_4 . The standard deviations for Si_3N_4 and hBN were calculated as $8.1089 \mu\text{m}$ and $14.3121 \mu\text{m}$ respectively. After performing ball milling process according to DOE, a uniform distribution of particle size was revealed as shown in Figs 4 (a-d) and Fig. 5 (a-d). The Fig. 4 (a) and Fig. 5 (a) correspond to experiment no. 1 with experimental setting of 1.5 hrs of Milling Time, BPR of 8:1 and Milling speed of 300 rpm. Similarly, Fig. 4 (b) & Fig. 5 (b), Fig. 4 (c) & 5 (c), and Fig. 4 (d) & 5 (d) correspond to experiment numbers 2, 3, and 4 respectively. The particle size and standard deviations improved which resulted in the reduction of the spread of the normal distribution curve corresponding to 4 different experimental settings. The 1st replication for experiments resulted in the standard deviation of $3.9939 \mu\text{m}$, $5.8367 \mu\text{m}$, $3.7248 \mu\text{m}$ and $3.2873 \mu\text{m}$ respectively. The APS was improved and lies between $10.5698 \mu\text{m}$ and $14.7910 \mu\text{m}$ for all 4 experiments.

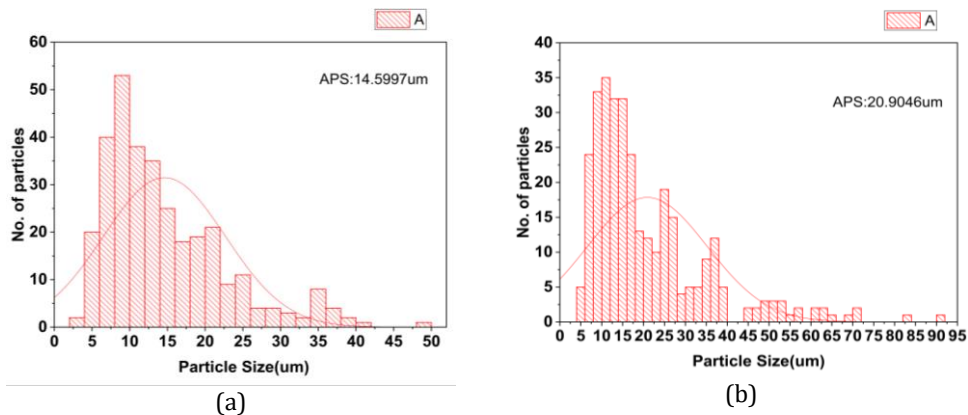
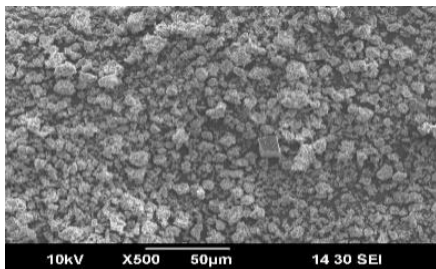
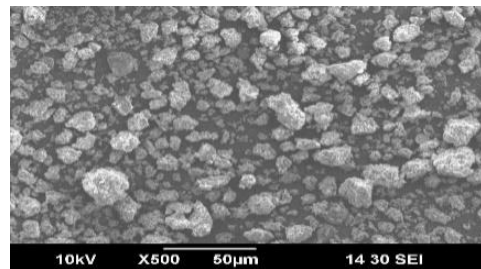


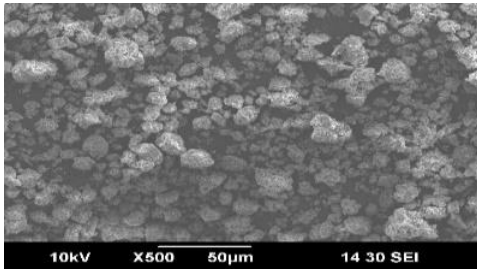
Fig. 3 (a, b): Particle size distribution for hBN and Si_3N_4



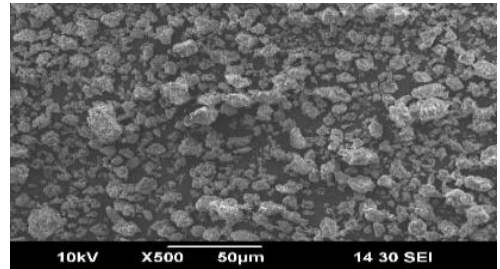
(a) corresponding to experiment no.1



(b) corresponding to experiment no.2

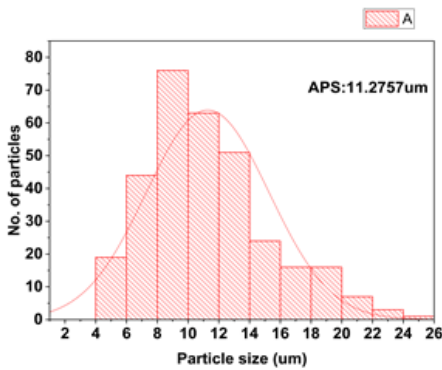


(c) corresponding to experiment no.3

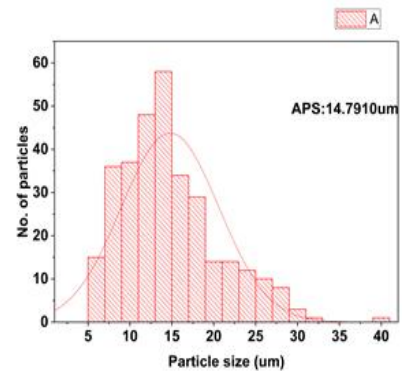


(d) corresponding to experiment no.4

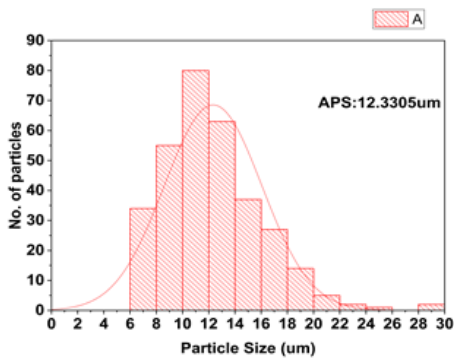
Fig. 4 (a-d): SEM images corresponding to Experimental Design



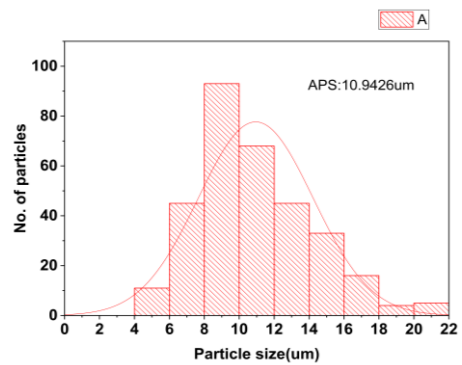
(a) corresponding to experiment 1



(b) corresponding to experiment 2



(c) corresponding to experiment 3



(d) corresponding to experiment 4

Fig. 5 (a-d): Histogram plots corresponding to experimental design

3.1 Influence of input factors on APS and EFO

The APS decreased as the milling time increased from 1.5 hrs to 2.5 hrs. The APS increased with increase in BPR from 8:1 to 12:1 and it also increased with increase in milling speed from 300 rpm to 500 rpm as shown in Fig. 6. The ball milling process resulted in increased EFO as the milling time changes from 1.5 hrs to 2.5 hrs. The EFO decreased with increase in BPR and milling speed as shown in Fig. 7.

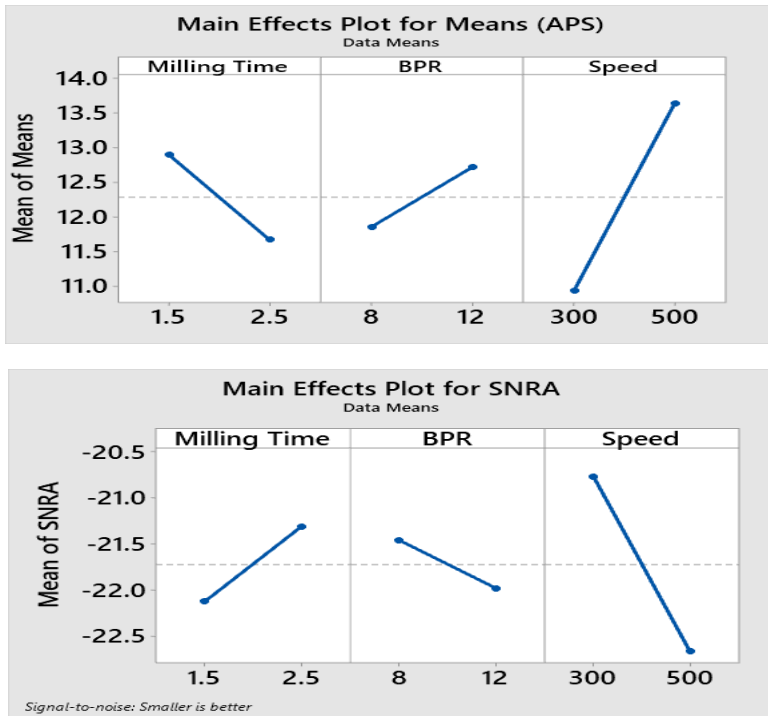


Fig. 6 Main effects plot for means and SNRA for APS

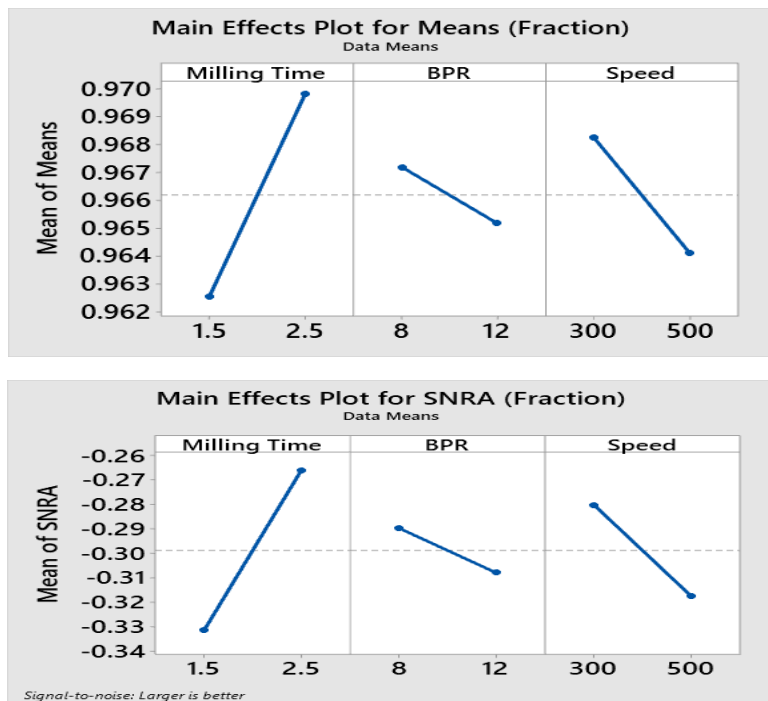


Fig. 7 Main effects plot for means and SNRA for EFO

3.2 Analysis of Responses

Analysis of Variance (ANOVA) is a statistical tool to determine the percentage contribution and significance of different factors on the selected response. The F-ratio test is a very widely used and trusted test for ascertaining the significance of the factors in any study. A factor is said to be significant at some stated level of confidence, say 95%, if the calculated value of F-ratio statistic for that factor is greater than the tabulated value of F-ratio for that factor (20).

Here, the tabulated value of F-ratio is 5.32 and all the calculated values are much greater than the tabulated F-value; hence all the factors are statistically significant in affecting the APS at 95% confidence level as given in Table 5. The most contributing factor was Milling Speed with 75.74% contribution, followed by Milling Time and BPR in that order.

Table 5. ANOVA table for average particle size

Source	DOF	SSS	Contribution	AMS	F-Value	P-Value
Regression	3	28.8247	99.00%	9.6082	264.05	0.000
Milling Time	1	4.5447	15.61%	4.5447	124.89	0.000
BPR	1	2.2283	7.65%	2.2283	61.24	0.000
Milling Speed	1	22.0517	75.74%	22.0517	606.01	0.000
Error	8	0.2911	1.00%	0.0364		
Total	11	29.1158	100.00%			

Tabulated F-value: $F_{0.05}(1,8) = 5.32$

Similarly, for EFO, the calculated F-Ratios of all the factors are greater than the tabulated F-Ratio as reported in Table 6. Therefore, all the factors are statistically significant at 95% confidence level in affecting EFO. The most contributing factor was Milling Time with 70.57% contribution, followed by Milling Speed and BPR in that order.

Table 6. ANOVA table for EFO

Source	DOF	SSS	Contribution	AMS	F-Value	P-Value
Regression	3	0.000223	98.89%	0.000074	237.88	0.000
Milling Time	1	0.000159	70.57%	0.000159	509.25	0.000
BPR	1	0.000012	5.41%	0.000012	39.04	0.000
Milling Speed	1	0.000052	22.91%	0.000052	165.34	0.000
Error	8	0.000002	1.11%	0.000000		
Total	11	0.000226	100.00%			

Tabulated F-value: $F_{0.05}(1,8) = 5.32$

3.3 Optimization and Predicted Value

The average particle size of the powder is a smaller the type of quality characteristic and the lowest points in the main effects plot for the means will correspond to the optimal settings of the process parameters leading to the best response. The EFO, on the other hand, is a larger the better type of quality characteristic and the highest points in the main effects plot for the means will correspond to the optimal settings of the process parameters resulting in the optimal value of the response.

As regards SNRA plots, the highest points in the plot will always correspond to the optimal settings of the factors leading to the best value of the response irrespective of the fact whether the quality characteristic is either smaller the better or larger the better.

Accordingly, Fig. 6 and Fig. 7 have been analysed for obtaining optimal settings of the parameters for individual responses. Second level of milling time, first level of BPR and first level of milling speed correspond to the highest points in SNRA ratio plots for APS as well as EFO. Hence, these values represent the optimal settings of the selected parameters for obtaining the best responses.

The predicted optimal value of APS corresponding to the optimal values of process parameters has been obtained by using Equation 5. Similar procedure was then adopted to find the predicted optimal value of EFO.

$$M_{APS} = \bar{P}_2 + \bar{N}_1 + \bar{O}_1 - 2\bar{T} \tag{5}$$

Where \bar{T} is the overall mean of APS = $(\sum R_1 + \sum R_2 + \sum R_3)/12$

\bar{P}_2 = Mean value of APS at level 2 of Milling Time

\bar{N}_1 = Mean value of APS at level 1 of BPR

\bar{O}_1 = Mean value of APS at level 1 of Milling Speed

The predicted optimal values for both the quality characteristics are given in Table 7. The SEM image of powder after performing ball mill at optimal factor setting is depicted in Fig. 8.

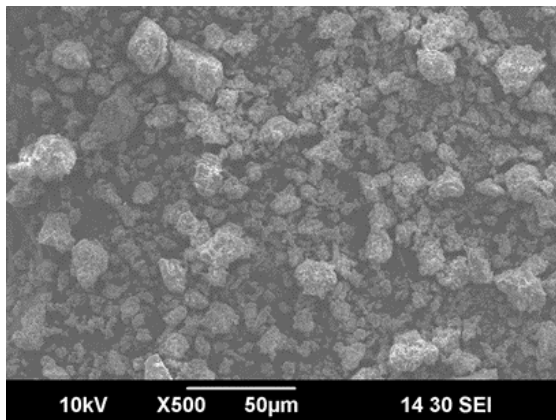


Fig. 8 SEM image of confirmation experiment

The 95% Confidence Intervals corresponding to Population and Confirmation Experiments were calculated by the using Equations 6 & 7.

$$CI_{CE} = \sqrt{(F_{\alpha}(1, d_e)E_v \left(\frac{1}{n_{eff}} + \frac{1}{A} \right))} \tag{6}$$

$$CI_{POP} = \sqrt{\frac{(F_{\alpha}(1, d_e)E_v}{n_{eff}})} \tag{7}$$

where, $F_{\alpha}(1, d_e)$ = The F ratio at the confidence level of $(1-\alpha)$ against DOF of mean, which is equal to 1, and error degrees of freedom d_e .

$$n_{\text{eff}} = \frac{N}{1 + [\text{DOF associated in the estimate of mean response}]} = 12 / (1+3) = 3$$

N = Total number of Observations = 4 x 3 = 12; A = Sample size for confirmation experiments = 3

E_v = Error variance (from ANOVA Table); d_e = error DOF = 8; $F_{0.05}(1, 8) = 5.32$

Table 7. Optimal factor level setting

1.	APS	2.5(P ₂)	8:1(N ₁)	300(O ₁)	9.8842 μm
2.	EFO	2.5(P ₂)	8:1(N ₁)	300(O ₁)	0.9729

The predicted values of confidence intervals at 95% confidence level for both the responses are reported in Table 8. The confirmation tests were performed at the optimal factor level setting and the average values of the confirmation experiments are found to lie within the predicted 95% confidence intervals as given in Table 8.

Table 8: Predicted values of confidence intervals at 95% level

Output Process Parameters	Input Optimal Process Parameters Settings	Predicted Confidence Intervals at 95% Confidence Level	Mean of three confirmation experiments
APS	P ₂ N ₁ O ₁	CI _{CE} : 9.5249 < μ _{APS} < 10.2435 CI _{POP} : 9.6301 < μ _{APS} < 10.1382	10.1234 μm
EFO	P ₂ N ₁ O ₁	CI _{CE} : 0.9720 < μ _{EFO} < 0.9738 CI _{POP} : 0.9722 < μ _{EFO} < 0.9736	0.9723

4. Conclusions

In this research article, optimization of ball milling process parameters for APS and EFO was accomplished through Taguchi’s DOE approach. Here, Orthogonal array L4 was selected and experiments were replicated 3 times. The number of observations falling under 4 σ limit was utilized to quantize the uniform distribution of particles. EFO term was coined for uniform distribution of particles. The nature of APS was minimizing and that of EFO was maximizing. Therefore, the SNRA for APS was chosen as per lower the better type of response, whereas the SNRA for EFO was chosen as per larger the better type of quality characteristic. The following conclusions were drawn from this paper:

- The ball milling process resulted in decreasing the range of Average Particle Size from 14.59972 μm-20.90461 μm to 10.5698-14.7909 μm.
- The standard deviation range of Average Particle Size improved from 8.10889 μm-14.3121 μm to 3.2873 μm - 5.8367 μm, i.e., most of the particles were of the same size.
- Experimental Fraction of Observations for the 4sigma limit resulted in uniform distribution of the particles.
- Milling speed, milling time and Ball to powder weight ratio were found as significant factors at 95% confidence level for both Average Particle Size and Experimental Fraction of Observations.
- The most significant factor affecting the Average Particle Size was the Milling Speed with 75.74% contribution.

- The most significant factor for Experimental Fraction of Observations was the milling time with 70.57% contribution.
- Milling Time of 2.5 hrs, Ball to Powder Weight Ratio of 8:1 and Milling Speed of 300rpm were optimal factor level settings for both Average Particle Size and Experimental Fraction of Observations.
- The confirmation tests were performed and the average values of responses were found to lie between the predicted 95% confidence intervals for both confirmation experiments and population.
- Authors have coined and introduced a novel quality characteristic, Experimental Fraction of Observations, to represent a measure of uniform distribution of particles in ball milling process.

Abbreviations

hBN	Hexagonal Boron Nitride	BPR (N)	Ball to Powder Weight Ratio
Si ₃ N ₄	Silicon Nitride	SNRA	Signal to Noise Ratio
APS	Average Particle Size	ANOVA	Analysis of Variance
EFO	Experimental Fraction of Observations	SEM	Scanning Electron Microscopy
DOE	Design of Experiments	DOF	Degrees of Freedom
SSS	Sequential Sum of Squares	MSD	Mean Squared Deviation
AMS	Adjusted Mean Squares	P	Milling Time
O	Milling Speed	hrs	hours

References

- [1] Lok YK, Lee TC. Processing of advanced ceramics using the wire-cut EDM process. *Journal of Materials Processing Technology*. 1997;63(1-3):839-43. [https://doi.org/10.1016/S0924-0136\(96\)02735-5](https://doi.org/10.1016/S0924-0136(96)02735-5)
- [2] Zhang C. Study of small cracks on nanocomposite ceramics cut by WEDM. *International Journal of Advanced Manufacturing Technology*. 2016;83(1-4):187-92. <https://doi.org/10.1007/s00170-015-7569-1>
- [3] Ming W, Jia H, Zhang H, Zhang Z, Liu K, Du J, et al. A comprehensive review of electric discharge machining of advanced ceramics. *Ceramics International* [Internet]. 2020;46(14):21813-38. <https://doi.org/10.1016/j.ceramint.2020.05.207>
- [4] Zakorzhevsky V V. Silicon Nitride. In: *Concise Encyclopedia of Self-Propagating High-Temperature Synthesis* [Internet]. Elsevier Inc.; 2017. p. 339-41. <https://doi.org/10.1016/B978-0-12-804173-4.00134-4>
- [5] Liang G, Sun G, Bi J, Wang W, Yang X, Li Y. Mechanical and dielectric properties of functionalized boron nitride nanosheets/silicon nitride composites. *Ceramics International* [Internet]. 2021;47(2):2058-67. <https://doi.org/10.1016/j.ceramint.2020.09.038>
- [6] Wang J, Ma F, Sun M. Graphene, hexagonal boron nitride, and their heterostructures: properties and applications. *RSC Advances*. 2017;7(27):16801-22. <https://doi.org/10.1039/C7RA00260B>
- [7] Eichler J, Lesniak C. Boron nitride (BN) and BN composites for high-temperature applications. *Journal of the European Ceramic Society*. 2008;28(5):1105-9. <https://doi.org/10.1016/j.jeurceramsoc.2007.09.005>
- [8] Duan X, Yang Z, Chen L, Tian Z, Cai D, Wang Y, et al. Review on the properties of hexagonal boron nitride matrix composite ceramics. *Journal of the European Ceramic Society*. 2016;36(15):3725-37. <https://doi.org/10.1016/j.jeurceramsoc.2016.05.007>
- [9] Gnanavelbabu A, Rajkumar K. Experimental Characterization of Dimensional and Surface Alternation of Straight and Angular Cutting on Self-lubricating Composite: A

- Wire EDM Approach. Arabian Journal for Science and Engineering [Internet]. 2020;45(7):5859-72. <https://doi.org/10.1007/s13369-020-04596-2>
- [10] Ahmadian H, Sallakhniknezhad R, Zhou T, Kiahosseini SR. Mechanical properties of Al-Mg/MWCNT nanocomposite powder produced under different parameters of ball milling process. Diamond and Related Materials [Internet]. 2022;121(September 2021):108755. <https://doi.org/10.1016/j.diamond.2021.108755>
- [11] Zhang P, Jia D, Yang Z, Duan X, Zhou Y. Influence of ball milling parameters on the structure of the mechanically alloyed SiBCN powder. Ceramics International [Internet]. 2013;39(2):1963-9. <https://doi.org/10.1016/j.ceramint.2012.08.047>
- [12] Sharma P, Khanduja D, Sharma S. Metallurgical and mechanical characterization of Al 6082- B4C/Si3N4 hybrid composite manufactured by combined ball milling and stircasting. Applied Mechanics and Materials. 2014;592-594:484-8. <https://doi.org/10.4028/www.scientific.net/AMM.592-594.484>
- [13] Qiu H, Huang W, Zhang Y, Chen J, Gao L, Omran M, et al. Preparation of nano-sized 6MgO-2Y2O3-ZrO2 powders by a combined co-precipitation and high energy ball milling process. Ceramics International [Internet]. 2022;48(13):19166-73.
- [14] Hlabangana N, Danha G, Muzenda E. Effect of ball and feed particle size distribution on the milling efficiency of a ball mill: An attainable region approach. South African Journal of Chemical Engineering [Internet]. 2018;25:79-84. <https://doi.org/10.1016/j.sajce.2018.02.001>
- [15] Wagih A, Fathy A, Kabeel AM. Optimum milling parameters for production of highly uniform metal-matrix nanocomposites with improved mechanical properties. Advanced Powder Technology [Internet]. 2018;29(10):2527-37. <https://doi.org/10.1016/j.apt.2018.07.004>
- [16] Tahamtan S, Halvae A, Emamy M, Zabihi MS. Fabrication of Al/A206-Al2O3 nano/micro composite by combining ball milling and stir casting technology. Materials and Design [Internet]. 2013;49:347-59. <https://doi.org/10.1016/j.matdes.2013.01.032>
- [17] Erdemir F. Study on particle size and X-ray peak area ratios in high energy ball milling and optimization of the milling parameters using response surface method. Measurement: Journal of the International Measurement Confederation [Internet]. 2017;112(July):53-60. <https://doi.org/10.1016/j.measurement.2017.08.021>
- [18] Arya R, Singh H. Optimization of Wire-cut EDM process parameters using TLBO algorithm. Engineering Research Express. 2022;4(3):035051. <https://doi.org/10.1088/2631-8695/ac8fcc>
- [19] Garg R. Effect Of Process Parameters On Performance Measures Of Wire Electrical Discharge Machining [Internet]. Vol. Ph.D. National Institute Of Technology, Kurukshetra-136 119, Haryana, India; 2010. Available from: http://nitkkr.ac.in/nit_kuk/docs/Ph.D_Thesis_by_Rohit_Garg.pdf
- [20] Ross PJ. Taguchi Techniques for Quality Engineering. 2nd ed. McGraw-Hill Education (India) Pvt Limited; 2005.

Blank Page



Research Article

Anchors for shear strengthening of damaged RC beam using bonded steel plate

Md Ashraful Alam^{*a}, Mohammad Al-Amin^b

Department of Civil Engineering, University of Asia Pacific, Dhaka, Bangladesh

Article Info

Abstract

Article history:

Received 30 Jan 2023

Accepted 05 Aug 2023

Keywords:

Reinforced concrete;

Damaged beam;

Shear strengthening;

EB method;

Steel plate;

Anchor

Appropriate anchor system has very important role for effective retrofitting of structure specially to prevent debonding of bonded plate for shear strengthening of damaged reinforced concrete beam. The debonding happens at concrete interface of externally bonded (EB) plate due to lower interfacial bond strength. Proper anchor system would enhance interfacial strength to prevent debonding failure. The main aim of the research work was to investigate the effectiveness of various anchor systems for externally bonded steel plate to enhance shear strength of damaged RC beams. A total of five full scale reinforced concrete beam had been fabricated, all beams were fully damaged in shear before strengthening. The damaged beams were then strengthened for shear using steel plates with double connector, multiple connectors, welded connector and near surface embedded bar anchor systems. Design guideline had been proposed to obtain dimension of steel plate for shear strengthening of damaged RC beam. Results exhibited that all anchors prevented debonding of steel plate at concrete-adhesive interface. Welded connector (WC) and embedded bar (EB) anchors had completely prevented debonding failures of steel plate at concrete-adhesive and plate-adhesive interfaces. Double and multiple connector anchors failed due to crushing of concrete at anchor zone followed by debonding of plate. Whereas, un-anchored strengthened beam showed premature debonding of plate at concrete-adhesive interface followed by shear failure. The results of the research exhibited that double and welded connector anchors had excellent performance in increasing shear strength to re-store original shear capacities of damaged beams. The theoretical results were comparable with the experimental findings.

© 2023 MIM Research Group. All rights reserved.

1. Introduction

Numerous reinforced concrete infrastructures around the world are considered unsafe due to environmental disasters such as earthquake and tsunami, increased load specification in the design codes, over-loading and also for building degradation due to age. Strengthening of reinforced concrete (RC) structures for those conditions would be the best alternative to enhance the capacities of structure. Because of sudden and catastrophic collapse of shear failure, strengthening of RC beam for shear become one of the most essential parts to ensure ductile failure of structure through enhancement of shear capacity. Researchers proposed various methods of shear strengthening for RC beams such as external pre-stressing [1], externally bonded steel plates [2], near surface mounted (NSM) [3], jacketing of beam [4], and externally bonded reinforcement (EBR) [5]. Strengthening materials include carbon fiber reinforced cementitious matrix (FRCM) composite [6], glass fiber reinforced polymer [7], steel plates [2], cement-based composite [8], highly ductile fibre reinforced concrete [9], CFRP grid [10], CFRP NSM [11], glass fiber textile mesh [12], textile reinforced mortar [13] and ramie fiber reinforced polymer

^{*}Corresponding author: dr.ashraful@uap-bd.edu

^a <https://orcid.org/0000-0003-4237-3713>; ^b <https://orcid.org/0009-0001-2131-0388>

DOI: <http://dx.doi.org/10.17515/resm2023.678st0130>

Res. Eng. Struct. Mat. Vol. 9 Iss. 4 (2023) 1361-1377

(FRFRP) [14] have been used to obtain the expected outcome. As compared to others, externally bonded method using steel plate has been widely used for shear strengthening of RC beam.

The major limitation of externally bonded method for shear strengthening of RC beam is premature debonding failure of plate as it prevents the beams to attain its ultimate strength. Recent works investigated the performance of anchors using bolt, fan, spike and embedded connectors to eliminate debonding of plate for shear strengthening of un-cracked RC beams [15-24]. Anchors of bolts, fan and spike require hole on externally bonded plate which reduce the effective cross-sectional area of plate. Moreover, fan and spike anchors are prepared using carbon fibre. In general fibre is unable to resist shear along its cross section, thus, could not be effective as anchor for shear strip. The fan anchor system has mostly been used in FRP wrap to prevent complete separation of wrap [24]. In contrast, embedded connector anchor proposed by Alam et al. [18] had been investigated and was found to be effective in enhancing the bond strength to prevent debonding of plate at concrete-adhesive interface. However, the major limitation of embedded connector anchor was unable to prevent debonding of plate at plate-adhesive interface. Moreover, the effectiveness of existing anchor systems was investigated for shear strengthening of un-cracked RC beams. The presence of cracks in damaged beams might have the effects on anchor system, however, the effectiveness of anchor systems for shear strengthening of damaged RC beams yet to be investigated. The research work aimed to propose welded connector and embedded bar anchor system for shear strengthening of damaged RC beams. The effectiveness of embedded connectors (double and multiple), welded connector and embedded bar anchor systems had been investigated experimentally for shear strengthening of damaged RC beams.

2. Proposed Design Guideline for Shear Strengthening of Damaged Reinforced Concrete Beam Using Steel Plate

2.1 Maximum Design Shear Force for Strengthening of RC Beam

The existing beam may fail by flexure or shear. The beam would fail by flexure once the shear capacity of the beam exceeds its flexural capacity. Hence, the shear enhancement of the existing beam could be possible until the beam fails by flexure. The ultimate flexural capacity of the beam can be calculated in accordance to EC2 [25] as shown below,

$$M = Tz = A_s f_{tk} \left[d - \frac{0.588 A_s f_{tk}}{f_{ck} b} \right] \tag{1}$$

Where,

$$x = \frac{A_s f_{tk}}{0.85 f_{ck} (0.8) b} = \frac{A_s f_{tk}}{0.68 f_{ck} b} \tag{2}$$

$$z = d - 0.4x = \left[d - \frac{0.588 A_s f_{tk}}{f_{ck} b} \right] \tag{3}$$

The beam will fail by flexure once the bending moment exceeds the maximum flexural strength of the beam (as shown in Equation 1). The maximum bending moment could be considered as the maximum flexural strength of the beam. Thus, the design shear force of the beam is,

$$V_{ds} = \frac{M}{L_s} = \frac{A_s f_{tk}}{L_s} \left[d - \frac{0.588 A_s f_{tk}}{f_{ck} b} \right] \tag{4}$$

2.2 Design Shear Force to Re-store Original Capacity of Damaged Beam

The number of shear link to resist shear,

$$N = \frac{[d - d'] \cot \theta}{s_{link}} \tag{5}$$

Where, θ is the angle of shear crack. The shear crack inclination may vary between 22 degrees to 45 degrees [25]. Crack inclination of 22 degrees could be used for conservative calculation of shear capacity of beam. The shear force resisted by shear link,

$$V_{y,link} = A_{s,link} f_{y,link} \left[\frac{(d - d') \cot \theta}{s_{link}} \right] \tag{6}$$

As per EC2 [24], the shear contribution is only from shear link rather than concrete. Hence, the shear capacity of the un-damaged control beam is,

$$V_{cb} = V_{y,link} = A_{s,link} f_{y,link} \left[\frac{(d - d') \cot \theta}{s_{link}} \right] \tag{7}$$

2.3 Cross Sectional Area of Steel Plate to Re-store Original Capacity of Damaged Strengthened Beam

Since the beam is damaged, concrete shows cracks and shear link yields, only externally bonded steel plate will resist shear in strengthened beam as shown in Figure 1. The inclination of shear crack could be considered as 45 degrees for conservative design of externally bonded plate.

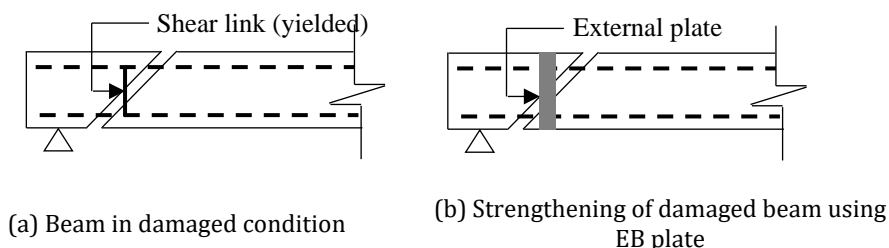


Fig. 1 Shear strengthening of damaged RC beam

The steel plate (two-sided plate) resists shear force as,

$$V_{sp} = 2A_p f_{yp} N_p = 2A_p f_{yp} \frac{h \cot \theta}{s_p} \tag{8}$$

The required optimal shear design of damaged beam to re-store original capacity is,

$$V_{sp} = V_{ds} = V_{y,link}$$

$$\frac{A_p}{s_p} = \frac{V_{y,link}}{2f_{yp}hcot\theta} = \frac{A_{s,link}f_{y,link} \left[\frac{(d-d')cot\theta}{s_{link}} \right]}{2f_{yp}hcot\theta} \quad (9)$$

The damaged shear strengthened beam could fail by flexure rather than shear also. In case, the beam fails in flexure, the maximum design shear could be obtained using Equation 4. Thus, the required optimal shear design of the damaged beam for the maximum capacity (up to flexural failure of beam) is,

$$V_{sp} = V_{ds} = \frac{A_s f_{tk}}{L_s} \left[d - \frac{0.588 A_s f_{tk}}{f_{ck} b} \right] \quad (10)$$

$$\frac{A_p}{s_p} = \frac{V_{ds}}{2f_{yp}hcot\theta} = \left\{ \frac{A_s f_{tk}}{L_s} \left[d - \frac{0.588 A_s f_{tk}}{f_{ck} b} \right] \right\} / (2f_{yp}hcot\theta)$$

2.4 Capacities of Damaged Shear Strengthened RC Beam

2.4.1 Debonding Load of Un-anchored Strengthened Beam

The guideline of Alam et al. [25] (as shown below) can be used to obtain the debonding strain of the plate;

$$\varepsilon_{deb,p} = \frac{F_{bp} w_p h}{A_p E_p} = \frac{F_{bp} w_p h}{w_p t_p E_p} = \frac{F_{bp} h}{t_p E_p} \quad (11)$$

Thus, $\varepsilon_p = \varepsilon_{deb,p}$

$$\text{Stress of steel plate, } \sigma_p = E_p \varepsilon_p = \frac{F_{bp} h}{t_p} \quad (12)$$

Shear force to cause debonding of plate,

$$V_{deb,p} = 2A_p \sigma_p N_p = 2A_p \left\{ \frac{F_{bp} h}{t_p} \right\} \left\{ \frac{h cot\theta}{s_p} \right\} \quad (13)$$

2.4.2 Shear Capacity by Yielding of External Steel Plate

Based on yielding of externally bonded steel plate, the shear capacity of damaged strengthened beam is,

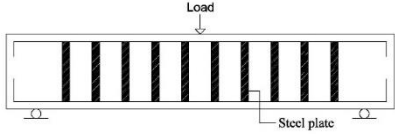
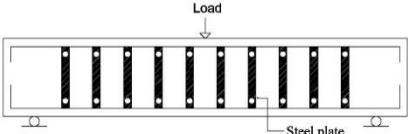
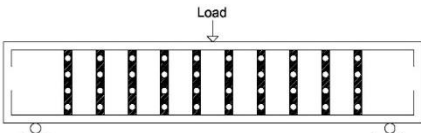
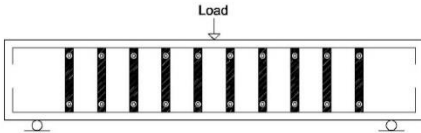
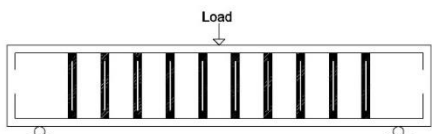
$$V_{sb} = V_{y,p} = 2A_p f_{yp} \left[\frac{h cot\theta}{s_p} \right] \quad (14)$$

3. Experimental Program

3.1 Test Specimens

In the experiment, five full-scale RC beams were fabricated and tested. The dimensions of all beams were 150 mm x 250 mm x 1300 mm. The beams were fully damaged before strengthening. Steel plate having the dimension of 3 mm x 20 mm x 300 mm was used with the spacing of 110 mm for shear strengthening of all damaged beams. The dimension of plate was obtained based on proposed design guideline shown in Equation 10. Double connector (DC), multiple connector (MC), welded connector (WC) and embedded bar (EB) anchor systems were used to eliminate premature debonding failure of EB steel plate. Strengthened beam of SB was left without anchor to compare the results with strengthened beams having anchors. Table 1 presents the details of all specimens.

Table 1. Details of specimens

Beam ID	Details of anchor		Figure of specimens
	Type	Material	
SB	No Anchor		
DC	Double connector	2-16 mm MS bar	
MC	Multi connector	4-16 mm MS bar	
WC	Welded connector.	2-16 mm MS welded bar	
EB	Embedded bar	6 mm MS surface mounted bar	

3.2 Preparation of Beams

The steel case of the beam was fabricated using 2-16 mm flexural reinforcement (at bottom), 2-12 mm hanger bar (at top) and 6 mm shear reinforcement with the spacing of 130 mm c/c. The details of reinforcements are shown in Figure 2. The shear reinforcement (6 mm bar) had yield and tensile strength of 420 MPa and 520 MPa respectively. Whereas, flexural reinforcement of 16 mm bar had 540 MPa and 620 MPa yield and tensile strengths respectively.

DOE method was used to design the concrete mix with the ratio of (cement, sand and stone aggregate) 1:1.96:3.07 for the target strength of 30 MPa. The water cement ratio of the mix was 0.6. The average slump of the concrete mix was found to be 130 mm approximately. All beams were cured under same condition by wet hessian cloth for 28 days after casting.

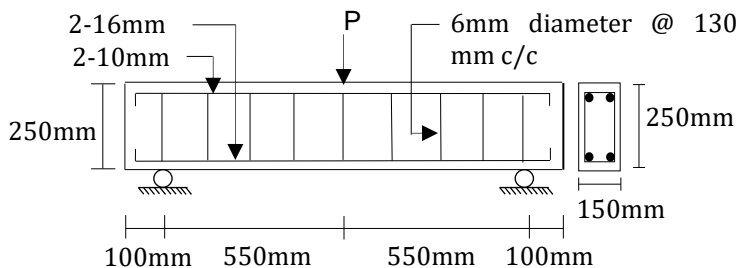


Fig. 2 Details of reinforcements of beam

3.3 Damaging of Beams

After 28 days of curing, all five beams were fully damaged before strengthening as shown in Figure 3. Beams were tested under three points bending. The clear span of the beam was 1100 mm.

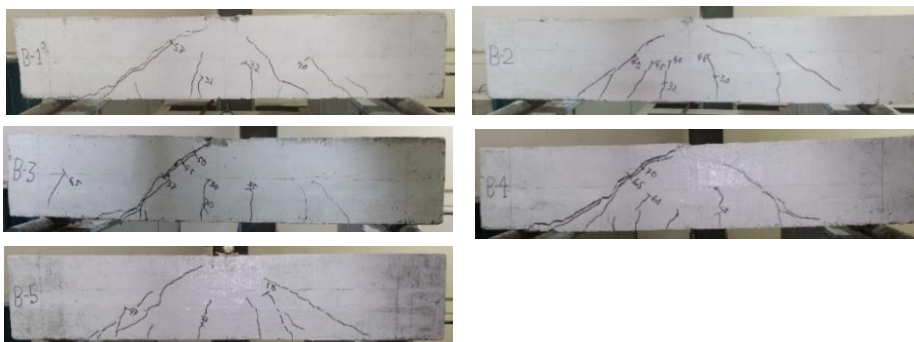


Fig. 3 Damaged beam specimens

The test was conducted by applying load with the increments of 5kN. Dial gauge was used to measure the deflection. All beams were fully damaged in shear by applying 136 kN load. The failure modes of all damaged beams are shown in Figure 3.

3.4 Strengthening

3.4.1 Preparation of Concrete Surface and Anchors

The strengthening process were conducted immediately after damaging of beams. The loose particles of concrete had been removed using diamond cutter from bonding face of the concrete beam as shown in Figure 4. The bonding face of steel plates were sand blasted to expose the original texture of the plate and to create a rough surface for ensuring excellent bond with adhesive and steel plate. Thinner was used to clean the prepared surfaces of concrete and steel plate. Two and four holes were made on concrete surfaces

at the locations of embedded double and multiple connector anchors respectively. Diameter and depth of the holes were 20 mm and 25 mm respectively.

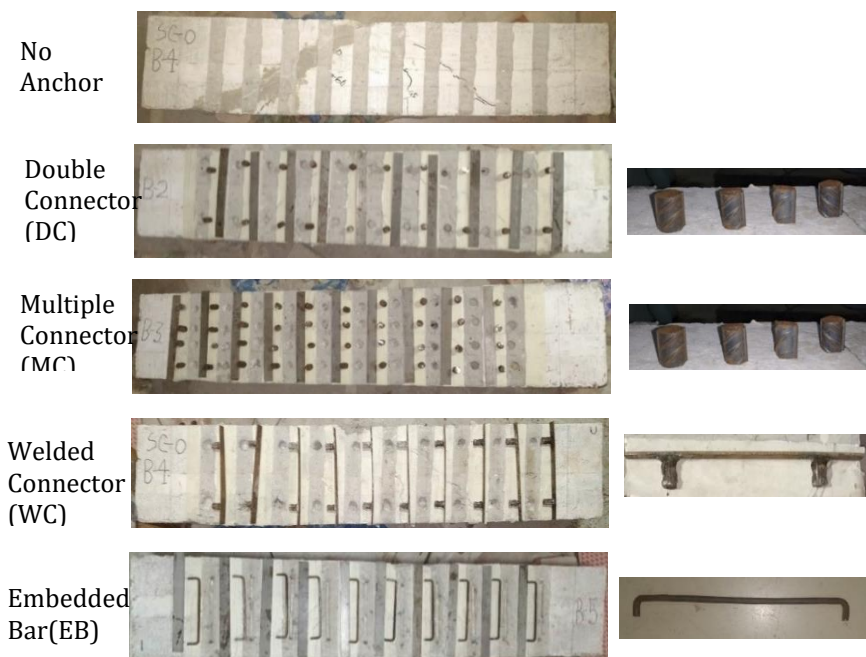


Fig. 4 Preparation of concrete surface and anchors

16 mm bar with 25 mm length was used for double and multiple connectors as shown in Figure 4. Holes were also prepared for welded connector anchor system. Two 16 mm steel bar of 25 mm length were welded near ends of steel plate to prepare welded connector anchor. For embedded bar anchor, 6 mm steel bar as shown in Figure 4 was used. Proper groove was prepared at bonding surface of concrete beam to fix embedded bar. The details of all anchor systems are shown in Figure 4. Before, fixing of plates and anchors, the holes and surrounding area of anchors were properly cleaned from dust using compressed air and thinner.

3.4.2 Fixing of Anchors and Steel Plates

Sikadur 31 epoxy was used to fix anchors and steel plates. Resin and hardener of the epoxy was properly mixed before applied on bonding face of concrete, anchors and plates. The holes of connectors and groove of embedded bar were fully filled with epoxy before placing of anchors. 16 mm steel connectors were then pressed inside epoxy filled holes to avoid air gaps in anchor systems (Figure 5). Embedded bars were also inserted in epoxy filled groove. Once the anchors were fixed properly, epoxy was placed at bonding face of concrete and surface of steel plate. The bonding face of the steel plate was then positioned properly on the beam as shown in Figure 5. The whole strengthening process were conducted in same day to ensure the consistency of the age of strengthening process. After fixing of plates, the strengthened beams were cured by air for seven days before testing.

3.5 Test Set Up and Testing of Beam

All beams were tested under three points bending (single point load) at simply supported condition. The clear and shear spans of the beam were 1100 mm 550 mm respectively as shown in Figure 6. Loading frame was used to test the beams. Mid-span deflection was

recoded using dial gauge. The load was applied slowly by controlling the pressure pump. Reading of deflection dial gauge had been recorded at every 5 kN interval. The debonding load, crack load, failure load, crack patterns and failure modes of all beams were also recorded during testing of beams.



Fig. 5 Fixing of anchors and steel plate

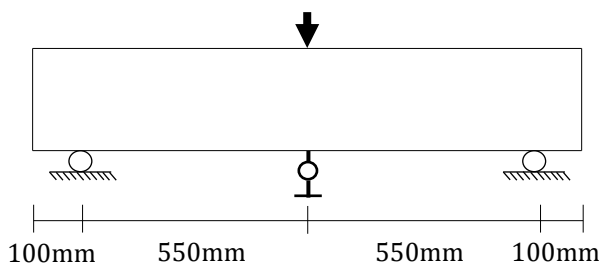


Fig. 6 Test setup and testing of beam

4. Experimental Results

4.1 Effects of Anchors for Shear Strengthening of Damaged RC Beams

4.1.1 Double Connector

The un-strengthened damaged beam had failed by shear as shown in Figure 7 (a). Shear strengthened damaged beam with double connector anchor system (DC) failed by flexure and flexural-shear followed by crushing of concrete as shown in Figure 7 (b). Double connector prevented debonding of steel plate at concrete-adhesive interface. It was noticed that the plate was partially deboned at plate-adhesive interface near the anchors beside the large cracks. Since, the connector was incapable to prevent debonding of plate at plate-adhesive interface, had shown flexural and flexural-shear failure. Whereas, beam without anchor (SB) failed by premature debonding of steel plate followed by shear as shown in Figure 7 (c), the debonding was noticed at concrete-adhesive interface. Double connector anchor system enhanced interfacial bond strength of plate at concrete-adhesive interface which resulted prevention of debonding failure of plate at concrete-adhesive interface.

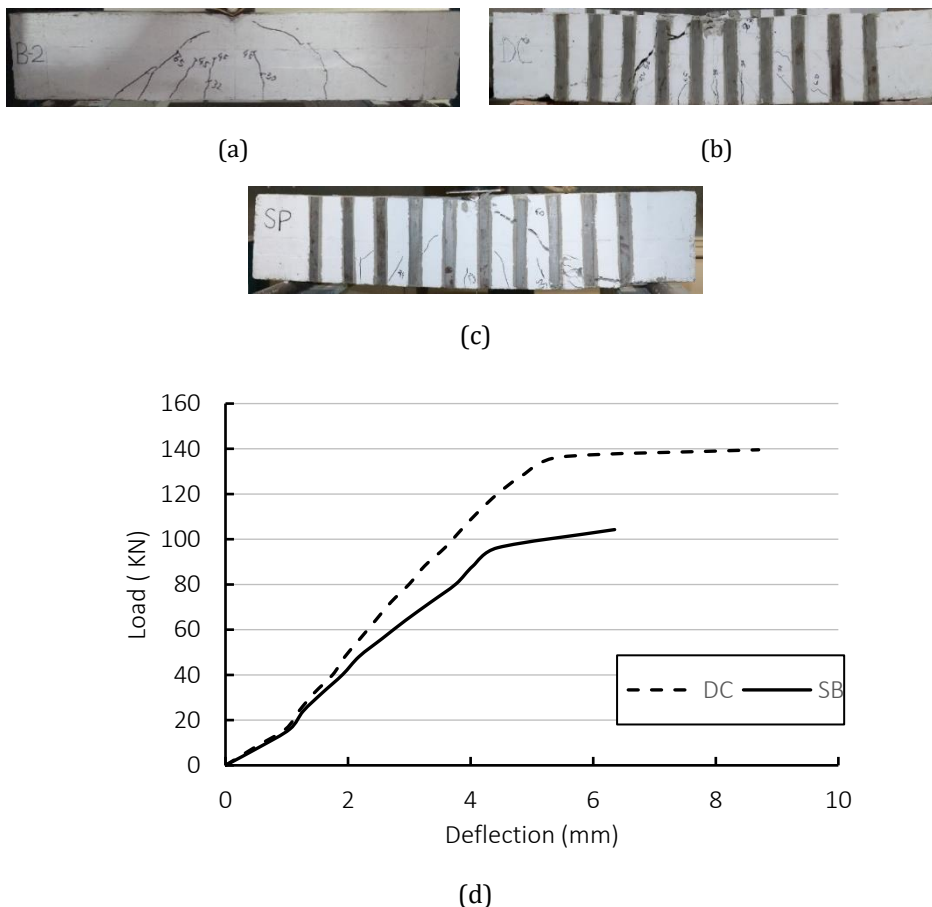


Fig. 7 (a) Damaged beam for DC, (b) Failure mode of beam DC, (c) Failure mode of beam SB, (d) Deflections of beams DC and SB

Results showed that the ductility performance of strengthened beam with double connector anchor system was better than strengthened beam without anchor system (Figures 7 (d)). Since, the strengthened beam (DC) had failed by partial flexure, the ductility of the beam was higher as compared to beam without anchor (SB). The failure loads of strengthened beams DC and SB were 139 kN and 104 kN respectively, while un-strengthened beam had failed by 136 kN load when it was damaged. The double connector anchor system fully restored the shear capacity of damaged beam and it showed 33.65% higher failure load than those of without anchor (SB). As compared to existing research, the shear capacity enhancement of damaged strengthened beam using hybrid composite plate was found to be maximum of 97% [27]. Existing research also reported that U-shaped cementitious composite material restored the shear capacity of damaged strengthened RC beams by 67% [28].

4.1.2 Multi Connector Anchor System

The beam was damaged in shear before strengthening using externally bonded steel plate and multi connector anchor system (Figure 8-a). The shear strengthened damaged beam with multi connector anchor (MC) failed by flexural-shear with crushing of concrete as shown in Figure 8(b). The connector failed immediately after crushing of concrete, and the

plate was debonded at plate-adhesive interface near the location of connector. Since, the beam had failed by flexural-shear rather than premature debonding of plate, the failure mode was bit ductile.

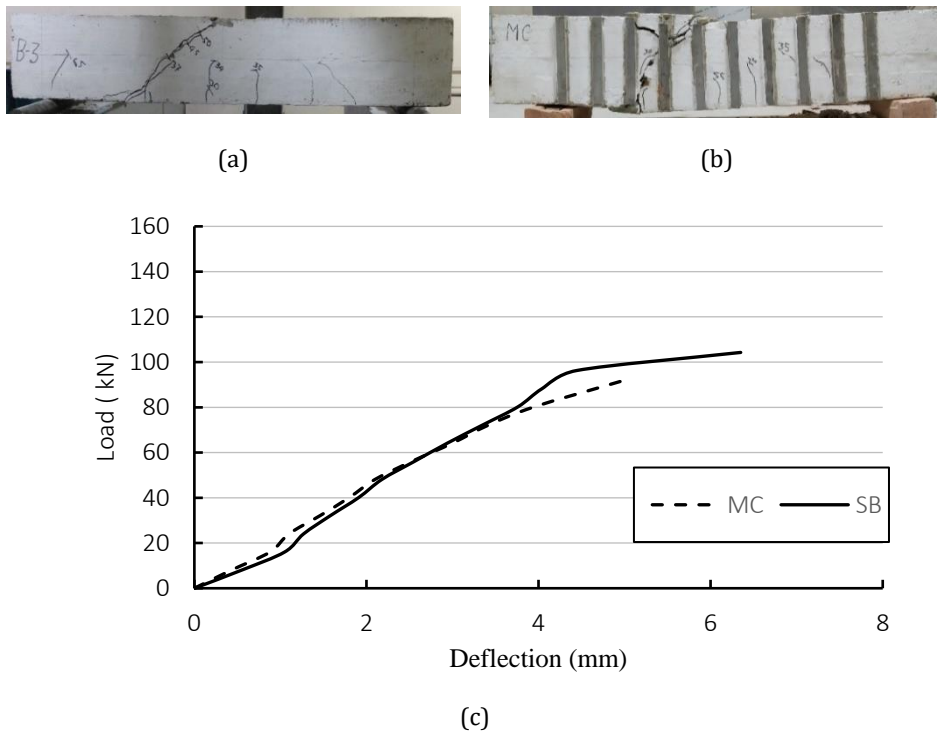


Fig. 8 (a) Damaged beam for MC, (b) Failure mode of beam MC, (c) Deflections of beams MC and SB

The multi connector anchor system prevented premature debonding of steel plate at concrete-adhesive interface. However, once the connector failed, the plate started to debond from plate-adhesive interface. Results also showed that the concrete of beam MC had crushed near the major cracking area of the damaged beam. The multi connector anchor strengthening system had enhanced 91 kN load of damaged beam. Since, the connector of the beam (MC) had failed due to crushing of concrete, the failure load of the strengthened beam was lower than that of without anchor system (Figure 8 (c)).

4.1.3 Welded connector

The beam was damaged in shear (Figure 9(a)) before strengthening. The strengthened beam with welded connector (WC) had failed by flexural-shear followed by crushing of concrete at top compression zone of the beam as shown in Figure 9(b). The welded connector anchor system completely prevented premature debonding of externally bonded steel plate from concrete-adhesive and plate-adhesive interfaces.

The concrete near the major cracking zone of the beam had crushed, once the concrete crushed, the connector had failed. Results also showed that the welded connector had failed because of concrete cover separation as well. The strengthened beam with welded connector anchor failed by 134 kN load which was higher as compared to strengthened beam without anchor as shown in Figure 9(c). Since, the welded connector was effective to prevent premature debonding of externally bonded steel plate at concrete-adhesive and

plate-adhesive interfaces, the failure load of the beam was found to be 28.8% higher as compared to strengthened beam without anchor.

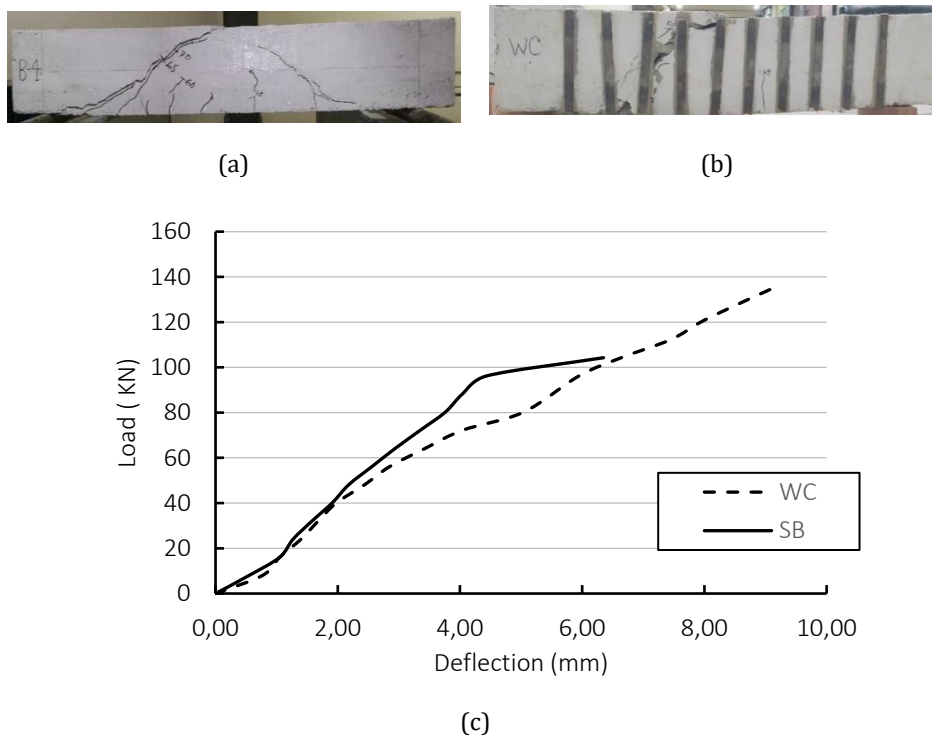


Fig. 9 (a) Damaged beam for WC, (b) Failure mode of beam WC, (c) Deflections of beams WC and SB

4.1.4 Embedded Bar

The embedded bar anchor system was excellent in complete prevention of debonding failure as shown in Figure 10(b). The beam did not show any kinds of debonding failure. The embedded bar provided sufficient interfacial bond strength at concrete-adhesive and plate-adhesive interfaces, thus, premature debonding failure of externally bonded steel plate had been prevented. Finally, the beam had shown flexural failure with crushing of concrete. The mode of failure was ductile rather than catastrophic brittle as shown in Figure 10(b,c).

Results showed that shear strengthened beam with embedded bar anchor had failed by 112 kN load. The beam was failed by flexure, the flexural capacity of that particular beam was lower, thus, the shear enhancement of that beam was found to be lower as well. Based on the results of that beam it could be concluded that the shear enhancement capacity of the strengthened beam depends on flexural capacity of that particular beam also.

4.2 Comparative Structural Behavior of Various Anchor Systems

4.2.1 Premature Debonding of Plate and Failure Behaviour of Strengthened Beam

The steel plate of double connector anchor system debonded from plate-adhesive interface near the location of connector. Once the plate detached from the connector, it was progressively deboned from concrete-adhesive interface. Finally, the plate was separated and caused flexural-shear failure of the beam (DC) with brittle mode of failure as shown in

Figure 11(DC). The steel plate of multi-connector anchor did not debond at concrete-adhesive interface, the plate debonded at plate-adhesive interface. In general, the plate had two interfaces i.e. concrete-adhesive interface and plate-adhesive interface, the plate could be debonded from any of the interfaces. The bond strength of plate at concrete-adhesive interface could be sufficiently increased by multi-connector anchor, thus, debonding at concrete-adhesive interface had been prevented. However, connector was unable to prevent debonding of plate at plate-adhesive interface (Figure 11). Results showed that both connectors failed because of crushing of concrete near the large crack of damaged beam.

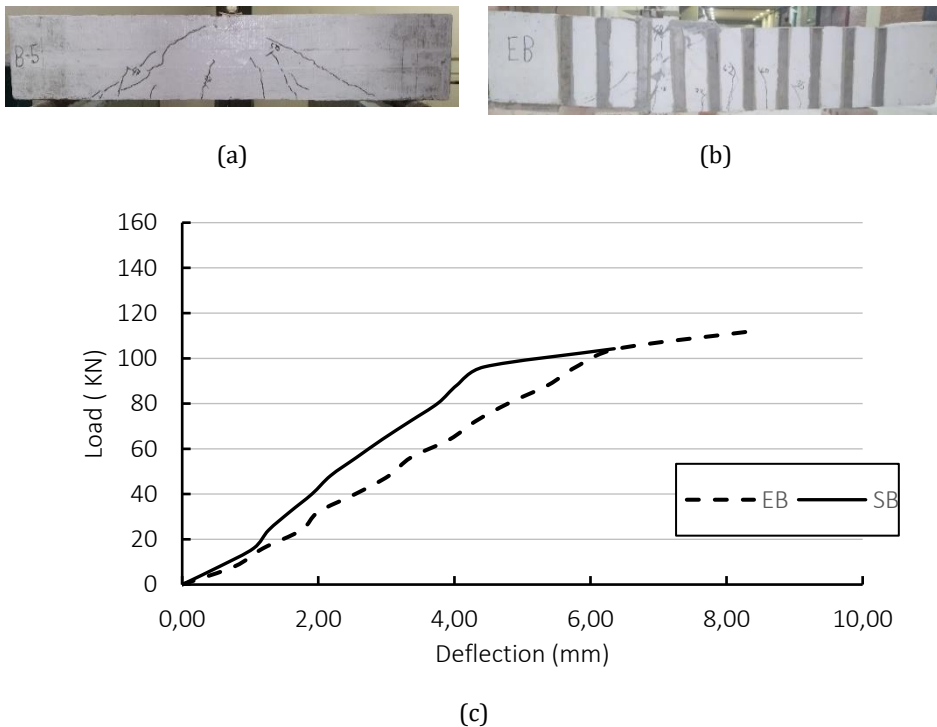


Fig. 10 (a) Damaged beam for EB, (b) Failure Mode of beam EB, (c) Deflections of beams EB and SB

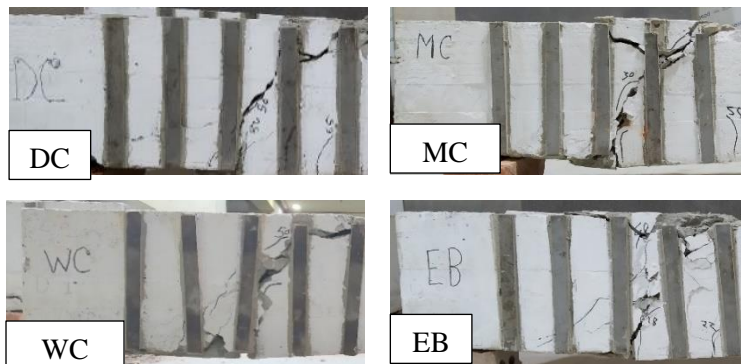


Fig. 11 Failures of shear strengthened beams with various anchors

The debonding of steel plate had been completely prevented by welded connector and embedded bar anchors. In WC, as the connector was welded with steel plate, the plate did not debond at plate-adhesive interface. The anchor of welded connector had failed because of peeling-off concrete cover. Embedded bar anchor was found to be excellent in preventing premature debonding failure, the beam with embedded bar anchor had shown ductile flexural failure as shown in Figure 11 (EB).

4.2.2 Debonding and Failure Loads

Table 2 shows the summary of experimental and theoretical results of all strengthened beams. Shear strengthened beam without anchor (SB) had failed by 104 kN load with debonding of plate at concrete-adhesive interface, the debonding initiated at 80 kN load. Steel plate of double connector strengthened beam (DC) partially debonded at 128 kN load, double connector anchor enhanced interfacial bond strength which resulted higher debonding load of strengthened beam (DC). Multi connector anchor completely prevented debonding of plate at concrete-adhesive interface, however, because of anchor failure due to crushing of concrete, the plate debonded at 90 kN load from plate-adhesive interface. Since, the connector failed, the shear enhancement of that beam was comparatively low.

Table 2. Results of shear strengthened damaged RC beams

Beam ID	Anchor type	Experimental results				Theoretical prediction	
		Debonding load (kN)	Failure load (kN)	Increased shear capacity (%)	Failure mode	Shear capacity (kN)	Flexural capacity (kN)
SB	No anchor	80	104	104	Debonding at concrete interface	135	153
DC	Double connector	128	139.6	139.6	Partial debonding at concrete and plate interface	135	153
MC	Multi connector	91.4	91.4	91.4	Debonding at plate interface	135	153
WC	Welded connector		136.3	136.3	No debonding, cover separation	135	153
EB	Embedded bar		112.3	112.3	No debonding, flexural failure	135	153

Before strengthening, all beams were fully damaged for shear and thus the un-strengthened damaged beams were not able to sustain shear force. Shear strengthened beam with welded connector prevented premature debonding of externally bonded steel plate, and thus, the shear capacity enhancement was 136.3% as compared to damaged beam. Embedded bar anchor prevented premature debonding of steel plate and concrete cover separation failure. The shear capacity enhancement of that beam (EB) was 112.3% as compared to damaged beam. However, the shear capacity of EB was found to be lower as compared to the design shear capacity (136 kN). The shear capacity of that beam even could be higher if the beam had sustained higher flexural capacity. Results showed that the degree of damage and size of cracks influenced the effectiveness of ancho system to

enhance the shear capacity of strengthened beams, especially for multi connector anchor system. In terms of capacity enhancement, double connector, welded connector and embedded bar anchor systems were found to be more effective. The concrete of damaged beam near shear cracks was relatively weak, the anchors near the shear crack might not be effective because of weaker concrete. The multi connector supposed to ensure higher bond strength to prevent premature debonding failure of steel plate. However, because of crushing of concrete at the location of connector, the capacity of strengthened beam with multi connector anchors were found to be lower as compared to others.

4.3 Theoretical Predictions

Flexural and shear capacities of all strengthened beams could be calculated based on the Equation of 15 and 16 respectively as shown below.

$$\text{Flexural capacity: } M = A_s f_{tk} \left[d - \frac{0.588 A_s f_{tk}}{f_{ck} b} \right] \tag{15}$$

$$\text{Shear capacity: } V_{sb} = 2 A_p f_{yp} \left[\frac{h \cot \theta}{s_p} \right] \tag{16}$$

Table 3. Parameters and theoretical capacities of strengthened beam

Parameters of strengthened beam (mm, mm ² , N/mm ²)										Flexural capacity (kN)	Shear capacity (kN)
A _s	f _{tk}	d	f _{ck}	b	A _p	f _{yp}	h	θ	S _p		
377	620	211	30	150	54	275	250	45	110	153	135

The particulars and theoretical capacities of beams are shown in Table 3. Results showed that theoretical flexural and shear capacities of strengthened beams were 153 kN and 135 kN respectively. Theoretical shear capacity of un-strengthened control beam was 136 kN, the shear contribution of externally bonded steel plate was almost same with the original shear capacity of damaged beam. All beams were designed for shear strengthening using steel plate to restore the original capacity. Since all beams were fully damaged in shear before shear strengthening, theoretical model considered the shear contribution of externally bonded steel plate only to predict shear capacity of strengthened beam. Results showed that shear strengthened beams DC and WC fully re-stored the shear capacity (139 kN and 136 kN respectively) and had almost similar values of theoretical shear capacities (135 kN) of beams.

5. Conclusions

Externally boded steel plate of shear strengthened damaged RC beam without anchor had debonded from concrete-adhesive interface. Whereas, embedded connector, double connector, welded connector and embedded bar anchor systems were found to be effective in prevention of premature debonding of externally bonded steel plate from concrete-adhesive interfaces of shear strengthened RC beams. The steel plate of double and multi connector anchor systems were debonded at plate-adhesive interface near the connector, the connectors were incapable to prevent debonding of EB steel plate at plate-adhesive interface near the anchors. The anchors could not function once the concrete had crushed or the plate had debonded at plate-adhesive interface. The debonding of plate and failure

of anchors caused shear failure of strengthened beams rather than flexural failure. Welded connector and embedded bar anchors were found to be very excellent in preventing premature debonding of externally bonded steel plate both at plate-adhesive and concrete-adhesive interfaces for shear strengthening of damaged RC beams. Strengthened beam with welded connector anchor had failed by separation of concrete cover. In general, all anchors significantly enhanced shear capacities of damaged beams, the anchor system enhanced maximum of 139% shear capacities of damaged beam through strengthening using externally bonded steel plate. Double and welded connector anchors had shown the highest enhancement of shear capacities of strengthened beams and were able to re-store the original capacities of damaged beams. The degree of damage, cracks and flexural capacity influenced the shear enhancement of strengthened beams. Larger crack of damaged beams caused failure of anchor systems which resulted lower enhancement of shear capacities of strengthened beams. The beam with lower flexural capacity caused lower enhancement of shear capacity as well. The dimension of steel plate for shear strengthening of damaged RC beam based on proposed design was sufficient to restore the full shear capacities of damaged beams. The shear capacity of strengthened beam based on the proposed theoretical model considering contribution of externally bonded steel plate was found to be comparable with the experimental results.

Acknowledgements

The research was funded by Ministry of Education (MOE), Peoples Republic of Bangladesh under the grant of SD2018781. The authors are very much thankful to the ministry for providing the fund. Appreciations are also due to my students, staff and Department of Civil Engineering, University of Asia Pacific for facilitating the laboratory supports to conduct the research.

Nomenclature

M	: Moment resisting capacity of beam
T	: Tensile force of flexural reinforcement
z	: Moment arm
A_s	: Cross sectional area of flexural reinforcement
f_{tk}	: Tensile strength of flexural reinforcement
f_{ck}	: Concrete compressive strength based on cylinder test
b	: Width of beam
x	: Depth of neutral axis
d	: Effective depth of beam
d'	: Depth of compression reinforcement (top bar)
V_{ds}	: Design shear force
L_s	: Shear span
N	: Number of shear link
s_{link}	: Spacing of shear link
V_{cb}	: Shear capacity of un – strengthened control beam
V_c	: Shear force resisted by concrete
$V_{y,link}$: Shear force of beam due to yielding of shear reinforcement
$A_{s,link}$: Cross sectional area of shear link
$f_{y,link}$: Yield strength of shear link
V_{sp}	: Shear force resisted by steel plate
A_p	: Cross sectional area of single steel plate
N_p	: Number of steel plate to resist shear (from one side of beam)
s_p	: Spacing of steel plate

f_{yp}	: Yield strength of steel plate
h	: Depth of beam
$\varepsilon_{deb,p}$: Debonding strain of plate
F_{bp}	: Bond strength of plate
w_p	: Width of plate
E_p	: Modulus of elasticity of plate
t_p	: Thickness of plate
σ_p	: Stress of plate
ε_p	: Strain of plate

References

- [1] Libreros JHG, Sneed LH, Antino TD', Pellegrino C. Behavior of RC beams strengthened in shear with FRP and FRCM composites. *Engineering Structures*, 2017; 150: 830-842. <https://doi.org/10.1016/j.engstruct.2017.07.084>
- [2] Alshaikhly AS, Alam MA, Mustapha KN. An Advanced Method for Repairing Severely Damaged Beams in Shear with Externally Bonded Steel Plates Using Adhesive and Steel Connectors. *Arabian Journal for Science and Engineering*, 2016; 41: 4077-4097. <https://doi.org/10.1007/s13369-016-2079-5>
- [3] Baghi H, Joaquim AO, Barros MF. Shear strengthening of reinforced concrete beams with Hybrid Composite Plates (HCP) technique: Experimental research and analytical model. *Engineering Structures*, 2016; 125: 504-520. <https://doi.org/10.1016/j.engstruct.2016.07.023>
- [4] Lourenço L, Zamanzadeh Z, Barros JAO, Rezazadeh M. Shear strengthening of RC beams with thin panels of mortar reinforced with recycled steel fibres. *J. of Cl. Produc*, 2018; 194: 112-126. <https://doi.org/10.1016/j.jclepro.2018.05.096>
- [5] Sundarraja MC, Rajamohan S. Strengthening of RC Beams in Shear Using Composites Fabrics an Experimental Study. 2008. NBMCW. <https://doi.org/10.1177/0731684407081772>
- [6] Swetha KS, James RM. Strengthening of RC Beam with Web Bonded Steel Plates. *International Journal of Engineering and Techniques*, 2018; 4 (3).
- [7] Younis A, Ebead U, Shrestha KC. Different FRCM systems for shear-strengthening of reinforced concrete beams. *Construction and Building Materials*, 2017; 153: 514-526. <https://doi.org/10.1016/j.conbuildmat.2017.07.132>
- [8] Szabó ZK, Balázs GL. Near surface mounted FRP reinforcement for strengthening of concrete structures. *Civil Engineering*, 2007; 51(1): 33-38. <https://doi.org/10.3311/pp.ci.2007-1.05>
- [9] Li R, Deng M, Chen H, Zhang Y. Shear strengthening of RC shear-deficient beams with highly ductile fiber-reinforced concrete. *Structures*, 2022; 44: 159-170. <https://doi.org/10.1016/j.istruc.2022.08.013>
- [10] Cai L, Liu Q, Guo R. Study on the shear behavior of RC beams strengthened by CFRP grid with epoxy mortar. *Composite Structures*, 2021; 275: 114419. <https://doi.org/10.1016/j.compstruct.2021.114419>
- [11] Alwash D, Kalfat R, Al- Mahaidi R, Du H. Shear strengthening of RC beams using NSM CFRP bonded using cement-based adhesive. *Construction and Building Materials*, 2021; 301. <https://doi.org/10.1016/j.conbuildmat.2021.124365>
- [12] Baraghith AT, Mansour W, Behiry RN, Fayed S. Effectiveness of SHCC strips reinforced with glass fiber textile mesh layers for shear strengthening of RC beams: Experimental and numerical assessments. *Construction and Building Materials*, 2022; 327. <https://doi.org/10.1016/j.conbuildmat.2022.127036>

- [13] Guo L, Deng M, Chen H, Li R, Ma X, Zhang Y. Experimental study on pre-damaged RC beams shear-strengthened with textile-reinforced mortar (TRM). *Engineering Structures*, 2022; 256. <https://doi.org/10.1016/j.engstruct.2022.113956>
- [14] Gai X, He D, Wang H. Shear strengthening of RC beam using RFRP composites. *Magazine of Civil Engineering*, 2022; 114(6).
- [15] Koutas L, Triantafyllou TC. Use of anchors in shear strengthening of reinforced concrete T-beams with FRP. *J Composites for Construction*, 2013; 17(1): 101-107. [https://doi.org/10.1061/\(ASCE\)CC.1943-5614.0000316](https://doi.org/10.1061/(ASCE)CC.1943-5614.0000316)
- [16] Galal K, Mofidi A. Shear strengthening of RC T-beams using mechanically anchored unbonded dry carbon fiber sheets. *Journal of Composites for Construction*, 2010; 24(1): 31-39. [https://doi.org/10.1061/\(ASCE\)CF.1943-5509.0000067](https://doi.org/10.1061/(ASCE)CF.1943-5509.0000067)
- [17] Mofidi A, Chaallal O, Benmokrane B, Neale K. Performance of end-anchorage systems for RC beams strengthened in shear with epoxy-bonded FRP. *Journal of Composites for Construction*, 2012; 16(3): 322-331 [https://doi.org/10.1061/\(ASCE\)CC.1943-5614.0000263](https://doi.org/10.1061/(ASCE)CC.1943-5614.0000263)
- [18] Alam MA, Alshaikhly AS, Mustapha KN. An experimental study on the debonding of steel and CFRP strips externally bonded to concrete in the presence of embedded shear connectors. *Arabian Journal for Science and Engineering*, 2016; 41 (10): 4171-4186. <https://doi.org/10.1007/s13369-016-2123-5>
- [19] Guan YH, Jiang BS, Jiang YD. Experimental study on RC beams strengthened in shear with the FRP-bolt strengthening technology. *Geotechnical Special Publication*, 2011; 219: 57-64. [https://doi.org/10.1061/47630\(409\)8](https://doi.org/10.1061/47630(409)8)
- [20] Belarbi A, Acun B. FRP Systems in shear strengthening of reinforced concrete structures. *Procedia Engineering*, 2013; 57: 2-8. <https://doi.org/10.1016/j.proeng.2013.04.004>
- [21] Chen GM, Zhang Z, Li YL, Li XQ, Zhou CY. T-section RC beams shear-strengthened with anchored CFRP U-strips. *Composite Structures*, 2016; 144: 57-79. <https://doi.org/10.1016/j.compstruct.2016.02.033>
- [22] Tetta ZC, Koutas LN, Bournas DA. Shear strengthening of full-scale RC T-beams using textile-reinforced mortar and textile-based anchors. *Composites Part B: Engineering*, 2016; 95: 225-239. <https://doi.org/10.1016/j.compositesb.2016.03.076>
- [23] Ghani Razaqpur A, Cameron R, Mostafa AAB. Strengthening of RC beams with externally bonded and anchored thick CFRP laminate. *Composite Structures*, 2020; 233. <https://doi.org/10.1016/j.compstruct.2019.111574>
- [24] Saribiyik A, Abodan B, Balci MT. Experimental study on shear strengthening of RC beams with basalt FRP strips using different wrapping methods. *Engineering Science and Technology, an International Journal*, 2021; 24 (1): 192-204. <https://doi.org/10.1016/j.jestch.2020.06.003>
- [25] EC2. General rules and rules for building. *Eurocode 2: Design of concrete structures Part 1-1 1992-1-1*. 2004.
- [26] Alam MA, Hassan A, Muda ZC. Development of kenaf fibre reinforced polymer laminate for shear strengthening of reinforced concrete beam. *Materials and Structures*, 2016; 49: 795-811. <https://doi.org/10.1617/s11527-015-0539-0>
- [27] Baghi H, Barros JAO, Rezazadeh M. Shear Strengthening of Damaged Reinforced Concrete Beams with Hybrid Composite Plates. *Composite Structures*, 2017; 178: 353-371. <https://doi.org/10.1016/j.compstruct.2017.07.039>
- [28] Hassan A, Baraghith, AT, Atta AM, El-Shafiey TF. Retrofitting of shear-damaged RC T-beams using U-shaped SHCC jacket. *Engineering Structures*, 2021; 246 (112892). <https://doi.org/10.1016/j.engstruct.2021.112892>

Blank Page



Research Article

Bi-diaphragm elastoplastic haunch retrofit solution for ill-detailed RC beam-column joints

Abhay Gujar^{*a}, Sachin Pore^b

Department of Civil Engineering, DBATU, Lonere, Maharashtra, India

Article Info

Article history:

Received 07 Mar 2023

Accepted 10 May 2023

Keywords:

Ill-detailed joint;
In-fill masonry;
Haunch;
Push-over;
Retrofit;
Soft-storey

Abstract

Failure of ill-detailed connections is a primary cause of catastrophic, cascading failure of Reinforced cement concrete (RC) frame subjected to seismic loading. A performance based, 3 dimensional (3D), Bi-Diaphragm bolted metallic haunch retrofit solution is proposed, to avoid brittle shear damage to the connection panel zone. Welding is avoided in fabrication of the proposed device to avoid brittle failure in any part of the assembly. The haunch is designed to alter the strength hierarchy of connection subassembly, ensuring plastic hinge formation in beam before any other type of failure occurs. Assessments reveal that, 3D geometry improves torsional stiffness (+277%) and resilience (+94%) over those of an equivalent planer haunch. Numerical analysis is done to estimate the stiffness of haunch. A flow-chart illustrating procedure to design the proposed haunch is presented. The efficacy of proposed solution is evaluated by performance comparison of a Parking+6 storey frame, with and without retrofit solution, subjected to push-over (+87% rise in lateral load at yield, resilience increased by +37 %) and non-linear seismic analysis (Max. roof displacement reduced by -106% and storey drift by -154%). Masonry walls in habitable floors are modeled as equivalent diagonal struts to replicate much essential soft-storey effect. This study is focused on retrofitting exterior beam-column connections owing to their vulnerability reported in the literature. Analytical and numerical assessments confirm the efficacy of proposed solution in mitigating failure during seismic excitations.

© 2023 MIM Research Group. All rights reserved.

1. Introduction

Experiments [1-2] and forensics [3] of earthquake-damaged structures have exposed inherent deficiencies in buildings designed and detailed for gravity-only loads. The absence of capacity design principles and inadequate ductile detailing are responsible for failure of such structures [4]. Hakuto et al. [2] conducted a series of investigations, pertaining to sub-standard column-beam connections. For a few of the specimens, the longitudinal bars of beams were hooked away from joint core. Remaining specimens had bars hooked inside the joint panel. Subassembly with bars hooked inside connection panel zone appeared to be more efficient in resisting joint shear owing to development of diagonal compressive concrete strut mechanism and reinforcement truss action. Reinforcement truss action is composed of bond between concrete and steel along with tensile strength of rebar. Vulnerability of joint core zone for deficient connections was highlighted by experiments [3] on scaled down (2/3) sub-standard joints. Pampanin et al. [5] proposed that principal stresses are a better measure of connection performance. A value of principal stress (P_t), giving rise to 1st shear crack in connection, can be assumed as $P_t = 0.2\sqrt{f_{ck}}$.

Column-beam joint is found to be the weakest link causing a progressive collapse of the building subjected to lateral loading. Efficient strengthening or retrofitting solution,

*Corresponding author: abhay.gujar@dbatu.ac.in

^a orcid.org/0000-0003-3294-3321; ^b orcid.org/0000-0001-8924-3823

DOI: <http://dx.doi.org/10.17515/resm2023.702st0507>

Res. Eng. Struct. Mat. Vol. 9 Iss. 4 (2023) 1379-1402

generating required protection to joint panel zone, while altering hierarchy of strength between different components of subassembly, is required to enhance the performance of building frame during seismic activity. Accounting for stiffness of infill brick masonry on upper floors is essential while performing seismic analysis of buildings with parking story. Sudden change in stiffness above parking floor tends to develop a soft story mechanism.

Improvement in performance of ill-detailed connections can be achieved through various active and passive retrofitting techniques. Ghobarah et al. [6] employed corrugated sheets for joint wrapping, carbon Fiber Reinforcement Polymers (CFRP) was used by [4], diagonally welded singular plate haunch by [7]. Jayasooriya et al. [8-9] employed diagonal haunches in the form of buckling resistant braces. Geo-Polymer [10] wrapping was also used to enhance the performance of the substandard connections.

Several investigations using different configurations of 'X', 'K' and, 'V' braces, were carried out by researchers in order to improvise lateral load resilience of RC frames, with sub-standard joints. It was observed during an analytical investigation [11] that, use of rigid, non-buckling diagonal braces tends to improvise plastic zone behavior of frames with weak column-strong beam type of configurations. Experimental investigations [12] revealed that use of X-braces as diagonal stiffeners improvise shear-capacity of structures, in the plane of braces. Another study [13] noted that X type diagonal braces are more efficient in case of shallow buildings, rather than tall buildings. Experiments [14] also revealed that ultimate load carrying capacity (LCC) and initial stiffness is considerably enhanced due to use of eccentric and concentric 'X' braces and with 'V' or reversed 'V' braces. Hu et al. [15] conducted investigations on 'X' type braces. It was observed that rather than increasing number of columns, provision of 'X' braces efficiently improvise the performance of the building. Another Investigation on 'X' type braces [16] claimed that transverse load carrying capacity of deficient frames increases three times due to the proposed bracing system. Rahimi et al. [17] carried our numerical assessment of 'X' type braces to conclude that 'X' braces decrease the lateral drift of the frame and the shear demand on the connections. Jafari et al. [18] studied non-linear performance of RC frames retrofitted by diagonal knee braces. It was observed that, knee braces can increase column axial load by 15% for a G+2 building and by about 7% for a moderately tall (8-12 storey) building.

Dynamic time-history analysis [19] was done on 5 storey and 7 story RC frames retrofitted using eccentric steel-braces. Significant reduction in storey drifts as compared to as built frames was observed. In past, a number of researchers Rahai et al. [20]; Ramin et al. [21]; Naghavi et al. [22]; Ozelik and Erdil [23]; Qian et al. [14]; Sutcu [24]; Godinez et al. [25]; Fateh and Hejazi [26]; Du et al. [27]; Kaviani et al. [28] investigated efficacy of various types of 'X' type, diagonal concentric or eccentric braces. The practical difficulty while using diagonal braces, across the bay, is that they pose a hinderance to an unobstructed passage within the habitable floor space. A better solution to cater this problem would be to use a knee brace type retrofit haunch element adjacent to beam-column connections. If the geometric dimensions of haunch element are designed keeping in view the headroom requirements, it will not cause any hinderance and will facilitate unobstructed use of the floor space.

Uang and Lee [29] were the first to propose a haunch retrofit solution for repairing and strengthening steel-moment-resistant frames damaged during Northridge-California (1994) earthquakes. Further investigations by Chen [30] established the utility of a haunched retrofit solution. Further study [30] of different haunch configurations yielded some conclusions, such as

- Haunch with stiffness below a lower bound, cannot arrest damage in joint panel zone.

- Column-beam connections have limited elastic deformation capacity thus, plastic deformation of haunches does not ensure enhanced resilience of the sub-system
- Having a haunch design, ensuring elastic behavior during entire loading range ensures best performance of the subassembly.

Haunch retrofit solution was improvised by Pampanin et al [31]. G. Genesio [7] devised a diagonal singular plate welded haunch, which was attached to beam column subassembly, through post installed anchor fasteners. The Bi-Diaphragm Haunch (BDH) retrofit solution proposed here is a modified bolted version of retrofit solution proposed by Genesio [7].

The practicability of any retrofit solution depends on factors like cost, reliability, replicability, invasiveness during installation, etc. This work presents the efficacy of a cost-effective, less invasive, 3-D bolted haunch, which can be introduced during or after the construction of a building. The primary concept is based on capacity design principles, wherein the stress path is deviated from passing through the weak connection zone. The path is altered in such a way that, a plastic hinge is formed in beam location, away from column face. Analytical and numerical investigations show that the haunch retrofit strategy increases strength and ductility of subassembly, and thus improves the over-all seismic performance of the building [30, 7].

2. Need for Proposed Retrofitting Solution

Typical deficiencies as reported in the literature [31-32] for gravity-only designed and ill-detailed connections are summarized as follows,

- Insufficient anchorage length in connection core for longitudinal reinforcement.
- Inadequate end hook detailing for transverse reinforcement.
- Inadequate amount of longitudinal and transverse reinforcement at connection core.
- Insufficient confinement in connection panel zone.

These deficiencies lead to catastrophic pancake failure of buildings subjected to seismic loading (Fig.1). To mitigate such failure, it is imperative to devise a solution, that can shift the critical stress path away from the beam-column joints, while ensuring failure governed by plastic hinge formation in the beam, away from face of the connection. Planer welded haunches [7] do not offer adequate post-buckling resilience. To avoid buckling, single plate haunch needs to be substantially thick. More-over, welded connections are prone to brittle failure. Other passive techniques like wrapping or increasing the strength of concrete in the connection zone by some means, do not remove connection zone from the critical stress path. The proposed BDH is expected to impart better resilience to the structure, while shifting critical stress path away from the connection panel zone. Further, literature study reveals that most of the performance evaluation done, does not consider the stiffness of infill brick masonry walls [31, 33] on the storeys above parking floor. Inclusion of brick masonry to structural stiffness explicitly shows vulnerability of parking floor joints and underlines the need for strengthening the same. In this work contribution of infill brick masonry to stiffness of upper floors is considered. Unlike planer haunches [7], proposed BDH is expected to impart a reasonable degree of lateral as well as torsional resilience to the subassembly. Although this solution seems to provide a practical cost-effective retrofit strategy, a systematic design procedure and numerical validation of the proposed technique is essential.

3. Performance of Ill-Detailed Connections

A series of tests [1, 2, 34, 35, 36, 37] highlight vulnerability of joint panel zone during seismic activity. It is reported that, absence of capacity design and insufficient quantity of

confining and longitudinal reinforcement along with inadequate anchorage detailing are the primary causes of this vulnerability.



Fig. 1 Pancake failure Islamabad 2005 earthquake (Seismic design characterization of RC special moment resisting frames in Pakistan-field survey to laboratory experiments.)

In such cases a brittle shear failure is observed in exterior beam-column joints before occurrence of flexural hinges in the beam or column. The mode of failure changes depending on the location and detailing of the joint. In absence of confining reinforcement performance solely depends on concrete compression strut. Thus, for an exterior joint, strength degrades rapidly after the formation of first crack. Strain hardening can only be expected for interior joints [30]. Further discussion is especially pertaining to strengthening of exterior beam-column connections.

4. Effect of Haunch on Beam-Column Subassembly

A free body diagram of exterior column-beam subassembly assuming points for contraflexure at mid spans of beam and column is illustrated in Fig. 2. Introduction of a haunch re-routes stress flow around column-beam subassembly as shown in Fig. 2. Moments and shear forces around the joint panel zone are significantly reduced. The critical moment in beam is shifted away from connection. This relocation of beam maximum moment can be exploited to ensure formation of a plastic hinge in beam before occurrence of any other failure mechanism. The efficacy of the proposed solution depends on X , α (Fig.6) and axial stiffness (K_a) of haunch [30]. The provision of haunch at top and bottom of beam eliminates axial force generation in the beam.

If the shear force in beam due to haunches is denoted by βV_b then BMD and SFD in terms of β can be drawn as shown in Fig. 3. Reduced beam moment at the face of connection is given as [30]

$$M_b = M_{bmax} \left[1 - \frac{\beta a_b}{2L \tan \alpha} - \frac{(1-\beta)X}{L} \right] \quad \text{where, } L = \left(\frac{L_{Bc}}{2} \right) - X \quad (1)$$

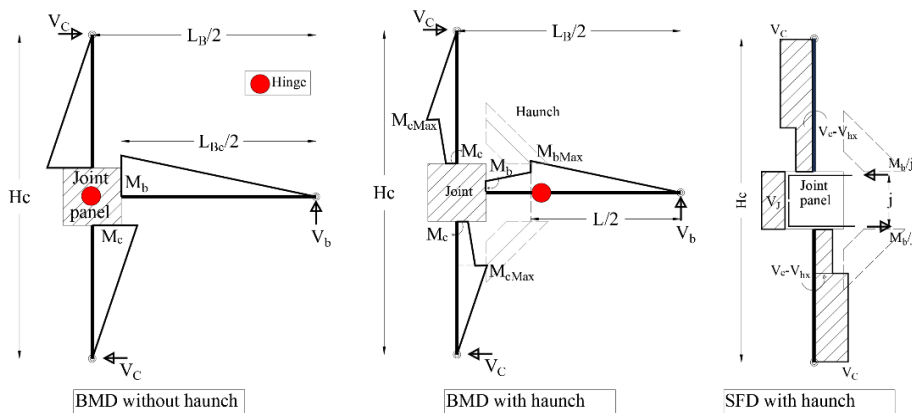


Fig. 1 Effect of haunch on SFD and BMD (Gujar & Pore, 2023)

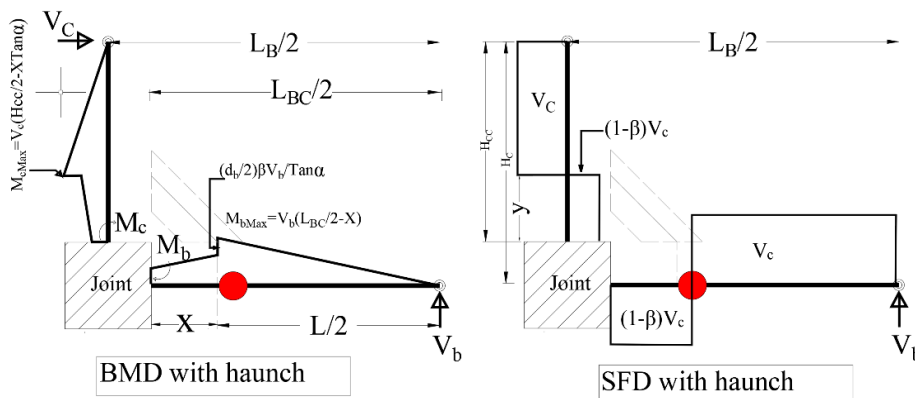


Fig. 3 BMD and SFD of haunched joint as a function of β

Reduced moment in column at connection interface is given as,

$$M_c = M_{cmax} \left(\frac{1 - \beta_1 d_c \tan \alpha}{2H_1} + \frac{(1 - \beta_1) X \tan \alpha}{H_1} \right) \tag{2}$$

Where

$$H_1 = \frac{H_{cc}}{2} - X \tan \alpha$$

and

$$\beta_1 = \beta \left(\frac{H_c}{L_B \tan \alpha} \right)$$

Maximum moment in column (M_{cmax}) corresponding to maximum moment in beam (M_{bmax}) is given as [30],

$$M_{cmax} = M_{bmax} \left(\left(\frac{H_c}{2} - \frac{d_b}{2} - X \tan \alpha \right) \left(1 + \frac{d_c}{L_{BC}} \right) / H_c \right) \tag{3}$$

Referring to moment diagram in Fig. 3 for details of symbols in the above expression, value of $\beta > 1$ will yield negative shear force. Negative shear force will be more desirable to

protect beam column joint in a better way [30]. β value is calculated from deformation compatibilities, between deformations of column and beam at the location of haunch and axial deformation of haunch. When flexural deformation of beam and column is also accounted for, then β is given as [30],

$$\beta = \left(\frac{y}{x}\right) \cdot \frac{6Ld_b + 3X \cdot d_b + 6y \cdot L + 4XY + \frac{2I_b L_b y^3}{I_c X H_c} + \frac{3I_b L_b y^2}{I_c X H_c} + \frac{3I_b d_c L_b y^3}{I_c X^2 H_c} + \frac{3I_b d_c H L_b y^2}{I_c X^2 H_c}}{3d_b^2 + 6y d_b + 4y^2 + \frac{12EI_b}{2K_{dav} X \cos^2 \alpha} + \frac{6I_b y^2}{X^2 A_c} + \frac{2I_b y^3}{X I_c} + \frac{3I_b d_c y^2}{I_c X^2} + \frac{3I_b d_c^2 y^3}{2I_c X^3}} \quad (4)$$

$$L = L_{BC} - 2X, \quad H = H_{CC} - 2y \text{ and } H_{CC} = H_c - d_b$$

(Note: If only one haunch is used, $2K_{dav}$ is replaced by K_{dav})

Where, I_b and I_c are major moment of inertias of beam and column respectively.

For details of X , Y , α please refer Fig. 6 L_b is c/c span of beam d_c and d_b are effective depths of column and beams.

K_{dav} is average elastic stiffness of haunch. E is modulus of elasticity of concrete.

5. Proposed Retrofit Strategy

The primary concept is based on altering strength hierarchy by relocating plastic hinge in beam through axial straining of haunch element. Haunch is designed in such a way as to reduce moment acting on joint thereby protecting it from brittle shear failure. Principal stresses are found to be more reliable measure [3, 40] of predicting response of any element subjected to multidirectional loads, hence performance evaluation in this work is based on state of principal stress pertaining to an element. Elasto-plastic performance of haunch is so designed that while dissipating the energy, stresses in connection zone remain well below critical principal stress levels. It is further ensured that moment at connection does not exceed its moment capacity before beam hinging takes place. In short strength hierarchy of subassembly is altered to ensure,

$$V_{beamHinge} < \gamma 1 \cdot V_{columnHinge} < \gamma 2 \cdot V_{joint} < \gamma 3 \cdot V_{beamShear} < \gamma 4 \cdot V_{columnShear}$$

$\gamma 1, 2, 3, 4$ are factor of safety assumed in consistency with code provisions

$$\text{(May be assumed between 0.7 to 0.85) [30]}$$

6. Design Steps for BDH Element

6.1 Limit State of Column Hinging

It is imperative to check that column hinging does not take place prior to beam hinging. Haunch design should be such that beam hinging occurs prior to maximum column yielding capacity moment capacity M_{pc} is reached. Thus, first threshold is limit of column story shear given as,

$$V_{capacit\ column\ hinge} = \frac{M_{pc}}{\frac{H_c}{2} - \frac{d_b}{2} - X \cdot \tan \alpha} \quad (5)$$

M_{pc} is plastic moment capacity of column. It can be obtained from moment curvature plot based on geometric properties of column. Knowing $V_{col-hinge}$, with some factor of safety $\gamma 1$ requirement for V beam-hinge can be obtained. ($\gamma 1$ may be assumed to be 0.8)

$$V_{capacity\ Beam\ hinge} = \gamma 1 \cdot V_{capacit\ column\ hinge} \quad (6)$$

6.2 Limit State of Connection Shear Capacity

It is essential that joint does not fail prior to beam or column. Hence equivalent story shear capacity of joint, must be greater than $V_{capacit\ column\ hinge}$. Principal stresses are reliable criteria for accessing performance of the joint (Pampanin, Calvi, & Moratti, Seismic Behaviour of R.C.Beam Column joints Designed for gravity loads, 2002). Critical value of principal stress (f_{pc}) is given as $f_{pc} = 0.29\sqrt{f_{ck}}$ for exterior connections [30]. Equivalent story shear for connection hinging in terms of β is defined as,

$$V_{capacit\ joint} = \frac{A_e \sqrt{(f_{pc}^2) - \frac{f_{pc}P}{A_c}}}{1 - \frac{\beta H_c}{(L_{Bc} + d_c) \tan \alpha} - \frac{H_c(L_{Bc} - 2X)}{j(L_{Bc} + d_c)} \left(1 - \frac{\beta d_b}{2L \tan \alpha} + \frac{(1-\beta)X}{L}\right)} \quad (7)$$

Where, $L = L_{Bc} - 2X$ and 'P' is axial load on column

Knowing $V_{capacit\ column\ hinge}$ from Eq. (5) and assuming factor of safety γ_2 , required $V_{capacit\ joint}$ can be obtained for a value of β from Eq. (7).

6.3 Ensuring Beam Hinging Prior to Any Other Failure

In order to ensure beam hinging moment at haunch, max. moment in beam (M_{bmax}) must reach yield moment capacity M_{pb} of beam. Thus, equivalent story shear corresponding to beam hinging is given as,

$$V_{capacit\ beam\ hinge} = \frac{M_{pb} \left(1 + \frac{d_c + 2X}{L_{Bc} - 2X}\right)}{H_c} \quad (8)$$

Value of 'X' needs to be so adjusted that Eq. (6) is justified.

6.4 Thickness of Haunch Plate

Approximate thickness of haunch diaphragm required for K_{ten} is obtained as follows (Fig.7)

$$t = K_{ten} \cdot \frac{L_{he}}{w_h E_s} \quad (9)$$

L_{he} and w_h are width and length of shaded portion of haunch plate in Fig. 7)

(E_s is Modulus of elasticity of haunch material)

Total thickness required t is divided in two diaphragm plates. These two diaphragm plates are separated by distance ' Z_h ' and are connected through lateral bolts in order to fabricate an integrated 3-dimensional haunch. Details of bolting are illustrated in Fig. 7.

7. Effect of Haunch Retrofit Solution on As Built Connection

Numerical analysis of as built and haunch retrofitted subassembly is done to ascertain efficacy of proposed solution. A similar type of performance assessment is done by Pampanin et al. [41]. A two-dimensional beam-column subassembly is modelled in Finite Element analysis (FEA) software Etabs. The sectional properties of beam and column are as depicted in Fig.9. The column is 3.2 m in height and beam is 2 m in span. Load is applied at the tip of the beam. Displacement controlled loading protocol along with plastic hinge assignment on the subassembly is shown in Fig. 4. Haunch was modelled as spring with stiffness 150000 kN/m as illustrated in Fig. 4. Performance evaluation of as built and retrofit subassembly is shown graphically in Fig.5. The pattern of graph resembles to that presented in Pampanin et al. [41]. Lateral load carrying capacity of retrofitted subassembly

increases by 30 % as compared to that of the as built specimen. The energy dissipation is calculated by estimating area under hysteresis loops. It is observed that haunch retrofit solution increases resilience of the subassembly by 27% and initial stiffness by 30 %. It is also noted that haunch retrofit solution ensures formation of plastic hinge with-in portion of beam beyond the outer-face of diagonal haunch. In addition, beam side sway mechanism is ensured in retrofit assembly as compared to joint shear side sway mechanism causing soft storey effect in case of as built subassembly.

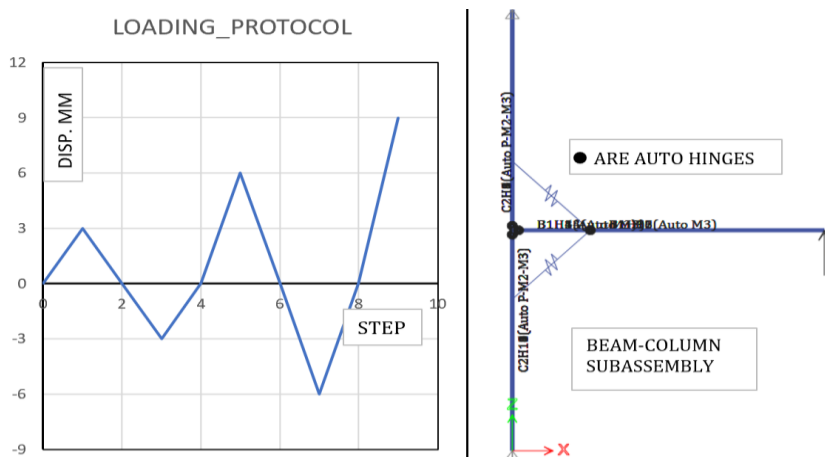


Fig. 4 Loading protocol and 2 -D subassembly model with plastic hinge assignment

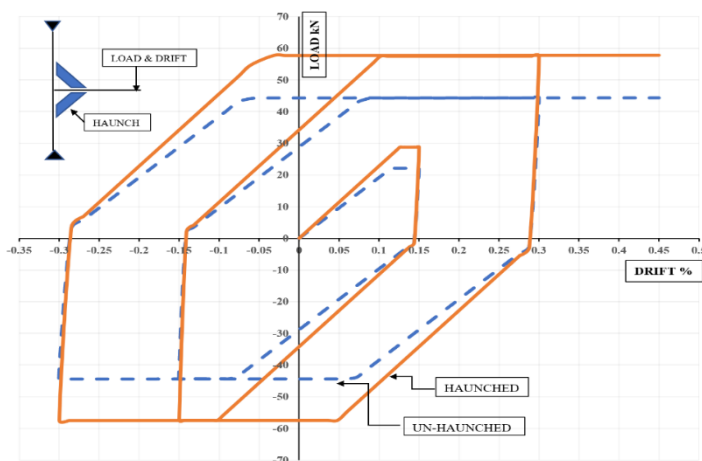


Fig. 5. Effect of retrofitting on performance of connection subassembly (Drift calculated as $(\text{displacement}/2000) \times 100\%$)

8. Optimum Value of Haunch Stiffness

In case of ill detailed connections, it is essential to ensure that inadequate anchorage of beam reinforcement does not cause flexure failure at joint due to slipping of reinforcement, before formation of plastic-hinge, at the location of haunch in the beam. It is generally observed that beam bars are anchored in connection between 60 to 70 % of required development length. Thus, maximum beam moment capacity at the column-face is

calculated to be $0.6 M_{pb}$. (M_{pb} is plastic moment capacity of beam for fully developed reinforcement, which can be obtained from moment curvature relation for given properties of beam). Eq. (1) can be rewritten for

$$M_{bmax} = M_{pb} \text{ as,}$$

$$M_{bc} = 0.6 \gamma_1 M_{pb} = M_{pb} \left[1 - \frac{\beta d_b}{(2 L \tan \alpha)} + \frac{(1 - \beta)X}{L} \right]$$

$$\text{for } \gamma_1 = 0.8 \text{ and } \alpha = 45 \quad \beta = \frac{L+2X}{d_b+2X} \tag{10}$$

Value of β from Eq. (10) is substituted in Eq. (4) to calculate optimum stiffness of haunch for given set of geometrical and material properties of the structure. It is observed that further increase in stiffness of haunch, beyond this value, does not have considerable effect on performance of the retrofitted assembly.

Fig. 6 illustrates a set of lateral loads against displacement curves obtained by numerical analysis for different values of haunch stiffness for same geometrical and material properties of a structural subassembly. It is observed that any increase in stiffness beyond 150000 kN/m, does not have substantial effect on performance of retrofitted subassembly for given set of structural parameters.

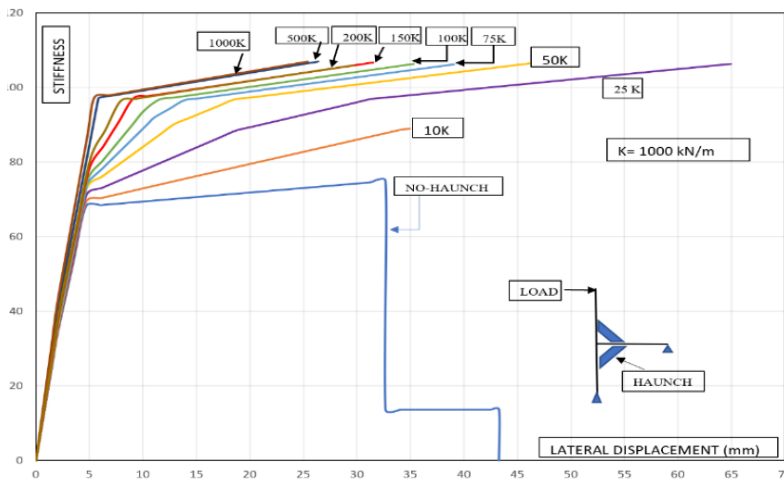


Fig. 6 Performance of joint subassembly for different haunch stiffnesses

9. Geometric Design of Haunch

Buildings with parking floor are most vulnerable during earthquakes owing to soft story effect. While designing the haunch it is essential to ensure adequate headroom below haunch element. Vertical projected length 'Y' (Fig.3) of haunch should be such that minimum headroom of 2.1 m is maintained below center of the haunch.

Higher values of α produce more efficient haunches [30]. However, ' α ' and headroom are inversely proportional depth of 600 mm. For such cases, practicable geometric dimensions of haunch are as shown in Fig. 7. Numerical investigations, done during this work, indicate that, $\alpha=45^\circ$ yields a reasonably efficient haunch. Another parameter affecting performance of haunch is its axial stiffness, (Kd). Kd can be determined experimentally or numerically.

If K_d is different in tension and compression, then average of the two is taken for calculation of β . For most of the buildings parking floor height is 3.15 m with average beam depth of 600 mm. For such cases, practicable geometric dimensions of haunch are as shown in Fig. 7.

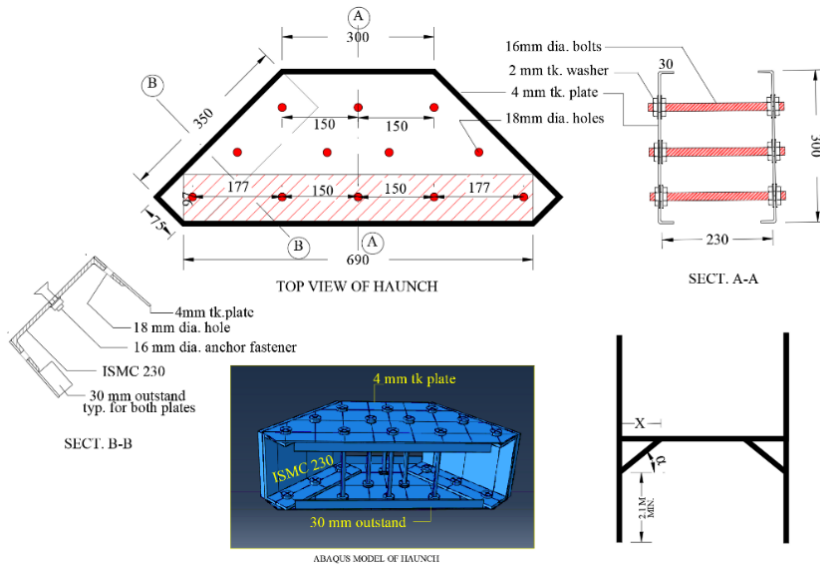


Fig. 7 Details of 4 BDH Haunch (4 BDH to indicate 4 mm thick haunch plates)

10. Comparison Between Single Plate and Equivalent BDH Solution

Comparative performance analysis of a 8 mm thick Single plate haunch (Genesio, 2012) as shown in Fig. 8 and a BDH made of two, 4mm thick diaphragm plates as shown in Fig. 7 is done in FEM analysis software ABAQUS. Axial, Lateral, and torsional stiffnesses of both haunch elements are evaluated. Results of this analysis are presented in Table 1. constitutive properties of haunch materials are illustrated in Table 3.

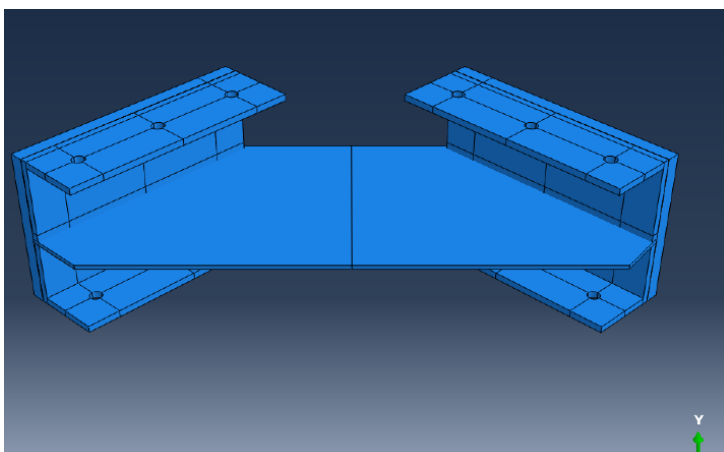


Fig. 8 Single Plate 8 mm tk. Welded Haunch

Table 1. Comparison between single plate and BDH Haunch

Parameter	Single plate 8 mm thick	BDH 4 mm tk. plates	% Rise
Comp. yield strength	313 kN	497 kN	59
Ulti. Comp. strength	446 kN	580 kN	30
Comp. stiffness initial	743000	662000	-12
Secant stiffness @ 3mm axial displacement	46505 kN/m	104500 kN/m	124
Tensile yield strength	389 kN	523 kN	34
Tensile ultimate strength	504 kN	636 kN	26
Torsional Stiffness	40kNm/rad	151kNm/rad	277
Torsional yield strength	3 kN m	12 kN m	300
Avg. energy dissipation @ 3 mm displacement	653050 N-mm	1267164 N-mm	94

11. Case Study (Parking+6 Storey Frame)

11.1 Details of As Built Structure

The efficacy of proposed retrofit strategy is assessed by push over analysis of a parking + 6 story 2-D frame, designed and detailed only for gravity loading as per IS 456-2002 (BIS, 2002). Geometrical and structural details of frame are illustrated in Fig. 9. Infill walls with less than 20% opening have been modelled as diagonal struts for habitable floors as shown in Fig. 9.

Various parameters and constitutive properties required for design of a haunch are presented in Table 2. It is assumed that beam longitudinal rebars are anchored in column core for 65% of required development length. Thus, effective area of a 16 mm diameter bar available as a fully developed bar is $201 \times 0.65 = 131 \text{ mm}^2$. So, support section of beam is provided with 131 mm^2 for each reinforcement bar.

All beam and column ends are modelled with default non-linear hinge parameters (ASCE 41-17) as available in FEM analysis software Etabs.

Table 2. Parameters and constitutive properties of as built structure for seismic assessment

Concrete module Elastic/Shear	22360 MPa /9316 MPa
Distance between top and bottom bars of beam (j_d)	390mm
c/c height of column (H_c)	3150 mm
Effective joint area ((A_j))	121900 mm^2
c/c beam span (L_B)	5000 mm
Clear beam span (L_c)	2235 mm
Diameter of main reinforcement	16 mm
Effective depth of beam(d_b)/column(d_c)	420/500 mm
Area of shear reinforcement leg (A_{sv})	100 mm^2
Limit state of principal stresses $P_t = 0.29 \sqrt{f_{ck}}$	1.296 MPa
Spacing of shear reinforcement for beam/column	120/150 mm
Yield strength of main reinforcement (f_y)	415 MPa
Yield strength of shear reinforcement (f_s)	415 MPa
Maximum moment capacity of beam (M_{bmax})	73 kN-m
Maximum moment capacity of column (M_{cmax})	169 kN-m

Displacement controlled Push Over analysis is carried out to access performance of the structure while being subjected to lateral loading.

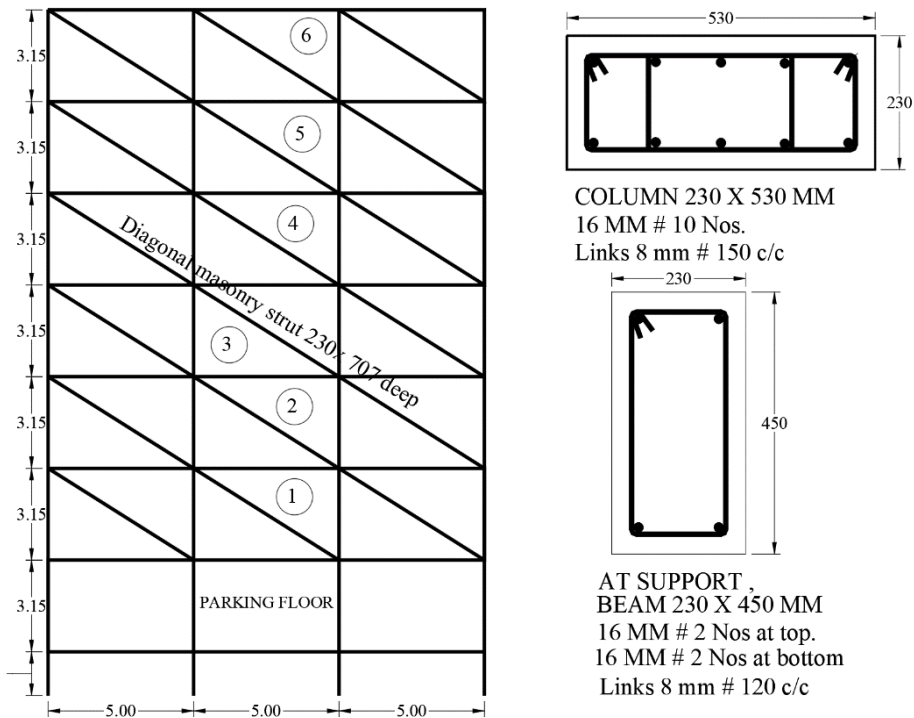


Fig. 9 Details of as built structure (Same sections are used for assessment of subassembly in Fig.4)

11.2 Modelling of Brick Masonry

Infill masonry walls are modelled as diagonal struts with hinged ends connected at beam-column connections as shown in Fig. 9. Pore [43] has done extensive study on constitutive properties of brick masonry across India. Strength of masonry (σ_p) for 1:6 mortar given by [43] is considered in this study.

$$\sigma_p = 0.175[\sigma_{cb}^{1.22} + \sigma_{mo}^{0.2}]$$

It is also observed (Pore, 2007) that compressive strength of brick (σ_{cb}) across India varies to a great extent. Except for Uttar Pradesh and West Bengal, strength of brick varies between 3 to 10 N/mm². For western Maharashtra region assuming, $\sigma_{cb} = 5 \text{ N/mm}^2$ and σ_{mo} (strength of mortar) = 6 N/mm² (Pore, 2007) for 1:6 mortar

(For 1:6 mortar) Strength of masonry is calculated as, $\sigma_p = 1.5 \frac{N}{\text{mm}^2}$.

IS 1893:2016 (BIS-IS-1893, 2016) gives value of elastic modulus of brick masonry as $E_m = 550 \sigma_p$ and width of strut as $w_{ds} = 0.175 \alpha_h L_{ds}$

Clause 7.9.2.2 of IS 1893:2016 (BIS-IS-1893, 2016) may be referred for further details of the terms mentioned above. Modulus of elasticity and width of strut for assumed data of prototype structure are calculated as 825 N/mm² and 707 mm respectively.

11.3 Performance of As Built Structure

Push over analysis of as built structure reveals formation of connection hinges (Fig.10) at parking storey slab level leading to soft storey mechanism. All upper habitable floors do not develop any type of non-linear hinge owing to diagonal masonry struts. Detailed results of push over analysis are discussed in later sections.

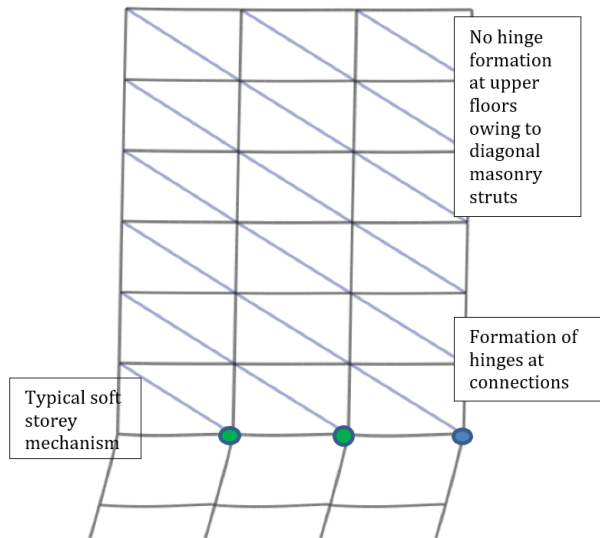


Fig. 10 Hinge formation at parking floor in as built frame

11.4 Retrofit Strategy

Based on performance of as built structure, it is decided to retrofit parking slab beam column connections by BDH elements. Eq. (9) and Table 2 yield $\beta = 3$ For required strength hierarchy. Substituting $\beta = 3$ in Eq. (4), optimum haunch stiffness is calculated as $K_{d\ av} = 380000$ kN/m. Referring to Eq. (10) and details of haunch shown in Fig. 7, thickness of haunch diaphragm works out to be 4 mm on each side. 16 mm(M16) diameter nominal lateral confining bolts are used to assemble the BDH unit.

11.5 Stiffness of Haunch Assembly

Analytical calculation of compressive and tensile stiffness is difficult due to non-standard geometry and overall configuration of the 3-D haunch. It is observed in literature [31] that it is a common practice to assume stiffness of haunch element only. Effect of joineries is usually accounted for by assuming a certain factor of safety. In this work numerical analysis software ABAQUS is used to determine the actual stiffnesses of haunch assembly. Numerical model of haunch during compression test is shown in Fig.11. All the elements are modelled as 3-D solids. Constitutive properties of haunch material are presented in Table 3. All components are meshed with C3D8R Brick elements with hour-glass control. Mesh Size of each element is adjusted, to properly maintain hierarchy between slave and master components. Diaphragm plate was discretized with 15 mm size mesh element and so on. Boundary conditions were imposed to avoid over-constraining as well as numerical singularities during analysis. Displacement controlled Ramp load with a limiting value of 6 mm was applied to cause axial deformation of BDH element. Static general analysis procedure was adopted. The Compressive and tensile load carrying capacities of haunch are presented in Fig. 11. Preliminary analysis of frame with nominal stiffness of 400000

kN/m indicates axial displacement of haunch element as 1.25 mm. Thus, modelled haunch should retain a stiffness of at-least 400000 kN/m at 1.25 mm displacement. Table 3 gives values of load carrying capacity of haunch assembly against displacement for tension and compression. It is observed that lowest stiffness of proposed haunch geometry is 480000 kN/m in compression (Table 4).

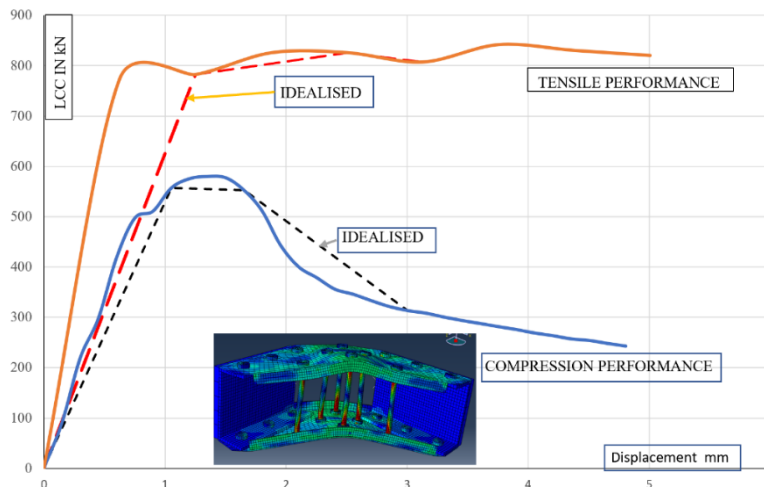


Fig. 11 Axial load carrying capacity of BDH element. (LCC on ‘Y’ axis indicates axial Load Carrying Capacity of the BDH element)

Table 3. Constitutive material properties for BDH specimen in Fig.7

Properties of diaphragm plate		Properties of M16 bolts	
E= 2e5 MPa	fu=450 MPa	E= 2e5 MPa	fu=827 MPa
fy=250 MPa	Poisson’s ratio=.3	fy=640 MPa	Poisson’s ratio=.3
stress	plastic strain	stress	plastic strain
250.8125	0	643.328	0
271.2852405	0.001504126	662.9481015	0.001241986
292.0436072	0.003777478	683.0245297	0.003082307
313.2355569	0.007138458	703.7899065	0.005800029
335.0687107	0.011998233	725.5847446	0.009788564
357.8281624	0.018874993	748.9024348	0.01559459
381.8979864	0.028405786	774.4510102	0.023965632
407.7869165	0.041353305	803.2372476	0.035904932
436.1587006	0.058604279	836.6802921	0.052729014
467.8676583	0.081155536	876.7640328	0.076118091
504	0.110083955	926.24	0.108142159

11.6 Modelling of Haunch in Etabs

A haunch assembly is made of two different types of link elements in Etabs (Fig.13)

- Rigid link for connecting basic haunch element to beam column centerlines
- Elasto-plastic haunch modelled as non-linear link element having constitutive properties derived from FEM analysis and illustrated in Table 4

Table 4. Stiffness variation of haunch against axial displacement

Displacement (-) is compression mm	Load in kN	Stiffness available kN/m
-3	-300	100000
-1.65	-570	345000
-1.2	-577	480000
0	0	0
1.2	780	650000
2.5	825	330000
3	750	250000

11.7 Analysis of Frame

Modal push over analysis for first mode of vibration and a response spectrum analysis as per IS 1893:2016, in global X direction, is done to access performance of as built and retrofitted frames.

12. Results and Discussion

(For numerical values of parameters in the formulae please refer Table. 2)

To understand need for retrofitting, it is essential to establish strength hierarchy of as built frame. It is done by comparing inter-storey column shear requirements for formation of plastic hinges in column and beam.

Column storey shear required to form a plastic hinge in beam (V_{CHB}) is given as,

$$V_{CHB} = 2 \frac{M_{BMax}}{L_{BC}} = \frac{73}{2.235} = 32.66 \text{ kN}$$

Column storey shear required to form a plastic hinge in column (V_{CHC}) is given as,

$$V_{CHC} = \frac{L_B V_{CHB}}{2H_C} = \frac{5 * 32.66}{2 * 3.15} = 25.92 \text{ kN}$$

$$actored = (0.7 * 25.92) = 18.14 \text{ kN}$$

Column storey shear required to form plastic shear hinge in joint (V_{CHJ}) is given as

$$V_{CHJ} = \left(\frac{M_{BMax}}{jd} \right) - V_{CHC} = 132.36 \text{ kN}$$

$$factored(0.7 * 0.7) = 64.68 \text{ kN}$$

Thus, $V_{CHC} < V_{CHB} < V_{CHJ}$. Joint shear capacity is more than other shear capacities however this hierarchy indicates column hinge formation at a connection, before beam hinge formation and hence is not acceptable. More-over, numerical analysis reveals formation of flexural hinges at connections (Fig. 10). So, connections at parking slab level need to be strengthened by BDH element.

12.2 Analytical Assessment of Retrofitted Frame

It is decided to adopt a BDH element with $\beta=3$ as already discussed. Inter-storey shear capacities are calculated as follows

Shear capacity for column hinging

$$V_{CR\text{COLUMNHINGE}} = \frac{M_{CMax}}{\frac{H_c}{2} - \frac{d_b}{2} - X \tan\alpha} = 192.82 \text{ kN}$$

Factored capacity = 0.7*192.82 = 134.97 kN

Shear capacity for beam hinging

$$V_{CR\text{BRAMHINGE}} = \frac{M_{BMax}}{H_c} * \left(1 + \frac{d_c + 2X}{L_{BC} - 2X}\right) = 105 \text{ kN}$$

Shear capacity of Joint hinging is given as,

$$V_{CR\text{JOINT HINGE}} = \frac{A_c \sqrt{\left(\frac{f_{pc}^2}{A_c}\right) - \frac{f_{pc}P}{A_c}}}{1 - \frac{\beta H_c}{(L_{BC} + d_c) \tan\alpha} - \frac{H_c(L_{BC} - 2X)}{j(L_{BC} + d_c)} \left(1 - \frac{\beta d_b}{2L \tan\alpha} + \frac{(1 - \beta)X}{L}\right)}$$

= -91 kN factored (0.7*-91) = -63.7 kN.

Negative sign indicates shear force will be required from opposite direction to cause tensile failure of joint. $\beta > 1$ will always yield negative shear capacity at joint (Fig.3). Having negative capacity is even better for protection of connection [30].

Thus,

$$V_{\text{beam-hinge-capacity}} \text{ (as (-)ve)} < \text{factored } V_{\text{column-hinge-capacity}} < \text{factored } V_{\text{joint-capacity}}$$

indicating proper strength hierarchy being maintained after retrofitting of the prototype structure.

12.3 Comparative Push Over Analysis

Comparative results of displacement-based push over analysis for first mode are plotted in Fig. 12.

Table 5. illustrates comparison of un-haunched and haunched frames based on key performance parameters. Location of first 'Immediate Occupancy'(IO) hinge formation is plotted on load-displacement graph. It is observed that, there is a substantial increase in the performance parameters of retrofitted frame over those of as built frame.

Table 5. Comparison of push over performance of as built and retrofitted frames

Parameter	Un-Haunched Frame	Haunched Frame	% Change
Ultimate lateral force capacity	417 kN	594 kN	+ 42
Lateral load at yield point	247 kN	464 kN	+ 87
Energy dissipation till formation of first LS hinge	38.55 kN-m	52.34 kN-m	+36

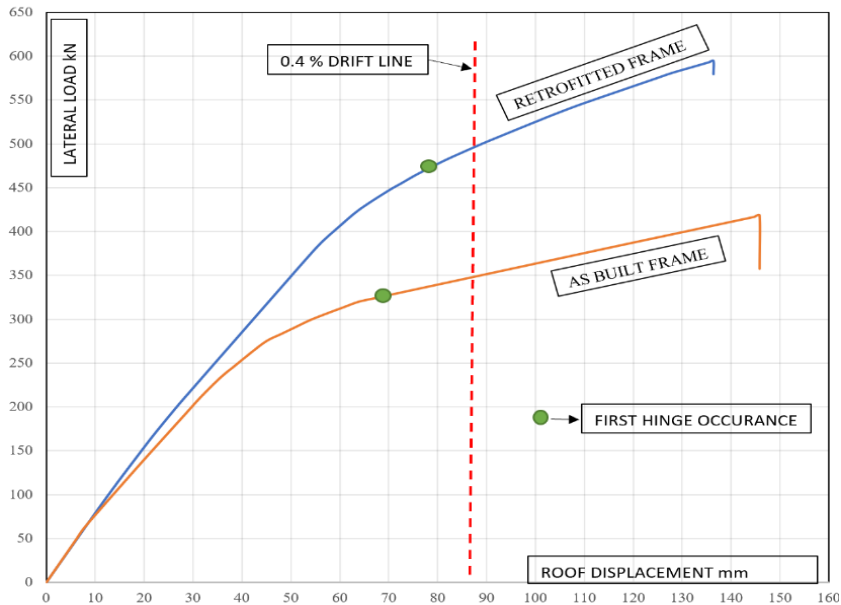


Fig. 12 Comparative push over analysis

Fig.13 shows hinge formation in retrofitted frame. It is observed that all hinges form only at haunch location and none of the hinges are formed in the connection region.

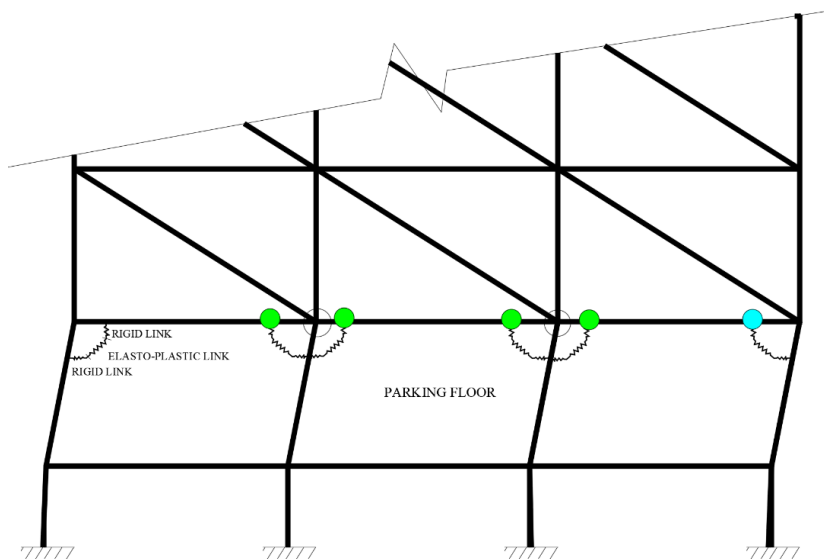


Fig. 13 Hinge formation at parking level in retrofitted structure (Green indicate IO hinges and cyan indicate LS hinges)

12.4 Comparative Seismic Analysis

Haunched and un-haunched frames are subjected to response spectrum loads as per IS1893:2016 [44]. Both linear and non-linear response spectrum analysis was carried out.

Table 6. illustrates comparative performance of as built and retrofitted structures while subjected to same seismic loads. It is observed that performance of retrofitted frame is better than as built frame with reference to maximum roof displacement and maximum storey drift by 14.6 and 42 % respectively. In case of non-linear response spectrum analysis, it is observed that as built frame yields much before retrofitted frame and maximum roof displacement and drifts for as built frame are more by 106 % and 154 % respectively. It is also observed that for as built structure the hinges form at connections whereas in case of retrofitted structure, hinges were formed only at the haunch-beam interface. Graphical performance of as built and retrofitted frames for non-linear response spectrum analysis is shown in Fig. 14.

Table 6. Comparative results of response spectrum analysis

Response spectrum analysis (Linear performance)			
Parameter	As built frame	Retrofitted frame	% Change
Max. roof displacement	51 mm	45 mm	- 14.6
Max. storey drift	4.7e-3	3.3 e -3	- 42

Response spectrum analysis (Nonlinear performance)			
Max. roof displacement	126 mm	61 mm	-106
Max. storey drift	2.7 e -3	1.06 e -3	- 154

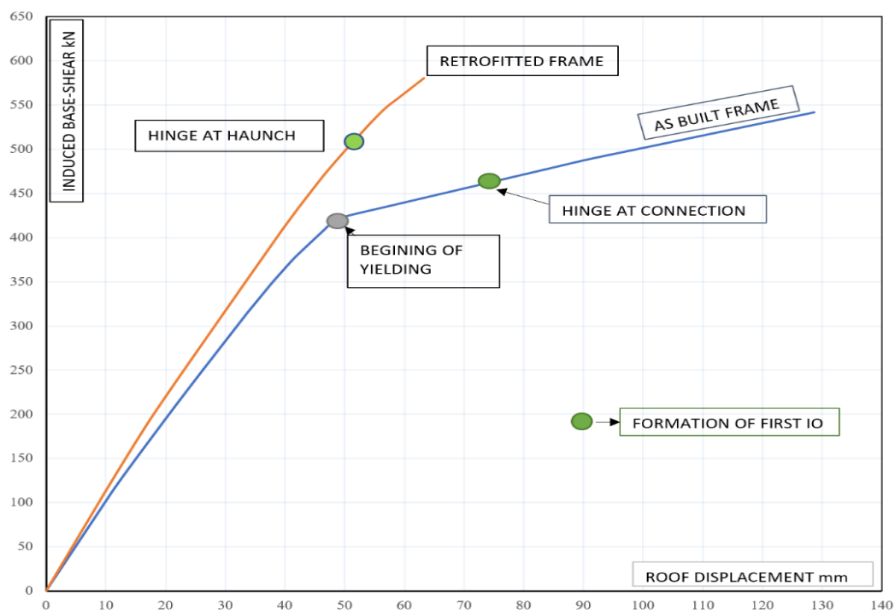


Fig. 14. Non-linear performance for as built and retrofitted structure

13. Experimental Validation of Retrofit Solution

A haunch retrofit solution was designed based on the methodology proposed in in this paper. Experiments on 1/3 scaled down specimen were carried out [39]. Details of haunch designed for the experimental program are shown in Fig.14. Abstract of experimental finding is depicted in Fig. 15. For details of experimental verification procedures [39], may be referred.

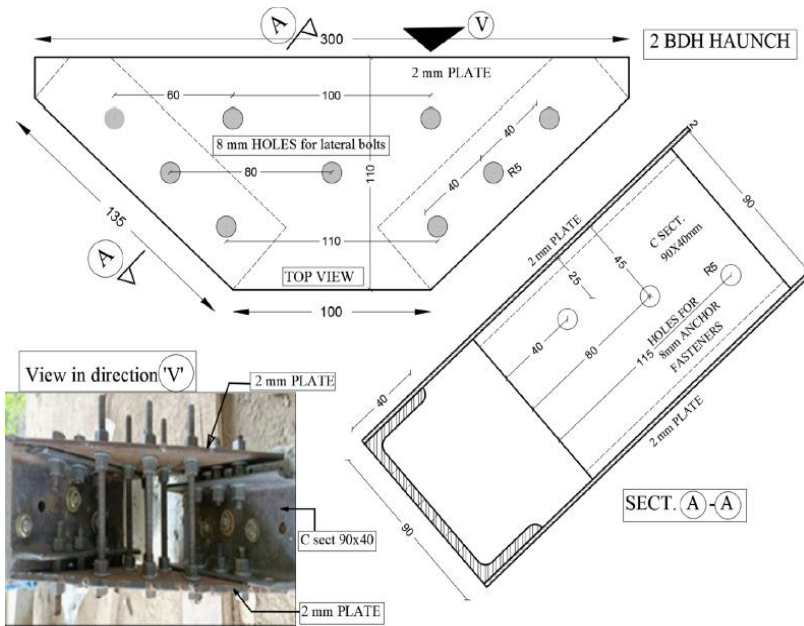


Fig. 14 Details of haunch used for experimental verification [39]

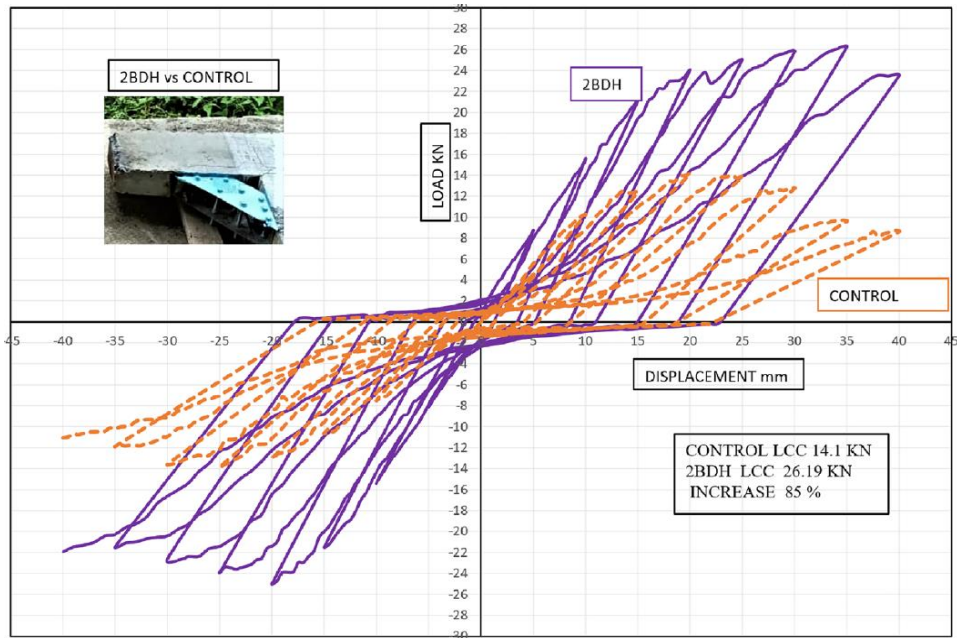


Fig. 15 Performance enhancement due to retrofit haunch [39]

Table 7 presents abstract of performance enhancement due to use of proposed BDH retrofit solution. [39]

Table 7. Performance evaluation of retrofit solution (Experimental)

Parameter →	Initial stiffness kN/mm	Resilience kN-mm	ductility	Load carrying capacity kN
Control (As built specimen)	0.962	20.39	1.13	14.10
2-BDH Retrofitted specimen	1.67	49.5	2.67	26.19
% Rise	85	94	136	85

14. Conclusions

Ill-detailed frames undergo critical brittle failure in joint region due to lack of capacity design considerations.

Modelling brick masonry as equivalent diagonal struts leads to formation of soft storey mechanism at parking floor. Hinges at connections are developed at parking storey slab level inducing a pan cake failure. Introduction of haunch re-routes critical stress path in subassembly excluding joint panel location.

Numerical analysis confirms that introduction BDH element near beam column connection substantially improves overall performance of beam-column connection subassembly. BDH retrofit unit has 277 % more torsional stiffness, 94 % more resilience and 59 % more yield strength, as compared to an equivalent single plate haunch. Higher yield strength ensures that BDH remains in elastic zone for higher loads, imparting higher resilience to beam-column connection subassembly.

A BDH element for given set of structural data can be designed and detailed adopting step by step flow-chart illustrated in this paper.

Elasto-plastic, bolted nature of BDH element enhances overall resilience of the structure.

A study of performance enhancement of retrofitted subassembly for different haunch stiffnesses reveals that, there is an optimum level of haunch stiffness for given set of structural properties, beyond which any increase in haunch stiffness has very marginal effect on performance of retrofitted beam column subassembly.

A BDH element not only shifts formation of plastic hinges in beam, away from connection region but also improves load carrying capacity, resilience, and rotational stiffness of connection subassembly.

The push over and seismic performance analysis of a parking+6 storey frame, designed for gravity loads, with and without retrofitting underlines advantages of retrofit strategy. It is observed that lateral load capacity at yield point of retrofitted frame increases by 87%, Ultimate lateral load capacity by 42% and resilience by 36 %. Comparative non-linear response spectrum analysis of retrofitted frame reveals that maximum roof displacement is reduced by 106 % and maximum storey drift by 154 %. Experimental investigations on 1/3 scaled down specimens indicate increase of 85 % in load carrying capacity, 136 % increase in ductility and 94 % rise in resilience.

It is concluded that this performance enhancement is due to (i) protection of exterior beam column joints (ii) rerouting of critical stress path excluding connection region (iii) reduction of inter-storey drift and maximum roof displacement for given seismic excitation.

Scope for Further Study

BDH elements connected to parent structure through anchor fasteners tend to exhibit slip in anchors subjected to reversed cyclic loading. A better anchoring technique needs to be investigated.

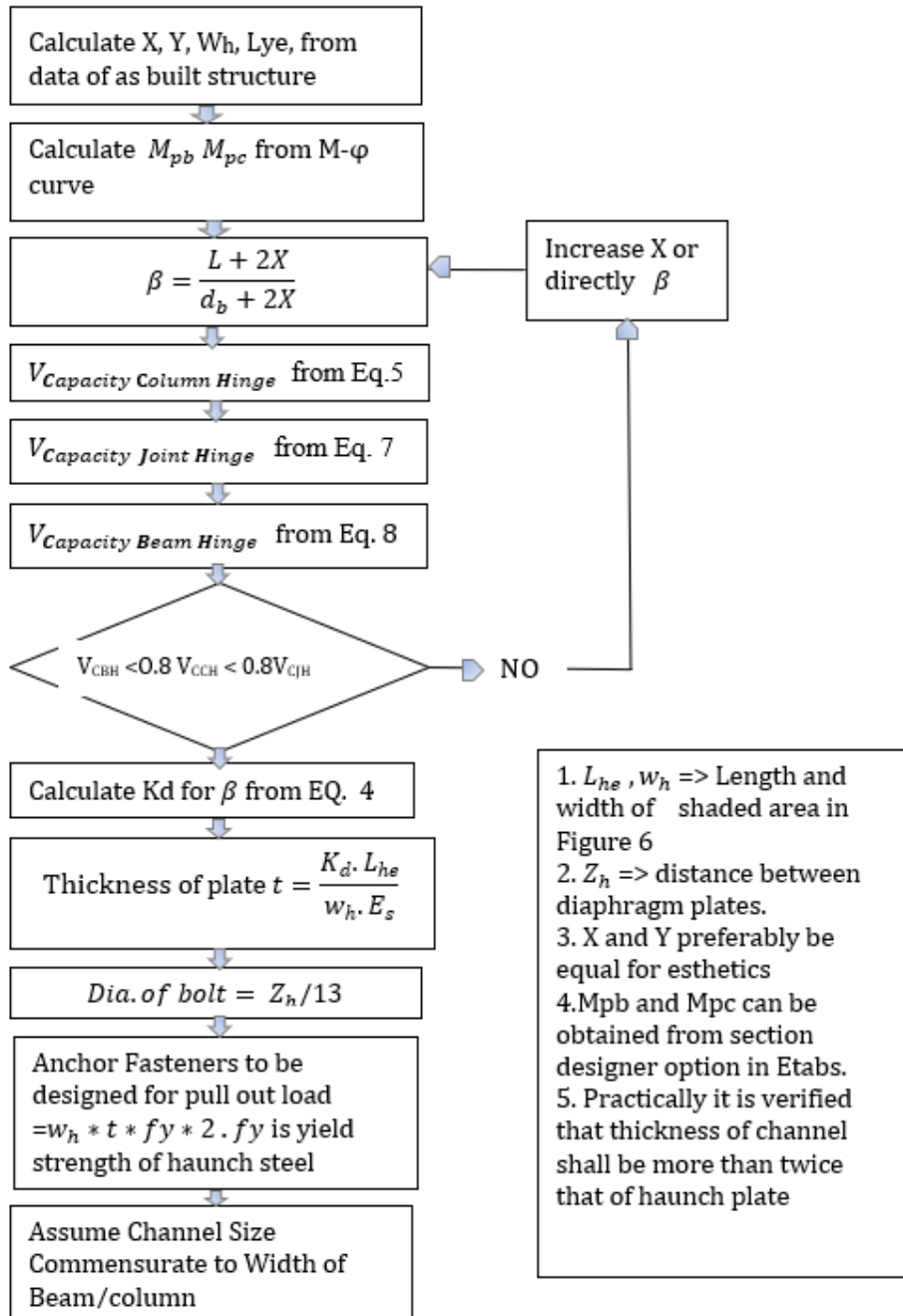


Fig.16 Flow Chart for Design of BDH Element

References

- [1] Calvi G, Magenes, Pampanin, S. Experimental test on three storey R.C. Frame designed for gravity only. 12th European conference on earthquake engineering, London, Paper. No. 727, 2002.
- [2] Hakuto S, Park R, Tanaka H. Seismic Load Tests on Interior and Exterior Beam Column Joints with Substandard Reinforcing Details. ACI Structural Journal. 2000;97:11-25. <https://doi.org/10.14359/829>
- [3] Pampanin S, Calvi G, Moratti M. Seismic response of reinforced concrete buildings designed for gravity loads part 1: experimental test on beam-column subassemblies, ASCE journal of structural engineering, 2003.
- [4] Pantelides CP, Clyde C, Reaveley LD. Performance-Based Evaluation of Reinforced Concrete Building Exterior Joints for Seismic Excitation. Earthquake Spectra. 2002 Aug;18(3): 449-80. <https://doi.org/10.1193/1.1510447>
- [5] Pampanin, S, Calvi, GM, Moratti, M. Seismic Behavior of R.C. Beam-Column Joints Designed for Gravity Only. 12th European Conference on Earthquake Engineering, London, paper no. 726, Sept 2002
- [6] Ghobarah A, El-Amoury T. Seismic rehabilitation of deficient exterior concrete frame joints. Journal of Composites for Construction. 2005; 9 (5):408-416. [https://doi.org/10.1061/\(ASCE\)1090-0268\(2005\)9:5\(408\)](https://doi.org/10.1061/(ASCE)1090-0268(2005)9:5(408))
- [7] Genesio G. Seismic Assessment of RC Exterior Beam Column Joints and Retrofit with Haunches Using Post-Installed Anchors, PhD Thesis, Institut für Werkstoffe im Bauwesen der Universität Stuttgart, Stuttgart, Germany, 2012.
- [8] Jayasooriya EMSD, Indika DWU, Wijesundara KK, Rajeev P. Equivalent viscous damping for steel eccentrically braced frame structures with buckling restraint braces. Innov Infrastruct Solut. 2021 Dec;6(4). <https://doi.org/10.1007/s41062-021-00503-2>
- [9] Bhat JA. An innovative technique of anchoring lacing bars with CFS sections for shear strengthening of RC beams. Innov Infrastruct Solut. 2022 Feb;7(1). <https://doi.org/10.1007/s41062-021-00722-7>
- [10] Saranya P, Nagarajan P, Shashikala AP. Seismic performance of geopolymer concrete beam-column joints under reverse cyclic loading. Innov Infrastruct Solut. 2021 Jun;6(2). <https://doi.org/10.1007/s41062-021-00474-4>
- [11] Badoux M, Jirsa J. Steel bracing of RC frames for seismic retrofitting. Journal of Structural Engineering (United States). 1990;1(16):55-74. [https://doi.org/10.1061/\(ASCE\)0733-9445\(1990\)116:1\(55\)](https://doi.org/10.1061/(ASCE)0733-9445(1990)116:1(55))
- [12] Bush T, Jones E, Jirsa J. Behavior of rc frame strengthened using structural steel bracing. Journal of Structural Engineering. 1991;117(4):1115-26. [https://doi.org/10.1061/\(ASCE\)0733-9445\(1991\)117:4\(1115\)](https://doi.org/10.1061/(ASCE)0733-9445(1991)117:4(1115))
- [13] Rahimi A, Maheri M. The effects of steel X-brace retrofitting of RC frames on the seismic performance of frames and their elements. Engineering Structures. 2020 Mar;206:110-149, doi.org/10.1016/j.engstruct.2019.110149 <https://doi.org/10.1016/j.engstruct.2019.110149>
- [14] Qian K, Weng Y, Li B. Improving Behavior of Reinforced Concrete Frames to Resist Progressive Collapse through Steel Bracings. J Struct Eng. 2019 Feb;145(2) [https://doi.org/10.1061/\(ASCE\)ST.1943-541X.0002263](https://doi.org/10.1061/(ASCE)ST.1943-541X.0002263)
- [15] Hu B, Lv H, Kundu T. Experimental study on seismic behavior of reinforced concrete frame in primary and middle schools with different strengthening methods. Construction and Building Materials. 2019 Aug; 217: 473-86. <https://doi.org/10.1016/j.conbuildmat.2019.05.040>
- [16] Kheyroddin A, Sepahrad R, Saljoughian M, Kafi MA. Experimental evaluation of RC frames retrofitted by steel jacket, X-brace and X-brace having ductile ring as a

- structural fuse. J Build Rehabil. 2019 Dec;4(1):1-13. <https://doi.org/10.1007/s41024-019-0050-z>
- [17] Rahimi A, Maheri MR. The effects of retrofitting RC frames by X-bracing on the seismic performance of columns. Engineering Structures. 2018 Oct; 173:813-30. <https://doi.org/10.1016/j.engstruct.2018.07.003>
- [18] Jafari V, Akbarpour A. Effect of near-field earthquake excitation on seismic behavior of knee-braced moment frames. Asian J Civ Eng. 2018 May 19; <https://doi.org/10.1007/s42107-018-0052-1>
- [19] Khan MS, Basit A, Khan U. Seismic upgrade of deficient RC frames using different configurations of eccentric steel braces. Asian J Civ Eng. 2021 Apr;22(3):461-75. <https://doi.org/10.1007/s42107-020-00325-0>
- [20] Rahai A, Lashgari M. Seismic strengthening of nine storey RC building using concentric and buckling resistant bracing, Proceedings of 31st conference on concrete structures, 421-426, 2006.
- [21] Ramin K, Maheri MR. The Seismic Investigation of Off-Diagonal Steel Braced RC Frames. Slovak Journal of Civil Engineering. 2018 Sep 1;26(3):49-64. <https://doi.org/10.2478/sjce-2018-0020>
- [22] Naghavi M, Rahnavard R, Thomas R, Malekinejad M. Numerical evaluation of the hysteretic behavior of concentrically braced frames and buckling restrained brace frame systems. Journal of Building Engineering. 2019 Mar;22:415-28. <https://doi.org/10.1016/j.jobe.2018.12.023>
- [23] Ozcelik R, Erdil E. Pseudo dynamic Test of a Deficient RC Frame Strengthened with Buckling Restrained Braces. Earthquake Spectra. 2019 Aug;35(3):1163-87. <https://doi.org/10.1193/122317EQS263M>
- [24] Sutcu F, Bal A, Fujishita K, Matsui R, Celik OC, Takeuchi T. Experimental and analytical studies of sub-standard RC frames retrofitted with buckling-restrained braces and steel frames. Bull Earthquake Eng. 2020 Mar;18(5):2389-410. <https://doi.org/10.1007/s10518-020-00785-4>
- [25] Godínez-Domínguez EA, Tena-Colunga A. Behavior of ductile steel X-braced RC frames in seismic zones. Earthq Eng Vib. 2019 Oct;18(4):845-69 <https://doi.org/10.1007/s11803-019-0539-0>
- [26] Fateh A, Hejazi F. Experimental Testing of Variable Stiffness Bracing System for Reinforced Concrete Structure under Dynamic Load. Journal of Earthquake Engineering. 2020 Feb 24;26(3):1416-37. <https://doi.org/10.1080/13632469.2020.1724216>
- [27] Du K, Cheng F, Bai J, Jin S. Seismic performance quantification of buckling-restrained braced RC frame structures under near-fault ground motions. Engineering Structures. 2020 May; 211:110447. <https://doi.org/10.1016/j.engstruct.2020.110447>
- [28] Kaviani A, Dabiri H, Kheyroddin A. Effect of beam and column dimensions on the behavior of RC beam-column joints. Asian Journal of Civil Engineering. 2021 Mar 15;22(5):941-58. <https://doi.org/10.1007/s42107-021-00356-1>
- [29] Uang CM, Lee CH. Analytical Modelling of Dual Panel Zone in Haunch Repaired Steel MRFs. Journal of Structural Engineering. 1997;123(1): 20-29. [https://doi.org/10.1061/\(ASCE\)0733-9445\(1997\)123:1\(20\)](https://doi.org/10.1061/(ASCE)0733-9445(1997)123:1(20))
- [30] Chen H. Retrofit strategy of non-seismically designed frame systems based on a metallic haunch system. thesis, university of canterbury, New Zealand, 2006.
- [31] Pampanin S, Christopoulos C, Chen T. Development, and validation of a metallic haunch seismic retrofit solution for existing under-designed RC frame buildings. Earthquake Engineering & Structural Dynamics. 2006;35(14):1739-1766. <https://doi.org/10.1002/eqe.600>, 2006. <https://doi.org/10.1002/eqe.600>
- [32] BIS-IS-13920. Ductile Design and Detailing of Reinforced Concrete Structures Subjected to Seismic Forces, Bureau of Indian Standard, New Delhi, India, 2016.

- [33] Chen HT . Retrofit strategy of non-seismically designed frame systems based on a metallic haunch system, M.E. Thesis, University of Canterbury, New Zealand, 2006.
- [34] Pampanin S, Magenes G, and Carr A. Modelling of shear hinge mechanism in poorly detailed RC beam-column joints, Fib Symposium on Concrete Structures in Seismic Regions, Athens, Greece, Paper 171, 6-8 May 2003
- [35] Aycardi L, Mander J, Reinhorn A. Seismic resistance of Reinforced concrete frame structures designed only for gravity loads: experimental performance of subassemblies. ACI Journal. 1994; 91(5): 552-563. <https://doi.org/10.14359/4170>
- [36] Nadir W, Ali AY. The key factors affecting the behavior of reinforced concrete beam-column joints under cyclic load. Asian Journal of Civil Engineering. 2022 Jun 15;23(6):907-27. <https://doi.org/10.1007/s42107-022-00464-6>
- [37] Park R. A Summary of Results of simulated seismic load tests on reinforced concrete beam-column joints, Beams, and columns with substandard reinforcing details. Journal Of Earthquake Engineering. 2002 Apr;6(2):147-74. <https://doi.org/10.1080/13632460209350413>
- [38] Seismic design characterization of RC special moment resisting frames in Pakistan-field survey to laboratory experiments.
- [39] Gujar AV, Pore SM. Strengthening of partially ductile RC beam-column connections. Asian Journal of Civil Engineering. 2022 Sep 6;24(1):93-108. <https://doi.org/10.1007/s42107-022-00490-4>
- [40] Priestley M. Displacement based seismic assessment of reinforced concrete buildings. Journal of earthquake engineering. 1997;1(1):157-192. <https://doi.org/10.1080/13632469708962365>
- [41] Pampanin S , Constantin C. Non-invasive retrofit of existing RC frames designed for gravity loads only, conference contributions, University of Canterbury, Civil Engineering, canterbury, New Zealand, 2342, 2003.
- [42] BIS. code of Indian standards, IS 456:2002, 2002.
- [43] Pore S. Performance based seismic design of low to medium rise framed buildings for India, PhD Thesis, IIT Roorkee, India, 2007.
- [44] BIS-IS-1893. Criteria for earthquake resistant design of structures- Code of Practice, Bureau of Indian Standard, New Delhi, India, 2016.



Research Article

Investigation of the effect of boron inhibitor on reinforced concrete by using the accelerated corrosion technique

Arda Uzunömeroğlu^a

Department of Civil Engineering, Eskişehir Osmanğazi University Eskişehir, Turkey

Article Info

Abstract

Article history:

Received 24 Mar 2023

Accepted 19 Jun 2023

Keywords:

Concrete;

Accelerated corrosion;

Corrosion inhibitors;

Chemical additives;

Boron inhibitor

Reinforcement corrosion induced by chloride is one of the most common reasons accounting for the premature deterioration of reinforced concrete (RC) structures. In this study, the effects of the use of chemical additives and corrosion inhibitors on the durability properties of the concrete and the potential of reinforcement corrosion were experimentally investigated. In this context, the effects of commercially common inhibitors and green inhibitors due to preventing corrosion and the interactions of these additives with each other were revealed. The reinforced concrete samples were prepared with four different chemical additives and two different corrosion inhibitors. Utilized chemical additives are; set accelerator, set retarder, super-plasticizer, and hyper-plasticizer; also, two different corrosion inhibitors were commercially common calcium nitrite-based corrosion inhibitor, and boron inhibitor which is obtained from natural boron. According to the laboratory experiments, concrete properties were enhanced with the synergistic collaboration of chemical additives and corrosion inhibitors. These effects are more acceptable than if chemical additives are applied individually in the concrete mix. Among all series, the concrete sample containing boron and hyper-plasticizer provided significant corrosion protection by reducing the initial corrosion current by 146,2 %. Moreover, as a result of the accelerated corrosion tests, latest damage occurrence time was calculated at 264 hours for the samples containing boron inhibitors, which is 106 hours for the control sample.

© 2023 MIM Research Group. All rights reserved.

1. Introduction

Corrosion is the chemical and electrochemical decomposition of metals and alloys as a result of various effects of the environment or damage as a result of physical dissolution. Due to the direct and indirect economic losses caused by corrosion, studies for corrosion protection are increasing day by day [1-3]. Metals tend to return to their natural state; therefore, it is impossible to completely eliminate corrosion but this process can be slowed down by taking the necessary precautions [4-9]. In order for reinforced concrete structures to continue their functions during their design life, some corrosion precautions should be taken. Research reveals that a reinforcement exposed to corrosion loses 50 percent of its bearing capacity at the end of 5 years, 90 percent at the end of 15 years, and completely at the end of 24 years [10]. Therefore, even without any external factors, a structure might collapse only with the effect of reinforcement corrosion. Today, corrosion of reinforcement is the primary reason of the destructive effect of earthquakes. A structure that is properly designed and protected from external influences (according to post-earthquake research) can stand statically for many years. The examples given below show that the insidious progress caused by corrosion, in fact, a structure that seems to be strong from the outside may have deteriorated and lost its mechanical strength in the depths.

Corresponding author: ardauzunomeroglu@gmail.com

^aorcid.org/0000-0003-4204-0564

DOI: <http://dx.doi.org/10.17515/resm2023.715st0324>

Res. Eng. Struct. Mat. Vol. 9 Iss. 4 (2023) 1403-1416

On-site images of the earthquake that occurred in Turkey on February 6, 2023 are given on Fig. 1. The damage caused by the corrosion effect on the reinforced concrete structures can be observed. Internal cracks formed as a result of volume expansion caused significantly high corrosion damage. When the site was examined, it was understood that many old buildings were under the influence of corrosion for many years, but this was not noticed by the residents. Since the formation of corrosion cannot be observed clearly from the surface of concrete, no previous corrosion progression applications have been made in the structures that were destroyed in the earthquake.



Fig. 1 On-site images of corrosion formation in earthquake site, Turkey

As a result of the research made on microstructures of concrete, especially in Hatay, some salt elements and sea shells were determined in the concrete mix. This is a shred of obvious evidence that sand was supplied from the sea. The biggest danger of sea sand is that it disrupts the structure of the concrete due to its high salt content. Therefore, concrete cannot preserve the design strength for the intended duration. It has been observed that sea sand causes corrosion of the rebar in the buildings, that is, its diameter decreases, and also causes it to rust and rot. As a result of on-site measurements, it was noticed that while the diameter of the reinforcement was 16 mm in the non-corroded parts of the structure, it decreased to 10 mm in the corroded areas.

There is a necessity for designers to produce high-quality and durable concrete in order to prevent the rapid deterioration of concrete in adverse environmental conditions. However, chlorine ions degrade the natural passive layer on the surface of the steel reinforcement and often cause corrosion of the reinforcement in concrete structures [11]. Various preventive methods such as producing impermeable concrete by increasing the consistency of concrete by using superplasticizers, covering the steel by using organic, inorganic, and metallic coatings, coating concrete with epoxy and resin-based waterproof chemicals, cathodic protection methods, and using corrosion inhibitors (addition to the concrete mix or application to surface) are applied to prevent the corrosion mechanism. In addition, during the production stage of concrete, the resistance of the reinforcement against corrosion could be also increased by using mineral additives that reduce the permeability of the concrete. One of the most commonly used methods to prevent or control corrosion by reducing the corrosion rate is the use of inhibitors [12]. In order for inhibitors to be effective in the concrete they are used in; it is important to choose the most suitable inhibitor and also the inhibitor amount for the building design.

In recent years, many commercial inhibitors, especially calcium nitrite, have been tried in concrete mixtures to protect the reinforcement from corrosion. The majority of researchers are of one mind that corrosion inhibitors used currently in the construction industry are known synthetic chemicals that are toxic to the earth [13,14,15]. For this reason, it has become a need for harmless inhibitors that might be considerably protectable to nature. These demands are significantly increased in recent years so researchers are focusing their studies in this field.

Eyu et al. [16] discussed the anticorrosive performance of *Vernonia amygdalina* extracts for carbon steel in concrete in 3.5M NaCl solution. Corrosion study was performed by using weight loss tests, corrosion potential calculations, half-cell calculations, concrete resistivity measurements as well as visual analysis. The outcomes acquired were also correlated with commercially available inhibitor like sodium nitrite or calcium nitrites. Phytochemical constituents of *Vernonia amygdalina* extract were described to contain alkaloids, saponins and tannins. Corrosion tests were illustrated by the plots against weight loss, inhibitor efficiency as well as corrosion rate. Outcomes achieved evidently discussed that *Vernonia amygdalina* extract showed analogous corrosion resistance when compared to commercially available inhibitors which are sodium and calcium nitrate.

Abdulrahman et al. [17] has broadly discussed and illustrated the anticorrosive behaviour of *Bambusa arundinacea* (BA) extract for reinforced steel corrosion in concrete. It was investigated to enhance the strength of concrete contaminate by chloride or sulphate environment. The obtained data was correlated with calcium nitrite and ethanolamine inhibitors. Effect of inclusion of $MgCl_2$ and $MgSO_4$ over concrete strength had been estimated and elucidated. Fundamental advantages of present analyses illustrate that inclusion of inhibitor shows negligible adverse effect on concrete durability. *Bambusa arundinacea* did not comprise and heavy metal that also eliminates the risk of production of dioxin on interacting with chloride contaminated water.

The above-mentioned studies were carried out to promote the use of natural (green) inhibitors rather than commercial inhibitors with known toxic effects such as calcium nitrite and sodium nitrite. In recent years, studies on boron have been increasing rapidly which can be utilized to obtain sustainable and ecological concrete additives. Boron inhibitor, which is obtained from boron and accepted as a green inhibitor, does not harm to nature and human thanks to the borane complex it contains [18]. The novelty of this study is the investigation of the effects of boron inhibitor on concrete with advanced corrosion techniques. One of the main reasons for choosing a boron inhibitor is that it is derived from natural boron. Toxic compounds that are harmful to nature and living things, which are found in many concrete additives, are not contained by this inhibitor [19]. The acceleration of studies with boron in recent years, the number of components synthesized from boron is increasing [20]. This inhibitor is just one of many compounds synthesized from boron. Considering all these reasons, the effect of boron inhibitor on concrete should be examined.

Boron inhibitor is a colourless liquid containing triethylamine borane complex. This inhibitor is a kind of boronium cation compound. Due to their low reactivity and high stability, their usage areas are increasing [21]. After the synthesis process, it was diluted in water and turned into a concrete additive. In this study, the effectiveness of natural boron inhibitors against reinforcement corrosion was investigated by the application of the accelerated corrosion method. The chosen method while determining the efficiency of the boron inhibitor was making a comparison of green inhibitors with the commercial calcium nitrite inhibitors, which are widely used in the construction industry and have known harmful effects. Nowadays, concrete additives are used in almost every type of concrete. Thus, reactions of these chemicals with new-generation corrosion inhibitors are not clearly known and corrosion mechanism had to be investigated. The aim of this study, is to examine the interactions between different chemical admixtures and to develop a concrete mixture with high corrosion and durability properties.

2. Materials and Measurements

In this section, detailed information is given about the materials used in the production of standard concrete and the mechanical and durability measurements. The materials in the concrete mix are ensured to the standards and also the measuring devices have been calibrated.

2.1. Materials

The dosage of cement in the concrete mix was 350 kg/m^3 and the water-cement ratio was 0,5. The interaction of boron inhibitor and calcium nitrite inhibitor with chemical additives was investigated by determining two different mixture series. Four different chemical additives were mixed with each inhibitor and laboratory experiments were applied consecutively. These chemical additives are set accelerator, set retarder, super-plasticizer and hyper-plasticizer. Chemical additives were added to the mixtures at the rate recommended by the standards. Tap water is used in concrete mixes and the pH of the water is 7,85.

2.2. Sample Types and Curing Conditions

Concrete samples are cylinders of $\phi 100 \times 200$ mm size. These cylinders have 14 mm diameter rebar at their centres. The samples were cured in the laboratory environment for one day and then they removed from the molds were kept in the curing condition until the relevant experiments were carried out. Reinforced concrete samples were kept in lime-saturated water pools with a temperature of $20 \pm 2 \text{ }^\circ\text{C}$ until the test time (standard curing).

The samples, whose curing period was completed, were taken out of the pool for accelerated corrosion test on the 28th and 90th days.

Each of the chemical additives used in this article can affect the slump value of fresh concrete. The slump test was carried out in accordance with the TS EN 12350-2 (2019) [22]. The fresh concrete mix was filled into the measuring cup by skewering 25 times in 3 layers. After the swelling of each layer, the air bubbles remaining in the concrete were removed by tapping the edges of the container 10-15 times. The excess part on the container was stripped off. After the cone is removed, the measurement is made between the cone and the top of the concrete mix.

2.3. Compressive Strength Test

The positive effect of chemical additives on the compressive strength of concrete has known. The compressive strength test was used on cubic samples with a dimension of 150 mm. Samples were loaded with a constant velocity of 0,3 MPa/s due to the TS EN 12390-3 (2019) standard [23]. With the help of a 2000 kN capacity concrete press, force was applied to the samples until the crack occurred on the sample.

2.4. Accelerated Corrosion Test

The accelerated corrosion laboratory test has different parts, these are; reinforced concrete, a plastic chamber, water with % 4 content of sodium chloride, a data logger device, and a direct current power source. The sample was produced by embedding 180 mm of 16 mm diameter reinforcement into a cylindrical sample $\phi 100 \times 200$ mm size. The reinforcement bar (working electrode) is connected to the positive pole of the direct current source, which applies a constant 20 Volt to the system, and plates (counter electrode) are connected to the negative pole [24-29]. The time-dependent corrosion current graphs were drawn according to the damage formation times after the application of experiments was ended. Accelerated corrosion test was applied on the samples in curing conditions at 28th and 90th days [Figure 2].

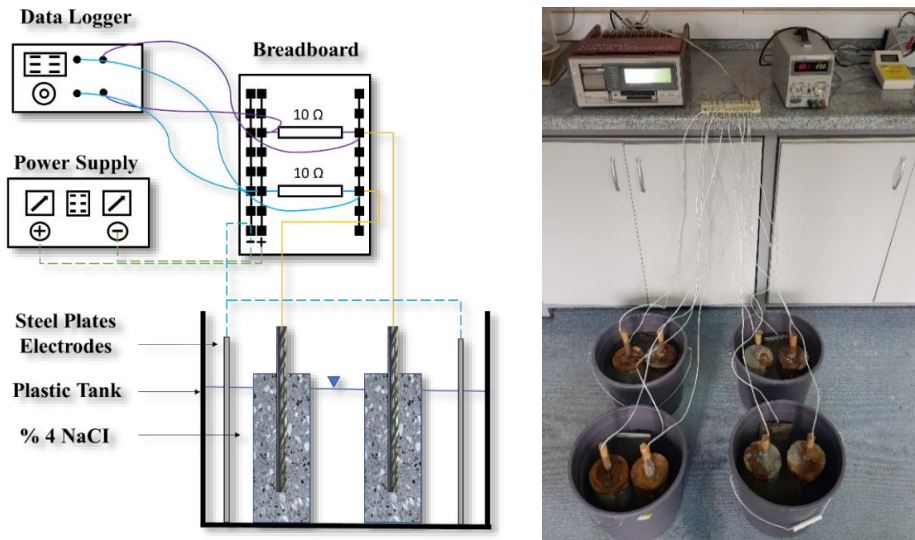


Fig. 2 Reinforced sample during accelerated corrosion; schematic illustration on the left and test setup on right

2.5. Micro Analysis on Concrete

Thanks to its natural compounds, the boron inhibitor creates a less porous microstructure in both early and late ages. Figure 3a shows ettringite formation in the microstructure of the control sample without inhibitor cured for 28 days. The boron inhibitor improved the hydration reactions occurring in the cement and caused the formation of non-pointed and denser ettringite. As evident from the SEM image on Figure 3b, the reactional activities which occurred by boron inhibitor and hyper plasticizer also contribute to the flowability of the concrete mix and improve the micro-filling ability.

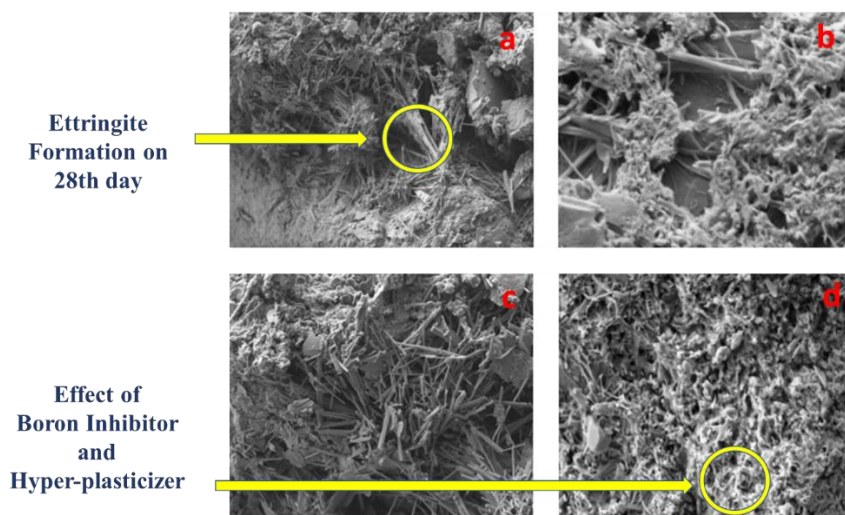


Fig. 3 a) Ettringite formation of the control sample on the 28th day b) Control sample on 90th day c) Effect of boron inhibitor and hyper-plasticizer on 28th day d) Sample with boron inhibitor and hyper-plasticizer on 90th day

The cement paste matrix demonstrated in Figure 3c is proof that more ettringites are developed according to 90 days of curing time. Figure 3d is the SEM images of the samples containing boron inhibitor and hyper-plasticizer after 90 days of curing. While the curing time increased, by the time porosity of the concrete samples containing the boron inhibitor started to decrease. By dint of all these, the porosity of the concrete was reduced, resulting in enhanced durability properties for concrete design including compressive strength and damage occurrence time of accelerated corrosion test.

3. Results and Discussion

3.1. Slump Values

In the series with chemical additives, the slump values increased in the series containing super and hyper-plasticizers. Considering the series with boron inhibitor and chemical additives, an increase in slump values was observed compared to the series in which only chemical additives were used. The slump values saw a slight rise when using the calcium nitrite-based corrosion inhibitor, although the amount of water was reduced and added to the mixture. Generally, with the addition of chemical admixtures to a concrete mix, slump values witnessed an increase. Especially, with the use of super and hyper-plasticizers in concrete series, the slump values rose significantly [Figure 4].

Since corrosion inhibitors are liquids with high water content, they affect the water/cement ratio of the concrete to a great extent, which might reduce the strength. The

water/cement ratio was kept constant by reducing the amount of water with the added inhibitor value, however, the slump value of the BORIN series increased by 11% compared to the control concrete. The slump value of the FERRO series increased compared to the control series but remained lower than the BORIN series.

In the series with chemical additives, the set retarders generally did not have a considerable effect on the slump values. However, as a result of the plasticizing effect of the setting accelerator additives, an increase was experienced in the slump values. Utilizing plasticizers was by far the most noticeable result. The slump values increased by approximately 51.4 % in the series containing super and hyper-plasticizers. In the series with boron inhibitor and chemical additives, the slump value of each series increased by an average of 35.2% compared to the series in which only chemical additives were used. The calcium nitrite-based corrosion inhibitor also shows moderate change in slump values. The series used calcium nitrite and set retarder increased the slump value accounting for 17.6% compared to the series with contain only set retarder.

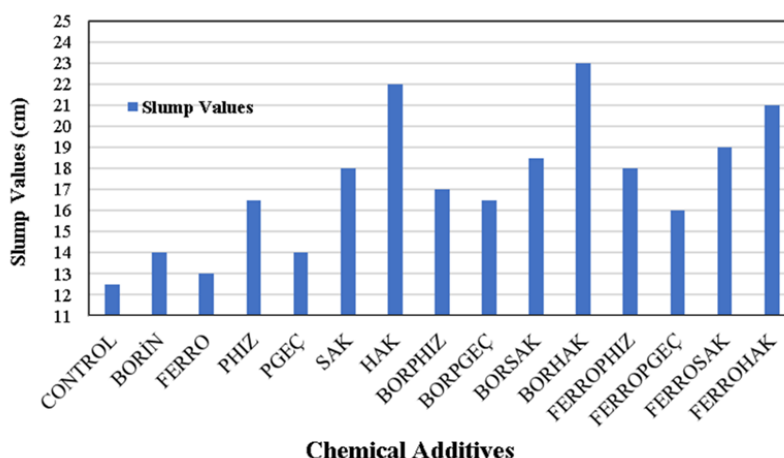


Fig. 4 Variation of slump values according to concrete series

3.2. Compressive Strength Values

In Figure 5, the variation of the compressive strength results of concrete with boron inhibitor and chemical additives over time is shown. When the figure was examined, it was seen that with the extension of curing times, compressive strength values also increased. Thus, hydration reactions occur better, new C-S-H gels are formed, and this affects positively the mechanical strength. As can be seen from Figure 5, it was concluded that the boron inhibitor did not degrade the chemical structure of the concrete (although it was used as a concrete additive for the first time) and it increased the compressive strength values more than the samples with calcium nitrite. The inhibitor obtained from boron did not cause any negative results when used with chemical additives. The use of the two chemicals together provided an increase in the compressive strength of concrete by creating a synergistic effect.

In the concrete samples where the setting accelerator and boron inhibitor were used together, an increase of 11.23% was observed in the concrete compressive strength compared to the concrete samples using only the set accelerator. Within the scope of this article, the highest compressive strength result is 50.4 MPa in the 90th day of curing, which is obtained as a result of the use of hyper-plasticizer additives and boron inhibitor

together. Hyper-plasticizer admixtures used together with boron inhibitor increased the concrete compressive strength by 27.59% compared to the control sample, and superplasticizer admixtures used together with boron inhibitor increased the concrete compressive strength by 17.42%. From this, it can be said that the green boron inhibitor increases the mechanical strength of the concrete and this will positively affect the corrosion resistance.

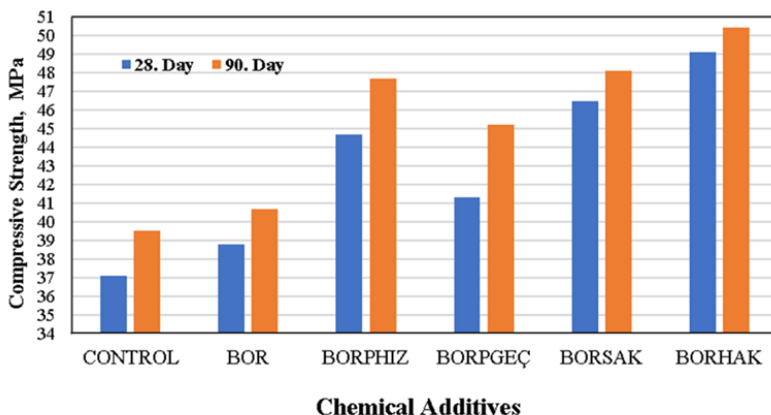


Fig. 5 Compressive strength of boron inhibitor and chemical additives

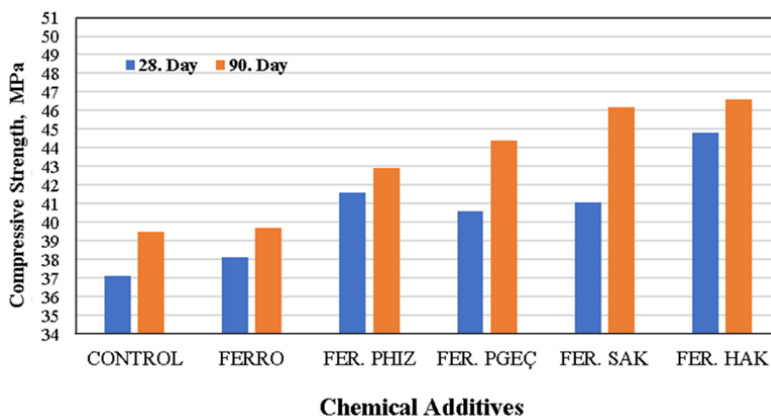


Fig. 6 Compressive strength of calcium nitrite and chemical additives

Figure 6 shows the variation of compressive strength results of concrete with calcium nitrite inhibitor and chemical additives over time. It was concluded that when calcium nitrite inhibitor and chemical additives are used together, they increase the compressive strength of concrete. The hyper-plasticizer admixtures used together with the calcium nitrite inhibitor increased the concrete compressive strength by 11.27%, and the superplasticizer admixtures used together with the calcium nitrite inhibitor increased the concrete compressive strength by 8.61% compared to the control sample. With the increase of curing time, an increase in compressive strength of approximately 6.11% was observed in all series. Although this increase is less than the boron inhibitor, it was seen that calcium nitrite inhibitor had a positive effect on the concrete compressive strength.

Boron inhibitor generally increased the compressive strength of concrete more than the calcium nitrite inhibitor, which is known as the market inhibitor. It was observed that the two inhibitors did not give harmful reactions with other chemicals during use in concrete and it was concluded that it increased the mechanical properties. When calcium nitrite is used in reinforced concrete with other chemical additives, the structure of the concrete mixture does not deteriorate. This is because nitrite components do not react with sulfonate and phosphate-based chemicals.

3.3. Accelerated Corrosion Test Results

After the accelerated corrosion test, the reinforcements inside the samples were corroded and damaged (Figure 7). Since the volume of corrosion products (rust) is 3-8 times larger than the volume of reinforcement involved in corrosion, rust products have created huge forces in the hardened concrete and it results in cracks and crumbles because of these increased internal stresses.



Fig. 7 Final stage of control and BORHAK sample after accelerated corrosion test

The variation of the accelerated corrosion test results of concretes with calcium nitrite inhibitor and chemical additives according to the concrete series is given in Figure 8. As seen in the figure, sudden current increases occurred in corrosion currents at the time of damage. The damage occurrence times of concrete samples were determined from these sudden current increases. It has been observed that the use of calcium nitrite in concrete samples generally reduces the initial corrosion current and prolongs the damage formation time. The FERROSAK90 sample increased the damage formation time by 37.9% compared to the control concrete with 163 hours. On the other hand, the FERROHAK90 sample gave better results, keeping the initial corrosion current at 94 mA and prolonging the damage formation time up to 192 hours by increasing 78.9%.

The rebar used in reinforced concrete structures corrodes rapidly in mediums containing Cl^- ions (especially if the permeability of the concrete is high). The passive film layer formed by the inhibitors generally has a protective effect around the reinforcement and prevents corrosion mechanism from occurring on the reinforcement surface. In the samples where these effects are less visible, the initial corrosion currents also rise. The use

of inhibitors in concrete samples gave positive results for both inhibitor types. The nitrite and borane compounds in the inhibitors protected the passive film layer around the reinforcement and the passage of chloride ions was prevented. This result was more prominent in the natural boron inhibitor. As a result, the use of chemical additives and inhibitors improved the corrosion resistance of concretes and extended the damage formation period. The synergistic effect of these chemicals improved the durability properties of concrete and gave better results. In the graph, it was determined that the strength results differ according to the curing time. For instance, the use of super and hyper-plasticizers decreased the permeability of the concrete and extended the first crack formation time at 28th days compared to the 90th day strength of the control sample.

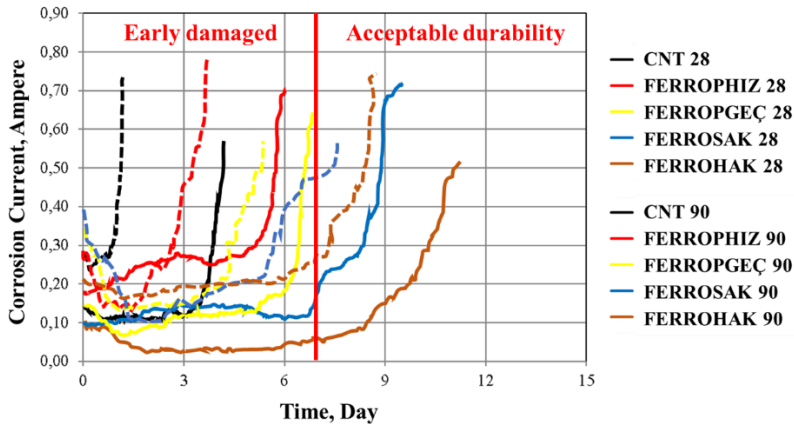


Fig. 8 Time-dependent corrosion current graph for concrete mix with calcium nitrite inhibitor

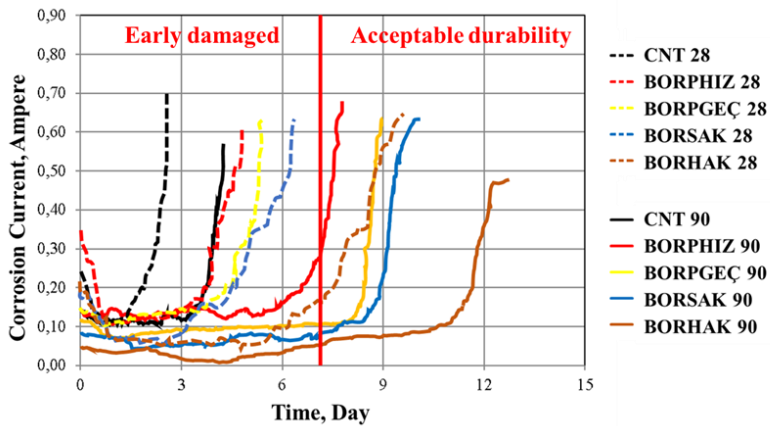


Fig. 9 Time-dependent corrosion current graph for concrete mix with natural boron inhibitor

In this study, the lowest initial corrosion current value and the longest damage formation time obtained from the samples using boron inhibitor (Figure 9). The BORHAK90 sample is the last damaged sample within the scope of the accelerated corrosion test performed with 264 hours, and it showed an increase of two times compared to the control sample. In addition, the BORHAK90 sample draws the lowest initial corrosion current with 47 mA. It can be understood from this that the boron inhibitor does not allow the formation of

corrosion reactions in the sample by forming an impermeable compact structure. BORSAK28 sample increased the initial crack formation by 124,92%. The borane complex contained in the boron inhibitor protected the passive film layer around the reinforcement, and this synergistic effect between them, together with the reduction of the impermeability of the hyper plasticizer, gave the latest damage formation time (Table 1).

Table 1. Corrosion current and damage occurrence time of samples

Series	Corrosion Current (Ampere)		Damage Occurrence Time (Hour)	
	28 th Day	90 th Day	28 th Day	90 th Day
Control	289	127	68	106
FERROPHIZ	205	170	102	135
FERROPGEC	152	124	118	146
FERROSAK	131	102	142	163
FERROHAK	106	94	175	192
BORPHIZ	151	123	121	176
BORPGEC	135	112	167	199
BORSAK	109	92	196	209
BORHAK	83	47	227	264

4. Conclusions

In this study, the definition of corrosion mechanism and the importance of the application of newly produced concrete additives (green natural inhibitors) was emphasized rather than traditional inhibitors with known toxic effects on earth. One of the most important compounds obtained from boron in recent years is a boron inhibitor. In this research, the boron inhibitor, which was used to protect the base metal in different sectors, was used as a concrete additive to protect the reinforcement. Combinations of boron inhibitor with other concrete additives significantly reduced the corrosion potential of the reinforcement and extended the damage formation time. As a result of the laboratory tests, it has been seen that the curing time, the chemical additives, and the type of corrosion inhibitor have an important effect on mechanical and durability properties of concretes in various ways.

According to the analysis, the following results were obtained;

- The use of green boron inhibitor in concrete significantly improved the mechanical and durability properties of concrete. Increasing the curing times is absolutely necessary and important.
- It has been observed that the mechanical properties of the concrete are significantly improved when a calcium nitrite-based corrosion inhibitor is used as a chemical additive. The use of calcium nitrite and hyper-plasticizers filled the micro-voids in the concrete (with the help of enhanced consistency) and increased the compressive strength by 21,6% compared to the control sample. Among all results, the highest compressive strength result is 50,4 MPa, which is obtained as a result of the use of hyper plasticizer additives and boron inhibitor together. BORHAK concrete series increased the concrete compressive strength by 27,59% compared to the control sample.
- On the perspective of durability properties, it was concluded that the damage occurrence time obtained as a result of the accelerated corrosion test was prolonged. While the damage formation time was measured as 192 hours with the use of commercial calcium nitrite inhibitor and hyper-plasticizer in concrete mixtures, this time was found to be 264 hours with the use of boron inhibitor and

hyper-plasticizer. Both inhibitors increased the damage formation time compared to the control samples by 81,1% and 146,2%, respectively.

- BORHAK90 sample draws the lowest initial corrosion current with 47 mA. It is understood from this that the boron inhibitor does not allow the formation of corrosion reactions in the sample by forming an impermeable compact structure. BORSAK28 sample increased the initial crack formation by 124,92%. The borane complex contained in the boron inhibitor protected the passive film layer around the reinforcement.
- The efficiency of the boron-containing green inhibitor is way higher compared to the other inhibitors obtained from plant extracts according to the literature review in previous sections. Considering the corrosion protection potential and cost of all other green inhibitors, it is thought that these inhibitors will be more difficult to manufacture and hard to become commercially available. The fact that boron reserves are abundant and can be easily processed, especially in Turkey, makes boron inhibitors to be more utilizable and economical.

References

- [1] Shahid KA, Bunnori NM, Johari MM, Hassan MH, Sani A. Assessment of corroded reinforced concrete beams: Cyclic load test and acoustic emission techniques. *Construction and Building Materials*. 2020; 233, 117291. <https://doi.org/10.1016/j.conbuildmat.2019.117291>
- [2] Topcu IB, Uzunomeroglu A, Pat S. Enhanced Corrosion Behavior of Reinforcing Steel in Concrete Using Titanium Nano-composite Thin Films, *Jordan Journal of Civil Engineering*. 2022; 16(2): 294 - 306.
- [3] Lapiro I, Mezhov A, Kovler K. Performance of corrosion inhibitors in reinforced concrete elements under electrical voltage. *Construction and Building Materials*. 2022; 342, 127656. <https://doi.org/10.1016/j.conbuildmat.2022.127656>
- [4] Alraeeini AS, Nikbakht E. Corrosion effect on the flexural behaviour of concrete filled steel tubulars with single and double skins using engineered cementitious composite. In *Structures*. 2022; Vol. 44, pp. 1680-1694. <https://doi.org/10.1016/j.istruc.2022.08.095>
- [5] Vivek DR, Sudeep YH. A Review of Accelerated Corrosion Studies on Reinforced Concrete Samples Using Voltage Impressed Test. *International Journal of Research in Engineering and Science (IJRES)*, Volume 10 Issue 5, 2022; 10-14.
- [6] Li Q, Dong Z, He Q, Fu C, Jin X. Effects of Reinforcement Corrosion and Sustained Load on Mechanical Behavior of Reinforced Concrete Columns. *Materials*, 2022; 15(10), 3590. <https://doi.org/10.3390/ma15103590>
- [7] Zhang S, Tian B, Chen B, Lu X, Xiong B, Shuang N. The Influence of Freeze-Thaw Cycles and Corrosion on Reinforced Concrete and the Relationship between the Evolutions of the Microstructure and Mechanical Properties. *Materials*. 2022; 15(18): 6215. <https://doi.org/10.3390/ma15186215>
- [8] Van Steen C, Nasser H, Verstrynghe E, Wevers M. Acoustic emission source characterisation of chloride-induced corrosion damage in reinforced concrete. *Structural Health Monitoring*. 2022; 21(3): 1266-1286. <https://doi.org/10.1177/14759217211013324>
- [9] Liang C, Cai Z, Wu H, Xiao J, Zhang Y, Ma Z. Chloride transport and induced steel corrosion in recycled aggregate concrete: A review. *Construction and Building Materials*. 2021; 282, 122547. <https://doi.org/10.1016/j.conbuildmat.2021.122547>
- [10] Erdogdu S. Determination of the State of Corrosion of Epoxy-coated Rebar in Concrete, Doctoral dissertation, University of New Brunswick. 1992.

- [11] Wang N, Wang Q, Xu S, Lei L. Green fabrication of mechanically stable superhydrophobic concrete with anti-corrosion property. *Journal of Cleaner Production*. 2021; 312, 127836. <https://doi.org/10.1016/j.jclepro.2021.127836>
- [12] Zhang W, François R, Wang R, Cai Y, Yu L. Corrosion behavior of stirrups in corroded concrete beams exposed to chloride environment under sustained loading. *Construction and Building Materials*. 2021; 274: 121987. <https://doi.org/10.1016/j.conbuildmat.2020.121987>
- [13] Topcu IB, Uzunomeroglu A. Properties of Corrosion Inhibitors in Reinforced Concrete, *Journal of Structural Engineering & Applied Mechanics*. 2020; 3(2): 93-109. <https://doi.org/10.31462/jseam.2020.02093109>
- [14] Goyal A, Ganjian E, Pouya HS, Tyrer M. Inhibitor efficiency of migratory corrosion inhibitors to reduce corrosion in reinforced concrete exposed to high chloride environment, *Construction and Building Materials*. 2021; 303: 124461. <https://doi.org/10.1016/j.conbuildmat.2021.124461>
- [15] Peng L, Zeng W, Zhao Y, Li L, Poon CS, Zheng H. Steel corrosion and corrosion-induced cracking in reinforced concrete with carbonated recycled aggregate. *Cement and Concrete Composites*. 2022; 133: 104694. <https://doi.org/10.1016/j.cemconcomp.2022.104694>
- [16] Eyu DG, Esah H, Chukwuekezie C, Idris J, Mohammad I. Effect of green inhibitor on the corrosion behaviour of reinforced carbon steel in concrete. *ARPN J. Eng. Appl. Sci*. 2013; 8(5): 326-332.
- [17] Abdulrahman AS, Ismail M. Assessment of green inhibitor on the crystal structures of carbonated concrete. *Journal Technology*. 2014; 69(3):1-9. <https://doi.org/10.11113/jt.v69.3137>
- [18] Iyigundogdu Z, Saribas I. The effect of various boron compounds on the antimicrobial activity of hardened mortars. *Construction and Building Materials*. 2022; 351: 128958. <https://doi.org/10.1016/j.conbuildmat.2022.128958>
- [19] Uzunömeroğlu A, Boğa AR, Pat S, Topcu IB. Improving the Corrosion Resistance of Reinforcement Embedded in Concrete with High Strength Zinc, Zinc-Boron and Zinc-Boron-Nitrogen Nanocrystal Composite Coating. *Arabian Journal for Science and Engineering*. 2022. <https://doi.org/10.1007/s13369-022-06619-6>
- [20] Topcu IB, Uzunomeroglu A. Experimental Investigation of Utilizing Chemical Additives and New Generation Corrosion Inhibitors on Reinforced Concrete, *Research on Engineering Structures and Materials*. 2021; 7(1): 13-34.
- [21] Zhang W, Han B, Yu X, Ruan Y, Ou J. Nano boron nitride modified reactive powder concrete. *Construction and Building Materials*. 2018; 179: 186-197. <https://doi.org/10.1016/j.conbuildmat.2018.05.244>
- [22] TS EN 12350-2 (2019). Testing fresh concrete - Part 2: Slump test, Turkish Standardization Institute. Ankara.
- [23] TS EN 12390-3 (2019). Testing hardened concrete - Part 3: Compressive strength of test specimens, Turkish Standardization Institute. Ankara.
- [24] Fan L, Shi X. Techniques of corrosion monitoring of steel rebar in reinforced concrete structures: A review. *Structural Health Monitoring*. 2022; 21(4): 1879-1905. <https://doi.org/10.1177/14759217211030911>
- [25] Li CZ, Song XB, Jiang L. A time-dependent chloride diffusion model for predicting initial corrosion time of reinforced concrete with slag addition. *Cement and Concrete Research*. 2021; 145: 106455. <https://doi.org/10.1016/j.cemconres.2021.106455>
- [26] Feng W, Tarakbay A, Memon SA, Tang W, Cui H. Methods of accelerating chloride-induced corrosion in steel-reinforced concrete: A comparative review. *Construction and Building Materials*. 2021; 289: 123165. <https://doi.org/10.1016/j.conbuildmat.2021.123165>
- [27] Li X, Kulandaivelu J, O'Moore L, Wilkie S, Hanzic L, Bond PL, Jiang G. Synergistic effect on concrete corrosion control in sewer environment achieved by applying surface

- washing on calcium nitrite admixed concrete. *Construction and Building Materials*. 2021; 302: 124184. <https://doi.org/10.1016/j.conbuildmat.2021.124184>
- [28] Xu W, Li Y, Li H, Wang K, Zhang C, Jiang Y, Qiang S. Corrosion mechanism and damage characteristic of steel fiber concrete under the effect of stray current and salt solution. *Construction and Building Materials*. 2022; 314: 125618. <https://doi.org/10.1016/j.conbuildmat.2021.125618>
- [29] Liu Y, Shi J. Corrosion resistance of carbon steel in alkaline concrete pore solutions containing phytate and chloride ions. *Corrosion Science*. 2022; 205: 110451. <https://doi.org/10.1016/j.corsci.2022.110451>



Research Article

Estimating vibration period of reinforced concrete moment resisting frame buildings

Thaer Alrudaini^a

Department of Civil Engineering, University of Basrah, Basrah, Iraq

Article Info

Article history:

Received 31 Mar 2023

Accepted 21 Aug 2023

Keywords:

Fundamental period;

Modal analysis;

Moment resisting

frame;

Vibration;

Reinforced concrete buildings

Abstract

One of the initial steps in the analysis and design of buildings subjected to lateral loads is estimating the fundamental vibration period of the building. Design codes and standards recommend conducting modal analysis to investigate the fundamental vibration period of the building. On the other hand, these design codes and standards specify simple empirical models that relate the fundamental period to the building height as an alternative approach to modal analysis. In this study, extensive modal analyses were conducted to investigate the fundamental period of 382 building models. Modal analyses were conducted to evaluate the effect of design parameters on the fundamental vibration period of reinforced concrete moment resisting frame buildings. The effect of each design parameter was identified using sensitivity analysis. Finally, a simple model was developed in this study based on the results of modal analysis to estimate the fundamental vibration period of the buildings. Main design parameters including building height, spans length, columns elasticity and columns size were considered in the developed model. The proposed model was validated against modal analysis in which a mean value of the proposed model to modal analysis predictions ratio equal to 1.00 ± 0.155 with coefficient of variation equal to 15.38 were obtained.

© 2023 MIM Research Group. All rights reserved.

1. Introduction

The fundamental vibration period is a main parameter that appears in base shear and lateral forces equations used for the analysis and design of buildings subjected to either wind loads or seismic excitation. The fundamental vibration period is mainly depending on stiffness and mass of the building which is a function of several parameters including building height, structural system, material properties, members dimensions and plan area of the building. Design codes and standards recommended using either modal analysis or a specified simple time period building height relation in order to predict the fundamental period of the buildings [1–3]. Researchers used recorded vibration time during earthquakes or ambient vibration experiments for developing empirical models. Goel and Chopra [4] and Salama [5] considered vibration of reinforced concrete moment-resisting frame buildings during earthquake in different regions in the United States. Hong and Hwang [6] and Chiauzzi et al. [7] considered vibration of reinforced concrete buildings during earthquake in Taiwan and Canada, respectively. On the other hand, several models were developed based on the recorded ambient vibrations of the buildings in different regions in the world. Guler et al. [8], Inel et al. [9] and Kaplan et al. [10] considered buildings in Turkey. Velani and Ramancharla [11] and Velani and Kumar [12] considered buildings in India. Jalali and Milani [13], Gallipoli et al. [14], Al-Nimry et al. [15] and Pan et al. [16] considered ambient vibration of buildings in Iran, Europe, Jordan and Singapore, respectively. Almost all the previous developed models give direct relations of the

Corresponding author: thaer.abdulhameed@uobasrah.edu.iq

^aorcid.org/0000-0003-2033-9979

DOI: <http://dx.doi.org/10.17515/resm2023.724st0331>

Res. Eng. Struct. Mat. Vol. 9 Iss. 4 (2023) 1417-1432

fundamental vibration period to buildings height. However, it was shown that previous simple models resulted in significantly large variations in predictions [17–24].

Several models to predict fundamental vibration time were developed in the literature based on modal analysis considering numerical modelling of the buildings. Crowley and Pinho [25] and Crowley and Pinho [26] studied several existing European buildings and developed an equation that relates fundamental vibration periods to building height. Amanat and Hoque [27] modified code specified fundamental period to building height relation by introducing span length, number of spans and infill amount factors based on finite element modeling and modal analyses. Rimal and Maskey [28] considered building height, building plan and number of bays in their proposed model that developed based on finite element modelling and modal analyses results. Koçak et al. [29] proposed empirical relation of fundamental period to building height, modulus of elasticity of infill walls and thickness of the infill walls based on numerical analysis considering 270 building models. Kewate and Murudi [30] modeled 21 existing reinforced concrete moment resisting frame buildings in India and proposed an equation that relates the fundamental vibration period to building height. Multiple fundamental period to building height relations for different seismic intensities were developed by Verderame et al. [31] based on modal analyses results. Mohamed et al. [32] used applied element method in modeling reinforced concrete buildings and conducted nonlinear dynamic analysis in which the fundamental period was extracted from the time history curve. An equation relates fundamental vibration period to building height, building width to length ratio and column size was developed. Joshi et al. [33] analyzed 206 building models to generate vibration period data and used the generated data in genetic programming for developing multiple models according to different limits of building height. Also, Hadzima-Nyarko and Draganic [34] used genetic algorithms to develop a fundamental period formulas based on the modal analysis results of finite element models. Asteris et al. [35] proposed using artificial neural network to predict the fundamental vibration period of buildings considering the effect of several design parameters including building height, spans length, number of spans, infill strength and amount. The developed artificial neural network model was trained and verified against numerical modeling and modal analyses results. Al-Balhawi and Zhang [36] investigated and developed a vibration period model for reinforced concrete tall buildings having moment resisting frames with shear walls system. Noor et al. [37] modeled 21 existing reinforced concrete buildings in India and proposed simple fundamental period to building height model based on the analyses results. Sharma et al. [38] developed artificial neural network model to predict fundamental period of reinforced concrete buildings based on finite element analysis results of modal analyses considering the effect of pile soil interaction. Gravett et al. [39] developed fundamental period formula based on the analyses results of 475 building models considering the effect of soil structure interaction and foundation types including separate footings and mat foundations. Ruggieri et al. [40] modeled newly constructed 40 reinforced concrete buildings using finite element method and conducted modal analyses. The results were utilized in regression analysis to derive a model to estimate fundamental period of buildings. Mirrashid and Naderpour [41] proposed fundamental period models of infilled reinforced concrete buildings using artificial neural network and neuro fuzzy methods considering the influence of number of stories, number of spans, spans length, infill stiffness and ratio of openings to infill.

In this study, recorded vibration periods of buildings located in different regions in the world were collected and compared with predictions of different models. Also, extensive modal analyses were conducted considering 382 reinforced concrete moment resisting frame (RC MRF) building models developed in this study to investigate the effect of different design parameters on the fundamental vibration period of the buildings. Models were built and modal analyses were conducted using commercially available structural

analysis and design software SAP 2000 [42]. Sensitivity analyses were conducted in which the effects of main design parameters including building height, spans length, columns stiffness was considered. The main objective of this study was to develop a simple but more precise model to estimate the fundamental vibration period of reinforced concrete moment resisting frame buildings based on the results of the modal analyses and considering the main influencing design parameters. The developed model is recommended for practicing engineers as an alternative to modal analysis.

The following section includes collecting some of actual records of fundamental periods as well as exploring several available models to predict fundamental period in which the results are compared. The third section includes presenting numerical modeling and modal analyses to investigate the fundamental period of 382 building models developed in this study. A proposed model in this study to estimate the fundamental vibration period is presented in fourth section followed by section five that includes the sensitive analysis to investigate the influence of each design parameter of the proposed model based on the results of modal analysis presented in this study. Then, the proposed model has verified in the sixth section. Finally, study considerations are highlighted and main conclusions points are drawn.

2. Available Period of Vibration Models

The design codes and standards specify different fundamental period to building height relations [1–3]. Also, several models were presented in the literature. Most of the available models consider the fundamental period of the building as a function of to its height or a number of stories. The available models were derived by regression analysis considering actual vibration records during earthquakes or ambient vibration of buildings located in different regions in the world. Table 1 presents some of these available models. The terms T_f and H represent the time of the fundamental vibration period and the building height, respectively.

Table 1. Available vibration time model

Researcher	Model	Location
ASCE/SEI 7-16 [1]	$T_f = 0.0466 H^{0.9}$	USA
Eurocode 8 [2]	$T_f = 0.075 H^{3/4}$	Europe
FEMA 450 [3]	$T_f = 0.0524 H^{0.9}$	USA
Hong and Hwang [6]	$T_f = 0.0294 H^{0.804}$	Taiwan
Michel et al. [43]	$T_f = 0.013 H$	France
Chiauzzi et al. [7]	$T_f = 0.037 H^{0.76}$	Canada
Guler et al. [8]	$T_f = 0.026 H^{0.9}$	Turkey
Velani and Ramancharla [11]	$T_f = 0.009 H^{1.1}$	India
Inel et al. [9]	$T_f = 0.0343 H^{0.762}$	Turkey

To evaluate the validity of the available models, predictions using these models are compared with actual records gathered from published works. Data of vibration period of 255 RC MRF buildings located in different regions in the world were collected and presented in Table 2 with measured time periods illustrated in Fig. 1. A comparison between predictions using available models and actual records of fundamental vibration time is presented in Fig. 2. Fig. 2 shows that almost all the existing formulas resulted in substantially different predictions. Also, a significant discrepancy between the predictions and measured values have been demonstrated. Consequently, adopting simple relation of building height to fundamental period resulted in inadequate predictions.

Table 2. Data of measured fundamental period of RC MRF buildings published in the literature

Reference	Location	No. of data	Building height (m)
Goel and Chopra [4]	USA	34	9 – 56
Hong and Hwang [6]	Taiwan	19	27 – 77
Jalali and Milani [13]	Iran	11	17 – 53
Guler et al. [8]	Turkey	6	12 – 30
Chiauszi et al. [7]	Canada	12	12 – 70
Gallipoli et al. [14]	Europe	113	3 – 51
Ditommaso et al. [44]	Italy	14	5.2 – 24.7
Al-Nimry et al. [15]	Jordan	25	4.4 – 20.5
Velani and Ramancharla [11]	India	21	72 – 147
	Total	255	3 – 147

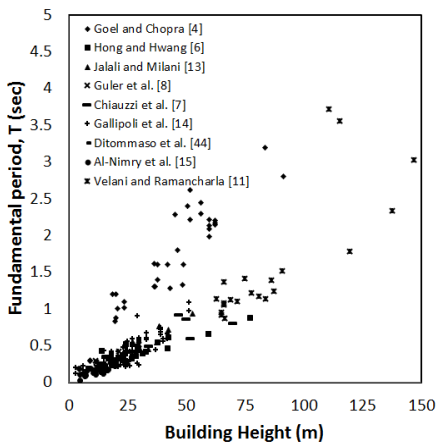


Fig. 1 Recorded fundamental vibration time of RC MRF buildings located in different regions in the world

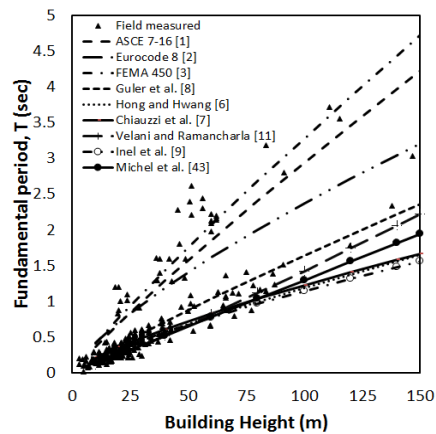


Fig. 2 Comparison between the recorded and predicted fundamental vibration time of RC MRF buildings

3. Numerical Investigations

In this study, modal analysis was conducted considering 382 models of reinforced concrete moment resisting frame buildings to determine the fundamental time period. Buildings were modelled using three-dimensional finite elements using the structural analysis and design software SAP2000 [42]. Beams and columns were simulated using three-dimensional frame elements and slabs were modelled using three-dimensional plate rectangular elements. The slabs thickness was assigned equal to 180 mm for all building models and the beams web width and total depth were set equal to 0.3 m and 0.50 m, respectively. The parametric investigations include the effect of building height, column size, span length and material properties on the time period of the buildings (T). The considered height of each storey of was 3 m. Table 3 gives the limits of the design parameters of the building models that considered in the investigations. Figure 3 illustrates a model structure of the buildings using the structural analysis and design program SAP2000 [42]. Table 4 illustrates the details of the parameters of the considered models in this study including height of the building (H), the span length (L), the

compressive strength of concrete (f'_c), the side dimension of the column (D) and the number of spans in orthogonal directions (Bx and By). Results of modal analyses for the considered models are illustrated in Table 4 and Fig. 4. Fig. 4 shows very wide range of predicted vibration periods corresponding to building height. The variation in the fundamental period can be seen to stem from the effect of different design parameters other than the building height. Also, it is shown that the numerical results presented in Fig. 4 cover the range of almost all measured values that shown in Figs. 1 and 2.

Table 3. Limits of the design parameters of the considered building models in the numerical analysis

Parameter	Values	Range
Building height (m)	3, 15, 30, 45, 60, 90	3 – 90
Columns side dimension (m)	0.3, 0.4, 0.5, 0.6, 0.7, 0.8, 0.9, 1.0, 1.2	0.3 – 1.2
Compressive strength of concrete f'_c (MPa)	30, 40, 50, 60, 70, 80, 90	30 – 90
Span length (m)	4, 5, 6, 7	4 – 7

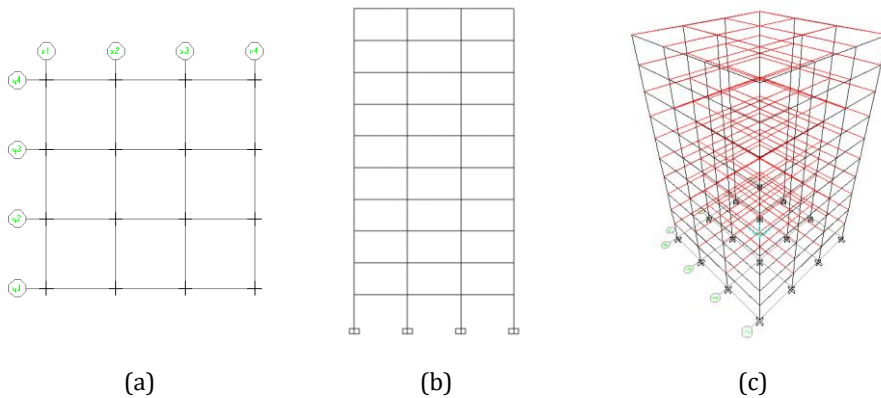


Fig. 3 Building Model considered in this study using SAP2000 [42], a) plan view, b) side view and c) three dimensional view

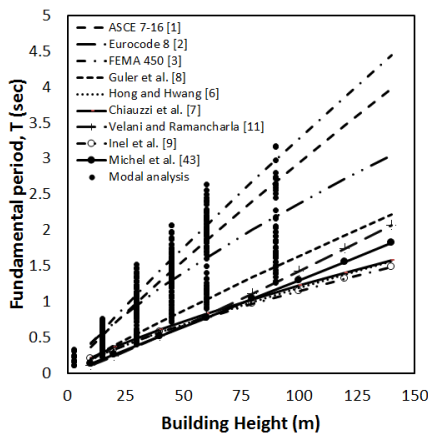


Fig. 4 Comparison of numerical fundamental period of buildings with different specified models

Table 4. Details of the design parameters of the considered models

Mod.	H (m)	L (m)	F'c (MPa)	D (m)	Bx (m)	By (m)	T (sec.)	Mod.	H (m)	L (m)	F'c (MPa)	D (m)	Bx (m)	By (m)	T (sec.)
1	3	4	70	0.3	3	3	0.1556	59	30	4	70	0.6	3	3	0.7301
2	15	4	70	0.3	3	3	0.6178	60	45	4	70	0.6	3	3	1.1468
3	30	4	70	0.3	3	3	1.2317	61	60	4	70	0.6	3	3	1.5995
4	45	4	70	0.3	3	3	1.8965	62	15	4	60	0.6	3	3	0.3532
5	15	4	60	0.3	3	3	0.6421	63	30	4	60	0.6	3	3	0.7588
6	30	4	60	0.3	3	3	1.2800	64	45	4	60	0.6	3	3	1.1919
7	45	4	60	0.3	3	3	1.9710	65	60	4	60	0.6	3	3	1.6623
8	15	4	50	0.3	3	3	0.6720	66	15	4	50	0.6	3	3	0.3697
9	30	4	50	0.3	3	3	1.3397	67	30	4	50	0.6	3	3	0.7942
10	45	4	50	0.3	3	3	2.0630	68	45	4	50	0.6	3	3	1.2474
11	3	4	40	0.3	3	3	0.1789	69	60	4	50	0.6	3	3	1.7399
12	15	4	40	0.3	3	3	0.7106	70	15	4	40	0.6	3	3	0.3909
13	30	4	40	0.3	3	3	1.4166	71	30	4	40	0.6	3	3	0.8397
14	15	4	30	0.3	3	3	0.7635	72	45	4	40	0.6	3	3	1.3190
15	30	4	30	0.3	3	3	1.5222	73	60	4	40	0.6	3	3	1.8397
16	15	4	70	0.4	3	3	0.4393	74	15	4	30	0.6	3	3	0.4200
17	30	4	70	0.4	3	3	0.8972	75	30	4	30	0.6	3	3	0.9023
18	45	4	70	0.4	3	3	1.3963	76	45	4	30	0.6	3	3	1.4174
19	15	4	60	0.4	3	3	0.4566	77	60	4	30	0.6	3	3	1.9769
20	30	4	60	0.4	3	3	0.9325	78	15	5	70	0.4	3	3	0.5088
21	45	4	60	0.4	3	3	1.4511	79	30	5	70	0.4	3	3	1.0393
22	60	4	60	0.4	3	3	2.0288	80	45	5	70	0.4	3	3	1.5576
23	3	4	50	0.4	3	3	0.1063	81	60	5	70	0.4	3	3	2.1995
24	15	4	50	0.4	3	3	0.4779	82	15	5	60	0.4	3	3	0.5288
25	30	4	50	0.4	3	3	0.9760	83	30	5	60	0.4	3	3	1.0801
26	45	4	50	0.4	3	3	1.5188	84	45	5	60	0.4	3	3	1.6188
27	60	4	50	0.4	3	3	2.1234	85	60	5	60	0.4	3	3	2.2859
28	3	4	40	0.4	3	3	0.1124	86	15	5	50	0.4	3	3	0.5534
29	15	4	40	0.4	3	3	0.5053	87	30	5	50	0.4	3	3	1.1305
30	30	4	40	0.4	3	3	1.0319	88	45	5	50	0.4	3	3	1.6943
31	45	4	40	0.4	3	3	1.6059	89	15	5	40	0.4	3	3	0.5852
32	60	4	40	0.4	3	3	2.2452	90	30	5	40	0.4	3	3	1.1953
33	15	4	30	0.4	3	3	0.5430	91	15	5	30	0.4	3	3	0.6288
34	30	4	30	0.4	3	3	1.1089	92	30	5	30	0.4	3	3	1.2845
35	45	4	30	0.4	3	3	1.7257	93	15	5	70	0.5	3	3	0.4235
36	60	4	30	0.4	3	3	2.4127	94	30	5	70	0.5	3	3	0.8851
37	15	4	70	0.5	3	3	0.3711	95	45	5	70	0.5	3	3	1.3357
38	30	4	70	0.5	3	3	0.7762	96	60	5	70	0.5	3	3	1.8852
39	45	4	70	0.5	3	3	1.2138	97	15	5	60	0.5	3	3	0.4401
40	60	4	70	0.5	3	3	1.6964	98	30	5	60	0.5	3	3	0.9198
41	15	4	60	0.5	3	3	0.3857	99	45	5	60	0.5	3	3	1.3882
42	30	4	60	0.5	3	3	0.8067	100	60	5	60	0.5	3	3	1.9593
43	45	4	60	0.5	3	3	1.2615	101	15	5	50	0.5	3	3	0.4607
44	60	4	60	0.5	3	3	1.7631	102	60	5	80	0.7	3	3	1.1800
45	15	4	50	0.5	3	3	0.4037	103	30	5	50	0.5	3	3	0.9627
46	30	4	50	0.5	3	3	0.8444	104	45	5	50	0.5	3	3	1.4529
47	45	4	50	0.5	3	3	1.3203	105	60	5	50	0.5	3	3	2.0507
48	60	4	50	0.5	3	3	1.8453	106	15	5	40	0.5	3	3	0.4871
49	15	4	40	0.5	3	3	0.4269	107	30	5	40	0.5	3	3	1.0180
50	30	4	40	0.5	3	3	0.8928	108	45	5	40	0.5	3	3	1.5363
51	45	5	60	0.7	6	3	0.9160	109	60	5	40	0.5	3	3	2.1683
52	45	4	40	0.5	3	3	1.3961	110	15	5	30	0.5	3	3	0.5234
53	60	4	40	0.5	3	3	1.9512	111	30	5	30	0.5	3	3	1.0939
54	15	4	30	0.5	3	3	0.4587	112	15	5	70	0.6	3	3	0.3831
55	30	4	30	0.5	3	3	0.9594	113	30	5	70	0.6	3	3	0.8215
56	45	4	30	0.5	3	3	1.5002	114	45	5	70	0.6	3	3	1.2487
57	60	4	30	0.5	3	3	2.0967	115	60	5	70	0.6	3	3	1.7591
58	15	4	70	0.6	3	3	0.3399	116	15	5	60	0.6	3	3	0.3981

Table 4. Continued

Mod.	H (m)	L (m)	F'c (MPa)	D (m)	Bx (m)	By (m)	T (sec.)	Mod.	H (m)	L (m)	F'c (MPa)	D (m)	Bx (m)	By (m)	T (sec.)
117	30	5	60	0.6	3	3	0.8538	172	15	6	30	0.5	3	3	0.5991
118	45	5	60	0.6	3	3	1.2977	173	30	6	30	0.5	3	3	1.2262
119	60	5	60	0.6	3	3	1.8283	174	15	6	70	0.6	3	3	0.4339
120	15	5	50	0.6	3	3	0.4167	175	30	6	70	0.6	3	3	0.9108
121	30	5	50	0.6	3	3	0.8936	176	45	6	70	0.6	3	3	1.4051
122	45	5	50	0.6	3	3	1.3582	177	60	6	70	0.6	3	3	1.9230
123	60	5	50	0.6	3	3	1.9135	178	15	6	60	0.6	3	3	0.4510
124	15	5	40	0.6	3	3	0.4406	179	30	6	60	0.6	3	3	0.9466
125	30	5	40	0.6	3	3	0.9449	180	45	6	60	0.6	3	3	1.4603
126	45	5	40	0.6	3	3	1.4362	181	60	6	60	0.6	3	3	1.9986
127	60	5	40	0.6	3	3	2.0233	182	15	6	50	0.6	3	3	0.4720
128	15	5	30	0.6	3	3	0.4734	183	30	6	50	0.6	3	3	0.9908
129	30	5	30	0.6	3	3	1.0171	184	45	6	50	0.6	3	3	1.5284
130	45	5	30	0.6	3	3	1.5433	185	60	6	50	0.6	3	3	2.0918
131	45	5	70	0.7	3	3	1.2159	186	15	6	40	0.6	3	3	0.4991
132	60	5	70	0.7	3	3	1.7121	187	30	6	40	0.6	3	3	1.0476
133	45	5	60	0.7	3	3	1.2637	188	45	6	40	0.6	3	3	1.6161
134	60	5	60	0.7	3	3	1.7794	189	60	6	40	0.6	3	3	2.2118
135	45	5	50	0.7	3	3	1.3226	190	15	6	30	0.6	3	3	0.5363
136	60	5	50	0.7	3	3	1.8624	191	30	6	30	0.6	3	3	1.1257
137	45	5	40	0.7	3	3	1.3985	192	45	6	30	0.6	3	3	1.7366
138	60	5	40	0.7	3	3	1.9692	193	45	6	70	0.7	3	3	1.3542
139	45	5	30	0.7	3	3	1.5028	194	60	6	70	0.7	3	3	1.8566
140	15	6	70	0.4	3	3	0.5899	195	45	6	60	0.7	3	3	1.4075
141	30	6	70	0.4	3	3	1.1811	196	60	6	60	0.7	3	3	1.9295
142	45	6	70	0.4	3	3	1.8003	197	45	6	50	0.7	3	3	1.4731
143	60	6	70	0.4	3	3	2.4584	198	60	6	50	0.7	3	3	2.0195
144	15	6	60	0.4	3	3	0.6131	199	45	6	40	0.7	3	3	1.5576
145	30	6	60	0.4	3	3	1.2275	200	60	6	40	0.7	3	3	2.1354
146	45	6	60	0.4	3	3	1.8711	201	45	6	30	0.7	3	3	1.6737
147	60	6	60	0.4	3	3	2.5549	202	15	7	70	0.4	3	3	0.6458
148	15	6	50	0.4	3	3	0.6417	203	30	7	70	0.4	3	3	1.2821
149	30	6	50	0.4	3	3	1.2847	204	60	5	90	0.7	3	3	1.1400
150	45	6	50	0.4	3	3	1.9583	205	45	7	70	0.4	3	3	1.9654
151	15	6	40	0.4	3	3	0.6785	206	60	7	70	0.4	3	3	2.6429
152	30	6	40	0.4	3	3	1.3585	207	15	7	60	0.4	3	3	0.6711
153	45	5	70	0.7	6	3	0.8800	208	30	7	60	0.4	3	3	1.3325
154	15	6	30	0.4	3	3	0.7291	209	45	7	60	0.4	3	3	1.9803
155	30	6	30	0.4	3	3	1.4598	210	15	7	50	0.4	3	3	0.7024
156	15	6	70	0.5	3	3	0.4847	211	30	7	50	0.4	3	3	1.3947
157	30	6	70	0.5	3	3	0.9921	212	45	7	50	0.4	3	3	2.0726
158	45	6	70	0.5	3	3	1.5212	213	15	7	40	0.4	3	3	0.7427
159	60	6	70	0.5	3	3	2.0806	214	30	7	40	0.4	3	3	1.4747
160	15	6	60	0.5	3	3	0.5038	215	15	7	70	0.5	3	3	0.5162
161	30	6	60	0.5	3	3	1.0311	216	30	7	70	0.5	3	3	1.0452
162	45	6	60	0.5	3	3	1.5810	217	45	7	70	0.5	3	3	1.5632
163	60	6	60	0.5	3	3	2.1623	218	60	7	70	0.5	3	3	2.1723
164	15	6	50	0.5	3	3	0.5273	219	15	7	60	0.5	3	3	0.5364
165	30	6	50	0.5	3	3	1.0792	220	30	7	60	0.5	3	3	1.0862
166	45	6	50	0.5	3	3	1.6547	221	45	7	60	0.5	3	3	1.6246
167	60	6	50	0.5	3	3	2.2632	222	60	7	60	0.5	3	3	2.2576
168	15	6	40	0.5	3	3	0.5575	223	15	7	50	0.5	3	3	0.5615
169	30	6	40	0.5	3	3	1.1411	224	30	7	50	0.5	3	3	1.1369
170	45	6	40	0.5	3	3	1.7496	225	45	7	50	0.5	3	3	1.7003
171	60	6	40	0.5	3	3	2.3930	226	60	7	50	0.5	3	3	2.3629

Table 4. Continued

Mod.	H (m)	L (m)	F'c (MPa)	D (m)	Bx (m)	By (m)	T (sec.)	Mod.	H (m)	L (m)	F'c (MPa)	D (m)	Bx (m)	By (m)	T (sec.)
227	15	7	40	0.5	3	3	0.5937	285	30	4	60	0.7	3	9	0.5080
228	30	7	40	0.5	3	3	1.2021	286	30	4	70	0.7	3	9	0.4890
229	45	7	40	0.5	3	3	1.7979	287	30	4	80	0.7	3	9	0.4730
230	60	7	40	0.5	3	3	2.4985	288	30	4	90	0.7	3	9	0.4590
231	15	7	70	0.6	3	3	0.4540	289	30	4	30	0.6	3	9	0.7140
232	30	7	70	0.6	3	3	0.9398	290	30	4	40	0.6	3	12	0.6640
233	45	7	70	0.6	3	3	1.4144	291	30	4	50	0.6	3	12	0.6280
234	60	7	70	0.6	3	3	1.9661	292	30	4	60	0.6	3	12	0.6000
235	15	7	60	0.6	3	3	0.4718	293	30	4	70	0.6	3	12	0.5780
236	30	7	60	0.6	3	3	0.9767	294	30	4	80	0.6	3	12	0.5590
237	45	7	60	0.6	3	3	1.4699	295	30	4	90	0.6	3	12	0.5420
238	60	7	60	0.6	3	3	2.0434	296	45	5	30	0.8	3	12	0.9500
239	15	7	50	0.6	3	3	0.4938	297	45	5	40	0.8	3	12	0.8800
240	30	7	50	0.6	3	3	1.0223	298	45	5	50	0.8	3	15	0.8300
241	45	7	50	0.6	3	3	1.5385	299	45	5	60	0.8	3	15	0.8000
242	60	7	50	0.6	3	3	2.1386	300	45	5	70	0.8	3	15	0.7700
243	15	7	40	0.6	3	3	0.5221	301	45	5	80	0.8	3	15	0.7400
244	30	7	40	0.6	3	3	1.0809	302	45	5	90	0.8	3	15	0.7200
245	45	7	40	0.6	3	3	1.6268	303	45	5	30	0.7	3	15	1.0900
246	60	7	40	0.6	3	3	2.2613	304	45	5	40	0.7	3	15	1.0100
247	15	7	70	0.7	3	3	0.4178	305	45	5	50	0.7	3	15	0.9600
248	30	7	70	0.7	3	3	0.8870	306	90	5	60	1.2	3	3	1.3900
249	45	7	70	0.7	3	3	1.3450	307	45	5	90	0.7	6	3	0.8300
250	60	7	70	0.7	3	3	1.8710	308	45	5	30	0.6	6	3	1.3000
251	15	7	60	0.7	3	3	0.4342	309	45	5	40	0.6	6	3	1.2000
252	30	7	60	0.7	3	3	0.9219	310	45	5	50	0.6	6	3	1.1400
253	45	7	60	0.7	3	3	1.3978	311	45	5	60	0.6	6	3	1.0900
254	60	7	60	0.7	3	3	1.9445	312	45	5	70	0.6	9	3	1.0500
255	45	5	80	0.7	6	3	0.8500	313	45	5	80	0.6	9	3	1.0100
256	15	7	50	0.7	3	3	0.4545	314	45	5	90	0.6	9	3	0.9900
257	30	7	50	0.7	3	3	0.9648	315	3	5	30	0.3	9	3	0.2440
258	45	7	50	0.7	3	3	1.4630	316	3	5	40	0.3	9	3	0.2300
259	60	7	50	0.7	3	3	2.0352	317	3	5	30	0.25	9	3	0.3300
260	15	7	40	0.7	3	3	0.4806	318	3	5	40	0.25	9	3	0.3050
261	30	7	40	0.7	3	3	1.0202	319	15	5	30	0.8	9	3	0.3000
262	45	7	40	0.7	3	3	1.5469	320	15	5	40	0.8	12	3	0.2800
263	60	7	40	0.7	3	3	2.1520	321	15	5	50	0.8	12	3	0.2600
264	90	6	70	0.8	3	3	2.7410	322	15	5	60	0.8	12	3	0.2500
265	90	6	70	0.9	3	3	2.7200	323	15	5	70	0.8	12	3	0.2400
266	90	6	80	0.9	3	3	2.6310	324	15	5	80	0.8	12	3	0.2300
267	90	6	90	1	3	3	2.5580	325	15	5	90	0.8	12	3	0.2250
268	90	6	60	0.7	3	3	2.8060	340	15	5	30	0.7	12	3	0.3400
269	90	6	90	1.2	3	3	2.5970	341	15	5	40	0.7	12	3	0.3200
270	90	6	90	1	3	3	2.5150	342	15	5	50	0.7	15	3	0.3000
271	90	4	70	0.7	3	3	2.6550	343	60	5	60	0.8	3	3	1.1100
272	90	4	50	0.7	3	3	2.9800	344	60	5	70	0.8	3	3	1.0700
273	90	4	40	0.7	3	3	3.1600	345	60	5	80	0.8	3	3	1.0300
274	90	4	40	0.6	3	6	3.1800	346	60	5	90	0.8	3	3	1.0000
275	30	4	30	0.8	3	6	0.5290	347	60	5	30	0.7	3	3	1.5000
276	30	4	40	0.8	3	6	0.4920	348	60	5	40	0.7	3	3	1.4000
277	30	4	50	0.8	3	6	0.4660	349	60	5	50	0.7	3	3	1.3200
278	30	4	60	0.8	3	6	0.4450	350	60	5	60	0.7	3	3	1.2600
279	30	4	70	0.8	3	6	0.4280	351	60	5	70	0.7	3	3	1.2200
280	30	4	80	0.8	3	6	0.4140	352	90	5	70	1.2	3	3	1.3400
281	30	4	90	0.8	3	6	0.4000	353	90	5	80	1.2	3	3	1.2900
282	30	4	30	0.7	3	9	0.6040	354	90	5	90	1.2	3	3	1.2600
283	30	4	40	0.7	3	9	0.5630	355	90	5	30	1	3	3	1.8400
284	30	4	50	0.7	3	9	0.5320	356	90	5	40	1	3	3	1.7100

Table 4. Continued

Mod.	H	L	F'c	D	Bx	By	T	Mod.	H	L	F'c	D	Bx	By	T
	(m)	(m)	(MPa)	(m)	(m)	(m)	(sec.)		(m)	(m)	(MPa)	(m)	(m)	(m)	(sec.)
357	90	5	50	1	3	3	1.6200	370	90	5	40	0.8	3	3	2.0300
358	90	5	60	1	3	3	1.5500	371	90	5	50	0.8	3	3	1.9200
359	90	5	70	1	3	3	1.4900	372	90	5	60	0.8	3	3	1.8300
360	90	5	80	1	3	3	1.4400	373	90	5	70	0.8	3	3	1.7600
361	90	5	90	1	3	3	1.4000	374	90	5	80	0.8	3	3	1.7000
362	90	5	30	0.9	3	3	1.9800	375	90	5	90	0.8	3	3	1.6500
363	90	5	40	0.9	3	3	1.8500	376	90	5	30	0.7	3	3	2.4500
364	90	5	50	0.9	3	3	1.7500	377	90	5	40	0.7	3	3	2.2800
365	90	5	60	0.9	3	3	1.6700	378	90	5	50	0.7	3	3	2.1600
366	90	5	70	0.9	3	3	1.6100	379	90	5	60	0.7	3	3	2.0600
367	90	5	80	0.9	3	3	1.5500	380	90	5	70	0.7	3	3	1.9800
368	90	5	90	0.9	3	3	1.5100	381	90	5	80	0.7	3	3	1.9200
369	90	5	30	0.8	3	3	2.1800	382	90	5	90	0.7	3	3	1.8600

4. Proposed Formula

The proposed fundamental time model in this study incorporates the main design parameters that affect the fundamental period of buildings. The considered parameters in the proposed model include buildings height, spans length and columns stiffness (size and material properties). The proposed fundamental time model is presented as:

$$T_f = \alpha_1 (H)^{\alpha_2} (L)^{\alpha_3} (f'_c)^{\alpha_4} (D)^{\alpha_5} \quad (1)$$

In which, D , f'_c and L are the column side dimension, compressive strength of the concrete and span length, respectively. The constants α_1 , α_2 , α_3 , α_4 and α_5 are the proportional factors that determined by adopting sensitive analyses on 382 modal analysis results.

5. Sensitivity Investigations

Sensitivity analyses are conducted to evaluate the effect of different design parameters on the vibration period of the building models. The sensitivity investigations are conducted considering the numerical results of 382 models of RC MRF buildings presented in this study. The parameters that considered in this study are illustrated in Table 4. The results of the sensitivity analyses are presented in the following subsections.

5.1. Effect of Buildings Height

A relation between the building height and the fundamental period of the buildings was presented in which the best fit curve was obtained and illustrated in Fig. 5. The fundamental time period to building height relation becomes;

$$T_f = 0.0537 H^{0.828} \quad (2)$$

Fig. 5 shows that the vibration period T_f is directly proportional to the height of the building with a power of 0.828. In comparison with previous simple models, it is shown that equation 2 is closest to the model specified by FEMA [3] that presented in Table 1.

5.2. Effect of Span Length

To investigate the effect of span length L on the vibration period of the buildings, the vibration periods are normalized by $(H^{0.828})$ to exclude the effect of building height. The resulted normalized vibration period is given by;

$$T_{f1} = T_f / H^{0.828} \tag{3}$$

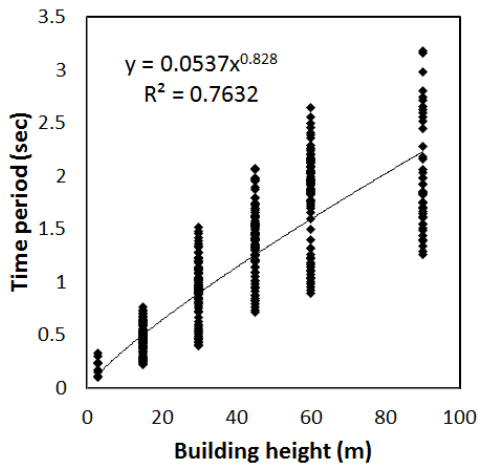


Fig. 5 Varying the fundamental period of the buildings with building height

Fig. 6 shows that the normalized vibration period T_1 increased with increasing span length with a power of 0.55.

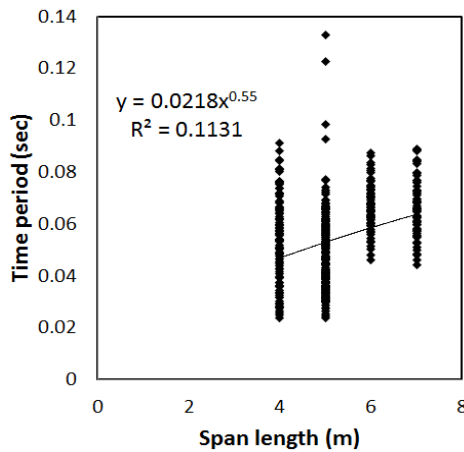


Fig. 6 Varying the normalized fundamental period of the buildings with spans length

5.3. Effect of Members Elasticity

In modeling reinforced concrete members, the elasticity of concrete is considered for defining members elasticity in which it is directly proportional to compressive strength of the concrete. In order to investigate the effect of concrete compressive strength on the vibration period of the buildings, the vibration periods (T_{f1}) are normalized by ($L^{-0.55}$) to exclude the effect of column size. The resulted normalized vibration period is given by;

$$T_{f2} = T_{f1} / L^{-0.55} \tag{4}$$

Fig. 7 shows that the normalized vibration period T_{f2} decreased with increasing compressive strength with a power of - 0.358.

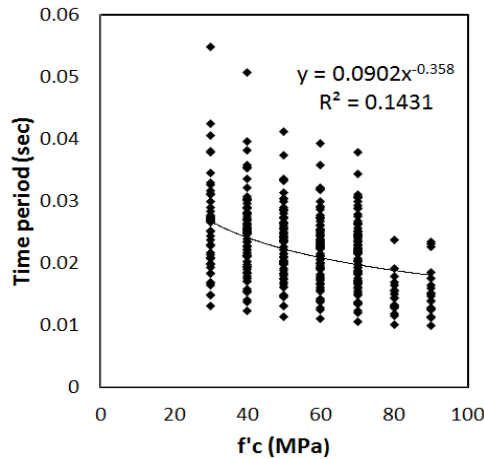


Fig. 7 Varying of normalized fundamental period of the buildings with concrete compressive strength

5.3 Effect of Columns Size

To investigate the effect of columns size on the vibration period of the buildings, the vibration periods (T_{f2}) are normalized by ($f'_c{}^{-0.358}$) to eliminate the effect of concrete compressive strength. The resulted normalized vibration period is given by;

$$T_{f3} = \frac{T_{f2}}{f'_c{}^{-0.358}} \tag{5}$$

Fig. 8 shows that the normalized vibration period T_{f3} decreased with increasing columns size with a power of - 0.665.

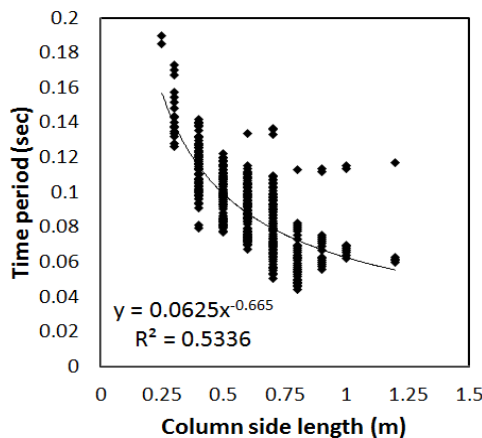


Fig. 8 Varying of normalized fundamental period of the buildings with columns size

5.4 Proportional Factor α_1

The obtained powers 0.828, 0.55, -0.358 and -0.665 of the parameters H, L, f'_c and D, respectively that obtained from curves of Figs. 5-8 are substituted in equation 1 in which becomes;

$$T_{f4} = \alpha_1 (H)^{0.828} (L)^{0.55} (f'_c)^{-0.358} (D)^{-0.665} \tag{6}$$

In order to obtain the value of the coefficient α_1 , a relation between numerical period T_f and T_{f4} is presented in which the best fit curve is obtained. A value of 0.0314 for the coefficient α_1 and a normalized period with a power of 1.2459 are obtained with R^2 equal to 0.953. By substituting the coefficient α_1 and refining equation 6 by multiplying the parameters powers by the obtained new power from Fig. 9 resulted in new powers for parameters H, L, D and f'_c that equals to 1.032, 0.69, -0.83 and -0.45, respectively. Substituting the new powers in equation 1 resulted in;

$$T_f = 0.0314 (H)^{1.023} (L)^{0.69} (f'_c)^{-0.45} (D)^{-0.83} \tag{7}$$

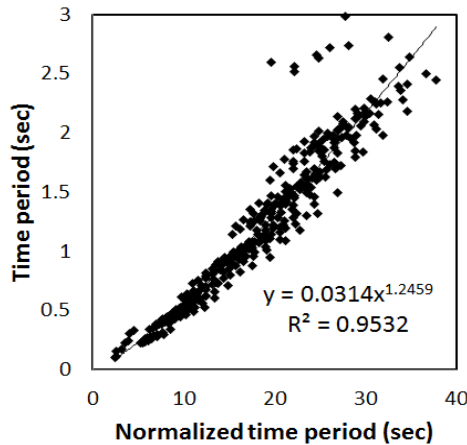


Fig. 9 Varying of fundamental period of the buildings with normalized time period

6. Validation of the Proposed Model

The calculated fundamental period using the developed simple equation is verified against the results of modal analysis of the 382 numerical models of buildings. Verification results in terms of the ratio of proposed model to modal analysis predictions demonstrated very good performance of the developed model. A mean value of the prediction's ratio (proposed model predictions to modal analysis predictions) equal to 1.00 ± 0.15 and a coefficient of variation of 15.38 are obtained. On the other hand, statistical measures are compared with those corresponding to predictions using the models available in the literature as illustrated in Table 5. It is obvious that the proposed model results in the most accurate predictions compared with other models as it provides the least standard of deviation and coefficient of variation as well as the closest results between the modal analysis and model predictions.

Additional ten models were considered for comparison in which haven't used in the sensitivity analyses and verification of the developed model. Table 6 illustrates the comparison results of the predicted fundamental vibration period of the ten models by using modal analysis and the proposed model. Comparison results have demonstrated very good agreement between the predictions using the proposed model and the modal analysis. The mean value of the proposed model to modal analysis ratio of 1.00 ± 0.12 and a coefficient of variation of 11.79 were obtained.

Table 5. Comparison of the predicted fundamental periods using the proposed model and other available models

Researcher	Mean	St. Deviation	CoV %
ASCE/SEI 7-16 [1]	0.936	0.289	30.89
Eurocode 8 [2]	0.991	0.290	29.22
FEMA 450 [3]	0.832	0.257	30.89
Hong and Hwang [6]	1.462	0.453	31.01
Michel et al. [43]	2.366	0.834	35.25
Chiauzzi et al. [7]	1.938	0.565	29.17
Guler et al. [8]	1.677	0.518	30.89
Velani and Ramancharla [11]	2.424	1.029	42.45
Inel et al. [9]	2.075	0.605	29.17
Proposed model	1.00	0.155	15.38

Table 6. Comparison of the predicted fundamental periods using the proposed model and numerical modal analysis

Span (m)	Col. width (m)	f'_c (MPa)	Building Height (m)	Time period		
				Modal analysis	Proposed model	Prop. /Modal
4	0.4	30	30	1.1089	1.2317	1.1108
4	0.4	50	30	0.9760	0.9788	1.0029
4	0.4	70	30	0.8972	0.8412	0.9376
4	0.6	70	30	0.7301	0.6008	0.8230
5	0.4	30	30	1.2845	1.4367	1.1185
5	0.5	70	30	0.8851	0.8154	0.9213
6	0.4	30	30	1.4598	1.6293	1.1162
6	0.4	70	30	1.1811	1.1128	0.9422
7	0.5	70	30	0.8870	1.0284	1.1595
7	0.7	70	45	1.3450	1.1782	0.8760
Mean						1.00
St. Deviation						0.12
CoV %						11.79

7. Conclusions

Fundamental vibration period of buildings is an essential factor for the analysis and design of buildings subjected to lateral loads. Design codes and standards recommended either conducting modal analysis on numerical models or using a specified simple formula that relates the fundamental vibration period to either building height or number of floors. The specified formulas by design standards and guidelines to predict the fundamental vibration period of buildings were empirically derived based on limited actual records of buildings vibration in different regions around the world. In contrast, modal analyses entail careful and time consuming numerical modelling process that include defining specific design parameters. The aim of this study is to propose a simple but more accurate model to estimate fundamental vibration period of reinforced concrete moment frame buildings. The first part of this study includes collecting some of the published recorded vibration period of buildings in different regions in the world. Some of the collected records were adopted by previous researcher in regression analyses for developing vibration time to building height relations. Also, several simple models available in the literature were explored. The collected data were compared with predictions of the available models in which shows large scatters in actual building vibrations compared to the estimations of the simple formulas. Also, investigations show different and diverse

estimations of vibration periods using the available simple models. The large discrepancy between predictions using different model and the large scatters of actual values compared with empirical predictions stem from neglecting the main design parameters in the developed models. In this paper, fundamental periods of moment frame buildings have extensively investigated considering 382 building models by using numerical modal analyses. A sensitivity analysis considering the modal analysis results is conducted in which a model is developed to estimate the fundamental period of the buildings considering the main influencing design parameters. The main design parameters include building height, spans length, members stiffness. Then, the effect of each design parameter is evaluated using sensitivity analyses in which assist in developing the proposed model. Sensitivity analysis showed that fundamental vibration period was directly proportional to the height of the building and span length with powers equal to 1.032 and 0.69, respectively. On the other hand, the fundamental period was inversely proportional to the lateral size of the columns and compressive strength of the concrete with powers equal to 0.83 and 0.45, respectively. Finally, a simple model is proposed based on modal analyses results and considering the effect of main design parameters. The proposed model is validated against modal analysis results of the 382 numerical models of buildings in which results in modal analysis to proposed model ratio equal to 1.00 ± 0.155 with coefficient of variation of 15.38. Additional ten models haven't used in the sensitivity analyses and verification of the developed model shows mean value of the proposed model to modal analysis ratio equal to 1.00 ± 0.12 and a coefficient of variation of 11.79. Also, the predictions of the proposed model were compared with the predictions of the available simple models and showed the most accurate results. Accordingly, adopting the developed model by practicing engineers rather than using simple models or complex modal analysis for predicting time of fundamental vibration provides efficient solution.

Acknowledgement

The author acknowledges that the research described in this paper was unfunded by any organization, institutions or people.

References

- [1] ASCE/SEI 7-22. Minimum Design Loads and Associated Criteria for Buildings and Other Structures.
- [2] Eurocode 8: Design of structures for earthquake resistance - Part 1 : General rules, seismic actions and rules for buildings. Eur Comm Stand 2004.
- [3] FEMA 450. NEHRP Recommended Provisions for Seismic Regulations for New Buildings and Other Structures. Part 1 2003:338.
- [4] Goel RK, Chopra AK. Period Formulas for Moment-Resisting Frame Buildings. J Struct Eng 1997;123:1454-61. [https://doi.org/10.1061/\(ASCE\)0733-9445\(1997\)123:11\(1454\)](https://doi.org/10.1061/(ASCE)0733-9445(1997)123:11(1454))
- [5] Salama MI. Estimation of period of vibration for concrete moment-resisting frame buildings. HBRC J 2015;11:16-21. <https://doi.org/10.1016/j.hbrj.2014.01.006>
- [6] Hong LL, Hwang WL. Empirical formula for fundamental vibration periods of reinforced concrete buildings in Taiwan. Earthq Eng Struct Dyn 2000;29:327-37. [https://doi.org/10.1002/\(SICI\)1096-9845\(200003\)29:3<327::AID-EQE907>3.0.CO;2-0](https://doi.org/10.1002/(SICI)1096-9845(200003)29:3<327::AID-EQE907>3.0.CO;2-0)
- [7] Chiauzzi L, Masi A, Mucciarelli M, F CJ. Estimate of fundamental period of reinforced concrete buildings: code provisions vs. experimental measures in Victoria and Vancouver (BC, Canada) Hazards View project RINTC-Implicit seismic risk of code-conforming Italian buildings View project Estimate o. vol. 3033. 2012.

- [8] Guler K, Yuksel E, Kocak A. Estimation of the fundamental vibration period of existing RC buildings in Turkey utilizing ambient vibration records. *J. Earthq. Eng.*, vol. 12, Taylor & Francis; 2008, p. 140-50. <https://doi.org/10.1080/13632460802013909>
- [9] Inel M, Ozmen HB, Cayci BT. Determination of period of RC buildings by the ambient vibration method. *Adv Civ Eng* 2019;2019. <https://doi.org/10.1155/2019/1213078>
- [10] Kaplan O, Guney Y, Dogangun A. A period-height relationship for newly constructed mid-rise reinforced concrete buildings in Turkey. *Eng Struct* 2021;232:111807. <https://doi.org/10.1016/j.engstruct.2020.111807>
- [11] Velani PD, Ramancharla PK. New Empirical Formula for Fundamental Period of Tall Buildings New Empirical Formula for Fundamental Period of Tall. 16th World Conf. Earthq. Eng., 2017.
- [12] Velani PD, Kumar RP. Approximate natural period expression for reinforced concrete tall buildings in India. *Curr Sci* 2023;124:1412.
- [13] Jalali A, Salem Milani A. Fundamental periods of buildings measured from ambient vibration measurements. 2005 World Sustain. Build. Conf., vol. 2729, 2005, p. 2577-84.
- [14] Gallipoli MR, Mucciarelli M, Šket-Motnikar B, Zupančić P, Gosar A, Prevotnik S, et al. Empirical estimates of dynamic parameters on a large set of European buildings. *Bull Earthq Eng* 2010;8:593-607. <https://doi.org/10.1007/s10518-009-9133-6>
- [15] Al-Nimry H, Resheidat M, Al-Jamal M. Ambient vibration testing of low and medium rise infilled RC frame buildings in Jordan. *Soil Dyn Earthq Eng* 2014;59:21-9. <https://doi.org/10.1016/j.soildyn.2014.01.002>
- [16] Pan TC, Goh KS, Megawati K. Empirical relationships between natural vibration period and height of buildings in Singapore. *Earthq Eng Struct Dyn* 2014;43:449-65. <https://doi.org/10.1002/eqe.2356>
- [17] Oliveira CS, Navarro M. Fundamental periods of vibration of RC buildings in Portugal from in-situ experimental and numerical techniques. *Bull Earthq Eng* 2010;8:609-42. <https://doi.org/10.1007/s10518-009-9162-1>
- [18] Aninthaneni PK, Dhakal RP. Prediction of fundamental period of regular frame buildings. *Bull New Zeal Soc Earthq Eng* 2016;49:175-89. <https://doi.org/10.5459/bnzsee.49.2.175-189>
- [19] Kose MM. Parameters affecting the fundamental period of RC buildings with infill walls. *Eng Struct* 2009;31:93-102. <https://doi.org/10.1016/j.engstruct.2008.07.017>
- [20] Ricci P, Verderame GM, Manfredi G. Analytical investigation of elastic period of infilled RC MRF buildings. *Eng Struct* 2011;33:308-19. <https://doi.org/10.1016/j.engstruct.2010.10.009>
- [21] Asteris PG, Repapis CC, Tsaris AK, Di Trapani F, Cavaleri L. Parameters affecting the fundamental period of infilled RC frame structures. *Earthq Struct* 2015;9:999-1028. <https://doi.org/10.12989/eas.2015.9.5.999>
- [22] Perrone D, Leone M, Aiello MA. Evaluation of the infill influence on the elastic period of existing RC frames. *Eng Struct* 2016;123:419-33. <https://doi.org/10.1016/j.engstruct.2016.05.050>
- [23] Al-Balhawi A, Zhang B. Investigations of elastic vibration periods of reinforced concrete moment-resisting frame systems with various infill walls. *Eng Struct* 2017;151:173-87. <https://doi.org/10.1016/j.engstruct.2017.08.016>
- [24] Soni P, Sangamnerkar P, Dubey SK. Analysis of natural time period of moment resisting frame buildings. *AIP Conf. Proc.*, vol. 2158, AIP Publishing LLC; 2019, p. 20016. <https://doi.org/10.1063/1.5127140>
- [25] Crowley H, Pinho R. Period-height relationship for existing European reinforced concrete buildings. *J Earthq Eng* 2004;8:93-119. <https://doi.org/10.1080/13632460409350522>
- [26] Crowley H, Pinho R. Simplified equations for estimating the period of vibration of existing buildings. *Proc 1st Eur Conf ...* 2006;3:3-8.

- [27] Amanat KM, Hoque E. A rationale for determining the natural period of RC building frames having infill. *Eng Struct* 2006;28:495-502. <https://doi.org/10.1016/j.engstruct.2005.09.004>
- [28] Rimal JC, Maskey PN. Fundamental Time Period of RC Moment Resisting Frames. *Proc. IOE Grad. Conf.*, 2019.
- [29] Koçak A, Borekci M, Zengin B. Period formula for RC frame buildings considering infill wall thickness and elasticity modulus. *Sci Iran* 2018;25:118-28..
- [30] Kewate SP, Murudi MM. Empirical Period-Height Relationship for reinforced Concrete Moment Resisting Buildings in India. *IOP Conf. Ser. Mater. Sci. Eng.*, vol. 481, IOP Publishing; 2019, p. 12018. <https://doi.org/10.1088/1757-899X/481/1/012018>
- [31] Verderame GM, Iervolino I, Manfredi G. Elastic period of sub-standard reinforced concrete moment resisting frame buildings. *Bull Earthq Eng* 2010;8:955-72. <https://doi.org/10.1007/s10518-010-9176-8>
- [32] Mohamed AN, El Kashif KF, Salem HM. An Investigation of the Fundamental Period of Vibration for Moment Resisting Concrete Frames. *Civ Eng J* 2019;5:2626-42. <https://doi.org/10.28991/cej-2019-03091438>
- [33] Joshi SG, Londhe SN, Kwatra N. Determination of natural periods of vibration using genetic programming. *Earthq Struct* 2014;6:201-16. <https://doi.org/10.12989/eas.2014.6.2.201>
- [34] Hadzima-Nyarko M, Nyarko EK, Morić D, Draganić H. New Direction Based (Fundamental) Periods of RC Frames Using Genetic Algorithms. *15 World Conf. Earthq. Eng.*, vol. 15, 2012.
- [35] Asteris PG, Tsaris AK, Cavaleri L, Repapis CC, Papalou A, Di Trapani F, et al. Prediction of the fundamental period of infilled rc frame structures using artificial neural networks. *Comput Intell Neurosci* 2016;2016. <https://doi.org/10.1155/2016/5104907>
- [36] Al-Balhawi A, Zhang B. Investigations of elastic vibration periods of tall reinforced concrete office buildings. *Wind Struct An Int J* 2019;29:209-23.
- [37] Noor SM, Halim NSM, Ibrahim A, Majid TA, Hassan SH. Fundamental period of vibrations influencing characteristics of torsional irregularity in reinforced concrete buildings. *IOP Conf. Ser. Earth Environ. Sci.*, vol. 244, IOP Publishing; 2019, p. 12021. <https://doi.org/10.1088/1755-1315/244/1/012021>
- [38] Sharma N, Dasgupta K, Dey A. Natural period of reinforced concrete building frames on pile foundation considering seismic soil-structure interaction effects. *Structures*, vol. 27, Elsevier; 2020, p. 1594-612. <https://doi.org/10.1016/j.istruc.2020.07.010>
- [39] Gravett DZ, Mourlas C, Taljaard V-L, Bakas N, Markou G, Papadrakakis M. New fundamental period formulae for soil-reinforced concrete structures interaction using machine learning algorithms and ANNs. *Soil Dyn Earthq Eng* 2021;144:106656. <https://doi.org/10.1016/j.soildyn.2021.106656>
- [40] Ruggieri S, Fiore A, Uva G. A new approach to predict the fundamental period of vibration for newly-designed reinforced concrete buildings. *J Earthq Eng* 2022;26:6943-68. <https://doi.org/10.1080/13632469.2021.1961929>
- [41] Mirrashid M, Naderpour H. Computational intelligence-based models for estimating the fundamental period of infilled reinforced concrete frames. *J Build Eng* 2022;46:103456. <https://doi.org/10.1016/j.jobe.2021.103456>
- [42] Csi. ETABS Integrated Software for Structural Analysis and Design. *Comput Struct Inc, Berkeley, CA, USA* 1995:1-74.
- [43] Michel C, Guéguen P, Lestuzzi P, Bard PY. Comparison between seismic vulnerability models and experimental dynamic properties of existing buildings in France. *Bull Earthq Eng* 2010;8:1295-307. <https://doi.org/10.1007/s10518-010-9185-7>
- [44] Ditommaso R, Vona M, Gallipoli MR, Mucciarelli M. Evaluation and considerations about fundamental periods of damaged reinforced concrete buildings. *Nat Hazards Earth Syst Sci* 2013;13:1903-12. <https://doi.org/10.5194/nhess-13-1903-2013>



Review Article

The evaluation of behavior of geopolymer reinforced concrete and conventional reinforced concrete beams: A critical review

Banu D. Handono^a, Ronny E. Pandaleke^b, Reynaldo J. Sela^c, Dody M.J. Sumajouw^{*d}, Steenie E. Wallah^e, Servie O. Dapas^f, Reky S. Windah^g

Department of Civil Engineering, Sam Ratulangi University, Manado, Indonesia

Article Info

Abstract

Article history:

Received 26 Mar 2023

Accepted 19 Jun 2023

Keywords:

Reinforced beams;
Conventional concrete;
Geopolymer;
Deflection;
Ductility

As concrete technology has evolved, Geopolymer Concrete (GPC) has emerged as an ecologically friendly material compared to Ordinary Portland Cement (OPC) concrete, which has several complex environmental impacts. Without using OPC, which is typically used as a binder, the GPC has been developed. The base constituent material of GPC, like fly ash, is used to produce binder for geopolymer-reinforced concrete as an alternative. In building construction, the most frequently used component of the reinforced concrete element is a beam made by combining OPC concrete and steel reinforcement. This research involves a critical investigation of the bending behavior of control beams made of conventional reinforced concrete (CRC) and geopolymer reinforced concrete (GRC) beams. This critical review intentions to clarify how to differentiate a flexural behavior between GRC and CRC beams. Data from different experimental studies, which are divided into five parameters namely cracks and failure patterns, failure loads, load and deflection relationships, deflections, and ductility, provide the basis for the research. The results of the analytical review support the claim that the flexural behavior of the two beams exhibits similarities, and is quite typical. Therefore, it is possible to analyze and design GRC beams using the theory and standards used by CRC beams.

© 2023 MIM Research Group. All rights reserved.

1. Introduction

Concrete remains a dominant material that cannot be separated from the construction industries. It is a versatile and proven construction material, capable of being utilized in various forms and finishes. When considering concrete for construction purposes, it is crucial to take into account its ease of use, durability, and simplicity of production. However, past research indicates that the global man-made carbon dioxide (CO₂) released from the cement sector is approximately 8% of the overall. This is because producing OPC emits one ton of CO₂ into the atmosphere. Roughly 3.75 billion tons of OPC were manufactured worldwide in 2013 alone. It is projected that by 2050, an additional 4.4 billion tons of CO₂ will be released into the atmosphere due to the expected growth in cement consumption and production globally [1]. Therefore, there is a need to explore alternative binders for making concrete because the production of OPC contributes significantly to CO₂ emissions.

Initially, the mineral admixture is employed with positive outcomes as a partial replacement for cement. To create environmentally friendly concrete, a variety of industrial waste materials, including fly ash, are utilized to replace OPC [2]. The utilization

*Corresponding author: dody_sumajouw@unsrat.ac.id

^a orcid.org/0009-0003-3805-0388; ^b orcid.org/0009-0007-4232-642x; ^c orcid.org/0009-0005-2993-0177;

^d orcid.org/0000-0002-0135-6389; ^e orcid.org/0000-0001-5989-9581; ^f orcid.org/0009-0002-6482-8504;

^g orcid.org/0009-0001-1532-8039

DOI: <http://dx.doi.org/10.17515/resm2023.719st0326>

Res. Eng. Struct. Mat. Vol. 9 Iss. 4 (2023) 1433-1457

of fly ash in GPC, a less conventional type of concrete, is a relatively recent advancement in concrete technology. Apart from fly ash, GPC is produced using waste materials for example ceramic waste, clay, kaolin, blast furnace slag, palm oil clinker, rice husk ash, agricultural waste, and lime-based natural resources. For instance, Kaya, M [3] made GPC by combining powdered ceramic with Sodium Hydroxide (NaOH) and Sodium Silicate (Na_2SiO_3). Consequently, the application of industrial by-product materials in GPC is considered a viable environmentally friendly solution for future construction and building materials [4].

Davidovits [5] used the term "Geopolymer" to characterize a group of mineral binders based on silicoaluminates. In GPC, a single raw material or a mixture of various precursor materials can be utilized for polymerization [6]. Generally, alkaline activators are used to generate a geopolymer gel out of the silica and alumina that are already present in the source materials. Furthermore, the unreacted constituents and loose aggregates in the mixture are bonded together by the geopolymer gel that generates the GPC. Sodium or potassium silicate and sodium or potassium hydroxide have frequently been used as alkaline activators [7, 8, 9, 10, 11]. Additionally, sodium sulfate (Na_2SO_4) and sulfuric acid (H_2SO_4) were both present in the solution at 5% and 2% mass concentrations, respectively [12, 13, 14]. Polymeric Si-O-Al-O linkages in an amorphous form are generated by a chemical reaction on Si-Al minerals under highly alkaline circumstances. Additionally, the geopolymer material is said to have great fire resistance [15], and even in the presence of significant alkalinity, the alkali-aggregate interaction does not occur [5].

The novelty studies on making GPC are the utilization of low calcium Class F fly ash conducted by several experimental studies [16-23]. Additionally, the variables influencing the characteristics of geopolymers have been encountered by a number of research, as reported by Davidovits [24, 25, 26], for example geopolymer material achieves a compressive strength of 20 MPa, and between 70 and 100 MPa at the end of a 28-day curing period. Besides, fresh geopolymer is often cured at elevated temperatures because heat accelerates chemical processes. The mechanical strength is discovered to be significantly influenced by the curing time and form of activators [7, 9, 26]. Compressive strength increases dramatically while curing at 60°C for 24 hours, resulting in a range of 47 to 53 MPa at one day [36]. Higher curing temperatures and longer curing times often provide materials with higher compressive strengths, but care must be made to prevent water loss during elevated temperatures curing. Though, using calcined raw materials of pure geological origin, such as metakaolin curing at ambient temperatures has been achieved successfully [5, 6, 8, 9, 10, 11, 25].

Even though fly ash-based geopolymers' mechanical strength is found to be significantly influenced by the curing time and variety of activators, the test findings from various investigations reveal that GPC cured at room temperature also produces results that are equivalent to those of heat curing [27-31]. GPC may reach its optimum 28-day strength at room temperature when slag or OPC material is added [32-36], and it can reach high strength at an earlier age when exposed to increased curing temperatures. The improved polymerization-induced intrinsic structure is what led to the improvement in physical characteristics [37, 38].

Despite having a higher tensile strength than OPC, GPC's behavior is still depending on the steel bars bonding and concrete. An important consideration for assessing the material's structural performance is the strength of bonding between the longitudinal reinforcement and the concrete. Because of its increased tensile strength, GPC exhibits a better bonding strength to the reinforcement [39-41]. The existing design formulas for bonding strength between reinforcement bars and CRC can still be applied to GPC since the failure behavior of GPC and CRC is similar [39-41]. Additionally, test results indicate that the GPC water

content mixture, expressed as the water-to-geopolymer solid ratio, significantly affects its compressive strength [42]. Furthermore, fresh geopolymer concrete may be handled for roughly 120 minutes without showing signs of setting and without reducing compressive strength [43]. Furthermore, the results of the experiments reveal that GPC has reduced creep [44]. Overall, fly ash-based GPC is very essential for building and construction, as a renewable cement substitute for green material [45]. This is because the usage of GPC may decrease the amount of CO₂ produced during the manufacture of OPC. The environmental harm carried on by the construction industry's CO₂ emissions could be minimized as a result of this.

Reinforced concrete beams play a vital role in supporting the loads in the building by withstanding them. The ability of the beam to resist failure under bending is referred to as flexural bending. To gain a deeper understanding of how beams behaves under bending, it is important to thoroughly comprehend five key parameters namely cracks and failure patterns, failure loads, load and deflection relationships, deflections, and ductility. These parameters are of utmost significance, and are commonly utilized by researchers to investigate the behavior of beams during bending. The reviewed study thoroughly examines and compares these parameters to enhance our understanding of how beams respond when is subjected to bending.

Previously, the investigation of reinforced GRC structural element behavior had received limited attention until a research team at Curtin University in Australia initiated a study on this topic [46-51]. Their research specifically focused on understanding the behavior of fly ash-based GRC structural members. Following this pioneering work, numerous studies on GRC structural members have been conducted and continue to be pursued.

Kumaravel et al. [52] examined the bending behavior of CRC control beams and GRC beams. The specimens were cast over an actual span of 3.200 mm, and they were put through monotonous load testing until failure. The beams were only supported, and they must withstand two concentrated loads that were distributed symmetrically across the beam span. Both types of beams' load with displacement responses were predicted through numerical analysis using the FEA software ANSYS. To compare with the theoretical findings, the displacement responses of the GRC and CRC beams were measured. The outcomes demonstrated greater flexural strength in the GRC beams. It was also found that the deflections at different stages were higher for GRC beams.

Furthermore, to evaluate the mechanical characteristics of GRC beams with CRC beams of equivalent grade, Abraham et al. [53] conducted experimental investigations. In this study, twenty beams, twelve GRC beam specimens, and eight CRC beam specimens were taken into consideration. All specimens were evaluated under two-point loads and were made with tensile reinforcement ratios of 0.55%, 0.83%, 1.02%, and 1.3%. Both kinds of beams' failure modes and the mechanical characteristics, such as load capacity, ultimate load, deflection, moment-curvature, first fracture load, crack width, and spacing, were examined. The test results show that when related to CRC beams of the same grade, GRC beams have better mechanical properties. This might be because the geopolymer paste bonds better than cement paste.

Dattatreya et.al [54] investigated the behavior of GRC beams. A total of 18 GRC beams, cured at room temperature, experienced flexure testing. The longitudinal reinforcement ratio was from 82 to 110 percent of the balanced condition, and the beam's dimensions were 100x150x1500 mm. All examples underwent two-point static loading testing. According to the report, the GRC beams' typical service loads were 12% lower than those of the CRC beams. The number, spacing, and width of the cracks, as well as the failure modes, were noted in the cracking patterns. With CRC beams, all produced essentially the same outcomes. The test results and the standard equations given by code to calculate the

cracking and ultimate moment, and maximum deflection demonstrated a reasonable relationship even though they were not identical in all aspects.

Additionally, an experimental study on the short-term mechanical characteristics and flexural behavior of GRC and CRC beams was taken by Ojha, P.N., et al [55]. Geopolymer concrete with slag-fly ash based was used to make the GRC beams. It was discovered that GRC beams had short-term mechanical properties that were comparable to those of CRC beams in terms of flexural strength. Despite this, the modulus elasticity of the GRC beam was lower than the CRC beams for comparable strength. Moreover, this study demonstrated that both types of beams display comparable load-deflection relationships, yield loads, and yield moments. It was also determined, based on the noticeable cracks which were developed along the beam span, that the GRC beams and CRC beams exhibited a comparable quantity and type of cracks in flexure.

Also, in a study [56], fly ash was used in place of cement to a whole extent. By constructing a physical model in the form of reinforced concrete beams, laboratory testing was carried out. The structural beams with dimensions of 150x350 mm with a 4000 mm span were made to test the strength of GRC and CRC beams. ACI 437.1R-07 was followed while testing structural beams, and the outcomes of the laboratory tests were then contrasted with those of the theoretical analysis. Based on the test result, it was discovered that the strength of beams formed by GRC was practically identical to that of CRC. However, the findings of the theoretical analysis were lower than the structural capacity test results of both GRC and CRC beams.

Furthermore, Laskar et al. [57] found that GRC beams outperformed CRC beams in terms of capacity when subjected to cyclic loading effects. Compared to CRC beams, the GRC beams' capacity had increased by almost 30%. The GRC beams also demonstrated a slower rate of stiffness deterioration over time. The test findings also revealed that the GRC beams were about 45% more capable of dissipating energy than the CRC beams. This fact implies that the GRC beams can withstand earthquakes more effectively than the CRC beams.

The purpose and importance of this critical review are that it is essential to comprehend the distinction between pure bending and non-uniform bending of the GRC beams. In contrast to CRC beams, GRC beams have unique processes for the development of strength. Therefore, before using GRC beams in buildings for applications, the existing approaches for the analysis and design of GRC beams must be examined and confirmed with existing codes and standards applied for CRC beams.

2. Flexural Behavior of Conventional Reinforced Concrete (CRC) Beams

The loads acting on the beams result in deformational strain caused by the flexural stresses due to the externally applied load [58]. When the load is increased, a supplementary strain and deflection are continuously added to the beam, which causes additional deformation and strain resulting from flexural cracks along the span of the beam. Additional increases in the level of the load initiate failure of the beam. When the load reaches the beam's capacity, more cracks propagate along the beam. In such a situation eventually, the beam has no acceptable safety and reserve strength to support the applied load, and it can finally lead to the results of beam failure.

2.1. Failure Loads

The beam is expected to fail because it lacks the required safety and reserve strength to withstand the applied load. The failure modes of the CRC beam, as shown in Figure 1, can be grouped into three conditions namely the Balanced condition, Over-reinforced condition, and Under-reinforced condition [58]. These conditions are explained as follows:

- In the balanced condition, a beam section under flexure is considered to fail when the concrete strain exceeds the failure strain in bending compression, which is typically equal to 0.003. At this point, the tensioned steel reaches its yield strain simultaneously that the concrete experiences failure strain.
- In the over-reinforced condition, the beam sections of reinforced concrete have an excess of reinforcement. In such cases, the failure occurs in the concrete before the steel reinforcement reaches its yield strain. If these beams are constructed and loaded to their maximum capacity, the tensioned steel will not yield significantly until the concrete achieves its maximum strain of 0.003.
- In the under-reinforced condition, the beam section refers to the situation where steel reinforcement in a reinforced concrete section fails by yield before the occurrence of concrete failure. The yielding of steel reinforcement indicates failure, and it occurs at loads smaller compared to those at which the concrete approaches its failure strain.

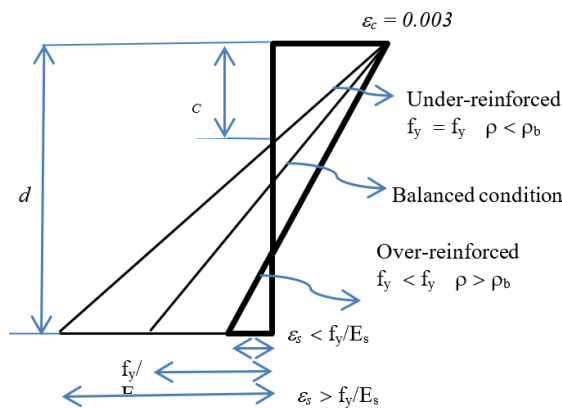


Fig. 1 Cross-section strain distribution [58]

2.2. Load and Deflection Relationship

A load-deflection relationship of CRC beams can be essentially idealized into a trilinear shape. The best possible load-deflection curve for mid-span beams is depicted in Figure 2. These occurrences are identified in the sequence as follows: initial cracking at point A, tensile reinforcing yielding at point B, crushing of concrete in the compression zone accompanied spalling of concrete cover at point C, and failure of the concrete compression zone due to reinforcement steel buckling at point D. Such sequential points are typical CRC beam flexural characteristics [59].

Three regions for the distinctive relationship of load-deflection for CRC beam are explained in three regions that are Pre-crack level (region I), Post-crack load level (region II), and Post serviceability crack level (region III) [59].

2.3. Crack and Failure Pattern

The type of failure that occurs in the beam structural elements depends on the cross-sectional stiffness (EI) of the beams. Flexural failure, shear compression failure, and diagonal tension failure are the three types of failure [58]. The type of failure for all literature on this study is considered a flexural failure.

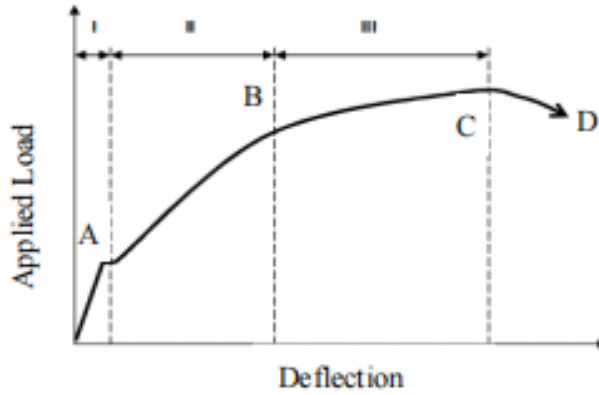


Fig. 2 Relationship between Load-Deflection for CRC Beam [59]

2.4. Deflection

The most essential aspect of reinforced concrete beams is the deflection problem. If the beam has a long span, the value of the deflection will also be large, and to reduce the deflection is usually by increasing the cross-sectional stiffness (EI). Mechanically the relationship of deflection (v), cross-sectional strength (EI), and bending moment (M) is:

$$\frac{d^2v}{dx^2} = \frac{M}{EI} \tag{1}$$

Using the differential equation, the deflection for a beam supported by simple supports with the load (P) at the middle of the beam mid-span is:

$$\delta = v_{max} = \frac{PL^3}{48 \times EI} \tag{2}$$

The maximum amount of deflection that occurs as a result of uniform load (q) and concentrated load (P) can be specified by using equation (3).

$$\delta = \frac{5}{384} q \frac{L^4}{EI} + \frac{Pa}{48EI} (3L^2 - 4a^2) \tag{3}$$

2.5. Ductility

Ductility behavior due to loading on the beam with a load exceeding the ultimate load can be illustrated in Figure 3 [59]. The difference between brittle and ductile behavior can be seen in contrast.

The ratio of maximum to yield deflection, stated by the following equation, can be used to quantitatively estimate the ductility of a beam:

$$\mu_d = \frac{\Delta_u}{\Delta_y} \tag{4}$$

where:

- μ_d = ductility of beam
- Δ_u = maximum deflection
- Δ_y = yield deflection

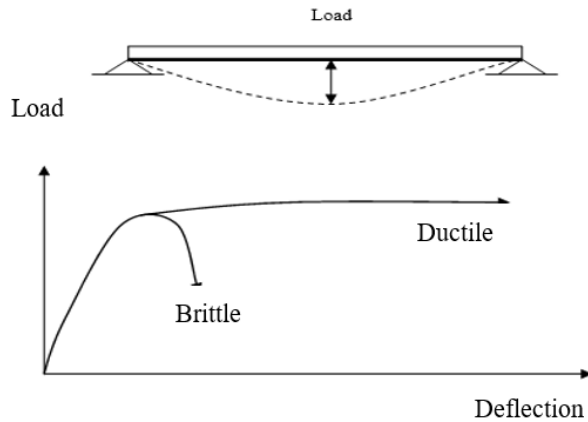
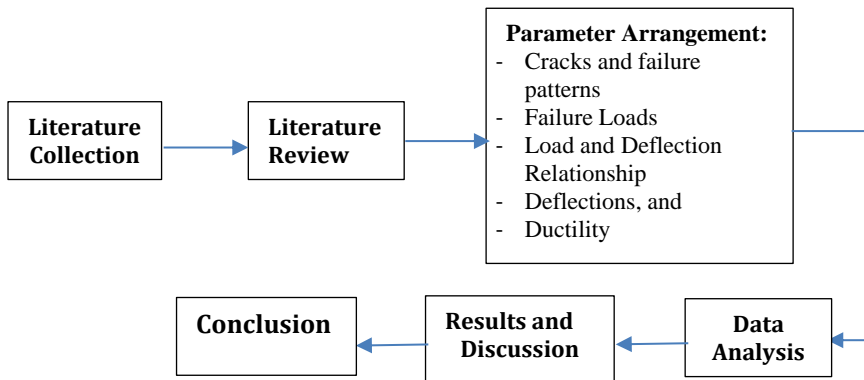


Fig. 3. Deflection Behavior Due to Loading

3. Methodology

In this study, the critical review is conducted based on data from various experimental studies which are grouped into five parameters, namely cracks and failure patterns, failure loads, load and deflection relationships, deflections, and ductility from both types of beams. The most significant indicator for comprehending the bending behavior of beams is understanding those five parameters. The study's progress is displayed as follows:



3.1. Materials and Mix Proportion

The experimental study presented in Research Report GC-1 by Hardjito and Rangan [32] was commonly prepared by most researcher to develop the mixture proportions of low-calcium fly ash-based GPC. Three composition mixtures were chosen for generating 40, 50, and 75 MPa compressive strengths [47]. Table 1 contains detailed mix combinations of GPC.

Dattatreya et.al [54], studied GRC beams that were made using various binder configurations, curing at room temperature, and having compressive strengths varying from 17 to 63 MPa. As the control (CRC) beams of the test examples, OPC, drinking water, fine aggregates, and coarse aggregates that complied with IS 12269 were used. Conventional concrete mixes prepared for CRC beams suggested by standards of IS

10262:2009 and ACI 211.1 were made to compare the outcomes of tests carried out using GRC beams.

In this study [56], physical models of the beams were made in 2 (two) variations of the mixture. The first mixture is GRC beams with 100% fly ash, and the second mixture is conventional reinforced concrete (CRC) beams with the use of 100% OPC.

Ojha et. al [55] investigated the mix design detail for the GRC beam dan CRC beam for normal and high-strength concrete. The CRC beam was designed according to IS 10262: 2009. The ratio of aggregate had been maintained at 60%: 40% of coarse aggregate to fine aggregate for normal-strength concrete mix [M40], and 35%: 65% for high-strength concrete mix [M70]. All the concrete mixes were kept between 75-100 mm for slump value. Superplasticizer was used for CRC beam mixes to reach the required slump value.

Table 1. The Detail Mix Composition of GPC [47]

Material	Mass (kg/m ³)
Aggregates (10mm)	550
Aggregates (7mm)	550
Fine Sand	640
Fly ash	404
Sodium hydroxide solution (14M)	41
Sodium silicate solution	102
Superplasticizer	6.0
Extra water*	GBI=25.5; GBII=17.0; GBIII= 13.5

* The amount of additional water added is the only difference between the three mixes.

3.2. Specimen Details and Test Set Up

To determine the cross-sectional capacity of GRC beams and CRC beams, physical models of the beam examples were created to carry out loads as shown in Figure 4 [56]. The compressive strength and tensile splitting test of both types of concrete were evaluated using the cylinder and beam specimens.

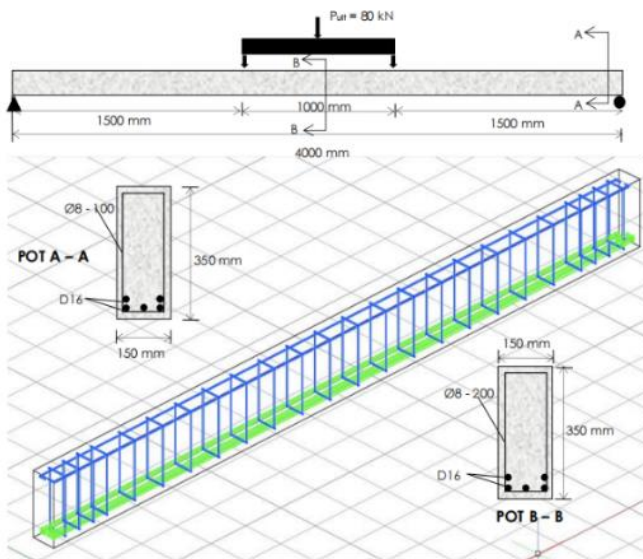


Fig. 4 Longitudinal reinforcement of GRC beam and CRC beam [56]

To prevent cracks due to sliding near the supports, and to ensure that a crack happens in the mid of the span (on the maximum moment), reinforced concrete cross sections were constructed with a specific amount of tensile reinforcement. The test configuration is displayed in Figure 5 below [56].



Fig. 5 Test Configuration for CRC beam Flexural Test [56]



Fig. 6 Test Arrangement for Flexure [54]

Figure 6 depicts the configuration for the flexural test [54]. The 1000kN capacity Universal Machine Test (UTM) was used to test the beam specimen. To quantify deflections at the midspan and under the load locations, dial gauges were used. At various load levels, the dial gauge readings were verified. The load was set at 2.5kN intervals until the first crack was noticed. Following that, the load was increased in 5kN increments.

The simply supported beam over a 3000mm span, was put under two concentrated loads that were distributed symmetrically across the span [52]. Several Linear Variable Data Transformers (LVDTs) were positioned under the beam's load spots and in the middle of the span. The load was delivered in 2.5kN intervals. Figure 7 depicts the test configuration.

The 500kN capacity of the Flexural Testing Machine was used to test the beam prototype [55]. Every beam was intended to fail simply from pure bending. The beam was merely about 2400 mm long span, and 2000 mm clear beam span, and was put to two concentrated static point loads that were applied symmetrically to the span. The examples were cured at $27 \pm 2^\circ\text{C}$ ambient temperature and at least 65% relative humidity. Figure 8 depicts the load-test configuration for a beam in flexure.



Fig. 7 Test Configuration for Flexure [52]



Fig. 8 Test Configuration for Beams [55]

4. Findings and Discussion

4.1. Cracks pattern and failure mode

The cracking pattern on the beams can be observed in Figures 9. a [56] for the CRC beam and 9. b [47] for the GRC beam. The specimen's failure pattern was confirmed, and both beams exhibit typical cracks brought by flexural bending loading.

The cracks and failure patterns between the GRC beam and reinforced CRC beams show similarities. Research conducted by both Sumajouw & Rangan [47] and Setiati & Irawan [58] with fewer reinforcement designs shows that the initial cracks formed in the beams occur in the pure bending zone at the mid-span area, precisely at the bottom of the load.

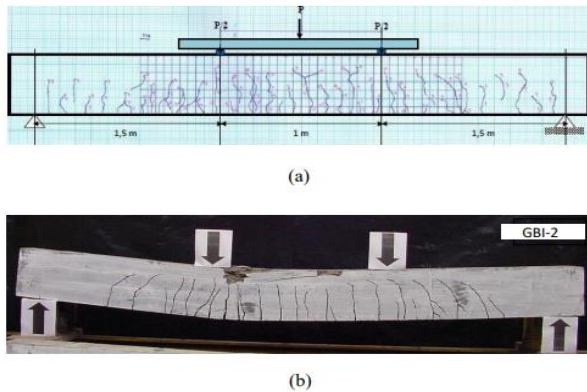


Fig.9 Failure pattern of the beams: (a) Conventional Reinforced Concrete Beam [56];
(b) Geopolymer Reinforced Concrete Beam [47].

Similar to other cases, some flexural fractures in the shear span of beams with higher tensile reinforcement ratios became inclined cracks as a result of the shear force. Along the span, the cracks' width and spacing changed. Overall, the crack patterns found in GRC beams were comparable to those found in CRC beams. When the compression face of the concrete beams was ultimately crushed, the longitudinal compressive steel also buckled. The mechanism was typical of an under-reinforced beam failure [47].



Fig. 10 RCC and GPC Beam Crack Pattern [52]

Table 2. Beam Failure modes, Crack Width, and Initial Crack Load.

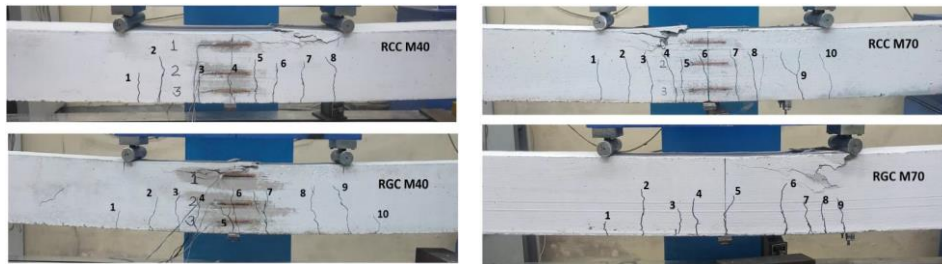
Authors	Beam ID	Beam Types	Type of Failure	
Kumaravel S et. Al [52]	CRC-I	Conventional Reinforced Concrete (CRC) Beams	Flexural mode	
	CRC-II		Flexural mode	
Sumajouw DMJ, Rangan BV [47]	GRC-I	Geopolymer Reinforced Concrete (GRC) Beams	Flexural mode	
	GRC-II		Flexural mode	
		Crack Width (mm) at Service Load-40 kN		
	CRC-1	0.125	Flexural mode	
	CRC-2	0.210	Flexural mode	
	CRC-3	0.230	Flexural mode	
	FAB1	-	Flexural mode	
	FAB2	0.130	Flexural mode	
	FAB3	0.280	Flexural mode	
Dattatreya JK et.al [54]	GRC-1	0.180	Flexural mode	
	GRC-2	0.240	Flexural mode	
	GRC-3	0.450	Flexural mode	
		Beam Types	First Crack Load (kN)	
	CRC ₁	Conventional Reinforced Concrete (CRC) Beams	16.75	Flexural mode
	CRC ₂		18.5	Flexural mode
	CRC ₃		20	Flexural mode
	CRC ₄		24	Flexural mode
Abraham R et.al [53]	GRC ₁	Geopolymer Reinforced Concrete (GRC) Beams	18	Flexural mode
	GRC ₂		20	Flexural mode
	GRC ₃		22	Flexural mode
	GRC ₄		24	Flexural mode

Figures 9 b and 10 illustrate that the cracking patterns and failure mechanisms shown for GRC beams are identical to those observed for CRC beams. This is by studies [47 and 52]. The failure processes of the CRC beams and GPC beams are displayed by the flexure behavior in Table 2 [47] and [52].

The same situation also arises in Dattatreya et al.'s experimental research [54]. In general, the GRC beam specimens developed flexural cracks in identical order to the CRC beam specimens for any given load. The failure modes of the two types of beams were essentially identical, and the crack pattern at various phases was also very similar. As shown in Table 2, flexure modes are the causes of failure for CRC and GRC beams, and both beams have similar fracture widths, crack spacing, and crack numbers.

According to a study by Abraham et al. [53], the observed GRC beam crack patterns were almost identical to those in CRC beams under all conditions. Because the load was increased linearly at first, cracks were originally not seen during the test. Using the load increase, flexure cracks started to appear as predicted in the bending zone at the center of the beams. The span experience both the development of new cracks and the widening of

existing cracks as the load increased. Table 2 [52, 47, 53, 54] displays the crack patterns of both beams. During the test, Ojha, P.N. et al. [55] noted the crack pattern for both beams. Flexural cracks first became apparent at the very beginning of loading, and spread at the tension zone between the loading arrangements. Figures 11 (a) and (b) demonstrated how normal-strength CRC beams and normal-strength (M40) GRC beams have fewer and smaller visible cracks, respectively. High-strength (M70) CRC beams and the equivalent GRC beams have identical crack patterns and sizes.



(a) M40 CRC and GRC

(b) M70 CRC and GRC

Fig. 11 Cracks width and pattern [55]

For all cases, when the applied load approaches the cracking moment limit, cracks initiate to develop on the tension side of the beams and begin to extend upward. Typically the first cracks appear at the tested GRC and CRC beams at comparable stress values in the middle of the span and spread upwards. More flexural cracks develop at the mid-span and near the support areas as the load increases, and the pre-existing vertical cracks significantly widen and deepen. Vertical cracks near the supports begin to develop inclined cracks when the loading is increased even further. The reinforcing ratio affects the number, and distribution of cracks as well as the size and length of the cracks. As the beam is designed for under-reinforced conditions, the failure modes of all beams occur by yielding steel reinforcement followed by reaching failure strain on the concrete.

4.2. Failure Load Parameters

The designed failures of under-reinforced concrete beams are comparable to the failure load of GRC and CRC beams. Every beam fails in the flexural phase. However, compare to CRC beams, the failure of GRC beams is more ductile, and followed by concrete in the compression zone being crushed. Table 3 displays the failure loads for both beams [53] and [52].

The expected failure loads [52] were calculated by using FEA software (ANSYS). It demonstrated that the failure load of the test results was very close to the calculated results. Table 3 compares the failure loads of CRC beams and GRC beams. As predicted, the tensile steel first yield, then the concrete in the compression face is crushed.

Numerous studies have investigated the failure behavior of CRC beams under flexure. The majority of the examinations were carried out on typical reinforced concrete beams with longitudinal reinforcement, and higher compressive strength. Table 4 displays the load-carrying capacities at different stages [54]. It demonstrates that, despite GRC beams' somewhat higher compressive strength, the load at the beginning of the initial crack is nearly identical in the case of CRC and GRC beams. Due to their slightly lower flexural rigidity than CRC beams, GRC beams also demonstrate reduced service load and ultimate load-carrying capability. The GRC beams have bigger maximum load-carrying capacities than the CRC beams, and this is due to their greater compressive strength, this might be

the case. The beams' final failure involves concrete crushing in the compression zone after the yielding of the tensile steel. This review generally confirms the performance of both beams, and that the load-carrying capability of GRC beams is comparable to that of CRC beams [55].

Table 3. Evaluation of the beam Failure loads [53] and [52]

Authors	Beam types	Beam ID	Failure loads (kN)		
Abraham R et.al [53]	Conventional Reinforced Concrete (CRC) Beams	CRC ₁	58.25		
		CRC ₂	60.25		
		CRC ₃	76.00		
		CRC ₄	88.00		
	Geopolymer Reinforced Concrete (GRC) Beams	GRC ₁	59.25		
		GRC ₂	69.75		
		GRC ₃	82.00		
			88.00		
Kumaravel S et.al [52]	Conventional Reinforcement Concrete (CRC) Beams	CRC ₁	72.00	75.00	96.0
		CRC ₂	74.50	75.00	99.3
	Geopolymer Reinforced Concrete (GRC) Beams	GRC-I	74.00	77.50	95.5
		GRC-II	76.50	77.50	98.7

4.3. Loads and Deflection Relationship

The load and deflection relationship between GRC beams and CRC beams exhibit an excellent correlation, according to Dattatreya et al. [54]. Figures 12. a and 12. b represent the mid-span deflection for the two specimens. For CRC beams and just a little bit more for GRC beams, the first crack deflection was a lesser amount than 1% of the ultimate deflection. The higher elastic modulus of CRC beams was what gives better serviceability.

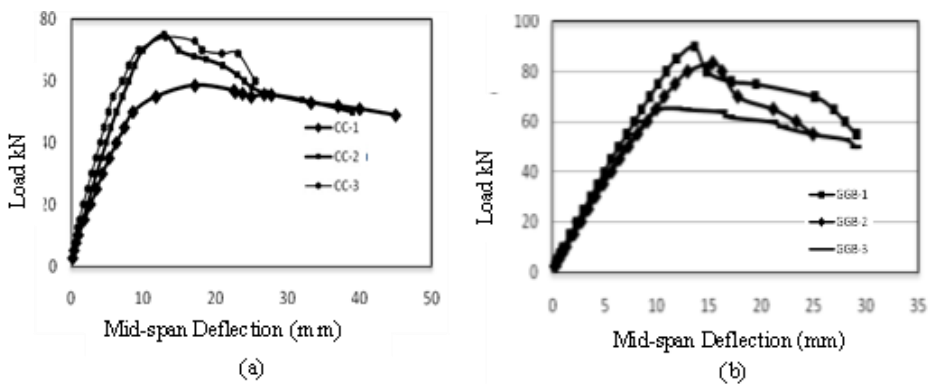


Fig. 12 Deflection at mid-span for both Beams [54]

According to Sumajouw and Rangan [47], in the case of GRC beams, the load and deflection relationship was a sign of the important steps that were performed throughout the test

(Figure 13). All the beams perform in a distinctive manner that is consistent with Figure 2 the typical relationship between the load-deflection curve [59].

Table 4. Load-carrying capacities at various stages [54-55]

Authors	Beam ID	Service Load (kN)	First Cracking Load (kN)	Yield Load (kN)	Ultimate Load (kN)
Dattatreya JK et.al [54]	CRC-1	39.0	9.5	58.90	58.90
	CRC-2	48.0	10.0	75.65	75.65
	CRC-3	56.0	10.0	79.65	79.65
	FAB1	26.0	6.75	37.50	37.50
	FAB2	38.0	9.5	84.74	84.74
	FAB3	39.0	8.75	89.80	89.80
	GRC-1	48.0	10.0	90.60	90.60
	GRC-2	45.0	10.0	85.45	85.45
	GRC-3	44.0	8.0	69.75	69.75
		Compressive Strength			P_y/P_u
	CRC Beam-1- M40	46.11	60.25	159.90	98.40
	CRC Beam-2- M40	44.61	64.75	161.90	97.77
	GRC Beam-1- M40	50.72	66.85	171.10	95.75
	GRC Beam-2- M40	51.47	57.90	159.90	96.44
Ojha PN et.al [55]	CRC Beam-1- M70	82.15	79.92	222.70	98.06
	CRC Beam-2- M70	83.90	82.25	224.60	96.56
	GRC Beam-1- M70	77.80	87.65	227.10	99.00
	GRC Beam-2- M70	79.80	80.75	224.00	96.34

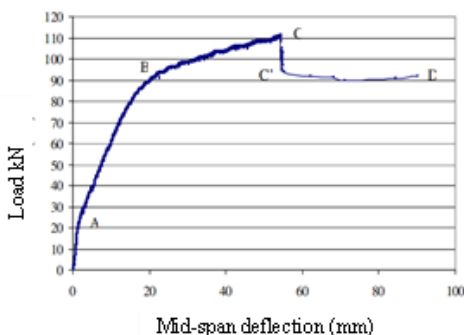


Fig. 13 Deflection at mid-span for GPC Beam [47]

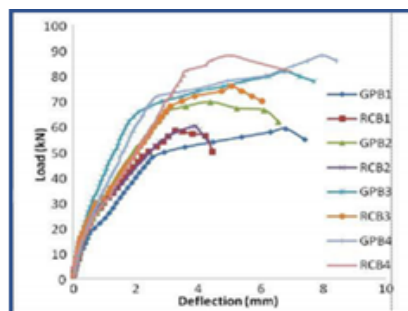


Fig. 14 Deflection at mid-span of the Beam [53]

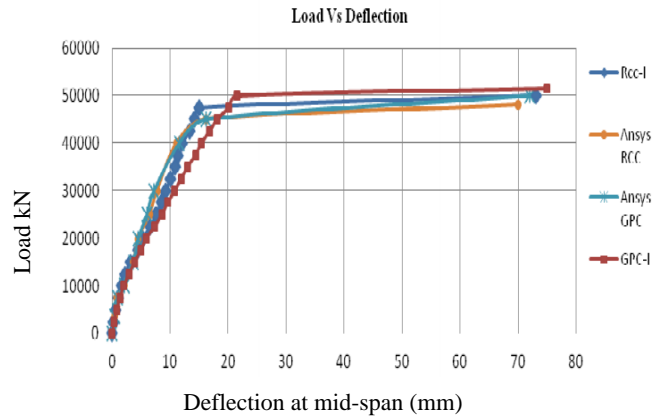


Fig. 15 Mid-span deflection of Beam [52]

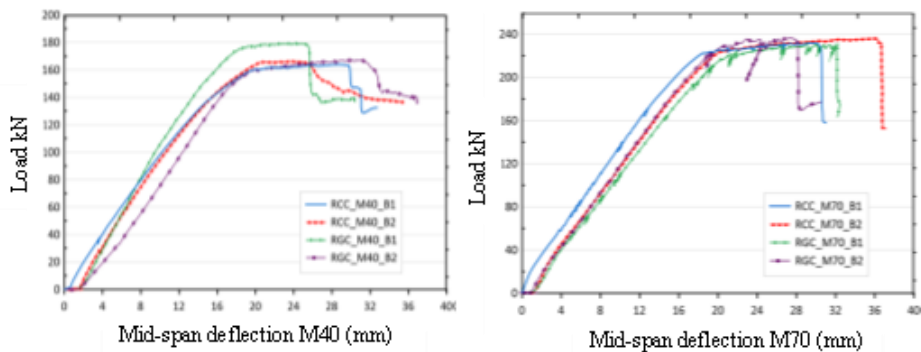


Fig. 16 Mid-span deflection of the Beam [55]

By Abraham et al. [53] the ductility factor was calculated by plotting the load versus deflection curve using the measured values. The load-deflection behavior of GRC and CRC beams using various steel reinforcement ratios is depicted in Figure 14. Additionally, it can be seen that both beams' load-deflection behavior is identical in nature. According to Kumaravel et al. [52], as shown in Figure 15, the mid-span deflection gained for the CRC beams and GRC beams almost have identical curvature. The GRC beams behave similarly to control beams based on the load and mid-span deflection. When compares to CRC beams, GRC beams have a higher ultimate load capacity (Figure 15).

The load versus displacement curves for GRC and CRC beams made of M40 and M70 grade concrete are shown in Figure 16. The load-deflection curve was used to directly identify the yield point. All of the beams' deflection increased linearly up until the first crack was detected. The failure was indicated by the decrease in curvatures for all combinations. The curves indicate that both kinds of beams exhibit similar flexural behavior. Using IS 456 [55], the expected moment values are determined.

The findings show that the load-deflection curves for all studies of GRC beams are similar to three regions for the typical relationship of load-deflection of CRC beam as shown in Figure 2 [59]. The uncracked state of the beams is represented by the sharp linear response in the first section (region 1). Once the load exceeds the tensile strength of concrete or the

modulus of rupture, the constant moment zone of the CRC beams begins to crack. After that point, the curves shift to the second section called a post-crack load level (region II), which represents the beams' cracked state. This segment, which continues until the peak compressive strain, has a lower slope compared to the first segment because of expanding cracking. The load decreases every time a significant crack shows up. Following the second segment, which experiences a beam rupture due to concrete crushing, is the third segment, called post serviceability level (region III). Based on the CRC's mechanical and material characteristics, this segment exhibits a nonlinear response.

4.4. Deflection Parameters

According to [56], based on the calculation from equation (3), the maximum amount of deflection of the GRC beam was larger than the CRC beam. This was due to the specific gravity of the GRC beam being larger but having a smaller modulus of elasticity compared to the CRC beam. This was obvious from the mid-span load deflection that the GRC beams behave similarly to the control beams (Table 5).

As stated by [53], the deflection of all beams developed linearly and remained proportional to load until the appearance of the first cracks. It was discovered that GRC beams exhibit greater deflection at ultimate load than CRC beams. Furthermore, it was found that the load-deflection behavior of CRC and GRC beams was identical. The capacity of energy absorption of the GRC beams had been improved by their greater load-carrying capacity and larger deflections as shown in Table 5 [53].

According to [52], the test and predicted result (ANSYS) of load-deflection curves were comparable for both GRC beams and control beams as shown in Table 5. The investigation by Abraham et. al [53] and Kumaravel et. al. [52] found that the deflection values carried by GRC beams were greater than CRC beams. But overall, the carried-out value of the deflection of the tests is proportional to the calculation results.

Figure 13 displays the mid-span deflection curve created by Sumajouw and Rangan [47], while Table 7 displays the greatest deflection. These characteristics describe reinforced concrete beams' typical flexure behavior [59]. In Figure 2, at points A, B, C, C' dan D, the gradual increment of deflection as an increasing load function is displayed. The deflection curves show specific instances of what happened during the test. The final load and mid-span deflection for CRC beams and GRC beams, which are studied by [47], are shown in Figure 13.

Dattatreya et al [54] claimed that a comparable technique was used to obtain the peak load deflection. When compared to the actual measurements, the testing load and the corresponding predicted deflections revealed a generally acceptable agreement. In general, there was good agreement between the test result of deflections and the calculated deflections that were computed according to the provisions of IS 456:2000, and conventional CRC theory.

The deflection response of CRC elements is a complicated process with a wide variety of impacts, such as differing strength and deformation characteristics of steel and concrete, cracking, and bond slip between reinforcement and concrete. Concrete between cracks increases stiffness whereas the impact of reinforcing is dominant when the beams are cracked. Generally, it finds in this review, that GRC beams often show greater deflection than CRC beams at service load and peak load levels, as well as other load levels. Furthermore, multiple investigations for fly ash-based low calcium GRC beams show that these beams have an equivalent initial load to crack, crack width, deflection, ultimate load, and failure mechanism to CRC beams undergoing flexural stress. [47, 52, 53, 54].

Table 5. Comparison of Deflection values [56, 53, 52]

Authors	Beam ID	Load at First Cracking (kN)	Crack at Mid-Span Deflection (mm)	Maximum Deflection (mm)
Setiati NR, Irawan RR. [56]	CRC-B1	18.59	2.26	10.553
	CRC-B2	19.41	2.52	
	GRC-B1	20.34	2.32	11.365
	GRC-B2	20.16	2.60	
		Ultimate Load Deflection (mm)		The capacity of Energy absorption (kNmm)
Abraham R, et.al [53]	CRC ₁	3.273		122.392
	CRC ₂	3.92		161.797
	CRC ₃	5.071		269.756
	CRC ₄	5.016		284.583
	GRC ₁	6.814		320.181
	GRC ₂	4.397		216.347
	GRC ₃	6.762		433.700
	GRC ₄	7.98		531.781
		Deflection (mm)		Ratio between Test/ Predicted result
		Test result	Predicted result (ANSYS)	
Kumaravel S, et.al [52]	CRC-I	73.00	70.00	1.04
	CRC-II	70.00	70.00	1.00
	GRC-I	75.00	72.00	1.04
	GRC-II	76.00	72.00	1.06

4.5. Ductility Index Parameters

Table 6 displays the ductility index, which was determined by the load-displacement and moment-curvature [53]. All GRC beams have better curvature ductility values than the corresponding CRC beams. All specimens failed in a flexural mode, but the failure of GRC beams was more ductile than that of CRC beams and was followed by concrete being crushed in the compression zone, providing additional proof that all of the beams failed in tension.

Table 6. Comparison of Ductility Index [53]

Beam Types	Beam ID	Bending Behavior	
		Displacement Ductility Index	Curvature Ductility Index
Conventional Reinforcement Concrete (CRC) Beams	CRC ₁	2.98	7.72
	CRC ₂	1.64	3.59
	CRC ₃	1.85	3.47
	CRC ₄	1.11	1.24
Geopolymer Reinforced Concrete (GRC) Beams	GRC ₁	5.12	8.17
	GRC ₂	2.68	3.68
	GRC ₃	4.30	4.94
	GRC ₄	1.44	1.38

The ductility is calculated by dividing the deflection at the ultimate moment by the deflection at the yield moment [47]. The yield moment, M_y is calculated for this purpose using the elastic theory [59]. The load-deflection test curves shown in Figure 13 are used to calculate the deflections related to the yield moment (M_y) and ultimate moment (M_u).

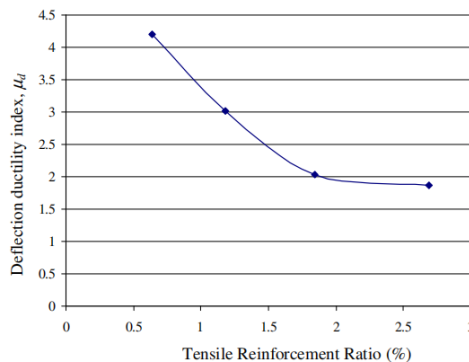


Fig. 17 Ductility Index of Tensile Reinforcement Ratio (GBI Series) [47]

Figure 17 depicts the effect of tension reinforcement on the ductility index. This graph shows how the ductility index declines with increasing tensile reinforcement. Deflection ductility increases significantly in specimens with a reinforcement ratio of less than 2.0%; however, deflection ductility is only marginally affected in beams with a reinforcement ratio of more than 2.0%. These test trends reflect those that are seen with CRC concrete beams [59]. The ductility index of test beams is provided in Table 7 as previously mention.

Study [54] found that the proportion of curvature at peak load to ultimate curvature at failure varied between 1.47 to 1.75 for GRC beams compared with 1.38 to 2.33 for CRC beams, indicating that GRC beams have less post-peak ductility than CRC beams. For GRC specimens, the deflections at several phases, together with the service and peak load phases, were higher. The ductility factor was similar to CRC beams. The review of all types of beams confirms that ultimate moment capacity and deflection for GRC flexural beams could be calculated using the CRC beam theory.

Table 7. Index of Ductility and Mid-span Deflection at Failure Loads [47]

Beam ID	Compressive Strength	Reinforcement Ratio (%)	Deflection (mm)	Ductility Index
GRC-I.1	37.0	0.64	56.53	4.20
GRC-I.2	42.0	1.18	46.01	3.01
GRC-I.3	42.0	1.84	27.87	2.03
GRC-I.4	37.0	2.69	29.22	1.87
GRC-II.1	46.0	0.64	54.27	3.8
GRC-II.2	53.0	1.18	47.20	3.28
GRC-II.3	53.0	1.84	30.01	2.25
GRC-II.4	46.0	2.69	27.47	1.70
GRC-III.1	76.0	0.64	69.75	4.95
GRC-III.2	72.0	1.18	40.69	3.24
GRC-III.3	72.0	1.84	34.02	2.74
GRC-III.4	76.0	2.69	35.85	2.41

4.6 Correlation of Test to Predicted Result

Sumajouw and Rangan [47] determined the GRC flexural strength according to the AS3600 specification for concrete structures [58]. Table 8 and Figure 18 compare the results of the evaluations with the estimated values. The overall ratio of test to expected results was 1.11, with a standard deviation of 0.135. The ultimate moment capacity was computed using IS456 in the study by Dattatreya et al. [54] with standard deviations of 0.142.

The borderline of the ultimate moment between the test results and the theoretical calculation shows the agreement as presented in Table 8 concerning the comparison ratio between the two values. The relationship in the form of a diagram shows in Figure 18.

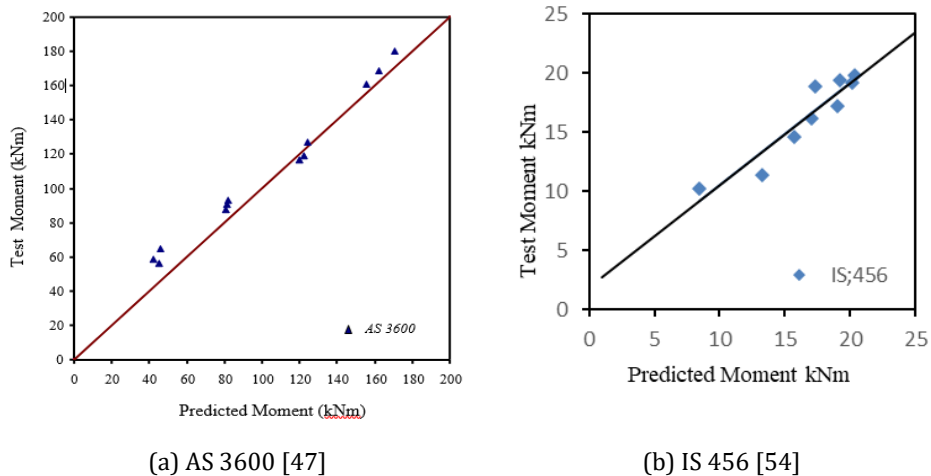


Fig.18 Predicted and test results

The experimental maximum moment (M_e) of beams was calculated as per the dimensions of the beam and the reinforcements following IS 456:2000. The moment of resistance (M_p) was calculated as per IS-456. The experimental maximum value was obtained from beam testing of mid-span. Table 9 shows the ratio between the test to predicted results [55].

Table 8. Evaluation of predicted and test results based on AS 3600 [47] and IS 456 [54]

Authors	Beam ID	Ultimate Moment (kN-m)		Ratio between Test / Predicted result
		Test result	Predicted result (AS3600)	
Sumajouw DMJ, Rangan BV. [47]	GRC-I.1	56.30	45.17	1.24
	GRC-I.2	87.65	80.56	1.09
	GRC-I.3	116.85	119.81	0.98
	GRC-I.4	160.50	155.31	1.03
	GRC-II.1	58.35	42.40	1.28
	GRC-II.2	90.55	81.50	1.11
	GRC-II.3	119.00	122.40	0.97
	GRC-II.4	168.70	162.31	1.04
	GRC-III.1	64.90	45.69	1.42
	GRC-III.2	92.90	82.05	1.13
	GRC-III.3	126.80	124.17	1.02
	GRC-III.4	179.95	170.59	1.05
	Average number			1.11
	Standard Deviation			0.135
Dattatreya JK et.al [54]	CRC-1	13.25	11.44	1.24
	CRC-2	17.03	16.19	1.05
	CRC-3	17.33	18.87	0.92
	FAB1	8.44	10.25	0.82
	FAB2	19.06	17.18	1.28
	FAB3	20.21	19.22	1.05
	GRC-1	20.39	19.78	1.03
	GRC-2	19.24	19.41	0.99
	GRC-3	15.71	14.62	1.07
	Average			1.05
	Standard Deviation			0.142

Table 9. The maximum strength of Beams [55]

Beam Code	Compressive Strength (MPa)	Moment (kN-M)		Predicted Moment M_p (kN-M)	Ratio between Test/Predicted result M_e/M_p
		Yield	Ultimate M_e (Experimental)		
M40 CRC Beam - 1	46.11	53.30	54.17	44.01	1.23
M40 CRC Beam - 2	44.61	53.97	55.20	44.01	1.25
M40 GRC Beam - 1	50.72	57.03	59.57	44.01	1.35
M40 GRC Beam - 2	51.47	53.30	55.27	44.01	1.26
M70 CRC	82.15	74.23	75.70	67.37	1.12

Beam - 1					
M70 CRC Beam - 2	83.90	74.87	77.53	67.37	1.15
M70 GRC Beam - 1	77.80	75.70	76.47	67.37	1.14
M70 GRC Beam - 2	79.80	74.67	77.50	67.37	1.15

5. Conclusions

This paper presents significant findings and results along with the current grouping parameters to analyze the flexural behavior of GRC and CRC beams. After conducting a critical review, the conclusion is as follows:

- The crack patterns and failure mechanisms mentioned in the literature for CRC beams are found to be equivalent to those considered for GRC beams. All beams collapse in flexure in a ductile way as the steel reinforcing yield in tension and the concrete is crushed in the area known as the compression zone.
- The flexural behavior of both GRC and CRC beams in load-deflection relationships exhibits a typical similarity to the description of significant test steps. These stages are listed in the following order; initial crack, yielding of the tensile steel, the concrete crushing associated with spalling of the concrete cover, and disintegration of the concrete compression zone due to buckling of the longitudinal steel at the compression area.
- The comparison between predicted and test results indicates that the deflection performance of GRC and CRC beams is nearly identical. Furthermore, the calculated deflection values based on AS3600 serviceability provisions are compared to the observed deflection during testing, and a good agreement is observed between the two. The test to calculated deflection ratio has a mean value of 1.15 and a standard deviation of 0.06, indicating a reasonably close match between the experimental and computed values. Additionally, there is reasonable agreement between the deflection test results and the predicted deflections calculated using the guidelines of IS456:2000 (Indian Standard Code for Plain and Reinforced Concrete) and CRC theory.
- The ductility of GRC beams increases as the tensile reinforcement ratio decreases, specified by the ratio of mid-span deflection at the ultimate moment to mid span deflection at the yield moment. According to test results, ductility increases significantly with ratio of beam's tensile reinforcement of smaller than 2%. The ductility is only slightly influenced by tensile reinforcement ratios of higher than 2%. These test patterns match the behavior of CRC beams closely.
- There is a comparable relationship between the test and predicted values for the test beams when the ultimate moment carrying capacities are calculated using the CRC principles and strain compatibility approach. On top of that, according to the findings, GRC beams can be evaluated using the same computational techniques that are used to assess the performance parameters of CRC beams at various phases. It has been confirmed that the design guidelines in the Indian Standard (IS 456) and Australian Standard for Concrete Structures (AS3600) for CRC apply to GRC beams. Therefore, it might be concluded, the behavior of GRC and CRC beams depicts a similar type, thus the standards that are developed for CRC, can also certainly be applied to GRC beams.

References

- [1] Blaszczyński TT, Krol MM. The durability of Green-Concrete, Proceedings of 8th International Conference AMCM, Poland. 2014; 530-540.
- [2] Davidovits J. Global Warming Impact on the Cement and Aggregates Industries, World Resource Review. 1994; 6(2): 263-278.
- [3] Kaya M. Mechanical properties of ceramic powder-based geopolymer mortars. Magazine of Civil Engineering, 2022. 112(4). Article No. 11207.
- [4] Sumajouw DMJ, Malingkas G, Pandaleke R, Handono BD. Geopolymer Concrete (GPC) as a Suitable Green Solution for Building and Construction Material, Journal of Mechanical and Civil Engineering (IOSR-JMCE). 2023; 20: 61-72
- [5] Davidovits J. Chemistry of Geopolymeric Systems, Terminology. In: Joseph Davidovits, Davidovits R, James C, editors. Geopolymer '99 International Conference; 1999 June 30 to July 2, 1999; France; 1999; 9-40.
- [6] Xu H, van Deventer JSJ. Geopolymerisation of Multiple Minerals. Minerals Engineering 2002;15(12):1131-1139. [https://doi.org/10.1016/S0892-6875\(02\)00255-8](https://doi.org/10.1016/S0892-6875(02)00255-8)
- [7] Palomo A, Grutzeck MW, Blanco MT. Alkali-Activated Fly Ashes, A Cement for the Future. Cement and Concrete Research 1999; 29(8):1323-1329. [https://doi.org/10.1016/S0008-8846\(98\)00243-9](https://doi.org/10.1016/S0008-8846(98)00243-9)
- [8] Xu H, van Deventer JSJ. The Geopolymerisation of Alumino-Silicate Minerals. International Journal of Mineral Processing 2000; 59(3): 247-266. [https://doi.org/10.1016/S0301-7516\(99\)00074-5](https://doi.org/10.1016/S0301-7516(99)00074-5)
- [9] van Jaarsveld JGS, van Deventer JSJ, Lukey GC. The Effect of Composition and Temperature on the Properties of Fly Ash and Kaolinite-based Geopolymers. Chemical Engineering Journal 2002; 89(1-3): 63-73. [https://doi.org/10.1016/S1385-8947\(02\)00025-6](https://doi.org/10.1016/S1385-8947(02)00025-6)
- [10] Swanepoel JC, Strydom CA. The utilization of fly ash in a geopolymeric material. Applied Geochemistry 2002;17(8):1143-1148. [https://doi.org/10.1016/S0883-2927\(02\)00005-7](https://doi.org/10.1016/S0883-2927(02)00005-7)
- [11] Barbosa VFF, MacKenzie KJD, Thaumaturge C. Synthesis and Characterisation of Materials Based on Inorganic Polymers of Alumina and Silica: Sodium Polysialate Polymers. International Journal of Inorganic Materials 2000; 2(4): 309-317. [https://doi.org/10.1016/S1466-6049\(00\)00041-6](https://doi.org/10.1016/S1466-6049(00)00041-6)
- [12] Standards-ASTM, Standard Test Method for Length Change of Hydraulic-Cement Mortars Exposed to a Sulfate Solution. 1995; C 1012 -95a.
- [13] Hime WG. Comments on Geopolymer Concrete. 2003.
- [14] Li G, and Zhao X. Properties of concrete incorporating fly ash and ground granulated blast-furnace slag. Cement & Concrete Composites, 2003; 25(3): p. 293-299. [https://doi.org/10.1016/S0958-9465\(02\)00058-6](https://doi.org/10.1016/S0958-9465(02)00058-6)
- [15] Cheng TW, Chiu JP. Fire-resistant Geopolymer Produced by Granulated Blast Furnace Slag. Minerals Engineering. 2003; 16(3): 205-210. [https://doi.org/10.1016/S0892-6875\(03\)00008-6](https://doi.org/10.1016/S0892-6875(03)00008-6)
- [16] Hardjito D, Wallah SE, Rangan BV. Study on Engineering Properties of Fly Ash-Based Geopolymer Concrete. Journal of the Australasian Ceramic Society 2002; 38(1): 44-47.
- [17] Hardjito D, Wallah SE, Sumajouw DMJ, Rangan BV. Fly Ash-Based Geopolymer Concrete. Australian Structural Engineering Journal, Engineers Australia, 2005. <https://doi.org/10.1080/13287982.2005.11464946>
- [18] Hardjito D, Wallah SE, Sumajouw DMJ, Rangan BV. On The Development of Fly Ash-Based Geopolymer Concrete. ACI Materials Journal, American Concrete Institute, December 2004. <https://doi.org/10.1080/13287982.2005.11464946>
- [19] Hardjito D, Wallah SE, Sumajouw DMJ, Rangan BV. Introducing Fly Ash-based Geopolymer Concrete: Manufacture and Engineering Properties. In Proceedings of the

- International Conference Our World in Concrete, Singapore, August 2005. <https://doi.org/10.1080/13287982.2005.11464946>
- [20] Sumajouw DMJ, Hardjito D, Wallah SE, Rangan BV. The Behavior of Geopolymer Concrete Columns Under Equal Load Eccentricities. In: Proceedings of the Seventh International Symposium on Utilisation of High Strength/High-Performance Concrete; Washington DC, USA: American Concrete Institute; June 2005.
- [21] Sumajouw DMJ, Hadrjito D, Wallah SE, Rangan BV. Flexural Behaviour of Reinforced Fly Ash-Based Geopolymer Concrete Beams. In Proceedings of CONCRETE 05 Conference, Melbourne, Concrete Institute of Australia, October 2005. <https://doi.org/10.1080/13287982.2005.11464946>
- [22] Wallah SE, Hardjito D, Sumajouw DMJ, Rangan BV. Creep and Drying Shrinkage Behaviour of Fly Ash-Based Geopolymer Concrete. In Proceedings of CONCRETE 05 Conference, Melbourne, Concrete Institute of Australia, October 2005. <https://doi.org/10.1080/13287982.2005.11464946>
- [23] Wallah SE, Hardjito D, Sumajouw DMJ, Rangan BV. Sulfate and Acid Resistance of Fly Ash-Based Geopolymer Concrete. In Proceedings of the Australian Structural Engineering Conference, Newcastle, Engineers Australia, September 2005. <https://doi.org/10.1080/13287982.2005.11464946>
- [24] Davidovits J. Geopolymers: Inorganic Polymeric New Materials. Journal of Thermal Analysis, 1991; 37: 1633-1656. <https://doi.org/10.1007/BF01912193>
- [25] Davidovits J. Properties of Geopolymer Cements. In: First International Conference on Alkaline Cements and Concretes; 1994; Kyiv, Ukraine, 1994: SRIBM, Kyiv State Technical University, 1994; 131-149.
- [26] Davidovits J. High-Alkali Cements for 21st Century Concretes. Concrete Technology, Past, Present, and Future, In proceedings of V. Mohan Malhotra Symposium. Editor: P. Kumar Metha, ACI SP- 144, 1994; 383-397.
- [27] Nath P, Sarker PK. Use of OPC to improve the setting and early strength properties of low calcium fly ash geopolymer concrete cured at room temperature, Cement & Concrete Composites Journal, 2014; (55): 205-214. <https://doi.org/10.1016/j.cemconcomp.2014.08.008>
- [28] Krishnaraja AR, Sathishkumar NP, Kumar TS, Kumar PD. Mechanical Behavior of Geopolymer Concrete under Ambient Curing, International Journal of Scientific Engineering and Technology, 2014; 3(2): 130-132.
- [29] Nath P, Sarker PK, Rangan BV. Early age properties of low-calcium fly ash geopolymer concrete suitable for ambient curing, The 5th International Conference of Euro Asia Civil Engineering Forum (EACEF-5), 2015. <https://doi.org/10.1016/j.proeng.2015.11.077>
- [30] Shinde BH, and Kadam KN. Properties of Fly Ash based Geopolymer Mortar with Ambient Curing, International Journal of Engineering Research, 2016; (5): 203-206.
- [31] Manjunath G, Giridhar C. Compressive strength development in Ambient Cured geopolymer mortar, International Journal of Earth Sciences and Engineering, 2011; (4-6): 830-834.
- [32] Hardjito D, Rangan BV. Development and Properties of Low-Calcium Fly Ash-based Geopolymer Concrete, Research Report GC-1, Faculty of Engineering, Curtin University of Technology, Perth, 2005.
- [33] Kong DL, Sanjayan JG. Damage behavior of geopolymer composite exposed to elevated temperatures, Cement and Concrete Composites, 2008; 30(10): 986-991. <https://doi.org/10.1016/j.cemconcomp.2008.08.001>
- [34] Guo X, Shi H, Dick WA. Compressive strength and microstructural characteristics of Class C fly ash geopolymer, Cement and Concrete Composite, 2010; 32(2): 142-147. <https://doi.org/10.1016/j.cemconcomp.2009.11.003>

- [35] Nasvi M, Gamage RP, Sanjayan JG. Geopolymer as well cement and the variation of its mechanical behavior with curing temperature, *Greenhouse Gases: Science and Technology*, 2012; 2(1): 46-58 <https://doi.org/10.1002/ghg.39>
- [36] Yost JR, Radlinska A, Ernst S, Salera M, and Martignetti. Structural behavior of alkali-activated fly ash concrete. Part 2: structural testing and experimental findings, *Material and Structures Journal*, 2013; (46): 449-462. <https://doi.org/10.1617/s11527-012-9985-0>
- [37] Kumar S, Kumar P, Mehrotra S. Influence of granulated blast furnace slag on the reaction, structure, and properties of fly ash geopolymer, *Journal of Material and Sciences*, 2010; 45(3): 607-615. <https://doi.org/10.1007/s10853-009-3934-5>
- [38] Kumar S, and Kumar R. Mechanical activation of fly ash: Effect on reaction, structure, and properties of resulting geopolymer, *Ceramic International*, 2011; 37(2): 533-541 <https://doi.org/10.1016/j.ceramint.2010.09.038>
- [39] Sarker PK. Bond Strength of geopolymer and cement concrete, *Advances in Science and Technology*, 2010; 69:143-151. <https://doi.org/10.4028/www.scientific.net/AST.69.143>
- [40] Sarker PK. Bond strength of reinforcing steel embedded in fly ash-based geopolymer concrete, *Mater. Structures*, 2011; 44: 1021-1030 <https://doi.org/10.1617/s11527-010-9683-8>
- [41] Sofi M, van Deventer JSJ, Mendis PA, Lukey GC. Bond performance of reinforcing bars in organic polymer concrete (IPC), *Journal of Material Sciences*, 2007; 42: 3107-3116. <https://doi.org/10.1007/s10853-006-0534-5>
- [42] Hardjito D, Wallah SE, Sumajouw DMJ, Rangan BV. Properties of Geopolymer Concrete with Fly Ash as Source Material: Effect of Mixture Composition. Presented at the Seventh CANMET/ACI International Conference on Recent Advances in Concrete Technology, Las Vegas, USA, 2004.
- [43] Hardjito D, Wallah SE, Sumajouw DMJ, Rangan BV. Properties of Geopolymer Concrete With Fly Ash as Its Source Material. Presented at the 21st Biennial Conference Of The Concrete Institute of Australia, Brisbane, Australia: Concrete Institute of Australia, 2003
- [44] Wallah SE, Hardjito D, Sumajouw DMJ, Rangan BV. Creep Behavior of Fly Ash-Based Geopolymer Concrete. Presented at the Seventh CANMET/ACI International Conference on Recent Advances in Concrete Technology, Las Vegas, USA, 2004.
- [45] Palomo A, Grutzeck MW, Blanco MT. Alkali-activated fly ashes A cement for the future. *Cement And Concrete Research*, 1999; 29(8): 1323-1329. [https://doi.org/10.1016/S0008-8846\(98\)00243-9](https://doi.org/10.1016/S0008-8846(98)00243-9)
- [46] Sumajouw DMJ, Dapas SO. *Elemen Struktur Beton Bertulang Geopolymer (Structural Elements for Geopolymer Concretes)*, Publisher CV. Patra Media Grafindo, Bandung-Indonesia, Third edition, ISBN:978-623-5776-51-4, 2023
- [47] Sumajouw DMJ, Rangan BV. Low-Calcium Fly Ash-Based Geopolymer Concrete: Reinforced Beams and Columns, Ph.D. Thesis, Faculty of Engineering, Curtin University of Technology, Perth-Australia, 2006.
- [48] Sumajouw DMJ, Hardjito D, Wallah SE, Rangan BV. Fly Ash-Based Geopolymer Concrete: An Application for Structural Members, In *Proceeding of the World Congress GEOPOLYMER 2005: Geopolymer; Green Chemistry and Sustainable Development solutions*, Saint-Quentin, France, 2005. <https://doi.org/10.1080/13287982.2005.11464946>
- [49] Sumajouw DMJ, Hardjito D, Wallah SE, Rangan BV. Behavior and Strength of Geopolymer Concrete Column, In *Proceeding of the 18th Australasian Conference on the Mechanics of Structures & Materials (ACMSM)*, Perth, A.A. Balkema Publishers, The Netherlands, Perth, Australia, 2004.

- [50] Sumajouw DMJ, Hardjito D, Wallah SE, Rangan BV. The behavior of geopolymer Concrete Columns under Equal Load Eccentricities, ACI Special Publication 228, 2005; 577-594.
- [51] Sumajouw DMJ, Hardjito D, Wallah SE, Rangan BV. Fly Ash-based Geopolymer Concrete: Studied of Slender Reinforced Columns. Journal of Material Sciences, 2007; 42(9): 3124-3130. <https://doi.org/10.1007/s10853-006-0523-8>
- [52] Kumaravel S, Thirugnanasambandam S, Jeyasehar CA. Flexural Behavior of Low Calcium Fly Ash Based Geopolymer Concrete Beams. International Journal of Engineering and Applied Sciences, 2013; 5(1): 24-31.
- [53] Abraham R, Raj DS, Abraham V. Strength and Behavior of Geopolymer Concrete Beams. International Journal of Innovative Research in Science, Engineering and Technology, 2013; 2: 159-166.
- [54] Dattatreya JK, Rajamane NP, Sabitha D, Nataraja MC. Flexural Behavior of Reinforced Geopolymer Concrete Beams. International Journal of Civil and Structural Engineering, 2011; 2(1): 138-159.
- [55] Ojha PN, Singh B, Trivedi A, Singh P, Singh A, Pedde C. Short-term Mechanical Performance and Flexural Behavior of Reinforced Slag-fly Ash-based Geopolymer Concrete beams in Comparison to OPC-based Concrete Beams, Journal of Research Engineering Structures & Materials, 2023; 9(1): 31-51. <https://doi.org/10.17515/resm2022.515me0902>
- [56] Setiati NR, Irawan RR. Perbandingan Sifat dan Karakteristik Beton Geopolymer terhadap Beton Semen Portland untuk Kekuatan Struktur Balok. Jurnal Jalan-Jembatan, 2018; 35(2): 125-138.
- [57] Laskar SM, Mozumder RA, Roy B. Behavior of geopolymer concrete under static and Cyclic Loads, Advances in Structural Engineering, 2015; 1643-1653. https://doi.org/10.1007/978-81-322-2187-6_125
- [58] Nawy EG. Reinforced Concrete: A Fundamental Approach, Six Edition Prentice Hall-Upper Saddle River, New Jersey, 2009:07458, ISBN-13:978-0-13-241703-7.
- [59] Warner RF, Rangan BV, Hall AS, & Faulkes KA. Concrete Structures, Melbourne, Longman, 1999:34010099, ISBN:0 582 802347 4.

Blank Page



Research Article

Effect of wind and structural parameters on across wind load of super high-rise buildings

Ashish Singh^{*a}, Sasankasekhar Mandal^b

Department of Civil Engineering, IIT(BHU), Varanasi, India

Article Info

Abstract

Article history:

Received 03 Apr 2023

Accepted 07 June 2023

Keywords:

*Across wind equivalent static wind loads;
Super high-rise building;
Wind and Structural parameters.*

Designing a super high-rise building requires careful consideration of wind loads. The across wind load plays a critical role for super high-rise buildings. A super high-rise building's across-wind load is highly dependent on wind parameters as well as building parameters. It is still unclear how these parameters affect across wind load. Within a possible practical range, this paper attempts to measure the effect of wind and structural parameters on across wind load of a super high-rise building. The wind parameters considered in this study are exponent of mean velocity profile, turbulence intensity, background peak factor and, peak factor for resonant response. Structural parameters influencing across wind load are also considered, such as natural frequency, and structural damping ratio. An analytical method is employed to evaluate the across wind loads to carry out the study. From the results, it can be concluded that among the structural parameters, natural frequency of the structure is the most dominant parameter for the evaluation of across wind loads. In terms of wind parameters, the exponent of mean wind profile has the most impact on the across wind load. The across wind load is not affected by turbulence intensity. This study assists the designers in determining the most appropriate values for wind and structural parameters while estimating the across wind loads.

© 2023 MIM Research Group. All rights reserved.

1. Introduction

Scientific and technological advancements have led to structures becoming taller and slender, and more susceptible to strong winds. Tall buildings are typically subjected to wind loads determined by wind characteristics and aerodynamic properties. It is particularly difficult for tall buildings in coastal areas to withstand severe wind loads due to frequent cyclones. Tall buildings are subjected to dynamic loads due to the turbulent nature of wind. High-rise structures vibrate in a number of ways when exposed to wind, including torsional, across-wind, and along-wind motions. Windward and leeward pressure fluctuations cause along wind vibrations, which typically follow changes in the approach flow, particularly at low frequencies [1,2]. Alternatively, vortex shedding inside the wake zone or galloping can result in transverse or lateral aerodynamic behavior. Both can be attributed to incident turbulence and potentially triggered by turbulence-induced buffeting [3]. The wind-induced torsional load comes into the picture due to structural as well as architectural framework (non-symmetric cross-section, non-symmetrical mass & stiffness distribution) [4] or by wind flow characteristics (uneven pressure distribution across the face, flow approaching at an oblique angle to the face [5,6].

A wind tunnel study conducted by Gu and Quan [7] examined various factors affecting across wind loads on distinctive tall buildings. Studies indicate that across wind dynamic responses of super-tall structures sometimes might be greater than the along-wind ones

^{*}Corresponding author: ashishsingh.rs.civ18@iitbhu.ac.in

^a orcid.org/0000-0001-7907-6179; ^b orcid.org/0000-0002-5495-3793

DOI: <http://dx.doi.org/10.17515/resm2023.727st0403>

Res. Eng. Struct. Mat. Vol. 9 Iss. 4 (2023) 1459-1475

[7,8]. Zhou *et al.* [9] formulated a guideline to estimate equivalent static wind load (ESWL) on structures. The maximum acceleration of the Jin Mao building in the across wind direction is about 1.2 times that in the along wind direction at the design wind speed [10]. Li *et al.* [11] carried out full-scale study of the Jin Mao building and observed the dynamic response of the structure during typhoon Rananim. While the typhoon occurred, acceleration responses were generally higher in across wind directions when compared to the along-wind directions. The measured and calculated natural frequencies of the Jin Mao building differ nearby 10.6-17%. These studies indicate the importance of across wind load in high rise buildings. Zheng and Alex [12] conducted a comparative study on across wind loads on tall building with different codal provisions and discussed the Chinese code [13] in detail. They concluded that there is wide variability in defining the far field wind profile (wind spectrum, turbulence profile, turbulence integral scale and correlation) for specific locations calculated by various codal provisions. They also emphasized that a specific model from full-scale can reduce the significant uncertainty on the design wind load versus the design wind speed. Kwon and Kareem [14] examined the most important wind standards for tall buildings due to adverse wind implications. Holmes *et al.* [15] compared the wind loads for low, medium, and high-rise structures using fifteen distinct international codes.

Quan and Gu [16] have developed an analytical method to estimate the across wind ESWL of a super high-rise building. The term "super high-rise building" refers to buildings that are 300 meters or higher in height. Singh and Mandal [17] investigated the impact of plan and height aspect ratios on across wind loads using this analytical approach and contrasted it with along wind loads. A tall building's wind load is influenced by a number of structural, geometrical, and wind characteristics. The impact of geometrical characteristics on the across wind load through aerodynamic modification has been examined in a number of studies [18]. Many studies also discuss the influence of structural damping in reducing the across wind load [19].

Due to insufficient knowledge regarding the role of wind and structural parameters on across wind load, an analytical method is utilized to identify the effect of various parameters on across wind loads. Out of structural parameters, the Natural frequency of the structure (f) and structural damping ratio (ζ_s) are selected due to their key role in the calculation of across wind load. Four parameters (Exponent of mean velocity profile (α), turbulence intensity (I_H), peak factor for resonant response (g_R), and the background peak factor (g_B)) are selected out of wind parameters because of their significance in defining the characteristics of wind approaching the structure. Thus, the effects of these parameters on the across wind load are examined in this paper. A hypothetical 300 m super high-rise building with a square cross-section, assumed to be located in urban terrain, is adopted for the analysis. In order to comprehend the range of parameters, several international codes are used for each parameter evaluation. For suitability, we have referred to the codes that explicitly provided the corresponding parameters. Various international codes/ Standards have provided certain values of these parameters applicable to their specific site conditions. An understanding of how these parameters affect the across wind load will greatly assist engineers in accurately calculating the across-wind load for the structure. Accurate estimation of wind and structural parameters is essential because inaccurate estimation of these parameters will lead to underestimation or overestimation of across wind load. An incorrect load calculation will result in a faulty building design.

2. Analytical Method

Analytical method utilized in the study is derived from the wind tunnel studies. The analytical method calculates the across wind ESWL, based on the geometrical & structural configuration of the structure and approaching wind parameters. Quan and Gu [16]

provided detailed instructions to evaluate the across wind ESWL. The procedure to evaluate across wind load is described briefly in the following steps:

First the dimensions of the buildings *viz.* height(H), width(B) & Depth(D) must be determined then find out the structural parameters *viz.* fundamental frequency (f_i) of the building, structural damping ratio (ζ_s), first mode shape $\phi_i = (z/H)^\beta$. Mode shape index (β)=1. The equation (1) denotes the generalized mass, where, $m(z)$ = mass per unit height at height z .

$$M_i^* = \left[\int_0^H m(z) \times \phi_i^2(z) dz \right] \quad (1)$$

Acquire the wind related parameters *viz.* turbulence intensity (I_H), mean wind velocity profile exponent (α), The wind pressure exerted at the uppermost section of a building (w_H), and mean velocity at the top of the building (U_H).

Coefficient of background base moment (C_{M-B0}) is evaluated using equation (2).

$$C_{M-B0} = \{ 0.182 - 0.019\alpha_{db}^{-2.54} + 0.54\alpha_w^{-0.91} \} \quad (2)$$

Where, $\alpha_{db} = D/B$; eventually, it will ultimately turn into one since a square building is taken into consideration. α_w is function of turbulence intensity (I_H) expressed as

$$\alpha_w = 4.2 - 4e^{3.7-60I_H} \quad (3)$$

Davenport [1] proposed an empirical formula to evaluate the peak factor for resonant response (g_R) as shown in equation (4).

$$g_R = \sqrt{2 \ln(600f_1)} + \frac{0.5772}{\sqrt{2 \ln(600f_1)}} \quad (4)$$

$S_M^*(n)$ is expressed as

$$S_M^*(n) = \frac{S_p \eta (n/f_p)^\lambda}{\left\{ 1 - (n/f_p)^2 \right\}^2 + \eta (n/f_p)^2} \quad (5)$$

In equation (5), f_p = Location parameter, S_p = Amplitude parameter, η = bandwidth parameter, λ = deflection parameter and α_{hr} = height ratio, Reduced frequency (n) = $f B/U_H$. Equations (6) to (10) are employed to compute these factors.

$$S_p = \{ (0.1\alpha_w^{0.4} - 0.0004e^{\alpha_w}) \times (0.84\alpha_{hr} - 2.12 - 0.05\alpha_{hr}^2) \times (0.422 + \alpha_{db}^{-1} - 0.08\alpha_{db}^{-2}) \} \quad (6)$$

$$f_p = \{ 10^{-5} (191 - 9.48\alpha_w + 1.28\alpha_{hr} + \alpha_{hr}\alpha_w) \times (68 - 21\alpha_{db} + 3\alpha_{db}^2) \} \quad (7)$$

$$\eta = \{ (1 + 0.00473e^{1.7\alpha_w}) \times (0.065 + e^{1.26 - 0.63\alpha_{hr}}) e^{1.7 - 3.44/\alpha_{db}} \} \quad (8)$$

$$\lambda = \{ (-0.8 + 0.06\alpha_w + 0.0007e^{\alpha_w}) \times (-\alpha_{hr}^{0.34} + 0.00006e^{\alpha_{hr}}) \times (0.414\alpha_{db} + 1.67\alpha_{db}^{-1.23}) \} \quad (9)$$

$$\alpha_{hr} = H/\sqrt{BD} \quad (10)$$

The aerodynamic damping ratio ζ_a derived by Quan et al. [20] is computed as

$$\zeta_a = \frac{\{ 0.0025 (1 - (U^*/9.8)^2) (U^*/9.8) + 0.000125 (U^*/9.8)^2 \}}{\{ (1 - (U^*/9.8)^2)^2 + 0.0291 (U^*/9.8)^2 \}} \quad (11)$$

where, U^* = Reduced wind speed and expressed in equation (12).

$$U^* = [U_H / f_1 B] \tag{12}$$

The across wind ESWL, $\hat{p}(z)$ is calculated using equation (13), where, G_B = Background load coefficient, G_R = Resonant load coefficient, they are expressed in equations (14) & (15) respectively.

$$\hat{p}(z) = W_H B \sqrt{G_B^2(z) + G_R^2(z)} \tag{13}$$

$$G_B(h) = \{ (0.65 + 1.3h + 7h^2 - 7.5h^3) g_B C_{M-B0} \} \tag{14}$$

$$G_R(z) = \frac{H m(z)}{M_i^*} \left(\frac{z}{H} \right)^\beta g_R \sqrt{\frac{\pi \Phi S_M^*(f_1)}{4(\zeta_{s1} + \zeta_{a1})}} \tag{15}$$

Where, $\Phi=1$ for first mode [21], ζ_{s1} = Structural damping ratio, and ζ_{a1} = Aerodynamic damping ratio, accordingly for the first mode.

The peak acceleration can be calculated using equation (16).

$$\hat{a}(z) = \frac{H}{M_i^*} B g_R W_H \left(\frac{z}{H} \right)^\beta \sqrt{\frac{\pi \Phi S_M^*(f_1)}{4(\zeta_{s1} + \zeta_{a1})}} \tag{16}$$

3. Fixed Parameters of the Building

This research investigates a theoretical tall structure located within the city environment. The wind direction and the plan of the building are shown in Fig.1. The plan dimension, height & other parameters of the building which are kept constant throughout this study are enumerated in Table 1. A discussion of the parameters which are varied will follow in the next section.

Table 1. Building parameters that are kept constant throughout the study

H(m)	B(m)	D(m)	β	$M_1^*(\text{kg})$
300	50	50	1	5.0×10^7

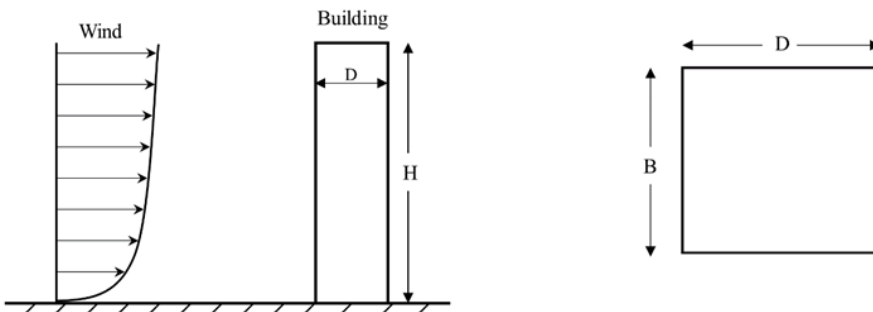


Fig. 1 Direction of wind and plan of the building

4. Structural Parameters

4.1 Natural Frequency of the Structure (f)

When it comes to determining wind loads, the natural period of a building holds the utmost importance. Table 2 shows the formulations available to calculate time period of tall RC buildings for wind design. The natural frequency of high-rise buildings with a height of H meter would be $f_1 = \frac{1}{T_1}$.

Natural time period is calculated according to the various codal provisions. There exists wide variability in the expressions for natural period provided by different codes and researchers. It is clearly visible from Table 2 that only Indian standard takes into account the base dimension in the formulation of time period. All other expressions are function of total height of the building only.

Table 2. Various recommendation of natural period (H & D are shown in Fig.1)

Code	Natural Time Period (T)	Natural Frequency (f)
ASCE 7-16 [22]	$T = H^{0.9}/43.5$	0.2565
Eurocode [23]	$T = 0.022H$	0.1515
Ha <i>et al.</i> [24]	$T = 0.0196H$	0.1700
IS 875 (Part 3)[25]	$T = 0.09H/\sqrt{D}$	0.2619
KBC [26]	$T = 0.073H^{0.75}$	0.1900
Lagomarsino [27]	$T = 0.018H$	0.1852
Tamura [28]	$T = 0.015H$	0.2222

4.2 Structural Damping Ratio (ζ_s)

From the perspective of structural response under dynamic loading, structural damping is a crucial parameter. Table 3 lists the various single value structural damping ratios of the numerous codal provisions.

Table 3. Structural Damping ratios of tall RC building

Code	Structural damping ratio(ζ_s)
ASCE 7-16 [22]	2%
AS/NZ1170 [29]	1%
Eurocode [23]	1.57%
ISO [30]	1.2%
IS 875 (Part 3)[25]	2%

5. Wind Parameters

5.1 Exponent of Mean Velocity Profile (α)

Exponent of mean velocity profile(α) is a pivotal parameter in defining the approaching wind profile. Equation (17) shows the power-law profile of approaching wind.

$$U(H) = U_{\text{ref}} \left(\frac{H}{H_{\text{ref}}} \right)^{\alpha} \quad (17)$$

Where, UH is the wind speed at height H, Href is the reference height taken as 10 meters. Uref is called as reference wind speed which is defined at the reference height. In this case Uref is considered as 25.2326 m/s. Href and Uref are kept constant, and only exponent of

mean wind velocity(α) is varied. Various international standards recommend the values of exponent of mean velocity profile for different types of terrain categories. The value of α for the urban terrain is shown in Table 4.

Table 4. Exponent of mean velocity profile for urban terrain

Code	Exponent of mean velocity profile for urban terrain (α)	Wind speed at the height of target building (U_H) in m/s
AIJ [31]	0.35	82.98
ASCE 7-16 [22]	0.25	59.05
GB 50009[13]	0.3	70
ISO [30]	0.40	98.36
NBCC [32]	0.36	85.84

5.2 Turbulence Intensity (I_H)

Turbulence intensity gives an understanding of wind turbulence in the approaching flow and it affects the effective wind loads on the structure. International codes have provided formulations to assess the turbulence intensity at the location of the building based on the terrain category parameters as presented in Table 5.

Table 5. Turbulence intensity profile and its parameters for urban terrain

Code	Turbulence intensity for urban terrain	Different parameters and their values for urban terrain	Turbulence Intensity in Percentage
ASCE 7-16 [22]	$I_z = c \left(\frac{10}{z}\right)^{1/6}$	$c=0.30,$ $\bar{z} = 0.6h$	18.53
AS/NZ1170 [29] (formulated)	$I_z = c \left(\frac{10}{z}\right)^d$	$c=0.40, d=0.24$	17.68
Eurocode [23]	$I_z = \left(\frac{1}{\ln(z/z_0)}\right)$	$z_0=1, z=h$	17.53
IS 875 (Part 3)[25]	$I_{z,4}$ $= 0.466 - 0.1358 \log_{10} \left(\frac{z}{z_{0,4}}\right)$	$z_{0,4} = 2, z=h$	17
ISO [30]	$I_z = \left(\frac{1}{\ln(z/z_0)}\right)$	$z_0=3, z=h$	21.71

5.3 Peak Factor for Resonant Response (g_R)

g_R is influenced by the averaging time (T) and the up-crossing rate (v), which is nearly equivalent to the natural frequency of the structure under the assumption that the development is narrow banded Gaussian. Quan and Gu [16] used the peak factor related to averaging time 10-minutes (600 sec), so here, for the conformity, we have opted the international standards, which specifically use 10-min averaging time. Here, f_1 is fundamental natural frequency of the building. Quan and Gu [16] used the fundamental frequency as 0.2 Hz so for comparison of different peak background factor, fundamental frequency is kept constant as 0.2 Hz for all cases. Various codal provisions for estimating the peak factor for resonant response are presented in Table 6.

Table 6. Peak factor for resonant response for various codes and its magnitude at fundamental frequency 0.2 Hz

Code	Peak factor for resonant response (g_R)	f = 0.20 Hz
AIJ [31]	$g_R = \sqrt{2\ln(600f_1) + 1.2}$	3.2825
AS/NZ1170 [29]	$g_R = \sqrt{2\ln(600f_1)}$	3.0943
Eurocode [23]	$g_R = \sqrt{2\ln(600f_1) + \frac{0.6}{\sqrt{2\ln(600f_1)}}$	3.2882
ISO [30]	$g_R = \sqrt{2\ln(600f_1) + \frac{0.577}{\sqrt{2\ln(600f_1)}}$	3.2808
GB 50009[13]	2.5	2.5

5.4 Background Peak Factor (g_B)

Almost all codes use a single value for the background peak factor. The Japanese and European codes use the value of g_B same as g_R . Table 7 shows the background peak factor for the various codal provisions. In contrast to other codes, the Chinese code specifies a fixed value of 2.5 for g_B and g_R , leading to significantly lower values. There is no clear explanation for this choice.

Table 7. Background Peak factor for various codes

Code	Background Peak factor (g_B)
AIJ [31]	$g_B = g_R = 3.2825$
AS/NZ1170 [29]	3.7
Eurocode [23]	$g_B = g_R = 3.2882$
ISO [30]	3.4
GB 50009[13]	2.5

6. Methodology

Following the instructions of the section analytical method, a MATLAB code is developed in the present study to evaluate all the parameters and compute the across wind ESWL and responses. The MATLAB code is provided in Appendix A. The validation of the code is done by comparing the results with Quan and Gu [16] as shown in Fig. 2. The evaluation of parameters is conducted using a variety of international codes in order to understand the range of parameters. There is a total of six parameters, whose effect on wind load is studied. Out of six parameters, only one is varied at a time, while the other independent parameter remains constant. Table 8 contains the fixed values of parameters. The effect of each parameter on across wind load and response is analyzed.

7. Results and Discussion

7.1 Effect of Natural Frequency (f) of the Structure

The across wind load of the super tall building is calculated on different natural frequencies. Table 8 lists the parameters that are kept constant in this section. The provisions for determining natural frequencies according to various codes are presented in the section structural parameters. The calculation procedures for calculating the across-wind ESWL and response are succinctly discussed in the section analytical method. Figures 3(a)-(d) show the variation in ESWL, shear force, bending moment, and peak acceleration along the height of the building. Peak factor for resonant response (g_R) is dependent on fundamental natural frequency of the structure. Therefore, g_R is automatically varied

while varying the natural frequency in this case. The parameters other than these two are kept constant. The Eurocode [23] proposes the lowest natural frequency for the building, while IS 875 (Part 3)[25] recommends the highest. As per the Fig 3, it is evident that the results obtained are maximum for Eurocode [23], while the results for IS 875 (Part 3)[25] are the minimum. It is evident from the results that as the natural frequency of the building is decreasing, the across wind load and responses are increasing. It is happening because the background components are highly sensitive to reduced frequency (n) which is a function of natural frequency.

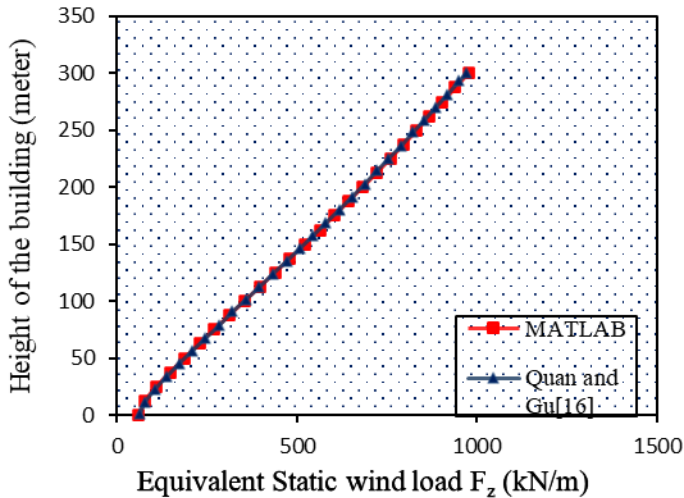


Fig.2 Comparison of Quan and Gu[16] and MATLAB results

Table 8. Fixed value of parameters.

Parameter	Value
Natural frequency(f) of the structure	0.20 Hz
Structural damping ratio (ζ_s)	1%
Exponent of mean velocity profile (α)	0.30
Turbulence intensity (I_H)	11%
Peak factor for resonant response (g_R)	3.281
Background peak factor (g_B)	3.5

7.2 Effect of Structural Damping Ratio (ζ_s)

In this section, the across wind load is calculated at different structural damping ratio (ζ_s) and keeping all the other parameters constant. As mentioned in Table 3, AS/NZ 1170 [29] recommends the lowest value of the structural damping ratio of the building, while ASCE 7-16 [22] and IS 875 (Part 3)[25] suggest the highest value. Fig. 4(a) -(d) delineates the variation of ESWL, shear force, bending moment, and peak acceleration along the building height. It can be observed from Fig 4(a)-(d) that AS/NZ 1170 [29] gives the maximum wind load. Since both ASCE 7-16 [22] and IS 875 (Part 3)[25] recommend the same, and high value of structural damping ratio, the across wind load is similar and minimum. A conclusion can be drawn that as the structural damping ratio increases the across wind load decreases. This study's findings agree with Wang et al. [33] and Li et al. [34], which found a decrease in cross-wind response as structural damping increased.

7.3 Effect of Exponent of Mean Velocity Profile (α)

Figure 5(a)-(d) illustrates the impact of wind velocities provided in Table 4 on the across wind loads and responses. Across wind load is maximum for ISO [30] because it has the maximum exponent value and due to this, it proposes the maximum wind velocity at height of target building. ASCE 7-16 [22] proposes the minimum value of exponent among other codes; hence the across wind load is minimum in this case. Based on Fig. 5 the conclusion can be drawn that as the wind speed increases across wind load and response also increases. Gu *et al.* [35] also concluded the same in their study. According to their statement, the susceptibility of the across-wind response is greater to the approaching wind speed as compared to the along-wind response. In general, longitudinal wind loads are more prominent at lower wind velocities, whereas transverse wind loads are predominant at higher velocities. The inherent frequencies of exceptionally tall structures are comparatively low, and the velocity of wind is greater at the uppermost tiers of the boundary layer. Consequently, the reduced frequency of a skyscraper at the wind speed for which it was designed may correspond to the reduced frequency at which the maximum force spectrum across the wind direction transpires.

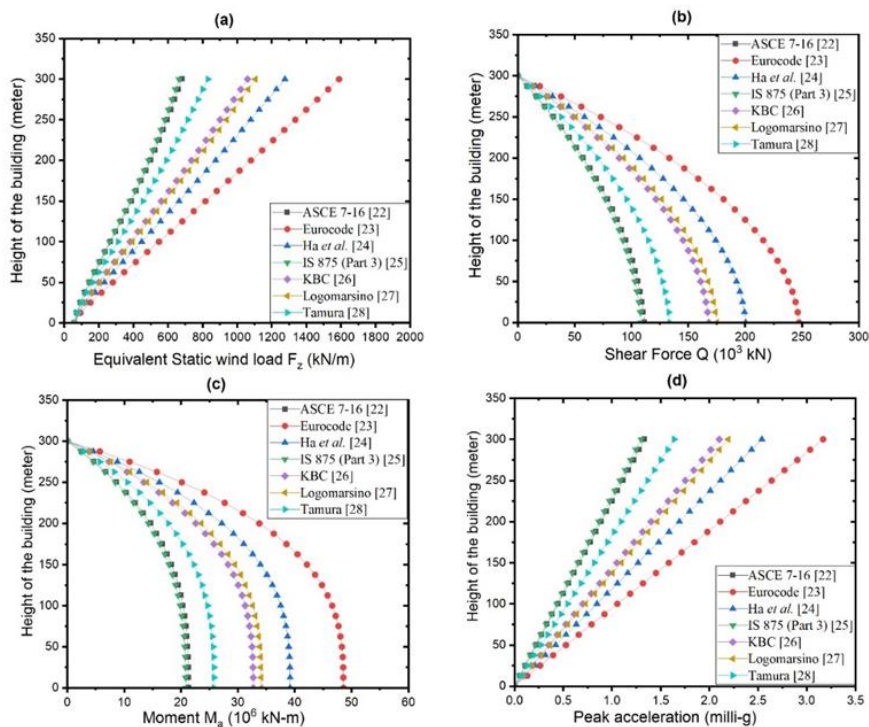


Fig. 3 ESWL, Shear Force, Moment and Peak acceleration along the height of the building for various natural frequencies

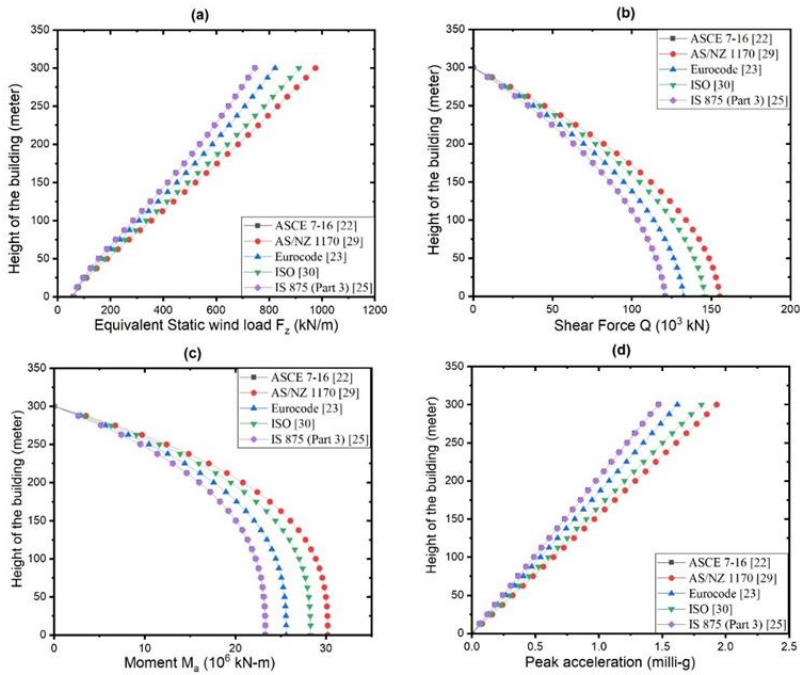


Fig.4 ESWL, Shear Force, Moment and Peak acceleration along the height of the building for various structural damping ratio

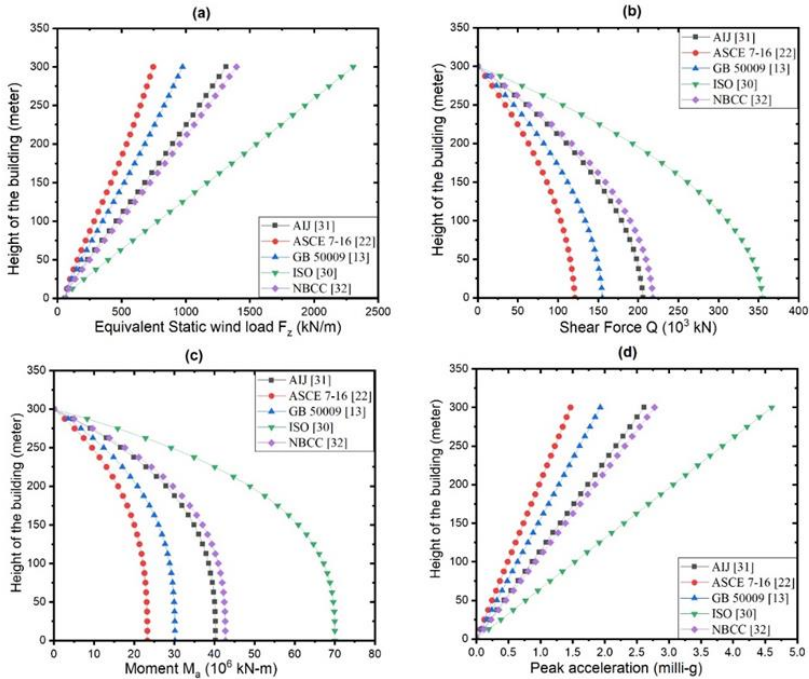


Fig. 5 ESWL, Shear Force, Moment and Peak acceleration along the height of the building for various exponent of mean velocity profile

7.4 Effect of Turbulence Intensity (I_H)

This section involves the calculation of the across wind load of tall building at different turbulence intensity values while keeping the other five parameters constant. Through the results obtained in the study, it can be inferred that turbulence intensity has a minimal effect on the across wind loads. The results collected from the various turbulence intensities produced similar outcomes. Table 9 exhibits the across wind load values (kN/m) from the analysis of five international codes. Cheng et al. [36] have previously deduced that the lift coefficient, an indicator of the across wind load, does not exhibit a correlation with changes in turbulence intensity. The current study has corroborated these findings. While the along-wind force spectrum primarily reflects the wind turbulence approaching the structure, the across-wind force spectrum is mostly influenced by vortex formation and flow separation. Therefore, the turbulence intensity has minimal impact on the across-wind response.

Table 9. Across wind ESWL of a 300 m super high-rise building at various turbulence intensity

Height	ASCE 7-16 [22]	AS/NZ1170 [29]	Eurocode [23]	IS 875 (Part 3) [25]	ISO [30]
0.00	60.54	60.54	60.54	60.54	60.54
12.50	77.98	77.98	77.99	77.99	77.98
25.00	110.16	110.17	110.17	110.18	110.15
37.50	147.89	147.90	147.91	147.92	147.88
50.00	187.96	187.98	187.98	188.00	187.94
62.50	229.20	229.22	229.22	229.24	229.17
75.00	271.08	271.10	271.11	271.13	271.05
87.50	313.31	313.34	313.34	313.37	313.27
100.00	355.68	355.72	355.72	355.76	355.64
112.50	398.05	398.09	398.10	398.13	398.00
125.00	440.28	440.32	440.33	440.37	440.23
137.50	482.25	482.30	482.31	482.35	482.19
150.00	523.86	523.91	523.92	523.97	523.80
162.50	565.02	565.07	565.08	565.14	564.95
175.00	605.63	605.69	605.71	605.76	605.56
187.50	645.65	645.71	645.73	645.79	645.57
200.00	685.02	685.09	685.10	685.17	684.94
212.50	723.72	723.79	723.81	723.88	723.63
225.00	761.76	761.83	761.85	761.92	761.66
237.50	799.15	799.23	799.25	799.33	799.05
250.00	835.98	836.06	836.08	836.16	835.87
262.50	872.34	872.43	872.45	872.53	872.22
275.00	908.38	908.48	908.50	908.59	908.26
287.50	944.31	944.41	944.43	944.53	944.18
300.00	980.37	980.47	980.50	980.60	980.24

7.5 Effect of peak factor for resonant response (g_R)

The study analyzed the across wind loads of a super tall building at various peak factors for resonant response (g_R) while holding the other five parameters constant (as shown in Table 8). The results were visualized in Fig. 6 (a)-(d), which displayed the variation of ESWL, shear force, bending moment, and peak acceleration along the height of the building. The findings from AIJ [31], ISO [30], and Eurocode [23] were quite similar. However, GB

50009 [13] showed the lowest across wind loads, primarily due to the lowest value of the resonant factor. It is observed that as the resonant factor increased, the across wind load also increased.

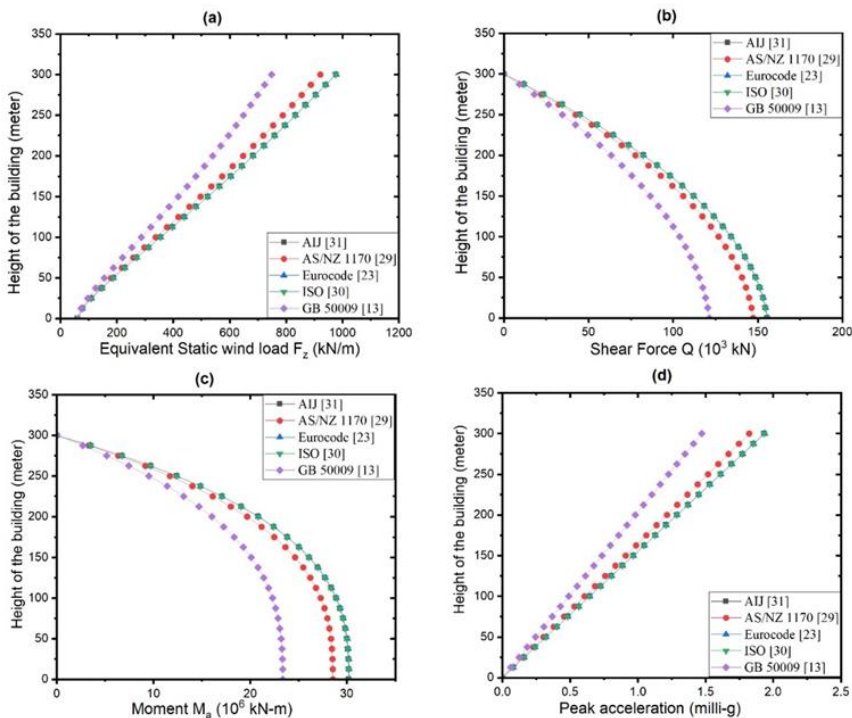


Fig.6 ESWL, Shear Force, Moment and Peak acceleration along the height of the building for g_R

7.6 Effect of Background Peak Factor (g_B)

The background response refers to a type of quasi-static response that occurs by variations in turbulence wind at low frequencies, which are too low to instigate any resonant response [37]. This section examines the across wind loads of the structure calculated at different background peak factor (g_B) and keeping the other five parameters constant. It can be seen from Fig.7(a)-(c) that effect of background peak factor on across wind load is minimum. Peak acceleration does not depend on the background peak factor (Equation 16). Therefore in Fig.7(d), all the codes produce equal peak acceleration.

7.7 Variations in the Across Wind Load Caused by Various Parameters

Variation of all the parameters with the maximum across wind ESWL is plotted in Fig. 8. A constant vertical axis of across wind ESWL is maintained for all the parameters. There is a rapid decrease in across wind load as the natural frequency increases. As the structural damping ratio increases the across wind load decreases. As the exponent of mean velocity profile increases, the across wind load also increases exponentially. Turbulence intensity does not influence the across wind load. As the peak factor for resonant response increases, the across wind load also increases. As the background peak factor increases the across wind load increases gradually. Out of the six parameters, the exponent of mean velocity profile affects the across wind load the most.

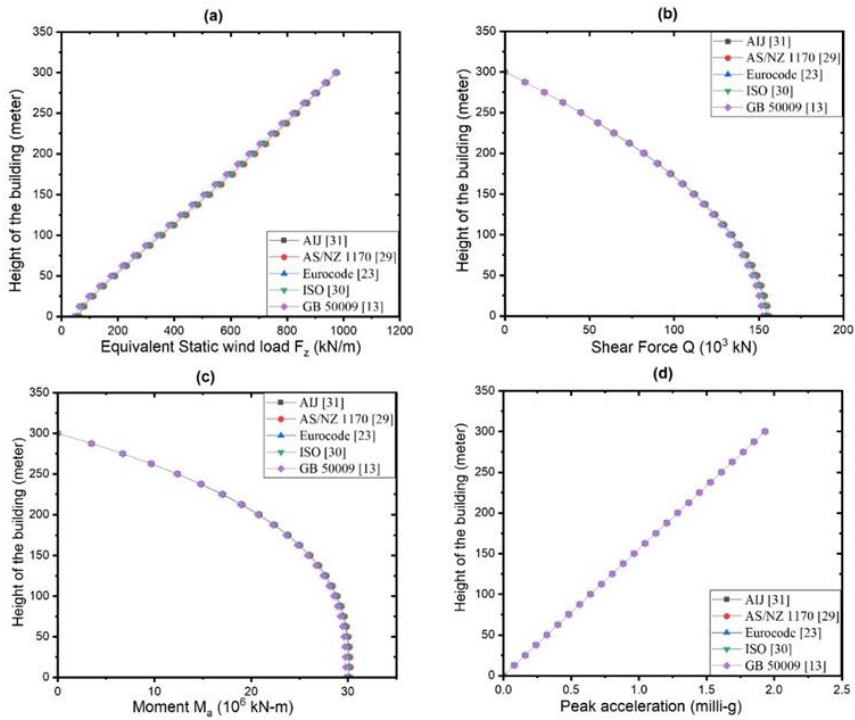


Fig. 7 ESWL, Shear Force, Moment and Peak acceleration along the height of the building for g_B

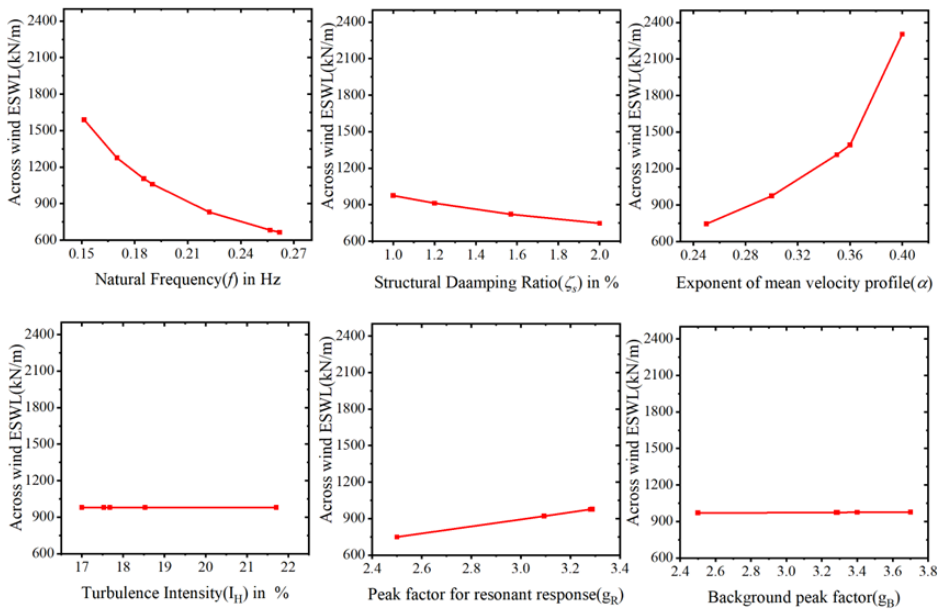


Fig.8 Variation of across wind load with various parameters

8. Conclusions

When designing a super high-rise building, it is crucial to take into account the wind loads it will be subjected to, particularly the across-wind load. Both wind and structural parameters heavily influence this type of load, and their impact on the across-wind load is still uncertain. This paper studies the effect of wind and structural parameters on across wind load. A hypothetical super high-rise building of 300 m in height and square cross-section, assumed to be located in urban terrain, is selected for analysis. Evaluation of the parameters is carried out in accordance with several international standards. To determine the across wind ESWL and responses, a MATLAB code is developed. The results are presented in the form of ESWL, Shear Force, Bending Moment, and Peak Acceleration. The following are critical outcomes of the present study.

- The results clearly show that as the natural frequency changes from 0.1515Hz to 0.2619 Hz, there is a change in the across wind ESWL from 1589kN/m to 664 kN/m. It is because the background components of the building are highly responsive to the natural frequency.
- The exponent of mean velocity profile (α) influences the cross wind load the most compared to other parameters. As the α changes from 0.36 to 0.4, there is a 65% increase in wind load. At high wind speed, there is an intense across-wind response.
- This study has demonstrated that when the structural damping ratio increases, there is a decrease in the cross-wind load. As the structural damping ratio increases from 1% to 2%, the across-wind ESWL decreases from 975 to 746kN/m.
- Across wind load is minimally affected by the turbulence intensity of the surrounding wind. As the turbulence intensity changes from 17% to 21.71%, the across wind ESWL remained unchanged as 980kN/m
- The peak factor for resonant response (g_R) affects the cross wind loads more in comparison to the background peak factor (g_B), and Peak acceleration is independent of the Background peak factor (G_B). As the g_R changes from 2.5 to 3.2882, the cross wind ESWL, the across wind ESWL increases from 748 kN/m to 977 kN/m. The background peak factor(g_B) changes from 2.5 to 3.7, there is a small increase in across wind ESWL as 971kN/m to 976kN/m.

This study substantially helps to understand the variation in wind loading due to the variability of the key parameters involved. It is crucial to have precise estimations of wind and structural parameters. It is essential to accurately determine these parameters to avoid underestimating or overestimating the wind load exerted on a structure, which may lead to flawed load calculations and faulty building design. Additionally, wind tunnel studies and full-scale experiments should be conducted to study the same in greater detail.

References

- [1] Davenport AG. Gust loading factors. Journal of the Structural Division. 1967;93(3):11-34. <https://doi.org/10.1061/JSDEAG.0001692>
- [2] Chen X, Kareem A. Dynamic wind effects on buildings with 3D coupled modes: Application of high frequency force balance measurements. Journal of Engineering Mechanics. 2005;131(11):1115-25. [https://doi.org/10.1061/\(ASCE\)0733-9399\(2005\)131:11\(1115\)](https://doi.org/10.1061/(ASCE)0733-9399(2005)131:11(1115))
- [3] Liang S, Liu S, Li QS, Zhang L, Gu M. Mathematical model of acrosswind dynamic loads on rectangular tall buildings. Journal of Wind Engineering and Industrial Aerodynamics. 2002;90(12-15):1757-70. [https://doi.org/10.1016/S0167-6105\(02\)00285-4](https://doi.org/10.1016/S0167-6105(02)00285-4)

- [4] Tallin A, Ellingwood B. Analysis of torsional moments on tall buildings. *Journal of wind engineering and industrial aerodynamics*. 1985;18(2):191-5. [https://doi.org/10.1016/0167-6105\(85\)90097-2](https://doi.org/10.1016/0167-6105(85)90097-2)
- [5] Cheung JC, Melbourne WH. Torsional moments of tall buildings. *Journal of Wind Engineering and Industrial Aerodynamics*. 1992;42(1-3):1125-6. [https://doi.org/10.1016/0167-6105\(92\)90119-U](https://doi.org/10.1016/0167-6105(92)90119-U)
- [6] Lythe GR, Surry D. Wind-induced torsional loads on tall buildings. *Journal of Wind Engineering and Industrial Aerodynamics*. 1990;36:225-34. [https://doi.org/10.1016/0167-6105\(90\)90307-X](https://doi.org/10.1016/0167-6105(90)90307-X)
- [7] Gu M, Quan Y. Across-wind loads and effects of super-tall buildings and structures. *Science China Technological Sciences*. 2011;54:2531-41. <https://doi.org/10.1007/s11431-011-4543-5>
- [8] Gu M, Quan Y. Across-wind loads of typical tall buildings. *Journal of Wind Engineering and Industrial Aerodynamics*. 2004;92(13):1147-65. <https://doi.org/10.1016/j.jweia.2004.06.004>
- [9] Zhou Y, Kareem A, Gu M. Equivalent static buffeting loads on structures. *Journal of Structural Engineering*. 2000;126(8):989-92. [https://doi.org/10.1061/\(ASCE\)0733-9445\(2000\)126:8\(989\)](https://doi.org/10.1061/(ASCE)0733-9445(2000)126:8(989))
- [10] Gu M, Zhou Y, Zhang F, Xiang HF. Dynamic responses and equivalent wind loads of the Jin Mao Building in Shanghai. In *Proceedings of the tenth international conference on wind engineering, Copenhagen, Denmark, Vol. 3*, pp. 1497-504,1999.
- [11] Li QS, Xiao YQ, Fu JY, Li ZN. Full-scale measurements of wind effects on the Jin Mao building. *Journal of Wind Engineering and Industrial Aerodynamics*. 2007;95(6):445-66. <https://doi.org/10.1016/j.jweia.2006.09.002>
- [12] Zheng WZ, Alex PT. Comparative study of along-wind and across-wind loads on tall buildings with different codes. *Proceedings of 14th international Symposium on Structural Engineering*. Beijing, China, 723-728, 2016.
- [13] Ministry of Housing and Urban-Rural Development of the People's Republic of China. GB 50009-2012 Load Code for the Design of Building Structures. 2012.
- [14] Kwon DK, Kareem A. Comparative study of major international wind codes and standards for wind effects on tall buildings. *Engineering Structures*. 2013;51:23-35. <https://doi.org/10.1016/j.engstruct.2013.01.008>
- [15] Holmes J, Tamura Y, Krishna P. Comparison of wind loads calculated by fifteen different codes and standards, for low, medium and high-rise buildings. In *11th Americas conference on wind engineering, San Juan, Puerto Rico, 1-10, 2009*.
- [16] Quan Y, Gu M. Across-wind equivalent static wind loads and responses of super-high-rise buildings. *Advances in Structural Engineering*. 2012;15(12):2145-55. <https://doi.org/10.1260/1369-4332.15.12.2145>
- [17] Singh A, Mandal S. Effect of plan and height aspect ratios on along wind and across wind loads on super high rise buildings. *Jordan Journal of Civil Engineering*. 2022;16(2):335-354.
- [18] Sharma A, Mittal H, Gairola A. Mitigation of wind load on tall buildings through aerodynamic modifications. *Journal of Building Engineering*. 2018;18:180-94. <https://doi.org/10.1016/j.jobe.2018.03.005>
- [19] Jafari M, Alipour A. Methodologies to mitigate wind-induced vibration of tall buildings: A state-of-the-art review. *Journal of Building Engineering*. 2021;33:1-25. <https://doi.org/10.1016/j.jobe.2020.101582>
- [20] Quan Y, Gu M, Tamura Y. Experimental evaluation of aerodynamic damping of square super high-rise buildings. *Wind & structures*. 2005;8(5):309-24. <https://doi.org/10.12989/was.2005.8.5.309>
- [21] Xu YL, Kwok KC. Mode shape corrections for wind tunnel tests of tall buildings. *Engineering Structures*. 1993;15(5):387-92. [https://doi.org/10.1016/01410296\(93\)90042-3](https://doi.org/10.1016/01410296(93)90042-3)

- [22] American Society of Civil Engineers. ASCE/SEI 7-16. Minimum design loads and associated criteria for buildings and other structures. American Society of Civil Engineers. 2016.
- [23] European Committee for Standardization (C.E.N.). Eurocode 1: Actions on Structures—Part 1–4: General Actions—Wind Actions; pr EN 1991-1-4.6; European Committee for Standardization (C.E.N.): Brussels, Belgium. 2004.
- [24] Ha T, Shin SH, Kim H. Damping and natural period evaluation of tall RC buildings using full-scale data in Korea. *Applied Sciences*. 2020;10(5):1-16. <https://doi.org/10.3390/app10051568>
- [25] IS 875 (Part 3): 2015, Bureau of Indian Standards, Indian Standard Code of Practice for design loads (other than earthquake) for buildings and structures. Part 3 – Wind loads, 2015.
- [26] Architectural Institute of Korea. Korean Building Code (KBC). Structural 2009; Ministry of Construction and Transportation of Korea: Seoul, Korea. 2009.
- [27] Lagomarsino S. Forecast models for damping and vibration periods of buildings. *Journal of Wind Engineering and Industrial Aerodynamics*. 1993;48(2-3):221-39. [https://doi.org/10.1016/0167-6105\(93\)90138-E](https://doi.org/10.1016/0167-6105(93)90138-E)
- [28] Tamura Y. Damping in buildings for wind resistant design. International Symposium on Wind and Structures for the 21st Century, Cheju, Korea, 115-130, 2000.
- [29] Australia/New Zealand (AS/NZS). Australian/New Zealand Standards, Structural Design Actions—Part 2, Wind Actions. AS/NZS 1170.2:2011; Standards Australia: Sydney, Australia, 2011
- [30] ISO 4354 (E) Second Edition: Wind Actions on Structures; International Organization for Standardization: Geneva, Switzerland, 2009.
- [31] Architecture Institute of Japan (AIJ).: Recommendations for loads on buildings. Architectural Institute of Japan. Tokyo, Japan. 2004 (In Japanese)
- [32] NBCC.: National building Code of Canada. National Research Council of Canada, Ottawa, Canada. 2020.
- [33] Wang M, Nagarajaiah S, Sun FF. A novel crosswind mitigation strategy for tall buildings using negative stiffness damped outrigger systems. *Structural Control and Health Monitoring*. 2022;29(9):2988. <https://doi.org/10.1002/stc.2988>
- [34] Li SY, Liu M, Li HX, Hui Y, Chen ZQ. Effects of structural damping on wind-induced responses of a 243-meter-high solar tower based on a novel elastic test model. *Journal of Wind Engineering and Industrial Aerodynamics*. 2018;172:1-11. <https://doi.org/10.1016/j.jweia.2017.10.027>
- [35] Gu M, Su L, Quan Y, Huang J, Fu G. Experimental study on wind-induced vibration and aerodynamic mitigation measures of a building over 800 meters. *Journal of Building Engineering*. 2022 Apr 1;46:103681. <https://doi.org/10.1016/j.jobbe.2021.103681>
- [36] Cheng CM, Lu PC, Chen RH. Wind loads on square cylinder in homogeneous turbulent flows. *Journal of Wind Engineering and Industrial Aerodynamics*. 1992 ;41(1-3):739-49. [https://doi.org/10.1016/0167-6105\(92\)90490-2](https://doi.org/10.1016/0167-6105(92)90490-2)
- [37] Holmes JD. Resonant dynamic response and effective static load distributions. *Wind loading of structures*, 3rd edition, New York CRC press, 2018: 113-148, ISBN 1978-1-4822-2922-6

Appendix A: MATLAB Code for Calculation of across wind ESWL

```

H=300;
pp=H/24;
h=[0,pp/H,(2*pp/H),(3*pp/H),(4*pp/H),(5*pp/H),(6*pp/H),(7*pp/H),(8*pp/H),(9*pp/H),(10*pp/H),(11*pp/H),(12*pp/H),(13*pp/H),(14*pp/H),(15*pp/H),(16*pp/H),(17*pp/H),(18*pp/H),(19*pp/H),(20*pp/H),(21*pp/H),(22*pp/H),(23*pp/H),1];
B=(300/6);
D=(300/6);
f1=1/T; %T=H^0.9/43.5%, %(Euro)T=0.022H
beta=1;
zetas=.01; %2,1,1.57,1.2,2%
rhoS=200;
mz=(B*D*rhoS);
syms k real
Mi=int(mz/(H^2))*k^2,k,[0 H]);
alpha=0.3;
Ih=0.11;
Uh=82.98;
Us=Uh/(f1*B);
wh=2996; % wh=(0.5*1.225*(Uh^2))%
alphadb=D/B;
alphaw=4.2-4*exp(3.7-60*Ih);
Cmbo=0.182-0.019*(alphadb^-2.54)+0.054*(alphaw^-0.91);
gr=sqrt(2*log(600*f1))+(0.5772/sqrt(2*log(600*f1))); % gr=2.5;%
phi=1;
alphahr=H/(sqrt(B*D));
fp=(10^-5)*(191-9.48*alphaw+1.28*alphahr+alphahr*alphaw)*(68-21*alphadb+3*alphadb*alphadb);
Sp=(0.1*(alphaw^-0.4)-0.0004*exp(alphaw))*(0.84*alphahr-2.12-0.05*alphahr*alphahr)*(0.422+(alphadb^-1)-0.08*(alphadb^-2));
neta=(1+0.00473*exp(1.7*alphaw))*(0.065+exp(1.26-0.63*alphahr))*(exp(1.7-(3.44/alphadb)));
lambda=(-0.8+0.06*alphaw+0.0007*exp(alphaw))*((-alphahr^0.34)+0.00006*exp(alphahr))*(0.414*alphadb+1.67*(alphadb^-1.23));
n=f1*B/Us;
Sm=(Sp*neta*(n/fp)^lambda)/((1-(n/fp)^2)^2+(neta*(n/fp)^2));
zetaaa=(0.0025*(1-(Us/9.8)^2)*(Us/9.8)+0.000125*(Us/9.8)^2)/((1-(Us/9.8)^2)^2+0.0291*(Us/9.8)^2);
%zetaaa=0.0040;
gb=3.5;
ptotal=zeros(1,25);
atotal=zeros(1,25);
for i=1:25
GbZ=((0.65+1.3*h(1,i)+7*(h(1,i))^2-7.5*(h(1,i))^3)*gb*Cmbo);
%GbZ=((0.65+1.3*h+7*h^2-7.5*h^3)*gb*Cmbo);
Grz=(H*mz/Mi)*(h(1,i))^beta*gr*(sqrt(pi*phi*Sm/(4*(zetas+zetaaa))));
%Grz=(H*mz/Mi)*h*gr*(sqrt(pi*phi*Sm/(4*(zetas+zetaaa))));
pz=wh*B*(sqrt(GbZ^2+Grz^2));
az=(H/Mi)*(h(1,i))^beta*gr*B*wh*(sqrt(pi*phi*Sm/(4*(zetas+zetaaa))));
ptotal(1,i)=pz/1000;
atotal(1,i)=az;
end

```

Blank Page



Research Article

Crack healing and flexural behaviour of self-healing concrete influenced by different bacillus species

Cherreddy Sonali Sri Durga^{1,a}, Chava Venkatesh*^{1,b}, T. Muralidhararao^{1,c}, Ramamohana Reddy Bellum^{2,d}

¹Department of Civil Engineering, CVR College of Engineering, Hyderabad, India

²Department of Civil Engineering, Aditya Engineering College (Autonomous), India

Article Info

Abstract

Article history:

Received 23 Apr 2023

Accepted 05 Aug 2023

Keywords:

Bacillus species;
Crack healing;
Cell concentration;
Flexural strength;
Ultra-sonic pulse velocity

The main aim of this investigation is to determine the influence of Bacillus species on the crack healing ability and flexural strength of concrete. In this regard, four bacillus species, such as "*Bacillus halodurans* (BH), *Bacillus cereus* (BC), *Bacillus licheniformis* (BL), and *Bacillus subtilis* (BS), and two bacterial cell concentrations are selected (viz., 10^8 and 10^9 cells/ml of water), and the concrete specimens are cracked with a 65% stress level concentration. To identify the crack healing ability of selected bacillus species, three different curing conditions are adopted: calcium lactate, water, and ambient curing conditions. The ultrasonic pulse velocity test (UPV) has been conducted to identify the crack healing ability of the selected bacillus species. From the results, calcium lactate-based cured concrete specimens showed better UPV values and crack healing ability. whereas *Bacillus halodurans* (BH) effectively filled the crack with calcite precipitation, which is the reason for 90% of crack healing ability and the high flexural strength recovery compared to other selected bacillus species. There is not much difference observed between the bacteria with cell concentrations of 10^9 and 10^8 ; however, 10^9 has a high healing ability and recovers flexural strength.

© 2023 MIM Research Group. All rights reserved.

1. Introduction

As concrete is a brittle substance, it is prone to cracking, which has major consequences for the durability of concrete structures [1-3]. Cracks will easily allow for entry of harmful substances into structures, accelerating deterioration and necessitating intensive repair and maintenance. Repair and rehabilitation of concrete structures is a difficult task nowadays because of the limited resources available to reconstruct a structure and budget required is more from an economical point of view. In the U.S, almost £40 billion are spent per year for maintenance of concrete structures in which cement plays a major role [4-5] and the reports from highway agency of England states that £80 million are used every year for the upcoming 20 years towards repair and rehabilitation of bridge works [6-7]. Moreover, for strengthening hammersmith flyover in London, nearly £70 million are spent since 2011 by its transport authority [8] and also in the U.K, it was found since from 2000, the amount spent for repair works has crossed than for new constructions [9-12]. To address the above issues, self-healing concrete was introduced for healing the cracks on the concrete surface.

Generally, animals and plants are capable of healing wounds by themselves without any external influences. For example, mammalian skin has an ability to recover from serious damage to its full extent [13]. In addition to that, a lot of organisms and natural systems

*Corresponding author: chava.venkatesh@cvr.ac.in

^a orcid.org/0000-0003-0942-9252; ^b orcid.org/0000-0003-0028-7702; ^c orcid.org/0000-0002-7768-3298;

^d orcid.org/0000-0002-0040-5812

DOI: <http://dx.doi.org/10.17515/resm2023.744st0423>

Res. Eng. Struct. Mat. Vol. 9 Iss. 4 (2023) 1477-1488

are capable to heal itself; so, from these examples, the idea of healing was applied to engineering problems. This idea has come to existence through experimental work from previous decades and still it is in fantasy. Self-healing concrete is the one that heals itself when it comes into air, water and produces lime on the outer layer of the concrete. The self-healing process can be broadly classified into two types, i.e., autogenous self-healing and autonomous self-healing and the healing methods are shown in Fig 1. The healing can be done with many materials like biological agents [14-19], chemical agents, superabsorbent polymers, crystalline materials, pozzolanic materials [20-22] and mineral admixtures that are added and replaced with cement in order to arrest the cracks of concrete which shortens their production.

The bacterial agents/mediums usage for the crack healing comings under the autogenous healing method. During this process, the bacteria facilitate the precipitation of calcite (CaCO₃) crystals by producing the urease enzyme. This precipitation occurs through the heterogeneous nucleation of the bacterial cell wall until supersaturation is reached. It highlights the potential of bacteria as effective self-healing agents [23]. The mechanical properties of the concrete are evaluated by using *Bacillus subtilis* bacteria and the study concluded there is an increase in mechanical properties due to the production of calcium carbonate and this is the reason for a fill of cracks [24]. Another study was done by using bacteria (*Bacillus subtilis*) and lactate derivative-based material which acts as a carbon source for crack healing. The spores of the bacteria get active and consume the nutrients, carbon source which precipitates the hydration products responsible for healing, improves the mechanical properties and water tightness enriches the durability behaviour of concrete structures [25-26].

As per the literature, several ways to carried out bacterial incorporation into the concrete for crack healing; bacterial direction injection [27], bacterial spraying on concrete cracked surface [28], bacteria encapsulation [29], and bacterial addition at time of mixing, and ect., Jonkers [30] said that addition of bacterial agents at the time of concrete mixing is better than above other methods and having optimum crack healing.

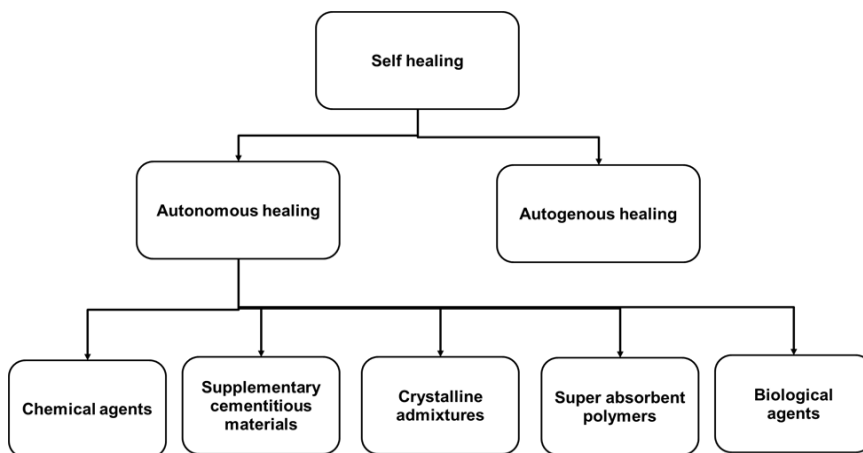


Fig. 1. Self-healing methods

The fissures underwent healing as a result of microbial precipitation induced by bacterial urealytic activity. This process of microbial precipitation is contingent upon various factors, including pH levels, the concentration of dissolved inorganic carbon, the quantity of calcium ions present, and the choice of bacterial nucleation site [31]. Many studies have mentioned that bacterial incorporation improves the mechanical strengths of concrete,

especially compressive and split tensile strength. Jena [32] used *Bacillus subtilis* (BS) with different cell concentrations ranging from 10^2 to 10^6 and investigated the mechanical properties. His study concluded that BS with 10^5 cells/ml has shown the optimum strength increments, such as a 32% increase in compressive strength, a 14.01% increase in split tensile strength, and a 29.14% increase in flexural strength. Akindahunsi [33] also mentioned that BS with 10^5 cells/ml has shown a 13% increase in compressive strength and a 15% increase in flexural strength compared to the control mix.

In the present study, four different *Bacillus* species, namely BH, BS, BL, and BC, with two different cell concentrations (10^8 cells/ml and 10^9 cells/ml), are selected. Additionally, three different curing conditions (calcium lactate, water, and ambient air) are identified to evaluate the potential of *Bacillus* species for crack healing ability and strength recovery. These parameters are considered as research gaps in the present study. The rate of crack healing is monitored daily using UPV, and the flexural strength is monitored to evaluate strength recovery.

2. Materials and Experimental Methodology

2.1 Materials

The required materials for preparing the concrete collected from local forums and its properties (i.e., physical and chemical) match the IS 12269-2013 [34], IS 383-2016 [35], and IS 456-2000 [36]. Subsequently, ordinary Portland cement contains 64.2% of CaO, 19.6% of SiO₂, 4.62% of Al₂O₃, 3.89% of Fe₂O₃, 1.86% of Na₂O₃, 0.78% of K₂O, 0.65% of TiO₂, 0.92% of MgO, and 3.48% of loss of ignition. Similarly, fine aggregates have 2.70, 1.45, and 2.56 specific gravity, bulk density, and fineness modulus, respectively. Similarly, coarse aggregates have specific gravity of 2.75, and bulk density of 1.51, respectively.

2.2 Bacteria

In the present study, the selected bacterial agents were purchased from the "National Collection of Industrial Microorganisms (NCIM), CSIR-National Chemical Laboratory (NCL), Pune, India," and cultured according to the nutrient broth medium method [18]. Based on the biological laboratory studies, all the bacterial agents exhibited a rod-like shape and were gram-positive. Furthermore, additional characteristics of the bacterial agents are listed in Table 1.

Table 1. characteristics of bacterial agents

Name of bacteria	Size, B×L (µm)	Shape	Pigmentation	Gram staining properties	Medium	Temperature	pH
<i>Bacillus halodurans</i>	0.5×1.8	Rod shaped	Pink	Gram positive	Nutrient broth	37°C	7
<i>Bacillus licheniformis</i>	1×4.2	Rod shaped	Red	Gram positive	Nutrient	30°C	6-8
<i>Bacillus cereus</i>	3×4	Rod shaped	Green	Gram positive	broth	28°C	4.6
<i>Bacillus subtilis</i>	0.2×1.2	Rod shaped	Brown	Gram positive	Nutrient	30°C	6-9

2.3 Experimental Methodology

According to IS 10262-2009 [37], the mix calculations for 40MPa strength concrete are evaluated and listed in Table 2. Additionally, two different bacterial cell concentrations,

namely 5.79×10^8 and 5.79×10^9 , are used in the concrete throughout the present research work. The crack healing ability of bacterial agents and the flexural behavior of bacterial agent-induced concrete are carried out. All the prepared concrete samples are cured in normal water for 28 days before testing. The surface cracks are formed using 65% and 75% stress level concentrations [16]. To evaluate the healing ability of bacterial agents, three different curing conditions are adopted, namely water, calcium lactate, and air (i.e., ambient curing).

Table 2. Mix calculations (Kg/m^3)

Cement	Fine aggregates	Coarse aggregates	Water	Bacteria (cells/ml of water)
450	624	1220	186	(5.79×10^8) & (5.79×10^9)

2.4 Ultrasonic Pulse Velocity Test

The non-destructive studies were carried out on the hardened concrete by performing an ultrasonic pulse velocity test as per IS: 13311 (Part 1) – 1992 [38]. An Ultrasonic Pulse Velocity (UPV) test is an in-situ, non-destructive test to check the concrete quality. In this, the strength and quality of concrete are evaluated by measuring the velocity of an ultrasonic pulse passing through a concrete structure. Higher velocities indicate good quality and continuity of the material, while a lower velocity indicates concrete with many cracks or voids. The pulse velocity will be calculated by using Eq 1. The specimens (prisms) are cracked from the mean strengths as shown in Fig 2 and are placed in different curing agents such as calcium lactate, water and air in Fig 3. The experimental setup of UPV measurement to the concrete specimen is represented in Fig 4. A white precipitate was formed on the concrete specimen’s surface indicating crack healing shown in Fig 5.

$$\text{Pulse velocity} = \text{Width of structure} / \text{Time taken by the pulse to go through} \tag{1}$$



Fig. 2. Setup of cracked concrete specimens



Fig.3 Concrete specimens cured at various curing agents

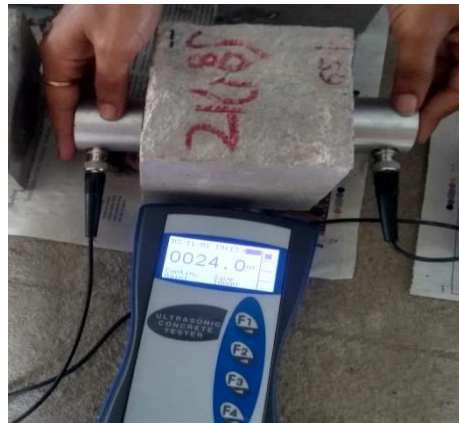


Fig.4 Setup of UPV measurement

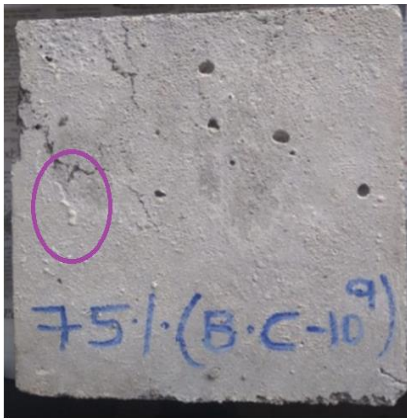


Fig. 5. Crack healed specimens

2.5 Flexural Strength Test

The flexural strength is the beam or prism's capability to resist failure in bending action; it can also be termed modulus of rupture. The size of specimens adopted is 500mm×100mm×100mm to test flexural strength using a flexural testing machine with a capacity of 100KN at a loading rate of 180kg/min. As per IS 516-1959 [36] requirements, the test was carried out for the specimens cured for 28 days. The flexural strength can be calculated with the following formulae in Eq 2.

$$\text{Flexural strength } (f_b) = \frac{3PL}{2bd^2} \quad (2)$$

4. Results and Discussion

4.1 Ultra Sonic Pulse Velocity

The ultrasonic pulse velocity (UPV) values are used presently to evaluate the crack healing ability of the selected Bacillus species, namely BS, BH, BL, and BC. The bacteria-induced concrete specimens are cracked with a stress level concentration of 65% and cured in

calcium lactate, water, and ambient air, respectively. Table 3 illustrates the UPV values when the cracked specimens are cured in calcium lactate. Based on Table 3, BH has a UPV value of 4.36@14 days, and its corresponding crack healing ability is 90%, which is the highest among the bacterial cell concentration 10^9 induced specimens. This effect is due to the reaction between the bacteria and calcium lactate within the concrete pores and cracks. The calcium lactate crystallizes within the cracks, leading to crack healing or sealing, thereby increasing the UPV values [39-40]. The principle of repair or crack healing involves the formation of calcium carbonate from the bacteria's spores by consuming nutrients such as calcium lactate, water, and oxygen [41-42]. The chemical agent calcium lactate has an alkaline nature, indicated by its pH value of 8, which is favorable for the concrete environment. Similarly, BC has a UPV value of 4.26@21 days, BL has 4.32@14 days, and BS has 4.11@21 days, with corresponding crack healing abilities of 87%, 88%, and 86%, respectively. A similar behavior was observed in the case of bacterial cell concentration of 10^8 induced concrete specimens.

Table 3. UPV (km/sec) crack healing after cured in calcium lactate

		Cell concentration, 10^9					Cell concentration, 10^8					
		NC	BC	BH	BL	BS	NC	BC	BH	BL	BS	
UPV values (Km/Sec)	Before Crack	4.85	4.85	4.85	4.86	4.85	4.85	4.86	4.87	4.88	4.86	
	After Crack	2.37	2.34	2.31	2.36	2.39	2.37	2.33	2.34	2.34	2.38	
	Curing age (days)	3	2.65	2.85	2.62	2.68	2.98	2.65	2.61	2.48	2.54	2.66
		7	3.01	3.67	3.37	3.59	3.86	3.01	3.54	3.24	3.3	3.67
		14	3.16	3.96	4.36	4.32	4.11	3.16	3.82	4.35	4.3	3.95
		21	3.44	4.26	4.36	4.32	4.21	3.44	4.25	4.35	4.3	4.19
		28	3.86	4.26	4.36	4.32	4.21	3.86	4.25	4.35	4.3	4.19
		35	3.86	4.26	4.36	4.32	4.21	3.86	4.25	4.35	4.3	4.19
Healing ability (%)	Before Crack	100	100	100	100	100	100	100	100	100	100	
	After Crack	49	48	48	49	49	49	48	48	48	49	
	Curing age (days)	3	55	59	54	55	61	55	54	51	52	55
		7	62	76	69	74	80	62	73	67	68	76
		14	65	82	90	89	85	65	79	89	88	81
		21	71	88	90	89	87	71	87	89	88	86
		28	80	88	90	89	87	80	87	89	88	86
		35	80	88	90	89	87	80	87	89	88	86

Table 4 lists the UPV values and crack healing ability percentages of bacteria-induced cracked concrete specimens cured in water for their crack healing. The bacteria with a cell concentration of 10^9 induced greater healing ability than bacteria with a cell concentration of 10^8 . The optimum UPV values and their corresponding healing ability percentages are as follows: NC has 3.49 @ 72% for 28 days, BC has 3.55 @ 73% for 21 days, BH has 3.65 @ 75% for 14 days, BL has 3.58 @ 74% for 14 days, and BS has 3.5 @ 72% for 21 days, respectively. The bacterial agents are capable of excreting calcite on the cracked surfaces when they react with the available moisture in their surroundings, according to [23],[43]. Similar results were observed in the bacteria with a cell concentration of 10^8 induced concrete specimens, as shown in Table 4.

The UPV values and crack healing ability percentages for bacteria-induced cracked specimens cured in ambient air are shown in Table 5. Results show that BH has the highest healing ability, i.e., 70%, which is optimum in the respective ambient air-cured concrete specimens. Whereas, BL has 68%, BS has 65%, BC has 67%, and NC has 64% in 14 days, 21

days, 21 days, and 28 days, respectively, and its corresponding optimum UPV values are 3.31 km/sec, 3.23 km/sec, 3.26 km/sec, and 3.13 km/sec, respectively. For bacteria with a cell concentration of 10⁸, the optimum UPV values are 3.13 Km/sec for NC, 3.23 Km/sec for BC, 3.39 Km/sec for BH, 3.29 Km/sec for BL, and 3.11 Km/sec for BS, respectively, for corresponding curing ages of 28 days, 21 days, 14 days, and 21 days, as shown in Table 5. According to [44&45], the selected bacillus species are sealed with a cracked concrete surface with calcite when it reacts with surrounding ambient air, which is the reason for crack healing.

Table 4. Crack healing after cured in water

		Cell concentration,10 ⁹					Cell concentration,10 ⁸				
		NC	BC	BH	BL	BS	NC	BC	BH	BL	BS
UPV values (Km/Sec)	Before Crack	4.86	4.87	4.87	4.85	4.87	4.85	4.85	4.86	4.87	4.88
	After Crack	2.36	2.31	2.32	2.32	2.41	2.37	2.32	2.35	2.35	2.4
	3	2.53	2.67	2.59	2.59	2.83	2.65	2.54	2.46	2.48	2.59
	7	2.99	3.13	3.11	3.17	3.39	3.01	3.07	3.03	3.01	3.29
	14	3.12	3.42	3.65	3.58	3.44	3.16	3.38	3.62	3.56	3.26
	21	3.4	3.55	3.65	3.58	3.5	3.44	3.51	3.62	3.56	3.48
	28	3.49	3.55	3.65	3.58	3.5	3.46	3.51	3.62	3.56	3.48
	35	3.49	3.55	3.65	3.58	3.5	3.46	3.51	3.62	3.56	3.48
Healing ability (%)	Before Crack	100	100	100	100	100	100	100	100	100	100
	After Crack	49	47	48	48	49	49	48	48	48	49
	3	52	55	53	53	58	52	52	51	51	53
	7	62	64	64	65	70	62	63	62	62	67
	14	64	70	75	74	71	64	70	74	73	67
	21	70	73	75	74	72	70	72	74	73	71
	28	72	73	75	74	72	71	72	74	73	71
	35	72	73	75	74	72	71	72	74	73	71

Summary of the results: Among the selected Bacillus species, BH has shown better crack healing ability than others under the given three curing conditions, namely calcium lactate, water, and ambient air curing. Concrete specimens cured with calcium lactate effectively sealed 90% of the cracked portion in a relatively shorter time, specifically 14 days, compared to the other conditions. Similar behavior was observed in both water and ambient air curing conditions. Subsequently, BL exhibited the second-largest healing ability (89% in 14 days) among the selected Bacillus species, followed by BC and BS. The bacterial agents ideally consume calcium lactate and excrete calcite in the surrounding voids or cracks in the concrete, which is the reason for achieving high UPV (ultrasonic pulse velocity) and observed healing ability in the calcium lactate curing conditions. Similarly, bacteria can also produce calcite precipitation by reacting with moisture and air, but these healing processes require slightly more time and have lower healing ability compared to calcium lactate conditioning.

3.2 Flexural Strength Test

Fig. 6 depicts the flexural strength of bacteria with cell concentrations of 10⁹ in concrete specimens before and after crack healing. In the selected bacillus species, BH has shown the greater flexural strength, i.e., 5.09 MPa, and it is considered optimum among other bacillus species. Based on biological studies, BH can survive effectively in a high alkaline environment (concrete pH > 12) compared to others and is primarily responsible for the calcium carbonate in the cracked portion of the concrete, which helps enhance the concrete's flexural strength. The calcium lactate curing-conditioned specimens have shown the highest recovery of the flexural strength, i.e., 99.61% in BH, 91.13% in BC, 96.02 in BL, 86.78 in BS, and 82.09 in NC, respectively. Similarly, BH has shown better strength

recovery under water and ambient air curing conditions, i.e., 98.23% and 96.46%, respectively. From the UPV values, it was observed that the bacteria can seal the crack by observing the surrounding moisture and air, which is the reason for the recovery of strength. Similar results were observed in the case of bacteria with a cell concentration of 10^8 , which are shown in Fig. 7.

Table 5. crack healing after cured in ambient air

		Cell concentration, 10^9					Cell concentration, 10^8				
		NC	BC	BH	BL	BS	NC	BC	BH	BL	BS
UPV values (Km/Sec)	Before Crack	4.87	4.88	4.88	4.87	4.9	4.87	4.87	4.89	4.89	4.89
	After Crack	2.35	2.32	2.34	2.3	2.42	2.35	2.3	2.32	2.33	2.39
	3	2.46	2.56	2.48	2.45	2.75	2.46	2.48	2.36	2.39	2.47
	7	2.97	2.92	2.86	2.71	3.14	2.97	2.86	2.84	2.6	3.04
	14	3.08	3.16	3.41	3.31	3.18	3.08	3.09	3.39	3.29	3.11
	21	3.09	3.26	3.41	3.31	3.23	3.09	3.23	3.39	3.29	3.2
	28	3.13	3.26	3.41	3.31	3.23	3.13	3.23	3.39	3.29	3.2
	35	3.13	3.26	3.41	3.31	3.23	3.13	3.23	3.39	3.29	3.2
Healing ability (%)	Before Crack	100	100	100	100	100	100	100	100	100	100
	After Crack	48	48	48	47	49	48	47	47	48	49
	3	51	52	51	50	56	51	51	48	49	51
	7	61	60	59	56	64	61	59	58	53	62
	14	63	65	70	68	65	63	63	69	67	64
	21	63	67	70	68	66	63	66	69	67	65
	28	64	67	70	68	66	64	66	69	67	65
	35	64	67	70	68	66	64	66	69	67	65

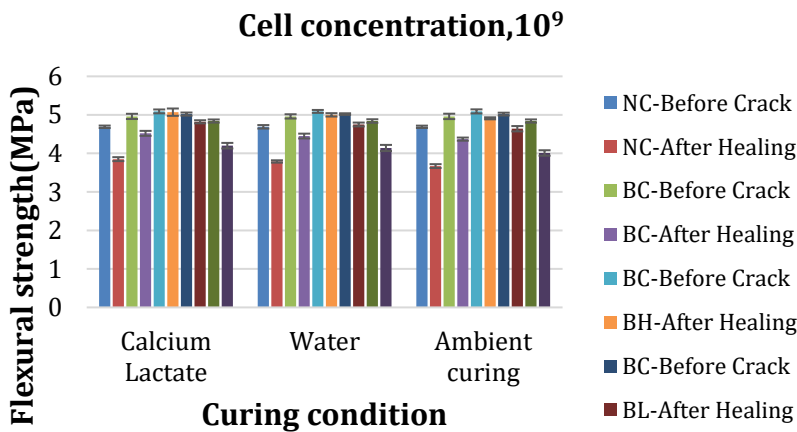


Fig. 6 Flexural strength of bacteria cell concentration of 10^9

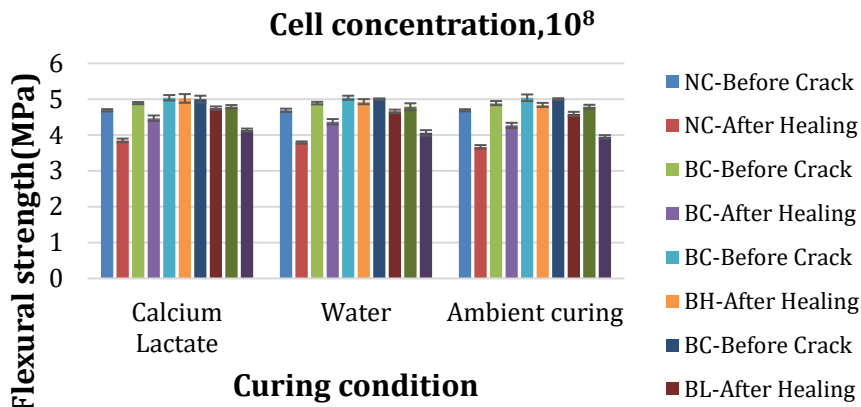


Fig. 7 Flexural strength of bacteria cell concentration of 10^8

5. Conclusions

In the present research study, the four bacteria (*Bacillus subtilis*, *Bacillus cereus*, *Bacillus licheniformis*, and *Bacillus halodurans*) were cultured, and the bio-concrete specimens were prepared using bacteria with two different cell concentrations of 10^8 and 10^9 . The specimens are cured for 28 days and checked for mechanical properties (flexural strength). The specimens are cracked with stress level concentrations of 65% mean strength and were placed in various curing conditions such as calcium lactate, air, water, and bacterial solution to determine the healing rate by conducting ultrasonic pulse velocity tests. The following are the conclusions drawn from the present research work:

- *Bacillus halodurans* has the highest crack healing ability compared to other *Bacillus* species used in the present study. Particularly, calcium lactate cured BH has the optimum performance in terms of crack healing and flexural strength recovery.
- The UPV values get constant for *Bacillus subtilis* (4.21 km/sec) and *Bacillus cereus* (4.26 km/sec) concrete specimens at 21 days, *Bacillus licheniformis* (4.32 km/sec), and *Bacillus halodurans* (4.36 km/sec) concrete specimens at 14 days, illustrating no further healing.
- In all the mixes, bacterial cell concentrations in 109 concrete samples showed better healing performance in the selected curing conditions, i.e., calcium lactate, water, and ambient air.
- The crack healing of BH is 90%, 75%, and 70% in calcium lactate, water, and ambient air curing, respectively. The name *Bacillus halodurans*, i.e., the term halo itself, indicates alkalinity, representing that this bacterium can sustain itself easily in a concrete environment and precipitate calcium carbonate.
- Subsequently, BL has shown the second highest performance, i.e., 89%, 74%, and 68% of crack healing in calcium lactate, water, and ambient air conditions, respectively.
- The selected bacillus species has shown considerable concrete specimen crack healing and recovery of flexural strength in ambient air and water curing conditions. From the results, it was found that ambient air and water can react with bacillus species and produce calcite precipitants.
- The *Bacillus halodurans* exhibited the highest flexural strength, measuring 5.07 MPa, while the control samples measured 5.09 MPa. This is attributed to the

bacteria's ability to survive in a high-alkaline environment and produce calcium carbonate, which fills the cracks and enhances the flexural strength of the concrete.

- From the obtained results, the present study concludes that *Bacillus halodurans* can be used for concrete repairs, particularly crack healing.

Future scope and limitations of the study

- The present investigation has proven that the selected *Bacillus* species are ideally suitable as self-healing agents in concrete repair works. It is necessary to study the performance of these *Bacillus* species in structural elements such as reinforced concrete beams, columns, and slabs. Additionally, it is advisable to study the behavior of the *Bacillus* species in adverse environments such as acid environments and elevated temperatures.
- From the observation, it can be noted that most of the time the crack healing ability of the selected *Bacillus* species is limited to surface cracks.

Acknowledgement

The author extends heartfelt thanks to Dr. Indira Mikkili, Associate Professor in the Department of Biotechnology at VFSTR Deemed to be University, and to the late Dr. Ruben, Associate Professor in the Civil Engineering Department at VFSTR Deemed to be University, for their continuous support and blessings.

References

- [1] Wang R, Zhang Q, Li Y. Deterioration of concrete under the coupling effects of freeze-thaw cycles and other actions: A review. *Construction and Building Materials*, 2022, 319, 126045. <https://doi.org/10.1016/j.conbuildmat.2021.126045>
- [2] Mohammadi A, Ghiasvand E, Nili M. Relation between mechanical properties of concrete and alkali-silica reaction (ASR); a review. *Construction and Building Materials*, 2020, 258, 119567. <https://doi.org/10.1016/j.conbuildmat.2020.119567>
- [3] Kabir H, Hooton RD, Popoff NJ. Evaluation of cement soundness using the ASTM C151 autoclave expansion test. *Cement and Concrete Research*, 2020, 136, 106159. <https://doi.org/10.1016/j.cemconres.2020.106159>
- [4] Joseph C, Jefferson AD, Isaacs B, Lark R, Gardner D. Experimental investigation of adhesive-based self-healing of cementitious materials. *Magazine of Concrete Research*, 2010, 62(11), 831-843. <https://doi.org/10.1680/macr.2010.62.11.831>
- [5] DTI (Department for Trade and Industry). *Construction Statistics Annual Report 2006*. TSO, London.
- [6] Das PC, *Maintenance planning for trunk road structures in England*. TRB Transport Research Circular, 1999.
- [7] Insaurralde CC, Rahman PK, Ramegowda M, Vemury CM. Follow-up methods for autonomic repairing process. In 2016 IEEE International Conference on Systems, Man, and Cybernetics (SMC) (pp. 004854-004859). IEEE 2016. <https://doi.org/10.1109/SMC.2016.7844997>
- [8] J Pryn, Hammersmith flyover needs £60m repair job after £10m emergency work two years ago. *London Evening Standard*.
- [9] Fib (Fédération Internationale du béton). *Bulletin 44: Concrete Structure Management: Guide to Ownership and Good Practice*. Fib, Lausanne, Switzerland, 2008.
- [10] McCarter W, Chrisp T, Starrs G, Holmes N, Basheer L, Basheer M, Nanukuttan SV. Developments in monitoring techniques for durability assessment of cover-zone concrete. *Computer-Aided Design*, 2010, 17(6), 294-303.
- [11] McCarter WJ, Chrisp TM, Starrs G, Adamson A, Owens E, Basheer PM, Holmes N. Developments in performance monitoring of concrete exposed to extreme

- environments. *Journal of infrastructure systems*, 2012, 18(3), 167-175. [https://doi.org/10.1061/\(ASCE\)IS.1943-555X.0000089](https://doi.org/10.1061/(ASCE)IS.1943-555X.0000089)
- [12] Suryanto B, Wilson SA, McCarter WJ, Chrisp TM. Self-healing performance of engineered cementitious composites under natural environmental exposure. *Advances in Cement Research*, 2016, 28(4), 211-220. <https://doi.org/10.1680/jadcr.15.00022>
- [13] Frei R, McWilliam R, Derrick B, Purvis A, Tiwari A, Di Marzo Serugendo G. Self-healing and self-repairing technologies. *The International Journal of Advanced Manufacturing Technology*, 2013, 69(5), 1033-1061. <https://doi.org/10.1007/s00170-013-5070-2>
- [14] Durga C, Ruben N. Assessment of various self-healing materials to enhance the durability of concrete structures. *Ann. Chim.-Sci. Matér*, 2019, 43(2), 75-79. <https://doi.org/10.18280/acsm.430202>
- [15] Durga CSS, Ruben N. A review of the mechanical behavior of substitution materials in self-healing concrete. *Sustainable Construction and Building Materials*, 2019, 135-144. https://doi.org/10.1007/978-981-13-3317-0_12
- [16] Durga CSS, Ruben N, Chand MSR, Venkatesh C. Evaluation of mechanical parameters of bacterial concrete. In *Annales de Chimie-Science des Matériaux*, 2019, (Vol. 43, No. 6, pp. 395-399). <https://doi.org/10.18280/acsm.430606>
- [17] Durga CSS, Ruben N, Chand MSR, Venkatesh C. Performance studies on rate of self-healing in bio concrete. *Materials Today: Proceedings*, 2020, 27, 158-162. <https://doi.org/10.1016/j.matpr.2019.09.151>
- [18] Durga CSS, Ruben N, Chand MSR, Indira M, Venkatesh C. Comprehensive microbiological studies on screening bacteria for self-healing concrete. *Materialia*, 2021, 15, 101051. <https://doi.org/10.1016/j.mtla.2021.101051>
- [19] Reddy S, Rao M, Aparna P, Sasikala CH. Performance of standard grade bacterial (*Bacillus subtilis*) concrete. *Asian J Civ Eng (Build Housing)*, 2010, 11, 43-55.
- [20] Ruben N, Venkatesh C, Durga CSS, Priyanka M, Reddy KHK. Evaluation of Flow Ability Properties of Cement Paste Incorporated with Bagasse Ash. *Indian journal of ecology*, 2020, Vol 47(11), 171-175.
- [21] Venkatesh C, Sri Rama Chand M, Ruben N, Sonali Sri Durga C. Strength Characteristics of Red Mud and Silica Fume Based Concrete. In *Smart Technologies for Sustainable Development* (pp. 387-393). Springer, Singapore 2021. https://doi.org/10.1007/978-981-15-5001-0_33
- [22] Venkatesh C, Ramanjaneyulu V, Reddy K, Durga C, Sathish P. A pilot strength studies on granite powder and silica fume based concrete. *International Journal of Innovative Technology and Exploring Engineering*, 2019, 8(7), 2278-3075.
- [23] Vijay K, Murmu M. Effect of calcium lactate on compressive strength and self-healing of cracks in microbial concrete. *Frontiers of Structural and Civil Engineering*, 2019, 13, 515-525. <https://doi.org/10.1007/s11709-018-0494-2>
- [24] Seifan M, Samani AK, Berenjian A. Bioconcrete: next generation of self-healing concrete. *Applied microbiology and biotechnology*, 2016, 100(6), 2591-2602. <https://doi.org/10.1007/s00253-016-7316-z>
- [25] Mors RM, Jonkers HM. Feasibility of lactate derivative based agent as additive for concrete for regain of crack water tightness by bacterial metabolism. *Industrial crops and products*, 2017, 106, 97-104. <https://doi.org/10.1016/j.indcrop.2016.10.037>
- [26] Rao MV, Reddy VS, Sasikala C. Performance of microbial concrete developed using *bacillus subtilis* JC3. *Journal of The Institution of Engineers (India): Series A*, 2017, 98(4), 501-510. <https://doi.org/10.1007/s40030-017-0227-x>
- [27] Sangadji S, Wiktor VAC, Jonkers HM, Schlangen HEJG. Injecting a liquid bacteria-based repair system to make porous network concrete healed. In *ICSHM 2013: Proceedings of the 4th International Conference on Self-Healing Materials*, Ghent, Belgium, 16-20 June 2013. Magnel Laboratory for Concrete Research.

- [28] Wiktor V, Jonkers HM. Field performance of bacteria-based repair system: Pilot study in a parking garage. *Case Studies in Construction Materials*, 2015, 2, 11-17. <https://doi.org/10.1016/j.cscm.2014.12.004>
- [29] Espitia-Nery ME, Corredor-Pulido DE, Castaño-Oliveros PA, Rodríguez-Medina JA, Ordoñez-Bello QY, Pérez-Fuentes MS. Mechanisms of encapsulation of bacteria in self-healing concrete. *Dyna*, 2019, 86(210), 17-22. <https://doi.org/10.15446/dyna.v86n210.75343>
- [30] Jonkers HM, Thijssen A, Muyzer G, Copuroglu O, Schlangen E. Application of bacteria as self-healing agent for the development of sustainable concrete. *Ecological engineering*, 2010, 36(2), 230-235. <https://doi.org/10.1016/j.ecoleng.2008.12.036>
- [31] Bang SS, Galinat JK, Ramakrishnan V. Calcite precipitation induced by polyurethane-immobilized *Bacillus pasteurii*. *Enzyme and microbial technology*, 2001, 28(4-5), 404-409. [https://doi.org/10.1016/S0141-0229\(00\)00348-3](https://doi.org/10.1016/S0141-0229(00)00348-3)
- [32] Jena S, Basa B, Panda KC, Sahoo NK. Impact of *Bacillus subtilis* bacterium on the properties of concrete. *Materials Today: Proceedings*, 2020, 32, 651-656. <https://doi.org/10.1016/j.matpr.2020.03.129>
- [33] Akindahunsi AA, Adeyemo SM, Adeoye A. The use of bacteria (*Bacillus subtilis*) in improving the mechanical properties of concrete. *Journal of Building Pathology and Rehabilitation*, 2021, 6, 1-8. <https://doi.org/10.1007/s41024-021-00112-7>
- [34] IS 12269-1987. Specifications for 53 grade ordinary Portland cement. Bureau of Indian Standards, New Delhi, India, 1987.
- [35] IS 383-2016. Coarse and fine aggregate for concrete - specification. Bureau of Indian Standards, New Delhi, India, 2016.
- [36] IS 456-2000. Plain and reinforced concrete - code of practice. Bureau of Indian Standards, New Delhi, India, 200.
- [37] IS 10262-2009. Concrete mix proportioning - guidelines. Bureau of Indian Standards, New Delhi, India, 2009.
- [38] IS 13311 (Part 1) - 1992. Non-destructive testing of concrete-methods of test. Bureau of Indian Standards, New Delhi, India, 1992.
- [39] IS 516-1959. Methods of tests for strength of concrete. Bureau of Indian Standards, New Delhi, India, 1959.
- [40] Vijay K, Murmu M. Self-repairing of concrete cracks by using bacteria and basalt fiber. *SN Applied Sciences*, 2019, 1(11), 1-10. <https://doi.org/10.1007/s42452-019-1404-5>
- [41] Khaliq W, Ehsan MB. Crack healing in concrete using various bio influenced self-healing techniques. *Construction and Building Materials*, 2016, 102, 349-357. <https://doi.org/10.1016/j.conbuildmat.2015.11.006>
- [42] Rao M, Reddy VS, Hafsa M, Veena P, Anusha P. Bioengineered concrete-a sustainable self-healing construction material. *Res. J. Eng. Sci.* ISSN, 2278, 9472, 2013.
- [43] Irwan JM, Anneza LH, Othman N, Alsharif AF, Zamer MM, Teddy T. Calcium Lactate addition in Bioconcrete: Effect on Compressive strength and Water permeability. In *MATEC Web of Conferences*, 2016, (Vol. 78, p. 01027). EDP Sciences. <https://doi.org/10.1051/mateconf/20167801027>
- [44] Achal V, Mukherjee A, Kumari D, Zhang Q. Biomineralization for sustainable construction-A review of processes and applications. *Earth-science reviews*, 2015, 148, 1-17. <https://doi.org/10.1016/j.earscirev.2015.05.008>
- [45] Chuo SC, Mohamed SF, Mohd Setapar SH, Ahmad A, Jawaid M, Wani WA, Mohamad Ibrahim MN. Insights into the Current Trends in the Utilization of Bacteria for Microbially Induced Calcium Carbonate Precipitation. *Materials*, 2020, 13(21), 4993. <https://doi.org/10.3390/ma13214993>
- [46] Seifan M, Sarmah AK, Samani AK, Ebrahiminezhad A, Ghasemi Y, Berenjian A. Mechanical properties of bio self-healing concrete containing immobilized bacteria with iron oxide nanoparticles. *Applied microbiology and biotechnology*, 2018, 102(10), 4489-4498. <https://doi.org/10.1007/s00253-018-8913-9>

Estimation of durability properties of self-healing concrete influenced by different bacillus species

Chereddy Sonali Sri Durga^{1,a}, Chava Venkatesh^{*1,b}, T. Muralidhararao^{1,c}, Ramamohana Reddy Bellum^{2,d}, B. Naga Malleswara Rao^{1,e}

¹Dept. of Civil Eng., CVR College of Engineering, Hyderabad, India

²Dept. of Civil Eng., Aditya Engineering College (Autonomous), India

Article Info

Abstract

Article history:

Received 23 Apr 2023

Accepted 06 Sep 2023

Keywords:

Bacteria;
Calcium carbonate;
Cell concentration;
Cracks;
Durability properties

The study was carried out with the influence of four Bacillus species, namely Bacillus subtilis (BS), Bacillus licheniformis (BL), Bacillus halodurans (BH), and Bacillus cereus (BC), in order to improve the impermeable nature of concrete. The selected bacterial agents were cultured according to the nutrient broth medium method and prepared with two variable cell concentrations of 10^8 and 10^9 . In this study, bacteria were used in two different modes, i.e., as an additive to the concrete and as a curing agent. However, all the concrete specimens were cracked with a 65% stress level concentration and then cured in calcium lactate (only for bacteria-induced concrete specimens) and bacterial solution (only for normal concrete specimens) for crack healing. The durability behavior of these concrete specimens was monitored before crack, after crack, and after healing. In this regard, the following durability tests were performed: Rapid Chloride Permeability Test (RCPT), Water absorption test, Open porosity test, and Acid attack test. From the experimental observations, a decline in the passage of coulombs by 1352 C, water absorption by 3.47%, open porosity by 4.61%, and increased resistance against acid attack was found in normal concrete specimens cured under bacterial solution (especially in Bacillus halodurans with cell concentrations of 10^9) compared to other ones. Based on the analysis of the results, bacterial cultures have enriched the durability of the concrete by filling the voids and cracks with calcite crystals. However, Bacillus halodurans has shown better durability performance in both types of concrete, i.e., bacterial concrete cured in calcium lactate and normal concrete cured in bacterial solutions.

© 2023 MIM Research Group. All rights reserved.

1. Introduction

Concrete is one of the most extensively utilized building material and also cracks are unavoidable because it is brittle in tension yet robust in compression [1-4]. When fractures appear in concrete, it can shorten the life of the structure. So, it is mandatory to attend the cracks and rebuilt them before failure of structure happens. A lot of cracks repairing and maintenance techniques are available, but they all are time consuming and extremely expensive [5]. Microbially induced carbonate precipitation (MICP) has been investigated as a solution for stone crack restoration because calcium carbonate minerals are a homogeneous substance that is compatible with concrete & stone which are environment friendly [6]. MICP is an old natural phenomenon that has altered the earth, as calcium carbonate minerals are generated from calcium and carbonate ions in this process [7-8]. This technology has been marketed for healing broken surfaces with induced CaCO_3 production named as self-healing concrete can be broadly classified into autogenous self-healing and autonomous self-healing. In most of the traditional concrete mixtures, 20-30%

*Corresponding author: chava.venkatesh@cvr.ac.in

^a orcid.org/0000-0003-0942-9252; ^b orcid.org/0000-0003-0028-7702; ^c orcid.org/0000-0002-7768-3298;

^d orcid.org/0000-0002-0040-5812; ^e orcid.org/0000-0002-5543-168X

DOI: <http://dx.doi.org/10.17515/resm2023.745st0423>

Res. Eng. Struct. Mat. Vol. 9 Iss. 4 (2023) 1489-1505

1489

of cement particles are left anhydrate. If the concrete's cracking occurs, the unreacted cement grains may become exposed to moisture and fill the cracks by precipitating calcite crystals termed as autogenous self-healing. If external agents, viz any chemical or biological agents are used for self-healing process, this process termed as autonomous healing [9].

The studies from various researchers stated that the healing process was carried out by introducing the bacteria into the concrete. The bacterial spores activate the healing process with the presence of moisture; thereby the cracks in concrete are healed by microbial-induced calcite precipitation [10]. The bacteria in the former are engineered to produce urease, an enzyme that catalyzes the conversion of urea to ammonium and carbonate. As ammonia dissolves, the pH shifts from neutral to alkaline, resulting in the formation of carbonate ions [11]. Bacterial cell walls are negatively charged, allowing them to capture positively charged calcium ions and deposit them on their surface. For the latter, the metabolic conversion of an organic calcium source, which mixes with the leached $\text{Ca}(\text{OH})_2$ to make additional CaCO_3 crystals, may result in the emission of carbon dioxide during the respiration process of some spore-forming alkali-resistant bacteria [12-13]. The investigations were continued in this area majorly focus on the mechanism of bacteria based self-healing concrete, characterization methodologies and crack self-healing ability. It was stated from the test results that there is an improvement in bacteria based self-healing concrete correlate to conventional ones in terms of healing percentage and reduction of crack width [14-15].

Along with the self-healing behavior of concrete study, the mechanical properties of concrete were also investigated [16-19]. Some researchers have also a study on engineered cementitious composites [20-22] consisting of cement, aggregate, water, fibers and chemical additives. As this fiber helps to improve the tensile strength of the concrete and acts as a crack resistor. The observation was done for both the specimen's engineered cementitious composites (ECC) and fiber-reinforced (FR) mortar. The specimen's load-bearing capacity characterized the strain hardening even after cracking was seen in ECC specimens as no changes were observed in FR mortar. However, the carbon dioxide present in atmosphere combines with moisture and reacts with calcium ions present in the concrete results in calcium carbonate formation [23]. This is why crack reduction happens and leads to repair of the whole crack, but the crack was healed to $100\mu\text{m}$ only due to natural process. To extend the reduction of crack width, both the biological and chemical agents need to be incorporated into concrete. Some of the bacterial studies focused on durability, as mentioned here. Liu et al. [24] used Denitrifying bacteria in concrete to improve concrete performance. This study concluded that compressive strength increased by around 30.3%, split tensile strength by 19.2%, and water absorption decreased by 33%. Naveet et al. [25] studied chloride ion permeability, water absorption, and compressive strength of *Sporosarcina pasteurii* bacteria-added concrete. Their study concluded that a 22% strength increment was observed. Compared to reference concrete, bacterial concrete exhibited 4 times more water absorption reduction and eight times less chloride ion penetration. Another study conducted by Priya et al. [26] utilized *Bacillus sphaericus* as a microbial agent in concrete to investigate durability and strength properties. The study concluded that compressive strength increased by 9.15%, while water absorption and sorptivity values decreased by 15.46% and 27.78%, respectively, compared to non-bacterial concrete. There is a need to focus on potential *Bacillus* species, particularly "*Bacillus subtilis* (BS), *Bacillus licheniformis* (BL), *Bacillus halodurans* (BH), and *Bacillus cereus* (BC)", due to the lack of sufficient literature. In the current research work, the methodology of incorporating both *Bacillus* species and calcium lactate into concrete to fill voids and cracks and decrease porosity and permeability was followed. The durability tests were performed to assess the fresh and hardened properties of the concrete in the present investigation.

2. Materials and Methods

2.1. Materials

The materials used in the current study are ordinary Portland cement of grade 53 confirming the specifications of ASTM C 150-19 [27][42], naturally available river sand and crushed stone aggregate are with the limitations of IS 383-2016 [28][43], potable water satisfying the limits of IS 456-2000 [29] for mixing of concrete. Along with these, four types of bacillus species were selected and purchased from National Collection of Industrial Microorganisms (NCIM)-Pune.

2.2. Experimental Methods

In the present study, all the concrete specimens were prepared with M40 grade concrete and mix proportions (as shown in Table 1) are determined as per the IS 10262-2009 [30]. The number of test specimens are used and their dimension are mentioned in the Table 2. All the samples cured in normal water at 28 days before its cracking.

Table 1. Mix calculations (Kg/m³)

Mix	Cement	Fine aggregates	Coarse aggregates	Water	Bacteria (cell/ml of water)
Normal concrete	450	624	1220	186	-
Bacterial agents induced concrete	450	624	1220	186	5.79×10 ⁸ 5.79×10 ⁹

Table 2. Details of specimens used in the entire research work

S.No.	Name of the test	Dimensions of specimen	Specimens for each Set	Total
1.	RCPT	100mm Φ and 50mm thick	Normal concrete - 30 Bacteria induced concrete - 24	54
2.	Open Porosity	150 mm × 150mm × 150mm	Normal concrete - 30 Bacteria induced concrete - 24	54
3.	Water absorption	150 mm × 150mm × 150mm	Normal concrete - 30 Bacteria induced concrete - 24	54
4.	Acid attack (HCl)	150 mm × 150mm × 150mm	Normal concrete - 30 Bacteria induced concrete - 24	54
			Total	216

2.3 Bacterial Culture Process

The four bacillus species (*Bacillus subtilis*, *Bacillus licheniformis*, *Bacillus halodurans* and *Bacillus cereus*) adopted in the present study are due to their calcium carbonate mineralization efficiency and capacity to survive in high alkaline environments. The bacterial cultures are grown using nutrient broth medium contains peptone 5gms, beef extract 3gms, sodium chloride 5gms diluted in 1000ml of distilled water that was sterilized at 121°C for 20 minutes. Allow time for the medium to cool before inoculating it with

culture and after inoculation, the solution was incubated for 24hrs at 37°C at a speed of 85rpm in an incubator shaker. In order to prepare the bacterial solution in terms of cell concentration, a serial dilution technique was utilized and again the cells were counted with hemocytometer method.

2.4 Direct Usage of Bacteria

In this process, the bacteria were cultured and two different cell concentrations of 10^8 and 10^9 are prepared and are incorporated into the concrete directly during its mixing process. After mixing, the specimens were cast in order to evaluate the performance of concrete by conducting various tests. Along with this, the specimens are placed in curing tank for a specified time of curing after 24hrs of casting.

2.5 Indirect Usage of Bacteria

This procedure entails to utilize the bacteria solution as one of the curing agents (indirectly to concrete) for healing purposes. The normal concrete specimens are prepared, cured for 28 days and are cracked artificially using 65% stress level concentration. The bacterial solution of two varied cells 10^8 and 10^9 are developed and the cracked normal concrete specimens are placed in this solution for sealing cracks.

2.6 Durability Studies on Concrete

Durability can be defined as the capability of concrete offering resistance against chemical attack, abrasion, attrition, and weathering actions by maintaining its desired properties. The durability of concrete was estimated by conducting water absorption, open porosity, acid attack, and rapid chloride permeability test in the present study. The test procedures are explained detailly in this section and there are many factors influencing the durability i.e., cement content, temperature, moisture, permeability, aggregate and water quality.

2.6.1 Rapid Chloride Permeability Test

The rapid chloride permeability test (RCPT) was used to calculate the resistance offered by concrete samples through chloride ion permeability. As per ASTM C 1202(2012) [31] specifications, the performance of concrete was evaluated using a specimen with size of 100mm diameter and 50mm height. Figure 1 shows the RCPT setup, which consists of two reservoirs as one is filled with 0.3M of NaOH and the other is filled with 3% NaCl solutions.



Fig. 1 RCPT setup

A constant voltage of 60V direct current was maintained and passed through the concrete specimens for chloride ions movement and readings were noticed. The total charge passed in 6hrs was estimated using Equation 1. The RCPT ratings as per ASTM C 1202(2012) were listed in Table 3.

$$Q = 900 \times (I_0 + 2 \times I_{30} + 2 \times I_{60} + 2 \times I_{120} \dots + I_{360}) \tag{1}$$

Table 3. RCPT ratings

Charge passed	> 4000	2000-4000	1000-2000	100-1000	< 100
Chloride ion permeability	High	Medium	Low	Very low	Negligible

2.6.2 Water Absorption Test

A water absorption test was conducted to measure the amount of water absorbed by the concrete specimens when submerged in water. This test was performed for the concrete specimens with size 150mm×150mm×150mm as per BS 1881-122:2011 [32] limitations. The water absorption was measured in percentage (%); the lower the value indicates better the result. The percentage of water absorption can be calculated by using the formulae in Equation 2. The experimental setup for the water absorption test was shown in Figure 2.

$$w(\%) = \frac{W_w - W_d}{W_d} \times 100 \tag{2}$$

Where W(%) = Percentage of water absorption, W_w = Wet weight of the samples, W_d = Dry weight of the samples



Fig. 2 Experimental setup for water absorption test

2.6.3 Open Porosity Test

The porosity can also be known as pore space, a measure of air and void space between the concrete particles. As per guidelines of ASTM C642-06 [33], the test was performed for the concrete specimens of size 150mm×150mm×150mm. The porosity of concrete is the ratio of the volume of pore space in a unit of material to the total volume of material. The porosity of concrete is calculated using the following Eq 3.

$$p = \frac{W_{ssd} - W_d}{W_{ssd} - W_w} \times 100 \tag{3}$$

Where p is the porosity, W_{ssd} is the specimen weight in saturated surface dry (SSD) condition, W_d is the specimen dry weight, W_w is saturated submerged specimen’s weight.

2.6.4 Acid Attack Test

A highly soluble calcium salt byproduct was formed from the reaction between the acid and calcium hydroxide portion of the cement paste in the acid attack test. The specimens

of size 150mm×150mm×150mm were prepared to execute the acid attack test as per ASTM C1898-20 [34] standards. The specimens were placed in the acid solution for 28 days which was diluted with 5% HCl. In the acid attack test, the acid durability loss factor (ADLF) is calculated by the product of acid mass loss factor (AMLF), acid attack factor (AAF), and acid strength loss factor (ASLF). The formula for ADLF is in Eq 4, and the test setup for the acid attack test is in Figure 3.

$$\text{Acid durability loss factor (ADLF)} = \text{AMLF} \times \text{AAF} \times \text{ASLF} \quad (4)$$

Where Acid mass loss factor (AMLF) = (Change in a mass of specimen after immersion in acid/Initial mass of specimen before immersion in acid) ×100

Acid attack factor (AAF) = (Change in a dimension of diagonals after immersion in acid/Original diagonal dimension before immersion in acid) ×100

Acid strength loss factor (ASLF) = (Change in strength after immersion in acid/Original strength before immersion in acid) ×100



Fig. 3 Experimental setup for acid attack test

3. Results and Discussion

3.1 Rapid Chloride Permeability Test

Figure 4 and Figure 5 illustrates chloride ions passage (measured in terms of coulombs) of normal concrete specimens cured in various bacterial solutions (such as *Bacillus subtilis*, *Bacillus cereus*, *Bacillus halodurans*, and *Bacillus licheniformis*) with two different cell concentration (10^8 and 10^9). However, the chloride ions passage was measured for the concrete specimens before cracking, after cracking and after healing with a stress level concentration of 65%. The passage of coulombs was measured in uncracked concrete samples were around 1900 C to 2001 C. Similarly, after cracking, the passage of coulombs has been increased up to 2828 C in *Bacillus subtilis*, 2886 C in *Bacillus cereus*, 2837 C in *Bacillus halodurans*, and 2802 C in *Bacillus licheniformis*. Afterward, the cracked concrete samples were cured in bacterial solutions (10^8 cell concentration) for 28days and once again, chloride ions permeability has been measured. Thus, the results have shown that the passage of coulombs was reduced up to 1941 C in *Bacillus subtilis*, 2033 C in *Bacillus cereus*, 1566 C in *Bacillus halodurans*, and 1729 C in *Bacillus licheniformis*. These results confirm the calcite precipitate formation by the bacterial solution that has filled the concrete cracks and voids. Similarly, the cracked concrete samples cured in bacterial solution with a cell concentration of 10^9 has been reduced from 2802 C to 1717 C in *Bacillus subtilis*, 2841 C to 1988 C in *Bacillus cereus*, 2820 C to 1452 C in *Bacillus halodurans*, and 2855 C to 1595 C in *Bacillus licheniformis*.

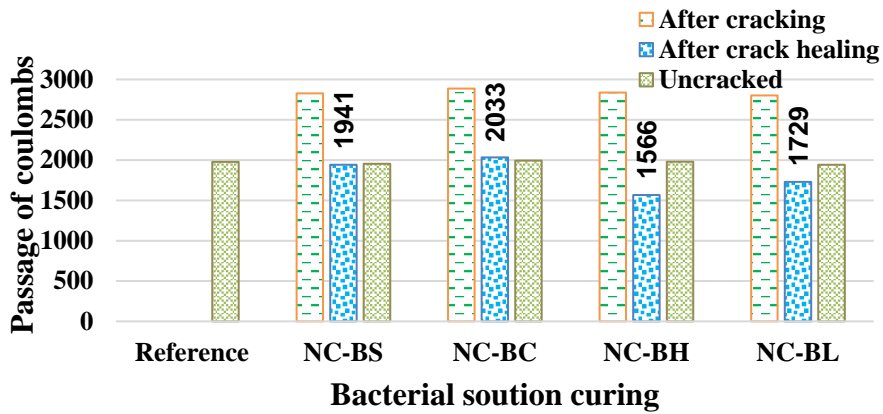


Fig. 4 Passage of coulombs Vs bacterial solution curing with cell concentration of 10^8

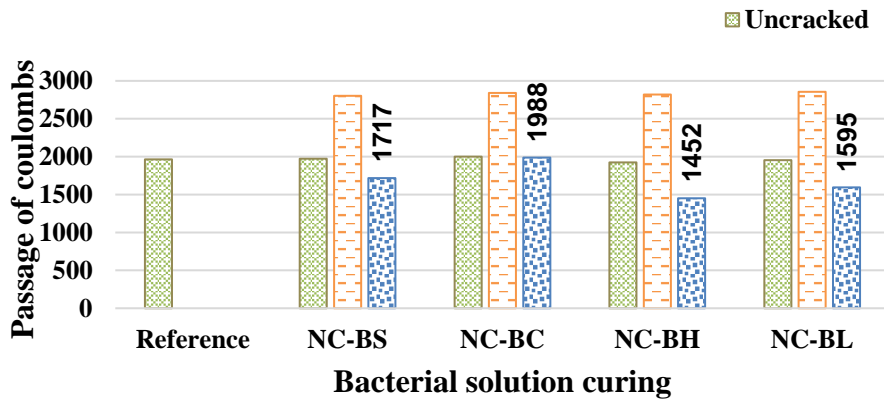


Fig. 5 Passage of coulombs Vs bacterial solution curing with cell concentration of 10^9

In the present research work, various bacterial concretes have been prepared with cell concentrations 10^8 and 10^9 . Moreover, all the concrete samples were cured in calcium lactate after cracking, and the chloride ions permeability has measured before cracking, after cracking, and after crack healing as represented in Figure 6 and Figure 7. No significant variations were observed in bacterial concrete than reference concrete from the obtained results in uncracked samples. Afterward, the crack was created for the concrete specimens with a stress level concentration of 65% in both cell concentrated samples via 10^8 and 10^9 , as all the cracked concrete samples have cured in calcium lactate solution, and it was observed that bacterial concrete permeability was reduced due to the filling of cracks by calcite formation. However, the passage of coulombs has reduced from 2868 C to 2467 C in reference concrete, 2914 C to 1984 C in *Bacillus subtilis*, 2866 C to 1954 C in *Bacillus cereus*, 2805 C to 1632 C in *Bacillus halodurans*, and 2857 C to 1787 C in *Bacillus licheniformis* for the bacterial concrete specimens with a cell concentration of 10^8 . Similarly, bacterial concrete with cell concentration 10^9 also reduced the passage of coulombs from 2852 C to 1962 C in *Bacillus subtilis*, 2852 C in 1866 C in *Bacillus cereus*, 2769 C in 1571 C in *Bacillus halodurans*, and 2798 C to 1659 C in *Bacillus licheniformis*. Similar results were found by this research work [35] that the bacterial concrete had reduced the electrical current passage through the concrete. The bacteria have formed

calcite sediments into the voids/pores. Hence the permeability of the concrete has been reduced.

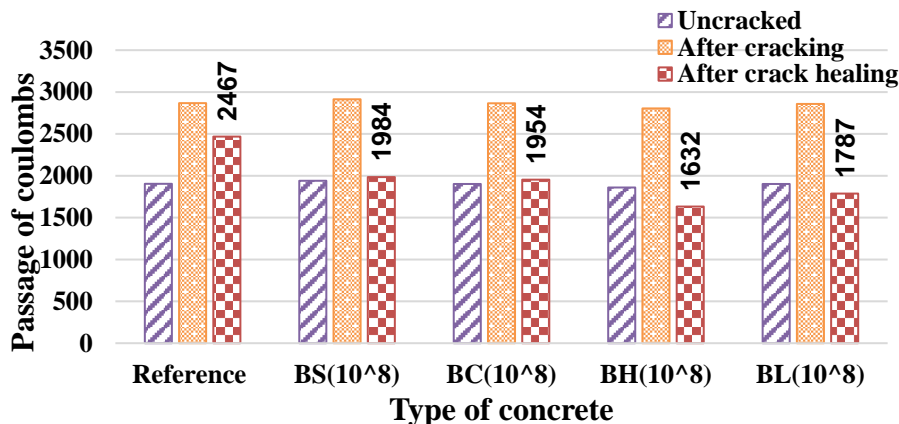


Fig. 6 Passage of coulombs Vs bacterial concrete cured in calcium lactate (10⁸)

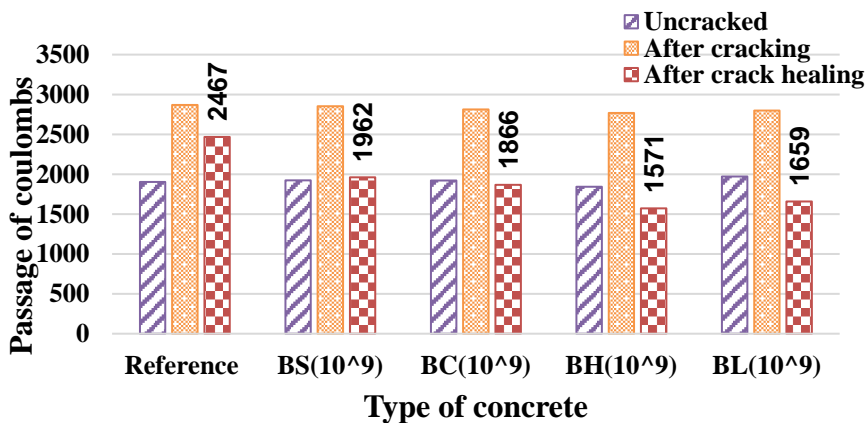


Fig. 7 Passage of coulombs Vs bacterial concrete cured in calcium lactate (10⁹)

4.3 Water Absorption Test

Figure 8 and Figure 9 show the water absorption of normal concrete samples cured in various bacterial solutions (such as *Bacillus subtilis*, *Bacillus cereus*, *Bacillus halodurans*, and *Bacillus licheniformis*) when concrete samples were cracked (with 65% of stress level concentration). The water absorption for the cracked concrete samples has increased from 4.81 % to 8.62%, 4.54 % to 8.56%, 4.75 % to 8.81%, and 4.87% to 8.59%. However, all the cracked concrete samples were cured in various bacterial solutions (cell concentration of 10⁸) for 28days. Afterward, once again, the water absorption has measured. The obtained results showed that water absorption of the cracked samples reduced to 5.58% in *Bacillus subtilis*, 5.63% in *Bacillus cereus*, 4.29% in *Bacillus halodurans*, and 4.56% in *Bacillus licheniformis*. This effect could be explained by the bacterial solution calcite precipitation, which has filled/sealed the cracks. Similarly, cracked samples cured in 10⁹ cells concentrated bacterial solution reduced the water absorption values from 8.69% to 5.08%

in *Bacillus subtilis*, 8.76% to 5.36% in *Bacillus cereus*, 8.85% to 4.17% in *Bacillus halodurans*, and 8.49% to 4.48% in *Bacillus licheniformis*.

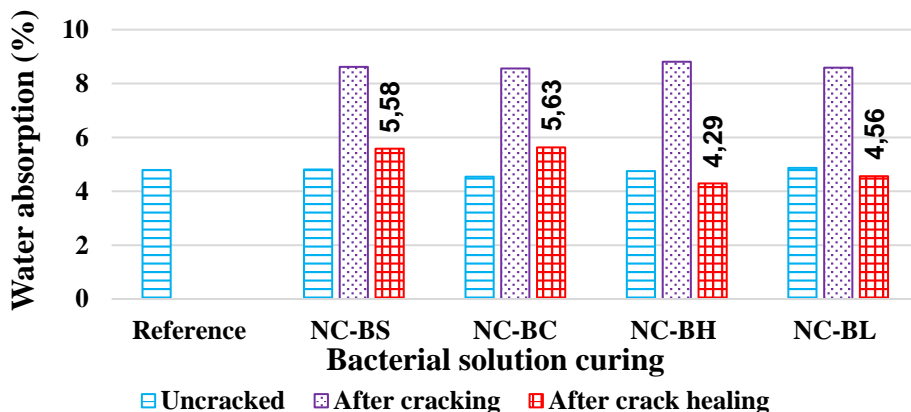


Fig. 8 Water absorption vs bacterial solution (10⁸)

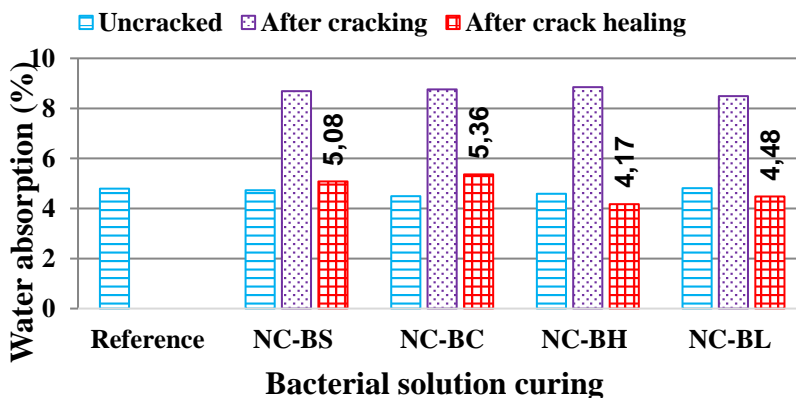


Fig. 9 Water absorption Vs bacterial solution (10⁹)

In the present research work, four selected bacteria cultures were incorporated into the concrete, and water absorption has measured before and after cracking. All the cracked concrete samples were cured in calcium lactate solution and once again, the water absorption for the cracked samples was measured. From the obtained results, the uncracked concrete samples have shown 4.91% in reference, 4.87% in *Bacillus subtilis*, 4.61% in *Bacillus cereus*, 4.74% in *Bacillus halodurans*, and 4.79% in *Bacillus licheniformis* of water absorption values. The water absorption for the cracked bacterial concrete samples with a cell concentration of 10⁸ has reduced from 8.86% to 7.15% in reference, 8.54% to 5.69% in *Bacillus subtilis*, 8.79% to 5.31% in *Bacillus cereus*, 8.5% to 4.23% in *Bacillus halodurans* and 8.82% to 4.48% in *Bacillus licheniformis* after cured into the calcium lactate as shown in Figure 10. Similarly, Figure 11 depicts the water absorption of cracked bacterial concrete specimens with a cell concentration of 10⁹ reduced from 8.6% to 5.26% in *Bacillus subtilis*, 8.42% to 5.45% in *Bacillus cereus*, 8.72% to 4.09% in *Bacillus halodurans*, and 8.44% to 4.39% in *Bacillus licheniformis* after cured into the calcium

lactate. A study [36] reported that water and gas permeability of concrete decreased after activation of bacterial spores in the concrete, as the calcite crystals are formed, and the cracks are filled. Similarly, in the study [37] it was reported that bacterial cultures would precipitate the calcite on the surface of the concrete which seals pores or voids. Moreover, there was a reduction of 65% to 95% water absorption, the permeability and sorptivity of concrete also will be reduced.

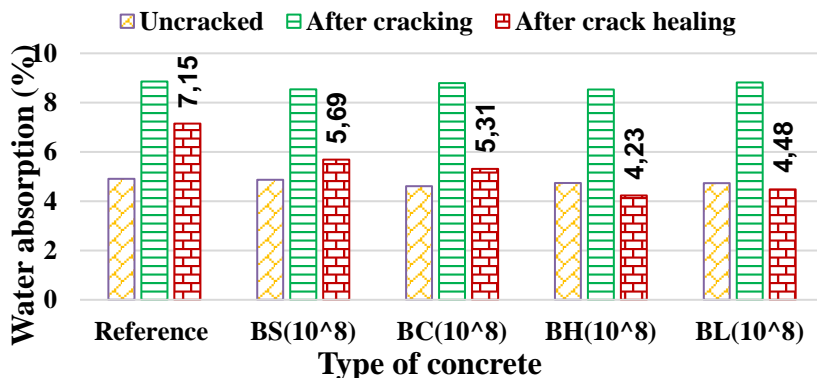


Fig. 10 Water absorption Vs bacterial concretes cured in calcium lactate (10⁸)

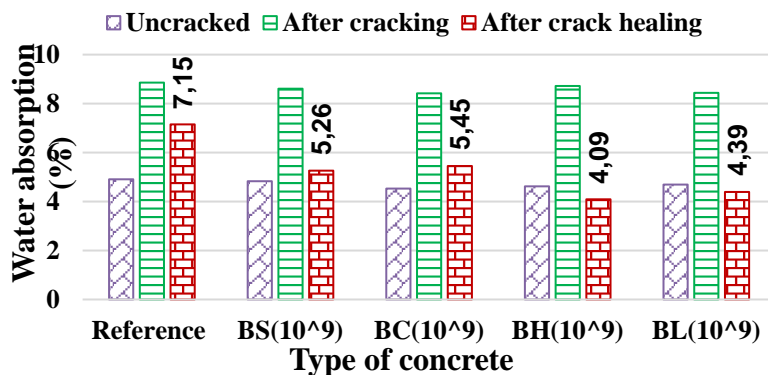


Fig. 11 Water absorption Vs bacterial concretes cured in calcium lactate (10⁹)

4.4 Open Porosity Test

In the present research work, open porosity test has been performed to know the bacterial cultures filling effect in the concrete pores and cracks. This test was conducted when concrete samples were uncracked, cracked (with 65% of stress level concentration), and after crack healing (cracked samples were immersed in various bacterial solutions such as *Bacillus subtilis*, *Bacillus cereus*, *Bacillus halodurans*, and *Bacillus licheniformis*). Thus, the obtained results in Figure 12 and Table 4 demonstrate that concrete's porosity has reduced, possibly due to calcite filling in the cracks and voids.

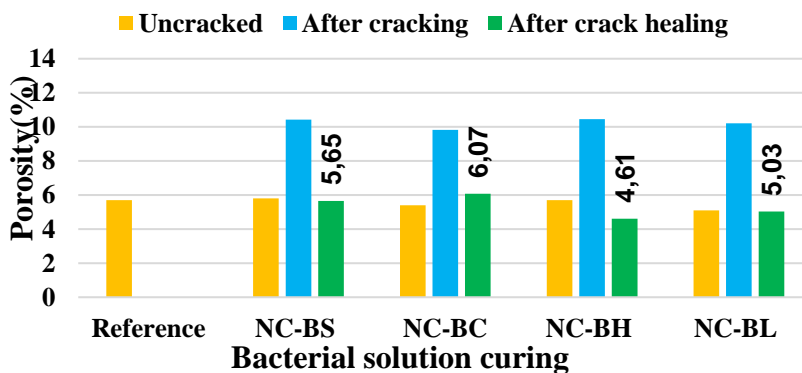


Fig. 12 Porosity Vs bacterial solution curing (10⁹)

However, the cracked samples (with cell concentration of 10⁹) porosity reduced from 10.42% to 5.65% in *Bacillus subtilis*, 6.82% to 6.07% in *Bacillus cereus*, 10.45% to 4.61% in *Bacillus halodurans*, and 10.21% to 5.03% in *Bacillus licheniformis*. Similarly, the results were observed in the concrete samples with 10⁸ cell concentrations curing, and there is a reduction of 9.73% to 5.65% in *Bacillus subtilis*, 9.66% to 6.28% in *Bacillus cereus*, 10.05% to 4.82% in *Bacillus halodurans*, and 10.01% to 5.24% in *Bacillus licheniformis*.

Table 4. Porosity Vs bacterial solution curing (10⁸)

	Porosity (%)				
	Reference	NC-BS(10 ⁸)	NC-BC(10 ⁸)	NC-BH(10 ⁸)	NC-BL(10 ⁸)
Uncracked	5.7	5.1	5.6	5.9	5.3
After cracking	-	9.73	9.66	10.05	10.01
After crack healing	-	5.65	6.28	4.82	5.24

Figure 13. and Table 5 shows the porosity of the bacterial concretes cured in calcium lactate. The results showed that cracked samples (with cell concentration of 10⁹) porosity reduced from 10.67% to 8.69% in the reference sample, 10.19% to 5.83% in *Bacillus subtilis*, 9.52% to 6.24% in *Bacillus cereus*, 10.25% to 5.14% in *Bacillus halodurans* and 10.31% to 5.35% in *Bacillus licheniformis* as shown in Figure 14. In this research work, [38] it was concluded that concrete porosity and water absorption had approximated and decreased from 48% to 55% and 50% to 55%. It might be due to calcite formation in the concrete microcracks and pores. A similar justification given by a researcher, [39] that bacillus species could precipitate CaCO₃ and act as a filler material and reduce the concrete's porosity implies strength and durability improvement.

Similarly, concrete samples incorporated with various bacterial cultures of cell concentration 10⁸ cured using calcium lactate has reduced the porosity values from 10.67% to 8.69% in the reference sample, 10.25% to 5.97% in *Bacillus subtilis*, 10.66% to 6.49% in *Bacillus cereus*, 10.35% to 5.43% in *Bacillus halodurans* and 10.41% to 5.51% in *Bacillus licheniformis* as illustrates in Table 5.

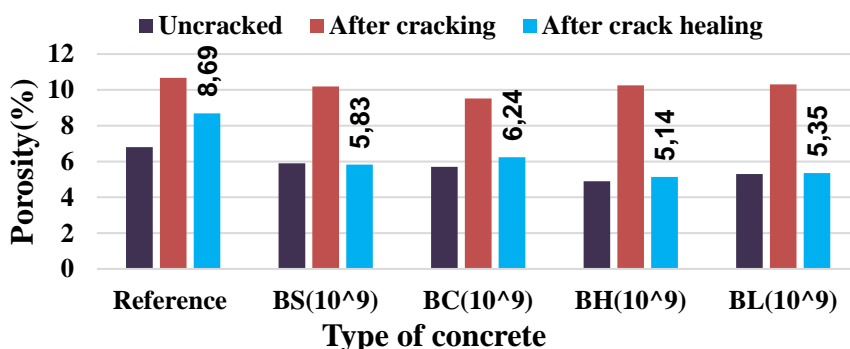


Fig. 13 Porosity Vs bacterial concretes cured in calcium lactate (10⁹)

Table 5. Porosity Vs bacterial concretes cured in calcium lactate (10⁸)

	Porosity (%)				
	Reference-CL	BS(10 ⁸)-CL	BC(10 ⁸)-CL	BH(10 ⁸)-CL	BL(10 ⁸)-CL
Uncracked	6.8	6.2	5.8	5.7	5.68
After cracking	10.67	10.25	10.66	10.35	10.41
After crack healing	8.69	5.97	6.49	5.43	5.51

4.5 Acid Attack Test

In the present research work, an acid attack test has been conducted to determine the durability behavior of bacterial concretes cured in calcium lactate, and normal concretes cured in bacterial solution. However, normal concrete samples cured in bacterial solutions have better durability than calcium lactate cured bacterial concrete samples as represented in Table 6. Similarly, bacterial cultures incorporated concrete having more durability than reference concrete. Moreover, *Bacillus halodurans* have shown better performance than other bacterial cultures as enlisted in Table 7. The bacterial cultures give protection to crack through calcite formation which enriches the structure’s lifespan.

Table 6. mass loss (%), strength loss (%) and dimension loss (%) of normal concrete samples cured in various bacterial solutions

CC	Mix	Mass Loss (%)			Dimension Loss (%)			Strength loss (%)		
		UC	AC	AH	UC	AC	AH	UC	AC	AH
10 ⁸	Ref	2.95	4.2	2.15	2.15	4.86	3.16	5.95	6.76	6.51
	NC-BS	2.43	4.32	2.12	2.15	4.52	2.29	4.5	6.21	4.6
	NC-BC	2.29	4.83	2.89	1.85	4.67	2.97	4.12	6.92	4.22
	NC-BH	2.6	4.36	2.97	1.34	4.92	1.39	4.14	6.64	3.14
	NC-BL	2.59	4.84	2.39	1.58	4.52	1.62	4.76	6.1	4.34
10 ⁹	NC-BS	2.41	4.45	2.98	2.09	4.37	2.16	4.38	5.94	4.49
	NC-BC	2.13	4.37	2.78	1.79	4.61	2.85	3.97	6.02	4.11
	NC-BH	2.48	4.84	2.74	1.27	4.21	1.31	3.95	6.35	2.99
	NC-BL	2.91	4.83	2.51	1.51	4.33	1.54	3.29	6.64	3.17

CC-Cell concentration, Ref-reference, UC- uncracked concrete, AC- after cracking, AH- after healing

Table 7. Mass loss (%), strength loss (%), and dimension loss (%) of bacterial concrete cured in calcium lactate

CC	Mix	Mass Loss (%)			Dimension Loss (%)			Strength loss (%)		
		UC	AC	AH	UC	AC	AH	UC	AC	AH
	Ref	2.75	5.86	4.22	2.5	3.12	3.56	6.03	7.12	6.15
10 ⁸	BS	2.37	5.06	3.99	2.29	3.1	2.36	4.61	7.02	5.81
	BC	2.12	5.94	3.73	1.96	3.96	2.11	4.21	7.36	5.42
	BH	2.54	5.26	2.79	1.43	3.23	1.5	4.21	7.97	4.19
	BL	2.87	5.57	2.27	1.67	3.5	1.75	4.45	7.02	4.89
10 ⁹	BS	2.33	5.84	3.86	2.17	3.42	2.29	4.47	7.56	4.67
	BC	2.08	5.05	3.54	1.85	3.61	2.98	4.09	7.37	4.29
	BH	2.42	5.36	3.54	1.34	3.57	1.42	4.12	7.01	2.1
	BL	2.83	5.22	3.04	1.58	3.46	1.67	4.37	7.1	2.78

CC-Cell concentration, Ref-reference, UC- uncracked concrete, AC- after crack, AH- after healing

Table 8. Acid durability loss factor for normal concretes cured in a bacterial solution

CC	Mix	Acid Durability Loss Factor		
		UC	AC	AH
	Ref	37.74	137.99	85.37
10 ⁸	NC-BS	23.51	121.26	32.87
	NC-BC	17.45	156.09	36.22
	NC-BH	14.42	142.44	12.96
	NC-BL	19.48	133.45	16.8
10 ⁹	NC-BS	22.06	115.51	28.9
	NC-BC	15.14	121.28	32.56
	NC-BH	12.44	129.39	10.73
	NC-BL	14.46	138.87	12.25

Table 9. Acid durability loss factor for bacterial concretes cured in calcium lactate

CC	Mix	Acid Durability Loss Factor		
		UC	AC	AH
	Ref	41.46	130.18	92.39
10 ⁸	BS	25.02	110.12	54.71
	BC	17.49	173.12	42.66
	BH	15.29	135.41	17.54
	BL	21.33	136.85	19.43
10 ⁹	BS	22.6	150.99	41.28
	BC	15.74	134.36	45.26
	BH	13.36	134.14	10.56
	BL	19.54	128.23	14.11

5. Conclusions

In the present research work, four different bacterial cultures "(i.e., *Bacillus subtilis* (BS), *Bacillus cereus* (BC), *Bacillus halodurans* (BH), and *Bacillus licheniformis*(BL))" are used in the concrete as additive and also as a curing agent. To assess the durability behaviour of bacterial concrete; "chloride ions permeability, open porosity, water absorption, and acid resistance tests" were conducted.

- The selected Bacillus species, namely Bacillus subtilis, Bacillus cereus, Bacillus halodurans, and Bacillus licheniformis, have the potential to heal surface cracks and enhance the durability of concrete when compared to non-bacterial concrete.
- The passage of coulombs (1352 C) has decreased significantly in normal concrete specimens cured under bacterial solution (Bacillus halodurans with a cell concentration of 10^9) compared to other bacterial solutions and calcium lactate curing, attributed to reduced void discontinuity.
- There is a decrease in water absorption (3.47%) and open porosity (4.61%) observed in normal concrete specimens cured under bacterial solution (Bacillus halodurans with a cell concentration of 10^9) in comparison to others.
- Normal concrete specimens cured with bacterial solution (Bacillus halodurans at a cell concentration of 10^9) exhibit higher resistivity of 9.94 against acid attack.
- Bacillus licheniformis has demonstrated optimal performance following Bacillus halodurans in all conditions.
- Although no significant difference in results was found between bacterial cell concentrations of 10^9 and 10^8 , samples with a concentration of 10^9 cells have exhibited greater durability.
- The analysis of results reveals that bacterial cultures have improved concrete durability by filling voids and cracks with calcite, leading to reduced coulombs, water absorption, porosity values, and enhanced resistance against chemical attacks.
- However, Bacillus halodurans has exhibited superior durability performance in both types of concrete (i.e., bacterial concrete cured with calcium lactate and normal concrete cured with bacterial solutions). Thus, this Bacillus species is recommended for use in real-time repair and rehabilitation projects.

Acknowledgement

The author extends heartfelt thanks to Dr. Indira Mikkili, Associate Professor in the Biotechnical Engineering Department at VFSTR Deemed to be University, and to the late Dr. Ruben, Associate Professor in the Civil Engineering Department at VFSTR Deemed to be University, for their continuous support and blessings.

References

- [1] Rong H, Wei G, Ma G, Zhang Y, Zheng X, Zhang L, Xu R. Influence of bacterial concentration on crack self-healing of cement-based materials. Construction and Building Materials. 2020 May 30;244:118372. <https://doi.org/10.1016/j.conbuildmat.2020.118372>
- [2] Arce GA, Hassan MM, Mohammad LN, Rupnow T. Self-healing of SMA and steel-reinforced mortar with microcapsules. Journal of Materials in Civil Engineering. 2019 Feb 1;31(2):04018366. [https://doi.org/10.1061/\(ASCE\)MT.1943-5533.0002568](https://doi.org/10.1061/(ASCE)MT.1943-5533.0002568)
- [3] Akhlaghi MA, Bagherpour R, Kalhori H. Application of bacterial nanocellulose fibers as reinforcement in cement composites. Construction and Building Materials. 2020 Apr 30;241:118061. <https://doi.org/10.1016/j.conbuildmat.2020.118061>
- [4] Siddique R, Rajor A. Influence of bacterial treated cement kiln dust on the properties of concrete. Construction and building materials. 2014 Feb 15;52:42-51. <https://doi.org/10.1016/j.conbuildmat.2013.11.034>
- [5] Vijay K, Murmu M, Deo SV. Bacteria based self healing concrete-A review. Construction and building materials. 2017 Oct 15;152:1008-14. <https://doi.org/10.1016/j.conbuildmat.2017.07.040>

- [6] Pei R, Liu J, Wang S, Yang M. Use of bacterial cell walls to improve the mechanical performance of concrete. *Cement and Concrete Composites*. 2013 May 1;39:122-30. <https://doi.org/10.1016/j.cemconcomp.2013.03.024>
- [7] De Muynck W, De Belie N, Verstraete W. Microbial carbonate precipitation in construction materials: a review. *Ecological engineering*. 2010 Feb 1;36(2):118-36. <https://doi.org/10.1016/j.ecoleng.2009.02.006>
- [8] Mastromei G, Marvasi M, Perito B. Studies on bacterial carbonate precipitation for stone conservation. In *Proc. of 1st BioGeoCivil engineering conference*, Delft, Netherlands. Delft University of Technology, Delft 2008 (pp. 104-106).
- [9] Aliko-Benítez A, Doblaré M, Sanz-Herrera JA. Chemical-diffusive modeling of the self-healing behavior in concrete. *International Journal of Solids and Structures*. 2015 Sep 1;69:392-402. <https://doi.org/10.1016/j.ijsolstr.2015.05.011>
- [10] Luo M, Qian CX. Performance of two bacteria-based additives used for self-healing concrete. *Journal of Materials in Civil Engineering*. 2016 Dec 1;28(12):04016151. [https://doi.org/10.1061/\(ASCE\)MT.1943-5533.0001673](https://doi.org/10.1061/(ASCE)MT.1943-5533.0001673)
- [11] Kalhori H, Bagherpour R. Application of carbonate precipitating bacteria for improving properties and repairing cracks of shotcrete. *Construction and Building Materials*. 2017 Sep 1;148:249-60. <https://doi.org/10.1016/j.conbuildmat.2017.05.074>
- [12] Stanaszek-Tomal E. Bacterial concrete as a sustainable building material?. *Sustainability*. 2020 Jan 17;12(2):696. <https://doi.org/10.3390/su12020696>
- [13] Jin C, Yu R, Shui Z. Fungi: A neglected candidate for the application of self-healing concrete. *Frontiers in Built Environment*. 2018 Oct 29;4:62. doi: 10.3389/fbuil.2018.00062. <https://doi.org/10.3389/fbuil.2018.00062>
- [14] Chuo SC, Mohamed SF, Mohd Setapar SH, Ahmad A, Jawaid M, Wani WA, Yaqoob AA, Mohamad Ibrahim MN. Insights into the current trends in the utilization of bacteria for microbially induced calcium carbonate precipitation. *Materials*. 2020 Nov 5;13(21):4993. <https://doi.org/10.3390/ma13214993>
- [15] Dakhane A, Das S, Hansen H, O'Donnell S, Hanoon F, Rushton A, Perla C, Neithalath N. Crack healing in cementitious mortars using enzyme-induced carbonate precipitation: Quantification based on fracture response. *Journal of Materials in Civil Engineering*. 2018 Apr 1;30(4):04018035. [https://doi.org/10.1061/\(ASCE\)MT.1943-5533.0002218](https://doi.org/10.1061/(ASCE)MT.1943-5533.0002218)
- [16] Hung CC, Su YF, Su YM. Mechanical properties and self-healing evaluation of strain-hardening cementitious composites with high volumes of hybrid pozzolan materials. *Composites Part B: Engineering*. 2018 Jan 15;133:15-25. <https://doi.org/10.1016/j.compositesb.2017.09.005>
- [17] Prasad CV, Lakshmi TV. Experimental investigation on bacterial concrete strength with *Bacillus subtilis* and crushed stone dust aggregate based on ultrasonic pulse velocity. *Materials Today: Proceedings*. 2020 Jan 1;27:1111-7. <https://doi.org/10.1016/j.matpr.2020.01.478>
- [18] Seifan M, Sarmah AK, Samani AK, Ebrahiminezhad A, Ghasemi Y, Berenjhan A. Mechanical properties of bio self-healing concrete containing immobilized bacteria with iron oxide nanoparticles. *Applied microbiology and biotechnology*. 2018 May;102:4489-98. <https://doi.org/10.1007/s00253-018-8913-9>
- [19] Siddique R, Jameel A, Singh M, Barnat-Hunek D, Ait-Mokhtar A, Belarbi R, Rajor A. Effect of bacteria on strength, permeation characteristics and micro-structure of silica fume concrete. *Construction and Building Materials*. 2017 Jul 1;142:92-100. <https://doi.org/10.1016/j.conbuildmat.2017.03.057>
- [20] Yildirim G, Alyousif A, Şahmaran M, Lachemi M. Assessing the self-healing capability of cementitious composites under increasing sustained loading. *Advances in Cement Research*. 2015 Nov;27(10):581-9. <https://doi.org/10.1680/adcr.14.00111>

- [21] Suryanto B, Wilson SA, McCarter WJ, Chrisp TM. Self-healing performance of engineered cementitious composites under natural environmental exposure. *Advances in Cement Research*. 2016 Apr;28(4):211-20. <https://doi.org/10.1680/jadcr.15.00022>
- [22] Yıldırım G, Khiavi AH, Yeşilmen S, Şahmaran M. Self-healing performance of aged cementitious composites. *Cement and Concrete Composites*. 2018 Mar 1;87:172-86. <https://doi.org/10.1016/j.cemconcomp.2018.01.004>
- [23] Andalib R, Abd Majid MZ, Hussin MW, Ponraj M, Keyvanfar A, Mirza J, Lee HS. Optimum concentration of *Bacillus megaterium* for strengthening structural concrete. *Construction and Building Materials*. 2016 Aug 15;118:180-93. <https://doi.org/10.1016/j.conbuildmat.2016.04.142>
- [24] Liu Z, Chin CS, Xia J. Novel method for enhancing freeze-thaw resistance of recycled coarse aggregate concrete via two-stage introduction of denitrifying bacteria. *Journal of Cleaner Production*. 2022 Apr 20;346:131159. <https://doi.org/10.1016/j.jclepro.2022.131159>
- [25] Chahal N, Siddique R, Rajor A. Influence of bacteria on the compressive strength, water absorption and rapid chloride permeability of fly ash concrete. *Construction and Building Materials*. 2012 Mar 1;28(1):351-6. <https://doi.org/10.1016/j.conbuildmat.2011.07.042>
- [26] Priya TS, Ramesh N, Agarwal A, Bhusnur S, Chaudhary K. Strength and durability characteristics of concrete made by micronized biomass silica and *Bacteria-Bacillus sphaericus*. *Construction and Building Materials*. 2019 Nov 30;226:827-38. <https://doi.org/10.1016/j.conbuildmat.2019.07.172>
- [27] ASTM AS. Standard Specification for Portland Cement. ASTM C150/C150M-19a.
- [28] IS 383-2016. (2016). Coarse and fine aggregate for concrete - specification. Bureau of Indian Standards, New Delhi, India.
- [29] IS 456-2000. (2000). Plain and reinforced concrete - code of practice. Bureau of Indian Standards, New Delhi, India.
- [30] IS 10262-2009. (2009). Concrete mix proportioning - guidelines. Bureau of Indian Standards, New Delhi, India.
- [31] ASTM C 1202. (2012). Standard test method for electrical indication of concrete's ability to resist chloride ion penetration. ASTM International, West Conshohocken, PA.
- [32] BS 1881-122:2011. (2011). Testing concrete-Method for determination of water absorption. British Standard Institute, London, United Kingdom.
- [33] ASTM C642-06. (2006). Standard test method for density, absorption, and voids in hardened concrete. ASTM International, West Conshohocken, PA.
- [34] ASTM C1898-20. (2020). Standard test methods for determining the chemical resistance of concrete products to acid attack. ASTM International, West Conshohocken, PA.
- [35] Vijay K, Murmu M. Self-repairing of concrete cracks by using bacteria and basalt fiber. *SN Applied Sciences*. 2019 Nov;1:1-0. <https://doi.org/10.1007/s42452-019-1404-5>
- [36] Tayebani B, Mostofinejad D. Self-healing bacterial mortar with improved chloride permeability and electrical resistance. *Construction and Building Materials*. 2019 May 30;208:75-86. <https://doi.org/10.1016/j.conbuildmat.2019.02.172>
- [37] Wang JY, Soens H, Verstraete W, De Belie N. Self-healing concrete by use of microencapsulated bacterial spores. *Cement and concrete research*. 2014 Feb 1;56:139-52. <https://doi.org/10.1016/j.cemconres.2013.11.009>
- [38] De Muynck W, Cox K, De Belie N, Verstraete W. Bacterial carbonate precipitation as an alternative surface treatment for concrete. *Construction and Building Materials*. 2008 May 1;22(5):875-85. <https://doi.org/10.1016/j.conbuildmat.2006.12.011>
- [39] Siddique R, Jameel A, Singh M, Barnat-Hunek D, Ait-Mokhtar A, Belarbi R, Rajor A. Effect of bacteria on strength, permeation characteristics and micro-structure of silica fume concrete. *Construction and Building Materials*. 2017 Jul 1;142:92-100. <https://doi.org/10.1016/j.conbuildmat.2017.03.057>

- [40] Andalib R, Abd Majid MZ, Keyvanfar A, Talaiekhazan A, Hussin MW, Shafaghat A, Zin RM, Lee CT, Fulazzaky MA, HAIDAR ISMAIL HA. Durability improvement assessment in different high strength bacterial structural concrete grades against different types of acids. *Sadhana*. 2014 Dec;39:1509-22. <https://doi.org/10.1007/s12046-014-0283-0>
- [41] Jonkers HM, Schlangen E. Development of a bacteria-based self healing concrete. *Taylor made concrete structures*. 2008 May 7;1:425-30. <https://doi.org/10.1201/9781439828410.ch72>
- [42] Narayana N, Rao BN, Rao TM. Application of optical microscopy techniques for the evaluation of raw materials for cement and concrete. *Materials Today: Proceedings*. 2023 May 5. <https://doi.org/10.1016/j.matpr.2023.04.447>
- [43] Madhavi C, Reddy VS, Rao MS, Shrihari S, Kadhim SI, Sharma S. The effect of elevated temperature on self-compacting concrete: Physical and mechanical properties. In *E3S Web of Conferences 2023* (Vol. 391, p. 01212). EDP Sciences. <https://doi.org/10.1051/e3sconf/202339101212>

Blank Page



Research Article

Effect of non-biodegradable waste materials on the strength performance of concrete

Ajibola Ibrahim Quadri^{a*}, Lekan Makanju Olanitori, Abdulhakeem Sadiq^b

Dept. of Civil and Environmental Eng.g, Federal University of Technology, Akure. P.M.B 704, Nigeria

Article Info

Abstract

Article history:

Received 28 Apr 2023

Accepted 21 Aug 2023

Keywords:

Concrete strength;

Waste glass;

Waste PET;

Slump;

Water absorption;

Waste reuse

Waste usage in the construction industry has reduced global environmental pollution. Reusing waste materials as substitutes for cement in concrete constituents and other construction materials can lower cement and concrete manufacturing costs, solid waste, and landfill space. Engineers are still unsure as to what extent waste can be repurposed to produce optimal strength for the production of concrete. Reutilization of waste materials has been employed in this paper by adopting 3.5%, 7%, and 10% of six wastes (plastic bags, rubber tires, cement sack strands, can waste, PET bottles, and waste from glass) as substitutes for aggregate in concrete production. At 10% replacement, the cement sack strand absorbed more water than other waste materials and about 5.8% less than the control specimen. Despite the fact that glass waste has a low water absorption rate, there was no discernible increase in strength after 28 days due to brittle damage under loading. At 10% and 7% partial replacement, can waste had about 9% and 12.5% higher compressive and tensile strengths than the control specimen. As a result, it is proposed that using wastes that may enhance concrete properties will lower the need for normal coarse and fine aggregates, enabling natural resource conservation.

© 2023 MIM Research Group. All rights reserved.

1. Introduction

Concrete constitutes nonhomogeneous materials of different aggregate types, cement, and water in varying proportions based on the strength requirements. It is a man-made material conglomerate with rock-like properties, and having varied compression and tensile strength properties. The tensile strength accounts for about 10% of its compressive strength, giving rise to low performance under tensile loading, and it is the most widely used for construction because of the availability of material constituents at a cheap rate [1,2]. During the production process, concrete can flow and take on different shapes based on various mix ratios and preparation techniques [3]. Many materials, including agricultural materials, synthetic materials, and industrial waste, are now being used to make concrete of varying strengths. To remove the effect of CO₂ in the environment, the most common material target from concrete constituent is cement. According to reports, a tonne of cement production always results in a tonne of CO₂ discharge into the surroundings [4]. consequently, the share of the cement industry to total global CO₂ discharge from fossil fuel combustion stood at about 7% [5]. Recently, these materials, particularly industrial wastes, have made significant inroads into concrete production by replacing a percentage of natural aggregate (fine or coarse aggregate) in concrete with them to produce lightweight concrete and a method of reducing environmental pollution.

Industries' waste is gradually increasing these days and causing huge environmental issues. It has been determined that recycling and reusing waste is the best option for

*Corresponding author: aiquadri@futa.edu.ng

^a orcid.org/0000-0001-5328-9379; ^b orcid.org/0009-0001-8985-7611

DOI: <http://dx.doi.org/10.17515/resm2023.751st0428>

Res. Eng. Struct. Mat. Vol. 9 Iss. 4 (2023) 1507-1519

reducing the volume of solid waste that could end up in disposal sites, with all the negative effects on the environment and financial loss that could result. Moreover, the world's rapid industrialization and urbanization drive infrastructure development. This process causes several issues, including a shortage of construction materials and increased productivity of waste and other products [6]. The continual advancement of concrete technology has increased the choices for incorporating cutting-edge and sustainable solutions into concrete designs and applications using industrial waste. Non-biodegradable waste, such as glass, plastics, rubber, etc., with substantial environmental impact, has been worked on using cutting-edge technology to reduce the impact of CO₂ generated during cement production and to produce lightweight concrete as an aggregate substitute. However, recycling some of these industrial wastes is often expensive and not sustainable for the green environment. According to [7], the majority of used non-biodegradable materials are not recycled but rather dumped, which contributes to several significant environmental issues. The pollution of rivers, lands, and oceans by waste plastic makes it a potential threat to aquatic life. However, because of their light weight, flexibility, moisture resistance, and cost-effectiveness, non-biodegradable materials will eventually replace many currently used composite materials, such as material used in producing concrete [8].

Over the last decade, varieties of industrial non-biodegradable wastes such as plastic waste, polystyrene, rubber tires, and waste glass have been used as alternatives for natural aggregate in concrete [9–11]. Research by Taha and Nounu [12] has proven that solid waste can substitute about 20% of fine aggregate in concrete with appropriate mechanical properties. The shapes and sizes of the substitute waste aggregate can affect the consistency of concrete [13]. There is always a reduction in strengths of concrete when the percentage replacement of waste aggregate is increased [14]. Vanitha et al., [6], investigated the use of plastic waste as a substitute for coarse aggregate in M20 concrete grade using 0-10% replacement with a 2% increment. The optimal concrete compressive strength was determined at 4% of the partial replacement. Manjunath [15], adopted electronic-plastic waste to partially replace coarse aggregate in M20 concrete grade, the flexural and compressive strengths improved substantially at 10% partial replacement. Plastic has some advantages in the partial replacement of concrete, such as non-degradability and durability, resistance to chemicals and moisture, and increased bonding capacity at high temperatures [16]. However, plastic materials have a low melting point and poor bonding properties at low temperatures, reducing the concrete strength. Islam et al., [17] adopted waste pet as an alternative in fresh and hardened concrete, an increase in the waste pet produced a lower compressive strength of concrete. PET aggregate concrete could have high workability at a low water-cement ratio. Choi et al., [18] reported that the structural efficiency of waste PET lightweight aggregate concrete and compressive strength decreased when the percentage replacement was increased; however, workability increased above 120% at 75% replacement compared with the natural aggregate. This implies that the consistency of PET concrete may not increase strength.

Thiruppathi, [19] investigated some factors influencing the performance of rubber tire concrete, such as aggregate shape, size, and curing time. Despite the low-strength development, rubber aggregate concrete demonstrated the potential to become a long-term solution for rubber waste management. When rubber tire waste was substituted for coarse aggregate in concrete with varying percentage by Ganjian et al., [20], there was no significant improvement in concrete strength at up to 5% replacement, however, with higher replacement ratios, appreciable changes were observed. On the use of waste glass as aggregate in concrete, Srivastava et al., [21] concluded that waste glass could be adopted as a coarse aggregate substitute for up to 50% replacement without substantial change in compressive strength. However, Keryou, [22] concluded that the optimum strengths of glass concrete was achieved at 25% replacement of coarse aggregate. It is essential to note

that the density, shape, size, and tensile properties of glass can significantly impact the performance of glass concrete [23].

A reassessment of the literature confirms that concrete strength can be improved using industrial waste as a partial substitute for natural aggregate in concrete. However, the question of to what extent the partial substitution of these natural aggregates can affect concrete strength and durability has not been answered. This study, therefore, investigates the consequences of the partial substitution of natural aggregate in concrete with non-biodegradable waste materials. Waste PET, plastic bags, rubber tires, glass waste, cement sack strands, and can waste are considered for the substitution of natural aggregate to ascertain concrete sustainability performance and serve as a panacea for industrial waste. In reality, cement sack strand and plastic bags cannot fully substitute the main function of coarse aggregate in concrete matrix, as coarse aggregate occupies over 50% of the volume of the concrete matrix and provides the majority of the strength in this study; however, these materials should be used as reinforced fiber in concrete [24]. Fig. 1 shows some selected waste materials in literature against their compressive strengths [25–36]. It can be seen that waste materials in concrete can produce high strength waste concrete depending on the mix proportion. In research by Evram et al. [25], the aggregate used was replaced by PET at 5% to 20%, the optimum concrete strength was at 15% partial replacement. Thorneycroft et al. [28] reported that replacing sand by 10% volume of recycled plastic can save above 800 million tons of sand every year by adopting suitable mix design for concrete.

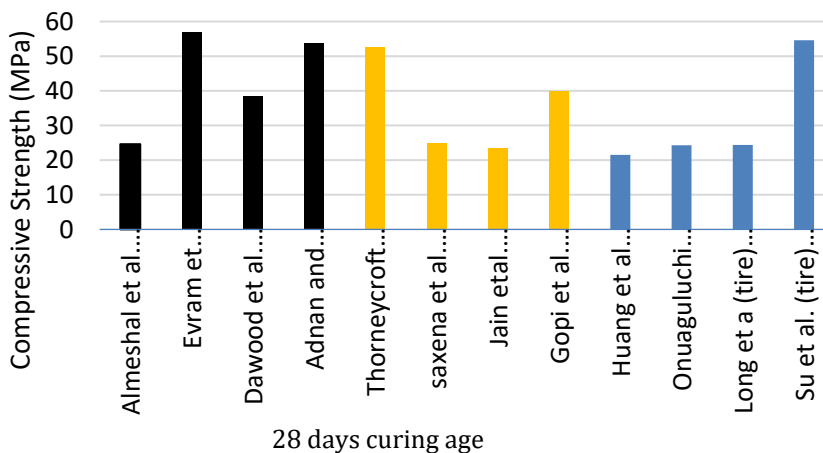


Fig. 1 Wastes materials versus compressive strength in 28 days

2. Methodology

The study used grade 43 Ordinary Portland Cement (OPC), the initial setting time was determined to be 30 minutes and a specific gravity (SG) of 3.2. The physical characteristics meet the requirements of [37]. The maximum size of coarse aggregate was measured as 20 mm with SG 2.81 and fine aggregate of 4.75 mm fine standard sieve were adopted having SG of 2.65. Six waste materials were employed in the current research to replace coarse aggregate in concrete; waste PET bottles, plastic bags, rubber tires, glass waste, cement sack strands, and tin waste as shown in Fig. 2. The glass waste is the mixture of broken glass bottles and mirrors collected from different household. Since the waste materials are lightweight, it may be inefficient to substitute the natural aggregate with the corresponding weight of waste. Three partial replacements of 3.5%, 7%, and 10% by

volume of coarse aggregate were therefore used. The waste materials were cut into the sizes of the coarse substitute aggregate up to the biggest size of 20 mm. The maximum length of plastic and cement sack strand used is 50 mm to be used as fiber in concrete. The concrete mix was designed following (BS 206-1) [38] recommended for M20 grade concrete. M20 concrete is commonly used in most construction projects. The concrete mix proportions adopted is 1:2:4, with a water-to-cement ratio (w/c) of 50%.



Fig. 2 Waste materials used for partial replacement of natural aggregate

2.1 Test on Aggregates

2.1.1 Sieve Analysis Test

To determine the soil gradation, particle size distribution evaluation with sieve gradation from 9.5 mm to 75 μ m arranged from top to bottom was performed on the sand according to the British Standards [39]. The sand sample was collected and dried in an oven for 24 hours to remove excess moisture. 400 g of oven-dried sample was measured for the sieve analysis, and the particle gradation was calculated using equations 1 and 2.

$$W_d = \left(\frac{100}{100 + m_n} \right) W_6 \tag{1}$$

$$P_p = \left(\frac{W_d - W_s}{W_d} \right) \times 100 \% \tag{2}$$

W_d Is the weight of the dried sample (in g), m_n is the moisture content (in %), and W_6 is the weight of the remaining sample to an accuracy of 0.01 g. The percentage of a particle passing the 75 μ m test sieve is denoted as P_p , the weight of the sample reserved in the sieve measured to an accuracy of 0.01 g is denoted as W_s .

2.1.2 Aggregate Soundness Test

The coarse aggregate was subjected to a soundness test. Aggregate passing the BS sieve size of 12.5 mm and reserved on a 10 mm was subjected to 110 $^{\circ}$ C for about 5 hours following (BS 812-121) [40]. The soundness apparatus was filled in three layers, with each layer given a 25-blow tamping rod, and then the compacted weight of the aggregate's

weight was measured and recorded as M_w . The aggregate surface was leveled before inserting the plunger. The apparatus containing the specimen was loaded uniformly on the compression testing machine until the sample failed. The sample was then run through a 2.36 mm sieve, and the portion that made it through was weighed and recorded as M_s . The aggregate impact value is expressed as given in Equation 3.

$$(AIV) = \frac{M_s}{M_w} \times 100 \quad (3)$$

2.2 Slump Test for Fresh Concrete

The fresh concrete slump test was performed on the different percentage replacements for each waste material and the control sample to establish the consistency of the fresh concrete following (BS 12350-2) [41]. The inner surface of the slump cone was lubricated and laid on a flat platform. The cone was then filled up with fresh concrete in three layers and tamped with 25 strokes of the tamping rod; the brim was level after the tamping process had been completed, the cone was gradually removed, and the slump height was measured.

2.3 Casting of Concrete

The design of normal concrete mixes according to (BS 206-1) [38] was used for concrete casting. The trial mixes of various cement, sand, granite, and water ratios were used to accomplish the required concrete strength for this study. Using the pre-determined concrete mix ratios, 228 concrete cubes of 150 mm and 246 cylindrical concrete samples of dimensions 200 mm × 100 mm in length and diameter were cast. For each percentage replacement strength test for the number of days (7, 14, 21, and 28), twelve specimens were considered. The mix ratio of 1:2:4 was used to determine substitute waste material in three different percentage proportions by volume of coarse aggregate.

2.4 Test on Concrete Water Absorption

This test was conducted following the BS 1881-122 [42]. The test aims to offer a means of comparing the tendency of water absorption of various waste substitutes used. After casting, the 200 mm × 100 mm cylindrical concrete was inserted in water for 28 days to ensure proper curing is achieved. The specimens were placed in an oven at 100 °C for about a day to remove excess moisture before being reweighed. The weight of the specimens was recorded as the dry weight (W_1), and they were immersed in water at 25 °C for 24 hours. This weight was recorded as the wet weight (W_2). The rate of absorption is expressed as.

$$W = \frac{w_2 - w_1}{w_1} \times 100 \quad (4)$$

2.4 Compressive and Splitting Strength Test

The compressive and tensile strength tests on concrete are important because they provide information about the material's strength. The tests were conducted following BS 12390-3 [43]. Compressive and splitting strength tests were performed on selected concrete specimens on the 7th, 14th, 21st, and 28th days, respectively. The specimen was carefully placed and adjusted with the center of the lower pressure plate of the compression machine as shown in Fig. 3; a flat plate was placed on the specimen to distribute the load during operation. The upper pressure plate of the machine was lowered to meet the top surface of the specimen, and the load was carefully applied in an increasing stress pattern until the specimen failed. In the splitting test, the height of the cylindrical specimen was positioned on the lower plate of the machine, while the upper plate was lowered until it made contact with the specimen. The splitting tensile strength is computed using Equation 5.

$$f_{cst} = \frac{2P}{\pi ld} \quad (5)$$

Where; f_{cst} = Split Tensile Strength, P is the breaking load, l is the length of the cylinder, and d is the diameter of the cylinder.



Fig. 3 Compressive strength test

3. Results and Discussion

3.1 Result of Sieve Analysis and Slump

The distribution curve for the fine aggregate and coarse aggregate is depicted in Figs. 4 and 5. During the particle size distribution test, the plastic and cement bags analysis were not considered because they could not pass through the set of sieves; moreover, they are often used in the concrete matrix as fiber reinforcement rather than as coarse aggregate. The aggregate is well-graded, ranging between fine gravel and fine sand. The uniformity (C_u) and curvature (C_c) coefficients have been numerically calculated to determine the particle distribution in the aggregate. The percentage fines of 60%, 30%, and 10% are evaluated here. C_u is the ratio of 60% finer to 10% finer, which yielded a value of 2.11, while C_c is the ratio of the square of 30% finer to 60% and 10% combined, yielding a value of 1.15, confirming that the fine aggregate is well graded. The gravel and coarse aggregate contents were higher than the fines, which can increase water absorption and, as a result, increase the capillary pores in concrete. The natural coarse aggregate as well as the waste samples range between medium gravel and coarse sand, indicating a well-graded particle.

The aggregate impact value AIV obtained from the soundness test of natural coarse aggregate is 18.71%, which is sufficient for concrete impact resistance. As a result, the coarse aggregate used can produce concrete with high impact resistance. Aggregate Impact Value also indicates how well aggregates absorb shock [44].

The slump test for different percentage replacements for various waste materials is presented in Fig. 6. The slump values increase with an increase in percentage replacement for all waste materials at an adopted water-cement ratio of 50%. The slump value of the control specimen is higher than the waste materials, up to 7% replacement, except for the glass waste. All the specimens showed a true slump, with can waste having the highest slump value.

3.2 Concrete Water Absorption Result

The average water absorption value of waste material concrete is presented in Fig. 7. The control mix recorded the highest water absorption value of 13.6%, far lower than the 18% recommended [45]. Pet bottles at partial replacement of 10% had the least water

absorption rate of 1.2%. This implies that concrete with a high-water absorption value may have a high permeability rate when exposed to inundation and thus become weakened. On the other hand, because can waste and pet bottles have a low absorption rate and affinity for water, their presence did not encourage moisture retention in concrete. This is because some capillary pores that retain water in concrete could be filled by the materials, reducing the voids left for water to occupy.

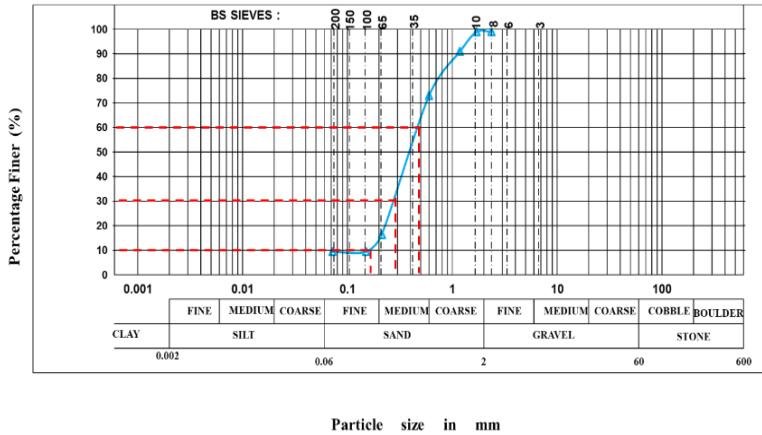


Fig. 4 Sand distribution particle curve

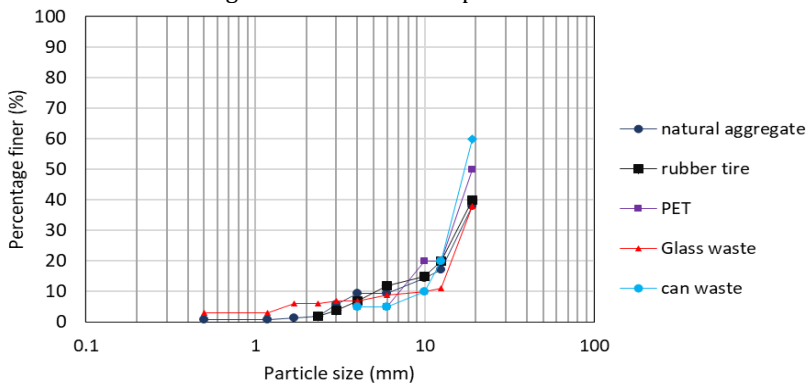


Fig. 5 Coarse aggregate distribution curve

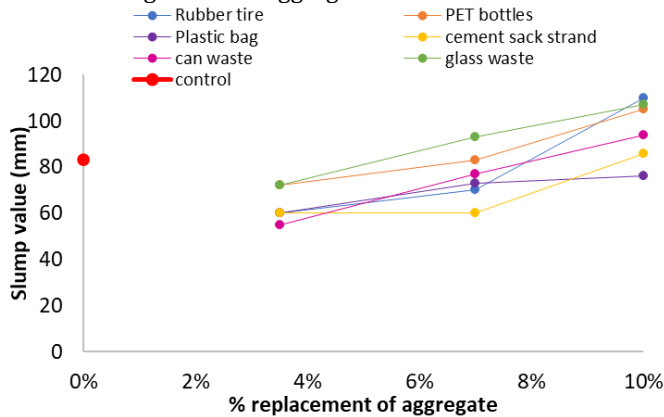


Fig. 6 Comparison of slump values for waste materials

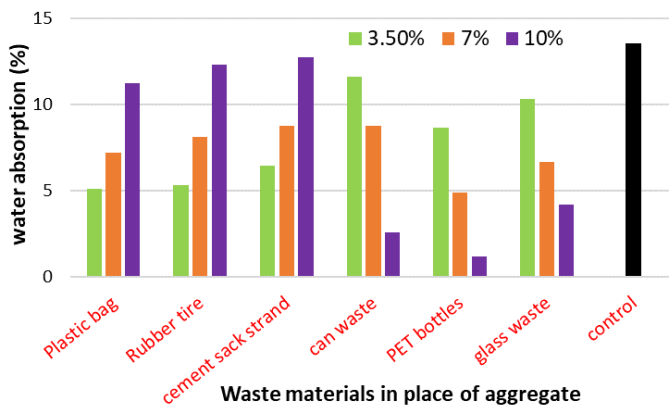


Fig. 7 Water absorption at different percentage replacement

3.3 Compressive Strength Result

The results of the average compressive strength obtained at the curing age of 7, 14, 21, and 28 days against the percentage replacement of coarse aggregate with waste materials are presented in Fig. 8. It can be seen that the compressive strengths of all specimens increase gradually with age. At 28-day curing, can waste has the highest compressive strength values at 10% replacement, followed by pet bottles and plastic bags at 3.5% replacement. This implies that waste material with high strength can act as reinforcement within the concrete. Although glass has a low water absorption rate, it was discovered during the compressive test that it did not contribute much to resisting the compressive load increment. Instead, it showed brittle failure (see Fig. 9). Concrete's heterogeneous material composition causes brittle failure under loading; combining a brittle material (glass) with its constituent does not improve Van der Waal's force in concrete but acts as an impurity in the concrete matrix. This could also prevent cement from completely hydrating in concrete.

3.4 Splitting Tensile Strength Result

Fig. 10 depicts the average tensile strength values of the waste materials and their respective percentage replacement. The can waste had the highest tensile strength at 7% partial replacement, which is approximately 44% higher than the control specimen. The cement sack strand had approximately 43% higher tensile strength than the control. Then, the glass waste had the lowest tensile strength, 19% lower than the control specimen. This confirms the unsuitability of glass waste as a coarse aggregate substitute in concrete production.

4. Conclusion

The properties of concrete incorporating various waste materials as coarse aggregate were investigated experimentally using 3.5%, 7%, and 10% replacement by volume of natural coarse aggregate with mix ratio 1:2:4. Consequently, the following conclusions have been drawn from the investigation.

- Can waste, pet bottles, and glass waste have low water absorption values as the percentage variation increases when compared to the control sample, which has the highest value of 13.55%. However, this does not translate to high concrete strength in this study because can waste and PET bottle concrete strengths are

lower when compared to other waste materials. Nonetheless, the compressive strength of these materials can be used where concrete strength is not a priority.

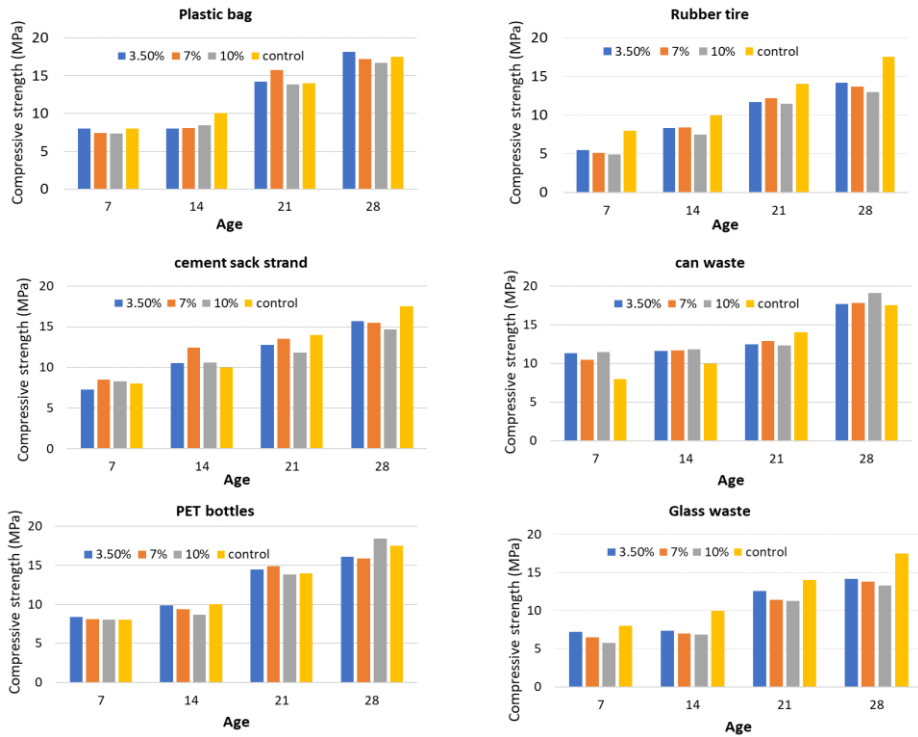


Fig. 8 Compressive strength results



Fig. 9 Failure mode of glass waste in concrete

- Glass waste had the highest workability and resistance to water absorption, implying that it can partially replace coarse aggregate in concrete; however, the glass-concrete had very low energy absorption under loading, resulting in brittle failure. This could be due to the low strength of the glass used. Glass waste with

high strength is recommended, which may increase the strength of concrete more than expected.

- All the waste materials showed a gradual increase in both compressive and tensile strength with age. Can waste produced an optimum compressive and tensile strength in 28 days. The compressive strength was 10% higher than the control specimen at 10% partial replacement while the splitting tensile strength was 44% higher than the control sample at 7% replacement of natural coarse aggregate.
- Although this study used industrial waste as a substitute for natural coarse aggregate in concrete, cement sack strands and plastic bags contributed as reinforced fiber, resulting in ductile behavior under loading. As a result, the material may not be suitable where strength is a higher priority than ductility. Quality control should thus be ensured in their use.

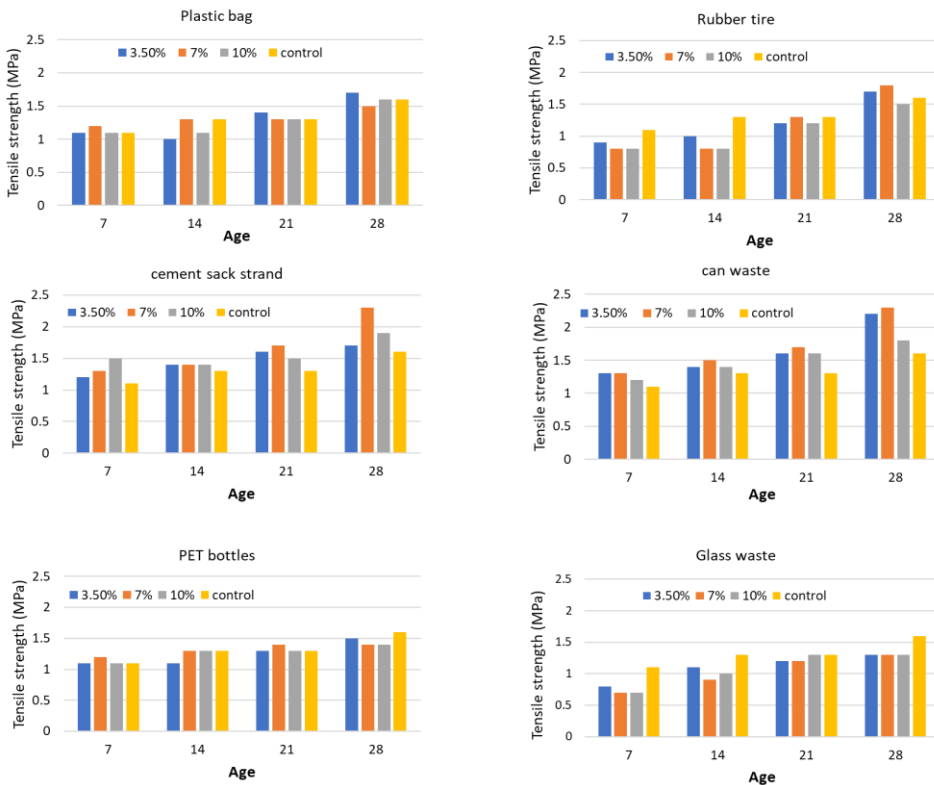


Fig. 10 Tensile strength results

References

- [1] Foti D. Recycled waste PET for sustainable fiber-reinforced concrete. Use of Recycled Plastics in Eco-efficient Concrete, Elsevier; 2019, p. 387-410. <https://doi.org/10.1016/B978-0-08-102676-2.00018-9>
- [2] Karthikeyan S, Arun P, Thiyaneswaran MP. Summary of non-biodegradable wastes in concrete, Namakkal, India: 2020, p. 020020. <https://doi.org/10.1063/5.0007586>
- [3] Pham TM, Elchalakani M, Hao H, Lai J, Ameduri S, Tran TM. Durability characteristics of lightweight rubberized concrete. Construction and Building Materials 2019;224:584-99. <https://doi.org/10.1016/j.conbuildmat.2019.07.048>

- [4] Liu B, Qin J, Shi J, Jiang J, Wu X, He Z. New perspectives on utilization of CO2 sequestration technologies in cement-based materials. *Construction and Building Materials* 2021;272:121660. <https://doi.org/10.1016/j.conbuildmat.2020.121660>
- [5] Oh D-Y, Noguchi T, Kitagaki R, Park W-J. CO2 emission reduction by reuse of building material waste in the Japanese cement industry. *Renewable and Sustainable Energy Reviews* 2014;38:796-810. <https://doi.org/10.1016/j.rser.2014.07.036>
- [6] Vanitha S, Natarajan V, Praba M. Utilisation of Waste Plastics as a Partial Replacement of Coarse Aggregate in Concrete Blocks. *Indian Journal of Science and Technology* 2015;8. <https://doi.org/10.17485/ijst/2015/v8i12/54462>
- [7] Park SB, Lee BC, Kim JH. Studies on mechanical properties of concrete containing waste glass aggregate. *Cement and Concrete Research* 2004;34:2181-9. <https://doi.org/10.1016/j.cemconres.2004.02.006>
- [8] Babafemi A, Šavija B, Paul S, Anggraini V. Engineering Properties of Concrete with Waste Recycled Plastic: A Review. *Sustainability* 2018;10:3875. <https://doi.org/10.3390/su10113875>
- [9] Quadri AI, Ogunsola NO. Influence of Cow bone Powder on Cement Partially Substitute in Sandcrete Blocks. *Proceedings of the Annual Conference of The School of Engineering & Engineering Technology, Nigeria: AIRASETA; 2021, p. 687-98.*
- [10] Quadri AI, Wasiu AT. Assessment of some mechanical properties of concrete by partial replacement of cement with cow bone powder. *JACEPR* 2020;10:10-8.
- [11] Suzuki M, Seddik Meddah M, Sato R. Use of porous ceramic waste aggregates for internal curing of high-performance concrete. *Cement and Concrete Research* 2009;39:373-81. <https://doi.org/10.1016/j.cemconres.2009.01.007>
- [12] Taha B, Nounu G. Properties of concrete contains mixed colour waste recycled glass as sand and cement replacement. *Construction and Building Materials* 2008;22:713-20. <https://doi.org/10.1016/j.conbuildmat.2007.01.019>
- [13] Batayneh M, Marie I, Asi I. Use of selected waste materials in concrete mixes. *Waste Management* 2007;27:1870-6. <https://doi.org/10.1016/j.wasman.2006.07.026>
- [14] Ali EE, Al-Tersawy SH. Recycled glass as a partial replacement for fine aggregate in self compacting concrete. *Construction and Building Materials* 2012;35:785-91. <https://doi.org/10.1016/j.conbuildmat.2012.04.117>
- [15] Manjunath BTA. Partial Replacement of E-plastic Waste as Coarse-Aggregate in Concrete. *Procedia Environmental Sciences* 2016;35:731-9. <https://doi.org/10.1016/j.proenv.2016.07.079>
- [16] Ahirwar S, Malviya P, Patidar V, Singh VK. An Experimental Study on Concrete by using E- Waste as Partial Replacement for Course Aggregate. *International Journal of Science Technology and Engineering* 2016;3:7-13.
- [17] Islam MJ, Meherier MS, Islam AKMR. Effects of waste PET as coarse aggregate on the fresh and harden properties of concrete. *Construction and Building Materials* 2016;125:946-51. <https://doi.org/10.1016/j.conbuildmat.2016.08.128>
- [18] Choi Y-W, Moon D-J, Chung J-S, Cho S-K. Effects of waste PET bottles aggregate on the properties of concrete. *Cement and Concrete Research* 2005;35:776-81. <https://doi.org/10.1016/j.cemconres.2004.05.014>
- [19] Thiruppathi R. Discarded tyre rubber as concrete aggregate: A possible outlet for used tyres. 2013 International Conference on Current Trends in Engineering and Technology (ICCTET), 2013, p. 202-7. <https://doi.org/10.1109/ICCTET.2013.6675946>
- [20] Ganjian E, Khorami M, Maghsoudi AA. Scrap-tyre-rubber replacement for aggregate and filler in concrete. *Construction and Building Materials* 2009;23:1828-36. <https://doi.org/10.1016/j.conbuildmat.2008.09.020>
- [21] Srivastava V, Gautam SP, Agarwal VC, Mehta PK. Glass Wastes as Coarse Aggregate in Concrete. *J Environ Nanotech* 2014;3:67-71. <https://doi.org/10.13074/jent.2013.12.132059>

- [22] Keryou DAB. Effect of Using Windows Waste Glass as Coarse Aggregate on some Properties of Concrete. Eng & Tech Journal 2014;32:1519-29. <https://doi.org/10.30684/etj.32.6A.14>
- [23] Pauzi NNM, Hamid R, Jamil M, Zain MFM. The effect of melted-spherical and crushed CRT funnel glass waste as coarse aggregates on concrete performance. Journal of Building Engineering 2021;35:102035. <https://doi.org/10.1016/j.jobe.2020.102035>
- [24] Ghernouti Y, Rabehi B, Bouziani T, Ghezraoui H, Makhloufi A. Fresh and hardened properties of self-compacting concrete containing plastic bag waste fibers (WFSCC). Construction and Building Materials 2015;82:89-100. <https://doi.org/10.1016/j.conbuildmat.2015.02.059>
- [25] Evram A, Akçaoğlu T, Ramyar K, Çubukçuoğlu B. Effects of waste electronic plastic and marble dust on hardened properties of high strength concrete. Construction and Building Materials 2020;263:120928. <https://doi.org/10.1016/j.conbuildmat.2020.120928>
- [26] Dawood AO, AL-Khazraji H, Falih RS. Physical and mechanical properties of concrete containing PET wastes as a partial replacement for fine aggregates. Case Studies in Construction Materials 2021;14:e00482. <https://doi.org/10.1016/j.cscm.2020.e00482>
- [27] Adnan HM, Dawood AO. Strength behavior of reinforced concrete beam using re-cycle of PET wastes as synthetic fibers. Case Studies in Construction Materials 2020;13:e00367. <https://doi.org/10.1016/j.cscm.2020.e00367>
- [28] Thorneycroft J, Orr J, Savoikar P, Ball RJ. Performance of structural concrete with recycled plastic waste as a partial replacement for sand. Construction and Building Materials 2018;161:63-9. <https://doi.org/10.1016/j.conbuildmat.2017.11.127>
- [29] Saxena R, Siddique S, Gupta T, Sharma RK, Chaudhary S. Impact resistance and energy absorption capacity of concrete containing plastic waste. Construction and Building Materials 2018;176:415-21. <https://doi.org/10.1016/j.conbuildmat.2018.05.019>
- [30] Jain A, Siddique S, Gupta T, Sharma RK, Chaudhary S. Utilization of shredded waste plastic bags to improve impact and abrasion resistance of concrete. Environment, Development and Sustainability 2020;22:337-62. <https://doi.org/10.1007/s10668-018-0204-1>
- [31] Gopi, K. Sai, Srinivas, Dr. T., Raju V, S. P. Feasibility Study of Recycled Plastic Waste as Fine Aggregate in Concrete. E3S Web Conf 2020;184:01084. <https://doi.org/10.1051/e3sconf/202018401084>
- [32] Huang W, Huang X, Xing Q, Zhou Z. Strength reduction factor of crumb rubber as fine aggregate replacement in concrete. Journal of Building Engineering 2020;32:101346. <https://doi.org/10.1016/j.jobe.2020.101346>
- [33] Onuaguluchi O, Banthia N. Durability performance of polymeric scrap tire fibers and its reinforced cement mortar. Materials and Structures 2017;50:158. <https://doi.org/10.1617/s11527-017-1025-7>
- [34] Almeshal I, Tayeh BA, Alyousef R, Alabduljabbar H, Mohamed AM. Eco-friendly concrete containing recycled plastic as partial replacement for sand. Journal of Materials Research and Technology 2020;9:4631-43. <https://doi.org/10.1016/j.jmrt.2020.02.090>
- [35] Long G, Ma K-L, Xie X, Xie Y-J. Effect of rubber aggregate on reduction of compressive strength of concrete. Jianzhu Cailiao Xuebao/Journal of Building Materials 2013;16:758-62.
- [36] Su H, Yang J, Ling T-C, Ghataora GS, Dirar S. Properties of concrete prepared with waste tyre rubber particles of uniform and varying sizes. Journal of Cleaner Production 2015;91:288-96. <https://doi.org/10.1016/j.jclepro.2014.12.022>
- [37] BS EN 197-1. Composition, specifications and conformity criteria for common cements. UK: The British Standards Institution; 2011.

- [38] BS 206-1. Concrete--complementary British Standard to BS EN 206-1. Part 1, Method of specifying and guidance for the specifier. 2nd ed. London: BSI; 2006.
- [39] BS 1377-2. British Standard methods of test for soils for civil engineering purposes. 1990.
- [40] BS 812-121. Testing aggregates. London: British Standards Institution; 1975.
- [41] BS 12350-2. Testing fresh concrete. Part 2, Slump-test. London: BSI; 2009.
- [42] BS 1881-122. Testing concrete. Part 122: Method for determination of water absorption. London: BSI; 2011.
- [43] BS 12390-3. Testing Hardened Concrete: Compressive Strength of Specimens. London: British Standard Institution; 2009.
- [44] Aderinola OS, Omolola OE, Quadri AI. Effect of Calcium Carbide Waste Powder on Some Engineering Properties of Bamboo Leaf Ash Concrete. OALib 2018;05:1-15. <https://doi.org/10.4236/oalib.1104990>
- [45] ASTM C90 C15 Committee. Specification for Loadbearing Concrete Masonry Units. US Department of Defence: ASTM International; 2017.

Blank Page



Research Article

Optimizing cost and strength by utilization of blast furnace slag aggregate and recycled concrete sand in concrete using response surface models

Poonam^{*a}, VP Singh^b

Department of Civil Engineering, National Institute of Technology, Kurukshetra, (Haryana) India

Article Info

Abstract

Article history:

Received 12 June 2023

Accepted 05 Aug 2023

Keywords:

Blast furnace slag aggregate;
Recycled concrete sand;
Optimize cost and concrete properties;
Response surface methodology;
Central composite design

The utilization of waste materials in concrete is crucial for sustainable construction, as it can contribute to environmental conservation and enhance concrete properties. Waste management and sustainable construction poses significant challenges in the construction industry. While numerous studies have focused on environmental conservation, only a limited number have explored the use of Blast furnace slag aggregate (BFSA) as coarse aggregate and recycled concrete sand (RCS) as fine aggregate to optimize cost and concrete properties using response surface models. In this study, response surface methodology (RSM) based on central composite design (CCD) was employed to evaluate the impact of BFSA (0-50%) and RCS (0-100%) replacement parameters on cost, compressive strength. ANOVA was used to verify the accuracy of the generated models. The RSM regression equations demonstrated high R² values exceeding 0.8 for all responses, indicating that the models could explain variability in the responses. The cost and compressive strength were found to be a suitable relation with BFSA and RCS replacement levels. In conclusion, RSM can help reduce costs by incorporating waste materials into concrete without significantly impacting concrete properties.

© 2023 MIM Research Group. All rights reserved.

1. Introduction

Rapid urbanization and industrialization have led to a continuous increase in the generation rate of construction and demolition (C&D) waste and a corresponding increase in the demand for natural resources [1-3]. Currently, a significant amount of C&D waste is disposed of through dumping and landfilling, which inevitably leads to land occupation and environmental issues. Additionally, there is a high demand for raw materials in the construction industry, leading to a depletion of natural resources [1-2]. Therefore, the reclamation of C&D waste is an essential step towards reducing the end-of-life impacts of structures and reducing their upstream impacts by minimizing the need for the extraction of natural resources [3]. Recycling C&D waste is a growing field, with a particular focus on recycling C&D waste into aggregates as sustainable building materials. The mechanical properties of recycled aggregate concrete (RAC) have been widely investigated, and it has been commonly accepted that the natural coarse aggregates can be replaced with recycled coarse aggregates (RCAs) by up to 30% without sacrificing the overall performance of concrete [4-6]. However, there is still a significant portion of concrete fines that cannot be recycled and reused.

On the other hand, recycled concrete powder (RCP) has also been recycled to replace fines aggregate in mortar or concrete. Existing studies [1,2,7,8] have demonstrated that the inferior properties of RCP mortar are mainly attributed to the higher porosity and water

^{*}Corresponding author: poonam_6170006@nitkkr.ac.in

^a orcid.org/0009-0002-2153-512X; ^b orcid.org/0009-0002-2153-512X

DOI: <http://dx.doi.org/10.17515/resm2023.797ma0612>

Res. Eng. Struct. Mat. Vol. 9 Iss. 4 (2023) 1521-1541

absorption of RCP particles. Additionally, the incorporation of RCP affects the particle packing status of aggregates in mortar under dry packing conditions, which is mainly caused by the change of particle size distribution after adding different contents and sizes of RCP particles. The packing status of granular materials can be characterized by the particle packing density, which is defined as the absolute volume to bulk volume ratio of the packed material. Red mud, Fly ash, silica fume (SF), metakaolin, blast furnace slag, and rice husk ash are the industrial by-products that different researchers [9-12] have used as cement replacement to improve concrete strength; due to, latent hydraulic properties, the compressive strength increased at an early stage, and flexural strength at later age showed better results.

In conclusion, recycling C&D waste, including RCP, as a sustainable construction material is a growing field. However, the use of RCP as replacement of sand in mortar or concrete has been found to have negative effects on the properties and microstructures of cementitious materials [13-15]. Further research is necessary to investigate ways to enhance the reactivity of RCP and improve its performance as fine aggregate in concrete is required.

Blast furnace slag is generated as a by-product during the iron-making process. Around 300 kg of molten slag is discharged for every 1000 kg of pig iron produced. The molten slag is cooled using various methods to produce Granulated Blast Furnace Slag (GBFS), which has high glass content and potential hydration activity when rapidly cooled by water quenching [16,17]. In recent years, GBFS has been extensively used in the cement and concrete industry, as well as in geopolymers, glass ceramics, agricultural fertilizers, and wastewater treatment [18-21]. Several investigations have been conducted on the problem of C&D wastes application to concrete, as reflected in the literature published studies [22-25]. Tam et al. [26] discovered that the presence of recycled fine/coarse aggregate with adhered old mortar can have detrimental effects on the early-age performance, strength development, and long-term performance of concrete. Boudali et al. [27] put forth a proposal suggesting that waste concrete/brick fines, which possess notable quantities of calcium, silicon, and aluminum, can be acquired through the grinding of discarded concrete/brick. These fine particles can subsequently be utilized as an alternative binder or supplementary cementitious material, effectively substituting cement in various construction applications.

According to Li et al. [28], the recycling of construction waste into recycled aggregate results in the generation of 10-20% waste concrete/brick fines. The inclusion of recycled concrete in concrete production can substantially influence the properties of cement. The utilization of recycled concrete as aggregates can have an impact on various aspects of concrete, including workability, compressive strength, splitting tensile strength, flexural strength, water absorption, and air permeability [29,30]. When recycled concrete is utilized as a substitute for natural aggregate, it has the potential to affect the workability of the concrete. This is primarily due to the presence of attached mortar, which can lead to an increased water demand in the mixture. However, through appropriate processing techniques, the amount of attached mortar can be minimized, resulting in an improvement in the mechanical properties of the concrete [31,32].

Every year, the global steel and iron industries generate an excess of 400 million tons of slag, a number that is continuously rising as the demand for steel and iron in diverse sectors continues to grow.

To obtain slag aggregates, smelter slag is crushed or fire-liquid slag melt is treated to produce molten slag aggregates [33]. These aggregates are experiencing growing utilization as binding constituents and fillers in various forms of concrete employed for construction objectives [34]. Synthetic aggregates, like blast furnace slag, are produced by

altering the physical and chemical properties of an original material. They can be intentionally created for use as synthetic aggregate or obtained as a by-product from manufacturing and combustion processes. Non-metallic blast furnace slag is formed through a chemical reaction between lime in the flux and the aluminates and silicates found in the ore and coke ash during the smelting process. Different types of blast furnace slag products, including aggregate for road asphalt production, are created using various cooling methods. Bottom ash, a waste product from coal-burning power plants, has the potential to replace specific aggregates used in asphalt pavement. In light of growing environmental concerns, bottom ash is being considered for multiple transportation applications such as embankment fill, roadway fill, sub-base, and base courses.

The utilization of slag as a substitute for cement in concrete production can enhance the properties of cement. Slag possesses pozzolanic properties, meaning it can react with calcium hydroxide to create additional cementitious compounds. Incorporating recycled concrete and slag into concrete production offers a practical and environmentally conscious approach for the construction sector. In recent years, there has been an increasing emphasis on using blast furnace slag (BFS) as a sustainable alternative to natural aggregate in concrete manufacturing. However, despite its popularity, there is a significant disparity between the demand for GBFS (Ground Granulated Blast Furnace Slag) in the cement industry and its supply. Some countries rely on imported GBFS to meet their demands.

The preparation of composite GBFS using solid wastes as raw materials is a viable method, but very few studies have been conducted on this topic, as indicated by a literature search. While some studies [35-37] have demonstrated that the mixture of solid wastes and GBFS offers superior properties, a summary of the specific synergistic effects is lacking. To successfully prepare composite GBFS, the synergistic effect between solid wastes and GBFS needs to be explored. The synergistic effect mainly lies in four aspects, including the alkali, sulfate, and particle filling effects, which significantly promote the hydration of GBFS. In systems consisting of three or more components, multiple synergistic effects are present, resulting in better properties. Therefore, the objective of this review is to provide new insights into using solid wastes to prepare composite blast furnace slag that can replace some or even all of the GBFS. The application of composite GBFS in cement, mortar, and concrete not only effectively addresses the high demand for high-quality GBFS but also improves the utilization rate of other solid wastes and promotes cross-industry cooperation among enterprises.

Abhishek et al. [38] the application of granulated blast furnace slag (GBS) was investigated in both normal vibrated and self-compacting concrete. The study focused on partially replacing the natural coarse aggregate with recycled concrete aggregate (RCA). The results revealed that the GBS-based self-compacting concrete specimens, where the natural coarse aggregate was replaced with recycled coarse aggregate, experienced a reduction in compressive strength exceeding 20%.

The study explored the application of air-cooled blast furnace slag aggregate (ACBFSA) as a substitute for limestone coarse aggregate in ultra-high-performance fiber-reinforced concrete. It was found that ACBFSA can be utilized partially or entirely as a replacement while maintaining crucial properties. However, as the replacement ratios increased, the workability of the concrete decreased [39].

The impact of incorporating Blast Furnace Slag Fine Aggregate (BFSFA) on the resistance to freezing and thawing in a chloride environment was examined. The study found that by utilizing BFSFA with a finer grain size and increasing the proportion of BFSFA in the mixture compared to natural sand, the freezing and thawing resistance was enhanced [40], the researchers investigated the incorporation of washing aggregate sludge (WAS) as an

additional component in alkali-activated paste and mortars. The findings of the study revealed several effects of WAS on the material properties. Firstly, the presence of WAS resulted in an extension of the setting time. Additionally, it led to an increase in water absorption and voids content within the paste and mortars. Consequently, the compressive strength was reduced. However, an interesting observation was made during wetting-drying cycles, where WAS demonstrated an efficient enhancement in residual compressive strength. In a study conducted by Alzaza et al. [41], an environmentally friendly construction material was developed by utilizing blast furnace slag (BFS) as a binder and fine aggregate in mortar. To enhance its suitability for construction in cold weather conditions, a calcium silicate hydrate seed accelerator was added. The study revealed that the inclusion of BFS aggregate in concrete led to enhanced resistance against frost and sulfuric acid attack. These findings underscore the potential of BFS as a feasible substitute for natural aggregate in concrete manufacturing. Nevertheless, it is crucial to take into account different factors, including the concrete type and the extent of substitution, as they can impact the properties and potential applications of concrete utilizing BFS.

The aim of this research was to examine the properties and behavior of M25 grade normal concrete by incorporating a blend of recycled concrete sand and blast furnace slag aggregate. The study aimed to identify the most suitable proportions of replacing both fine and coarse aggregates with waste materials in order to decrease the cost and carbon dioxide (CO₂) emissions related to concrete manufacturing.

1.1 Response Surface Methodology

An efficient method is required for optimizing the properties of concrete containing waste materials, as it is an important step towards sustainable construction that reduces the depletion of natural resources and promotes cleaner neighborhoods. Response surface methodology (RSM) has been used to generate models for independent variable optimization, which is a statistical, theoretical, and numerical technique [42,43]. The effect of independent parameters on one or numerous responses is considered by RSM, which employs partial factorial designs like central composite design (CCD) to generate response surfaces for second-order mathematical models. Mathematical models generated using RSM have been observed to be efficient in predicting the properties of concrete containing waste materials [44,45].

Several researchers [46-50] have applied the use of RSM in the optimization of concrete containing waste materials, and it has been found to be an effective method for identifying mixtures that yield the best compromises among the responses. Regression analysis, experimental designs, and recommended statistical tests are generated by RSM employing design of experiment (DOE) software packages such as Minitab and Design Expert [51]. Partial factorial designs used by RSM reduce the number of experiments required compared to full factorial designs, making it a practical method for researchers with limited time and resources [25,45].

A solution to cost-effective conventional concrete production is provided by this study through the use of waste materials such as BFS (0-50%) as coarse aggregate and RCS (0-100%) as sand replacement in concrete. The performance of concrete containing these waste materials is predicted by mathematical models generated in this study, which optimize their contents, cost, compressive strength. The response surface models generated in this research are distinct from those developed by other researchers and validate the practicability of the generated models. Overall, an efficient method that can bring about a revolution in sustainable construction is the use of RSM in optimizing the properties of concrete containing waste materials, as depicted in Figure 1.

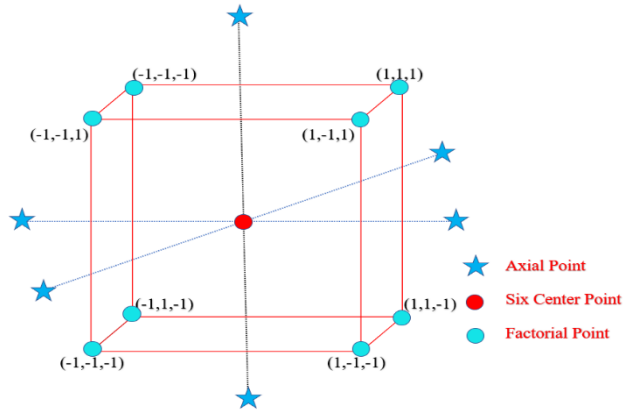


Fig. 1 Central Composite Design (CCD) augmented with hybrid points

In this study, RSM based on CCD was employed to evaluate the impact of two parameters, namely blast furnace slag aggregate (BFSA) and Recycled Concrete sand (RCS) replacement percentages, on four response variables: cost, compressive strength. The range of BFSA was set from 0 to 50%, while RCS was set from 0 to 100%. The response variables were measured for each experiment and used to generate mathematical models that would predict the response variables based on the input parameters.

The generated models were then analyzed using ANOVA (Analysis of Variance) to verify their accuracy [42,45,52]. ANOVA is a statistical method used to determine whether there are significant differences between the means of multiple groups. In this case, ANOVA was used to determine whether the models accurately predicted the response variables based on the input parameters. The results of the study showed that BFSA and RCS replacement percentages had a significant impact on all four response variables. The mathematical models generated from the experimental data showed good agreement with the measured values, as confirmed by the ANOVA analysis. The models were then used to determine the optimal conditions for each response variable. RSM based on CCD proved to be an effective method for evaluating the impact of BFSA and RCS replacement percentages on cost, compressive strength, split tensile strength, and flexural strength [53,54].

The mathematical model generated by the RSM based on CCD for evaluating the impact of BFSA and RCS replacement percentages on the response variables can be expressed in equation 1:

$$Y = \beta_0 + \beta_1X_1 + \beta_2X_2 + \beta_3X_1^2 + \beta_4X_2^2 + \beta_5X_1X_2 + \varepsilon \tag{1}$$

where, Y is the predicted response variable (e.g., cost, compressive strength) β_0 is the intercept term $\beta_1, \beta_2, \beta_3, \beta_4, \beta_5$ are the regression coefficients for linear, quadratic, and interaction terms X_1 and X_2 are the coded values of the independent variables (e.g., BFSA replacement and RCS replacement) ε represents the random error term [55].

By analyzing the CCD experimental design and fitting the data to the model, the regression coefficients ($\beta_0, \beta_1, \beta_2, \beta_3, \beta_4, \beta_5$) can be estimated, allowing us to predict the response variables for different combinations of BFSA and RCS replacement levels [45].

The mathematical models generated from the experimental data showed good agreement with the measured values and were used to determine the optimal conditions for each response variable. ANOVA analysis was used to verify the accuracy of the models and confirm their validity. This study highlights the potential benefits of using BFSA and RCS

in construction materials, as well as the importance of statistical optimization techniques in achieving optimal results.

1.2. Optimization Process

The optimization process for the RSM based on CCD involves finding the optimal values of BFSa and RCS replacement percentages that maximize or minimize the response variable of interest, subject to any constraints that may exist. The initial step in the optimization process involves generating a mathematical model using experimental data and conducting an analysis of variance (ANOVA) to validate the model's reliability. Once the model is confirmed, the subsequent step is to determine the optimal values of the input variables (BFSa and RCS) that will yield the desired response variable (e.g., cost or compressive strength). This can be accomplished through various optimization techniques, including response surface methodology, gradient-based optimization, or genetic algorithms.

One commonly employed technique is to employ a response surface plot, which visually depicts the relationship between the input variables and the response variable. This plot aids in identifying the optimal values. Another approach entails utilizing constrained optimization techniques, where the optimal input variable values are ascertained while considering any applicable constraints. For example, material costs may need to be minimized while fulfilling specific strength requirements, or the strength requirements may need to be met while minimizing the environmental impact of the materials.

Subsequently, the optimal input variable values can be validated by conducting experiments using the predicted values and comparing the results against the model's predictions. If the experimental outcomes align with the model predictions, the optimal values can be considered the final solution. If there is a disparity, it may be necessary to refine the model or conduct additional experiments to obtain a more accurate model.

2. Materials and Methods

2.1. Materials

The researchers in this study utilized 43-grade OPC cement that conforms IS: 8112 [32] standard and BFSa was collected from Ambala city, India. To determine various properties, standard laboratory tests were conducted, including normal consistency (28%), soundness (2.5mm), fineness (2%), initial setting time (126 minutes), final setting time (243 minutes), specific gravity (3.19), and compressive strength (recorded as 26.6 MPa at 3 days, 34.23 MPa at 7 days, and 45.60 MPa at 28 days).

Natural fine aggregate and coarse aggregates were obtained from local markets by the researchers and grading analysis was performed based on Indian standard (IS: 383) [56]. Blast furnace slag aggregate was purchased by the researchers online from the India Mart site and was converted into a coarse aggregate shape using a jaw crusher. The Specifications for the mechanical behavior of ordinary coarse aggregate and BFSa are presented in Table 1.

Feasible use of RCS was achieved by manually crushing 5- to 7-month-old and uncontaminated 150 mm³ size concrete cubes with a hammer. For the present study, the crushed products were sieved and recombined to obtain the required grading. Table 1 shows the fineness modulus of the recycled aggregate. Concrete casting was carried out using tap water that was purified in this experiment to eliminate harmful substances in compliance with IS: 10500-2012 [57].

Table 1. Specifications for the mechanical behavior of ordinary coarse aggregate and BFSA

Property	Normal coarse aggregate	Blast furnace slag aggregate
Fineness modulus	7.38	7.25
Flakiness index (%)	15.39	7.35
Bulk density(compact) (kg/m ³)	1565	1417
Los Angeles abrasion resistance (%)	22.56	35.45
Impact value (%)	9.60	17.30
Bulk density(loose) (kg/m ³)	1485	1310
Crushing value (%)	20.10	12.53
Elongation index (%)	10.31	18.65
Specific gravity	2.67	2.58

2.2. Experimental Design

The mix design for M25 grade concrete was conducted following the guidelines of the Indian Standard, as presented in Table 1. To generate precise optimum values and analyze a significant amount of experimental data, a Central Composite Design (CCD) within the framework of Response Surface Methodology (RSM) was employed. A total of 13 experimental runs were carried out based on the CCD, which is renowned for its adaptability in determining the number of center points and axial distances.

In this study, a set of 25 concrete mixes was generated using RSM, with varying proportions of cement, sand, RCS (Recycled Concrete Aggregate), BFSA (Blast Furnace Slag Aggregate), and coarse aggregate. The specific quantities used for each mix are outlined in Table 2, adhering to the M25 concrete mix design as specified in IS 456:2000 [58]. The independent parameters considered in the experimentation were BFSA and RCS. The response parameters evaluated in the study were denoted as R1 and R2, representing cost and compressive strength, respectively.

2.3. Experimental Procedure

Experimental designs for all 25 runs with control mix were obtained using Design Expert 13 as shown in Table 2.



Fig. 2 Experimental setup

Table 2. Mix design with replacement in (kg/m³)

Level	Mix Name.	RCS	BFSA	Cement	FA	RCS	CA	BFSA	Water	Extra water
0	0R0B	0	0	342	711.4	0	1174	0	153.9	0
1	10R5B	10	5	342	640.26	71.14	1115.3	58.7	153.9	1
2	25R5B	25	5	342	533.55	177.85	1115.3	58.7	153.9	1
3	50R5B	50	5	342	355.7	355.7	1115.3	58.7	153.9	1
4	75R5B	75	5	342	177.85	533.55	1115.3	58.7	153.9	1
5	100R5B	100	5	342	0	711.4	1115.3	58.7	153.9	1
1	10R15B	10	15	342	640.26	71.14	997.9	176.1	153.9	2
2	25R15B	25	15	342	533.55	177.85	997.9	176.1	153.9	2
3	50R15B	50	15	342	355.7	355.7	997.9	176.1	153.9	2
4	75R15B	75	15	342	177.85	533.55	997.9	176.1	153.9	2
5	100R15B	100	15	342	0	711.4	997.9	176.1	153.9	2
1	10R25B	10	25	342	640.26	71.14	880.5	293.5	153.9	5
2	25R25B	25	25	342	533.55	177.85	880.5	293.5	153.9	5
3	50R25B	50	25	342	355.7	355.7	880.5	293.5	153.9	5
4	75R25B	75	25	342	177.85	533.55	880.5	293.5	153.9	5
5	100R25B	100	25	342	0	711.4	880.5	293.5	153.9	5
1	10R35B	10	35	342	640.26	71.14	763.1	410.9	153.9	6
2	25R35B	25	35	342	533.55	177.85	763.1	410.9	153.9	6
3	50R35B	50	35	342	355.7	355.7	763.1	410.9	153.9	6
4	75R35B	75	35	342	177.85	533.55	763.1	410.9	153.9	6
5	100R35B	100	35	342	0	711.4	763.1	410.9	153.9	6
1	10R50B	10	50	342	640.26	71.14	587	587	153.9	8
2	25R50B	25	50	342	533.55	177.85	587	587	153.9	8
3	50R50B	50	50	342	355.7	355.7	587	587	153.9	8
4	75R50B	75	50	342	177.85	533.55	587	587	153.9	8
5	100R50B	100	50	342	0	711.4	587	587	153.9	8

The cement, FA, and CA were slowly mixed for two minutes, and water was added to achieve the desired workable consistency. After achieving a suitable mix, the freshly mixed concrete was then transferred into lubricated molds and compacted uniformly using a table vibrator and tested according to Indian standard codes of practice for its compressive strength after 28 of submersion in water at 27°C.

The cube specimens were tested at the age of 28 days in Compression Testing Machine (CTM) after drying at room temperature according to IS: 516-1959 [59], Without impacts and jerks and uniformly, the load was applied, and the failure load taken by each specimen was recorded and the results have been shown in Figure 2. Each independent run involved manual mixing of the concrete containing waste materials with water, ensuring homogeneity in the mix.

3. Results and Discussion

In this section, the results and discussion of the experimental data and the mathematical models for the cost, compressive strength, the analysis includes the validation of the model’s using ANOVA and the interpretation of the model coefficients and response surface plots. The optimization process for determining the optimal BFSAs and RCS replacement percentages that maximize or minimize the response input variables is also discussed in table 3. Insights into the impact of BFSAs and RCS replacement parameters on the properties of construction materials are provided by the results and discussion. The effectiveness of RSM based on CCD for modeling and optimizing construction materials is demonstrated.

Table 3. Input parameter

Factor	Name	Minimum	Maximum	Coded Low	Coded High	Mean	Std. Dev.
A	RCS	0	100.00	-1	+1	52.00	33.32
B	BFSAs	0	50.00	-1	+1	26.00	15.94

3.1. Models Fitting

The regression coefficients are estimated by minimizing the sum of squared errors between the predicted values and the actual values of the response variable. The statistical significance of the model as a whole and the individual terms within the model is assessed using the F-test and t-test, respectively.

Table 4. Fit Statistics table for cost and compressive strength

Coefficient	Cost	Compressive Strength
Std. Dev.	0.0007	0.8463
Mean	4122.99	35.07
C.V. %	0	2.41
R ²	1	0.8667
Adjusted R ²	1	0.8334
Predicted R ²	1	0.7853
Adeq Precision	NA	18.5066

After fitting and validating the model, it becomes a powerful tool for predicting the response variable at any given combination of BFSAs and RCS replacement percentages within the experimental range. Additionally, the model can be utilized to identify the optimal combination of BFSAs and RCS replacement percentages that either maximize or minimize the response variable, while considering any constraints that may be present. This allows for an informed decision-making process, ensuring that the desired outcome is achieved while adhering to specific requirements or limitations.

The Coefficient of Variation (CV%) is a measure of the relative variability of the data. In this table 4, the CV% values for Compressive Strength range from 1.40% to 3.30%. This suggests that the variability in the data for these properties is fairly consistent. However, the CV% for Cost is very low, at 0%. This suggests that the data for Cost is very consistent and has very little variability. All of the Predicted R^2 and Adjusted R^2 values for the various strength properties of the material were in agreement, with the difference between them being less than 0.2 for all cases. The Predicted R^2 of 1.0000 and Adjusted R^2 of 1.0000 for the property of Cost were found to be in agreement, while the Predicted R^2 of 0.7853 and Adjusted R^2 of 0.8334 for compressive strength were also in agreement. Moreover, the Adeq Precision ratio was greater than 4 for all models, indicating that there was adequate signal to noise ratio. This indicates that the models could be effectively used to navigate the design space.

3.2. Coded Factors

Predictions for the response are made based on the given levels of each factor using equations that incorporate coded factors. Typically, the high levels of the factors are represented as +1, while the low levels are represented as -1. The coded equation is advantageous in identifying the relative influence of the parameters by comparing the coefficients associated with each factor. In this study, Tables 5 and 6 present the regression equations in terms of coded factors, which were derived using Response Surface Methodology (RSM) for all responses.

Table 5. Final equation in terms of coded factors

Factor	Cost	Compressive Strength
	3925.7	35.7
A	-172.51	-0.6742
B	-739.62	-10.57
AB		0.2776
A ²		-0.0811
B ²		-13.81

It is worth noting that for a linear interaction between variables and responses, at least one regression coefficient in the model should not be zero. Table 5 displays the final equation obtained from the analysis, expressing the relationship between the coded factors (represented as A and B) and the dependent variable (represented as C). This equation demonstrates how the values of the coded factors are combined to determine the value of the dependent variable.

Table 6. Actual equation in terms of coded factors

Factor	Cost	Compressive Strength
	4837.83	33.3386
RCS	-6.9006	-0.0316
BFSA	-14.792	0.33521
RCS * BFSA		0.00022
RCS ²		-0.0001
BFSA ²		-0.0055

The coefficients assigned to the coded factors in this equation determine the magnitude of their impact on the dependent variable. On the other hand, Table 6 presents the actual equation in terms of coded factors for the specific study, providing further details and insights into the relationship between the factors and the dependent variable.

3.3. Cost Optimization

3.3.1. Linear Model Fit Summary and ANOVA Evaluation for Cost

The identification of the response surface model was assisted by the model statistics summary and ANOVA for the linear model for cost, as presented in Table 10 and Table 11, respectively. A perfect correlation in the cost response was observed in the tables. The strength of correlation of the response surface model was determined using model statistics summary, including R2 and adjusted R2.

Table 7. ANOVA for cost

Source	Sum of Squares	df	Mean Square	F-value	p-value	
Model	3.135E+06	2	1.568E+06	2.822E+12	< 0.0001	significant
A-RCS	1.381E+06	1	1.381E+06	2.486E+12	< 0.0001	
B-BFSA	1.464E+06	1	1.464E+06	2.636E+12	< 0.0001	
Residual	0.0000	23	5.555E-07			
Cor Total	3.135E+06	25				

The ANOVA analysis presented in Table 7 demonstrates a highly significant relationship between the factors and the cost variable. The overall model exhibits statistical significance ($p < 0.0001$), indicating its effectiveness in explaining the variation observed in the cost. Both factors, "A-RCS" and "B-BFSA," contribute significantly to the cost variable ($p < 0.0001$). The large F-values and very low p-values indicate that these factors have a substantial impact on the cost. Moreover, the absence of residual variation (error term) suggests a perfect fit of the model to the data.

The ANOVA results provided in Table 7 offer valuable insights into the relationship between the factors and the cost variable. This serves as a solid foundation for further analysis and decision-making. It should be noted that the factors have been coded, and the analysis employs Type III - Partial sum of squares. The significant model F-value, coupled with a very low probability (0.01%) of such a large F-value occurring due to noise, further confirms the model's capability to explain the variation in the dependent variable accurately. Furthermore, the p-values for the model terms indicate their significance. In this case, the coded factors A and B are both significant model terms, with p-values less than 0.0500.

This suggests that these factors have a substantial impact on the dependent variable and should be considered in the analysis. On the other hand, values greater than 0.1000 indicate that the model terms are not significant. If many model terms are insignificant, reducing the model may improve its accuracy. Overall, the analysis provides valuable insights into the significance of the model terms, guiding further analysis and decision-making.

3.3.2. Model Graphs and Diagnostic Findings

Diagnostic findings in Design Expert typically include statistical tests and numerical measures that assess the quality of the model. For example, the adequacy of the model fit to the data can be determined through the lack of fit test, and any patterns or outliers in the data that may indicate problems with the model can be identified using the residual plot.

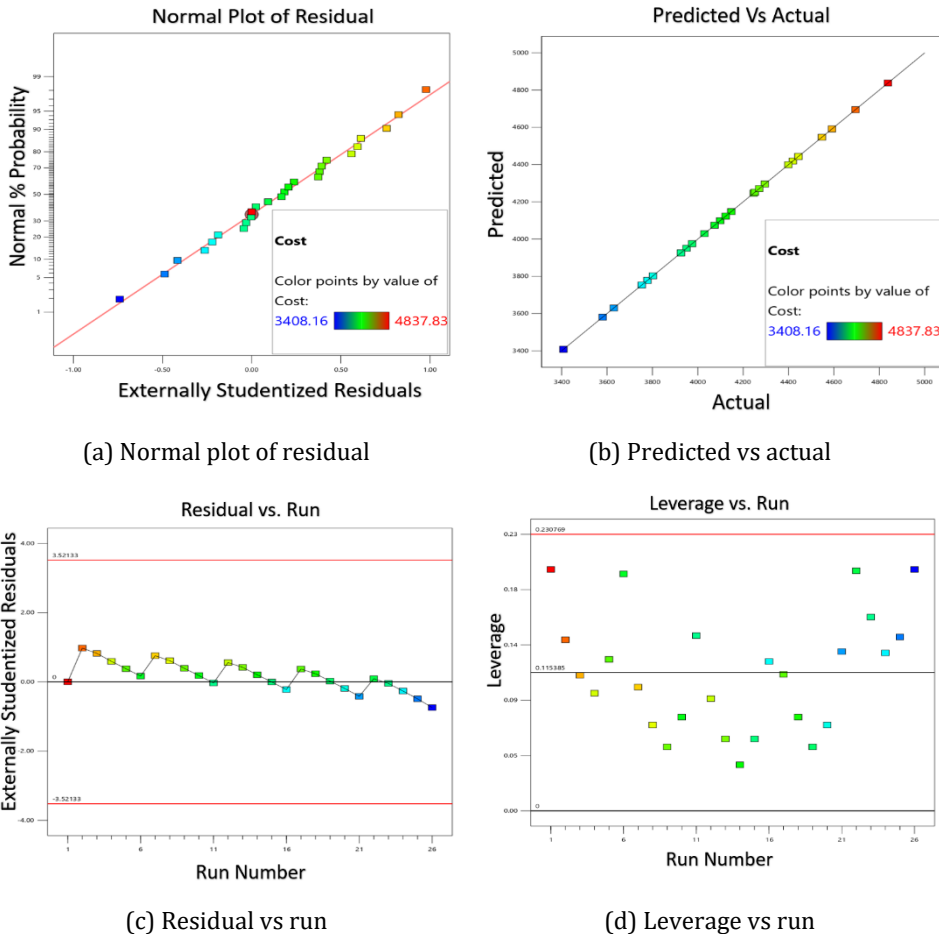


Fig. 3 Model graphs and diagnostic findings of cost

Measures of the model's predictive accuracy, such as the root mean square error (RMSE) or the coefficient of determination (R-squared), can also be included in the diagnostic findings. By examining these model graphs and diagnostic findings, the performance of the statistical model can be assessed, and any necessary adjustments can be made to improve its accuracy and predictive power.

Figure 3a shows that a normal plot of residuals can diagnose problems with a statistical model. Departures from normality in the plot may indicate a mis specified model or missing predictors. Figure 3b depicts a predicted vs actual plot, which compares predicted values to actual values. Deviations from the diagonal line indicate discrepancies between predicted and actual values and can indicate misspecification or missing predictors. Figure 3c shows how a predicted vs actual plot can identify systematic bias or non-linear

relationships. Figure 3d depicts how a leverage vs run plot can identify influential observations and evaluate model robustness over time or other variables. If influential observations are found, the model may need re-evaluation or exclusion of those observations. A residual vs run plot can identify trends or cycles in residuals, indicating the need to update the model with additional predictors. These plots can improve a model's accuracy and predictive power. The summary of ANOVA cost is presented in Appendix 1.

3.3.3. Model Graphs of Cost

Model graphs typically include graphical representations of the model, such as contour plots or surface plots, which allow the user to visualize the relationship between the input variables and the response variable.

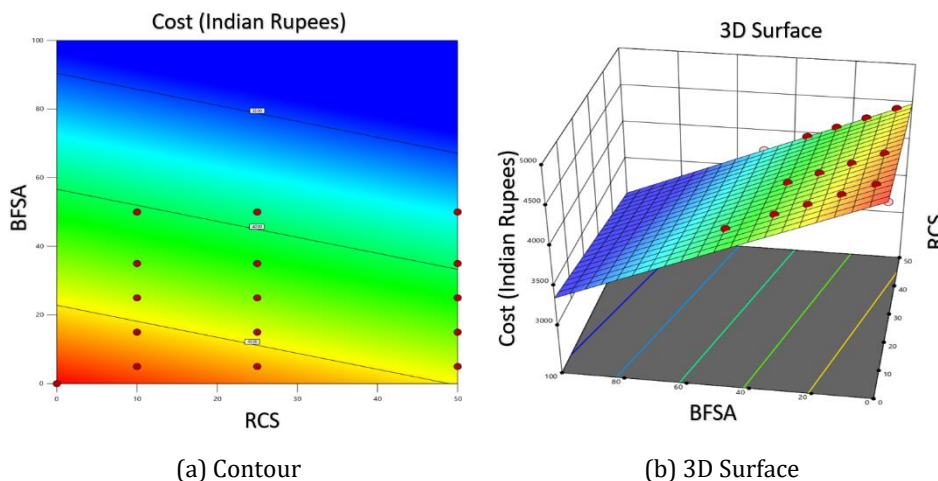


Fig. 4. Model graphs of cost

These plots can help identify any nonlinear relationships between the variables and can also help identify any interactions between the variables that may be important for the model. The relationship between cost, BFS, and RCS can be effectively visualized through contour plots (Figure 4(a)) and 3D plots (Figure 4(b)). Contour plots illustrate lines of constant cost on a grid of BFS and RCS values, providing a clear representation of how cost varies with different combinations of BFS and RCS percentages. On the other hand, 3D plots depict the cost on the z-axis, with BFS and RCS values represented on the x and y axes, respectively. This visualization allows for a comprehensive understanding of how changes in BFS and RCS impact the cost of the concrete mixture. By examining these plots, it becomes possible to identify regions in the input space where cost is highly sensitive to variations in BFS or RCS percentages. This information can be used to determine optimal values that minimize cost while still meeting the desired specifications and requirements.

Furthermore, a previous study discovered that when incorporating waste materials as replacements, it was necessary to decrease the mass of BFS and RCS while increasing the proportion of coarse aggregate. This adjustment in the composition of the concrete mixture resulted in cost optimization. The findings of this study can serve as a valuable reference for decision-making regarding the optimal utilization of waste materials, ensuring a balance between cost-effectiveness and meeting necessary construction criteria.

3.3.4. Linear Model Fit Summary and ANOVA Evaluation for Compressive Strength

The identification of the response surface model was assisted by the model statistics summary and ANOVA for the linear model for Compressive Strength. Table 8 presents the results of the ANOVA analysis for compressive strength. The table shows the sources of variation, sum of squares, degrees of freedom, mean square, F-value, and p-value for each factor. The model was found to be significant with a p-value of less than 0.0001. The factors A-RCS and AB were not significant as their p-values were greater than 0.05. However, the factors B-BFSA and B² were found to be highly significant with p-values of less than 0.0001. The factors A² was also not significant with a p-value of 0.5110. The residual sum of squares was 14.32, and the total sum of squares was 107.44. A perfect correlation in the Compressive Strength response was observed in tables 8.

Table 8. ANOVA for compressive strength

Source	Sum of Squares	df	Mean Square	F-value	p-value	
Model	93.12	5	18.62	26.00	< 0.0001	significant
A-RCS	2.22	1	2.22	3.10	0.0935	
B-BFSA	23.29	1	23.29	32.52	< 0.0001	
AB	0.3740	1	0.3740	0.5222	0.4783	
A ²	0.3208	1	0.3208	0.4480	0.5110	
B ²	40.77	1	40.77	56.93	< 0.0001	
Residual	14.32	20	0.7162			
Cor Total	107.44	25				

3.3.5. Model Graphs and Diagnostic Findings

The influence of BFSA and RCS on the compressive strength of concrete is elucidated in Figure 5. In Design Expert, diagnostic findings encompass statistical tests and numerical measures that assess the quality of the model. These findings aid in evaluating the model's fit to the data, with the lack of fit test determining if the model adequately represents the observed data. The residual plot helps identify any patterns or outliers that may indicate potential issues with the model. Additional diagnostic measures such as RMSE (Root Mean Square Error) or R-squared provide insights into the model's predictive accuracy. Analyzing these model graphs and diagnostic findings empowers users to assess the performance of their statistical model and make necessary adjustments to enhance its accuracy and predictive power.

In Figure 5(a), problems with a statistical model can be diagnosed using a normal plot of residuals. Departures from normality in the plot may indicate a mis specified model or missing predictors. Figure 5(b) compares predicted values to actual values using a predicted vs actual plot. Deviations from the diagonal line indicate discrepancies between predicted and actual values and can indicate misspecification or missing predictors. Figure 5(c) demonstrates how a predicted vs actual plot can identify systematic bias or non-linear relationships. Figure 5(d) shows how a leverage vs run plot can identify influential observations and evaluate model robustness over time or other variables. If influential observations are found, the model may need re-evaluation or exclusion of those observations. A residual vs run plot can identify trends or cycles in residuals, indicating the need to update the model with additional predictors. These plots can improve a model's accuracy and predictive power. The summary of ANOVA compressive strength is presented in Appendix 2.

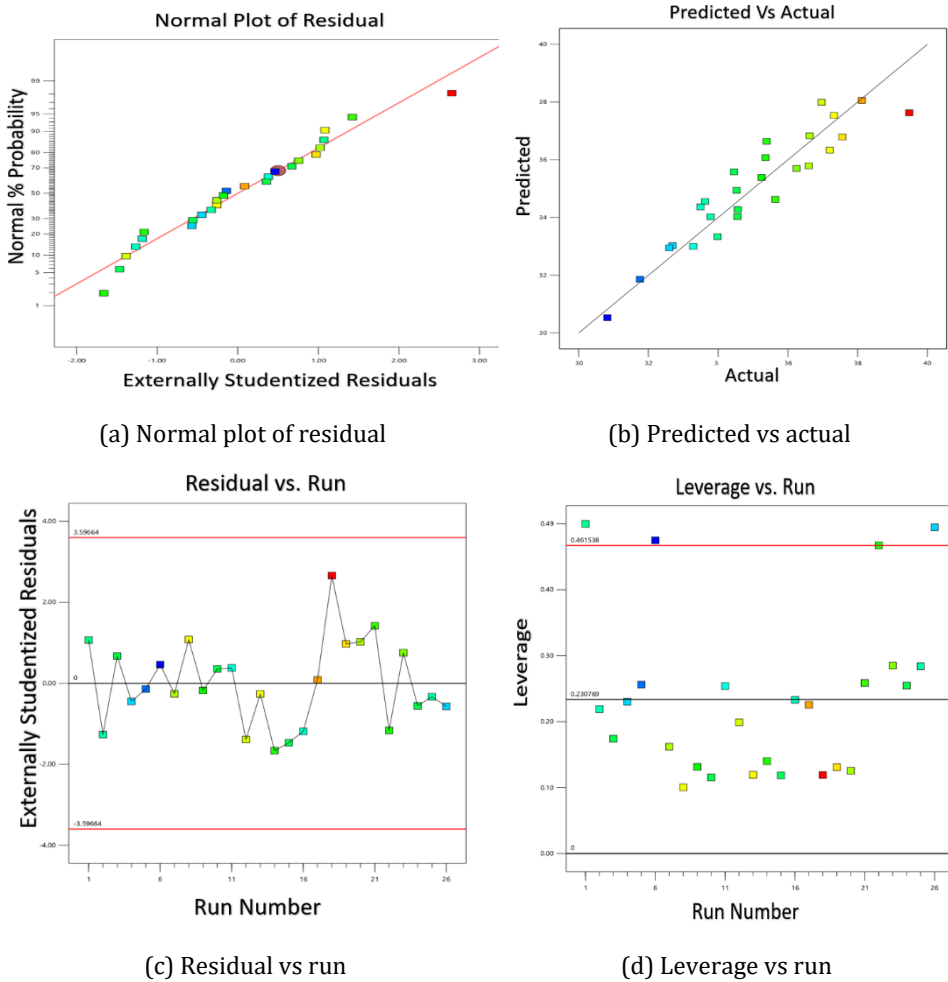


Fig. 5 Model graphs and diagnostic findings of compressive strength

3.3.6. Model Graphs of Compressive Strength

Model graphs typically include graphical representations, such as contour plots or surface plots, which allow the relationship between the input variables and the response variable to be visualized by the user. These plots enable the identification of nonlinear relationships between the variables, as well as the identification of any interactions between the variables that may be important for the model.

Figures 6(a) and 6(b) present the visualization of the relationship between Compressive strength, BFSa, and RCS using contour and 3D plots. The contour plot displays lines of constant Compressive strength on a grid of BFSa and RCS, while the 3D plot shows compressive strength on the z-axis and BFSa and RCS on the x and y axes, respectively. By examining the contours or the surface of the plot, it is possible to identify regions of the input space where Compressive Strength is particularly sensitive to changes in BFSa or RCS. This information can be used to identify optimal values of BFSa and RCS that minimize Compressive Strength or to explore the sensitivity of the model to changes in the input variables.

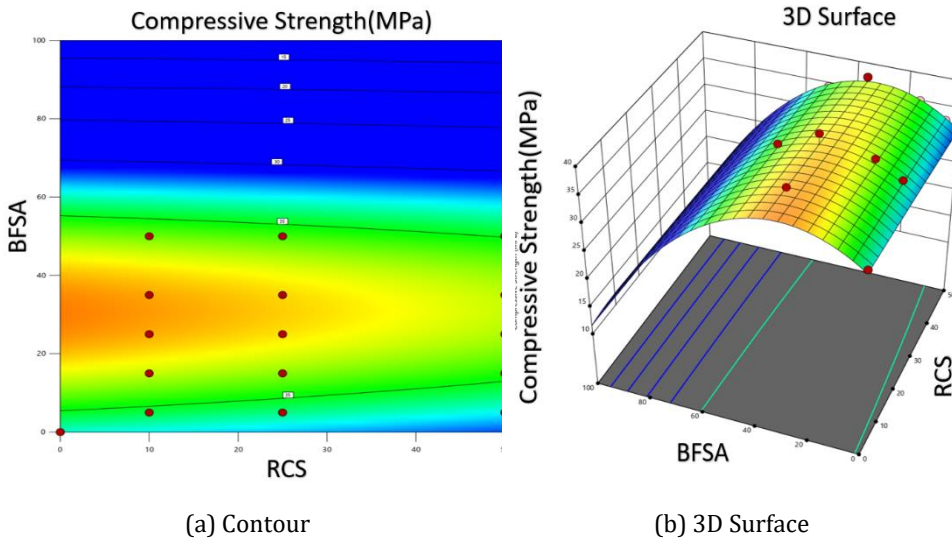


Fig. 6 Model graphs of compressive strength

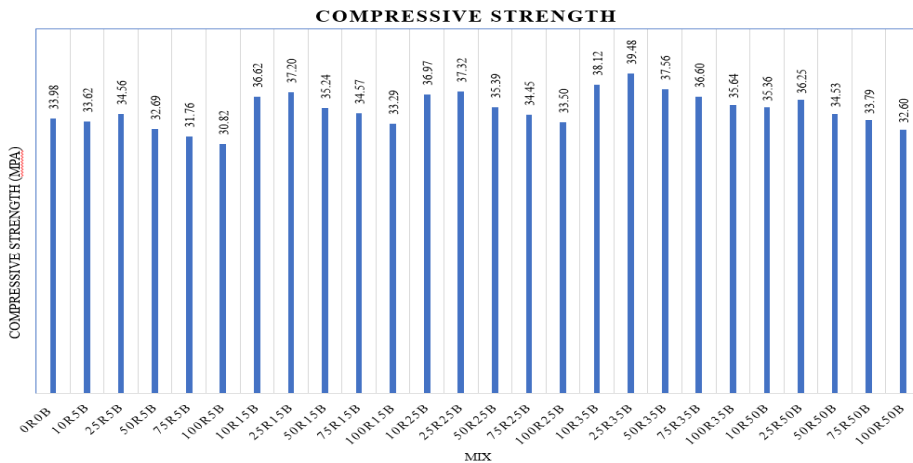


Fig. 7 Compressive strength values for the concrete mixtures

The provided Figure 7 offers a comparison of the percentage replacements of fine aggregate by RCS (Recycled Concrete Sand) and coarse aggregate by BFSa (Blast Furnace Slag Aggregate), along with the corresponding compressive strength values for the concrete mixtures. Analysing the data, several observations can be made regarding the impact of aggregate replacements on compressive strength. when both the fine aggregate replacement by RCS and the coarse aggregate replacement by BFSa remain at a constant percentage of 5%, the compressive strength values vary from 30.82 for the Mix with 100% fine aggregate replacement (100R5B) to 34.56 for the Mix with 25% fine aggregate replacement (25R5B). This indicates that higher replacement percentages of fine aggregate lead to a slight decrease in compressive strength. When, focusing on the replacement of coarse aggregate by BFSa, it can be observed that as the replacement percentage increases from 5% to 25%, the compressive strength generally increases. For instance, the compressive strength rises from 33.62 for the Mix with 5% fine aggregate

replacement and 10% coarse aggregate replacement (10R5B) to 37.32 for the Mix with 5% fine aggregate replacement and 25% coarse aggregate replacement (25R25B).

Lastly, considering a higher replacement percentage of coarse aggregate by BFS (35% and 50%), a decreasing trend in the compressive strength is evident. As the coarse aggregate replacement increases, the compressive strength gradually decreases. For example, the compressive strength drops from 38.12 MPa for the Mix with 35% fine aggregate replacement and 10% coarse aggregate replacement (10R35B) to 32.60 MPa for the Mix with 50% fine aggregate replacement and 100% coarse aggregate replacement (100R50B).

In summary, the data emphasizes the influence of both fine and coarse aggregate replacements on the compressive strength of concrete mixtures. It highlights the importance of carefully selecting and optimizing aggregate replacements to achieve the desired compressive strength in concrete production.

4. Conclusion

In summary, the prescribed limits have a crucial role in determining the permissible ranges for various parameters involved in the evaluation of construction materials. These limits provide essential guidelines for assessing parameters like Compressive Strength and Cost. By establishing lower and upper boundaries for each parameter, these limits ensure that values fall within acceptable ranges and comply with specific criteria or desired standards.

For the Compressive Strength parameter, the acceptable range is defined with a lower limit of 30.822 MPa and an upper limit of 39.48 MPa. These limits serve as benchmarks for evaluating the compressive strength of construction materials, guaranteeing that it meets necessary requirements and ensures quality and durability.

Similarly, the Cost parameter specifies a permissible range of cost values, with a lower limit of 3408.16 INR and an upper limit of 4837.83 INR. Adhering to these limits ensures that the cost remains within reasonable bounds, guiding the evaluation of the financial aspects of the construction project.

When replacing coarse aggregate with BFS at higher percentages (35% and 50%), a consistent trend emerges, showing a gradual decline in compressive strength. Increasing the percentage of coarse aggregate replacement correlates with a decrease in compressive strength in the concrete mixtures. This trend is evident in cases like the mix with 35% fine aggregate replacement and 10% coarse aggregate replacement (10R35B), where the compressive strength decreases from 38.12 to 32.60 in the mix with 50% fine aggregate replacement and 100% coarse aggregate replacement (100R50B). This observation emphasizes the significant influence of replacing coarse aggregate with BFS on the mechanical properties of concrete, particularly compressive strength.

Therefore, careful consideration of the percentage of coarse aggregate replacement is crucial to achieve desired properties and performance in concrete applications. By evaluating and determining the appropriate percentage, the mechanical properties of the concrete mix, specifically compressive strength, can be optimized. This ensures that the construction materials meet necessary standards, providing the required structural integrity and overall quality.

References

- [1] Pradhan B, Chand S, Chand S, Rout PR, Naik SK. Emerging groundwater contaminants: A comprehensive review on their health hazards and remediation technologies.

- Groundwater Sustainable Development 2023;20:100868.
<https://doi.org/10.1016/j.gsd.2022.100868>
- [2] Miller BG. 4 - the effect of coal usage on human health and the environment. Clean Coal Engineering Technology. 2011:85-132. <https://doi.org/10.1016/B978-1-85617-710-8.00004-2>
- [3] Pulkit K. Effect of stone slurry & recycled aggregate on properties of concrete waste management. Lap LAMBERT Academic Publication. 2018 Dec.
- [4] Kim J. Construction and demolition waste management in Korea: recycled aggregate and its application. Clean Technologies and Environmental Policy. 2021;23(8):2223-2234. <https://doi.org/10.1007/s10098-021-02177-x>
- [5] Marrero M, Puerto M, Rivero C, Freire-Guerrero A, Solís-Guzmán J. Assessing the economic impact and ecological footprint of construction and demolition waste during the urbanization of rural land. Resources, Conservation and Recycling. 2016;117. <https://doi.org/10.1016/j.resconrec.2016.10.020>
- [6] McAllister J. Factors influencing solid-waste management in the developing world. PhD Thesis, Master of Science, Utah State University, Logan, Utah, 5-2015
- [7] Russo N, Lollini F. Effect of carbonated recycled coarse aggregates on the mechanical and durability properties of concrete. Journal of Building Engineering. 2022;51:104290. <https://doi.org/10.1016/j.jobbe.2022.104290>
- [8] Makul N, Fediuk R, Amran M, et al. Zeyad AM, Murali G, Vatin N, Klyuev S. Use of recycled concrete aggregates in production of green cement-based concrete composites: A Review. Crystals. 2021;11(3). <https://doi.org/10.3390/cryst11030232>
- [9] Zhou C, Chen Z. Mechanical properties of recycled concrete made with different types of coarse aggregate. Construction and Building Materials. 2017;134:497-506. <https://doi.org/10.1016/j.conbuildmat.2016.12.163>
- [10] Grazia D, Trottier C, Dantas SRA, Nagarajun Y, Ziapour R, et al. Influence of recycled concrete aggregate type on rheological behaviour of mixtures proportioned using the equivalent volume method. Recent Progress in Materials. 2022;4(3):1-1. <https://doi.org/10.21926/rpm.2203017>
- [11] Duan Z, Hou S, Xiao J, Li B. Study on the essential properties of recycled powders from construction and demolition waste. Journal of Cleaner Production 2020;253:119865. <https://doi.org/10.1016/j.jclepro.2019.119865>
- [12] Zhu F, Yang C, Miao M. Experimental study on the properties of polyvinyl alcohol fiber reinforced cementitious composites with super early strength. Materials Letters 2023;330:133264. <https://doi.org/10.1016/j.matlet.2022.133264>
- [13] Goergens J, Belli R, Schulbert C, Goetz-Neunhoeffler F. Influence of different CA2/CA-ratios on hydration degree, AH3 content and flexural strength investigated for a binder formulation of calcium aluminate cement with calcite. Cement and Concrete Research. 2023;165:107090. <https://doi.org/10.1016/j.cemconres.2023.107090>
- [14] Yücel HE, Öz HÖ, Güneş M, Kaya Y. Rheological properties, strength characteristics and flexural performances of engineered cementitious composites incorporating synthetic wollastonite microfibers with two different high aspect ratios. Construction and Building Materials 2021;306:124921. <https://doi.org/10.1016/j.conbuildmat.2021.124921>
- [15] Solanke SS, Pawade PY, Ali Khan H. An experimental study on tensile as well as flexural strength of concrete by using sugarcane baggase ash & steel fiber. Materials Today: Proceedings. 2022;60:627-637. <https://doi.org/10.1016/j.matpr.2022.02.129>
- [16] Agarwal A, Ramana G V, Datta M, Soni NK, Satyakam R. Pullout behaviour of polymeric strips embedded in mixed recycled aggregate (MRA) from construction & demolition (C&D) waste - Effect of type of fill and compaction. Geotextiles and Geomembranes. Published online 2023. <https://doi.org/10.1016/j.geotexmem.2023.01.004>

- [17] Abera Y (Shanko) A. Performance of concrete materials containing recycled aggregate from construction and demolition waste. Results in Materials. 2022;14:100278. <https://doi.org/10.1016/j.rinma.2022.100278>
- [18] Bergonzoni M, Melloni R, Botti L. Analysis of sustainable concrete obtained from the by-products of an industrial process and recycled aggregates from construction and demolition waste. Procedia Computer Science. 2023;217:41-51. <https://doi.org/10.1016/j.procs.2022.12.200>
- [19] Bolan S, Padhye LP, Kumar M, et al. Review on distribution, fate, and management of potentially toxic elements in incinerated medical wastes. Environmental Pollution.2023;321:121080. <https://doi.org/10.1016/j.envpol.2023.121080>
- [20] Koelmel J, Prasad V, Velvizhi G, Butti S, Mohan S. Chapter 15 - metalliferous waste in India and knowledge explosion in metal recovery techniques and processes for the prevention of pollution. Environmental Materials and Waste (Resource Recovery and Pollution Prevention). 2016;339-390 <https://doi.org/10.1016/B978-0-12-803837-6.00015-9>
- [21] Ministry of transport. Transport Yearbook 2018. Ministry of Transport. Czech Republic.2018:52.
- [22] Zeng Q, Liu X, Zhang Z, Wei C, Xu C. Synergistic utilization of blast furnace slag with other industrial solid wastes in cement and concrete industry: Synergistic mechanisms, applications, and challenges. Green Energy and Resources 2023;1(2):100012. <https://doi.org/10.1016/j.gerr.2023.100012>
- [23] Horii K, Tsutsumi N, Kitano Y, Kato T. Processing and reusing technologies for steelmaking slag. Nippon Steel Technical Report. 2013;805(104):123-129.
- [24] Yu P, Wang S, Li Y, Xu G. A Review of Granulation Process for Blast Furnace Slag. MATEC Web of Conferences.2016;68:6007. <https://doi.org/10.1051/mateconf/20166806007>
- [25] Assaad JJ, Mikhael C, Hanna R. Recycling of waste expanded polystyrene concrete in lightweight sandwich panels and structural applications. Cleaner Materials.2022;4:100095. <https://doi.org/10.1016/j.clema.2022.100095>
- [26] Liu H, Li Q, Wang P. Assessment of the engineering properties and economic advantage of recycled aggregate concrete developed from waste clay bricks and coconut shells. Journal of Building Engineering 2023;68:106071. <https://doi.org/10.1016/j.jobe.2023.106071>
- [27] Chen W, Jin R. 7 - Recycled concrete for non-structural applications. Recycled Concrete. Technologies and Performance (Woodhead Publishing Series in Civil and Structural Engineering). 2023:233-263. <https://doi.org/10.1016/B978-0-323-85210-4.00006-0>
- [28] Ul Islam MM, Li J, Roychand R, Saberian M, Chen F. A comprehensive review on the application of renewable waste tire rubbers and fibers in sustainable concrete. Journal of Cleaner Production. 2022;374:133998 <https://doi.org/10.1016/j.jclepro.2022.133998>
- [29] Tam VWY, Butera A, Le KN, Li W. Utilising CO2 technologies for recycled aggregate concrete: A critical review. Construction and Building Materials. 2020;250. <https://doi.org/10.1016/j.conbuildmat.2020.118903>
- [30] Boudali S, Abdulsalam B, Rafiean AH, Poncet S, Soliman A, Elsafty A. Influence of fine recycled concrete powder on the compressive strength of self-compacting concrete (SCC) using artificial neural network. Sustainability (Switzerland). 2021;13(6). <https://doi.org/10.3390/su13063111>
- [31] Li S, Gao J, Li Q, Zhao X. Investigation of using recycled powder from the preparation of recycled aggregate as a supplementary cementitious material. Construction and Building Materials.2021;267. <https://doi.org/10.1016/j.conbuildmat.2020.120976>

- [32] Prakash Singh O, Singh Kulhar K, Choudhary S. Strength studies on concrete containing of recycled coarse aggregate and granite cutting waste as partial replacement of fine aggregate. *Materials Today: Proceedings*. 2023;76:481-487. <https://doi.org/10.1016/j.matpr.2022.11.153>
- [33] Cominato V, Benavente Canteras F, Andréia Gachet L, Cristina Cecche Lintz R. The effect of granulometry of natural and recycled coarse aggregate on permeable concrete properties. *Materials Today: Proceedings*. 2022;65:1711-1718. <https://doi.org/10.1016/j.matpr.2022.04.717>
- [34] Spaeth V, Djerbi Tegguer A. Improvement of recycled concrete aggregate properties by polymer treatments. *International Journal of Sustainable Built Environment*. 2013;2(2):143-152. <https://doi.org/10.1016/j.ijbsbe.2014.03.003>
- [35] Sarhan Alyaseen A, Shah S, Solanki R, Daxini B, Alwani YK. Reuse of Improved Recycled Concrete Aggregates (RCA) for Sustainable and Environmental-Friendly Rigid Pavements. *IOP Conf. Series: Materials Science and Engineering*. 2021. 1145; 012024 <https://doi.org/10.1088/1757-899X/1145/1/012024>
- [36] Yuksel I. Blast-furnace slag. *Waste and Supplementary Cementitious Materials in Concrete. Characterisation, Properties and Applications*. Woodhead Publishing Series in Civil and Structural Engineering. 2018, :361-415 <https://doi.org/10.1016/B978-0-08-102156-9.00012-2>
- [37] Naresh B, Saravanan M. Experimental study of replacement of cement with ground granulated blast furnace slag. *Materials Today: Proceedings*. 2022;62:3493-3496. <https://doi.org/10.1016/j.matpr.2022.04.302>
- [38] Salih MA. New geo-polymerization process for high strength alkali-activated binder with palm oil fuel ash and ground granulated blast furnace slag. *Proceedings of the National Academy of Sciences*. 2015.3:1-15
- [39] Owaid HM, Hamid RB, Taha MR. A review of sustainable supplementary cementitious materials as an alternative to all-portland cement mortar and concrete. *Australian Journal of Basic and Applied Sciences*. 2012;6(9):287-303.
- [40] Krishna Murthy H, Brijbushan S, Maneeth PD. An experimental research on partial replacement of river sand by silica sand and partial replacement of cement by GGBS in rigid pavements. *International Journal of Recent Technology and Engineering* 2019;8(3):4971-4977. <https://doi.org/10.35940/ijrte.C5631.098319>
- [41] Abhishek P, Ramachandra P, Niranjana PS. Use of recycled concrete aggregate and granulated blast furnace slag in self-compacting concrete. *Material Today Proceeding*. 2020;42:479-486. <https://doi.org/10.1016/j.matpr.2020.10.239>
- [42] Cao Q, Nawaz U, Jiang X, Zhanga L, Ansari WS. Effect of air-cooled blast furnace slag aggregate on mechanical properties of ultra-high-performance concrete. *Case Studies in Construction Materials*. Jan 2022;16:e01027. <https://doi.org/10.1016/j.cscm.2022.e01027>
- [43] Bilici S, Kabay N, Miyan N, Omur T, Ozkan H. Effect of washing aggregate sludge waste on the properties of alkali-activated blast furnace slag. *Journal of Building Engineering*. 2023;63(PA):105527. <https://doi.org/10.1016/j.jobbe.2022.105527>
- [44] Pulkit K, Saini B, Chalak H, Illikainen M. M Effect of various interface bond tests and their failure behavior on substrate and overlay concrete- A Review. *Research on Engineering Structures and Materials*.2022:1-22. <http://dx.doi.org/10.17515/resm2022.575me1103>.
- [45] Ahmed T, Ray S, Haque M, Tasnim Nahin T, Ferdous Mita A. Optimization of properties of concrete prepared with waste glass aggregate and condensed milk can fiber using response surface methodology. *Cleaner Engineering and Technology*. Aug 2022;8:100478. <https://doi.org/10.1016/j.clet.2022.100478>
- [46] Seetharaman R, Seeman M, Kanagarajan D, Sivaraj P, Saravanan I. A statistical evaluation of the corrosion behaviour of friction stir welded AA2024 aluminium alloy. *Materials Today: Proceedings* 2020;22:673-680 <https://doi.org/10.1016/j.matpr.2019.09.066>

- [47] Chong BW, Othman R, Jaya RP, Li X, Hasan M, Abdullah M. Meta-analysis of studies on eggshell concrete using mixed regression and response surface methodology. *Journal of King Saud University - Engineering Sciences*. April 2021. <https://doi.org/10.1016/j.jksues.2021.03.011>
- [48] Ali M, Kumar A, Yvaz A, Salah B. Central composite design application in the optimization of the effect of pumice stone on lightweight concrete properties using RSM. *Case Study in Construction Material*. Jan 2023;18 <https://doi.org/10.1016/j.cscm.2023.e01958>
- [49] Kursuncu B, Gencel O, Bayraktar OY, Shi J, Nematzadeh M, Kaplan G. Optimization of foam concrete characteristics using response surface methodology and artificial neural networks. *Construction and Building Material*. Jan 2022;337:127575. <https://doi.org/10.1016/j.conbuildmat.2022.127575>
- [50] Manohar DR, Anbazhagan P. Shear strength characteristics of geosynthetic reinforced rubber-sand mixtures. *Geotextiles and Geomembranes*. 2021;49(4):910-920. <https://doi.org/10.1016/j.geotexmem.2020.12.015>
- [51] Shi J, Zhao L, Han C, Han H. The effects of silanized rubber and nano-SiO₂ on microstructure and frost resistance characteristics of concrete using response surface methodology (RSM). *Construction and Building Material*. Feb 2022;344:128226. <https://doi.org/10.1016/j.conbuildmat.2022.128226>
- [52] Poorarbabi A, Ghasemi M, Azhdary Moghaddam M. Concrete compressive strength prediction using neural networks based on non-destructive tests and a self-calibrated response surface methodology. *Journal of Non-destructive Evaluation*. 2020;39(4):1-11. <https://doi.org/10.1007/s10921-020-00718-w>
- [53] Hamada HM, Al-Attar AA, Tayeh B, Bin Mat Yahaya F, Abu Aisheh YI. Optimising concrete containing palm oil clinker and palm oil fuel ash using response surface method. *Ain Shams Engineering Journal*. 2023;102150 <https://doi.org/10.1016/j.asej.2023.102150>
- [54] Guo L, Guo Y, Zhong L. Research on the back analysis and failure mechanism of recycled concrete aggregate meso-parameters based on Box-Behnken Design response surface model. *Journal of Building Engineering*. Jan 2022;51:104317 <https://doi.org/10.1016/j.jobbe.2022.104317>
- [55] Saboo N, Nirmal Prasad A, Sukhija M, Chaudhary M, Chandrappa AK. Effect of the use of recycled asphalt pavement (RAP) aggregates on the performance of pervious paver blocks (PPB). *Construction and Building Materials*. 2020;262:120581. <https://doi.org/10.1016/j.conbuildmat.2020.120581>
- [56] Sinkhonde D. Generating response surface models for optimisation of CO₂ emission and properties of concrete modified with waste materials. *Cleaner Materials*. June 2022;6:100146. <https://doi.org/10.1016/j.clema.2022.100146>
- [57] Bheel N, Ali MOA, Shafiq N, et al. Utilization of millet husk ash as a supplementary cementitious material in eco-friendly concrete: RSM modelling and optimization. *Structures*. Feb 2023;49:826-841 <https://doi.org/10.1016/j.istruc.2023.02.015>
- [58] Amiri H, Azadi S, Karimaei M, Sadeghi H, Farshad Dabbaghi. Multi-objective optimization of coal waste recycling in concrete using response surface methodology. *Journal of Building Engineering*. Oct 2022;45:103472. <https://doi.org/10.1016/j.jobbe.2021.103472>
- [59] IS 383-1970. Specification for coarse and fine aggregates from natural sources for concrete. Bureau of Indian Standard. Published online 1970.
- [60] IS 10500. Indian Standard Drinking Water Specification (Second Revision). Bureau of Indian Standards. May 2012;IS 10500:1-11
- [61] IS: 456. Plain and Reinforced Concrete. Bureau of Indian Standards. Published online 2000.
- [62] IS:516. Hardened Concrete -Methods of Test. Bureau of Indian Standards.1959

Blank Page



Research Article

Analytical study on seismic strengthening of existing reinforced concrete buildings by implementation of energy absorbers

Mehmet Cemal Genes^a, Pari Yaseen^b

Civil Engineering Department, Eastern Mediterranean University, Famagusta, Cyprus via Mersin 10, Turkey

Article Info

Article history:

Received 29 Jan 2023

Accepted 03 Jun 2023

Keywords:

*Nonlinear time history;
analysis;
Hysteretic;
Absorbers;
Energy;
Dissipating devices;
Seismic strengthening;
Seismic risk*

Abstract

Retrofitting of reinforced concrete (RC) buildings is generally made by jacketing of columns and/or implementing shear walls. However, this method increases the building mass and requires foundation strengthening which is not easy to apply. Recently, strengthening by absorbing the applied energy to the building during an earthquake by energy absorbers has become popular. In this study, an analytical study of an energy dissipation system for seismic strengthening of existing RC buildings is presented. The study was conducted to investigate the implementation of an energy absorber to the bracing system of an existing building located in Antakya/Türkiye. One of the considerable challenges is to establish the optimal design to retrofit buildings against the effect of predicted earthquakes with minimal disturbance to the structure and residents. The proposed system aims to provide high protection of the structure during severe earthquakes by controlling the maximum inter-story drifts. The used system performs as a bilinear hysteretic device. To investigate the performance of the proposed design and configuration, nonlinear time-history analyses were carried out on an 8-Story building. The main parameters which are Displacement, Inter Story Drift Ratio, Acceleration, and Input Energy are studied according to the different configurations. The obtained results showed that the seismic responses of the strengthened structures were significantly higher than the original structures. The maximum displacement and drift reduction values of the strengthened building were between 70% to 80%, the maximum acceleration reduction values were between 4% to 20%, and the input energy levels decreased between about 64% and 70%.

© 2023 MIM Research Group. All rights reserved.

1. Introduction

When a severe earthquake occurs near residential areas, it can cause damage to reinforced concrete (RC) structures and result in life and property losses. Furthermore, structural and nonstructural damages are essentially due to lateral displacements and acceleration [1]. Therefore, structures are required to be strong enough to resist seismic effects.

There is a seismic activity zone in Türkiye that ranks second on the planet which is known as the Alpine-Himalayan Belt. The highest level of seismic activity in Türkiye was known to be up to 0.8g. But after the 6th February 2023 Kahramanmaraş earthquakes depending on soil conditions the seismic activity could be more than 1.3g.

The major plate in which Türkiye is known as the Anatolian plate as shown in Figure 1. It is bounded by two great strike-slip fault zones, the 550 km-long East Anatolian Fault and the 1500 km-long North Anatolian Fault [2]. The fault as a result of the collision, the Anatolian Plate was formed of the complicated zone between the Eurasian Plate and both the Arabian and African Plates [3].

^{*}Corresponding author: cemal.genes@emu.edu.tr

^aorcid.org/0000-0002-9052-7361; ^borcid.org/0000-0001-7292-7049

DOI: <http://dx.doi.org/10.17515/resm2023.677ea0129>

Res. Eng. Struct. Mat. Vol. 9 Iss. 4 (2023) 1543-1571

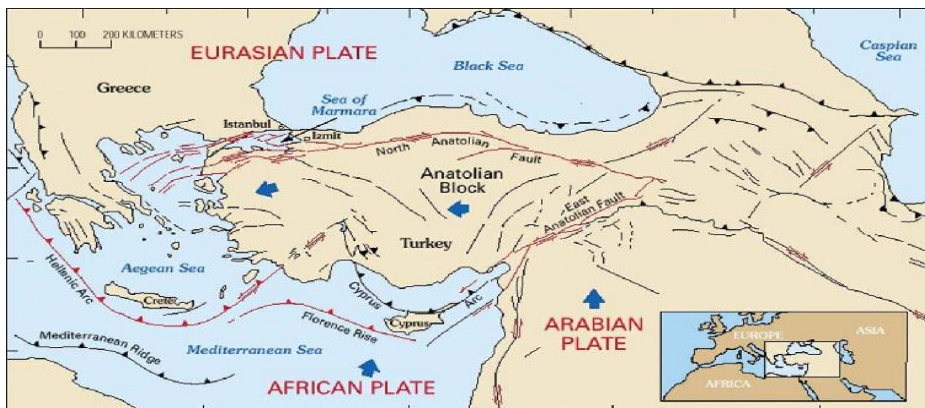


Fig. 1 Tectonic map of Türkiye [2]

Due to these fault ruptures, more than 800 earthquakes with various magnitudes have occurred in the last 120 years in Türkiye as given in Table 1 according to the obtained data from the Disaster and Emergency Management Presidency Earthquake Department (AFAD). However, after the recent earthquakes in Kahramanmaraş ($M_w:7.7$ and $M_w:7.6$) and Hatay ($M_w:6.4$), Table 1 should be modified with a new number of events which are shown in brackets.

Table 1. Past earthquakes in Türkiye between 1900 and 2020 [4]

Earthquake Magnitude	$6 > M \geq 5$	$7 > M \geq 6$	$M > 7$
No. of Events	702	81 (82)	17 (19)
Return Interval (years)	0.2	1.5	7

Moreover, due to the continued convergence between Eurasian Plate and both the Arabian and African Plates, there is generated energy that is stored and can be released at any moment in the form of considerable earthquakes magnitude. Therefore, at least one major earthquake of magnitude ≥ 7.0 can occur in the future [5, 6]. The major earthquake return period in Türkiye is around seven years according to AFAD which is a very short-term return interval for a major earthquake. In general, an earthquake magnitude between 7.0 and 7.9 is considered a considerable earthquake that can cause severe damage or collapse of buildings, injuries, as well as pose a risk to lives [7].

The existing buildings have much more crucial seismic resistance problems in comparison to the buildings that have been designed during recent 25 years according to seismic precautions. The buildings have been designed according to older codes, which primarily focus on resisting gravity loads only. The buildings which have been constructed in high seismic zones, if they are designed to resist earthquakes according to seismic codes, can resist the earthquake loads adequately [1, 8]. Moreover, the past forty years have witnessed a considerable increase in awareness about earthquake engineering that indeed modern structures don't meet the requirements of constantly evolving codes. Therefore, several deficiencies can be found in existing structures as well as inadequate lateral stiffness, irregular structural configuration, and inappropriate member detailing for ductility. However, the issue becomes more sophisticated when other aspects, beyond the reach of codes, are taken into consideration. Generally, it is usual for the owners of existing buildings to have structural modifications without any engineering consideration, resulting in further obstruction of the structures which might already have low seismic resistance. In addition, the construction quality may be poor because of deficient design

and execution. Thus, buildings that have seismic deficiencies may cause injuries and casualties besides economic loss [9]. Most of the existing buildings, which are older than 30 years in Türkiye, have been designed and constructed without or with weak methods of seismic resistance precautions. Therefore, the buildings are most likely to experience severe damage even when mild earthquake events occur. To resist earthquakes and prevent failure of the structures, strengthening both old buildings that have been designed according to old codes and new buildings designed according to recent codes but have insufficient seismic-resistant is critically needed.

A preliminary step in seismic strengthening is determining the essential structural characteristics of existing buildings as well as their earthquake resistance capacity. After that, rehabilitation performance objectives are set, and the seismic hazard level is determined, accordingly. However, it's not simple to work since complicated cooperation needs to be considered between technical, economic, and social factors, specified for each region. The social factor is considered by the decision on the performance level of the building seismic appraisal and retrofitting. According to engineering judgment, the most appropriate measures can be selected to improve the structure's behavior. In general, local evaluations are more suitable when some structure's components have inadequate capacity, while comprehensive measures are appropriate in case of major deformation, including irregularities and pounding. The Federal Emergency Management Agency (FEMA) using Seismic Techniques, Rehabilitation of Existing Structures can be used as guidance for Seismic Assessment and Retrofit [9].

The protection of buildings in seismically active zones is required to meet the following requirements:

- a.** The main system of the structure must have adequate resistance to be able to withstand medium-intensity earthquakes without being damaged, which can impact the structure at least once.
- b.** All the structure's elements should have ductility to decrease seismic input energy without collapse.

Modern structures can achieve these strengths and ductility benefits without anti-seismic devices if certain design and execution principles are adhered to. Conversely, buildings and structures built according to the old codes don't have high ductility, and even conventional strengthening techniques don't enhance ductility as they are primarily focused on resistance in the elastic range. Therefore, to achieve a sufficient response to seismic activity or to reduce the structure's vulnerability, the energy can be dissipated through the implementation of the structural control system.

To achieve seismic design, probabilistic analysis is essential because of the large uncertainties associated with forces and structural responses [10]. Moreover, it is not possible to predict the earthquake's occurrence, its magnitude, the features of the rupture surface, and the structure's dynamic response with absolute certainty. Therefore, to evaluate the impact of these uncertainties on the performance of structures and seismic design, probabilistic and statistical methods are required. The other essential seismic engineering concept is that materials must be designed and prepared to behave inelastically due to severe earthquake loading. The relationship between stress and strain is linear within Hooke's Law, but beyond this point, structural behavior becomes more complicated. Moreover, the Inelastic behavior of structures was largely investigated using analytical and experimental techniques established around the 1960s [11].

The earthquake-resistant design incorporates various types of seismic control systems to decrease the effects of seismic forces on the building's essential structural elements. In

general, structural control systems are classified into four general types based on the user device types: active, semi-active, hybrid, and passive [12].

Currently, seismic control devices are the most reliable and functional methods to reduce a structure's seismic response. Installing seismic control devices in a structure provides artificially increase structural damping, consumes the vibration energy under the earthquake, reduces the vibration response, and achieves the purpose of earthquake resistance of the structure. The effectiveness of these systems is highlighted through a detailed earthquake damage assessment, there can be a considerable reduction of seismic impacts on the main structure to be protected [13, 14]. One of the seismic controllers is energy dissipation devices, they are mechanical systems that are linked to the building frame to allow the structure to withstand earthquake shaking by absorbing a considerable amount of energy input resulting from seismic activity, without deforming and yielding [15]. Different types of energy dissipation systems are classified according to their ability to improve structural system dissipation energy.

The energy-dissipating devices in framed structures are generally inserted in braces of steel between two sequent stories of the structure as shown in Figure 2. The inter-story drifts accommodated by the building when a seismic event occurs stimulate the energy-dissipating devices before the essential members of the structure are involved in their inelastic behavior. Accordingly, the main objective of the current design strategy employed for energy-dissipating devices is to substantially reduce the demands for ductility on structural members made of RC as stated by Dolce et al. [16]. Thus, the system that supports gravity loads and the system that dissipates energy during an earthquake are discrete systems.

According to a study by Reinhorn et al. [17], it has been shown that the implementation of energy dissipation devices greatly improves the overall capacity of old seismic codes or RC frame structures designed to bear gravity loads. The energy-dissipating devices initially depend on the plastic hinges developed for columns that have low energy dispersal capacity and rapidly deteriorate in rigidity and strength. Accordingly, it's observed that structural vibrations have been significantly reduced [18].

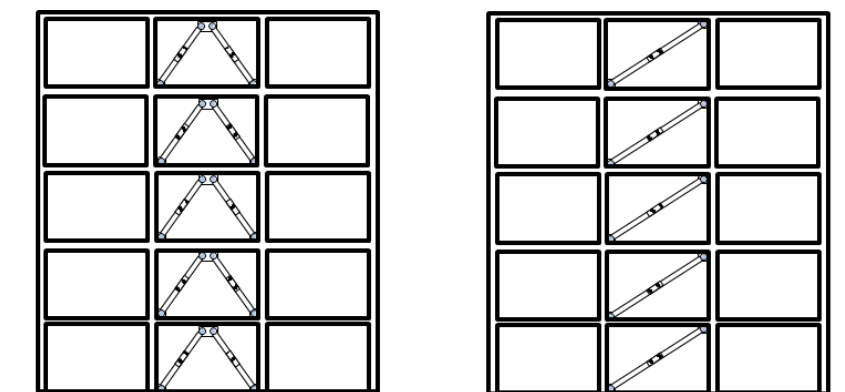


Fig. 2 Energy dissipation system in a structure [18]

There are several energy dissipation devices have been studied by scientist and some of them are applied in newly designed and strengthened buildings. These devices are Metallic Yielding Dampers [19, 20, 21], Energy Dissipative Bracing (EDB) [22, 13, 23, 24], Hysteretic Energy Dissipative Bracing (HEDB) [25, 26], Dissipative Energy Device Based On The Plasticity of Metals [15], Seismic Design of RC Braced Frames with Metallic Fuses [27, 28],

Saw Type Seismic Energy Dissipaters [29, 30], Re-centering Energy Dissipative Braces [31] and Adaptive Hysteretic Dampers [32], Impulsive Semi-Active Mass Dampers [33], Damped Braces [34], bolt connected buckling-restrained braces [35] [36] and visco-elastic dampers [37].

A new metallic-yielding piston (MYP) damper is presented by Ghandil et al. [21] for seismic control of structures. A set of rectangular metallic yielding plates has been considered as an energy-dissipating part of this damper. According to its yielding mechanism and its special configuration, the story high-performance in seismic protection of structures at low-value story drifts is presented.

Thongchom et al. [38, 28] proposed a new metallic damper consisting of five plates: shear plate, flange plate, X-stiffeners, middle plate, and boundary plates. The middle plate and boundary plates do not contribute to resisting the applied load while the shear plate, flange plate, and X-stiffeners share the shear strength.

In order to demonstrate the effectiveness of the dampers Zhu et al. [39] performed an experimental and numerical study of an X-type energy dissipation device under impact loads. They tested 20 specimens by using a drop hammer impact test machine, then established a model with finite elements by using the software LS-DYNA.

Due to its stable hysteretic behavior and the ability to transfer the inter-story shear force or axial load of a brace into the moment of the steel plate many analytical, experimental, and optimization studies were carried out [40].

In the present research, a seismic control technique that is based on Hysteretic Dissipative Energy Bracing Based on the plasticity of metals is used. The brand and name of the energy damper are MAURER and SHARK (Short-stroke Hysteretic Damper jack) [41], respectively. The energy dissipation system is incorporated into an existing reinforced concrete building located in Türkiye. This seismic system is developed to enhance the seismic performance of buildings by limiting inter-story drift while preventing the damage of the structure. Nonlinear Time-History Analysis is conducted to investigate the system performance to decrease the input energy, inter-story drift, top displacement, and top acceleration.

The main aim of this study is to introduce and recommend seismic control techniques for existing RC buildings to withstand minor earthquakes and avoid major damage and collapse during a severe earthquake. A strengthening procedure involves technical interventions in a building's structure that increase its structural stiffness, strength, or/and ductility to increase its seismic resistance. Furthermore, increase awareness about earthquake impact on existing buildings in highly seismic areas of Türkiye and assure knowledge in design and seismic rehabilitation. In addition, the strengthening existing structures assures to keep human life is safe, and that occupants or pedestrians will not be injured by a collapsed structure. Consequently, this study sought to define a design procedure for seismic retrofitting of existing RC-framed buildings using an energy dissipation device based on hysteretic damping.

The proposed study is carried out in two stages which include, collecting data and model analysis. Stage one is carried out to collect data about the selected building structure, seismic area, earthquake records, ambient vibration records [42] and the used energy absorber. The collected data was utilized in the second stage to develop and estimate an accurate calibrated three-dimensional model to perform analysis through ETABS software, in which the buildings configurations were modeled, the contribution of earthquakes and their impact on the structure of the building were elaborately investigated under Nonlinear Time History Analysis (NLTHA) considering and comparing the existing framed

building and the strengthened framed building by the implementation of SHARK energy dissipation device.

2. Research Methodology

A three-stage process is followed in this research methodology. The first stage consists of designing a building with different configurations and materials to calibrate the model and define the current performance of the building. The second stage consists of the implementation of the SHARK energy dissipation device in the braced frame of the designed building in different installation configurations. Finally, the third stage consists of evaluating the performance of the original and the strengthened building and comparing them based on the results obtained from nonlinear time-history analyses by applying 11 pairs of earthquakes to the buildings.

2.1. Introducing the Used Building Bracing System

SHARK is an inventive energy dissipation device that can provide absolute structural safety and reduce the risk of potential damage caused by earthquakes. The design, testing, and quality management of the bracing system comply according to [43]. The SHARK device shown in Figure 3 is made of steel. Its innovative design represents a simple but extremely efficient energy dissipation. When the structure is subjected to loads, the damper operates within its elastic system and acts as a rigid spring to provide structural support. When an earthquake occurs, the SHARK's specially shaped hysteretic lamellas experience plastic deformation to dissipate seismic energy. On the four faces of the hollow section of the dissipative core shown in Figure 3. For severe Ultimate Limit State (ULS) earthquakes, the damper provides stable and reliable performance. The damper can endure up to 3-4 MCE events without any failure due to the special shape of the lamellas. After an unavoidable failure of one lamella, the rest offer proportional resistance and damping functions. The configuration of SHARK is shown in Figure 4. Table 2 provides the size and performance data of SHARK. Furthermore, there is a second form known as SHARK-Adaptive which minimizes the accelerations at each level to ensure better protection of sensitive non-structural components. The SHARK-Adaptive damper features a unique "two-stage" hysteretic loop that allows for the adjustment of effective stiffness and damping based on the intensity of the earthquake [41].

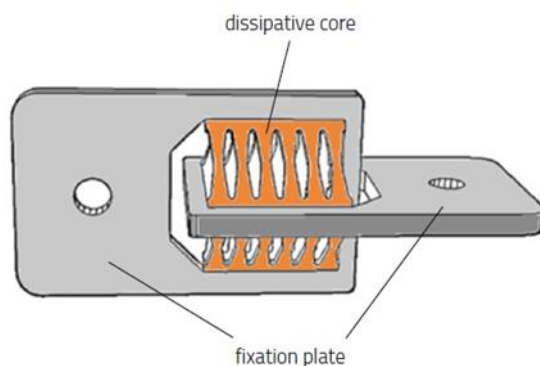


Fig. 3 SHARK damper dissipation core and fixation plate [41]

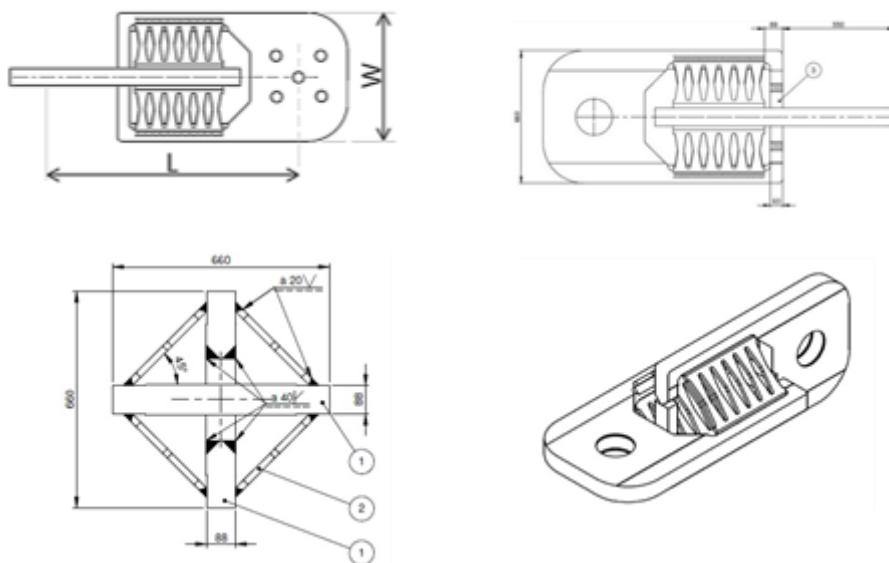


Fig. 4 MAURER SHARK (a) Configuration, (b) side view, (c) front view, (d) 3D view [41]

Table 2. Size and performance data of SHARK [41]

FMCE [kN] MASS	FYk [kN]	K_{el} [kN/mm]	K_{pl} [kN/mm]	dSLS [±mm]	dMCE [±mm]	d_{cd} [±mm]	L [mm]	W [mm]	d_y [mm]	F_{pl} (kN)
350	220	100	4	≤ 1	35	50	700	560	2.2	411.2
700	410	165	6	≤ 1	50	70	800	580	2.484	815.1
1000	615	245	9	≤ 1	50	70	900	600	2.510	1222.4
1400	820	325	12	≤ 1	50	70	1000	620	2.523	1629.7
1700	1020	410	15	≤ 1	50	70	1100	640	2.487	2032.7
2100	1230	490	18	≤ 1	50	70	1200	660	2.510	2444.8
2400	1430	570	21	≤ 1	50	70	1300	680	2.508	2847.3

The utilizing of the SHARK energy dissipation device has the following advantages: There is no need for regular maintenance and the use of only one material provides high reliability, The building structural systems have a similar service life, provide stable response of up to 3-4 MCE earthquake events without any failure [41], high level of safety due to the parallel configuration of hysteretic lamellas, uncomplicated bilinear model appropriate for analysis, having a compact size, a convenient visual inspection and replacement process if needed after a fire or other unforeseen event, exceptional fatigue strength in case of wind, as well as service loads, design following European Standard EN15129 or according to other standards upon request.

A typical installation layout is illustrated by two examples in Figure 5. In general, the connection to the construction can be screwed or welded, as appropriate for the project, it also can be connected directly to the original frame of the building by connections to the middle of the beam and ends of the columns [41]. However, as there is an additional shear force in the beam, particularly because of this diagonal force, the shear force should be transferred to the beam element by applying steel jacketing around the beam to show the

effectiveness of the connections to transfer the loads. For this study, installation layout A is applied to the buildings, and according to the first data provided in Table 3.

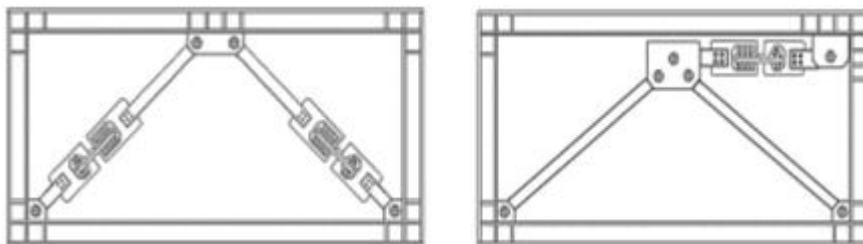


Fig. 5 Installation layout A and B [41]

The performance of the SHARK has been successfully tested as shown in Figure 6 and, showed a perfect hysteretic loop according to the European Standard EN 15129 at EUCENTRE Laboratory in Pavia (Italy) and Bundeswehr University of Munich. As part of nonlinear finite element analysis, SHARK has been designed and optimized [41, 32].

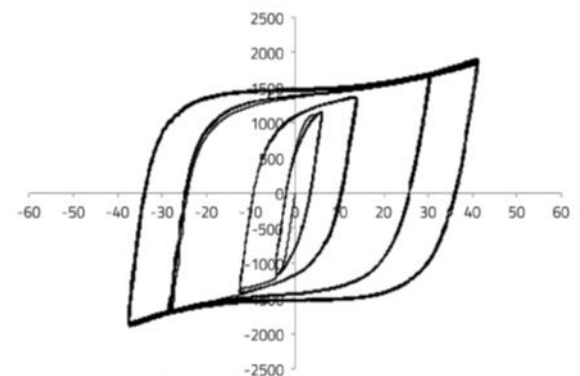


Fig. 6 Experimental bilinear hysteretic loop of Shark [41]

2.2 Modelling of Studied Building

The studied building was built in 1973 in Antakya/Hatay (Figure 7). In the frame of a project which is supported by TUBITAK with a project code TUBITAK (107M445), the building was studied by providing ambient vibration to calibrate its model and performing pushover analysis to define its performance level. During that project study, the project team found that this building has characteristic features that can represent approximately 71 of the reinforced concrete buildings in Antakya [42]. There are two apartments on each floor of the building. Therefore, it is not symmetrical concerning the X-axis.

The cross-section dimensions of the column elements used while modeling are given in Table 3. The building is an 8-story RC frame, with a height of 2.9 meters for each story. The total height of the structure above the basement is 23.2 meters. There is no earthquake-resisting shear walls or reinforced concrete core around the elevator in the building. There are 17 columns, and the sections and reinforcement ratios of these columns vary between stories. C16 concrete and St-I (S220) reinforcing steel properties were used in the modeling of the building. According to the region where the building is located (the

coordinate is Latitude: 36.210103° Longitude 36.159782°), the ground condition is very tight layers of sand, gravel, and hard clay or weathered, very cracked weak rocks [42].



Fig. 7 The studied apartment building

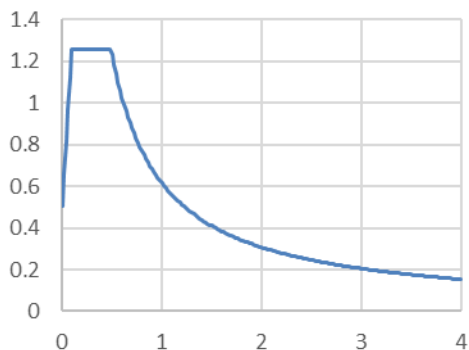


Fig. 8 The target response spectrum of soil class C

ETABS software has been used to create a three-dimensional model design and perform analysis. ETABS follows [44] to employ the performance-based design of the lateral load-bearing systems. According to TBEC-2018 [45], the soil class "C" is considered to define the spectrum curve of the site. Therefore, Figure 8 presents the target response spectrum curve corresponding to this region.

The ACI-318-11 [44] and ASCE 41-17 [46] design codes have been utilized in the design of the reinforced concrete building, and all details have been observed and considered according to these standards. Hinges were assigned according to [46]. Table 3 and Figure 9 illustrate the frame section property definitions of the members used in the modelling and analysis.

The dead and live loads based on the residential use of the building are used as 4.2 kN/m² and 2 kN/m², respectively. The design of the 8-story building is conducted according to the specified plan and sections without considering the infill walls. However, according to the original plan, there are balconies along the X-axis which prevent the possibility of energy absorber implementation. Therefore, the balconies on the edges of the X-axis are removed and the energy absorber is applied on the edges. Further, an analysis was conducted to define the structure's dynamic behavior parameters (vibration periods and mode shapes) and compare them with the real parameters obtained from the study of [42] to calibrate the analytical model of the building, and then to determine and evaluate the behavior of the strengthened structure with SHARK energy dissipator. The obtained vibration periods and frequencies after model calibration are presented in Table 4. The building model and the plan layout are presented in Figure 10.

The load combinations have been considered following [45] regulations to analyze the building.

As is clear from the 3D model and plan of the building (Figure 10), the building does not have a strong earthquake resistance system (i.e. Shear walls or RC core). The performance analysis results of the building are given in Table 5 and Figure 11. According to the results, the 4th floor of the building has a performance level of failure, as severely damaged columns are formed and all the shear forces on this floor are carried by the damaged columns.

According to the Turkish Building Earthquake Code [45] and Türkiye Earthquake Hazard Maps Interactive Web Application (AFAD), The Building Earthquake Ground Motion level have earthquake location with a 10% probability of exceedance in 50 years (recurrence period of 475 years) movement level. Further, Local Soil Class C has very tight layers of sand, gravel, and hard clay or weathered, very cracked weak rocks. The following factors and coefficients have been applied to analyze the building behavior when subjected to earthquakes. The applied factors and coefficients according to TBEC-2018 [45] are given in Table 6.

Table 3. Frame section property definitions

Name	Mat.	Depth/W idth (cm)	Bars	Design Type	Name	Mat.	Depth/W idth (cm)	Bars	Design Type
BEAM 30X70	C16	70/30		Beam	S17-GRNDFL	C16	20/100	6φ16	Col.
BEAM20X60	C16	60/20		Beam	S1-BASEM.	C16	20/70	6φ16	Col.
S10-1	C16	20/60	6φ14	Col.	S1-GRNDFL	C16	20/60	6φ16	Col.
S10-2	C16	20/40	6φ14	Col.	S2-1	C16	20/80	6φ16	Col.
S10-BASEM.	C16	20/70	6φ16	Col.	S2-2	C16	20/70	6φ16	Col.
S10-GRNDFL	C16	20/60	6φ14	Col.	S2-BASEM.	C16	25/100	8φ16	Col.
S1-1	C16	20/50	6φ14	Col.	S2-GRNDFL	C16	20/100	6φ16	Col.
S11-1	C16	20/60	6φ14	Col.	S3-1	C16	20/80	6φ16	Col.
S11-2	C16	20/50	6φ14	Col.	S3-2	C16	20/60	6φ14	Col.
S11-BASEM.	C16	20/80	6φ16	Col.	S3-BASEM.	C16	25/100	8φ16	Col.
S11-GRNDFL	C16	20/70	6φ16	Col.	S3-GRNDFL	C16	20/90	6φ16	Col.
S1-2	C16	20/40	4φ14	Col.	S4-1	C16	60/20	6φ14	Col.
S12-1	C16	90/20	6φ16	Col.	S4-2	C16	50/20	6φ14	Col.
S12-2	C16	40/20	6φ16	Col.	S4-BASEM.	C16	80/20	6φ16	Col.
S12-BASEM.	C16	100/30	8φ16	Col.	S4-GRNDFL	C16	70/20	6φ16	Col.
S12-GRNDFL	C16	100/20	6φ16	Col.	S5-1	C16	20/60	6φ14	Col.
S13-1	C16	60/20	6φ14	Col.	S5-2	C16	20/50	6φ14	Col.
S13-2	C16	40/20	6φ14	Col.	S5-BASEM.	C16	20/80	6φ16	Col.
S13-BASEM.	C16	70/20	6φ16	Col.	S5-GRNDFL	C16	20/70	6φ16	Col.
S13-GRNDFL	C16	60/20	6φ14	Col.	S6-1	C16	80/20	6φ16	Col.
S14-1	C16	20/60	6φ14	Col.	S6-2	C16	70/20	6φ16	Col.
S14-2	C16	20/40	6φ14	Col.	S6-BASEM.	C16	100/25	6φ14	Col.
S14-BASEM.	C16	20/70	6φ16	Col.	S6-GRNDFL	C16	100/20	6φ16	Col.
S14-GRDFL	C16	20/60	6φ14	Col.	S7-1	C16	50/20	4φ14	Col.
S15-1	C16	20/60	6φ14	Col.	S7-2	C16	40/20	4φ14	Col.
S15-2	C16	20/40	6φ14	Col.	S7-BASEM.	C16	70/20	6φ16	Col.
S15-BASEM.	C16	20/70	6φ16	Col.	S7-GRNDFL	C16	50/20	6φ14	Col.
S15-GRNDFL	C16	20/60	6φ14	Col.	S8-1	C16	60/20	6φ14	Col.
S16-1	C16	20/90	6φ14	Col.	S8-2	C16	50/20	6φ14	Col.
S16-2	C16	20/70	6φ16	Col.	S8-BASEM.	C16	80/20	6φ16	Col.
S16-BASEM.	C16	30/100	6φ16	Col.	S8-GRNDFL	C16	70/20	6φ16	Col.
S16-GRNDFL	C16	25/100	6φ14	Col.	S9-1	C16	20/80	6φ16	Col.
S17-1	C16	20/80	6φ16	Col.	S9-2	C16	20/70	6φ16	Col.
S17-2	C16	20/70	6φ16	Col.	S9-BASEM.	C16	25/100	6φ16	Col.
S17-BASEM.	C16	25/100	8φ16	Col.	S9-GRNDFL	C16	20/100	6φ16	Col.

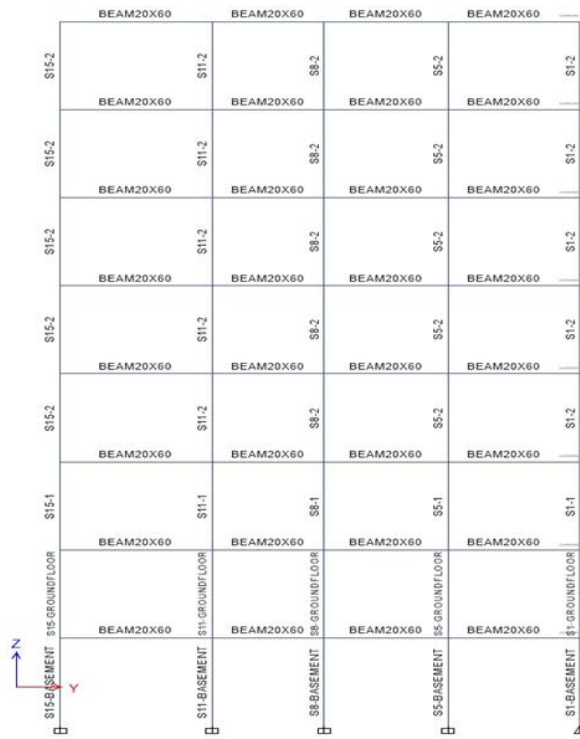


Fig. 9 Frame sections on the Y-Z plane

Table 4. Vibration periods and frequencies

Mode	Period (sec)	Frequency (cyc/sec)
1	1.232	0.812
2	1.058	0.945
3	1.011	0.99
4	0.41	2.44
5	0.355	2.819
6	0.336	2.981
7	0.243	4.111
8	0.21	4.752
9	0.195	5.127
10	0.17	5.884
11	0.146	6.854
12	0.133	7.537

Table 5. Joint properties of load-bearing elements on the 4th floor of the building

	A-B	B-IO (minimum)	IO-LS (pronounced)	LS-CP (advanced)	Total
Beam	0	79	0	0	79
Column	0	0	0	32	32

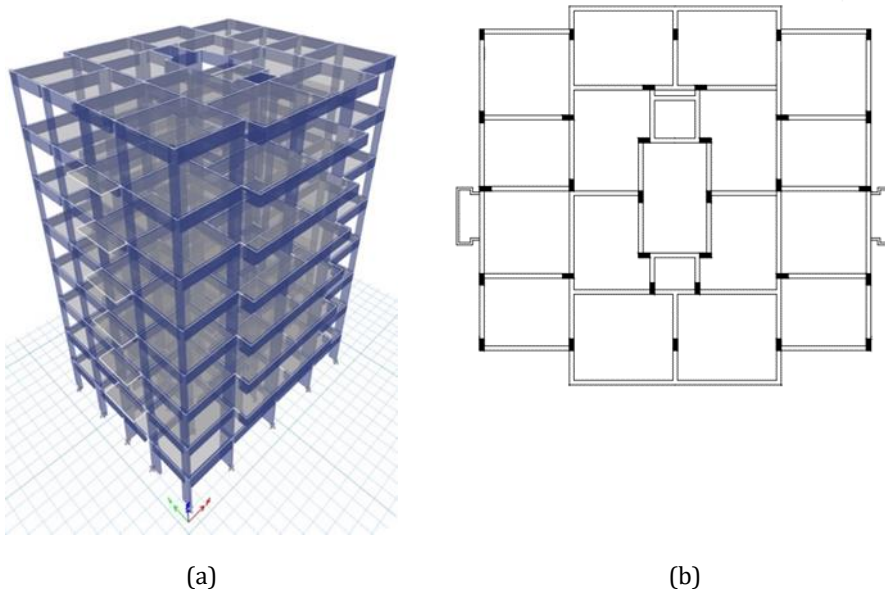


Fig. 10 8-Story building (a) Model layout in ETABS, (b) Plan Layout

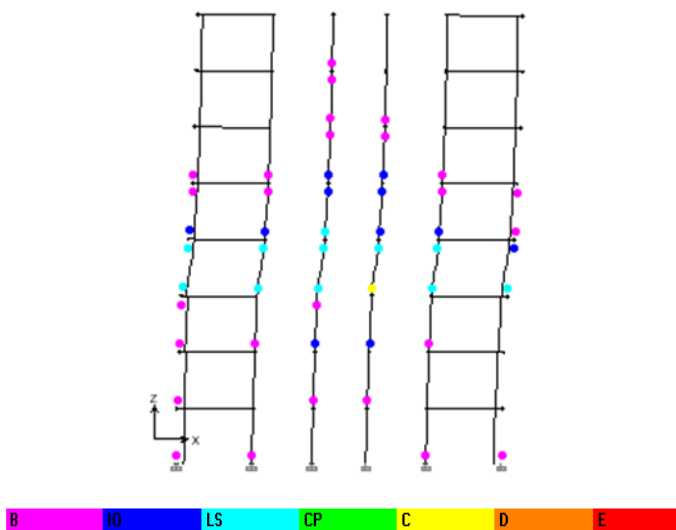


Fig. 11 Plastic hinges of the building - side view subjected to an earthquake event

Design spectral acceleration coefficients can be calculated by the following equations.

$$S_{DS} = S_S F_S \tag{1}$$

$$S_{D1} = S_1 F_1 \tag{2}$$

where, S_{DS} = Short period design spectral acceleration coefficient, S_{D1} = Design spectral acceleration coefficient for a period of 1.0 second, $F_S = 1.2$ (Site Coefficient (TBEC-2018 [45]: Table 2.1)), $F_1 = 1.5$ (Site Coefficient (TBEC-2018 [45]: Table 2.2))

Table 6. Applied Factor and coefficients according to TBEC-2018 [45].

Response Modification Factor (R)	4
System Overstrength Factor (Ω_0)	3
Importance Factor (I)	1
Short-period map spectral acceleration coefficient (S_s)	1.048
Map spectral acceleration coefficient for a 1.0 second period (S_1)	0.273
Maximum ground acceleration [g] (PGA)	0.445
Maximum ground speed [cm/sec] (PGV)	27.550

For this research, 11 pairs of ground motions shown in Table 7 were obtained from the PEER database [47] and the analyses were conducted by utilizing these motions. An earthquake-resistant structure's seismic design depends largely on the seismic response spectrum obtained from an earthquake-hazard analysis. Furthermore, an algorithm for generating realistic design acceleration time series is based on spectral matching in the time domain. For this study, the spectral matching method is applied with 5% damping by using SeismoMatch and ETABS programs to match the earthquake records to the target response band, the match is done according to the time domain and based on the [48].

Table 7. Selected earthquake records

No.	Earthquake	Year	Magnitude	Rjb (km)	Rrup (km)	Peer No.
1	"Duzce_Türkiye"	1999	7.14	12.02	12.04	1602
2	"Friuli_Italy-01"	1976	6.5	33.32	33.4	122
3	"Imperial Valley-06"	1979	6.53	15.19	15.19	164
4	"Kern County"	1952	7.36	38.42	38.89	15
5	"Kobe_Japan"	1995	6.9	24.85	24.85	1100
6	"Kocaeli_Türkiye"	1999	7.51	10.56	13.49	1148
7	"Landers"	1992	7.28	34.86	34.86	838
8	"Loma Prieta"	1989	6.93	39.32	39.51	762
9	"Manjil_Iran"	1990	7.37	12.55	12.55	1633
10	"Morgan Hill"	1984	6.19	23.23	23.24	450
11	"Northridge-01"	1994	6.69	35.66	36.77	942

Nonlinear time-history analyses were performed to estimate and evaluate the performance of the strengthened structure in compliance with TBEC-2018 [45] code specifications. The obtained results are used to determine whether the strengthened structure will survive and sustain earthquakes more than the normal structure.

3. Analysis Results and Discussion

A variety of results of NLTHA have been carried out considering a set of 11 accelerograms matching on both original and strengthened buildings, which are discussed, and compared to demonstrate the effectiveness of employing the proposed SHARK energy absorber in seismic strengthening.

The seismic responses, considered for investigation and comparison, includes story displacement, drift, and acceleration as well as input energy to the building. All the selected earthquake records have been subjected to the buildings as X-X Y-Y which is the X-Direction of the building and X-direction of the earthquake and Y-direction of the building and Y-direction of the earthquake. Furthermore, X-Y Y-X is the X-Direction of the building and Y-direction of the earthquake and Y-direction of the building and X-direction of the

earthquake. As stated by TBEC-2018 [45] which indicate that at least eleven earthquake ground motion sets are used in nonlinear calculations to be made in the time history.

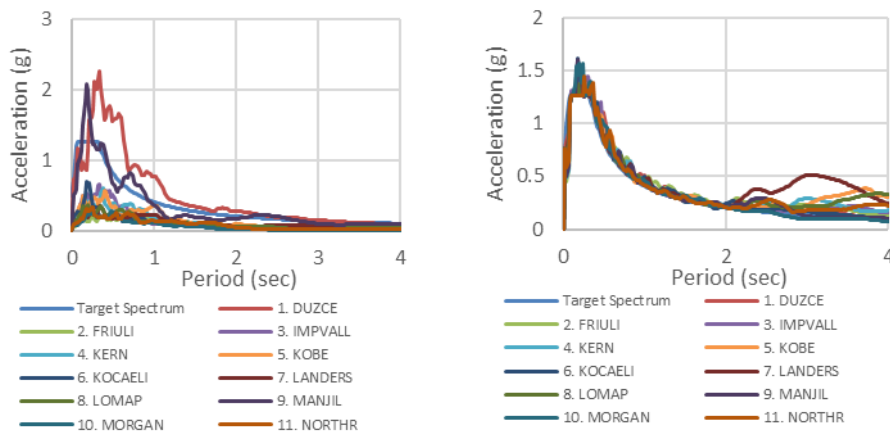


Fig. 12 The unscaled and scaled response spectrum of all earthquakes (x-direction)

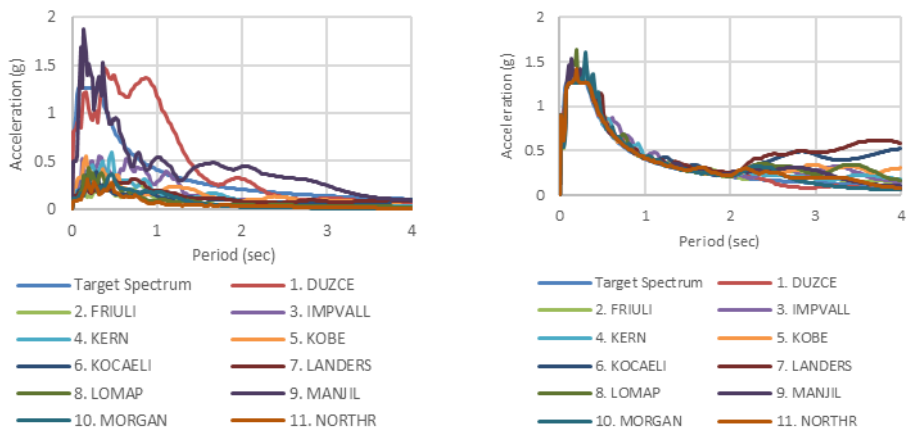


Figure 13. The unscaled and scaled response spectrum of all earthquakes (y-direction)

Acceleration records in two perpendicular horizontal directions are applied simultaneously in the direction of the (X) and (Y) principal axes of the system. Then, the axes of the acceleration records are rotated 90° and the calculations are repeated.

Figure 14 demonstrates the applied energy absorber configurations (CONF1, CONF2) which are used in the strengthening of the building. The connection of the SHARK device is applied to the beams and the bottom ends of the columns. As a representative of the numerical results of NLTHA, the time histories and responses of the buildings subjected to the DUZCE X-X Y-Y earthquake are presented in Figures 15-19.

For economical design, parameters of the smallest size of the energy absorber of SHARK (see Table 2) are used in the modelling of both configurations.

Figures 15 to 19 demonstrated that the implementation of SHARK in the building resulted in a considerable response. As can be seen in Figures 15a and 15b the time history response has resulted in a significant reduction of the Top Story Displacement for DUZCE X-X Y-Y in the X and Y directions of the building, respectively.

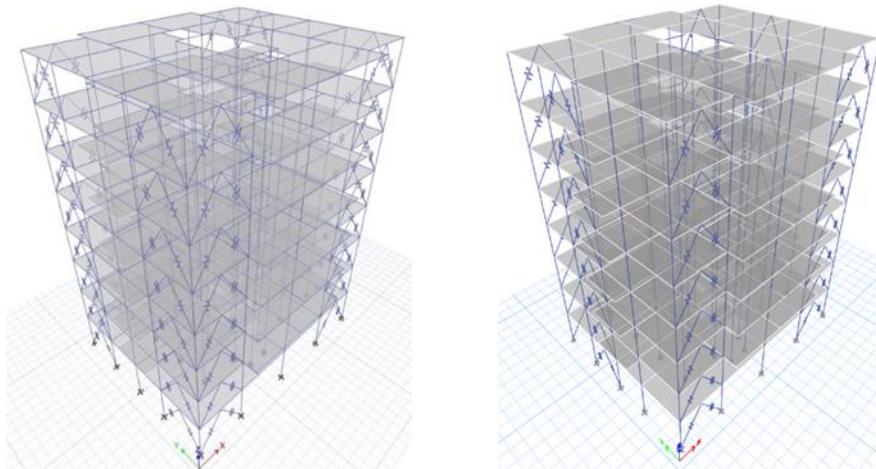


Fig. 14 8-Story building with two SHARK configurations a) CONF1, b) CONF2

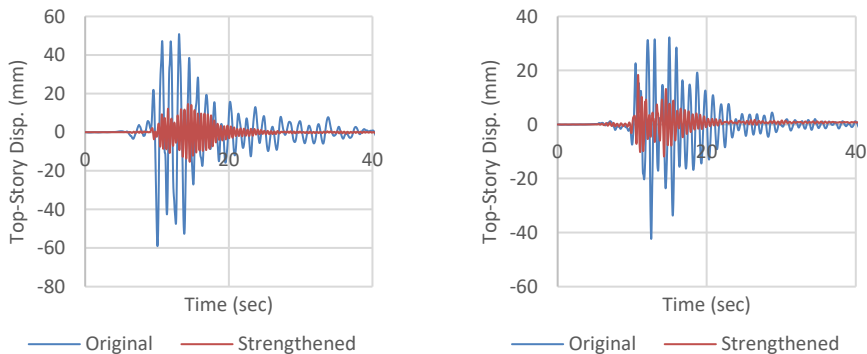


Fig. 15 Top-story displacement (DUZCE X-X Y-Y, CONF1) a) in the X-dir., b) in the Y-dir.

Further, Figures 16a and 16b showed a minimal reduction of the Top Story Acceleration for DUZCE X-X Y-Y in the X and Y directions of the building, respectively. However, in some cases during minor *Serviceability Limit State* (SLS) events, the SHARK generally operates within its elastic range and behaves like a stiff restrainer without much reduction of the earthquake input. This performance characteristic can lead to an increment of the peak story acceleration, which can be prejudicial to the non-structural components and technological contents for buildings such as hospitals, fire stations, police stations, data centers, emergency centers, or substantial commercial structures. To address this issue, the SHARK-Adaptive configuration can be utilized at a higher cost when compared to SHARK [32].

Moreover, Figures 17 and 18 demonstrate all stories' responses to displacement and drift. Figures 17 and 18 showed that there was significant displacement and drift reductions of all stories in both the X- and Y- direction of the building, respectively. Lastly, Figure 19 demonstrated the considerable input energy reduction of the strengthened building when compared to the original building.

In the interest of succinctness, this paper does not present graphical results for all the considered earthquakes that were applied. Instead, the maximum responses of the stories

under the applied scaled earthquakes are presented in Table 8 in X- and Y-directions of the building.

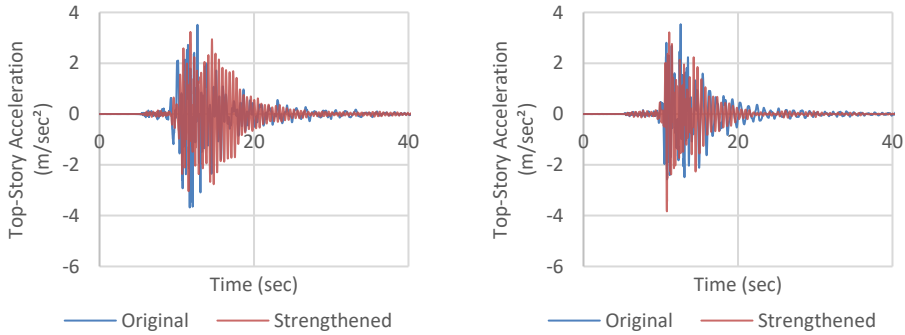


Fig. 16 Top-story acceleration (DUZCE X-X Y-Y, CONF1) a) in the X-dir., b) in the Y-dir.

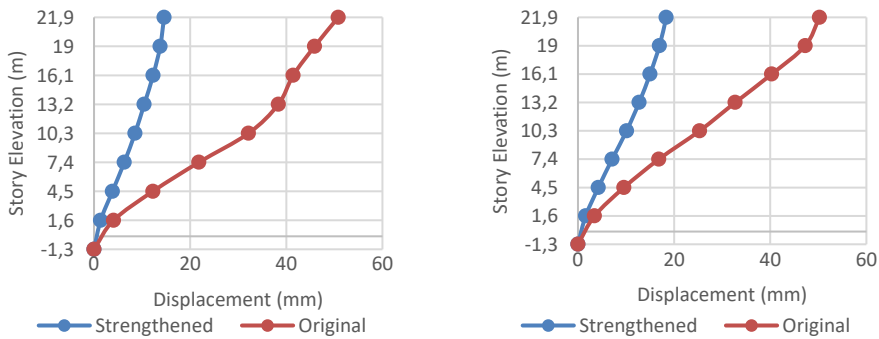


Fig. 17 Stories displacement (DUZCE X-X Y-Y, CONF1) a) in the X-dir., b) in the Y-dir.

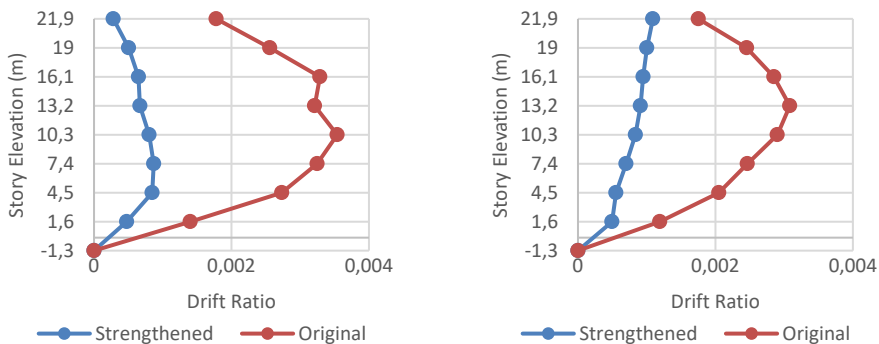


Fig. 18 Stories drift (DUZCE X-X Y-Y, CONF1) a) in the X-dir., b) in the Y-dir.

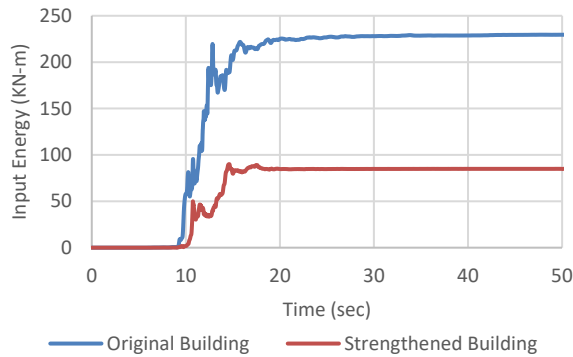


Fig. 19 Input energy to the building in the original and strengthened model with CONF1 (DUZCE X-X Y-Y)

Table 8 demonstrated the maximum responses of the 8-Story original and strengthened with configuration 1 buildings for story displacement, story drift, and story acceleration, all of which are significantly decreased compared to the original building. The reduction of the displacement in most of the cases is over 70% for the X-direction, while, in the Y-direction most of the cases are over 60%. The reduction of the drift in most of the cases is over 80% for the X-direction, while, in the Y-direction most of the cases are over 70%. Furthermore, the reduction of the acceleration in the X-direction varied between 8% to 44%, but in some cases showed below 1% reduction, while in the Y-direction varying between 4% to 28%. Further, 3 of the cases in the X-direction resulted in acceleration increments varying between 7% to 22%. While in the Y-direction 9 of the cases resulted in acceleration increments of 0.3% and 27%. The acceleration increment can be due to the fact the SHARK performance characteristic may behave like a stiff restrainer in some earthquake events which led to an increment of the story acceleration, or it can be due to long-period earthquakes, because of the close correlation between the period of the strengthened building and some of the selected earthquakes. Nevertheless, most of the strengthened building results have shown significantly better seismic performance than the original building results, which approve of the effectiveness of SHARK as an energy dissipation device.

The input energy caused by earthquakes subjected to original and strengthened buildings is shown in Table 9. According to the results, the strengthened building showed a significant decrease in the input energy as compared to the original building.

Table 8. Max story response in X- and Y-direction of the building with CONF1

Output Case			X-Direction			Y-Direction		
			Story Disp. (mm)	Story Drift (Ratio)	Story Acc. (m/sec ²)	Story Disp. (mm)	Story Drift (Ratio)	Story Acc. (m/sec ²)
1. DUZCE X-X Y-Y	Original	50.81	0.001778	3.27	50.26	0.001752	3.56	
	Strength.	14.58	0.000281	2.9	18.37	0.000495	2.73	
	Reduction %	71	84	11	63	72	23	
1. DUZCE X-Y Y-X	Original	73.24	0.002688	4.38	46.97	0.001374	4.08	
	Strength.	12.545	0.000243	2.64	17.89	0.000488	2.93	
	Reduction %	83	91	40	62	64	28	
2. FRIULI X-X Y-Y	Original	60.32	0.002108	2.88	49.9	0.001746	3.82	
	Strength.	16.08	0.000347	3.51	18.27	0.000501	3.32	
	Reduction %	73	83	-22	63	71	13	
2. FRIULI X-Y Y-X	Original	67.65	0.002437	3.55	42.23	0.001539	2.84	
	Strength.	15.46	0.000316	3.16	18.25	0.000473	3.9	
	Reduction %	77	87	11	57	69	-37	
3. IMPVAL X-X Y-Y	Original	65.87	0.002333	3.52	49.87	0.001598	2.83	
	Strength.	13.68	0.000293	2.62	16.94	0.000456	2.5	
	Reduction %	79	87	26	66	71	12	
3. IMPVAL X- Y Y-X	Original	64.1	0.002025	3.64	46.63	0.001381	2.83	
	Strength.	14.51	0.000282	2.82	16.39	0.000467	2.98	
	Reduction %	77	86	22	65	66	-5	
4. KERN X-X Y-Y	Original	72.1	0.002195	4.8	44.21	0.001355	2.62	
	Strengthened	15.98	0.000322	3.46	17.33	0.000483	3.32	
	Reduction %	78	85	28	61	64	-27	
4. KERN X-Y Y-X	Original	56.05	0.001999	2.82	52.11	0.001464	3.55	
	Strength.	13.67	0.000307	2.81	15.98	0.000463	2.74	
	Reduction %	76	85	0.35	69	68	23	
5. KOBE X-X Y-Y	Original	68.45	0.002648	4.7	48.96	0.001451	3.12	
	Strength.	16.13	0.000349	3.6	14.77	0.000418	2.88	
	Reduction %	76	87	23	70	71	8	
5. KOBE X-Y Y-X	Original	63.7	0.002387	3.12	41.94	0.001392	3.48	
	Strength.	12.4	0.00028	2.88	16.02	0.00041	3.17	
	Reduction %	81	88	8	62	70	9	
6. KOCAELI X- X Y-Y	Original	61.79	0.001786	4.35	41.23	0.001505	3.02	
	Strength.	14.82	0.000303	3.02	12.06	0.000405	2.73	
	Reduction %	76	83	31	71	73	10	
6. KOCAELI X- Y Y-X	Original	50.077	0.002164	3.11	42.35	0.001306	3.36	
	Strength.	11.91	0.000238	2.6	16.08	0.000424	2.45	
	Reduction %	76	89	16	62	68	27	
7. LANDERS X- X Y-Y	Original	63.73	0.002365	3.35	64.29	0.002458	3.66	
	Strength.	15.54	0.000298	2.88	15.83	0.000441	2.96	
	Reduction %	76	87	14	75	82	19	
7. LANDERS X- Y Y-X	Original	52.25	0.001851	3.19	45.73	0.001413	3.23	
	Strength.	14.94	0.000339	3.41	16.31	0.000509	3.52	
	Reduction %	71	82	-7	64	64	-9	
8. LOMA X-X Y- Y	Original	75.64	0.002401	4.06	41.38	0.001696	3.28	
	Strength.	13.77	0.000292	3.04	17.71	0.000547	3.29	
	Reduction %	82	88	25	57	68	-0.3	
8. LOMA X-Y Y-X	Original	73.8	0.00278	4.13	52.09	0.001554	3.5	
	Strength.	13.52	0.000315	2.71	17.83	0.000525	3.37	
	Reduction %	82	87	34	66	66	4	
9. MANJIL X-X Y-Y	Original	83.23	0.002287	3.73	53.33	0.001725	2.65	
	Strength.	11.9	0.000266	2.5	19.16	0.000577	3.22	
	Reduction %	86	88	33	64	67	-22	
9. MANJIL X-Y Y-X	Original	58.23	0.002207	3.25	51.4	0.001416	2.86	
	Strength.	13.77	0.000301	2.8	16.81	0.000453	2.88	
	Reduction %	76	86	14	67	68	-0.7	

10. MORGAN	Original	61.35	0.002433	4.11	31.72	0.001296	2.92
X-X Y-Y	Strength.	14.72	0.000281	2.48	17.47	0.000586	3.37
Reduction %		76	88	40	45	55	-15
10. MORGAN	Original	73.23	0.002769	2.41	54.83	0.001884	3.54
X-Y Y-X	Strength.	12.86	0.000256	2.77	18.07	0.000484	2.56
Reduction %		82	91	-15	67	74	28
11. NORTHR	Original	66.27	0.00286	3.6	49.65	0.001879	3.13
X-X Y-Y	Strength.	12.18	0.000285	2.97	14.39	0.000493	3.42
Reduction %		82	90	18	71	74	-9
11. NORTHR	Original	60.63	0.001949	3.8	41.66	0.001832	3.75
X-Y Y-X	Strength.	13.37	0.0003	2.95	17.92	0.000476	3.49
Reduction %		78	85	22	57	74	6

Table 9. Input energy to the building with the original model and CONF1

Output Case	Original kN-m	Strengthened kN-m	Reduction %
1. DUZCE X-X Y-Y	229.5858	90.0942	61
1. DUZCE X-Y Y-X	252.9478	113.9889	55
2. FRIULI X-X Y-Y	510.8472	153.1915	70
2. FRIULI X-Y Y-X	511.5960	208.5827	59
3. IMPVAL X-X Y-Y	1034.5741	257.7190	75
3. IMPVAL X-Y Y-X	829.4655	271.2382	67
4. KERN X-X Y-Y	483.8709	212.1759	56
4. KERN X-Y Y-X	555.8534	153.9982	72
5. KOBE X-X Y-Y	432.5402	109.6562	75
5. KOBE X-Y Y-X	469.9797	79.3143	83
6. KOCAELI X-X Y-Y	304.4265	86.4378	72
6. KOCAELI X-Y Y-X	221.4493	65.4920	70
7. LANDERS X-X Y-Y	324.9492	104.8087	68
7. LANDERS X-Y Y-X	336.4976	117.8001	65
8. LOMA X-X Y-Y	592.2024	191.5439	68
8. LOMA X-Y Y-X	589.2366	163.445	72
9. MANJIL X-X Y-Y	343.3354	100.8728	71
9. MANJIL X-Y Y-X	357.7581	119.9789	66
10 MORGAN X-X Y-Y	271.8399	99.4532	63
10 MORGAN X-Y Y-X	273.9571	104.7164	62
11. NORTHR X-X Y-Y	340.3192	115.6935	66
11. NORTHR X-Y Y-X	415.5953	138.7465	67

The variance of Inter Story Drift Ratio (ISDR) requirements along stories height of the strengthened building is shown in Table 10.

$$\Delta_i = u_i - u_{i-1} \tag{3}$$

$$\delta_i = \frac{R}{I} \Delta_i \tag{4}$$

$$\text{Max ISDR} \left(\frac{\delta_i}{h_i} \right) \leq \frac{0.008 k}{\lambda} \tag{5}$$

A building's drift demand is calculated by subtracting the consecutive story displacements, resulting from the analysis of the building under earthquake effects as specified by Eq. (3). By using Eq. (4), the effective story drift can be determined. The maximum ratio of story drift to story height is calculated as specified in Eq. (5) to determine the maximum ISDR of the building. The ISDR limit resulted to be 2.6%.

According to the results, the ISDR in the X-direction of the original building showed that stories 3 and 4 have more than the ISDR limit. However, the strengthened building reduced the ISDR and performed within the limit. Furthermore, the ISDR for the strengthened building showed much less when compared to the original building. The strengthening of the building is also accomplished by the implementation of the most economical size of SHARK in Configuration 2 (CONF2) (see Figure 14b).

Table 10. ISDR in X- and Y- directions of the building with CONF1

Story No.	X-Direction				Y-Direction			
	Original ISDR	Limit Check	Strengthened	Limit Check	Original ISDR	Limit Check	Strengthened	Limit Check
8	0.013546	WL	0.001120	WL	0.008215	WL	0.001951	WL
7	0.012327	WL	0.002016	WL	0.019213	WL	0.002699	WL
6	0.008473	WL	0.002571	WL	0.020939	WL	0.003130	WL
5	0.017146	WL	0.002639	WL	0.020470	WL	0.003600	WL
4	0.028507	ML	0.003069	WL	0.023357	WL	0.004154	WL
3	0.026357	ML	0.003398	WL	0.020065	WL	0.003966	WL
2	0.022601	WL	0.003390	WL	0.016867	WL	0.003628	WL
1	0.011206	WL	0.001909	WL	0.009525	WL	0.002216	WL

WL: Within Limit, ML: More than Limit

Figures from 20 to 24 demonstrated the implementation of SHARK to the building in configuration 2 (CONF2). As it can be seen in figures 20a and 20b, the time history response has resulted in a significant reduction of the Top-Story Displacement for DUZCE X-X Y-Y in the X- and Y-directions of the building, respectively.

Further, Figures 21a and 21b showed a minimal reduction of the Top-Story Acceleration for DUZCE X-X Y-Y in the X- and Y-directions of the building, respectively. Moreover, figures 22 and 23 demonstrate all stories' responses to displacement and drift. These figures showed that there was a significant displacement and drift reduction of all stories in both the X- and Y-directions of the building. Lastly, figure 24 demonstrated the considerable input energy reduction of the strengthened building when compared to the original building. This paper does not present graphical results for all the considered earthquakes that were applied. Instead, the maximum responses of the stories are presented in Table 12 in the X- and Y-directions.

Table 12 demonstrated the maximum responses of the original and strengthened building with configuration 2. Story displacement, story drift, and story acceleration are significantly decreased compared to the original building. The reduction of the displacement in most of the cases is over 65% for the X-direction, while in the Y-direction, most of the cases are over 55%. The reduction of the drift in most of the cases is over 80% for the X-direction, while in the Y-direction, most of the cases are over 70%, which is the same as for configuration 1. Furthermore, the reduction of the acceleration in the X-direction in most of the cases varies between 3% to 42% while in the Y-direction, in most of the cases vary between 2% to 39%. Further, 4 of the cases in the X-direction resulted in an acceleration increment varying between 11% to 45%. 5 of the cases in the Y-direction resulted in an acceleration increment varying between 1% to 12%.

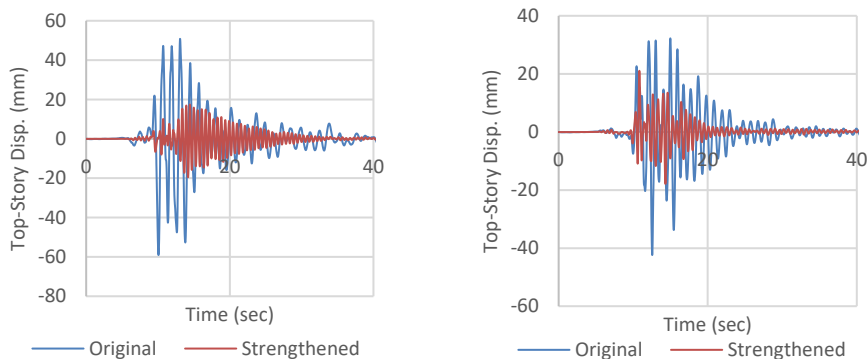


Fig. 20 Top-story displacement (DUZCE X-X Y-Y, CONF2) a) in the X-dir., b) in the Y-dir.

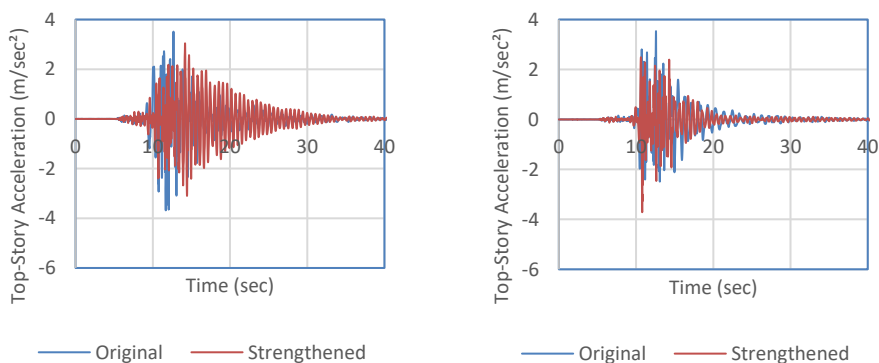


Fig. 21 Top-story acceleration (DUZCE X-X Y-Y, CONF2) a) in the X-dir., b) in the Y-dir.

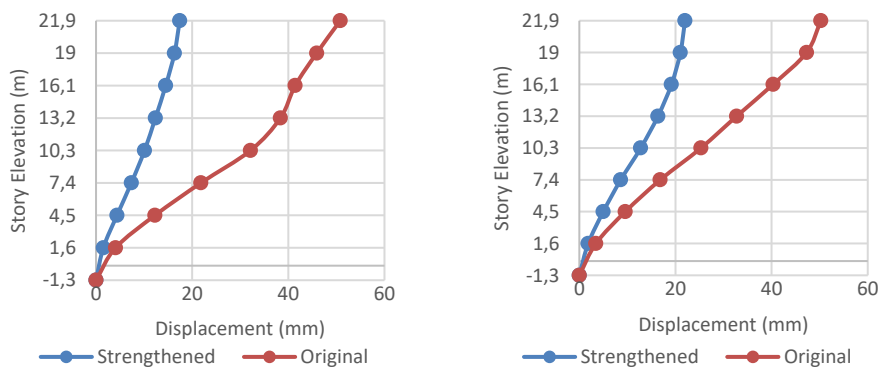


Fig. 22 Stories displacement (DUZCE X-X Y-Y, CONF2) a) in the X-dir., b) in the Y-dir.

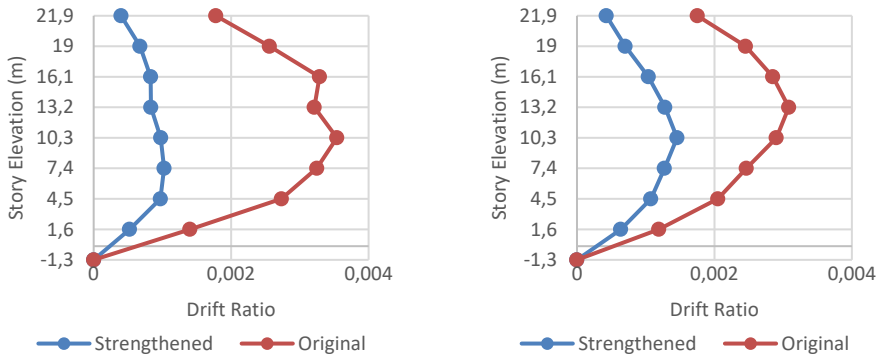


Fig. 23 Stories drift (DUZCE X-X Y-Y, CONF2) a) in the X-dir., b) in the Y-dir.

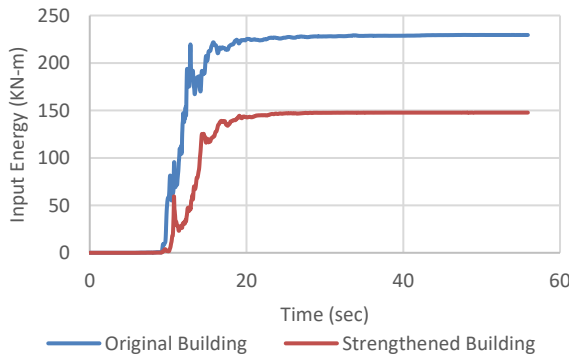


Fig. 24 Input energy to the building in the original and strengthened model with CONF2 (DUZCE X-X Y-Y)

By comparing the results of configuration 1 and configuration 2, it can be seen that displacement and drift results are very close. However, the acceleration results in the X-direction showed that there is a slight difference with the acceleration reduction percentage, but there is more acceleration increment percentage for configuration 2. While the Y-direction showed that configuration 1 has better performance in the acceleration reduction when compared to configuration 2. As mentioned earlier, the slight difference in the acceleration reduction can be due to SHARK performance may behave like a stiff restrainer in some earthquake events, in which this issue can be addressed by the usage adaptive shark which can provide effective protection of non-structural components and technological content of the building because of the flexible damper response (minimization of peak floor accelerations) under weak but frequent Serviceability Limit State (SLS) earthquakes. In addition, the acceleration increment percentage could be due to long-period earthquakes because of the close correlation between the period of the strengthened building and some of the selected earthquakes. Nevertheless, both configurations have shown significantly better seismic performance than the original ones, which approves the effectiveness of SHARK as an energy dissipation device in both configurations.

Table 12. Max story response in X- and Y-direction of the building with CONF2

Output Case		X-Direction			Y-Direction		
		Story Disp. (mm)	Story Drift (Ratio)	Story Acc. (m/sec ²)	Story Disp. (mm)	Story Drift (Ratio)	Story Acc. (m/sec ²)
1. DUZCE X-X Y-Y	Original	50.81	0.001778	3.27	50.26	0.001752	3.56
	Strengthened	17.41	0.000398	2.9	21.08	0.000428	2.61
	Reduction %	66	78	11	58	76	27
1. DUZCE X-Y Y-X	Original	73.24	0.002688	4.38	46.97	0.001374	4.08
	Strengthened	19.21	0.000403	3.03	15.22	0.000336	2.49
	Reduction %	74	85	31	68	75	39
2. FRIULI X-X Y-Y	Original	60.32	0.002108	2.88	49.9	0.001746	3.82
	Strengthened	17.89	0.000349	3.21	15.74	0.00034	2.37
	Reduction %	70	83	-11	68	80	38
2. FRIULI X-Y Y-X	Original	67.65	0.002437	3.55	42.23	0.001539	2.84
	Strengthened	19.67	0.000453	3.21	17.4	0.000367	2.66
	Reduction %	71	81	10	59	76	6
3. IMPVAL X-X Y-Y	Original	65.87	0.002333	3.52	49.87	0.001598	2.83
	Strengthened	18.39	0.000437	2.99	18.44	0.000431	2.93
	Reduction %	72	81	15	63	73	-3
3. IMPVAL X-Y Y-X	Original	64.1	0.002025	3.64	46.63	0.001381	2.83
	Strengthened	17.4	0.000367	2.92	15.59	0.000339	2.5
	Reduction %	73	82	20	67	75	12
4. KERN X-X Y-Y	Original	72.1	0.002195	4.8	44.21	0.001355	2.62
	Strengthened	16.53	0.000353	3.27	20.1	0.000435	2.93
	Reduction %	77	84	32	55	68	-12
4. KERN X-Y Y-X	Original	56.05	0.001999	2.82	52.11	0.001464	3.55
	Strengthened	19.65	0.00042	3.67	19.52	0.000366	2.91
	Reduction %	65	79	-30	62	75	18
5. KOBE X-X Y-Y	Original	68.45	0.002648	4.7	48.96	0.001451	3.12
	Strengthened	17.5	0.000369	3.17	17.2	0.000291	2.38
	Reduction %	74	86	32	65	80	24
5. KOBE X-Y Y-X	Original	63.7	0.002387	3.12	41.94	0.001392	3.48
	Strengthened	14.96	0.000358	2.49	19.6	0.00041	2.85
	Reduction %	76	85	20	53	71	18
6. KOCAELI X-X Y-Y	Original	61.79	0.001786	4.35	41.23	0.001505	3.02
	Strengthened	18.36	0.000361	2.53	15.39	0.000357	3.06
	Reduction %	70	80	42	63	76	-1.3
6. KOCAELI X-Y Y-X	Original	50.077	0.002164	3.11	42.35	0.001306	3.36
	Strengthened	12.59	0.000262	2.79	19.77	0.000369	2.97
	Reduction %	75	88	10	53	72	12
7. LANDERS X-X Y-Y	Original	63.73	0.002365	3.35	64.29	0.002458	3.66
	Strengthened	18.29	0.000482	4.44	17.22	0.000318	2.24
	Reduction %	71	80	-32	73	87	39
7. LANDERS X-Y Y-X	Original	52.25	0.001851	3.19	45.73	0.001413	3.23
	Strengthened	17.04	0.000327	2.52	16.76	0.000341	2.36
	Reduction %	67	82	21	63	76	27
8. LOMA X-X Y-Y	Original	75.64	0.002401	4.06	41.38	0.001696	3.28
	Strengthened	18.82	0.000424	2.96	17.32	0.000427	2.79
	Reduction %	75	82	27	58	75	15
8. LOMA X-Y Y-X	Original	73.8	0.00278	4.13	52.09	0.001554	3.5
	Strengthened	19.01	0.000447	3.28	15.94	0.000402	2.32
	Reduction %	74	84	21	69	74	34
9. MANJIL X-X Y-Y	Original	83.23	0.002287	3.73	53.33	0.001725	2.65
	Strengthened	18.65	0.000383	3.22	18.38	0.000413	2.74
	Reduction %	78	83	14	65	76	-3.4

9. MANJIL X-Y Y-X	Original	58.23	0.002207	3.25	51.4	0.001416	2.86
	Strengthened	19.34	0.000524	3.07	16.24	0.000419	2.79
Reduction %		67	76	6	68	70	2
10. MORGAN X-X Y-Y	Original	61.35	0.002433	4.11	31.72	0.001296	2.92
	Strengthened	19.43	0.000429	3.08	18.95	0.000353	2.87
Reduction %		68	82	25	40	73	2
10. MORGAN X-Y Y-X	Original	73.23	0.002769	2.41	54.83	0.001884	3.54
	Strengthened	21.03	0.000488	3.5	15.27	0.000325	2.44
Reduction %		71	82	-45	72	83	31
11. NORTH X-X Y-Y	Original	66.27	0.00286	3.6	49.65	0.001879	3.13
	Strengthened	16.94	0.000473	3.5	17.05	0.00031	2.89
Reduction %		74	83	3	66	83	8
11. NORTH X-Y Y-X	Original	60.63	0.001949	3.8	41.66	0.001832	3.75
	Strengthened	18.78	0.000464	3.53	18.25	0.000343	3.79
Reduction %		69	76	7	56	81	-1

Table 13. Input energy to the building with the original model and CONF2

Output Case	Original kN-m	Strengthened kN-m	Reduction %
1. DUZCE X-X Y-Y	229.5858	147.7328	36
1. DUZCE X-Y Y-X	252.9478	96.6466	62
2. FRIULI X-X Y-Y	510.8472	183.0025	64
2. FRIULI X-Y Y-X	511.596	200.9595	61
3. IMPVAL X-X Y-Y	1034.5741	531.0618	49
3. IMPVAL X-Y Y-X	829.4655	378.2784	54
4. KERN X-X Y-Y	483.8709	293.0583	39
4. KERN X-Y Y-X	555.8534	305.6324	45
5. KOBE X-X Y-Y	432.5402	128.5034	70
5. KOBE X-Y Y-X	469.9797	145.0765	69
6. KOCAELI X-X Y-Y	304.4265	106.6303	65
6. KOCAELI X-Y Y-X	221.4493	108.9572	51
7. LANDERS X-X Y-Y	324.9492	111.8569	66
7. LANDERS X-Y Y-X	336.4976	101.8414	70
8. LOMA X-X Y-Y	592.2024	257.867	56
8. LOMA X-Y Y-X	589.2366	204.2867	65
9. MANJIL X-X Y-Y	343.3354	178.379	48
9. MANJIL X-Y Y-X	357.7581	170.0593	52
10 MORGAN X-X Y-Y	271.8399	151.0671	44
10 MORGAN X-Y Y-X	273.9571	123.1499	55
11. NORTH X-X Y-Y	340.3192	199.1478	41
11. NORTH X-Y Y-X	415.5953	215.1773	48

The input energy caused by earthquakes subjected to the original and strengthened buildings as in Configuration 2 is shown in Table 13. According to the results, the strengthened building showed a significant decrease in the input energy as compared to the original building.

The variance of ISDR requirements along stories height of the 8-Story strengthened building is shown in Table 14. The building's drift demand is calculated by subtracting the

consecutive story displacements, resulting from the analysis of the building under earthquake effects. According to the results, the ISDR requirements should be less than 2.6%, which is a limit according to TBEC-2018 [45].

Table 14. ISDR in X- and Y-directions of the building with CONF2

Story No.	X-Direction				Y-Direction			
	Original ISDR	Limit Check	Strengthened	Limit Check	Original ISDR	Limit Check	Strengthened	Limit Check
8	0.013546	WL	0.001506	WL	0.008215	WL	0.001346	WL
7	0.012327	WL	0.002509	WL	0.019213	WL	0.002556	WL
6	0.008473	WL	0.002965	WL	0.020939	WL	0.003874	WL
5	0.017146	WL	0.003104	WL	0.02047	WL	0.004936	WL
4	0.028507	ML	0.003789	WL	0.023357	WL	0.005742	WL
3	0.026357	ML	0.004122	WL	0.020065	WL	0.005008	WL
2	0.022601	WL	0.003928	WL	0.016867	WL	0.004327	WL
1	0.011206	WL	0.00209	WL	0.009525	WL	0.002551	WL

WL: Within Limit, ML: More than Limit

According to the results, the ISDR in the X-direction of the original building showed that stories 3 and 4 have more than the ISDR limit. However, the strengthened building reduced the ISDR and performed within the limit. Furthermore, the ISDR for the strengthened building showed much less when compared to the original building.

4. Conclusions

This study carried out a procedure that includes model calibration parameters obtained from the analysis of ambient vibration records for seismic strengthening of multi-story existing RC buildings. This was done through the implementation of the SHARK Hysteretic Energy Dissipation Device. The proposed procedure for design and configurations has been evaluated through NLTHA by applying a pair of 11 selected earthquake records on an 8-Story RC building without and with SHARK. The implementation of the SHARK has been carried out in two configurations by the usage of the specified sizes and values that are provided by MAURER [41] and applied in the ETABS program to achieve the proper behavior of the energy dissipation system against earthquakes. First, the X- and Y-components of the earthquakes were applied to the X- and Y-directions of the building, and then the components of the earthquakes are rotated 90° and reapplied to the X- and Y-directions of the building. It was observed that the seismic responses of the strengthened structure were significantly higher than the original structure. The levels of input energy decreased considerably, and the structure was able to resist various earthquake events with less displacement, drift ratio, and acceleration. The following conclusions can be derived from the results of the conducted NLTHA:

- The maximum displacement reduction values of the strengthened building are between 70% and 80% in comparison to the original building. The reduction is on average about 78% and 72% for the x-direction. However, the y-direction resulted in a 64% and 62% reduction for CONF1 and CONF2, respectively.
- The maximum drift reduction values of the strengthened building are between 70% and 80% in comparison to the original building. The reduction is on average about 87% and 82% for the x-direction. However, the y-direction resulted in a 69% and 76% reduction for CONF1 and CONF2, respectively.
- The maximum acceleration reduction values of the strengthened building are between 4% and 20% compared to the original building. The reduction is on average about 17% and 10% for the x-direction of the building with CONF1 and CONF2, respectively. Furthermore, there were some cases with acceleration increment which can be due to the fact that the SHARK performance characteristic may behave like a stiff restrainer in some earthquake events which led to an

increment of the story acceleration. This issue can be addressed by the usage of adaptive-shark which can provide effective protection of non-structural components and technological content of the building because of the flexible damper response (minimization of peak floor accelerations) under weak but frequent Serviceability Limit States earthquakes. This beneficial performance is essential for very important buildings (e.g., hospitals, police stations, fire stations, data centers, important commercial structures, or emergency management centers) that are required to remain fully operational in the emergency response after an earthquake. In addition, the increase in acceleration in some cases can be due to long-period earthquakes, because of the close correlation between the period of the strengthened building and some of the selected earthquakes. Nevertheless, most of the strengthened building cases have shown significantly better seismic performance than the original one, which approves the effectiveness of SHARK as an energy dissipation device.

- The input energy of the strengthened building showed a significant decrease as compared to the original building. The reduction is on average about 64% and 70% for the 8-Story building with CONF1 and CONF2, respectively.
- All the results of the Inter Story Drift Ratio ISDR of the strengthened building are obtained less than the estimated limit according to TBEC-2018.

Based on the above conclusions, the use of the proposed MAURER SHARK-which provides high protection of the structure during severe Ultimate Limit State earthquakes, long-term reliability against wear and fatigue problems, high redundant safety level, easy visual inspection, and easy-to-replace at low cost- is highly recommended, either for seismic strengthening of the existing buildings or newly designed ones. Finally, it should be emphasized that this study was limited to a few multi-story RC buildings. For more encompassing conclusions, this study should be expanded to encompass several buildings.

The comprehensive analytical work conducted in this research has improved the understanding of earthquake effects on buildings, building behavior, seismic strengthening, and hysteretic energy absorbers. However, some investigation needs to be addressed. Further research studies in this area are recommended as follows:

- In this research, Non-Linear Time History Analysis is performed on a three-dimensional system model and then the building is strengthened. But the building model was a simplified model of a real building with basic structural framing which didn't include various elements such as walls, elevators, stairs, etc. A better realistic model can be used to get accurate results and perform safer strengthening.
- When the SHARK experiences minor serviceability limit states (SLS), like other conventional bilinear dampers, the damper primarily operates in its elastic range, acting as a stiff restraint without reducing the input of the earthquake. Therefore, it's recommended to use the SHARK-Adaptive configuration to address this issue effectively.
- Applying different installation configurations than the studied ones can give acceptable results with fewer Energy Dampers for more economical strengthening of old or designing new buildings.

It's recommended to make a study on the cost evaluation of applying the MAURER devices to the new and old buildings.

References

- [1] El-Betar SA. Seismic vulnerability evaluation of existing RC buildings. HBRC Journal, 2018; 14(2), 189-197. <https://doi.org/10.1016/j.hbrj.2016.09.002>

- [2] Gökkaya K. Geographic analysis of earthquake damage in Turkey between 1900 and 2012. *Geomatics, Natural Hazards and Risk*, 2016; 7(6), 1948-1961. <https://doi.org/10.1080/19475705.2016.1171259>
- [3] Isik V, Uysal IT, Caglayan A, Seyitoglu G. The evolution of intraplate fault systems in central Turkey: Structural evidence and Ar-Ar and Rb-Sr age constraints for the Savcili Fault Zone. *Tectonics*, 2014; 33(10), 1875-1899. <https://doi.org/10.1002/2014TC003565>
- [4] Atmaca B, Demir S, Gunaydin M, Altunisik AC, Husem M, Ates S, Angin Z. Lessons learned from the past earthquakes on building performance in Turkey, *Journal of Structural Engineering & Applied Mechanics*, 2020; 3(2), 61-84. <https://doi.org/10.31462/jseam.2020.02061084>
- [5] Bulut F, Aktuğ B, Yaltrak C, Doğru A, Özener H. Magnitudes of future large earthquakes near Istanbul quantified from 1500 years of historical earthquakes, present-day microseismicity and GPS slip rates. *Tectonophysics*, 2019; 764, 77-87. <https://doi.org/10.1016/j.tecto.2019.05.005>
- [6] Mojarab M, Memarian H, Zare M. Performance evaluation of the M8 algorithm to predict M7+ earthquakes in Turkey. *Arabian Journal of Geosciences*, 2015; 8(8), 5921-5934. <https://doi.org/10.1007/s12517-014-1624-3>
- [7] Cagatay IH. Experimental evaluation of buildings damaged in recent earthquakes in Turkey. *Engineering Failure Analysis*, 2005; 12(3), 440-452. <https://doi.org/10.1016/j.engfailanal.2004.02.007>
- [8] Pinho R. Selective retrofitting of RC structures in seismic areas, Ph.D. Thesis, Faculty of Engineering, University of London, 2000, London.
- [9] Tsionis G, Apostolska R, Tauver F. Seismic strengthening of RC buildings, Publications Office of European Union, 2014, Luxembourg.
- [10] Benjamin JR, Cornell CA. Probability, statistics, and decisions for civil engineers. Dover Publications, 2014.
- [11] Veletsos A, Newmark NM. Effect of inelastic behavior on the response of simple systems to earthquake motions. Second World Conference on Earthquake Engineering, 1960; 2: 895-912 Tokyo, Japan.
- [12] Castaldo P. Integrated seismic design of structure and control systems. Springer, 2014. <https://doi.org/10.1007/978-3-319-02615-2>
- [13] Constantinou MC, Soong TT, Dargush GF. Passive energy dissipation systems for structural design and retrofit, University of Buffalo, USA, 1998.
- [14] Gkournelos P, Triantafillou T, Bournas D. Seismic upgrading of existing reinforced concrete buildings: A state-of-the-art review. *Engineering Structures*, 2021; 240, 112273. <https://doi.org/10.1016/j.engstruct.2021.112273>
- [15] Franco J, Cahís X, Gracia L, López F. Experimental testing of a new anti-seismic dissipator energy device based on the plasticity of metals. *Engineering structures*, 2010; 32(9), 2672-2682. <https://doi.org/10.1016/j.engstruct.2010.04.037>
- [16] Dolce M, Cardone D, Ponzo FC, Valente C. Shaking table tests on reinforced concrete frames without and with passive control systems. *Earthquake Engineering and Structural Dynamics*, 2005; 34(14), 1687-1717. <https://doi.org/10.1002/eqe.501>
- [17] Reinhorn AM, Li C, Constantinou M. Experimental and analytical investigation of seismic retrofit of structures with supplemental damping: Part. 1-fluid viscous damping devices. Technical Report NCEER-95-0001, University of Buffalo, USA, 1995.
- [18] Aiken ID, Nims DK, Whittaker AS, Kelly JM. Testing of passive energy dissipation systems. *Earthquake Spectra*, 1993; 9(3), 335-370. <https://doi.org/10.1193/1.1585720>
- [19] Khampanit A, Leelataviwat S, Kochanin J, Warnitchai P. Energy-based seismic strengthening design of non-ductile reinforced concrete frames using buckling-restrained braces. *Engineering Structures*, 2014; 81(4), 110-122. <https://doi.org/10.1016/j.engstruct.2014.09.033>

- [20] Sahoo DR, Rai DC. Seismic strengthening of non-ductile reinforced concrete frames using aluminum shear links as energy-dissipation devices. *Engineering Structures*, 2010; 32(11), 3548-3557. <https://doi.org/10.1016/j.engstruct.2010.07.023>
- [21] Ghandil M, Riahi HT, Behnamfar F. Introduction of a new metallic-yielding piston damper for seismic control of structures. *J. Constr. Steel Res.* 2022; 194, 107299. <https://doi.org/10.1016/j.jcsr.2022.107299>
- [22] Sabelli R, Mahin S, Chang C. Seismic demands on steel braced frame buildings with buckling-restrained braces. *Engineering Structures*, 2003; 25(5), 655-666. [https://doi.org/10.1016/S0141-0296\(02\)00175-X](https://doi.org/10.1016/S0141-0296(02)00175-X)
- [23] Tsai KC, Chen HW, Hong CP, Su YF. Design of steel triangular plate energy absorbers for seismic-resistant construction. *Earthquake spectra*, 1993; 9(3), 505-528. <https://doi.org/10.1193/1.1585727>
- [24] Titirla MD. Using Friction-Yielding Damper CAR1 to Seismic Retrofit a Two-Story RC Building: Numerical Application. *Applied Sciences*, 2023; 13(3), 1527. <https://doi.org/10.3390/app13031527>
- [25] Di Cesare A, Ponzo FC, Nigro, D. Assessment of the performance of hysteretic energy dissipation bracing systems. *Bulletin of Earthquake Engineering*, 2014; 12(6), 2777-2796. <https://doi.org/10.1007/s10518-014-9623-z>
- [26] Di Cesare A, Ponzo FC. Seismic retrofit of reinforced concrete frame buildings with hysteretic bracing systems: design procedure and behaviour factor. *Shock and Vibration*, 2017. <https://doi.org/10.1155/2017/2639361>
- [27] Tena-Colunga A, Nangullasmú-Hernández H. Assessment of seismic design parameters of moment resisting RC braced frames with metallic fuses. *Engineering Structures*, 2015; 95, 138-153. <https://doi.org/10.1016/j.engstruct.2015.03.062>
- [28] Thongchom C, Mirzai N, Chang B, Ghamari A. Improving the CBF brace's behavior using I-shaped dampers, numerical and experimental study. *Journal of Constructional Steel Research*, 2022; 197, 107482. <https://doi.org/10.1016/j.jcsr.2022.107482>
- [29] Demir S, Husem M. Saw type seismic energy dissipaters: development and cyclic loading test. *Journal of Constructional Steel Research*, 2018; 150, 264-276. <https://doi.org/10.1016/j.jcsr.2018.08.015>
- [30] Chen Y, Ye D, Zhang L. (2022). Analytical development and experimental investigation of the casting multi-plate damper (CMPD). *Engineering Structures*, 2022; 250, 113402. <https://doi.org/10.1016/j.engstruct.2021.113402>
- [31] Zhang A, Ye Q. Design and testing of prefabricated steel frame with an innovative re-centering energy dissipative brace. *Engineering Structures*, 2019; 201, 109791. <https://doi.org/10.1016/j.engstruct.2019.109791>
- [32] Gandelli E, Chernyshov S, Distl J, Dubini P, Weber F, Taras A. Novel adaptive hysteretic damper for enhanced seismic protection of braced buildings. *Soil Dynamics and Earthquake Engineering*, 2021; 141, 106522. <https://doi.org/10.1016/j.soildyn.2020.106522>
- [33] Shih MH, Sung WP. Seismic Resistance and Parametric Study of Building under Control of Impulsive Semi-Active Mass Damper. *Applied Sciences*, 2021; 11(6), 2468. <https://doi.org/10.3390/app11062468>
- [34] Bruschi E, Quaglini V, Zoccolini L. Seismic Upgrade of Steel Frame Buildings by Using Damped Braces. *Applied Sciences*, 2023; 13(4), 2063. <https://doi.org/10.3390/app13042063>
- [35] Cao XY, Feng DC, Wu G, Wang Z. Experimental and theoretical investigations of the existing reinforced concrete frames retrofitted with the novel external SC-PBSPC BRBF sub-structures. *Engineering Structures*, 2022; 256, 113982. <https://doi.org/10.1016/j.engstruct.2022.113982>
- [36] Cao XY, Feng DC, Wu G, Wang Z. Parametric investigation of the assembled bolt-connected buckling-restrained brace and performance evaluation of its application into

- structural retrofit. *Journal of Building Engineering*, 2022; 48, 103988. <https://doi.org/10.1016/j.jobe.2022.103988>
- [37] Nasab M, Guo YQ, Kim J. Seismic retrofit of a soft first-story building using viscoelastic dampers considering inherent uncertainties. *Journal of Building Engineering*, 2022; 47, 103866. <https://doi.org/10.1016/j.jobe.2021.103866>
- [38] Thongchom C, Bahrami A, Ghamari A, Benjeddou O. Performance Improvement of Innovative Shear Damper Using Diagonal Stiffeners for Concentrically Braced Frame Systems. *Buildings*, 2022; 12(11), 1794. <https://doi.org/10.3390/buildings12111794>
- [39] Zhu X, Wang W, Li W, Zhang Q, Du Y, Yin Y. Experimental and numerical study of X-type energy dissipation device under impact loads. *Journal of Constructional Steel Research*, 2023; 204, 107876. <https://doi.org/10.1016/j.jcsr.2023.107876>
- [40] Zhang J, Fang C, Yam M, Lin C. Fe-Mn-Si alloy U-shaped dampers with extraordinary low-cycle fatigue resistance. *Engineering Structures*, 2022 264, 114475. <https://doi.org/10.1016/j.engstruct.2022.114475>
- [41] MAURER SHARK® Short-Stroke Hysteretic Damper, 2020. Retrived from MAURER: <https://www.maurer.eu/en/products/seismic-devices/dampers/index.html>
- [42] Genes MC, Gülkan PH, Bikçe M, Kaçın S. Combination of Instrumental and Numerical Data Based on the Mixed Approach of Reinforced Concrete Framed Structures Investigation of Damage and Seismic Characteristics, Tubitak (107M445)-IntenC Project final report, 2011.
- [43] EN 15129 Anti-seismic devices, 2009.
- [44] ACI 318-11 Building Code Requirements for Structural Concrete (ACI 318-11), An ACI Standard and Commentary. American Concrete Institute. Farmington Hills, USA, 2011.
- [45] TBEC Türkiye Earthquake Code for Buildings. Disaster and emergency management presidency. Ministry of Interior, Ankara, Turkey, 2018.
- [46] ASCE 41-17 Seismic evaluation and retrofit of existing buildings. American Society of Civil Engineers, USA, 2017.
- [47] PEER Peer ground motion database. Pacific Earthquake Engineering Research Center. <http://ngawest2.berkeley.edu>. University of California, Berkeley, CA, USA, 2021.
- [48] ASCE 7-16 Minimum Design Loads and Associated Criteria for Buildings and Other Structures, American Society of Civil Engineers, USA, 2017.

Blank Page



Review Article

Evaluation of physical testing for seismic behaviour of tunnels: A comprehensive review

Aashima Sharma^a, Heaven Singh^b

Civil Engineering Department, Thapar Institute of Engineering and Technology, Patiala, India

Article Info

Abstract

Article history:

Received 12 Jan 2023

Accepted 19 Jun 2023

Keywords:

Centrifuge test;
Shake-table test;
Soil structure
Interaction;
Tunnel;
Underground
structure

Underground structures are nowadays quite popular for urban construction. Since it is very difficult to begin post-damage construction immediately, the correct evaluation of its response during any seismic activity is an important factor for the analysis. Various physical models and numerical and analytical methods are recently introduced to study earthquake waves' effects on underground structures. This paper presents a brief review of the experimental tests, i.e., the Centrifuge test and Shake table test, used to analyze the performance of tunnels under a seismic environment with due consideration of the failure of the underground structure due to ground failure and ground shaking conditions. Besides this, the seismic behaviour of tunnels, factors influencing the behavior of tunnel structure and its failure patterns are also discussed. Subsequently, overall gaps in the study have been mentioned with the current understanding for its analysis.

© 2023 MIM Research Group. All rights reserved.

1. Introduction

Tunnels are enclosed reinforced concrete RC structures used for transportation purposes and play an important role in the infrastructure of modern society. Tunnel serves a major purpose to cross water and mountain hindrance, and due to increased traffic in urban areas, metro tunnels also serve as the main loop to run trains on the busiest routes to shorten the time. The tunnel construction growth in the country has been driven by many projects, developing the urban-rapid-mass-transit systems, improving the connectivity between road, rail etc. To facilitate the needs of densely populated areas, tunnels are constructed at an increasing rate. According to the tunnel market survey 2019, the global tunneling market in India has nearly doubled as compared to 2016, with the main growth from road and rail tunnels (1). Being such an important part of the infrastructure, tunnels should be structurally stable and should be capable enough to resist static as well as dynamic loads imposed on them. Hence, an insightful study of the effects of the earthquake on the analysis, construction and design of tunnels is an important factor under consideration.

The major difference between the behaviour of surface structures and underground (UG) structures during an earthquake (EQ) is due to surrounding soil, which dominates the seismic design of underground structures (2–4), whereas the seismic behavior of surface structures is affected by the inertial forces. The contribution of soil-structure interaction is therefore, more in defining the seismic behaviour of underground structures.

On the basis of shape, tunnels are broadly classified as (5) (figure: 2).

- Mined or bored tunnels

^{*}Corresponding author: sharmaaashima15@gmail.com

^a <https://orcid.org/0000-0003-0234-6403>; ^b <https://orcid.org/0000-0003-4719-7288>

DOI: <http://dx.doi.org/10.17515/resm2023.640ea0112>

Res. Eng. Struct. Mat. Vol. 9 Iss. 4 (2023) 1573-1591

- Cut-cover tunnels
- Immersed tunnels

Bored tunnels are most popular where there are significant excavation depths and the presence of overlying structures. These are constructed using TBMs (Tunnel Boring Machines) or by drill and blast in rocks and thus are circular in shape. Cut and cover tunnels are constructed by means of excavating the soil, constructing the structure and then filling the surrounding of tunnel with the excavated soil. This method is employed for rectangular tunnel construction where excavation depth is shallow. Cut and cover tunnels are generally more economical up to a depth of 10m-12m than mined or bored tunnels. An immersed tube tunnel is an underwater tunnel constructed elsewhere and then floated to the site, sunk and anchored in place. These tunnels are used to cross water bodies where it is not suitable to construct a bridge or bored tunnels.

Earlier, no seismic effects were considered while designing the underground facilities, but, the consequences of various damages observed in the past, highlighted those underground structures which were not properly designed were subjected to vulnerable effects of the wave propagation. Failure of various tunnel structures and their behaviour within the seismic environment is discussed in this paper with details signifying the methods used for its analysis by various researchers and designers and subsequently describing the current gaps in their experimental testing.

2. Seismic Performance of Tunnels

Though underground structures are very less susceptible to EQ effects than above-ground structures; but, during several strong EQs like San Fernando EQ (1971), Northridge EQ (1994), and Kobe EQ (1995), various researchers documented the failures of underground structures. Dowding et. al.(5)observed 71 cases of damage of tunnels during a seismic event and concluded that most damage cases were observed in tunnels in rocks rather than tunnels in the soil. Owen G.N. et. al.(6) extended this study to 127 cases considering failures of cut and cover tunnels also as an addition to the data collected by (5). The prime factors for the failure of tunnels are increase in lateral forces arising due to surrounding soil backfill and duration of strong EQ.

Sharma et al. (7) updated the work of previous researchers by analyzing 192 cases of damage under 85 earthquakes and correlated the damage characteristics of tunnels to various parameters, namely tunnel geometry, geotechnical features and EQ characteristics like peak-ground acceleration (PGA), epicentral distance and magnitude. They concluded that deeper tunnels were less vulnerable to EQ damage as compared to shallow tunnels primarily due to the more confining pressure of the surrounding ground. Due to large embedment depth and overburden pressure the deformation in under-ground structures are very less as compared to surface structures. Besides this, as the distance of the structure from the epicenter increases the severity of damage decreases. Power M.S. et. al.(8) further investigated 217 cases of bored tunnels damaged after the Hyogoken-Nambu earthquake leading to failure of most underground structures. Daikai subway station is one of the prominent cases considered for evaluation of failure criteria of underground subway station. During the 1995 Kobe EQ, Daikai subway station located in Kobe, Japan suffered a collapse of ceiling slab and settlement of soil cover by 2.5 m as shown in figure 1.

Though there were various factors that prevented the collapse, which includes adding zig-zag reinforcement in addition to hoop reinforcement in the centre columns that did not buckle in comparison to columns with hoop reinforcement only(2). Also, the transverse walls at the ends act as shear walls and prevented the collapse(3).During Loma-Prieta EQ, structural cracking was observed in the tunnels and due to liquefaction of the surrounding soil, significant leakage was reported within the structure(3). Another example was

observed during Chi-Chi EQ in Taiwan (Japan). Damage to the tunnel portals was due to slope instability, crack penetration, ground-water ingress, and collapse of lining, which leads to closing the entrance of tunnel at Chelungpu fault (figure: 3). One of the extensive damages caused during the 1999 Koceili EQ was the collapse of the twin Bolu tunnel. The left tunnel, which was still under construction during this period, suffered extensive damage (9). The major damage patterns observed were cracks and spalling of concrete lining, which might be due to tunnel crossing the fault.



(a)



(b)

Fig. 1 (a) Collapse of roadway overlying above Daikai subway station, (b) Collapse of central columns during Nyogoken- Nambu earthquake (1995) (3)

On the basis of the cases reported above, O'Rourke et. al. (10) classified the damage criteria of underground structures as:

- Ground shaking criteria
- Ground failure criteria

Ground shaking refers to the deformation produced by the shaking of the soil strata due to seismic waves propagating through it. Ground failure includes the failure of the surrounding soil like liquefaction, slope instability and fault displacement. The major factors influencing the dynamic behaviour of tunnels are tunnel geometry, ground conditions, the depth of the overburden and relative stiffness of the soil-tunnel interface etc., (3,7)(11–15). Most of the studies till now relate the damage criteria of tunnels during an earthquake to ground shaking, and very few have considered the damage due to failure of the ground (8,16,17). Chian and Madabhushi studied the effect of UG structures in liquefiable soil and concluded that lower unit weight of the tunnel structure as compared to the surrounding soil is the reason behind its vulnerability in liquefiable soil (16).

One of the major factors in the failure of the UG structure is the stresses generated in the lining (3,18,19). The past studies have considered the effect of the seismic environment under no-drainage conditions, Bobet analytically studied the effect of stresses induced in the tunnel-lining during an EQ considering the full-drainage and no-drainage conditions at the interface of the ground and the lining (20). Lining and ground were considered linearly elastic and plain-strain conditions were assumed at the cross-section of tunnel. The water table is assumed to be far from the tunnel hole and the effect of tunnel excavation on water table is neglected. To report the effect of water table, he considered 9 cases with different ground and liner stiffness. The results concluded that stresses in the tunnel lining are not affected by drainage conditions at the interface of ground and lining, if ground stresses are applied far from the centre of the tunnel, whereas the maximum stresses in the ground varies drastically. Sadiq et al. and Lu et al. (21,22) related the damage criteria to the flexibility ratio (F), which is defined as the relative stiffness of the structure to the soil. It has been observed that the F of the tunnel majorly influences the surface settlement and the deformation pattern. Stiff tunnels with $F < 1$ show slight bulging at the surface, whereas the flexible tunnels with $F > 1$ produce convex bending of both the roof and the floor slab (21). Singh and Mandal (23) studied the stresses induced in the tunnel considering different interface conditions with coefficient of friction varying as 0, 0.4 and 3, considering the effect of overburden pressure and PGA were analyzed. For validation of the numerical model, the results of collapse of Daikai subway station were considered. With increasing PGA, the axial stresses in the tunnel central column increases for varying coefficient of friction and overburden-depth.

It was observed that axial stresses in tunnels central column were same for coefficient of friction as 0.4 and 3, with overburden depth of 6.34 m and 12.68 m. This is because of increase of inertial forces due to soil-amplification. Various factors considered by the researchers, which could probably affect the seismic behaviour of the UG structures to a greater extent are summarized in table:1. The performance of the tunnels is also affected by the structures present in their vicinity. A large amount of energy is released during the earthquake. This energy is carried by different waves produced during the seismic activity. The behavior of the UG structure is affected when these waves transfer this energy to the tunnel while passing through the tunnel section [18][24].

2.1. EQ Effects on UG Structure

Earthquake leads to the propagation of waves through the volume of the earth and crust, which causes the most damage (3). These waves are further classified as: Surface waves and Body waves. Underground structures are affected by the propagation of body waves, i.e., primary waves and secondary waves. Primary waves (P-waves) are the fastest of seismic waves and move the particles of the soil in the direction of propagation of waves by simultaneous push and pull that leads to alternate compression and tension. Secondary waves (S-waves) shake the particles up, down or side to side perpendicular to the direction of propagation of the wave.

On the basis of deformations, the EQ response of UG structures can be grouped as (6):

- Longitudinal bending
- Axial compression and extension
- Ovaling and Racking

Axial deformations are caused by the components of seismic waves, which produce motion parallel to the tunnel axis and cause alternate compression and tension. Hence it is said to be caused by the P- waves. Bending deformations are generated by the components of the wave propagating perpendicular to the longitudinal axis of the tunnel. Ovaling and racking deformations develop due to shear waves propagating normal to the tunnel axis, thus distorting the cross-sectional shape of the tunnel. figure: 5 describes the deformation patterns generally observed in the tunnel section due to the propagation of seismic waves through it. The characterization of different types of crack patterns observed in various cases can thus be due to different earthquake waves passing through the cross- section of the tunnel. On the basis of the propagating waves, design considerations for bending and axial deformations are provided in the direction parallel to the tunnel axis and in the transverse direction for the racking deformation (3).

2.2. Seismic Analysis of Tunnels

The general method adopted in the seismic analysis of tunnels (12) (figure: 6) is broadly classified as:

- Free-Field Interaction approach (FFI)
- Dynamic Earth pressure approach
- Soil-Structure Interaction approach (SSI)

In FFI approach, the strains produced by a seismic wave propagating through the soil in the absence of the structure or excavation are considered while designing the tunnel, thus ignoring the effects of the interaction between the structure and the soil. A designer can impose these deformations directly on the structure(24,25). Though it is comparatively easy to formulate the results, it provides a conservative value if the structure is stiffer than the Ground and also provides less precise results for structure in variable ground conditions. San-Francisco BART subway station and LA metro were the structures designed with this approach and showed significantly good performance during the Loma Prieta Earthquake (1989) and Northridge Earthquake (1994), respectively.

Another approach used for the analysis of tunnel structures during EQ is the Dynamic Earth Pressure methods, which are based on the assumption that the inertial force of the surrounding soil is one of the criteria leading to its development. Mononobe-Okabe, given by Seed et al.(26) and the Japanese Society of Civil Engineering (27) is the widely used method for finding out the increase in the lateral earth pressure. This method was originally developed for retaining walls and considers that wall would move or tilt sufficiently so that an active earth yield wedge would form behind the wall. But for a UG structure, the structure and the surrounding ground move together, thus making it difficult for the yielding wedge to form. This method gives unrealistic results for the rectangular tunnel structures under plain-strain conditions and results in excessive shear deformations of the tunnel structure as compared to the surrounding soil. This effect becomes more prominent with the increase of depth of embedment because of reduction in deformation of structure and soil. Despite of all its shortcomings, this method is precisely applicable for tunnels with minimal soil-cover thickness.

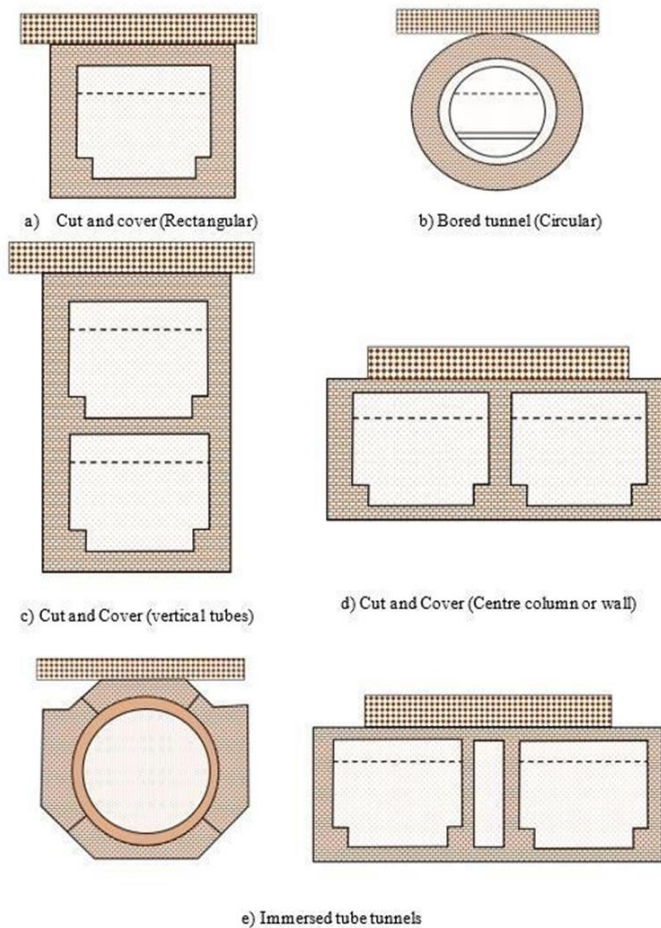


Fig. 2 Possible shapes of tunnels



Fig. 3 Tunnel portal failure due to slope instability after Chi-Chi earthquake(28)

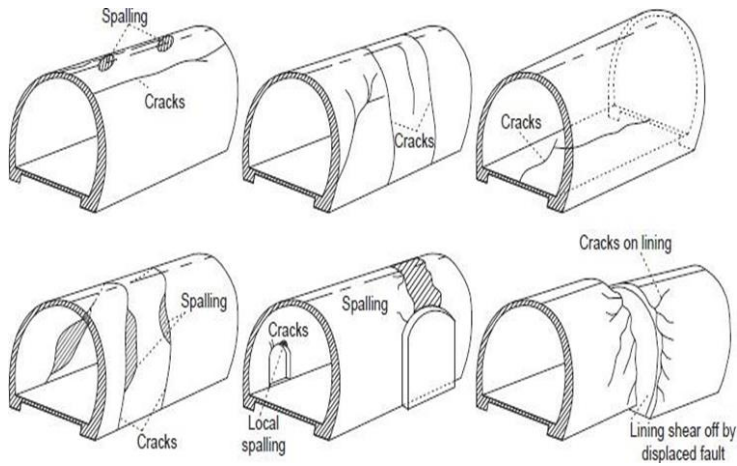


Fig. 4 Crack patterns (11)

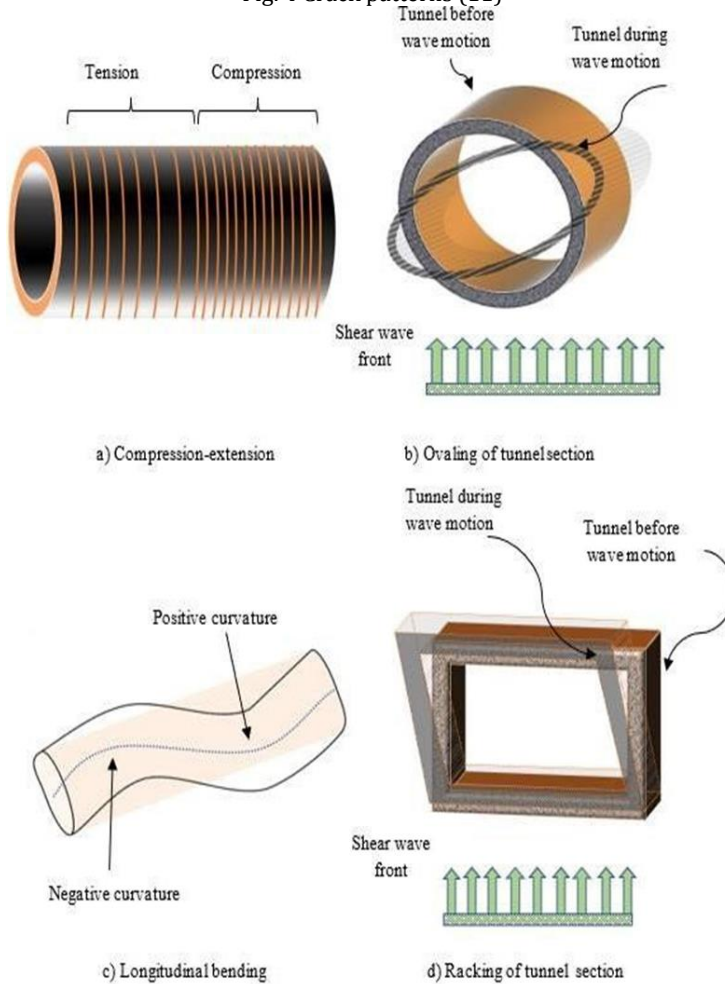


Fig. 5 Various deformation modes of the underground structure subjected to seismic waves (redrawn and modified after (6))

Table 1. Factors influencing the seismic analysis of tunnels

Author	Factors affecting	Parameters considered
(16),(29-33)	Shape and dimensions of the tunnel	
(13-16), (30,31,33,34)	Depth of overburden	
(29,31,33),(35) (12,13), (18,20,29),(30), (36-38) (17,20)	Tunnel lining Tunnel-soil interface Drainage conditions	Soil and structure parameters
(13),(17),(29), (39)	PGA and PGV	
(40,41) (40) (38,39) (40)	Frequency content Earthquake magnitude Intensity of earthquake Duration of earthquake	Seismic and ground motion parameters
(18), (33,34)		Effect of structures in vicinity

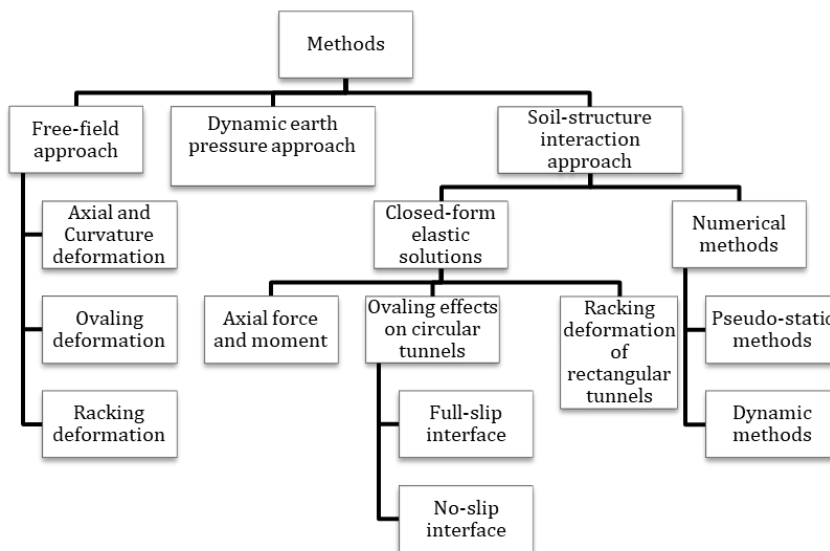


Fig. 6 Flow-chart representing methods of seismic analysis of tunnels

SSI considered the interaction between the structure and the soil, which is the major criteria affecting the seismic behavior of UG structures. Many researchers investigated the soil-structural response by various numerical and closed-form elastic solutions. The methods generally used comprise numerical dynamic analysis (21,42-47) frame-spring models (32,48,49) and subgrade reaction methods used to examine the seismic response of tunnel and the soil interface properties, the results of which can be validated through centrifuge testing.

3. Physical Testing of the EQ Response of Tunnels

3.1 Centrifuge Modelling

The actual behaviour of a tunnel structure can be verified by considering the "scaling effects," which are very difficult to consider fully in the laboratory. Centrifuge test is a reduced scale physical model which can apply the stress level that existed in the field to the prototype model (11). It is a widely used experimental set-up to examine the effects of both ground shaking and ground failure on the tunnel structure. The centrifuge applies an increased "gravitational" acceleration to the prototype model so as to produce stresses that are identical to the actual structure. The one-to-one scaling of stress increases the similarity of geotechnical models and makes it possible to obtain accurate data to help solve complex problems such as earthquake-induced liquefaction, soil-structure interaction etc. The basic mechanism of deformations induced and failure criteria can be well understood from this modeling technique. Further, it provides a useful benchmark for the verification of the numerical models. Earlier studies considered the effect of earth pressure and forces acting on the lining during shear deformation of the Ground to assess the damage induced in the tunnel (18),(35),(50). The later study mainly focused on the effect of vertically propagating transverse shear waves (35,51,52). Shibayama et al.(35) studied the effect of support conditions of tunnel lining on bending moment and axial forces induced during an EQ. For this purpose, he used two types of horse-shoe tunnel models to examine the effect of fixity conditions: for the first model, tunnel lining and invert were firmly fixed by welding, and for the second model, in order to transfer only axial force, the contact was modeled as a plastic hinge (non-welded). For tunnel lining to be rigidly fixed, the bending moment at the end of lining were quite large, whereas for lining to be rotational at the free end, the axial force at the shoulder end were high.

Kutter et al. (53) experimentally tested cut and cover tunnels by centrifuge modeling to understand the uplift mechanism and vulnerability during EQ-induced floatation. This study outlines the base to understanding the uplift behaviour of the tunnel during shaking, which is predominantly caused by the soil moving below the tunnel. The results reported a total uplift of 180 mm, which is verified by a numerical model with an error of 20%. The error could arise due to pore pressure generation, liquefaction and large strains in base course soil etc. Post-shaking uplift was also observed to be found as 30 mm in centrifuge testing and 5 mm with numerical testing. Chian et. al. (16) carries out their investigation on Ground susceptible to liquefaction during an earthquake, thus causing an uplift of the structure due to its lower unit weight as compared to the surrounding Ground. The depth of burial of the structure and its size are the major factors influencing the uplift behaviour of the structure. This could be due to increased resisting forces due to increased vertical earth pressure and inertial forces of the structure which resist the buoyant forces due to liquefied surrounding soil.

Chou et al. (17) continuing the previous research on the uplift performance of the tunnels consolidated the results by providing mechanisms observed during the uplift, i.e., the ratcheting mechanism in which the sand migrates underneath the tunnel with every cycle of relative shaking, pore-water mechanism and bottom-heave mechanism. Though, the fourth mechanism, i.e., viscous flow of liquefied soil, was not observed in these experimental results. Table: 2 provides a summary of the tests carried out by various researchers in the past and shows that very less work has been carried out till now for understanding the behaviour of tunnels in ground failure conditions. Since EQ-induced flotation failure has a great potential for loss of economy and life, methods to reduce its impact must be studied in detail for further study. One way to reduce the impact of flotation failure is the improvement of the ground; Taylor et al. (54) studied the use of coarse-grained granular backfill around the tunnel by replacing areas of liquefiable soil and

observed that ground improvement done below the tunnel was most effective in reducing the uplift of the structure.

Depth, shape, tunnel lining stiffness, nature of input motion and properties of surrounding soil strata affect the behaviour of the tunnel during an earthquake. Dynamic centrifuge experimentally evaluates these factors at different input ground motions with varying frequencies and amplitude. Cilingir et al. (14,40,55) studied the effect of the input motion on the seismic behaviour of both square and circular tunnels, which is influenced mostly by the intensity of the earthquake, peak ground velocity (PGV) and peak ground acceleration (PGA) value and are least influenced by the duration and frequency content. In this study, they experimentally observed three stages of failure: the transient stage, steady-state cyclic stage and residual stage. The tunnel structure reaches a dynamic equilibrium stage in the first few cycles; in the second stage, the earth pressure values get stagnant about a particular value and this oscillating value gets fixed during the third stage when the shaking stops.

Chen et al. (56) discussed various methods proposed for the seismic protection of tunnels. The isolation layer is generally used to protect the tunnels crossing different soil strata as it absorbs the deformations of the Ground that are caused by an EQ and thus, reduces the cross-sectional deformation of the tunnel cross-section, further reducing the dynamic bending moment. Chian and Madabhushi (15) observed that when the shaking of the model was gradually decreased to 40g, there was a decrease in the internal forces, which suggests that due to lowering confining stress, the sand dilates instead of contracting and hence, the lining recovers a part of the accumulated strain.

Chen et al. (56) evaluated the results of the effect of the presence of an isolation layer for a frequency of 50 Hz, and as shown in figure: 7, the dynamic bending moment at corners are much larger than those at other location and therefore, the corners of a rectangular tunnel are to be designed with proper seismic considerations. Presence of isolation layer reduces the moments at the corners, thus providing structural safety under seismic loading. The rectangular tunnel structure is more profound to show a rocking-racking deformation behaviour under transversal Ground shaking. This combined behaviour was verified by various centrifuge tests, in which a rigid tunnel is subjected to more rocking deformation with reduced racking, whereas flexible tunnels show prominent racking values and less rocking deformations. Since, racking deformation amplifies with flexibility of the structure, flexible tunnels are more prone to racking failure than rocking failure. Tsiniadis et al. (30) verified these results by conducting a centrifuge test on rectangular tunnel structures and the results have been evaluated in terms of the relative flexibility of soil-tunnel and soil-structure interface properties. Table 3 gives the values of the dynamic bending moment for rigid and flexible tunnel structures, and it has been observed that dynamic bending moment values are higher for rigid tunnels as compared to flexible tunnels.

Till now, most of the tests examined the behaviour of the underground structures without considering the structures in the vicinity. But ideally, the presence of other structures in their vicinity also influences their behaviour during an earthquake. Though very few studies have been carried out recently and are still undergoing investigation of the effects of nearby structures (could be another tunnel, above-ground structures like buildings etc.). Gillis et al.(18,57) studied the effect of the presence of temporary and permanent structures in the vicinity of a mid to high-rise building and study the effect in terms of inertial force of tall buildings, added confinement of the building and constraints added on the foundation. The added confinement by high-rise structures reduces the racking deformation of the structure but also, increases the lateral earth pressure. Particularly, they examined the results of seismic environment on isolated cut and cover structures, temporary excavation and the presence of mid to high-rise buildings in its locality. Hashash

et al. (58), using centrifuge modeling, implied that interaction between the building and the tunnel can majorly influence the seismic behaviour of cut and cover tunnels.

Various observations from centrifuge modeling give extremely useful results in examining the behaviour of tunnel structures, but there is certain limitation this method portrays in modeling minor details of the section and special components like joints between different segments of the lining. Further, to model the lining of the tunnel, the material used is often aluminium which poses the effect on the recorded response.

3.2 Shake Table Test (STT)

STT was invented in 1893 by the University of Tokyo and had a major application for the seismic analysis of above-ground structures. But for a few decades, it has been significantly used for the UG structures. It may be used as an alternative to the centrifuge test with the advantage of modeling much larger models in size and the use of more realistic materials for the tunnel lining. The shortcomings of plain concrete that need special attention are its low tensile strength and brittle behavior (59). To overcome this, various material has been proposed as the tunnel lining like rubber sheet lining (13), plexiglass (22), polypropylene fibre reinforced concrete (59), ultra-high-performance fibre reinforced concrete (60), using gypsum and water slurry (61), concrete lining (62), steel reinforced concrete lining, organic glass (63) and steel fiber concrete and steel-basalt fiber reinforced concrete lining (64).

Various tests have been carried out on decoding the parameters influencing the EQ response of the tunnel structures in different soil conditions. But very few studies have been carried out to investigate its behaviour into two different stratum. Liang et al. (62) proposed a similitude-ratio method to analyze the behaviour of circular tunnels under soft-hard soil stratum with a shake table test. This test is depended on the size of the laminar shear box, performance parameters of the shake-table, and the material characteristics of the model tunnel. The tunnel strain around the soft-hard interface increases significantly, which could be due to a change of relative stiffness at the junction of the soft-hard medium. Because of the different dynamic characteristics of the structures, the behavior of seismic waves will be different and thus, at the point of intersection the coherence between these waves decides the seismic performance of the tunnel. Zhang et al. (67) analyzed the behaviour of shaft-tunnel junction showing discrepant responses causing the bending deformation of the tunnel axis and enlargement of the strains at the junction. These additional strains are generally imposed on the shafts. Also, at the junction of the shaft and the tunnel, the longitudinal circumferential-joint extensions and the transverse dynamic strains are raised. This observation constitutes additional evidence of the damage to the tunnel.

Consideration of the uniform wave excitation has been carried out so far to analyze the behaviour of the tunnel, but Chen et al. (13) carried out the first STT on the tunnel under non-uniform excitation to examine the performance of rectangular tunnel with and without construction joints. The actual behaviour of the tunnel is very difficult to account for in the laboratory due to the "scale effects" (11). Though centrifuge modeling provides a compatible way to model scale effects; but, due to its limitation of modeling structures with larger dimensions because of size limitations, it is necessary to consider the issue for further investigation. Using a synthetic soil model (i.e., a mixture of sand and saw-dust) has been found to be a remedy to the scaling issues (68).

The isolation layer provides one of the effective methods used for reducing the dynamic earth pressure effects on the lining. It minimizes the intensity of seismic action and reduces the deformation transferred from ground to the tunnel lining (42). Xu et al. (61) using a shake table test, investigated the effect of using geof foam as a seismic isolation layer

between the rock and the tunnel lining. The results interpreted show that installation of a geofoam isolation layer reduces the dynamic earth pressure by 70-90% in comparison to cases without an isolation layer. The effects of reinforcing the rock with anchors, adding of steel wire mesh layer in the lining and provision of flexible joints in the tunnel lining were some other areas of research investigated in this study. Results revealed that provision of anchor reinforcement reduces the dynamic strain in the lining by 50 % to 60 %, as compared to non-anchored structure. These methods were found effective in dissipating the earthquake energy and thus, reduces the dynamic strain in the tunnel.


Table 2. Summary of experimental test results

Method	Author	Cross-section of tunnel			Ground Shaking	Ground Failure	Racking /Ovaling deformation	Rocking deformation	Uplift displacement/Floatation
		Rectangular	Circular	Other					
Dynamic Centrifuge test	(53)	✓				✓	✓		
	(17)	✓				✓			✓
	(40)	✓	✓		✓		✓		
	(16)		✓			✓	✓		✓
	(15)		✓				✓		
	(38,65)	✓					✓	✓	
	(18)	✓					✓		
	(66)	✓					✓		
Shake Table test	(41)	✓					✓		
	(34)	✓					✓		
	(67)		✓				✓		
	(68)	✓					✓		
	(54)			✓		✓			✓
	(69)			✓			✓		
	(70)		✓			✓			✓
(71)			✓			✓			

Some studies have contributed to study the effect of tunnels in liquefiable ground using shake-table testing (70,72), crossing faults (73)(74), effect of flexibility ratio (22) . Tsinidis et al. studies the effect of heavy buildings on the response of single or twin circular tunnels in the urban environment and signifies that the number of single-degree-of-freedom of the building and their position relative to an axis of tunnel majorly affects the seismic performance of the tunnel structure (34). Singh et. al.(75) studied the seismic behavior of tunnels damaged during aftershocks and concluded that damaged tunnels are more

vulnerable to low-frequency earthquake motion. The effect of after-shocks on damage characteristics of tunnels is still required to be studied in detail. One of the limitations of the shake table test was a little study on the similitude laws to study the post-cracking behaviour of the tunnel lining (69). Antoniou et al. (69) proposed scaling laws for the 1 g shake table test, simulating the post-cracking phase of lightly reinforced concrete lining found in rock, but still, much work has to be done on this. Increased scaling laws allow for investigating the urban conditions more easily and precisely in comparison to centrifuge tests. But this 1-g test is performed at confining stress much lower than in the field; therefore, there is a difference in the recorded response and the actual one; thus, the actual condition in the field is not accurately represented. Shake table tests are, therefore, of less importance for verification and validation of the numerical and analytical methods.

Table 3. Effect of the soil-tunnel interface properties and soil non-linear response on the dynamic lining bending moment (N-mm/mm) (38)

Considered points	Flexible-elastic		Flexible-elastoplastic		Rigid-elastic		Rigid-elastoplastic	
	D	C	No-slip	Full-slip	No-slip	Full-slip	No-slip	Full-slip
								
A	-4.871	-2.367	-6.294	-2.282	-10.946	-3.564	-6.27	-2.203
B	6.54	3.303	4.268	0.45	11.481	3.117	10.10	0.426
C	-5.524	-3.772	-5.235	0.154	-10.88	-3.974	-7.568	-1.757
D	5.596	4.358	4.084	-0.366	12.307	4.371	8.973	1.135
A	-4.784	-2.936	-3.563	0.403	-10.759	-3.859	-8.336	-1.243

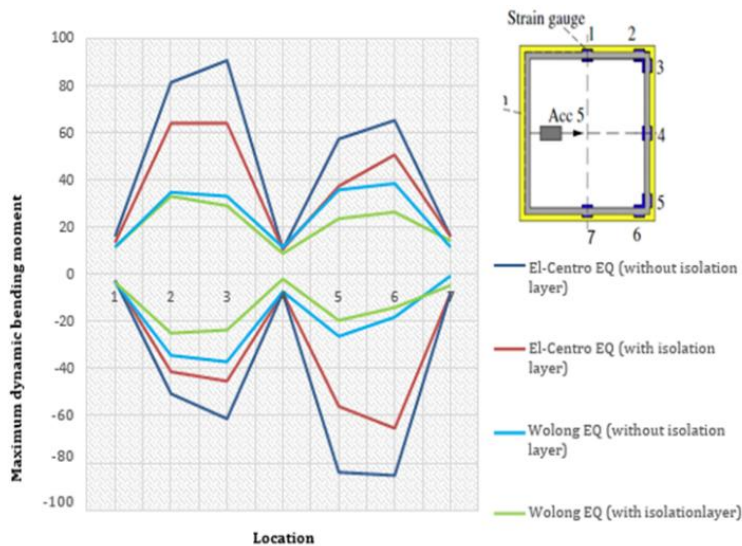


Fig. 7 Impact of isolation layer on Dynamic Bending Moment (56)

3. Conclusions and Recommendations

With the detailed study of the seismic environment on the performance characteristics of tunnels, the following conclusions can be made regarding their experimental testing:

- Major contributors to seismic response in tunnels are PGA, PGV, EQ intensity, shape and cross-section of the tunnel, interface properties and presence of another structure.
- Monobe-Okabe method does not give realistic values for rectangular tunnels and proposes much higher racking values in comparison to the encircling soil. Still, this method is suitable for tunnels with minimum soil cover.
- Corners of a rectangular tunnel develop maximum values of bending moment during an EQ, so joints should be designed with precision, but the presence of an isolation layer helps in reducing these values to some extent.
- Stiff rectangular tunnels tend to show bulging at the surface during deformation, whereas flexible tunnels show convex bending of both roof and floor slabs.
- Tunnels subjected to an environment with multi-stiffness characteristics (for example, the presence of structures in the surrounding or tunnel passing through soil with varying stiffness) show an increase in strain values at the joints. This could be due to the coherence between the waves propagating through different media.
- Centrifuge test, due to its inability to model buildings with high-fundamental frequency, resulted in studying the limited factors for structures in the vicinity of tunnels, whereas STT provides an easier way to model the structure at a larger scale but is of less importance to validation of numerical models.

This paper presented a brief review of the current approaches to experimentally understand the behaviour and performance of tunnels under an EQ. Based on it, further work that needs to be considered are:

- Experimental tests studied considers the uni-directional horizontal ground motions, but in the actual scenario, the motions are three-dimensional. So, instrumentation of tunnels under three-dimensional shaking conditions in order to measure both lateral and vertical response of the structure must be evaluated.
- The performance of tunnels has been evaluated for the simplistic soil conditions. Few recent studies have considered different soil-strata conditions and the effect of varying stiffness of the surrounding soil, but still, a detailed study to investigate the effect of non-linearity of soil on EQ performance of tunnels needs to be studied.
- The inelastic response of the tunnel lining needs to be considered for further work.
- The old tunnels are prone to the aging effects of lining, which affects their performance during seismic response. In order to develop cost-efficient retrofitting techniques and studying the residual life of existing old tunnels, further work needs to be carried out.
- Study of the influence of different isolation material in reducing the bending moment induced in a tunnel so as to maintain its structural integrity should be evaluated, in order to have a cost-efficient material for practical application.

References

- [1] Tunnel Market Survey [Internet]. 2019. Available from: <https://mtry.fi/tunnel-market-survey-2019-ita-aites/>

- [2] Iida Hiroomi, Hiroto Toshio, Yoshida Nozomu, Iwafuji Masahiko. Damage to Daikai subway station. Soils Found. 1996 Jan;283-300. https://doi.org/10.3208/sandf.36.Special_283
- [3] Hashash YMA, Hook JJ, Schmidt B, Yao JI-C. Seismic design and analysis of underground structures. Tunn Undergr Sp Technol. 2001;16:247-93. [https://doi.org/10.1016/S0886-7798\(01\)00051-7](https://doi.org/10.1016/S0886-7798(01)00051-7)
- [4] Yu H, Chen J, Bobet A, Yuan Y. Damage observation and assessment of the Longxi tunnel during the Wenchuan earthquake. Tunn Undergr Sp Technol. 2016 Apr 1;54:102-16. <https://doi.org/10.1016/j.tust.2016.02.008>
- [5] Dowding CH, Rozen A. Damage to rock tunnels from earthquake shaking. J Geotech Eng Div. 1978;104:175-91. <https://doi.org/10.1061/AJGEB6.0000580>
- [6] Owen G.N., Scholl R.E. Earthquake engineering of large underground structures. Washington, D.C.; 1981 Jan.
- [7] Sharma S.W.R., Judd W R. Underground opening damage from earthquakes. Eng Geol. 1991;30:263-76. [https://doi.org/10.1016/0013-7952\(91\)90063-Q](https://doi.org/10.1016/0013-7952(91)90063-Q)
- [8] Power M.S., Rosidi D., Kaneshiro J.Y. Seismic vulnerability of tunnels and underground structures revisited. In: Proceedings of North American Tunneling '98. Newport Beach, CA, Balkema Rotterdam.; 1998. p. 243-50.
- [9] Jaramillo CA. Impact of seismic design on tunnels in rock - case histories. Vol. 2, Underground Space (China). Tongji University; 2017. p. 106-14. <https://doi.org/10.1016/j.undsp.2017.03.004>
- [10] O'Rourke, M.J., Liu X. Response of buried pipelines subjected to earthquake effect. 1999.
- [11] Tsinidis G, de Silva F, Anastasopoulos I, Bilotta E. Seismic behaviour of tunnels: From experiments to analysis. Tunn Undergr Sp Technol. 2020 May 1;99. <https://doi.org/10.1016/j.tust.2020.103334>
- [12] Wang J. Seismic Design of Tunnels A Simple State-of-the-Art Design Approach. New York; 1993 Jun.
- [13] Chen J, Shi X, Li J. Shaking table test of utility tunnel under non-uniform earthquake wave excitation. Soil Dyn Earthq Eng. 2010 Nov;1400-16. <https://doi.org/10.1016/j.soildyn.2010.06.014>
- [14] Cilingir U, Madabhushi SPG. Effect of depth on the seismic response of square tunnels. Soils Found. 2011 Jun;449-57. <https://doi.org/10.3208/sandf.51.449>
- [15] Lanzano G, Bilotta E, Russo G, Silvestri F, Madabhushi SPG. Centrifuge modeling of seismic loading on tunnels in sand. Geotech Test J. 2012 Nov;35(6). <https://doi.org/10.1520/GT104348>
- [16] Chian SC, Madabhushi SPG. Effect of buried depth and diameter on uplift of underground structures in liquefied soils. Soil Dyn Earthq Eng. 2012 Oct;41:181-90. <https://doi.org/10.1016/j.soildyn.2012.05.020>
- [17] Chou JC, Kutter BL, Travararou T, Chacko JM. Centrifuge modeling of seismically induced uplift for the BART transbay Tube. J Geotech Geoenvironmental Eng. 2011 Aug;754-65. [https://doi.org/10.1061/\(ASCE\)GT.1943-5606.0000489](https://doi.org/10.1061/(ASCE)GT.1943-5606.0000489)
- [18] K.M. Gillis, S. Dasht, Y.M.A. Hashash, M.I. Romero Arduz. Seismic Response of a Cut-and-Cover Underground Structure in Dry Sand: Centrifuge Modeling. In: e 8th International Conference on Physical Modeling in Geotechnics., Perth, Australia.; 2014.
- [19] Penzien J, Wu CL. Stresses in linings of bored tunnels. 1998;27(August 1996):283-300. [https://doi.org/10.1002/\(SICI\)1096-9845\(199803\)27:3<283::AID-EQE732>3.0.CO;2-T](https://doi.org/10.1002/(SICI)1096-9845(199803)27:3<283::AID-EQE732>3.0.CO;2-T)
- [20] Bobet A. Effect of pore water pressure on tunnel support during static and seismic loading. Tunn Undergr Sp Technol. 2003;18:377-93. [https://doi.org/10.1016/S0886-7798\(03\)00008-7](https://doi.org/10.1016/S0886-7798(03)00008-7)

- [21] Sadiq S, Van Nguyen Q, Jung H, Park D. Effect of flexibility ratio on seismic response of cut-and-cover box tunnel. *Adv Civ Eng.* 2019;2019. <https://doi.org/10.1155/2019/4905329>
- [22] Lu S, Xu H, Wang L, Liu S, Zhao D, Nie W. Effect of flexibility ratio on seismic response of rectangular tunnels in sand: Experimental and numerical investigation. *Soil Dyn Earthq Eng.* 2022 Jun 1;157. <https://doi.org/10.1016/j.soildyn.2022.107256>
- [23] Singh DK, Mandal A. Dynamic Effect of Soil-Tunnel Interface Under Dynamic Loading. *Soil Mech Found Eng.* 2019;56(2):91-7. <https://doi.org/10.1007/s11204-019-09575-w>
- [24] Sanchez-Jimenez JL. Free-field racking deformation methodology applied to the design of shallow tunnel structures in high risk seismic areas. Practical considerations. In: Tenth US, National Conference of Earthquake Engineering. Anchorage, Alaska; 2014.
- [25] Wood JH. Seismic Analysis of a UG Structure by JH Wood - Shortcut.
- [26] Seed HB, Whitman R V. Design of earth retaining structures for dynamic loads. In: ASCE Specialty Conference on Lateral Stresses in the Ground and the Design of Earth Retaining Structures. Ithaca, New York; 1970. p. 103-47.
- [27] Japanese Society of Civil Engineers. Specifications for Earthquake Resistant Design of Submerged Tunnels. 1975.
- [28] Sun W, Yan S, Ma Q, Liang Q. Dynamic response characteristics and failure mode of a bias loess tunnel using a shaking table model test. *Transp Geotech.* 2021 Nov 1;31. <https://doi.org/10.1016/j.trgeo.2021.100659>
- [29] Abdel-Motaa MA, El-Nahas FM, Khiry AT. Mutual seismic interaction between tunnels and the surrounding granular soil. *HBRC J.* 2014 Dec;10:265-78. <https://doi.org/10.1016/j.hbrcj.2013.12.006>
- [30] Tsinidis G. Response characteristics of rectangular tunnels in soft soil subjected to transversal ground shaking. *Tunn Undergr Sp Technol.* 2017 Feb 1;62:1-22. <https://doi.org/10.1016/j.tust.2016.11.003>
- [31] Fakhriyeh H, Vahdani R, Gerami M. Seismic acceleration spectrum of ground surface under urban subway tunnels with circular cross sections in soil deposits based on SSI. *Shock Vib.* 2019;2019. <https://doi.org/10.1155/2019/2076961>
- [32] Nguyen DD, Lee TH, Nguyen VQ, Park D. Seismic damage analysis of box metro tunnels accounting for aspect ratio and shear failure. *Appl Sci.* 2019 Aug 1;9(16). <https://doi.org/10.3390/app9163207>
- [33] Naseem A, Kashif M, Iqbal N, Schotte K, De Backer H. Seismic behavior of triple tunnel complex in soft soil subjected to transverse shaking. *Appl Sci.* 2020 Jan 1;10(1). <https://doi.org/10.3390/app10010334>
- [34] Tsinidis G. Response of urban single and twin circular tunnels subjected to transversal ground seismic shaking. *Tunn Undergr Sp Technol.* 2018 Jun 1;76:177-93. <https://doi.org/10.1016/j.tust.2018.03.016>
- [35] Shibayama S, Izawa J, Takahashi A, Takemura J, Kusakabe O. Observed behaviour of a tunnel in sand subjected to shear deformation in a centrifuge. *Soils Found.* 2010 Apr;281-94. <https://doi.org/10.3208/sandf.50.281>
- [36] Penzien J. Seismically induced racking of tunnel linings. *Earthq Eng Struct Dyn.* 2000;29:683-91. [https://doi.org/10.1002/\(SICI\)1096-9845\(200005\)29:5<683::AID-EQE932>3.0.CO;2-1](https://doi.org/10.1002/(SICI)1096-9845(200005)29:5<683::AID-EQE932>3.0.CO;2-1)
- [37] Ertuğrul N. Analysis of seismic behaviour of underground structures: A case study on bolu tunnels. 2010.
- [38] Tsinidis G, Rovithis E, Pitilakis K, Chazelas J-L. Seismic Response of Rectangular Tunnels by Centrifuge Testing and Numerical Analysis. 2015; Available from: http://www.series.upatras.gr/DRESBUS_II https://doi.org/10.1007/978-3-319-10136-1_30

- [39] Chen J, Jiang L, Li J, Shi X. Numerical simulation of shaking table test on utility tunnel under non-uniform earthquake excitation. *Tunn Undergr Sp Technol.* 2012 Jul;30:205-16. <https://doi.org/10.1016/j.tust.2012.02.023>
- [40] Cilingir U, Gopal Madabhushi SP. A model study on the effects of input motion on the seismic behaviour of tunnels. *Soil Dyn Earthq Eng.* 2011 Mar;31:452-62. <https://doi.org/10.1016/j.soildyn.2010.10.004>
- [41] Hassanzadeh M, Bonab MH, Javadi AA. Experimental and numerical study of the behaviour of shallow rectangular tunnels. *J Vibroengineering.* 2018 Jun 1;20:1783-96. <https://doi.org/10.21595/jve.2018.19308>
- [42] Anato NJ, Assogba OC, Tang A, Youssouf D. Numerical Investigation of Seismic Isolation Layer Performance for Tunnel Lining in Shanghai Soft Ground. *Arab J Sci Eng.* 2021 Nov 1;46(11):11355-72. <https://doi.org/10.1007/s13369-021-05683-8>
- [43] Aygar EB, Gokceoglu C. A special support design for a large-span tunnel crossing an active fault (T9 Tunnel, Ankara-Sivas High-Speed Railway Project, Turkey). *Environ Earth Sci.* 2021 Jan 1;80(1). <https://doi.org/10.1007/s12665-020-09328-1>
- [44] Shao S, Shao S, Li J, Qiu B. An Analysis of Loess Tunnel Failure and Its Mechanism. *Adv Civ Eng.* 2021;2021. <https://doi.org/10.1155/2021/6671666>
- [45] Zheng G, Yang P, Zhou H, Zhang W, Zhang T, Ma S. Numerical Modeling of the Seismically Induced Uplift Behavior of Twin Tunnels. *Int J Geomech.* 2021 Jan;21(1). [https://doi.org/10.1061/\(ASCE\)GM.1943-5622.0001897](https://doi.org/10.1061/(ASCE)GM.1943-5622.0001897)
- [46] Choudhury D, Patil M, Ranjith PG, Zhao J. Dynamic Tunnel-Soil Interaction in Soft Soils Considering Site-Specific Seismic Ground Response. In 2019. p. 249-71. https://doi.org/10.1007/978-981-13-5871-5_12
- [47] Lu Q, Chen S, Chang Y, He C. Comparison between numerical and analytical analysis on the dynamic behavior of circular tunnels. *Earth Sci Res J.* 2018 Jun 1;22(2):119-28. <https://doi.org/10.15446/esrj.v22n2.72248>
- [48] Pitolakis K, Tsinidis G. Performance and seismic design of underground structures. Vol. 28, *Geotechnical, Geological and Earthquake Engineering.* 2014. p. 279-340. https://doi.org/10.1007/978-3-319-03182-8_11
- [49] Zlatanović E, Šešov V, Lukić D, Prokić A, Trajković-Milenković M. Tunnel-ground interaction analysis: Discrete beam-spring vs. continuous model. *Teh Vjesn.* 2017;24:61-9. <https://doi.org/10.17559/TV-20141001181339>
- [50] Lanzano G. Physical and analytical modelling of tunnels under dynamic loadings.
- [51] Yamada T, Nagatani H, Igarashi H, Takahashi A. Centrifuge model tests on circular and rectangular tunnels subjected to large earthquake-induced deformation. In: *Proceedings of the third symposium on geotechnical aspects of underground construction in soft ground.* Netherland: Taylor and Francis; 2002. p. 673-8.
- [52] Abuhajar O, El Naggar H, Newson T. Experimental and numerical investigations of the effect of buried box culverts on earthquake excitation. *Soil Dyn Earthq Eng.* 2015;130-48. <https://doi.org/10.1016/j.soildyn.2015.07.015>
- [53] Kutter BL, Asce M, Chou J-C, Asce SM, Travararou T, Asce AM. Centrifuge testing of the seismic performance of a submerged cut-and-cover tunnel in liquefiable soil. In: *Fourth Geotechnical Earthquake Engineering and Soil Dynamics Conference.* Sacramento, USA; 2008. [https://doi.org/10.1061/40975\(318\)204](https://doi.org/10.1061/40975(318)204)
- [54] Taylor EJ, Madabhushi SPG. Remediation of liquefaction-induced floatation of non-circular tunnels. *Tunn Undergr Sp Technol.* 2020 Apr 1;98. <https://doi.org/10.1016/j.tust.2020.103301>
- [55] Cilingir U, Madabhushi SPG. Effect of depth on seismic response of circular tunnels. *Can Geotech J.* 2011 Jan;117-27. <https://doi.org/10.1139/T10-047>
- [56] Chen ZY, Shen H. Dynamic centrifuge tests on isolation mechanism of tunnels subjected to seismic shaking. *Tunn Undergr Sp Technol.* 2014 May;42:67-77. <https://doi.org/10.1016/j.tust.2014.02.005>

- [57] Gillis KM. Seismic response of shallow underground structures in dense urban environments[Internet].2015.Availablefrom:https://scholar.colorado.edu/cven_grad_etdshttps://scholar.colorado.edu/cven_gradetds/184
- [58] Hashash YMA, Dashti S, Musgrove M, Gillis K, Walker M, Ellison K, et al. Influence of tall buildings on seismic response of shallow underground structures. *J Geotech Geoenvironmental Eng.* 2018 Dec;144(12):04018097. [https://doi.org/10.1061/\(ASCE\)GT.1943-5606.0001963](https://doi.org/10.1061/(ASCE)GT.1943-5606.0001963)
- [59] Xin CL, Wang ZZ, Zhou JM, Gao B. Shaking table tests on seismic behavior of polypropylene fiber reinforced concrete tunnel lining. *Tunn Undergr Sp Technol.* 2019 Jun 1;88:1-15. <https://doi.org/10.1016/j.tust.2019.02.019>
- [60] Nehdi ML, Abbas S, Soliman AM. Exploratory study of ultra-high performance fiber reinforced concrete tunnel lining segments with varying steel fiber lengths and dosages. *Eng Struct.* 2015;101:733-42. <https://doi.org/10.1016/j.engstruct.2015.07.012>
- [61] Xu H, Li T, Xia L, Zhao JX, Wang D. Shaking table tests on seismic measures of a model mountain tunnel. *Tunn Undergr Sp Technol.* 2016 Nov 1;60:197-209. <https://doi.org/10.1016/j.tust.2016.09.004>
- [62] Liang J, Xu A, Ba Z, Chen R, Zhang W, Liu M. Shaking table test and numerical simulation on ultra-large diameter shield tunnel passing through soft-hard stratum. *Soil Dyn Earthq Eng.* 2021 Aug 1;147. <https://doi.org/10.1016/j.soildyn.2021.106790>
- [63] Wang G, Yuan M, Miao Y, Wu J, Wang Y. Experimental study on seismic response of underground tunnel-soil-surface structure interaction system. *Tunn Undergr Sp Technol.* 2018 Jun 1;76:145-59. <https://doi.org/10.1016/j.tust.2018.03.015>
- [64] An D, Chen Z. Research on Seismic Performance of Fiber Concrete Lining Structure of Urban Shallow-Buried Rectangular Tunnel in Strong Earthquake Area. 2021;25:2748-57. <https://doi.org/10.1007/s12205-021-1721-2>
- [65] Tsinidis G, Heron C, Pitilakis K, Madabhushi G. Physical modeling for the evaluation of the seismic behavior of square tunnels. In: *Geotechnical, Geological and Earthquake Engineering.* Kluwer Academic Publishers; 2014. p. 389-406. https://doi.org/10.1007/978-3-319-00458-7_22
- [66] Chen Z, Bian M. Dynamic Centrifuge Test and Numerical Modelling of the Seismic Response of the Tunnel in Cohesive Soil Foundation. *Buildings.* 2022 Mar 1;12(3). <https://doi.org/10.3390/buildings12030337>
- [67] Zhang J, Yuan Y, Yu H. Shaking table tests on discrepant responses of shaft-tunnel junction in soft soil under transverse excitations. *Soil Dyn Earthq Eng.* 2019 May 1;120:345-59. <https://doi.org/10.1016/j.soildyn.2019.02.013>
- [68] Wu W, Ge S, Yuan Y, Ding W, Anastasopoulos I. Seismic response of subway station in soft soil: Shaking table testing versus numerical analysis. *Tunn Undergr Sp Technol.* 2020 Jun 1;100. <https://doi.org/10.1016/j.tust.2020.103389>
- [69] Antoniou M, Nikitas N, Anastasopoulos I, Fuentes R. Scaling laws for shaking table testing of reinforced concrete tunnels accounting for post-cracking lining response. *Tunn Undergr Sp Technol.* 2020 Jul 1;101. <https://doi.org/10.1016/j.tust.2020.103353>
- [70] Yue F, Liu B, Zhu B, Jiang X, Chen L, Liao K. Shaking table test and numerical simulation on seismic performance of prefabricated corrugated steel utility tunnels on liquefiable ground. *Soil Dyn Earthq Eng.* 2021 Feb 1;141. <https://doi.org/10.1016/j.soildyn.2020.106527>
- [71] Xu C, Jiang Z, Du X, Zhong Z, Shen Y. Seismic displacement and deformation analyses of a precast horseshoe segmental tunnel. *Tunn Undergr Sp Technol.* 2022 Jun 1;124. <https://doi.org/10.1016/j.tust.2022.104476>
- [72] Haiyang Z, Xu W, Yu M, Erlei Y, Su C, Bin R, et al. Seismic responses of a subway station and tunnel in a slightly inclined liquefiable ground through shaking table test. *Soil Dyn Earthq Eng.* 2019 Jan 1;116:371-85. <https://doi.org/10.1016/j.soildyn.2018.09.051>

- [73] Shen YS, Wang ZZ, Yu J, Zhang X, Gao B. Shaking table test on flexible joints of mountain tunnels passing through normal fault. *Tunn Undergr Sp Technol*. 2020 Apr 1;98. <https://doi.org/10.1016/j.tust.2020.103299>
- [74] Zhao X, Li R, Yuan Y, Yu H, Zhao M, Huang J. Shaking table tests on fault-crossing tunnels and aseismic effect of grouting. *Tunn Undergr Sp Technol*. 2022 Jul 1;125. <https://doi.org/10.1016/j.tust.2022.104511>
- [75] Singh DK, Mandal A, Karumanchi SR, Murmu A, Sivakumar N. Seismic behaviour of damaged tunnel during after shock. *Eng Fail Anal [Internet]*.2018;93(March):44-54. <https://doi.org/10.1016/j.engfailanal.2018.06.028>

Research on

Structures



Engineering

Materials

Scopus®



ULAKBİM



Open Academic Journals Index



ASOS indeks



ROOTINDEXING JOURNAL ABSTRACTING AND INDEXING SERVICE



Research Group

